NUREG/CR—4805 (1 of 2)
SAND86—2752 (1 of 2)
R3, R5, R7
Printed May 1987

8024

Reactor Safety Research Semiannual Report January – June 1986 Volume 35

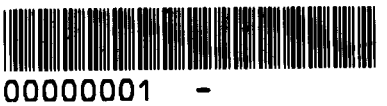

Reactor Safety Research Department 6420

Prepared by
Sandia National Laboratories
Albuquerque, New Mexico 87185 and Livermore, California 94550
for the United States Department of Energy
under Contract DE-AC04-76DP00789

Prepared for
U. S. NUCLEAR REGULATORY COMMISSION

Available from

Superintendent of Documents
U.S. Government Printing Office
Post Office Box 37082
Washington, D.C. 20013-7082

and

National Technical Information Service
Springfield, VA 22161

NUREG/CR-4805 (1 of 2)
SAND86-2752 (1 of 2)
Vol. 35
R3, R5, and R7

REACTOR SAFETY RESEARCH SEMIANNUAL REPORT
January-June 1986

Reactor Safety Research Program

Printed May 1987

APPROVED:

Jack V. Walker
Manager, Reactor Safety Research

David J. McLoskey
Director, Nuclear Regulatory Research

Sandia National Laboratories
Albuquerque, NM 87185
Operated by
Sandia Corporation
for the
U.S. Department of Energy

Prepared for
Division of Accident Evaluation
Office of Nuclear Regulatory Research
U.S. Nuclear Regulatory Commission
Washington, DC 20555
Under Memorandum of Understanding DOE 40-550-75
NRC FINs (A1016, A1019, A1030, D1124, A1181, A1218,
A1227, A1246, A1263, A1264, A1335, A1336,
A1340, A1342, A1383, A1385, A1390)

FORWARD

Sandia National Laboratories is conducting, under USNRC sponsorship, phenomenological research related to the safety of commercial nuclear power reactors. The research includes experiments to simulate the phenomenology of accident conditions and the development of analytical models, verified by experiment, which can be used to predict reactor and saftey systems performance behavior under abnormal conditions. The objective of this work is to provide NRC requisite data bases and analytical methods to (1) identify and define safety issues, (2) understand the progression of risk-significant accident sequences, and (3) conduct safety assessments. The collective NRC-sponsored effort at Sandia National Laboratories is directed at enhancing the technology base supporting licensing decisions.

CONTENTS

CONTENTS (Continued)

CONTENTS (Continued)

CONTENTS (Concluded)

LIST OF FIGURES

LIST OF FIGURES (Continued)

LIST OF FIGURES (Continued)

LIST OF FIGURES (Continued)

LIST OF FIGURES (Continued)

LIST OF FIGURES (Continued)

LIST OF FIGURES (Continued)

LIST OF FIGURES (Continued)

LIST OF FIGURES (Continued)

LIST OF FIGURES (Continued)

LIST OF FIGURES (Continued)

LIST OF FIGURES (Concluded)

LIST OF TABLES

LIST OF TABLES

NOMENCLATURE

ACRR	- Annular Core Research Reactor
AICC	- Adiabatic Isochoric Complete Combustion
APS	- Aerodynamic Particle Sizer
BCL	- Battelle Columbus Laboratories
BNL	- Brookhaven National Laboratories
BWR	- Boiling Water Reactor
CEA	- Commisariat a L'Energie Atomique
CDA	- Core Disruptive Accident
CMCI	- Core Melt-Coolant Interaction
CMOT	- Clad Motion Code
CORCON	- Core/Concrete Interaction Code
DCC	- Degraded Core Coolability
DC	- Dry Capsule
DF	- Damaged Fuel
DFR	- Debris Formation and Relocation
ECCS	- Emergency Core Cooling System
EOEC	- End of Equilibrium Core
EURATOM	- European Atomic Energy Community
EXO-FITS	- Outside of Fully Instrumented Test Sites
FCI	- Fuel-Coolant Interaction
FITS	- Fully Instrumented Test Sites
FLAME	- Flame Acceleration Measurements and Experiments
FRG	- Federal Republic of Germany
FPRF	- Fission Product Reaction Facility
HCDA	- Hypothetical Core Disruptive Accident
HDT	- Heated Detonation Tube
HECTR	- Hydrogen Even Containment Transient Response
HEDL	- Hanford Engineering Development Laboratory
HIPS	- High-Pressure Melt Ejection and Direct Containment Heating
HPIS	- High-Pressure Injection System
IDCOR	- Industry Degraded Core Rulemaking
IFCI	- Integrated Fuel Coolant Interaction
INPO	- Institute of Nuclear Power Operation
IRIS	- Inductive Ring Susceptor Technique
KfK	- Kernforschungszentrum Karlsruhe
LANL	- Los Alamos National Laboratory
LCS	- Limestone/Common Sand
LMF	- Large Melt Facility
LMFBR	- Liquid Metal Fast Breeder Reactor
LOAC	- Loss of Coolant Accident
LOF	- Loss of Flow
LWR	- Light Water Reactor
MAAP	- Modular Accident Analysis Program
MELPROG	- Melt Progression Code
NRC	- Nuclear Regulatory Commission
NTS	- Nevada Test Site
ORNL	- Oak Ridge National Laboratory
PIE	- Postirradiation Examination
PIXE	- Photon Induced X-Ray Emission

PNC	- Power Reactor and Nuclear Fuel Development Corporation
PRA	- Probabilistic Risk Assessment
PWR	- Pressurized Water Reactor
QUEST	- Quantitative Uncertainty Evaluation for the Source Term
RCS	- Reactor Coolant System
RSR	- Reactor Safety Research
RPV	- Reactor Pressure Vessel
S/A	- Subassembly
SARRP	- Severe Accident Risk Rebaselining Program
SASA	- Severe Accident Sequence Analysis
SEALS	- Steam Explosions at Large Scale
SHE	- Straight High Explosive
SHIP	- Small-Scale High Pressure
SPIT	- System Pressure Injection Test
ST	- Source Term
STAR	- Sandia Transient Axial Relocation
SWISS	- Sustained Water Interactions With Stainless Steel
TMBDB	- Thermal Margin Beyond Design Basis
TRAN	- Transition Phase
TURC	- Transient Urania Concrete
TWT	- Transient Water Tests
ULOF	- Unprotected Loss of Flow
UT	- Ultrasonic Thermometer
VGES	- Variable Geometry Experimental System

EXECUTIVE SUMMARY

1. CONTAINMENT LOADING AND RESPONSE

The containment of a reactor is the last barrier that prevents radionuclide release to the environment during a severe reactor accident. Considerable attention then needs to be devoted to accident phenomena that may threaten the integrity of reactor containments. Two important ex-vessel phenomena that will place significant loads on reactor containments are direct containment heating caused by pressure-driven expulsion of melt from the reactor vessel and the interactions of core debris with structural concrete. Highlights of recent experimental research on these phenomena are described in this report. The recent developments in models of core debris interactions with concrete--CORCON and VANESA--are also described. The results will not only be used to support model development for CORCON and VANESA, but also for the integrated systems development containment code, CONTAIN, and the melt progression code, MELPROG.

1.1 Ex-Vessel Core Debris Interactions

The SURC experiments will provide the first large scale tests of the sustained interactions of urania and zirconium melts with concrete. As such the SURC tests will be the most prototypic tests of the important core debris-concrete interaction phase of hypothetical severe reactor accidents. The tests will make a major improvement in the existing data base on such interactions.

Pretest calculations were done for the SURC experiments using the CORCON/VANESA severe accident analysis code. The concrete ablation rates for SURC are predicted to range from 15 to 120 cm/h, gas evolution rates are predicted to range from 50 to 250 L/min, and aerosol generation rates are predicted to range from 1 to 100 g/m^3. These calculations showed three things. First, that the SURC tests will exercise important heat transfer, gas chemistry, and aerosol release models in the CORCON/VANESA codes. Second, that the tests will be able to distinguish between competitive models currently under consideration for inclusion in CORCON and VANESA. Third, that significant and measurable variations in temperature response, gas chemistry, and aerosol release are predicted over the range of the experimental matrix. These results verify the geometry and instrumentation design for the SURC experiments, which have the stated goal of validating the heat transfer, gas chemistry, and aerosol release models used in the CORCON/VANESA code to analyze source terms resulting from ex-vessel/core-concrete interactions.

1.2 High-Pressure Melt Ejection and Direct Containment Heating

Experiments and analyses have shown that debris dispersed from a reactor cavity can potentially impart energy to the containment atmosphere and develop large quantities of aerosol. Most experiments to date have been unable to quantify either the extent of direct atmospheric heating or the amount of aerosolized material. The SURTSEY Direct Heating Test Facility was recently installed at Sandia to allow scaled cavity experiments to be performed in a confined volume. The DCH-1 test was the first experiment conducted in the SURTSEY facility. It was designed to provide the experimental data required to understand the phenomena associated with pressurized melt ejection and direct containment heating. The results will be used to develop phenomenological models for large containment response codes.

The DCH-1 test involved 20 kg of molten core debris ejected into a 1:10 scale model of the Zion reactor cavity. The melt was produced by a metallothermitic reaction of iron oxide and aluminum powders to yield molten iron and alumina. The cavity model was placed so that the emerging debris would propagate directly upwards along the vertical centerline of the chamber.

Results from the experiment showed rapid debris dispersal. Peak pressure from the six transducers ranged from 0.09 to 0.13 MPa (13 to 19 psig). The time interval from the start of debris ejection to pressure peak was 2 to 3 s. Posttest debris collection yielded 11.6 kg of material outside the cavity of which approximately 1.6 kg was attributed to the uptake of oxygen by the iron particles. Mechanical sieving of the recovered debris showed a lognormal size distribution with a mass mean size of 0.55 mm. Aerosol measurements indicated a substantial portion (5 to 29 percent) of the displaced mass was in the size range less than 10 mm. However, these results may have been affected by overloading of the aerosol sampling devices. A more realistic range would be 5 to 10 percent of the displaced mass.

An important development in the experimental efforts has been the ability to directly measure the dynamic shape factors as well as size distributions of aerosols produced in the experiments. Heretofore only average dynamic shape factors could be back calculated. In the DCH-1 test, it was found that shape factors are size dependent, varying from 7 to 11 at 1 μm to about 2 at 5 μm. This size dependency of the shape factor, if it also develops in aerosol produced from real reactor materials, has an important bearing on the

fraction of aerosol produced by pressure-driven melt expulsion that might be released from the plant.

1.3 CORCON Code Development

The later stages of a severe nuclear reactor accident are marked by the deposition of molten core debris into the reactor cavity, which leads to vigorous interactions between the core melt and structural concrete. Included in these interactions are rapid ablation of the concrete followed by intense aerosol generation and gas and fission-product release. These phenomena are an important concern in severe accident source term evaluation and risk and consequence assessment.

The CORCON computer code was developed at Sandia to model these ex-vessel core debris-concrete interactions. Early comparisons between experimental data and CORCON calculations indicated that the existing melt-concrete heat transfer models were inadequate. An improved melt-concrete heat transfer model has been developed that consists of the Kutateladze nucleate boiling correlation acting in series with a melted slag film. Comparison of experiment results to calculations made using this model indicate good to excellent agreement for the TURC, SWISS, and BETA tests that have been conducted at Sandia and KfK. The model was then used for the SURC3 and SURC4 pretest predictions. The pretest predictions demonstrated that SURC3 and SURC4 will provide validation of the heat transfer and chemistry models in CORCON.

1.4 Molten Fuel-Coolant Interactions

The objective of this program is to develop an understanding of the nature of fuel-coolant interactions (FCIs) during hypothetical accidents in light water reactors (LWRs). The understanding of FCIs achieved in this program is expected to resolve key reactor safety issues for both terminated and unterminated accidents. Models are being developed to quantitatively determine:

1. The rates and magnitudes of steam and hydrogen generation.

2. The degree of mixing and coarse fragmentation of the fuel.

3. The degree of the fine fragmentation of the individual droplets composing the coarse mixture.

4. The fraction of the available thermal energy that is converted into mechanical energy.

Experiments are being conducted to determine the influence on FCIs of three classes of important independent variables: thermodynamic conditions (temperature of the fuel and the coolant and the ambient pressure); scale variables (amount of fuel and coolant initially involved); and boundary conditions (pour diameter and rate, shape and degree of confinement of the interactions region, presence of structures, water depth, and fuel-coolant contact mode). Measurements made during the experiments include photographic observation of the FCIs, pressures generated in the coolant and the cover gas, steam and hydrogen generation, and the resulting debris characteristics.

At the request of the NRC, we have prepared a new program plan which addresses the important phenomena involving jets of molten fuel mixing and interacting with water. In the early phases of the program, the mixing behavior and explosibility of single jets of molten fuel in water are addressed in the EXO-FITS facility. Subsequent test series evaluate the influence of neighboring jets (three-jet matrix) and of a fully surrounded jet (five-jet matrix). The proposed jet diameter and hole pitch will represent either full- and half-linear-scale representations of the lower grid distributor plate or half- and quarter-linear-scale representations of the lower core support plate inside a TMI-Unit-2 "like" reactor.

We have conducted six preliminary experiments in the EXO-FITS facility investigating the behavior of molten jets of iron-alumina thermite falling through approximately 1.8 m of air. The purpose of these experiments is to develop the experimental technology needed to deliver unobstructed molten jets of iron-alumina into deep water chambers of various sizes. To date we have investigated two basic jet configurations: single- and three-jet. In the single jet experiments (MDJET-1, -2, -6, and -7), we observed some interesting and somewhat unexpected trends in the jet behavior. The integral behavior of this jet was unusual in that it could not be described by a single-jet characteristic. Rather, the jet behavior appeared as a combination of characteristics, depending upon the time into the pour. Early in the pour, the jet characteristic resembled the turbulent regime with a transverse disturbance, more commonly referred to as sinuous breakup of the jet. Subsequent to this early pouring phase, the behavior of the jet changed from sinuous to varicose.

Two experiments (MDJET-4 and -5) were conducted using a three-jet geometry. During these two experiments, we

observed the same general type of jet behavior, involving two classifications. Early in the pour, the jet behavior was dominated by turbulent sinuous wave breakup while at late times it was characterized by surface tension effects (i.e., varicose breakup). Furthermore, during the early pour times, the three jets appeared to spread away from one another and spin slightly about the center line. At late times during the pour, the jets fall vertically down when the influence of turbulence has subsided and surface tension effects again become important.

We have also conducted four experiments in which jets of molten iron-alumina were allowed to fall through saturated water. In these experiments, we observed significant breakup of the melt as it fell through the water chamber, independent of the initial jet diameter (4-, 8-, and 16-cm initial jet diameters). The 4- and 8-cm diameter jets displayed similar mixing and interaction behavior, although slight differences were observed. In contrast, the 16-cm diameter jet appeared different from the smaller jets. In particular, no mixing plateau was observed. It seems that discontinuous flow regime changes may be playing an important role in the fragmentation and mixing of these jets. We have speculated about the causes of these threshold mixing phenomena, but it is currently unclear exactly what causes this transient mixing behavior.

In the event of a severe accident involving core melting, molten jets can form as fuel pours through the water in the lower plenum. If the vessel fails, gravitational or pressure-driven jets can also form as the fuel is ejected into a cavity containing water. The breakup of these jets will determine the probability and energetics of in- and ex-vessel steam explosions, the rate of production of hydrogen and steam, the characteristics of the resulting debris bed, the characteristics of fission products released from the fuel, and the extent to which the fuel is dispersed. The information produced in the experiments described above are being used to develop one- and two-dimensional models of jet mixing and breakup. A study of liquid jet breakup has been performed by the University of Wisconsin under contract to us. Some results are discussed in the text.

1.5 Hydrogen Behavior

Sandia developed the HECTR code to analyze the transport and combustion of hydrogen during reactor accidents. IDOCR uses the MAAP code to perform similar analyses. These codes differ in the way that various phenomena are modeled. In order to estimate the impact of the modeling differences, a

standard problem, an S2HF accident sequence in a PWR ice-condenser containment, was defined to compare the HECTR and MAAP code predictions. Preliminary results of the first part of the problem show that the two codes yield very different pictures of the burning process. HECTR predicts three global deflagrations with very sharp, but brief pressure and temperature peaks. MAAP predicts a much more gradual increase in pressure and temperature, which resemble characteristics of diffusion flames rather than propagating deflagrations. Thus the calculated peak combustion pressures and temperature by MAAP are very low.

Improved combustion correlations for predictions of flame speed and combustion completeness have been developed. These correlations are based on measured or inferred data obtained from the NTS, VGES, FITS, ACUREX, and Whiteshell experiments. The effects of fans and sprays are also included in these correlations. The accuracy of these correlations is reasonably good (within 20 percent).

The FLAME facility is a large channel used to study combustion problems of hydrogen-air mixtures related to flame acceleration and deflagration-to-detonation transition (DDT). The results of 20 tests conducted with no obstructions in the channel and 10 tests with obstacles present are summarized. Hydrogen mole fraction was varied from 12 to 30 percent. The degree of transverse venting was varied by moving steel plates on the roof of the channel. Measurements included the speed of propagation of the flame down the channel, the overpressures generated, and the possible occurrence of DDT.

The most important variable is the hydrogen mole fraction. Flame speeds and overpressures increase rapidly with higher values. The presence of obstacles causes a great increase in flame speed, overpressure, and range of DDT over that seen in comparable tests in a clear channel. DDT was observed at 15 percent hydrogen mole fraction with obstacles and 24 percent without obstacles. The effect of transverse venting is complex: Large degrees reduce the severity of the combustion, small degrees increase it. In the latter case, the increase in flame speed caused by the turbulence generated dominates the effect of the loss of gas from the channel. The effects of geometric scale were determined using MINIFLAME, a one-twelfth scale model of FLAME. For the same combustible mixtures, flame speeds, overpressures, and range of DDT were greatly reduced at small scale. MINIFLAME and FLAME results indicate flame acceleration and DDT will not scale up accurately to full-size nuclear reactor containments with identical combustible mixtures. Limited experimental results from the FRG indicate that if

the scale-model combustible mixture is made more reactive than the full-scale mixture, such that the ratio of geometric size to detonation cell size is identical, then scale-model testing will be valid.

We have completed a simulation of FLAME Experiment F-23 with a modified version of the CONCHAS-SPRAY code. This was a burn of 14.5 percent hydrogen with no top venting. The side walls were fitted with 16 pairs of symmetrically placed obstacles. The blockage ratio was 0.33. The entire length of the 30-m facility was included in the simulation. The computational flame trajectory was in good qualitative agreement with the experimental data. In many respects the quantitative agreement was also quite good. The calculated flame velocity at the time the flame reached the end of the facility was 570 m/s, compared to 540 m/s measured in the experiment. The structure of the computed flame trajectory differed from the experiment in that it did not exhibit as sharp an acceleration in the middle of the burn. This computation was achieved through the use of a new FLAME model, which involved a minimum of adjustable paramters.

The possibility of local detonations during a hypothetical degraded core accident at the Bellefonte nuclear power plant was investigated for the Severe Accident Risk Rebaselining Program. The possibility that a mixture in a given compartment will propagate a detonation was studied using a chemical kinetics code based on a ZND model and the experimental H_2-air-steam data from the Heated Detonation Tube. The calculations from the code indicate that the propagation of a detonation is possible in one compartment of Bellefonte for two different types of accidents, but it is unlikely in other compartments.

1.6 Hydrogen Mitigative and Preventive Schemes

The objective of the Hydrogen Mitigative and Preventive Schemes Program is to provide the NRC with information to evaluate proposed equipment concepts and operational schemes to prevent or mitigate the effects of hydrogen combustion during hypothetical LWR accidents. To provide this information, we are investigating the operability and consequences of operation of deliberate ignition systems and their components during hypothetical hydrogen-producing accidents in nuclear power plants.

During the completion of the experiments and analyses of data relating to the behavior of resistively heated hydrogen igniters during the operation of water sprays in containment, we discovered several new aspects of the behavior of the igniters:

EXECUTIVE SUMMARY

1. Both the cylindrical and the helical igniters will withstand greater water fluxes when initially hot compared to initially cold when first exposed to the spray; the increase is in the range of 10 to 30 percent for the cylindrical igniter and almost threefold for the helical igniter.

2. The tip of the cylindrical igniter remains hot in airflows almost twice as great as the sides of the igniter.

3. The cylindrical igniter is much less affected by water sprays than the helical igniter in the presence of combined water sprays and airflows. Thus the airflows mostly govern the operating temperature of the cylindrical igniter, while a combination of airflows and water drop flux governs the surface temperature of the helical igniter. These new observations indicate more complex but in some instances less pessimistic limitations on the operability of resistively heated igniters during the operation of the containment spray system.

2. FISSION-PRODUCT SOURCE TERM

2.1 High-Temperature Fission-Product Chemistry and Transport

The purpose of the Fission-Product Chemistry and Transport Program is to obtain data on the chemistry and processes that affect the transport of fission products under accident conditions. Thermodynamic and chemical reactivity data are being collected for compounds of fission-product elements of particular interest. An experimental facility has been built to allow the chemistry of fission products in steam-hydrogen environments to be studied. The interaction of fission products with reactor materials such as stainless steel can be examined in this facility. Results of these experimental studies are compared to predictions of thermo-chemical models to determine if reaction kinetics play an important role in fission-product transport.

Reactor component surfaces can react with the environment of a nuclear reactor accident to influence the progress of that accident. Surface reaction studies using the experimental facility, the Fission Product Reaction Facility, have been accomplished by Sandia personnel. The results of studies using cesium hydroxide and cesium iodide in this facility to simulate the behavior of these fission-product species in severe reactor accident environments are described.

In all cases where the reaction was between CsOH and 304 stainless steel the cesium reaction product existed in the inner oxide formed on the steel. Where a correlation could be established, it was between cesium and silicon (as silica). In a few of these cases, where the reaction had gone to completion, the product was identified as $Cs_2Si_4O_9$. A model was developed for the kinetics of this reaction as controlled by the temperature, oxide growth, and availability of CsOH.

Results of early work showed CsI to be quite stable in a steam environment in the presence of structural materials. CsI instability was first observed in a radiation field and was attributed to the ionizing radiation. Subsequent work has shown that this instability could have been produced by only thermal effects. The magnitude of the instability varies from test-to-test. Some pattern to the instability may be obtained by examining the kinetics of the reaction of the cesium bearing compound resulting from decomposition of the CsI.

2.2 ACRR Source Term Tests

Understanding the release of radionuclides during fuel degradation in a core uncovery accident is the first stage in determining the amount and chemical nature of the radioactive species released from a damaged nuclear plant. Current estimates of the release of the principal fission products over the range of relevant accident conditions are subject to significant uncertainty (e.g., see the QUEST Study). A key element in reducing the uncertainty in predicted releases is an improved understanding of fission-product release from the fuel under severe fuel damage conditions. Major progress is being made in the development of mechanistic release models (e.g., MELPROG's VICTORIA model) to substantially reduce these uncertainties. The ACRR Source Term (ST) program is being conducted to provide a data base for fission-product release over a range of fuel temperatures, system pressures, and fuel damage states. Significantly, these experiments will be performed in the presence of ionizing radiation and at elevated pressure, where little or no data currently exist, to allow the validation of these improved fission-product release models.

The major activities in this program currently involve evaluation of filter sampler designs and components, the continued development of the VICTORIA code and application of VICTORIA to the ST experiments, completion of design and fabrication of the ST experiment package, and modification of the Sandia Area V Hot Cell Facility.

The design goals for the ST sampler system are to (1) measure the quantity of each primary fission product (Cs, I, Te, Ba, Sr, Sb, Ru, Ce, Eu, Kr, and Xe) and structural material (Sn) released from the fuel bundle; (2) determine the release rates; and (3) qualitatively establish some of the chemical forms that exist close to the fuel bundle under high-temperature accident conditions.

Tests are being conducted to evaluate various filter sampler designs for use in the ST experiments. In these tests, mixtures of stable forms of fission product species (Cs, CsI, I, Ba, and Te) are introduced into a gas stream, which then flows through the candidate filter sampler. The filters are then disassembled and analyzed for the various fission product species. For the ST-1 experiment, which will contain a very reducing atmosphere, VICTORIA predicts that metallic Cs will dominate the Cs species that will interact with the filter. Hence the initial tests of filter designs were run with Cs metal as the dominant species in extremely reducing conditions.

EXECUTIVE SUMMARY

In the first three filter systems tests, various geometries and materials were evaluated for reactive portions of the filters. The reactive segments were intended to be somewhat selective in their collection of various species. This selectivity would aid in identifying the chemical forms of the fission products in the gas stream. It was found, however, that there was little or no selectivity in the reactive portion of the filter with the exception of the reaction of tellurium species with stainless steel and nickel components. In general, the reactive portion of the filter assembly acted as no more than a thermal gradient tube. High overall filter efficiencies were attainable, but it became obvious that the fiber filter must be sealed to the filter thimble to prevent flow from bypassing the fiber filter.

The results of the first three filter systems tests led to a redesign of the filter. That next design was evaluated in filter systems test 4, which was run in early May. The stainless steel filter thimble contained three sections: (1) a 34-cm-long nickel thermal gradient tube that had 0.5-mm diameter wires of Ni, Pt, and Ag running parallel to its walls; (2) a 24-cm-long fiber filter composed of 0.076-mm diameter Pt-10%Rh wire with a graded packing density of 3 to 5 to 6.3 percent, and (3) a 3-cm-long granular charcoal filter. The wires that stretched along the length of the thermal gradient tube were inserted to provide better information on chemical speciation. The wires were analyzed using the new SEM located in the Sandia Area V Hot Cell Facility by wavelength and energy dispersive analyses. The Ni wire was included because it is the same material as the thermal gradient tube and will give an indication of chemical species deposited in the thermal gradient tube; the Pt wire was included because it is chemically inert to most fission products, except possibly Te at high temperatures; and the Ag wire was included to react with the gaseous iodine species HI and I_2.

The data from filter systems test 4 result in the following conclusions: The filter assembly appeared to be greater than 99 percent efficient. About 1.3 g of Cs were collected; most of the Cs deposited on the fiber filter as Cs metal aerosol. Wavelength dispersive analyses also identified individual particles composed of Cs alone (probably Cs_2CO_3 formed by oxidation of Cs metal and reaction with CO_2 after exposure to the atmosphere), CsI, and $Cs_{2-x}Te$ on the wires. The iodine generated appeared to exist primarily as CsI aerosol particles. The Sn appeared to be deposited as SnTe. However, since the Te to Sn ratio was about 8.6, Te probably also existed as Te, Te_2, H_2Te,

and $Cs_{2-x}Te$. Metallic Te vapor and H_2Te are known to react strongly with Ni and steel; however, under the test conditions, reaction of Cs_2Te with Ni and steel may be weak or even thermodynamically unfavorable. The quantities of Ba that were generated were so close to the detection limit that the measured values were meaningless. This filter systems test was successful in that the filter was very efficient and our analyses gave some insight into chemical speciation. The final filter design will not be much different from the one used in test 4.

The VICTORIA code is being developed both as a fission-product release/transport/chemistry module for MELPROG and as a stand-alone experiment analysis code. Both versions have been upgraded by the incorporation of a new chemical equilibrium solver which is more than an order-of-magnitude faster than the previous version. This solver reduces the number of equations to be solved at the expense of introducing significant additional nonlinearity into the problem.

The stand-alone version of VICTORIA is currently being modified for use in analyzing the results of the HI test series at ORNL. Changes in the code input to accommodate the different geometry of these tests have been made and a zirconium oxidation model has been developed. Once this latter model (based on the Urbanic and Heidrick data) has been verified, detailed modeling of these experiments and a comparison of the experimental results with calculations will be made.

The design of the ST experiment package has been completed, and all components for the first two ST experiments have been ordered or are being fabricated. It is anticipated that most components will be available in late August. The major modifications to the Sandia Area V Hot Cell facilities are nearing completion. The development of the posttest analysis methods and development of hot cell tooling and fixturing are continuing.

3. LWR DAMAGED FUEL PHENOMENOLOGY

Sandia's LWR Damaged Fuel Phenomenology Program includes analyses and experiments that are part of the integrated NRC Severe Fuel Damage (SFD) Research Programs. Sandia is investigating, both analytically and in separate-effects experiments, the important "in-vessel" phenomenology associated with severe LWR accidents. This investigative effort provides for two related research programs: (1) the Debris Formation and Relocation (DFR) Program and (2) the Degraded Core Coolability (DCC) Program. The focus of these activities is to provide a data base and improved phenomenological models that can be used to predict the progression and consequences of LWR severe core damage accidents. Radionuclide source term uncertainty studies (e.g., QUEST) indicate large sensitivity of source terms to core-temperature distributions, geometric configurations, and coolant flows. The DFR experiment program provides unique data on in-vessel fuel damage processes that are of central importance in determining the release and transport of fission products in the primary system. The DCC experiment program, completed early in this semiannual period, provided data on the ultimate coolability of damaged fuel configuration. Models coming from both programs are used directly in the MELPROG code.

3.1 ACRR Debris Formation and Relocation (DFR)

The focus of the LWR DFR experiment program is directed toward providing separate-effects phenomenological data on important severe in-vessel fuel-damage processes to aid in the development of second generation severe accident analysis codes. The core damage configuration, hydrogen generation, and fission-product release are the primary areas of interest. The DFR test series uses cinematography to record the fuel damage progression during the course of in-pile experiments in which accident conditions are simulated in a small LWR fuel bundle. Decay heating in these experiments is simulated by fission heating of the fuel in the ACRR. Steam conditions and clad preoxidation, similar to expected accidents in a local region of a degrading core, are provided.

Results from the DF-3 (PWR Control Rod Effects Test) on-line instrumentation are presented and a discussion on the interpretation of this data is given. This interpretation holds that the Ag-In-Cd control rod did not fail and relocate until the steel tube encasing the control alloy reached its melting point at ~1700 K. Further, the observation of aerosol in the file record did not occur

coincident with the control rod failure as expected, but appeared at the time that zircaloy melting temperatures were being attained. This would indicate that Sn, and not Cd, was the major source of the aerosol. The metallurgical characterization shows that the relocated silver did not interact significantly with Zr or any of the other test bundle components and appeared to be somewhat immiscible with other materials. Stainless steel components, namely Fe and Cr, were found in complex eutectics involving U-Zr-O, but were deemed as having little influence on fuel attack or dissolution.

Substantial planning and design work have been devoted to the DF-4 experiment, which includes a BWR control blade structure in a larger rod bundle in order to determine the effects of B_4C and stainless steel control blade materials on the melt and damage progression. A collaboration with SASA program members at ORNL has been arranged wherein information concerning the experiment outcome will be exchanged and analytical support and guidance for the experimental parameters will be provided. This cooperative effort has led to the development of an experiment analysis code based upon MARCON 2.1B subroutines. Titled MARCON-DF4, this code has been used to predict the DF-4 test section heatup for a proposed heating sequence. The results of these precalculations are presented. Completion of the test is expected near the end of FY86.

3.2 ACRR LWR Degraded Core Coolability (DCC)

The LWR Degraded Core Coolability (DCC) Program investigated the coolability of damaged core debris in water. The debris was fission heated in the Annular Core Research Reactor (ACRR) to simulate the decay heat expected in an LWR severe core-damage accident. The governing phenomenological uncertainties investigated were pressure effects, deep bed behavior, particle size distributions, stratified beds, bottom coolant feed, and coolability in three thermal regimes: (1) convention/boiling, (2) dryout, and (3) extended dryout. The staff used experimental results to confirm and modify the present analytical models used to predict degraded-core coolability.

Three experiments constituted the DCC Program. The DCC-1 experiment was designed to look at boiling in deep debris beds with a broad distribution of small particulate. The DCC-2 experiment was also a deep bed composed of a narrow distribution of medium-sized particles with a small amount of "fines" added. The DCC-3 experiment was a stratified bed in which a thin layer of small particulates (effective

diameter: 0.919 mm; 100-mm deep) was placed on top of a thick layer of large particles (effective diameter: 3.64 mm; 400-mm deep). In addition, DCC-3 provided for inlet flow of coolant at the bottom of the debris. The first two experiments were conducted over the full PWR pressure range (17 MPa) while DCC-3 was conducted only up to the peak of the predicted "pressure versus dryout heat-flux" curve (7 MPa). No other high-pressure data for debris coolability has been generated.

The three experiments have been successfully concluded and the analyses completed. Experiment hardware, test procedures, and results of the analyses for DCC-1 and -2 have been presented in previous quarterly and semiannual reports. The experiment hardware and procedures for DCC-3 were discussed in the July-December 1985 Semiannual Report. This report summarizes the results and analyses of DCC-3.

The DCC-3 experiment provided data to validate theoretical treatments of stratification and inlet flow in a deep bed of a large UO_2 particulate. The data demonstrated two important theoretical predictions of debris coolability: (1) Stratification can sharply reduce the coolability of a debris bed, and (2) inlet flow can significantly and effectively increase the coolability of a bed.

Without inlet flow, the DCC-3 debris bed would be uncoolable in a prototypic reactor accident. This is counterintuitive since a bed composed solely of the smaller particles (in the upper layer) would be coolable. The cause of the seemingly premature dryout is the surface tension force at the stratification interface. The top layer of smaller particles acts like a sponge and holds water, preventing it from flowing into the lower bed.

The great importance of surface tension in the DCC-3 experiments is at odds with the heuristic argument that surface tension is unimportant in beds composed of "large" particles. The justification for this argument is that the capillary rise in such particles is much smaller than the depth of the debris bed. The argument is valid for homogeneous beds where the length scale governing dryout is the height of the bed. In stratified beds, capillary forces can make strong changes in the saturation profile over a length equal to the capillary rise. The length scale governing dryout for such changes is much smaller than the bed height and, in DCC-3, is the same order of magnitude as the capillary rise.

The heuristic argument about particle size is not without appeal. One would not expect the same sort of behavior seen

in DCC-3 if the particles had been a factor of 10 larger. The difference in expected behavior probably lies in the question of stability.

If the absolute value of the capillary forces is sufficiently small, the pressure fluctuations will exceed the stabilizing force and the configuration can become unstable. The most probable result of the instability would be a two-dimensional flow of water and gas in which the water flows into the lower bed on one side and gas is released into the upper bed on the other side. The instability probably has a critical wavelength. Test sections having a diameter smaller than this wavelength will exhibit the stable behavior while those having a larger diameter will exhibit two-dimensional flow. It is possible that the DCC-3 dryout heat fluxes would have been larger if the debris bed diameter had been larger.

In agreement with our theoretical predictions, the injection of water at the bottom of the DCC-3 debris bed increased the dryout powers above that which would be observed in a reactor accident. The inlet flows required for this were within the capacity of the High Pressure Injection System (HIPS). This demonstrates that the HIPS might be useful in cooling debris beds in the pressure vessel. This is subject to the condition that the lower boundary of the debris bed is permeable.

The DCC experimental series has provided a data base for debris coolability in which prototypic materials were used and prototypic pressures were realized. DCC-1 exhibited an unexpected pressure dependence, and DCC-2 displayed the effects of inhomogenities. Both of these effects are believed to be due to the particle size distributions. In spite of these new effects, the data from DCC-1 and DCC-2 fit in well with the world data base obtained under less prototypic conditions. DCC-3 provided unique data on the effects of nonuniform beds and bottom inlet flow. The experiments have demonstrated that the models developed for LMFBR debris coolability and modified for LWR conditions are applicable to the LWR degraded core.

The behavior of debris beds at this point is reasonably well understood. Several analytical models, among them the Lipinski model, do a reasonable job of predicting dryout heat fluxes. The obvious problem is in determining the proper debris bed configuration for LWR reactor accidents. In particular, more information is needed on the particle size distribution, void fraction, bed depth, and degree of stratification (if it occurs). Given this information,

reasonably accurate predictions can be made about the coolability of an actual debris bed. Further efforts in the area of debris coolability should concentrate on the questions of debris formation and settling. This concludes the reporting of the DCC program in the semiannual reports.

4. MELT PROGRESSION CODE DEVELOPMENT (MELPROG)

The objective of this program is the development of a mechanistic computer model for the analysis of the in-vessel phases of severe accidents in LWRs. This model, MELPROG, is implicitly linked with the TRAC-PF1 thermal hydraulics code to provide a complete, integrated treatment of the reactor primary system from accident inception up to and through release of core materials and fission products from the reactor vessel. The model also provides materials and thermohydrodynamic input to the CONTAIN reactor containment analysis model.

The approach used in MELPROG has been to develop stand-alone modules to analyze specific phenomena that may be encountered during a severe accident sequence. These modules are then explicitly linked within the MELPROG code in order to treat the entire accident sequence in an integrated manner. In this way, one may obtain accurate predictions of both the various phenomena and the coupling between the phenomena. This approach allows key quantities, such as fission-product release and transport, to be calculated in a consistent manner. In addition, the modular structure has the advantage that it is relatively easy to improve or substitute new models into the code as warranted.

The first version of MELPROG, MELPROG-PWR/MOD0, was completed and is being tested prior to release. This version has emphasized the thermal-hydraulic modeling of the reactor vessel. It uses a one-dimensional fluid dynamics model (FLUIDS module) and contains PWR core structure models (STRUCTURES module). It also includes the DEBRIS module for debris bed analysis, the RADIATION module for radiation heat transfer analysis, and the PINS module for fuel and control rod analysis. Major development on this version has ceased in order to devote more effort to developing the improved versions of the code.

The second version, MELPROG-PWR/MOD1, is currently operational, but still under development. This version includes all features of the original code plus many significant enhancements. In particular, this version includes a two-dimensional fluid dynamics model (FLUIDS-2D module), a fission-product model (VICTORIA module), an improved core structures model (CORE module), a melt-water interaction model (IFCI module), and a melt ejection model (EJECT module). This version represents a major improvement over the original version.

The new FLUIDS-2D module replaces the one-dimensional fluid dynamics treatment in MOD0 with a full two-dimensional (R-Z)

capability. In addition, four momentum fields are treated instead of three (the corium field is split into solid and liquid fields). This version was completed at Los Alamos National Laboratory as part of the MELPROG effort. The major advantage gained through the new FLUIDS module is the ability to treat the important effects of natural circulation in the core and vessel.

The VICTORIA module in MELPROG treats release and transport of fission products in the core and vessel. It uses a detailed treatment of thermochemical equilibrium to establish equilibrium partial vapor pressures for the various fission-product molecular species in a high-pressure steam and hydrogen environment. The excess of the equilibrium vapor pressures over the existing partial pressures in the bulk overlying gas determines the local driving force for release. Three rate limitations to release, however, are explicitly calculated: (1) transport in the bulk fuel/clad phase, (2) Langmuir vaporization kinetics, and (3) boundary layer mass transport to the bulk gas. Chemical reactions in the gas phase are treated, as is condensation, to form aerosols onto existing aerosols and onto cold structures. Aerosol transport, deposition, and reentrainment are modeled, as is revaporization (due to decay heating) of condensed fission products. Finally, the partitioning of decay heat among corium, vapor, liquid, and structural fields is performed using the release and transport models. A stand-alone version of VICTORIA is complete, and development has progressed to the point where scoping calculations for the ACRR source term tests are being made.

The new core structures module (CORE) will treat PWR and BWR core structures such as fuel rods, control rods, poison rods, control blades, can walls, and grid spacers. This module will calculate both the thermal and mechanical response of these structures. Work has been completed on developing the basic models in this module.

The melt-water interaction module, IFCI, in MELPROG is essentially a flow regime controller for situations in which corium is brought into rapid contact with liquid coolant. Coarse mixing of the corium and water mixture is controlled by the respective volume fractions of the two materials, the respective temperatures (which in turn control film boiling dynamics), and their relative velocity. Similarly, fine melt fragmentation is controlled by hydrodynamic mechanisms based on film collapse and hydrodynamic instabilities among other candidate mechanisms. Finally, vapor generation is calculated subject to flow regime and (for explosive

interactions) inertial constraints. The module provides the flow regime and heat transfer information in an interactive mode with the FLUIDS module. Both explosive interactions and rapid boiling are treated by the module. A stand-alone version of the module has been completed.

The melt ejection module, EJECT, consists of models for the flow regime of existing core and coolant materials as well as models for ablation of the initial failure during blowdown. The module treats low-pressure, gravity-driven slumping through the lower vessel head, high-pressure blowdown, and (eventually) ejection through steam-explosion induced failures. This module is currently under development in a stand-alone version.

In addition to the development work, both MELPROG-PWR/MOD0 and MELPROG-PWR/MOD1 are undergoing extensive testing. The codes are being used to study the PBF and ACRR SFD experiments and to study a TMLB' accident sequence for Surry. This accident calculation covers the entire spectrum of meltdown phenomenology and as such is valuable for testing the code.

The first complete, coupled, and largely mechanistic analysis of a TMLB' (station blackout) core meltdown accident has been made with MELPROG-PWR/MOD1. The calculation was initiated at the point boiling began in the core region and ended with failure of the reactor vessel. Most of the important phenomena occurring in the accident sequence were modeled during this accident sequence. The important exceptions are a treatment of cladding motion prior to major disruption of the fuel rods (candling) and a treatment of the fission-product release, transport, and deposition (as treated by the VICTORIA module that is being implemented). While this calculation should be viewed as preliminary, it does demonstrate the advanced capabilities of this version of MELPROG.

5. ADVANCED REACTOR ACCIDENT ENERGETICS

The Advanced Reactor Accident Energetics Program was initiated in 1975 to address the important phenomenological uncertainties involved in LMFBR core disruptive accidents. The program consisted of 10 major in-pile experimental programs addressing all phases of in-core phenomenology. These programs drew significant international attention and were jointly funded and staffed by the German Kernforschungszentrum Karlsruhe (KfK), the Japanese Power Reactor and Nuclear Fuel Development Corporation (PNC) and the United Kingdom Atomic Energy Authority. With the completion of the STAR-7 test in the Initiation Phase; the GAP-2 experiment in the Transition Phase; and the irradiated Equation-of-State experiments in the Disassembly Phase, the major elements of the program have now been completed.

5.1 Initiation Phase

The Sandia Initiation Phase Fuel Dynamics Program provided experimental data and analysis for the initiation phase of an LMFBR core-disruptive accident. The motion of clad and fuel in the initiation phase of an LOF accident is an important consideration in the subsequent progression of the accident. Early fuel dispersal can lead to neutronic termination while limited dispersal and blockage formation continue the accident into the transition phase and the possibility of further neutronic activity.

To obtain data on the important phenomena involved in this phase of an LMFBR accident, the Sandia Transient Axial Relocation (STAR) experiments have been performed in the Annular Core Research Reactor (ACRR). The purpose of the seventh and last experiment in the STAR program, STAR-7, was to investigate the upper bound loss-of-flow (LOF) accident scenario for the MONJU fast breeder reactor. The experiment was performed successfully and analyses are currently in progress at PNC.

5.2 Transition Phase

If sufficient fuel dispersal does not occur in the initiation phase of a core disruptive accident, the accident may progress to a "transition" or "meltout" phase. The key questions in the transition phase, highlighted in the CRBR safety review, are whether fuel or clad blockages form, leading to a confined or "bottled" core configuration, and the behavior and reactivity implications of this pool of fuel-steel in the core region if the fuel blockages do lead to this state.

The TRAN program addressed the question of fuel-inventory reduction by penetration into the upper core structure through subassembly can wall gaps to the lower core structure. If deep penetrations occur, nonenergetic shutdown is probable while shallow penetrations will lead to a transition phase and the possibility of further energetics. First-of-a-kind in-pile experiments have been conducted to provide data to evaluate the various models describing fuel penetration.

The last experiment in the TRAN program, GAP-2, addressed the large fuel removal paths presented by the subassembly gap regions of the LMFBR core. This experiment involved the melting of a 1.7-kg UO_2 fuel load and the downward injection by applied gas pressure of this melt into a channel representative of the subassembly can wall gaps. The fuel load was successfully melted and a temperature of about 4000 K was attained. Analysis of the channel thermocouples indicated the arrival of a substantial amount of melt at all axial locations along the length of the channel (~70 cm). In addition, thermocouples situated at the bottom of the dump tank showed ~200 K heating of this massive component, an indication that a substantial amount of molten material penetrated the full length of the freezing channel. Preliminary interpretation of GAP-2 at KfK suggests that conduction freezing dominates fuel removal processes and that potentially a large fuel removal capability exists through these flow paths.

5.3 Disassembly Phase - The Effective Equation-of-State (EEOS) Experiments

In the safety evaluation of LMFBRs, the severity of core disruptive accidents (CDAs) is a primary concern. One of the significant sources of uncertainty in the mechanistic modeling of such CDAs is the lack of thermo-physical data for irradiated fuel. The Effective Equation-of-State (EEOS) experiments investigated the pressure source from irradiated mixed oxide fuels (U, Pu) under severe accident conditions. The tests are sponsored by the Fast Breeder Project/KfK through the NRC and are being conducted in the ACRR.

The working fluid during a CDA core expansion phase is generally liquid irradiated fuel. To calculate the mechanical excursion of the core disruption, the pressure-enthalpy and pressure-temperature relation of the fuel is needed up to about 6000 K.

The EEOS experiments have been designed to investigate the pressure buildup from irradiated fuel under three different conditions:

- o In-channel conditions
- o In-pin conditions
- o Vacuum environment

Three of the experiments, EEOS-10, -11, and -12, have been completed. Their individual test objectives were:

- o EEOS-10 Determine irradiated fuel vapor pressure for typical LMFBR coolant channel conditions (low fuel smear density and low ambient pressure).
- o EEOS-11 Determine irradiated fuel vapor pressure for typical in-pin conditions (high fuel smear density and high ambient pressure).
- o EEOS-12 Measure fission-product release kinetics without fill gas contribution. Compare to fresh fuel results.

The test parameters were carefully selected from the experimentally accessible parameter space to simulate the above given conditions as closely as possible.

The irradiated fuel test used the same experimental technique as previous ACRR EEOS tests. The test fuel was prepared from HEDL pin P15-2A, which had a peak burnup of 5.1 percent.

The three experiments have provided the first Equation-of-State data on irradiated mixed-oxide fuels. Although no detailed analysis of the new data has been performed, preliminary results appear to support the following findings:

- o Significant amounts of fission products are released from the solid fuel, generating pressures around 1 to 2 MPa.
- o Fission-product release continues as the fuel is heated to higher temperatures, which results in the pressure being raised by several MPa.
- o Somewhere between 4000 and 5000 K, fuel vapor pressure seems to become dominant over the fission-product species.
- o In all cases, however, this fuel vapor contribution itself appears to be below that of fresh fuel at the same temperature.

- Fill gas may hamper the vaporization of condensible fission products and fuel species.

The total pressure from liquid irradiated fuel should be some combination of the pressures from its individual constituents, e.g., different classes of fission products and fuel species. The measured raw data suggests that the interaction of these constituent pressures may not follow simple models, e.g., ideal solubility pressure addition, ideal insolubility behavior, or boiling point suppression.

A main goal of the final analysis will be to derive a model for the total pressure of irradiated fuel in terms of constituent pressures and ambient gas pressures. Such a model would allow some further extension of the experimental results to other fuels or vaporization conditions.

1. CONTAINMENT LOADING AND RESPONSE

The containment of a reactor is the last barrier that prevents radionuclide release to the environment during a severe reactor accident. Considerable attention then needs to be devoted to accident phenomena that may threaten the integrity of reactor containments. Two important ex-vessel phenomena that will place significant loads on reactor containments are direct containment heating caused by pressure-driven expulsion of melt from the reactor vessel and the interactions of core debris with structural concrete. Highlights of recent experimental research on these phenomena are described in this report. The recent developments in models of core debris interactions with concrete--CORCON and VANESA--are also described. The results will not only be used to support model development for CORCON and VANESA, but also for the integrated systems development containment code, CONTAIN, and the melt progression code, MELPROG.

1.1 Ex-Vessel Core Debris Interactions

(D. A. Powers and E. R. Copus, 6422; D. R. Bradley, 6425)

The high-temperature ablation of concrete by molten nuclear reactor core debris has been recognized as an important aspect in radioactive source term evaluations for core meltdown accident scenarios. A core melt-concrete interaction can produce large quantities of noncondensible gases and aerosols laden with fission products. Combustible gases such as hydrogen and carbon monoxide as well as heat are liberated simultaneously. If combustion of these gases occurs, then significant pressurization of the containment can be expected, possibly even threatening containment integrity. The long-term behavior of a core melt-concrete interaction may include significant erosion of the concrete basemat, possibly even melting through the floor.

A number of experiments have been conducted over the years to simulate core melt-concrete interactions. Several computer codes have been developed to model this behavior and to simulate reactor accidents. Among those computer codes are CORCON,[1] a model of core debris-concrete interactions, and VANESA,[2] a model of radionuclide release from core debris. A systematic validation of these codes is now in progress at Sandia. The validation process includes

comparison of code predictions with experimental data and modification of the computer code models when necessary.

The Sustained Uranium-Concrete (SURC) experimental tests are the experimental element in the CORCON/VANESA verification process. In addition to extending the existing data base to include more prototypic core-concrete interactions, the SURC experiments are designed to provide information necessary to validate three important aspects of ex-vessel/core-concrete interactions as modeled by CORCON and VANESA. These are (1) heat transfer mechanisms, (2) gas release chemistry, and (3) vaporization release of aerosols. Four experiments are scheduled in the CY86 test matrix. Tests one and two (SURC1 and SURC2) will investigate gas release, aerosol release, and concrete ablation during sustained corium-concrete interactions. In addition to being the largest tests to date using prototypic core materials, these two tests are expected to provide important validation data for heat transfer mechanisms involving high temperature oxides. The tests will also provide important data for evaluating the VANESA model of aerosol generation during core debris interactions with concrete. These tests will inductively heat 250 kg of 69 percent UO_2 - 22 percent ZrO_2 - 9 percent Zr over a 40-cm diameter concrete plug formed from either limestone concrete (SURC1) or basaltic (SURC2) concrete. Both the plug and the corium charge will be surrounded by a 10-cm thick MgO cylinder. The charge will be heated to the melting point and is expected to interact with and ablate the concrete plug for a duration of 20 to 60 minutes.

Pretest calculations were done for the SURC experimental matrix using the CORCON/VANESA severe accident analysis code. The concrete ablation rates for SURC are predicted to range from 15 to 120 cm/h, gas evolution rates are predicted to range from 50 to 250 L/min, and aerosol generation rates are predicted to range from 1 to 100 g/m^3. These calculations showed three things. First, that the SURC tests will exercise important heat transfer, gas chemistry, and aerosol release models in the CORCON/VANESA codes. Second, that the tests will be able to distinguish between competitive models currently under consideration for inclusion in CORCON and VANESA. Third, that significant and measurable variations in temperature response, gas chemistry, and aerosol release are predicted over the range of the experimental matrix. These results verify the geometry and instrumentation design for the SURC experiments, which have the stated goal of validating the heat transfer, gas chemistry, and aerosol release models used in the CORCON/VANESA code to analyze source terms resulting from ex-vessel/core-concrete interactions.

1.1.1 Preliminary CORCON Calculations for the QTB Experiment and Their Relationship to the SURC Pretest Calculations

The QTB experiment was a precursor to the SURC test series. QTB was designed in order to determine whether or not a UO_2-ZrO_2 mixture could be heated in place over a concrete plug and attack or erode the plug without loss of geometry or input power due to severe oxidation of the tungsten susceptor ring assembly. The test was done using a 30-kg charge of 69 percent UO_2 - 22 percent ZrO_2 - 9 percent Zr over a 20-cm diameter plug of limestone-common sand concrete. The plug and charge were surrounded by a 10-cm thick MgO cylinder or annulus. Instrumentation for the test consisted mainly of K-type thermocouples embedded both in the concrete plug and in the MgO walls. The test lasted 1 h at an average net power input of 30 kW.

During the first 30 min of the test, the tungsten susceptor assembly heated the simulated core debris to 2500°C and melted approximately 80 percent of the 30-kg charge. After 30 min, concrete ablation began. This attack lasted 30 min and ablated 10 cm of concrete. Power to the susceptors appeared to be constant. Posttest disassembly of the crucible showed that the tungsten rings were severely oxidized but still intact and functional, that roughly 10 to 12 cm of concrete had been eroded, and that the susceptor assembly had collapsed through the molten pool to a position within 2 cm of the melt-concrete interface.

Posttest analysis of the thermocouple data was done with CORCON. This anaysis will help validate the heat transfer models in CORCON and will provide boundary condition estimates for future analyses, such as the pretest calculations for the SURC test matrix.

The calculated results are similar to the pretest calculations for SURC1. This should not be too surprising since the melts in QTB and SURC1 are similar and thus the controlling influence in the SURC1 calculation, Zr oxidation, is also present in the QTB calculation. It is important to note that Zr oxidation has also been demonstrated as a controlling factor in ex-vessel aerosol and fission-product release in some severe accidents. This is especially true of accidents at BWR reactor plants that have high limestone reactor cavities.

The most significant differences between the SURC1 and QTB experiments are in their concrete types, specific power inputs, and geometries. The limestone-common sand concrete used in QTB has a lower gas content, lower ablation temperature, and lower enthalpy of ablation than the limestone concrete to be used in SURC1. These property differences

produce faster concrete ablation in the QTB calculation, which partially compensates for the lower gas content of the QTB concrete. The calculated gas fluxes for the two calculations are, therefore, very similar. The somewhat higher specific power input in QTB is partially compensated by the higher surface-to-volume ratio in QTB. Heat losses through the MgO sidewalls are assumed in the calculations to be 33 percent in QTB and 20 percent in SURC1. Generally, however, the similarities between the calculations indicate that experiment results from QTB should provide insight into what might be expected for the SURC1 test.

CORCON calculations are compared to QTB results for concrete ablation rate and melt temperature. The ablation rate is measured experimentally by thermocouple failure times, which in QTB were fairly distinct. Experimental melt temperature data is limited to a single pyrometer measurement. Unfortunately, the pyrometric data exhibited significant fluctuations during the period of concrete ablation, and therefore, only a qualitative comparison to the CORCON calculation is possible.

As in the SURC pretest calculations, the CORCON calculation for QTB demonstrates the importance of zirconium oxidation. During the 275 s in which Zr is oxidizing, ablation proceeds at greater than 2 cm/min. The melt temperature during this time is sustained at greater than 2400 K. When Zr oxidation is completed, the calculated melt temperature and ablation rate fall rapidly to steady state values of less than 1800 K and 0.5 cm/min.

In the QTB experiment, ablation proceeded rapidly for 7 min at an average rate of approximately 1 cm/min. After this time, ablation was much slower -- 0.2 to 0.4 cm/min. The pyrometric data is very erratic, but it appears to indicate a gradual decline in melt temperature to 1500°C (1770 K). This value is consistent with that calculated by CORCON.

Consider the qualitative similarities in behavior exhibited in the calculation and the experiment. In both cases, the initial period of extremely rapid ablation ends suddenly and is followed by a transition to a much slower ablation rate.

In the calculation, 9.3 cm of concrete is ablated during Zr oxidation. If the rapid ablation period in the experiment is assumed to be caused by Zr oxidation, between 7 and 8 cm are ablated during Zr oxidation in the experiment. This difference between the calculation and the experiment can be explained by considering preheating of the concrete and resulting gas release and Zr oxidation prior to the onset of ablation. The thermocouples in the concrete indicate that the surface of the concrete was heated to approximately

800°C prior to ablation while even at 4 cm into the concrete the temperature exceeded 150°C. From the measured temperature profile, the following is an estimate of gas release prior to ablation:

- o CO_2 released to 0.25 cm
- o Bound H_2O released to 1.25 cm
- o Free H_2O released to 4 cm

These (rough) estimates give gas release values of 6.9 g-mols of H_2O and 1.1 g-mols of CO_2. If this gas is assumed to react completely with Zr, 4 g-mols of Zr would be oxidized prior to the onset of ablation. This represents 16 percent of the initial Zr in the melt if we assume a 25-kg melt with 9 percent Zr. Reducing the 9.3 cm calculated by CORCON by 16 percent results in 7.8 cm of ablation required for complete Zr oxidation. This value is in the "ballpark" of the 7 to 8 cm of rapid ablation observed in the QTB experiment.

Unfortunately, since no gas composition data are available from QTB and the melt temperature results are somewhat unreliable, we cannot be certain that Zr oxidation produced the observed initial rapid ablation in the experiment. The gas composition and redundant temperature measurements in SURC1 should provide conclusive evidence of the influence of Zr oxidation on core debris-concrete interactions.

1.1.2 CORCON Pretest Calculations for SURC1 and SURC2

This summarizes the results from two recent CORCON pretest calculations for the first SURC experiments. The discussion outlines the preparation of the input to CORCON and then summarizes the most significant results from the calculations. More detailed results are presented in Tables 1.1-1 and 1.1-2 and Figures 1.1-1, -2, -3, and -4.

1.1.2.1 Preparation of the Input to CORCON

CORCON assumes that the cavity/crucible that the melt enters is composed entirely of concrete. Concrete ablation is, therefore, two-dimensional. The one-dimensional nature of the SURC experiments can be approximated by inputting an extremely large cavity radius (e.g., 10 m). This results in a bottom surface area that is much greater than the sidewall surface area. Sidewall melt-concrete interactions, therefore, have very little effect on the overall result. To maintain the same melt height as in the experiment configuration, the melt mass is scaled by the ratio of the bottom surface areas for the calculation and the experiment. The specific power input is also maintained in the calculation

Table 1.1-1

CORCON Results for SURC1 - Pretest
T_{melt} = 2850 K

Time (s)	Ablation Rate (cm/min)	Melt Temperature (K)	Gas Flow Rate (L/s)
0	2.00	2850	124
80	1.67	2722	102
160	1.44	2635	88
220	1.32	2586	79
230	1.30	2578	79
240	1.27	2565	79
360	0.77	2316	47
480	0.53	2169	32
600	0.39	2076	24
720	0.30	2012	19
840	0.25	1995	16
960	0.27	1989	15
1080	0.26	1982	15
1200	0.26	1976	15
1320	0.25	1970	15
1440	0.24	1965	15
1680	0.24	1959	14
1800	0.23	1954	14

Table 1.1-2

CORCON Results for SURC1 - Pretest
T_{melt} = 2750 K

Time (s)	Ablation Rate (cm/min)	Melt Temperature (K)	Gas Flow Rate (L/s)
0	0.12	2750	7.4
20	0.14	2761	8.7
40	0.18	2764	11.1
60	0.27	2762	16.7
70	0.45	2758	28
80	1.76	2744	109
100	1.46	2633	91
120	1.41	2613	87
180	1.19	2520	74
240	1.09	2477	68
300	1.02	2442	63
360	0.94	2406	58

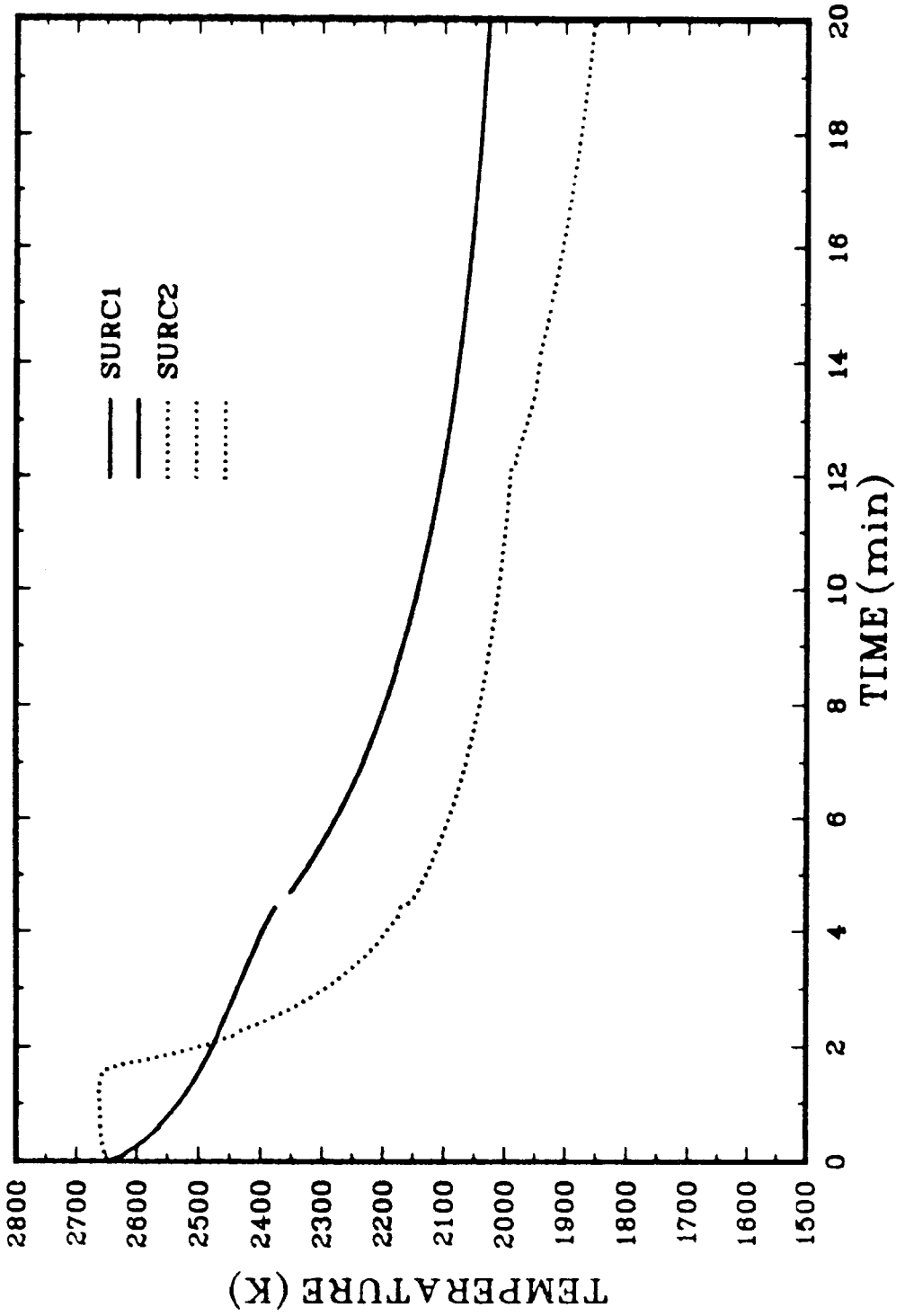

Figure 1.1-1. SURC1/2 Pretest Melt Temperature

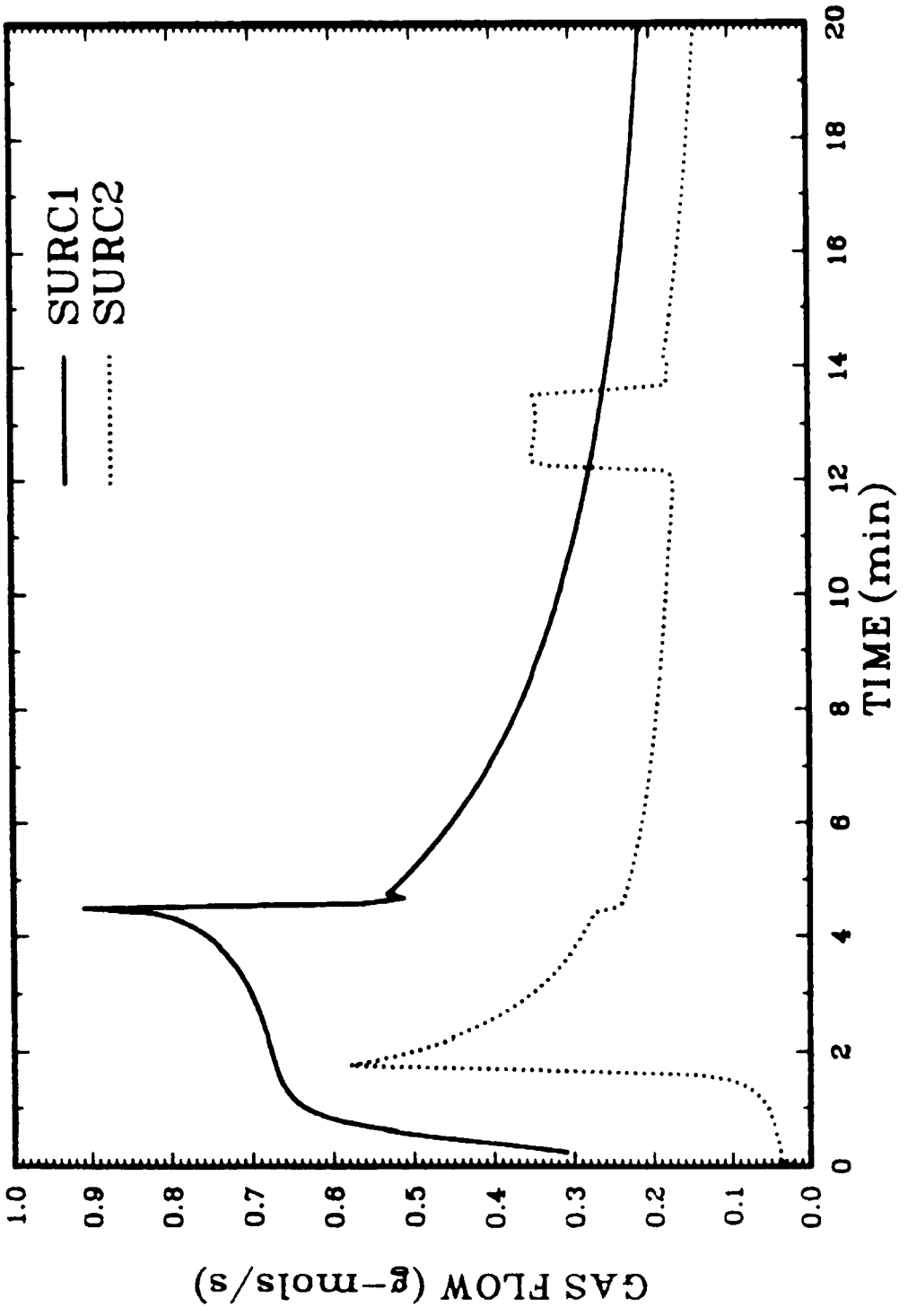

Figure 1.1-2. SURC1/2 Pretest Gas Flow

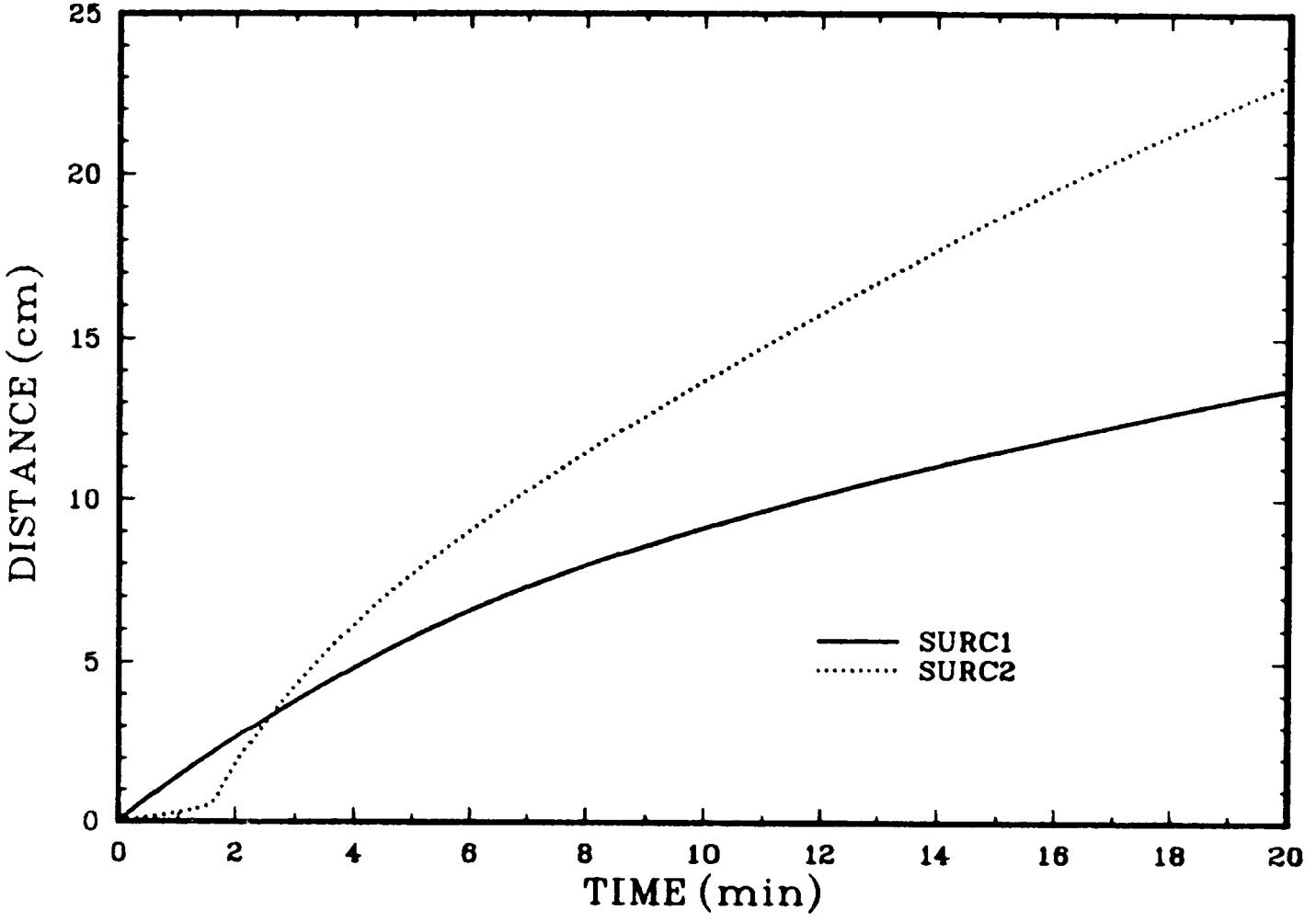

Figure 1.1-3. SURC1/2 Pretest Ablation Distance

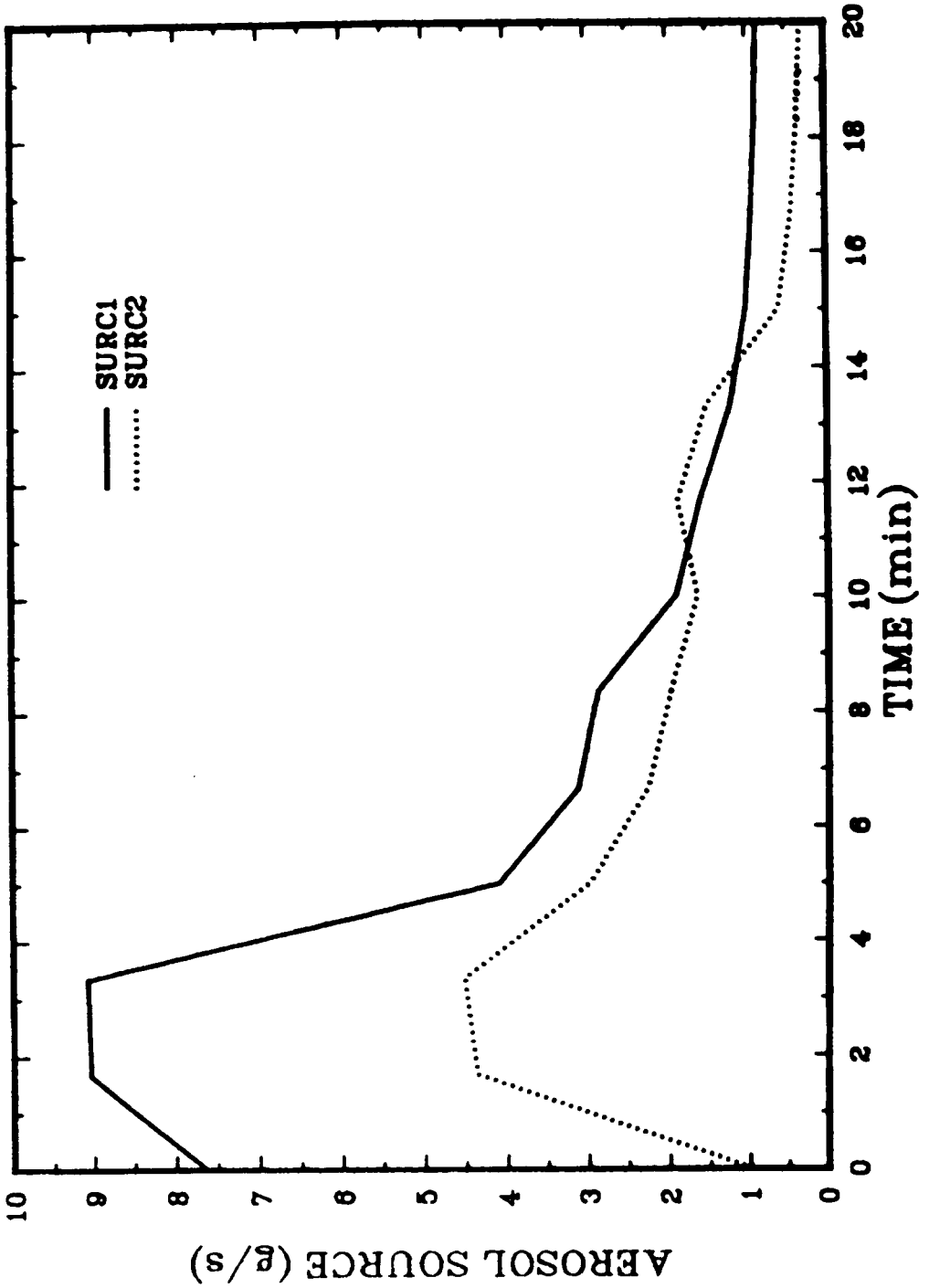

Figure 1.1-4. SURC1/2 Pretest Aerosol Source

by multiplying the experiment power input by this ratio. The power input to CORCON must also account for estimated sidewall heat losses since CORCON has no internal calculation of heat transfer to a nonablating sidewall. The predicted sidewall heat loss is subtracted from the input power, and it is this net power that is actually input to the CORCON code.

The two calculations presented here assume the following experiment conditions:

Total mass of melt:	110 kg
Composition of the melt:	64 percent UO_2, 27 percent ZrO_2, 9 percent Zr
Input power to the melt:	100 kW
Sidewall heat loss:	20 kW
Net power input:	80 kW

In the CORCON calculation all of the above quantities with the exception of the composition are scaled by multiplying by the area ratio (= 2500).

The calculations assume that the concrete used in the experiments is similar to the high limestone default concrete used in CORCON. An ablation temperature of 1780 K is assumed in the calculation. This temperature is approximately half of the way between the default liquidus and solidus temperatures for the high limestone concrete.

The calculation of radiative heat loss from the top surface of the melt requires specification of the temperature and emissivity of the surrounding surfaces. In the present calculations, the surface emissivity and temperature are assumed to be 0.9 and 1000 K, respectively.

The only significant code input that remains to be discussed is the initial melt temperature. Pretest calculations were performed for two different melt temperatures: one just above the liquidus temperature for the oxidic debris and one just below the solidus of the debris. For the first calculation, an initial temperature of 2850 K was chosen. This value is 15 K above the liquidus of the oxidic debris. The second calculation used 2750 K, which is 80 K below the solidus temperature of the debris. This calculation was performed to simulate the initial crusting behavior that was observed in the TURC2 and TURC3 experiments. Similar crusting should occur in SURC1 if the concrete is not significantly heated prior to penetration of the melt through the zirconia board.

1.1.2.2 Results From the CORCON Pretest Calculations

Table 1.1-1 presents the CORCON results for the pretest calculation which used the higher initial melt temperature.

In this calculation, no initial crusting was calculated and ablation proceeded at an initially rapid rate. The resulting large gas flow through the melt produced rapid Zr oxidation. The chemical reaction energy source during this period was 2 to 3.5 times greater than the net power input. This additional energy source allowed the temperature of the melt to remain elevated even though the ablation rate (i.e., heat transfer to the concrete) also remained high. While the Zr was oxidizing, CORCON predicted almost complete reduction of CO_2 and H_2O to CO and H_2. Zirconium oxidation was completed at approximately 4 min. Subsequently, the ablation rate and melt temperature fell rapidly to much lower steady state values. Since no metal was left in the melt, CORCON predicted no reduction of the CO_2 and H_2O released from the concrete. These results are summarized below:

- Calculation 1: T_{melt} = 2850 K

  Initial ablation rate: 2 cm/min

  Steady state during Zr oxidation:
  - Ablation rate: 1.3 cm/min
  - Melt temperature: 2600 K
  - Gas flow rate: 80 L/s at 1350 K
  - CO/CO_2 ratio: 5 to 10:1
  - H_2/H_2O ratio: 1 to 5:1

  Zr oxidation completed at 230 to 240 s

  New steady state at 720 s:
  - Ablation rate: 0.25 cm/min
  - Melt temperature: 1975 K
  - Gas flow rate: 15 L/s at 1350 K

Table 1.1-2 presents the early time results from the lower temperature calculation. As expected, the oxidic material is initially solidified and the ablation rate is, therefore, very low. CORCON assumes that the gases released during ablation pass through the debris regardless of whether it is solidified or not. It, therefore, calculates almost complete reduction of the released H_2O and CO_2 by the Zr in the debris. Complete melting of the oxidic material occurs at approximately 80 s and the interaction subsequently continues in a manner similar to that in the preceding calculation. These results are summarized below:

- Calculation 2: T_{melt} = 2750 K

  Initial ablation rate: 0.12 cm/min

  Ablation rate just prior to remelt: 0.45 cm/min

  Gas flow rate: 7 to 27 L/s at 1350 K

Remelt occurs at 70 to 80 s.

Subsequent behavior similar to Calculation 1 with times shifted by 100 s.

It should be noted that the quasi-steady ablation model in CORCON is not accurate for the initial transient hot solid-concrete interaction in this calculation. In this type of interaction, a significant fraction of the energy transferred to the concrete is conducted away from the surface and is not available for ablation. Energy conducted into subsurface concrete produces dehydration and decorboxylation of the concrete well in advance of the ablation front. The net result of this is that CORCON overestimates the concrete ablation rate while it may underestimate the gas release from the concrete. The calculated ablation and gas release rates should, however, be within a factor of 2 of the correct values.

1.2 High-Pressure Melt Ejection and Direct Containment Heating

(W. W. Tarbell and J. E. Brockmann, 6422; M. Pilch 6425)

Severe reactor accidents may involve degradation of the core while the reactor coolant system (RCS) remains pressurized. Experiments and analyses have indicated that the ejection of core debris into the reactor cavity may result in the molten material being lofted into the containment atmosphere. Transfer of chemical and thermal energy from the debris could cause heating and pressurizing of the containment atmosphere. If the energy transfer processes are efficient, only a fraction of the total core mass would be sufficient to threaten the integrity of some containment structures.[3] Containment response codes are under development to aid in the resolution of the safety issues associated with high pressure ejection of core debris and direct heating of the containment atmosphere.

The SURTSEY Direct Heating Test Facility has been designed and constructed to perform experiments where molten debris is ejected into a well defined and contained atmosphere. The size of the facility allows the use of realistically scaled cavity and containment models. The SURTSEY test chamber permits direct measurement of the pressure and temperature increases caused by the dispersal of debris from the cavity. The chamber also enables the debris and aerosol material to be sampled and recovered.

The DCH-1 test described here was the first experiment performed in the SURTSEY facility. It involved 20 kg of molten material ejected into a 1:10 linear scale model of the Zion reactor cavity. This report gives a description of the test apparatus, initial conditions, test observations

from camera records and visual inspections, and results from pressure, temperature, and aerosol measurements.

1.2.1 Test Apparatus

A schematic of the SURTSEY facility is shown in Figure 1.2-1. It consists of a pressure vessel (4 m in diameter by 12 m tall) oriented vertically with the lower head flange approximately 2 m above the concrete pad. A 1:10 linear scale model of the Zion cavity was placed in the vessel so that the floor of the cavity was at the elevation of the lower head-to-shell weld line (elevation 2.45 m). The cavity exit was located on the vertical centerline of the vessel. The concrete lined cavity was modified by the addition of a 0.36 x 0.36 x 0.9-m-tall steel "chute" attached to the exit of the cavity. The purpose of the chute was to direct the dispersed debris vertically upward to avoid ablation of the SURTSEY steel shell. The chute terminated approximately 2 m above the floor of the cavity (elevation 4.35 m). The molten material was produced in a melt generator attached to the cavity at the scaled height of the reactor pressure vessel (RPV). The annular gap around the RPV was not simulated.

The chamber and cavity were instrumented with the devices described in Table 1.2-1. The emphasis of the instrumentation was to quantify the pressure increase caused by the dispersed debris and to assess the generation of aerosol. The extensive aerosol instrumentation was designed to measure the mass concentration, size and number distributions, chemical content, and dynamic shape factors.

The six pressure transducers and three thermocouples that measured the chamber atmosphere were located in 12-inch flanged penetrations in the vessel sidewall (at elevations 3.36, 5.8, and 8.24 m). The pressure sensors were placed in tapped holes in the steel flange cover so that the sensing element was slightly recessed in a cavity (approximately 1-cm in diameter by 2.5 cm deep). The cavity was filled with stainless steel turnings to provide protection against debris particles in the atmosphere. This arrangement placed the sensing element nominally 30 cm outboard from the shell surface. The 1/16-inch-diameter sheathed thermocouples were inserted in 1.4-inch-diameter tubing to reduce their flexibility. The exposed sensing junction was located approximately 15 cm inward from the vessel sidewall.

The pressure and temperature gauges placed in the melt generator measured the condition of the gas in the free volume above the molten pool. The devices recorded the initial conditions prior to the start of the test, the change that occurred during the thermite reaction, and the blowdown of the gas following failure of the fusible plug.

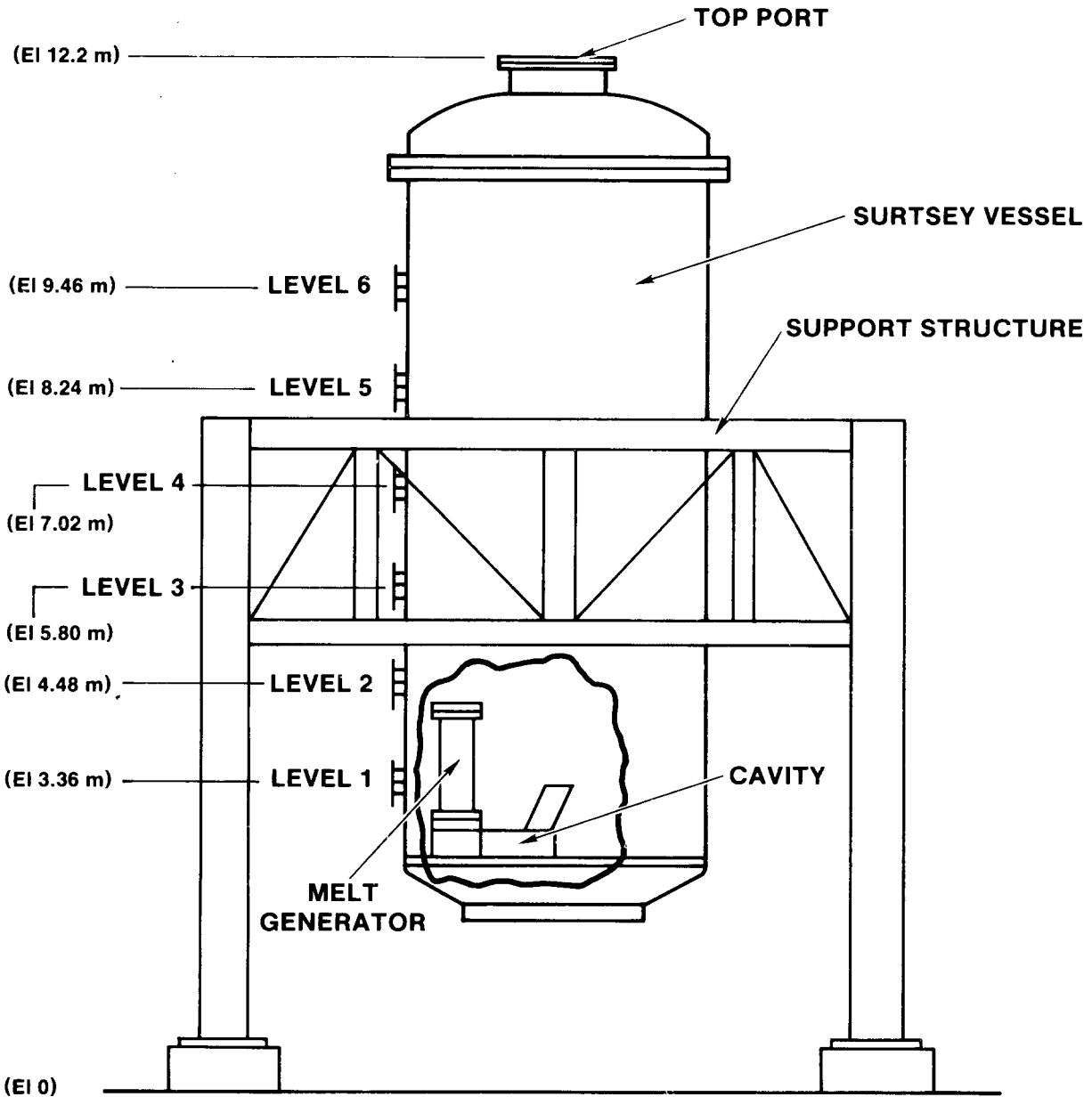

Figure 1.2-1. Schematic of DCH-1 Apparatus in the SURTSEY Direct Heating Test Facility

Table 1.2-1

DCH-1 Instrumentation

Device	Location	Range	Remark
Pressure gauge	Melt gen	1000 psig	Driving pressure
Bourdon gauge	Flange N-1[a]	100 psig	Chamber pressure
Pressure gauge	Flange S-1 (2 ea)	100 psig	Chamber pressure
Pressure gauge	Flange S-3 (2 ea)	100 psig	Chamber pressure
Pressure gauge	Flange S-5 (2 ea)	100 psig	Chamber pressure
Thermocouple	Melt gen	1400 K	Gas temperature
Thermocouple	Flange S-1	1400 K	Chamber temperature
Thermocouple	Flange S-3	1400 K	Chamber temperature
Thermocouple	Flange S-5	1400 K	Chamber temperature
Camera	Flange S-2	200 fps	Chamber observation
Camera	Top flange	200 fps	Chamber observation
TV camera	Flange S-2 & top flange	30 hz	Chamber observation
Filter samples	Flanges E-2 & E-4 (6 ea)	-	Aerosol mass concentration
Impactors	Flanges E-2 & E-4 (4 ea)	$\leq$10 μm	Size distribution
Cascade cyclone	Flange E-4	-	Size segregated bulk aerosol
Aerodynamic particle sizer	Flange E-5	-	Real-time particle size
Photometer	Flange E-4	-	Real-time mass concentration
Gas samples	Flange E-1	-	Chamber gas composition

[a]Flange locations: N - north, S - south, E - east, W - west; elevations: 1 @3.36 m, 2 @4.58 m, 3 @5.80 m, 4 @7.02 m, 5 @8.24 m. For example: S-1 is a south facing flange at elevation 3.36 m.

The two-color (λ = 0.7 and 1.05 μm) pyrometer was focused just above the exit of the chute to detect the temperature of the ejected debris. The device was placed outside the chamber behind a clear optical (Plexiglas) port cover. The Plexiglas had only a slight attenuation of light at the two operating frequencies and did not affect the results because the pyrometer evaluated the ratio between the two emittances. A high-speed motion picture camera was also positioned at this location and on the top port located on the upper head.

The aerosol devices were placed into large diameter steel pipes (flanges E-2 and E-4) so that the sampling location was near the vertical centerline of the vessel. The pipes protected the wiring and tubing connected to the devices.

1.2.2 Test Conditions

The initial conditions for the DCH-1 test are summarized in Table 1.2-2. The products of the thermite reaction simulated the predicted characteristics of core debris during this accident sequence. The melt was composed of both metallic (Fe) and ceramic (Al_2O_3) constituents, at estimated temperatures of 2100° to 2500°C. The 20-kg melt mass was less than the 80-kg quantity used on previous HIPS tests[4] to reduce the extent of direct atmosphere heating to a level known to be within the capacity of the SURTSEY vessel. The reduced melt quantity also provided information regarding the effect of mass scaling on the direct heating of the atmosphere. The weight fractions stated in the table have been corrected to include the materials placed in the melt to study the behavior of fission products (dopants). Dopants were selected to simulate the chemical behavior of the principal radionuclide groups. The gas volume of the melt generator was larger than in previous tests because of the reduced mass occupied by the thermite. The volume indicated was approximately one-third the value of a 1:10 linear scaling of the Zion RCS.

The dopants placed in the melt were designed to simulate the chemical behavior of several classes of radionuclides. The mass of these simulants was limited to less than 5 percent of the total quantity of melt in order to prevent significant depression of the temperature achieved during the reaction. The mass of the brass fusible plug (292 g) also contributed about 1.5 w/o of copper and 0.8 w/o of zinc to the initial mass of the melt.

1.2.3 Test Observations

The principal real time test observations were obtained by three TV cameras. One camera viewed the overall apparatus from a distance of approximately 70 m, a second was located

on the top flange of the SURTSEY vessel for an internal observation, and the third camera was focused on the large-face Bourdon tube gauge that measured chamber pressure. The first two cameras were intended primarily for observation to insure safe operation during the experiment. The third device gave an immediate indication of the pressure within the chamber although the response of the gauge was assumed to be too slow to accurately determine the transient pressure pulse.

Table 1.2-2

DCH-1 Initial Conditions

Melt mass	20 kg
Thermite composition	Iron oxide (Fe_3O_4) 73.7 w/o plus aluminum (Al) 22.9 w/o
Melt composition	Iron (Fe) 53.3 w/o plus alumina (Al_2O_3) 43.3 w/o
Dopants (674 g total)	Lanthanum oxide (La_2O_3) - 118 g Barium molybdate ($BaMoO_4$) - 313 g Niobium pentoxide (Nb_2O_5) - 143 g Nickel (Ni) - 100 g
Ambient temperature	26°C
Ambient pressure	12 psia (0.083 MPa)
Driving gas	Dry bottled nitrogen (N_2)
Melt generator gas volume	0.109 m^3
Initial gas pressure	270 psig (1.86 MPa)
Fusible plug diameter	4.8 cm

Upon ejection of the melt into the atmosphere of the vessel, the top-mounted camera recorded a brilliant flash that lasted several seconds. This was quickly followed by virtually total darkness within the chamber. In the same time frame, the Bourdon tube gauge was observed to rapidly increase to a value of approximately 15 psig before decaying to around 2 to 3 psig. No observable changes were detected with the overall camera.

When the chamber pressure stabilized at nominally 1 psig, experimenters investigated the facility to assess possible damage. No obvious damage was detected. It was observed through an optical port that the chamber was filled with suspended aerosol particles that appeared to move in random directions. Most of the upward facing horizontal surfaces

in the chamber were covered with a thick layer (~1 mm) of light-brown particulate. Aerosol was also detected in the dilution box used in conjunction with the aerodynamic particle sizer (APS) system.

When the chamber was opened the day following the test, the presence of the thick aerosol layer was confirmed. All exposed horizontal surfaces were heavily covered with fine, loose particulate material. The vertical shell wall and the underside of the top head also displayed a coating of fine particles. A few large globules of frozen melt (several centimeters in mean dimension) were seen atop the cavity apparatus, but not anywhere else in the chamber. A thin layer of melt was found attached to the underside of the aerosol pipe enclosure at level 4 and on one side of the top head. Debris particles were observed on horizontal surfaces and the floor among the settled aerosol.

1.2.4 Test Results

All of the recorded data were affected by electrical noise caused by ground loop currents circulating in the steel vessel. These records have been digitally filtered where necessary to remove the noise.

The melt generator pressure record is given in Figure 1.2-2. The record was from 20 s prior to melt ejection (zero time) to 10 s afterwards. The determination of the actual zero time was difficult because the optical probe placed on the fusible plug did not function. Zero time was established for the plots as the point in time where pressure first began to decrease.

Based on the recorded pressure, the total thermite reaction time was somewhat less than 8 s. Considering the reduced height of the thermite bed relative to the previous HIPS experiments,[4] the reaction rate was comparable. The "dip" in the pressure record just after ignition was not expected and had not been observed in any previous test. Inspection of the melt generator thermocouple record showed a similar, but inverted, pulse occurring at the same time. This behavior suggested electrical interference as the cause of the anomaly. The other gauge records also indicated the same effect, although much less pronounced.

The influence of the electrical interference on the remainder of the melt generator pressure record is not known. The thermocouple and other pressure gauges returned to the pretransient state following the duration of the interference (on the order of 1.6 s). For this reason, the recorded peak pressure and blowdown history are believed accurate. The pressure at the time of ejection was 370 psig (2.55 MPa), representing a 37 percent increase caused by the

heat from the thermite reaction. This value was less than anticipated because the larger gas volume caused a proportionate decrease in the heating of the gas and the release of gaseous reaction byproducts.

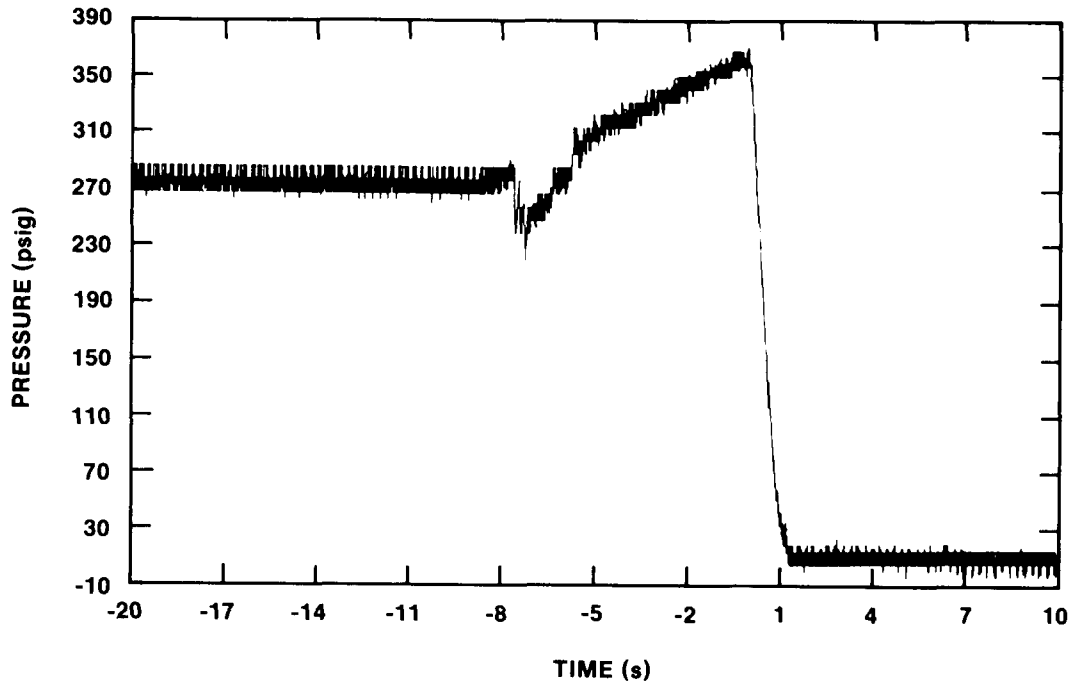

Figure 1.2-2. Melt Generator Pressurization History

The recorded debris temperature obtained with the two-color pyrometer is given in Figure 1.2-3. The plot shows an initial increase in temperature prior to the zero time established by the pressure record. This indicated that the debris dispersal occurred prior to a detectable drop in the melt generator pressure. The temperature record yielded a debris ejection interval on the order of 1.1 s with a peak temperature approaching 2000°C recorded at 0.1 s. The two records on the plot indicate the data as recorded and corrected for the influence of the acrylic port window. The correction factor was determined by calibrating the pyrometer with and without the window in place. The slightly nonlinear correction function caused the recorded temperatures to be reduced approximately 50°C. The measured temperatures in this experiment were slightly less than recorded in previous HIPS tests.[4] Some additional heat loss may have been incurred by the longer path length with the addition of the chute.

Two pressure gauges and one thermocouple were placed in each of three ports on the shell portion of the SURTSEY vessel.

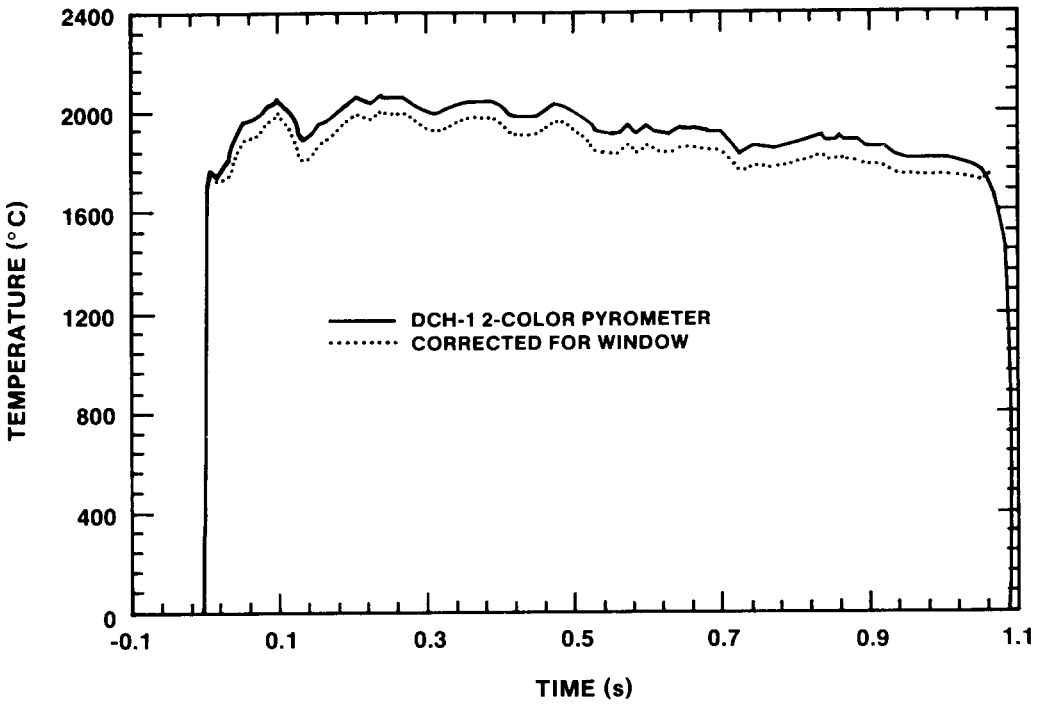

Figure 1.2-3. DCH-1 Measured Debris Temperature

The locations were commonly referred to as bottom, middle, and top to identify levels 1, 3, and 5, respectively. The recorded pressure histories for each pair of the six gauges are given in Figure 1.2-4. The best estimate of the peak pressure from each plot range from 13.4 to 19.4 psig (0.09 to 0.13 MPa). These values were obtained using the manufacturer's stated sensitivity for the individual gauges. The calibration was checked following the experiment and the deviation was less than 1 percent for all gauges.

Most of the gauge records demonstrated a pronounced degree of electrical interference, both before and after the pressure transient. The decay portion of the curves showed a cyclic pattern characteristic of several different frequencies forming harmonic behavior. The range of the frequencies was too high to be a mechanical phenomena such as vibration of the vessel.

All of the plots were characterized by a rapid increase in pressure (80 to 90 percent of the peak value in about 1 s) with the peak value occurring at nominally 3 s. Following this, the decay in pressure (without the interference pattern) was virtually exponential in form. Based on this assumption, an estimated time constant was found for each record. The values show that the apparent decay time constant was on the order of 30 to 40 s. This range was at

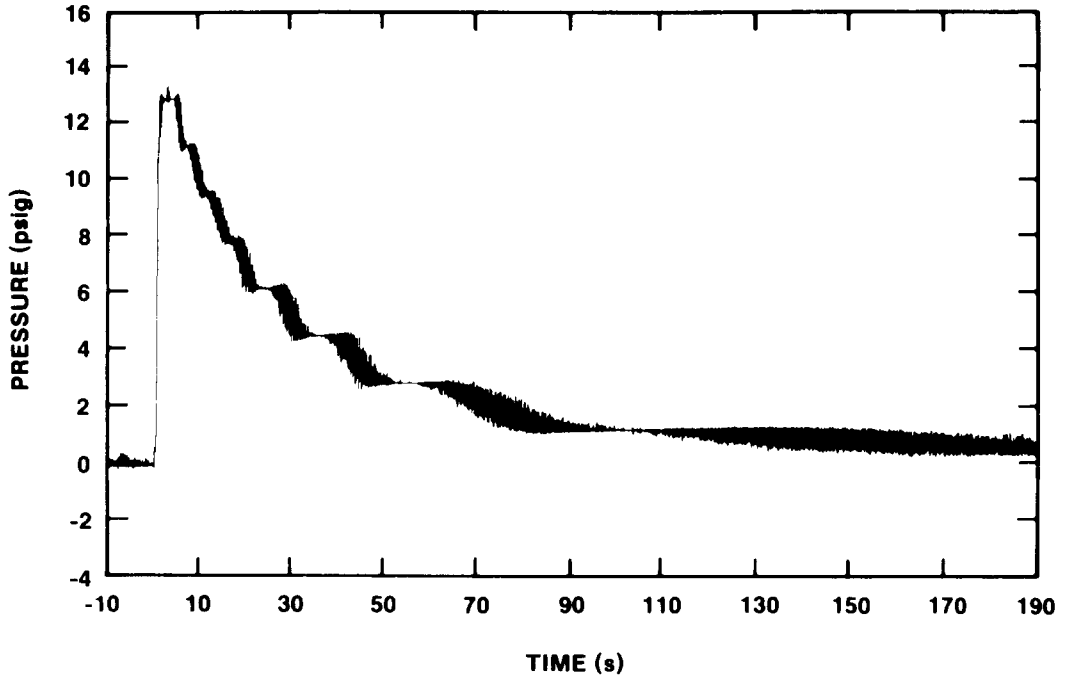

a. Gauge P-2

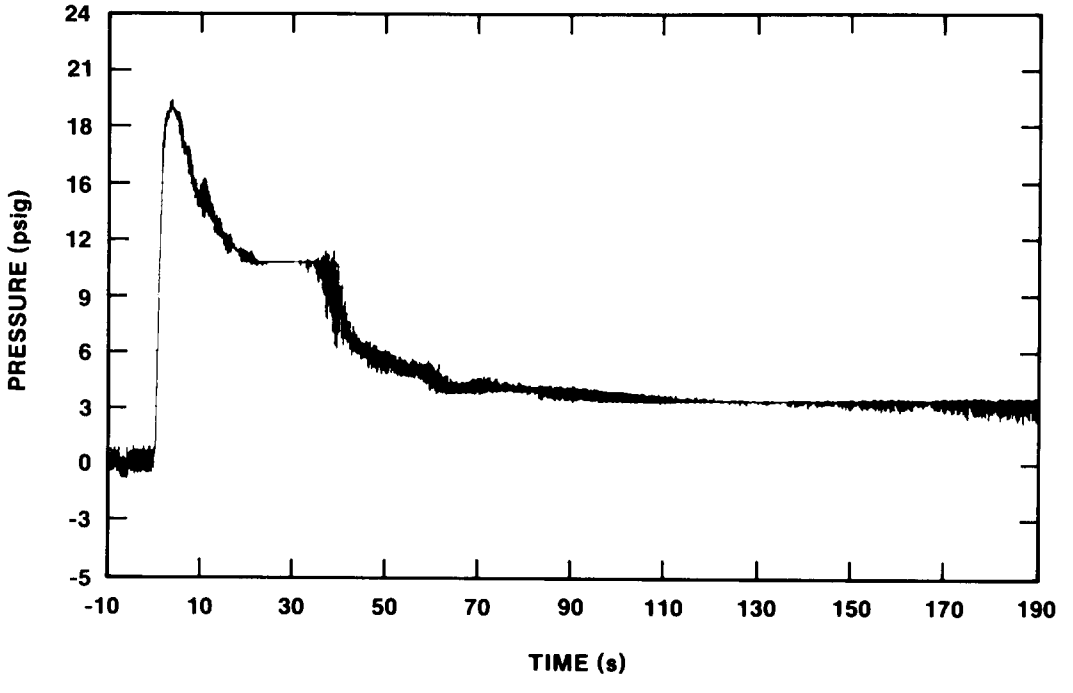

b. Gauge P-3

Figure 1.2-4. SURTSEY Chamber Pressure

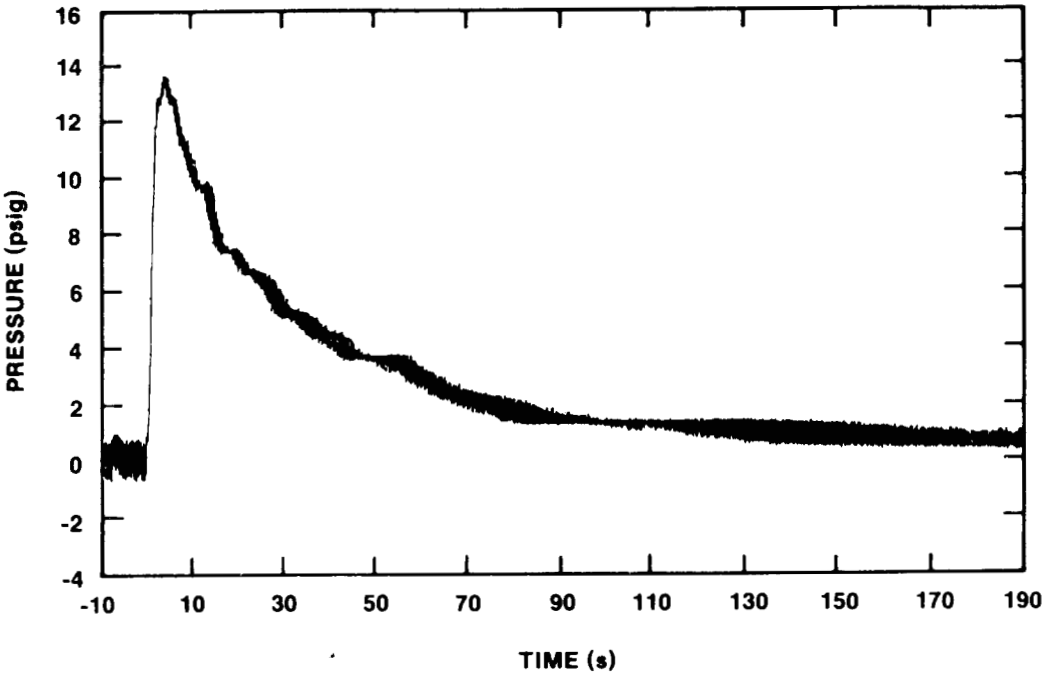

c. Gauge P-4

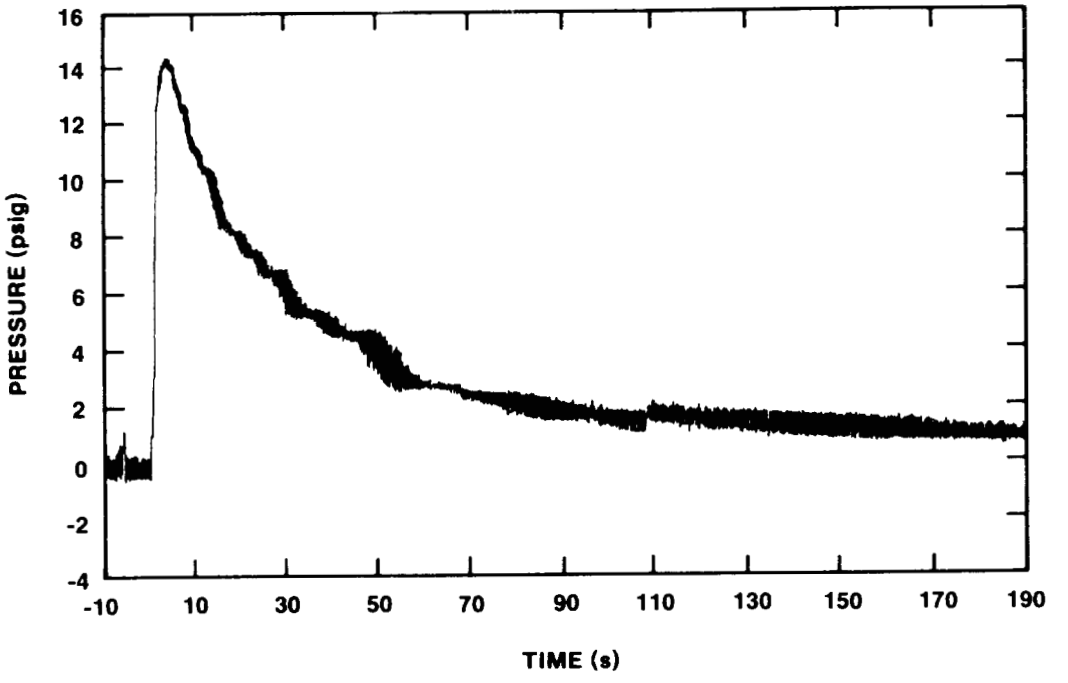

d. Gauge P-5

Figure 1.2-4. (continued)

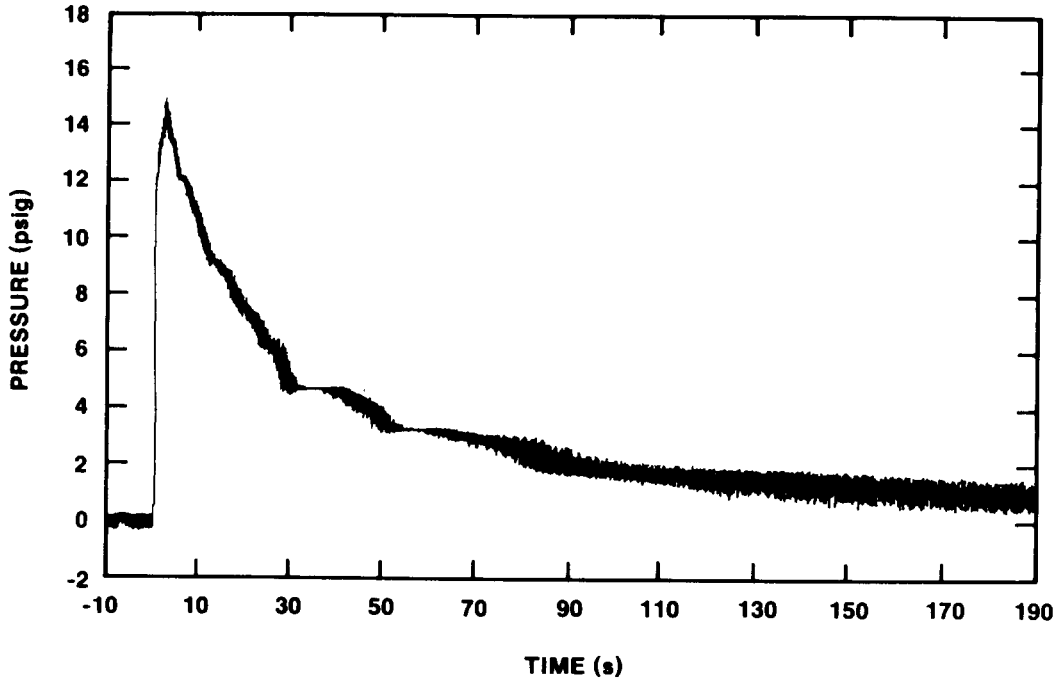

e. Gauge P-6

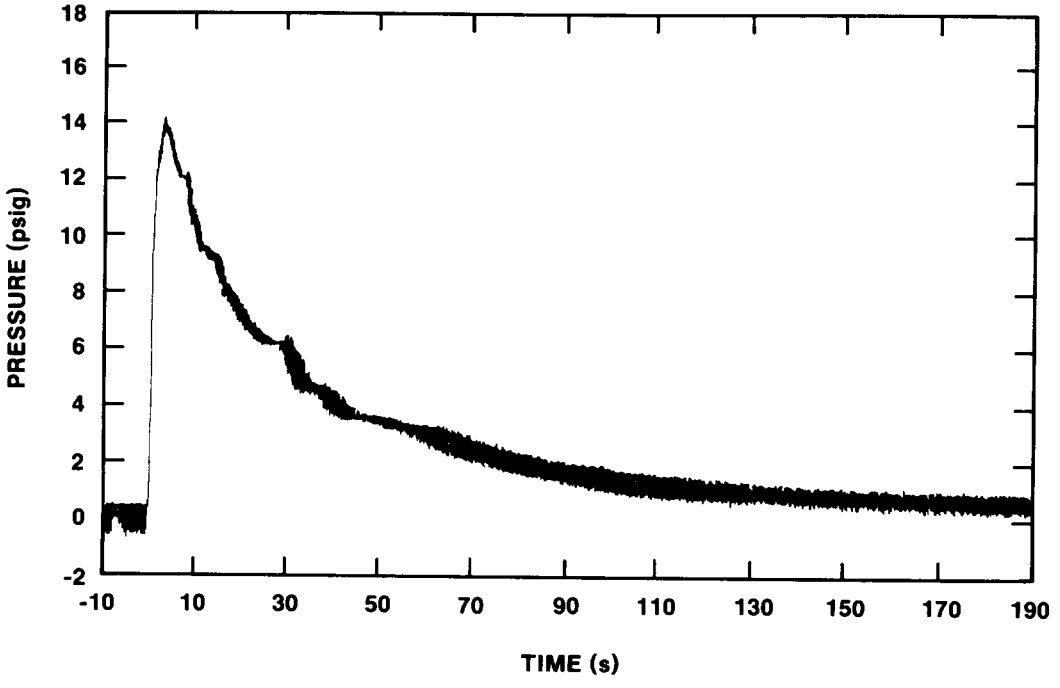

f. Gauge P-7

Figure 1.2-4. (continued)

least 10 times shorter than the leak rate of the chamber, which was determined prior to the test.

The pressure data from gauges P-2 and P-3 represent the low and high values, respectively, for all the devices. These gauges were placed approximately 5 cm apart on the same port. This location placed these gauges closest to the debris source. Despite the protection used with the pressure transducers, exposure of the sensing element to elevated temperature material may have induced ambiguous response.

The temperature histories recorded by the three thermocouples were very inconsistent and did not correspond to the recorded pressure. The bottom and middle sensors recorded temperature changes that were very low, while the top device was significantly higher. Likewise, the time constant for decay to 1/e of the peak value also varied considerably. The erratic behavior was attributed to deposition of debris and aerosol that affected the behavior of the devices. The data were not considered representative of the actual behavior of the gas in the chamber.

All relocated debris material was collected by vacuuming the inside of the chamber, both the floor and walls. A fine particulate filter element on the unit allowed all but the smallest material (<20 μm in diameter) to be retained. Material was also collected from the surfaces within the chamber that exhibited a crust layer, i.e., the undersides of the aerosol pipe devices and the upper head. The crust on the top head was difficult to remove because it was thin (~1 mm) and tightly bonded to the metallic surface.

After collection, the debris was weighed and mechanically sieved to determine particle size distribution. A Rotap 60 Automatic Sifter was employed with seven separate mesh sizes. The debris removed from the underside of the top head and the aerosol from the filters and impactors were not included in the sieve analysis. The results of the sieving are given in Table 1.2-3 and Figure 1.2-5. Data previously obtained from the SPIT-18 and SPIT-19 experiments[4] are also compared in the figure. The results suggest that the debris size distribution was nearly lognormal and intermediate between the two past data sets. The slight deviation from lognormal at the smallest size range reflects the improved collection efficiency afforded by the SURTSEY chamber. The calculated mass mean size was 0.55 mm with a geometric standard deviation of 4.2.

The total mass collected from the chamber yielded the amount of material dispersed from the cavity. Further, material retained within the cavity and melt generator was also evaluated to yield an overall mass balance. These results are summarized in Table 1.2-4.

Table 1.2-3

Debris Sieve Results

Sieve Size (mm)	Debris Mass (g)	(%)
> 2.38	1504	15.2
1.60-2.38	823	8.3
0.85-1.60	1559	15.7
0.417-0.85	1989	20.1
0.105-0.417	2973	30.0
0.075-0.105	397	4.0
0.053-0.075	215	2.2
< 0.053	446	4.5
Total	9906	100.0

The material taken from the cavity and chute was in the form of a crust layer, except for the single large mass found on the floor of the cavity at the base of the inclined shaft. The crust thickness averaged 2 to 3 mm where it was attached to the concrete sidewalls or floor. It had the appearance of a very dense material with little observable porosity. Some concrete was adhered to the crust layer and could not be removed. The crust in the steel chute was thinner, 1 to 2 mm, and was also very dense, but with some large embedded globules. The pattern of the crust matched the angle of inclination of the shaft with very little detectable lateral spreading of the debris stream. Close inspection indicated that the crust in both the cavity and chute was made of fine particles tightly bonded together.

Some areas within the cavity (primarily on the floor) showed a second crust layer atop the first. This second layer was much more porous than the underlying material and had a smooth upper surface. The large mass at the base of the shaft was also of this form. This material has been identified as melt that was not entrained by the gas blowdown. The large mass at the base of the inclined tunnel was probably from a film of material that was not carried out of the cavity. Because the melt alone did not propagate at high velocity, it could not escape the cavity under its own momentum. The large pores were developed as the heat from the debris decomposed the underlying concrete (chemically bound water was released but melting did not occur), causing gas to escape up through the soldifying mass.

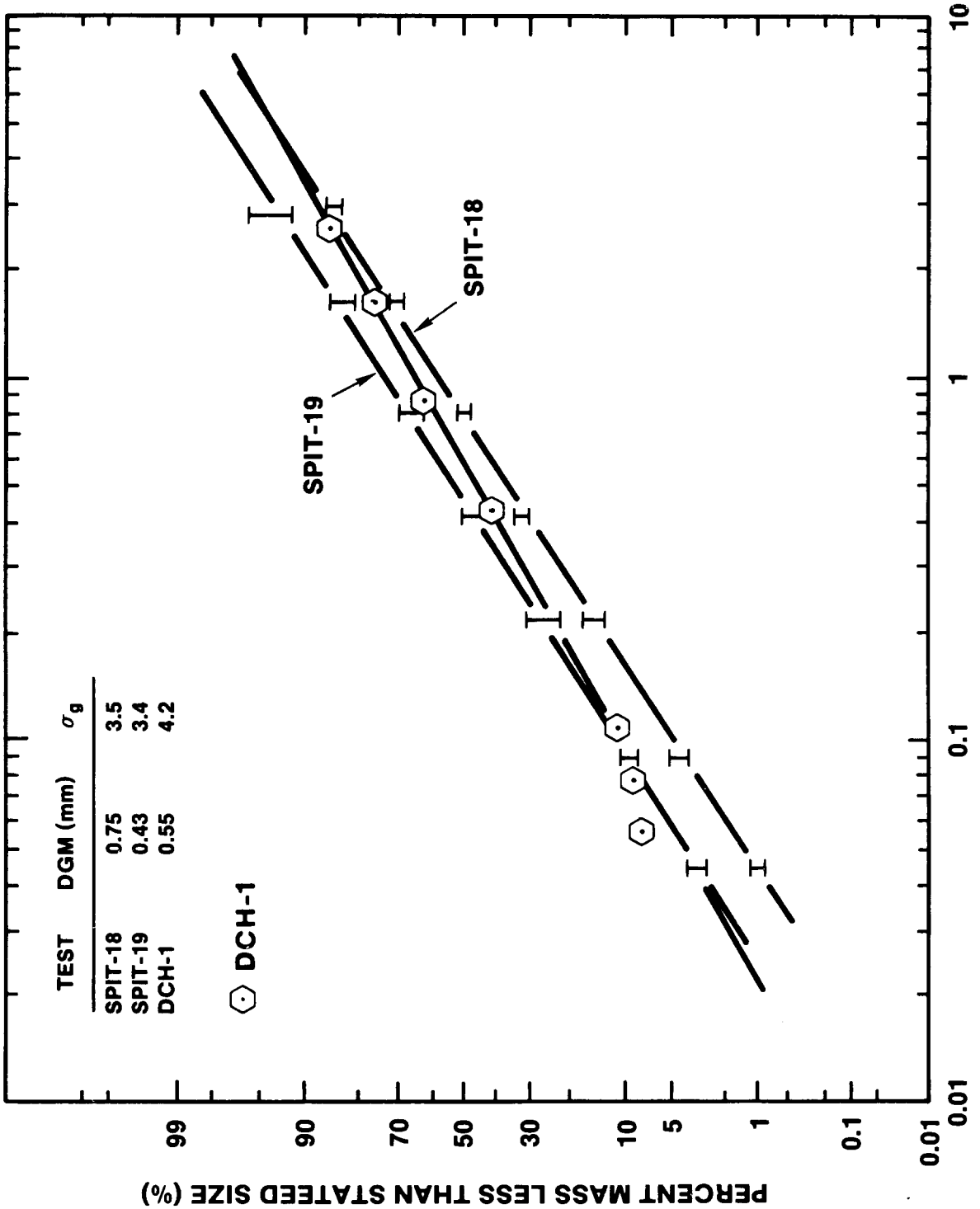

Figure 1.2-5. Debris Size Distribution From the DCH-1, SPIT-18, and SPIT-19 Tests

Table 1.2-4

Debris Mass Balance

Location	Mass (kg)
Chamber walls and floor	10.168
Underside of top head	1.462
(a) Total dispersed	11.620
Cavity and chute	7.963
Floor of cavity at inclined tunnel (single mass)	1.177
Melt generator lower flange	0.507
(b) Total in apparatus	8.647
Total mass (a + b)	21.277

The total mass of debris collected was greater than the initial mass of the thermite charge. The principal factor contributing to the increased mass was the uptake of oxygen by the metallic constituent of the debris. It is assumed that all of the aluminum oxidation (to Al_2O_3) occurred within the melt generator and all of the iron was oxidized to iron-oxide (Fe_2O_3) in the chamber. Based on this, it was estimated that 9.97 kg of debris was dispersed from the cavity. This represents an increase of 1.65 kg due to the oxidation of the iron (from 20 v/o to 18.4 v/o in the chamber). Subtracting this amount from the total in Table 1.2-4 yields a value slightly less than the original thermite mass plus brass plug (20 + 0.29 kg). Several factors may contribute to the potential error in the mass balance:

1. Some concrete residue was adhered to the debris collected from the cavity.

2. Small amounts of steel from the melt generator apparatus were ablated and discharged during the discharge process.

3. The iron bearing particles may not have been completely oxidized during the experiment.

The material recovered from the chamber was studied at high magnification to determine the geometric character of the debris. Table 1.2-5 gives a brief qualitative description of four different size groupings. Figure 1.2-6 shows photographs of the same four groupings.

Table 1.2-5

Qualitative Appearance of Collected Debris

Size (mm)	Description
>2.38	Mostly large agglomerates (>1 mm) with rough exterior appearance, some shrink holes, other very irregular shapes, and some smooth spheres.
1.6-2.38	Irregular agglomerates (~1 mm) of smaller particles, some irregular shapes with smooth external surfaces, some spheres with shrink holes and some with small particles attached.
0.85-1.60	Similar to above except more spheres present, spheres differ in diameter throughout the size range.
0.417-0.85	Almost totally composed of spheres and small irregular (angular) shapes, shrink holes obvious in many spheres.

Shrink holes were formed in the particles because of the manner that the liquid drops cooled in the atmosphere. Heat transfer from the drop caused a solid outer surface to form followed by cooling of the center portion. As the center of the drop lost heat, a large contraction occurred and the ensuing stress in the outer shell was relieved by the initiation of a fissure. The irregular shapes were attributed to some mechanical formation process such as cracking of larger solid particles.

The composition of the chamber atmosphere was ascertained before and after debris dispersal to determine the oxygen consumed by the metallic melt particles. Each sample bottle withdrew 75 mL through a small steel tube inserted into the chamber. Cycling time was determined by the valve actuation interval, or approximately 3 to 5 s per sample. Gas chromatography was used following the test to determine the chemical species of the sample. Figure 1.2-7 shows the oxygen concentration (volume percent) versus the time the

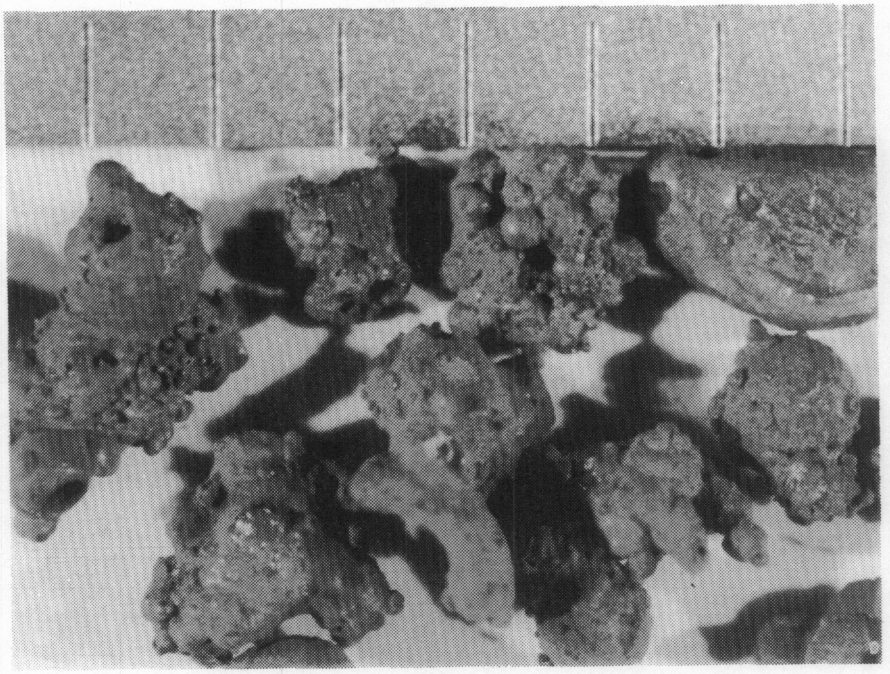

a. >2.38 mm

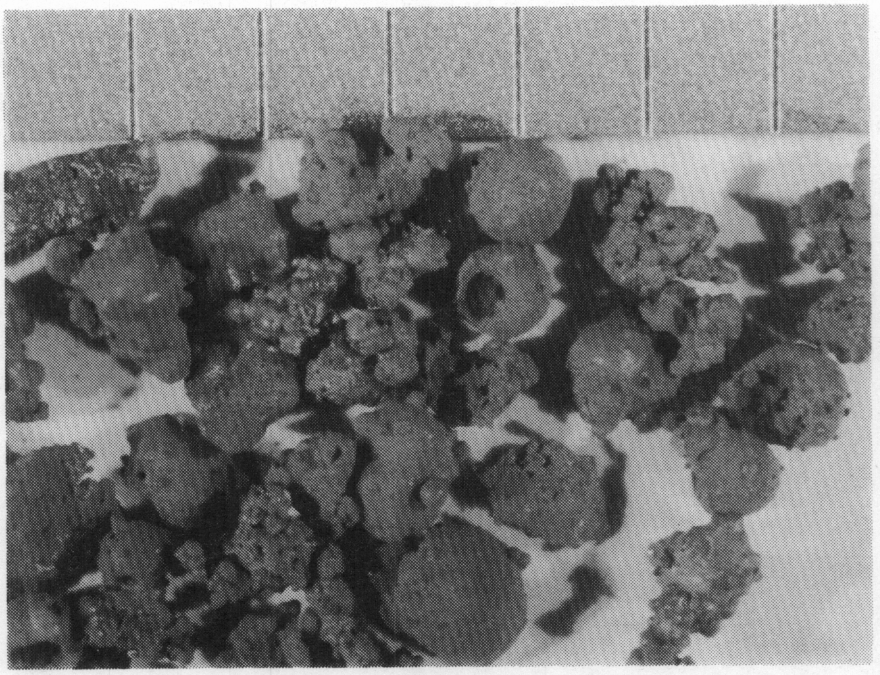

b. 1.6 - 2.38 mm

Figure 1.2-6. Photographs of Collected Debris From the DCH-1 Experiment. Scale marking is 1 mm.

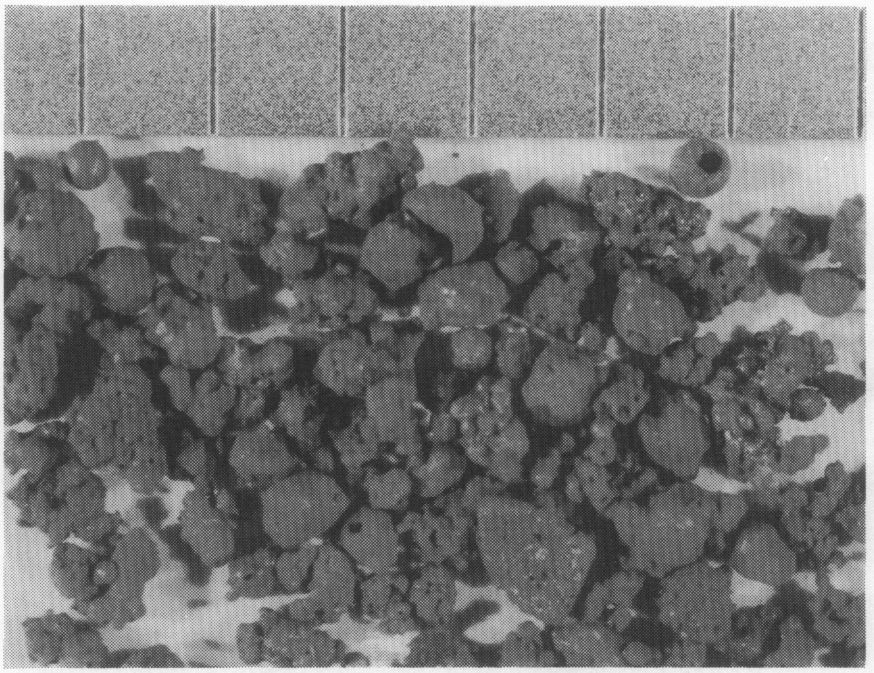

c. 0.85 - 1.6 mm

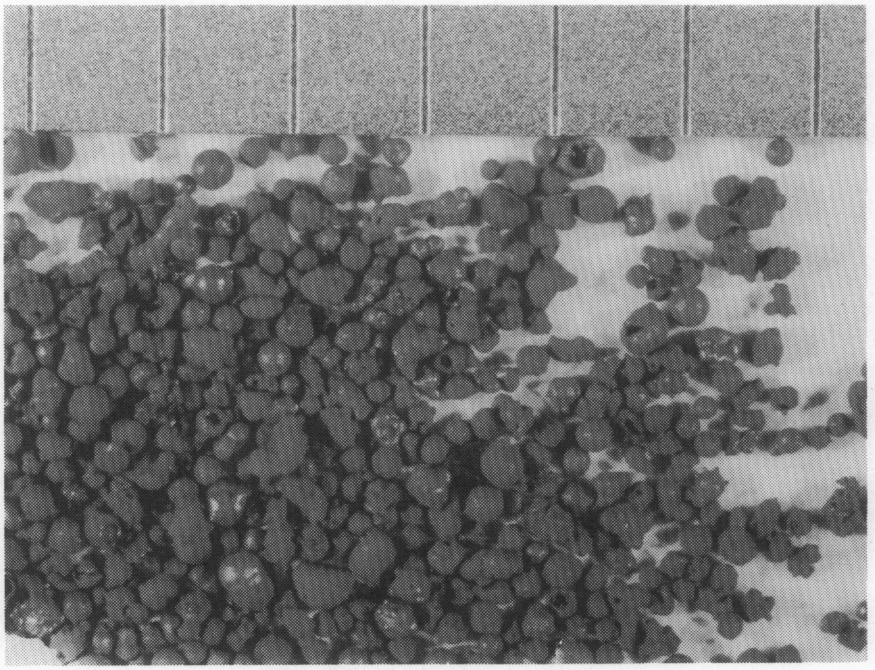

Figure 1.2-6. (continued)

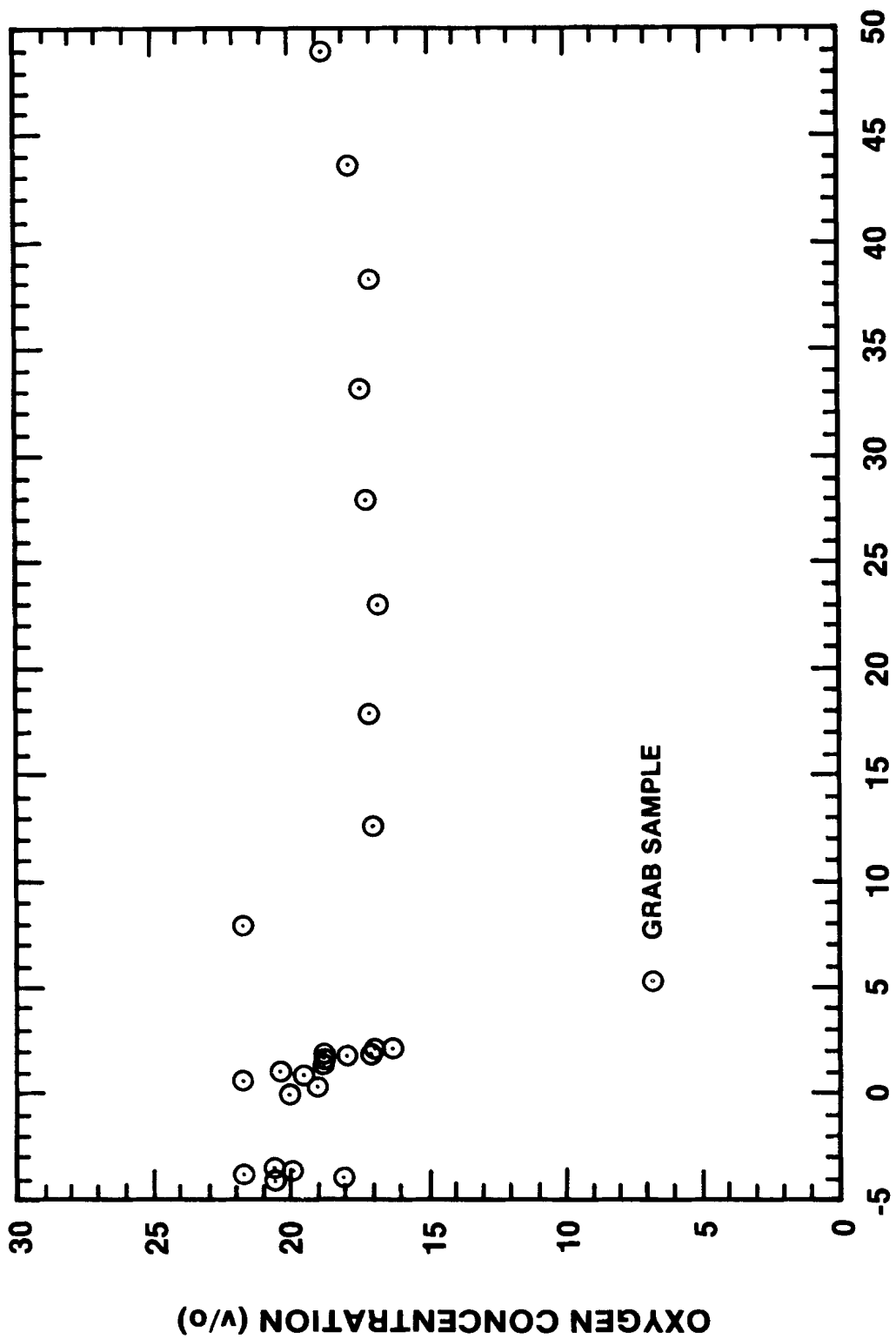

Figure 1.2-7. Oxygen Gas Concentration

sample was obtained. The results have not been corrected to account for the slight effect of the nitrogen gas ejected into the chamber from the melt generator. Further, the data were not adjusted to consider the change in the chamber pressure for the samples taken shortly after debris dispersal.

The results given in Figure 1.2-7 clearly show the oxygen consumption that occurred during the experiment. The first few samples following debris dispersal did not give this indication because of the "dead volume" of gas within the sampling line. It was estimated that five to eight samples were required in order to obtain gas that was representative of that in the atmosphere after debris ejection. The initial value of approximately 20 v/o was reduced to about 16 v/o within a few minutes. The added nitrogen from the melt generator caused this value to be lower than that determined considering the oxidation of the metallic particles (18.4 v/o). Beyond 15 min the data remained relatively constant at ~16 v/o.

Aerosol samples were taken in the SURTSEY chamber for the first 41 min (2463 s) following the ejection of debris. The sample times, locations, and inferred concentrations are given in Table 1.2-6. The locations correspond to those defined in Table 1.2-1.

Concentrations varied widely over time and between locations. Table 1.2-6 gives the concentrations at different times, the average concentration, and the standard deviation. The designations within parenthesis under the "Source" column indicate the type of device (impactor, filter, or cyclone) and its letter designation. The standard deviation was based on all the samples within a given sampling period. The 95 percent confidence level was calcuated from the standard deviation times the "Student t" distribution over the square root of the number of samples. It was based on the data from the sample interval 315 to 345 s because this interval contained the most points. The confidence level was assumed to apply to all sample averages and was used to calculate the ranges given in Table 1.2-6. The cascade impactor samples A and B appeared anomalously high and have not been included in these results.

The calculated concentrations given in Tables 1.2-6 and 1.2-7 are the actual concentrations at the chamber conditions. The concentration multiplied by the approximate 100 m^3 chamber volume gave the suspended aerosol mass. The calculated aerosolized mass was 0.5 to 2.9 kg or 5 to 29 percent of the mass of debris ejected from the cavity. The upper range of aerosolized melt (29 percent) is unrealistically high, especially considering the 40 min average concentration (2.1 g/m^3). This range was caused by the

statistical analysis of samples from what was once a highly heterogeneous aerosol; it may also have been affected by overloading of the aerosol sampling devices. A more realistic upper range would be 10 percent of the displaced mass. The range reflects the 95 percent confidence interval based upon first samples. Additional analyses employing an aerosol tagging technique are under way.

Table 1.2-6

Calculated Aerosol Concentration

Time (s)	Concentration Source[a] (g/m^3)	Concentration Mean (g/m^3)	Concentration Std Dev (%)	Range 95% Conf Int (g/m^3)
15-30	1.52 (FA)	1.52	-	
30-45	24.0 (FB) 6.7 (FH)	15.4	80	3.7-27.0
15-45	12.8 (FA&FB) 4.6 (IE) 3.5 (IF)	7.0	73	1.7-12.3
165-195	12.0 (FC) 21.0 (FI)	16.5	39	4.0-29.0
315-345	7.3 (FJ) 6.6 (IC) 8.7 (ID) 2.2 (IG) 2.4 (IH)	5.4	55	1.3-9.5
1343-1404	2.0 (FE) 3.4 (FK)	2.7	38	0.7-4.8
2403-2463	2.7 (FL)	2.7	-	0.7-4.8
15-2463	2.1 (FF) 2.1 (CI)	2.1	-	0.5-4.0

[a]F=filter, I=impactor, C=cyclone

The data indicated an initially high aerosol concentration (~10 g/m^3), which decreased very rapidly at first and then slower at later time. This is consistent with a bimodal source term where the large mode concentration dominates the early time behavior. The large particles rapidly fall out of suspension and take some of the smaller

Table 1.2-7

Aerosol Measurements

Device & Location		Sample Time (s)	Mass (mg) w/o PS[a]	Mass (mg) Total	Ave Temp (K)	Chamber Press (psia)	Gas Volume (L)[b]	Calc Conc (g/m^3)
Impactors								
A	E-2	15-45	558	863	455	18.4	11.35	49-76
B	E-2	15-45	500	707	455	18.4	7.8	64 91
E	E-4	15-45	23.3	52.2	455	18.4	11.35	2.1 4.6
F	E-4	15-45	16.0	26.9	455	18.4	7.8	2.1-3.5
C	E-2	315-345	68.4	98.8	300	12.2	7.5	4.6-6.6
D	E-2	315-345	54.6	98.2	300	12.2	5.15	5.3-8.7
G	E-4	315-345	15.9	33.2	300	12.2	7.5	1.1-2.2
H	E-4	315-345	15.4	24.6	300	12.2	5.15	1.5-2.4
Cyclone								
I	E-4	15-2463	-	1327.2	300	12.2	620.0	2.1
Filters								
A	E-2	15-30	-	2.7	485	19.7	1.8	1.5
G	E-4	15-30	-	-	485	19.7	1.8	-
B	E-2	30-45	-	37.8	424	17.2	1.6	24.0
H	E-4	30-45	-	10.5	424	17.2	1.6	6.7
C	E-2	165-195	-	27.1	310	12.5	2.3	12.0
I	E-4	165-195	-	46.6	310	12.5	2.3	21.0
D	E-2	315-345	-	-	300	12.2	2.2	-
J	E-4	315-345	-	16.1	300	12.2	2.2	7.3
E	E-2	1344-1404	-	8.6	300	12.2	4.4	2.0
K	E-4	1344-1404	-	15.1	300	12.2	4.4	3.4
F	E-2	15-2463	-	390.4	300	12.2	181.9	2.1
L	E-4	2403-2463	-	11.7	300	12.2	4.4	2.7

[a]PS - preseparator
[b]Actual volume of gas sampled at the chamber condition

particles by agglomeration. The remaining small-mode concentration then decays more slowly.

The aerosol size distribution was measured at two times in the chamber (15 to 45 and 315 to 345 s). Samples were simultaneously taken at the upper and lower locations. Each sample consisted of two impactors with flow rates of 15 and 10 L/min. This gave staggered cutpoints and the algebraic combination of the results from the two impactors yielded a distribution with more data points than either impactor separately.

The 15 to 45 s distribution data measured by impactors E and F were distinctly bimodal with peaks at 1 and >10 μm aerodynamic equivalent diameter. A third mode at 5 μm may also be present. Approximately one-half of the total mass was less than 10 μm in diameter. The smaller mode consisted primarily of floculated material and was described well by a lognormal distribution with a geometric mass median aerodynamic diameter of 1 μm and a geometric standard deviation between 1.7 and 1.9.

The distribution obtained from samples taken 5 min later indicated a single mode between 5 and 10 μm. These data were probably affected by overloading of the sampler which may have masked the bimodal character of the distribution. The overloading was attributed to the physical bulk of the collected material. The collected aerosol had a high void fraction so that large volumes collected at each stage interfered with the normal flow patterns through the devices.

A steel box of approximately 1-m^3 volume was used to dilute the aerosol samples drawn from the chamber for the APS. A cascade impactor was also used to provide a mass distribution along with the number distribution of the APS. The simultaneous measurement of these distributions and the material density of the aerosol yielded the dynamic shape factor, χ. The dynamic shape factor relates aerodynamic equivalent diameter and the mass equivalent diameter.[5] For a particle of given mass, a larger shape factor means that it will fall slower.

Preliminary examination of the data from 4 h after melt ejection indicated a bimodal mass distribution with modes at about 1 and 6 μm aerodynamic diameters. The χ for the smaller mode was estimated to be 6.5 to 7.4. For the larger mode particles, the χ was 1.8 to 2.4. Deposition of aerosol on the walls of the chamber was estimated by vacuuming six separated areas and collecting the material on a filter. Table 1.2-8 gives the results of this process. The mean surface concentration was 0.183 $\pm$0.029 mg/cm^2. Based on the total vertical surface area, it was estimated that 128 to 180 g of aerosol were deposited on the walls of the vessel.

Table 1.2-8

Aerosol Wall Deposition

Filter Location[a]	Collected Mass (mg)	Wall Area (cm^2)	Surface Concentration (mg/cm^2)
70/2	41.03	231	0.178
140/2	33.41	169	0.198
190/5	40.34	216	0.187
280/5	30.08	132	0.228
0/4	22.35	150	0.149
130/4	20.49	132	0.155
		Mean	0.183

[a]Designation refers to radial location in degress from North (70 = 70° N-NE) and elevation (2 = el 2 m)

The measurements indicated that 5 to 29 percent of the dispersed mass was aerosolized into particles with less than a 10-μm aerodynamic diameter.

1.3 CORCON Code Development

(D. A. Powers and J. E. Brockmann, 6422; D. R. Bradley, 6425)

In the event of a severe reactor accident in which molten core debris penetrates the reactor vessel, the interaction of the molten debris with structural concrete in the reactor cavity can be an important factor in the risk associated with the accident. Since the time of the Reactor Safety Study,[6] this aspect of reactor safety analysis has been poorly understood, with little substantive experimental data available. Out of necessity then, computer models were initially developed based on data from simulant experiments and on observations from the few existing melt-concrete experiments. The CORCON MOD1 computer code[7] was developed during this time at Sandia in work sponsored by the NRC. An improved version of the code, CORCON MOD2[1] has been released to the public and is now the core-concrete model used in the NRC Source Term Code Package.

In the last two years, experiment programs at Sandia[8,9,10] and at Kernforshungszentrum Karlsruhe (KfK)[11,12,13] have investigated prototypic melts interacting with concrete. Experiments at both facilities have been well-instrumented and have yielded an abundance of useful data. The availability of these data has allowed validation of existing core-concrete models.

Previous publications[8,14] have reported on comparisons of CORCON MOD2 calculations to the results of the Sandia and KfK experiments and these results are summarized here. In general, CORCON was found to underestimate the rapid concrete ablation observed in high-temperature metallic-melt experiments while it overestimated the much slower ablation observed in oxide-melt experiments. (The oxidic-melt data is limited to two transient experiments in which the melt was not internally heated. Therefore, steady state ablation could not be observed.)

It was apparent from these comparisons that the heat transfer models in CORCON MOD2 were inadequate. As a result, an extensive model development effect was initiated at Sandia. This summarizes the recent results of this work.

The section is organized in the following manner: First, a brief description of the CORCON MOD2 heat transfer model is provided. This is followed by a description of heat transfer model revisions that have been incorporated into a working version of the code (hereafter referred to as CORCON MOD2h). Comparisons between the model prediction and the results from several of the Sandia and KfK experiments are then presented. After completing a comparison of the new heat transfer model with existing data, the model is then applied to pretest predictions for the SURC3 and SURC4 experiments.

The SURC3 and SURC4 experiments have been designed to examine the effect of Zr metal on concrete ablation. In the pretest predictions both the new and the original heat transfer models were used. As will be shown, significant differences in the behavior of the experiment are predicted to occur, depending upon which heat transfer model is used. Thus it is expected that the performance of the SURC3 and SURC4 tests will add significant data to core-concrete heat transfer model validation. The experiments will also provide validation of the Zr oxidation model in CORCON.

1.3.1 The CORCON MOD2 Heat Transfer Model

The fundamental assumption in the CORCON MOD2 heat transfer model is that a stable gas film forms upon initial contact between the molten core debris and the concrete and is sustained throughout the interaction. This film is assumed to be present along both the bottom and sides of the concrete cavity. Heat transfer across the gas film is by combined radiation and convection. Gases released from the concrete flow perpendicular to the horizontal bottom surface and enter the debris. Gases released from the vertical concrete sidewalls flow parallel to the walls and are confined to the gas film. Convective heat transfer

coefficients vary in the film depending on flow direction and magnitude. Both laminar and turbulent flow correlations are used.

Within the core debris, heat transfer is by bubble driven convection if the debris is molten and by conduction if it is solidified. Different heat transfer correlations are used for vertical and horizontal interfaces. Between the stratified core melt layers, heat transfer enhanced by entrainment is modeled.

1.3.2 Heat Transfer Model Revisions

The initial step in the model development process was a review of the available literature on melt-concrete heat transfer and related fields. For the most part, the existing heat transfer models fell into two broad categories--those that assumed that a stable film was present and those that allowed direct contact between the melt and the concrete. These disparate models are analogous to film and nucleate boiling.

In order to determine which mode of heat transfer was most likely for most postulated reactor accident conditions, it was first necessary to determine under what conditions each would exist. In boiling heat transfer applications, a stable film is usually assumed to form at a critical heat flux, or equivalently, a critical superficial gas velocity. A similar gas velocity transition criterion should also apply to film formation at a melt-concrete interface.

Several equations have been proposed for the transition to stable film boiling at horizontal surfaces, and they all give similar results. Of these equations, the one that appears to have the greatest experimental support is one attibuted to Kutateladze and Malenkov.[15] This equation is:

$$V_{s,crit} = k_s \sqrt{\frac{\sigma}{\rho_g A}} \quad , \tag{1.3-1}$$

$$\text{where } k_s = \begin{cases} 30\ M_*^{2/3} & \text{for } Ar_* > 10^4 \text{ and} \\ 6.3\ M_*^{2/3}\ Ar_*^{1/6} & \text{for } Ar_* < 10^4 \quad . \end{cases} \tag{1.3-2}$$

$$A = \sqrt{\frac{\sigma}{g(\rho_l - \rho_g)}} \quad , \tag{1.3-3}$$

$$M_*^2 = \rho_g\ gA/p \quad , \text{ and} \tag{1.3-4}$$

$$Ar_* = gA^3/\nu^2 \quad . \tag{1.3-5}$$

In these equations, σ is surface tension, ρ_l and ρ_g are the densities of the liquid and gas phases, p is the pressure at the interface, and ν is the kinematic viscosity of the liquid.

When properties for steel melts and steam-carbon dioxide gas mixtures are inserted into the above equation, a superficial gas velocity of approximately 4.3 m/s is calculated. This extremely high gas velocity requires a concrete ablation rate of roughly 6 mm/s for a silicate concrete and 2 mm/s for a limestone concrete. These rates exceed those observed in any of the experiments conducted thus far. Under most reactor accident conditions, the ablation rate will probably be much slower.

The Kutateladze transition criterion has been incorporated into CORCON MOD2h to determine the appropriate mode of heat transfer for the horizontal bottom surface of the reactor cavity. The gas film model has been retained but is only invoked when the gas velocity is sufficiently high.

A review of existing heat transfer models for bubble-driven convection within liquids produced a large number of very different correlations, which were all based on simulant experiments. When applied to prototypic materials such as molten steel, these correlations give an order of magnitude variation in results. It is important, therefore, to determine which of the available correlations is validated for materials similar to those expected in a reactor accident.

Of the available correlations, only one attributed to Kutateladze[16] appears to be valid for both high and low Prandtl number fluids. For low Prandtl number fluids such as molten metals, most of the other correlations predict heat transfer coefficients that are high by a factor of 10 or more when compared to existing experiment data.[17] Such is the case for the correlation used in CORCON MOD2. The Kutateladze correlation has replaced this correlation in a working version of the code. The Kutateladze correlation is

$$Nu_A = \begin{cases} 1.5 \times 10^{-3}\ Ku^{2/3} \\ \qquad \text{for } V_s\mu/\sigma < 4.3 \times 10^{-4} \text{ and} \\ 3 \times 10^{-5}\ Ku^{2/3}\ (V_s\mu/\sigma)^{-0.5} \\ \qquad \text{for } V_s\mu/\sigma > 4.3 \times 10^{-4} \end{cases} \qquad (1.3\text{-}6)$$

Here Nu_A is the Nusset number based on a characteristic length A, where A is given by Equation (1.3-3). In Equation (1.3-6), Ku is defined by

$$Ku = \frac{Pr\ p\ V_s}{g\mu} \quad , \qquad (1.3\text{-}7)$$

where Pr is the Prandtl number for the liquid, μ is the viscosity of the liquid, and all other variables have the same meaning as defined earlier.

Although the Kutateladze correlation was developed to represent bubbling heat transfer at a horizontal surface, experimental evidence suggests that heat transfer adjacent to vertical bubbling surfaces may be very similar.[17] Due to the limited experimental data available for vertical surfaces, we have chosen to use the Kutateladze correlation to represent heat transfer in the core melt adjacent to the vertical sidewalls.

In the CORCON MOD2h heat transfer model, a concrete slag film is assumed to be present between the core debris and the horizontal bottom surface of the cavity. Heat transfer in the slag film is governed by convection, and a correlation similar to the Kutateladze churn-turbulent correlation is used. In this correlation, the heat transfer coefficient is assumed to be dependent on the superficial gas velocity raised to the one-sixth power. Due to uncertainty in the thermophysical properties of the slag film, the leading coefficient in this correlation was initially varied to determine a best fit to the Sandia TURC and SWISS experiments.[8,9,10] The resulting correlation is

$$H_{slag} = 4720\ V_s^{0.167} \left(\frac{W}{m^2 K}\right) \qquad (1.3\text{-}8)$$

Along the vertical sidewalls of the concrete cavity, the gas film model is still used. Assessment of alternate models is currently under way.

1.3.3 Comparisons to Experiment Results

In the following discussion CORCON MOD2h calculations are compared to the results of several Sandia and KfK experiments. Because the experiments at these two laboratories are fundamentally different in design, each will be addressed separately.

1.3.3.1 Comparison to the Sandia Experiments

CORCON calculations have been performed for several of the experiments in the TURC and SWISS test series. The TURC tests were transient experiments in which the molten material was not internally heated. Their purpose was to investigate the interaction of several different types of melt with concrete. The SWISS experiments used inductively

heated steel melts and included the addition of water to the crucible at some time after the interaction had begun. The primary purpose of these experiments was to investigate the affect of coolant addition on the progress of melt-concrete interactions.

Both groups of experiments used a crucible design with magnesia (MgO) sidewalls and a limestone-sand concrete bottom. This design was used in order to limit melt-concrete heat transfer to the axial direction. By eliminating the great uncertainty in radial heat transfer to the concrete, it was hoped that accurate heat transfer models could be developed for axial heat transfer. Radial heat losses from the melt were determined from the response of thermocouples embedded in the MgO sidewalls. Since the MgO is a well-characterized material, an inverse heat flux technique[18] was used to determine heat losses to the sidwalls.

Figures 1.3-1 and 1.3-2 present comparisons of the calculated and experimental concrete ablation rates for the TURC1SS and TURC1T experiments. In TURC1SS, which was a teem of approximately 100 kg of molten stainless steel, concrete ablation was rapid but very short-lived since the steel was not internally heated. As shown in the figure, the comparison between the calculation and the experiment is very good, both in terms of the ablation rate and the total extent of ablation during the experiment.

In the TURC1T experiment, which was a teem of approximately 135 kg of an iron-alumina thermite mixture, concrete ablation was somewhat slower but longer-lived than in TURC1SS due to the higher initial temperature of the thermite mixture. As shown in the figure, the comparison between the experiment and the calculation is not quite as good as for TURC1SS. This difference is attributed to the well-mixed initial state of the thermite in the experiment. In CORCON, the iron and alumina are assumed to be stratified. Ablation of the concrete is therefore by an extremely hot, high-thermal conductivity, molten metal rather than by a mixture of metal and lower thermal conductivity oxide.

Mixing models are now being developed at Sandia and several other laboratories. When these models become available, they will be incorporated into CORCON along with models for the thermophysical properties of immiscible mixtures.

Figure 1.3-3 presents a comparison of the measured and calculated concrete erosion for the SWISS1 experiment. Again, the comparison is very good both before and after the addition of water at 35 min. In both the experiment and the calculation, water had little effect on the calculated

ablation rate. The CORCON calculation indicates that heat transfer to the water was by film boiling. Therefore, both before and after water addition, upward heat loss is controlled by thermal radiation.

Calculations have also been performed for the TURC2 and TURC3 experiments in which melts consisting predominantly of UO_2 and ZrO_2 were teemed into crucibles. Comparisons for these experiments are not shown since in both the calculations and the experiments, concrete ablation was minimal (<5mm). Apparently ablation was limited because a thick crust formed soon after contact with the concrete. This behavior was calculated by the revised version of CORCON MOD2h. In previous calculations using CORCON MOD2, crusting did not occur. Instead, rapid ablation took place initially and continued until the oxide mixture solidified. Unfortunately, definitive statements regarding the accuracy of the revised heat transfer models for oxide melts cannot be made based on this limited data base. Experiments with internally heated oxidic melts are required. Such experiments are planned at Sandia and results from these experiments will soon be available. At that time more thorough testing of the models will be performed.

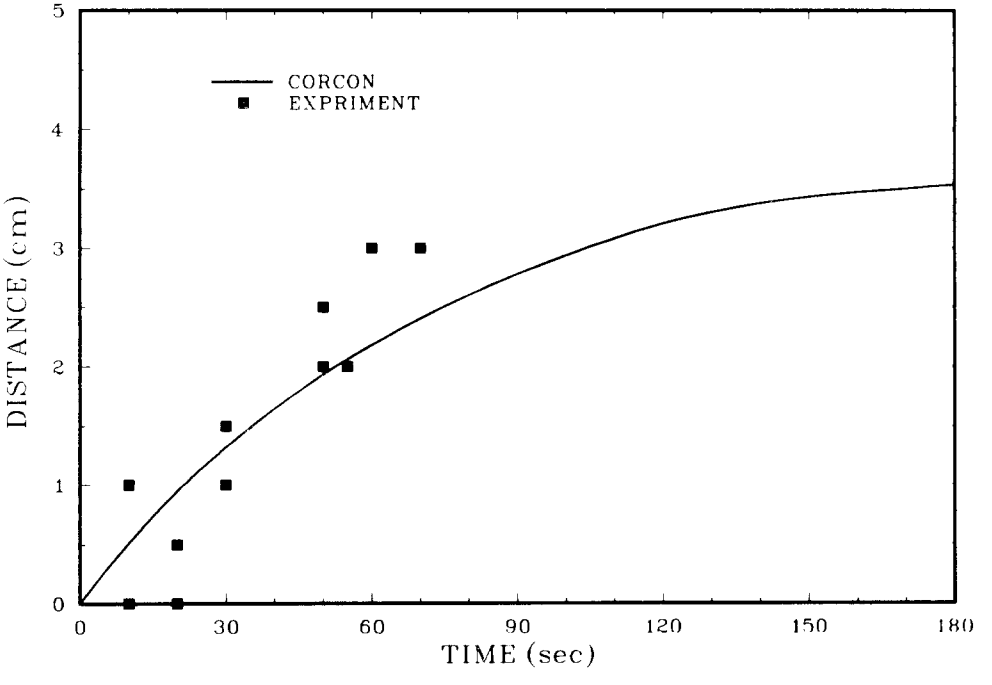

Figure 1.3-1. TURC1SS Ablation Distance

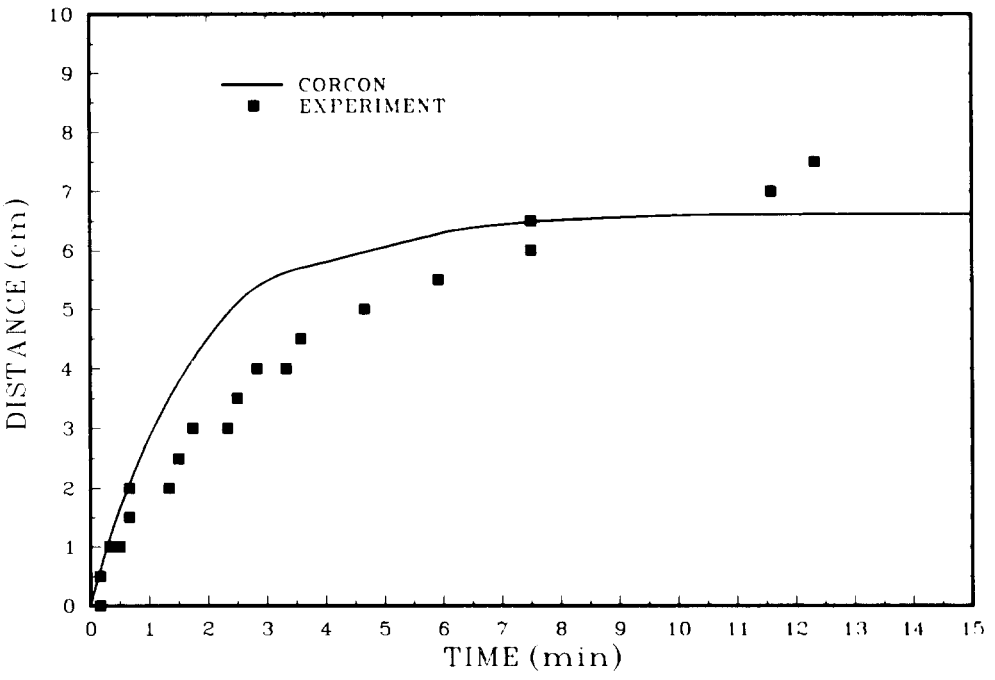

Figure 1.3-2. TURC1T Ablation Distance

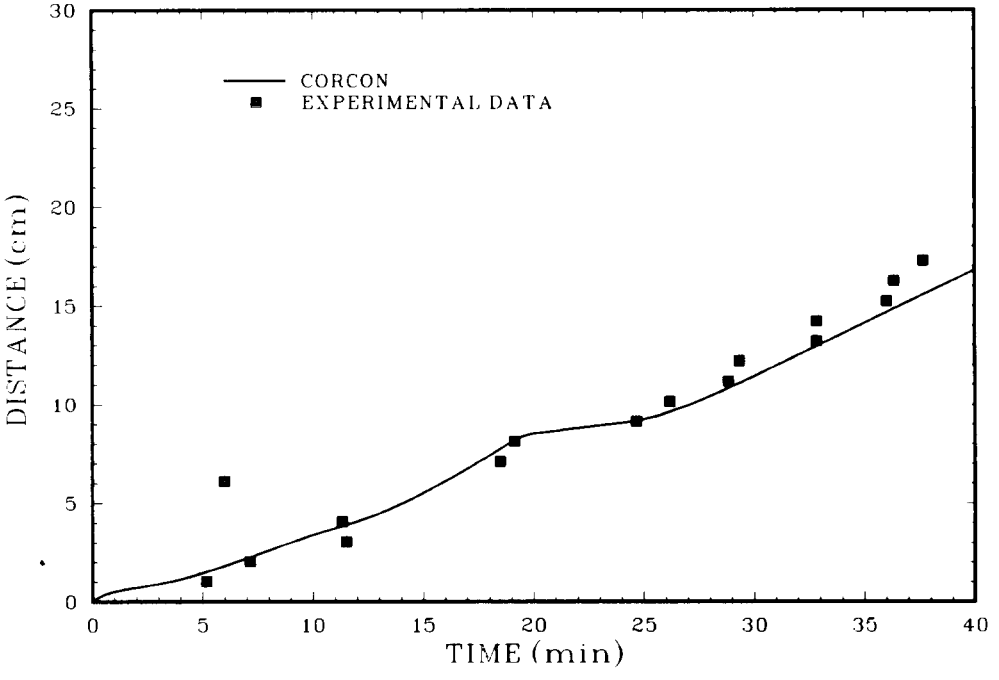

Figure 1.3-3. SWISS1 Ablation Distance

1.3.3.2 Comparison to the KfK Experiments

The design of the BETA experiments at KfK was quite different from that of the Sandia experiments. Most significantly, an all-concrete crucible was used and the melt-concrete interaction was therefore two-dimensional. The crucibles were usually made from silicate concrete though near the end of the BETA test series, several experiments were run using limestone or limestone-sand concrete crucibles similar in composition to those used in the Sandia experiments. The melts used in BETA were generated thermitically and were then poured into the concrete crucible where they were internally heated using induction techniques. The primary variables in the BETA experiments were the composition of the melt and the nominal induction power level. The melt composition varied from pure molten iron to molten steel with a low density molten oxide such as alumina. Nominal power levels varied from 100 kW to almost 2000 kW.

CORCON calculations were performed for five of the BETA experiments: V0.2, V1.6, V1.7, V2.1, and V3.3. The first four experiments used silicate concrete crucibles while the last one used a limestone-sand concrete crucible. The primary difference among the four silicate concrete experiments was in their nominal power levels. The nominal powers were: V0.2 - 40 kW, V1.6 - 1000 kW, V1.7 - 1700 kW, and V2.1 - 120 kW. The operating power usually changed significantly during the test, especially in the higher power experiments.

Figures 1.3-4 through 1.3-8 present comparisons of calculated and experimental concrete ablation for the five BETA experiments. The comparisons are in general excellent, especially in light of the sometimes nonuniform concrete erosion pattern observed in the experiments. The calculations were less accurate for the two low power BETA experiments, V0.2 and V2.1, where the axial erosion rate increased significantly in the latter part of the experiments even though the power supplied to the melt remained approximately the same or even decreased. One possible explanation is that the steel melt forms a crust at these low power levels soon after contacting the cold concrete. This is especially likely in the BETA experiments, which have a large surface-to-volume ratio. Eventually, after heating the adjacent concrete, the crust begins to remelt and the concrete ablation rate increases. Because CORCON assumes the concrete has already reached its ablation temperature and a steady state temperature profile has been established, it cannot match this initial behavior. Future plans are to incorporate a concrete heat conduction model into the code to handle this initial transient.

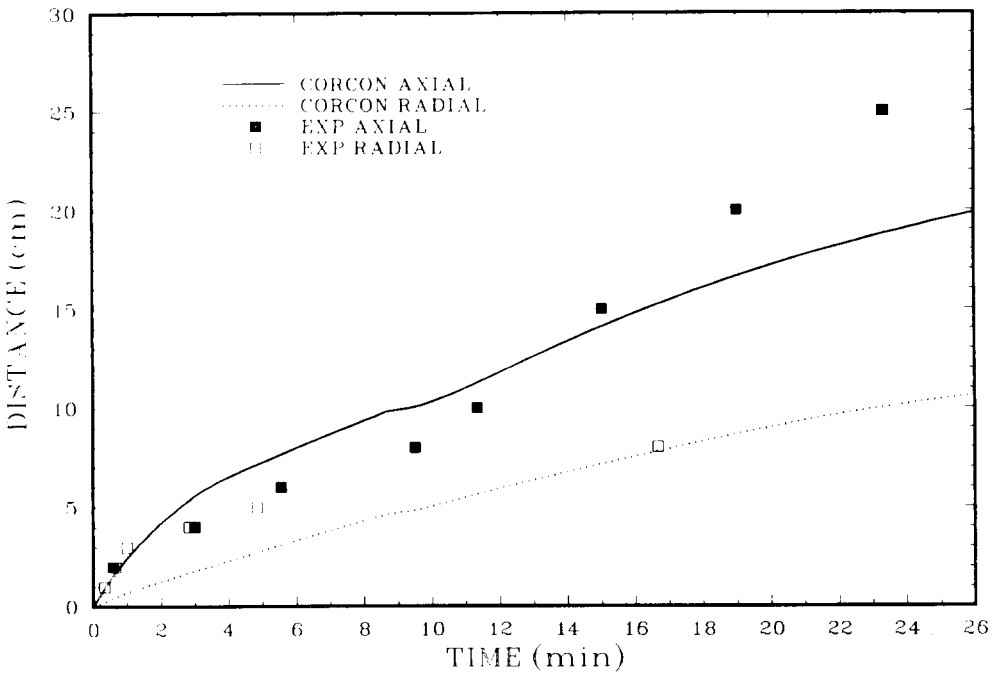

Figure 1.3-4. BETA V0.2 Ablation Distance

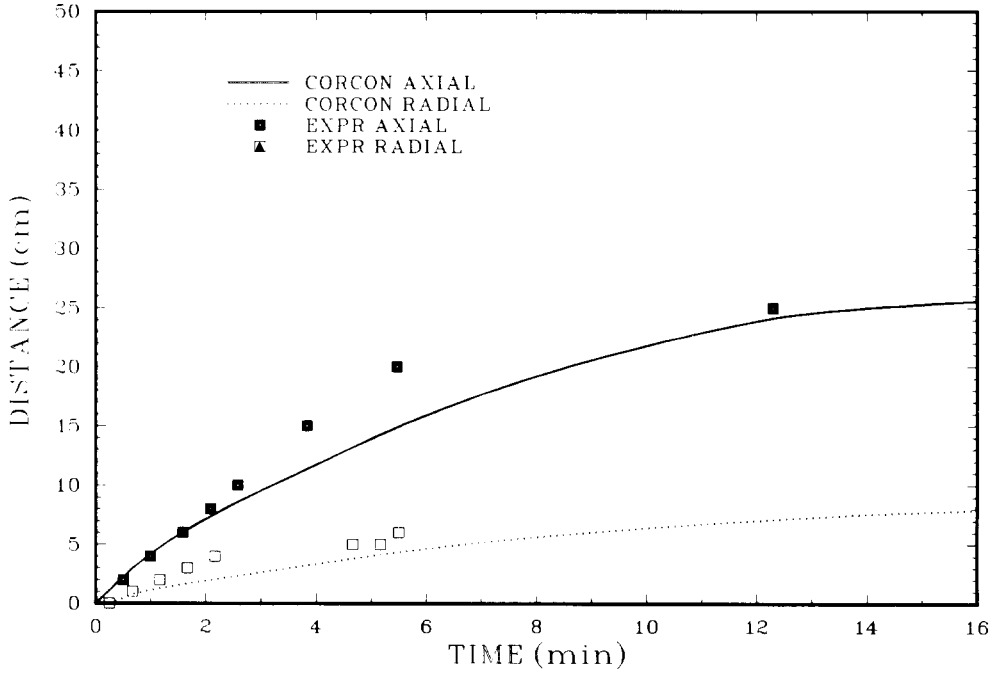

Figure 1.3-5. BETA V1.6 Ablation Distance

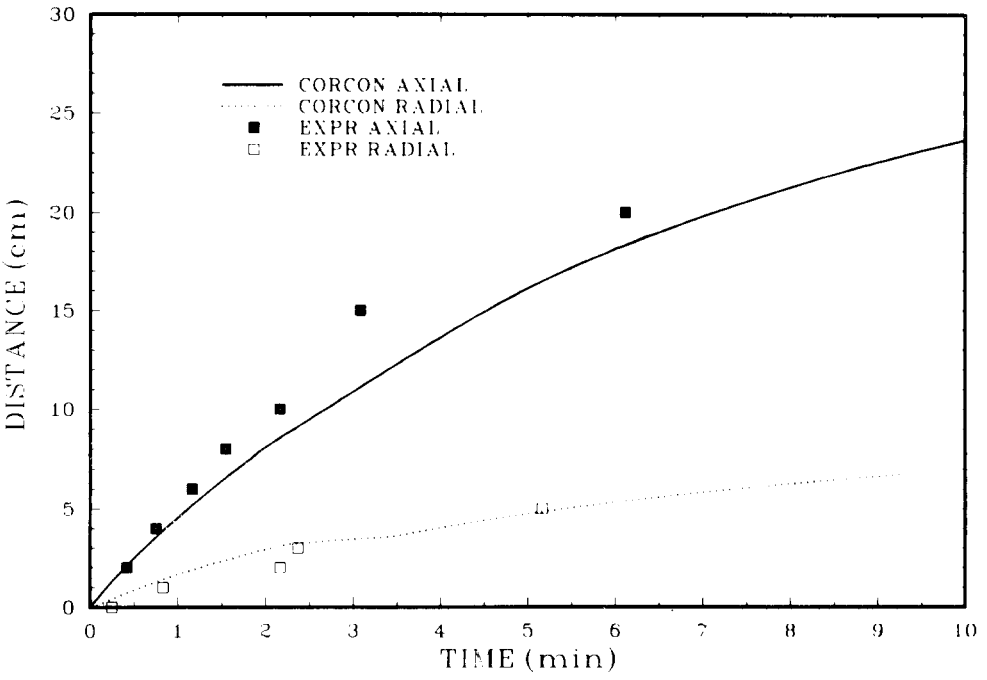

Figure 1.3-6. BETA V1.7 Ablation Distance

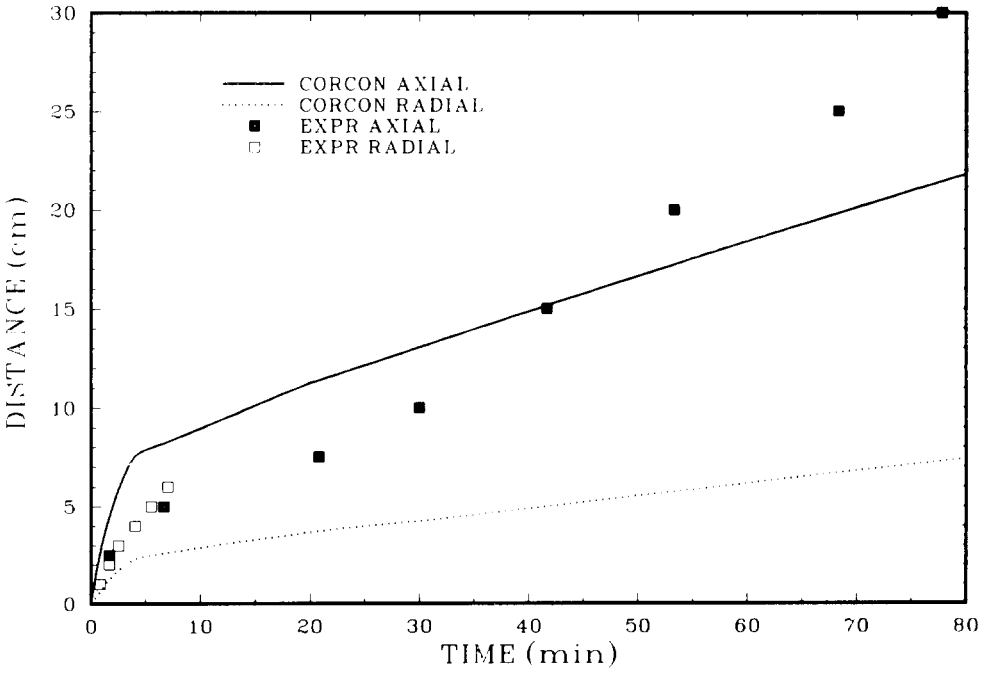

Figure 1.3-7. BETA V2.1 Ablation Distance

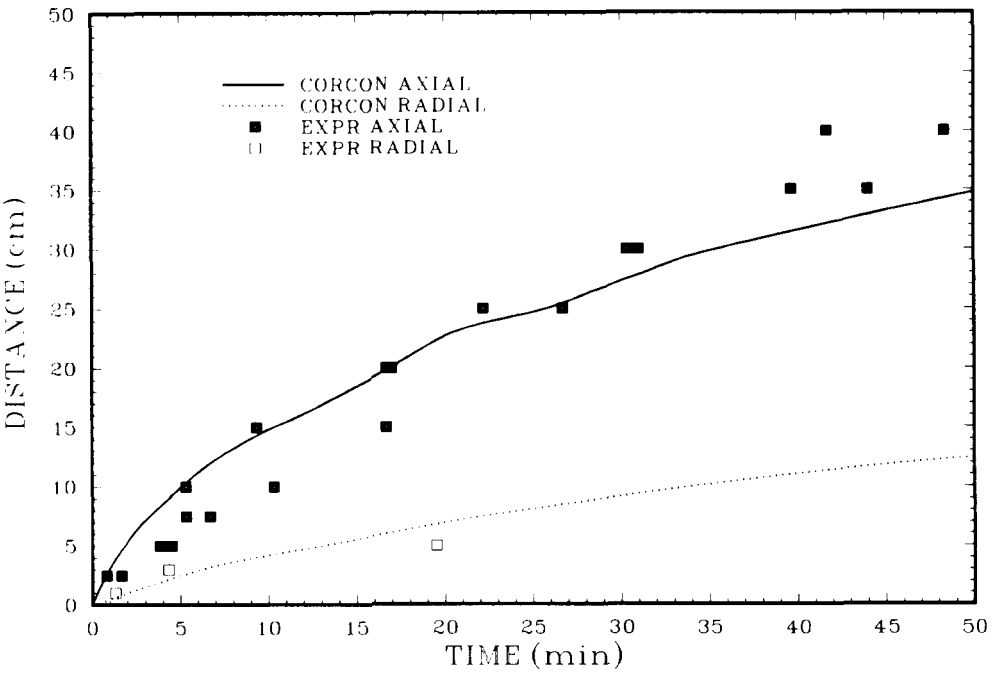

Figure 1.3-8. BETA V3.3 Ablation Distance

1.3.4 CORCON Pretest Predictions for SURC3 and SURC4

There are two primary concerns in the SURC3 and CURC4 experiments: Validation of the CORCON models for zirconium (Zr) oxidation and validation of the CORCON heat transfer models. Discussion of the heat transfer models in CORCON MOD2 and MOD2h has already been provided. The following discussion addresses the models for Zr oxidation in CORCON.

The chemistry package in CORCON assumes chemical equilibrium is achieved during reactions between the metal phase of the melt pool and the gases released from the concrete. Of particular importance are reactions between Zr and carbon dioxide (CO_2) released from the concrete. In most CORCON calculations, oxidation of Zr by CO_2 is calculated to proceed by the following reaction:

$$Zr + CO_2 \rightarrow ZrO_2 + C + 150 \text{ kcal/mol Zr} \quad .$$

This reaction is sometimes referred to as "coking."

The coking reaction is important for two reasons: It is very exothermic, which tends to increase the melt pool temperature, and it greatly reduces the flow of gas through the melt. When Zr oxidation is nearly complete, oxidation of the condensed carbon begins. The two oxidation reactions are $C + CO_2 \rightarrow 2\ CO$ and $C + H_2O \rightarrow CO + H_2$.

Both of these reactions are endothermic, which causes the melt pool temperature to decrease. They also produce a sudden increase in gas flow since two mols of gas are produced for every mol reacted.

In severe accident calculations performed using CORCON and VANESA, peak aerosol and fission-product release usually occur at the beginning of the carbon oxidation phase, when gas flow has increased while the temperature of the melt is still high. Also, during both Zr and C oxidation, the low oxygen potential of the melt promotes reduction of fission-product oxides such as La_2O_3 to more volatile species. It is therefore important to verify that Zr oxidation proceeds by the coking reaction. The SURC experiments are being designed to provide ample validation of the chemistry model in CORCON and the aerosol and fission-product release models in VANESA.

In order to observe the effects of coking on melt-concrete heat transfer and chemistry, the SURC3 and SURC4 experiments will be run for a period without Zr, and then Zr will be added to the melt. The only major difference between the SURC3 and SURC4 experiments will be the concrete used; SURC3 will use limestone concrete while SURC4 will use basaltic concrete. Coking is expected to have a major effect in the limestone concrete experiment (SURC3), but only a minor effect in the basaltic concrete experiment (SURC4). This is due to the much smaller CO_2 content of the basaltic concrete.

The experimental procedure to be used in SURC3 and SURC4 will be to create a mildly superheated melt of stainless steel, pour it into an inductively heated interaction crucible, wait until steady state conditions have been established, then add Zr, and observe any changes in the interaction. For the purpose of CORCON pretest calculations, the following example procedure was assumed:

1. Start with a 50-kg stainless steel melt at 1900 K.

2. Internally heat the melt with a net inductive power of 16 kW for 30 min.

3. At 30 min add 5 kg of Zr metal.

4. Continue the calculation for an additional 30 min.

Shown in Figure 1.3-9 are the CORCON predictions for the ablation rate as a function of time in the SURC3 experiment. The two curves shown in the figure represent calculations made using CORCON MOD2 and CORCON MOD2h. As can be seen, before Zr addition the two models predict almost the same result. However, after Zr addition, the

model predictions are significantly different. Figure 1.3-10 shows the concrete penetration resulting from the ablation rates shown in Figure 1.3-9. The penetration distance will be measured experimentally by noting the failure times of the thermocouples embedded in the concrete.

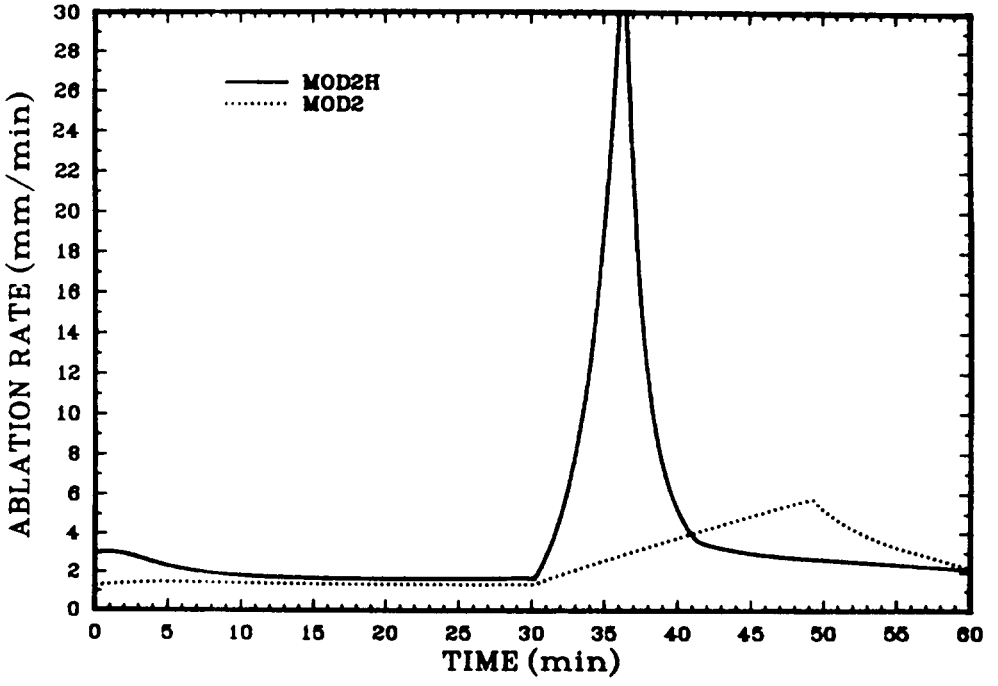

Figure 1.3-9. SURC3 Predicted Ablation Rate

Three things can be concluded from these results. First, Zr addition will have a pronounced effect on heat transfer to the concrete. Second, this effect will be detectable from thermocouple failure times. Third, the SURC3 experiment will provide a further basis for determining which of the two heat transfer models is more appropriate for melt-concrete interactions.

Figure 1.3-11 is a plot of the predicted melt pool temperature for SURC3. Both versions of CORCON calculate significant temperature increases during Zr oxidation. Such a large increase will be easily detectable by the pool temperature measuring devices in the experiment.

Figure 1.3-12 is a plot of the predicted gas flow rate for SURC3. Note that during the coking reaction almost no release of carbon monoxide (CO) is calculated while during the carbon oxidation phase, CO release is enhanced. These changes in gas composition are shown in Figure 1.3-13, which presents the molar ratio of CO + CO_2 to H_2 in the gas

stream exiting the melt. As the figure shows, this ratio is predicted to vary by orders of magnitude during the experiment. These dramatic changes in gas flow and gas composition will be easily measured by the diagnostic equipment used in the experiment.

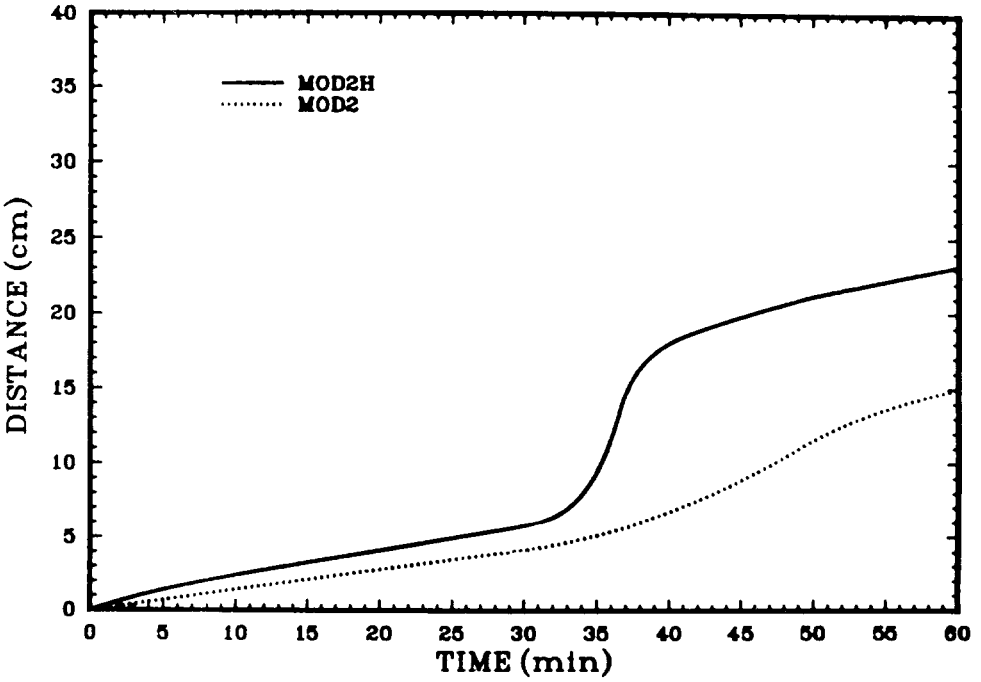

Figure 1.3-10. SURC3 Predicted Ablation Distance

Results of the CORCON pretest calculations for the SURC4 experiment are shown in Figures 1.3-14 through 1.3-18. The inputs to these CORCON calculations are identical to those for the SURC3 calculations except that basaltic concrete was selected rather than limestone concrete. As mentioned earlier, the low CO_2 content of the basaltic concrete is expected to minimize the effects of Zr oxidation on melt pool heat transfer, gas chemistry, and aerosol and fission-product release. This expectation is supported by the results presented in the figures. Changes in the concrete ablation rate (Figures 1.3-14 and 1.3-15) and melt pool temperature (Figure 1.3-16) would not be detectable. The same can be said for the gas flow rate (Figure 1.3-17). As shown in Figure 1.3-18, the coking and carbon oxidation reactions are apparent in the plot of CO + CO_2/H_2 ratio.

Aerosol and fission-product release calculations have not yet been performed for the SURC3 and SURC4 experiment because VANESA is not yet able to accept addition of mass after the start of the calculation. When the code has been

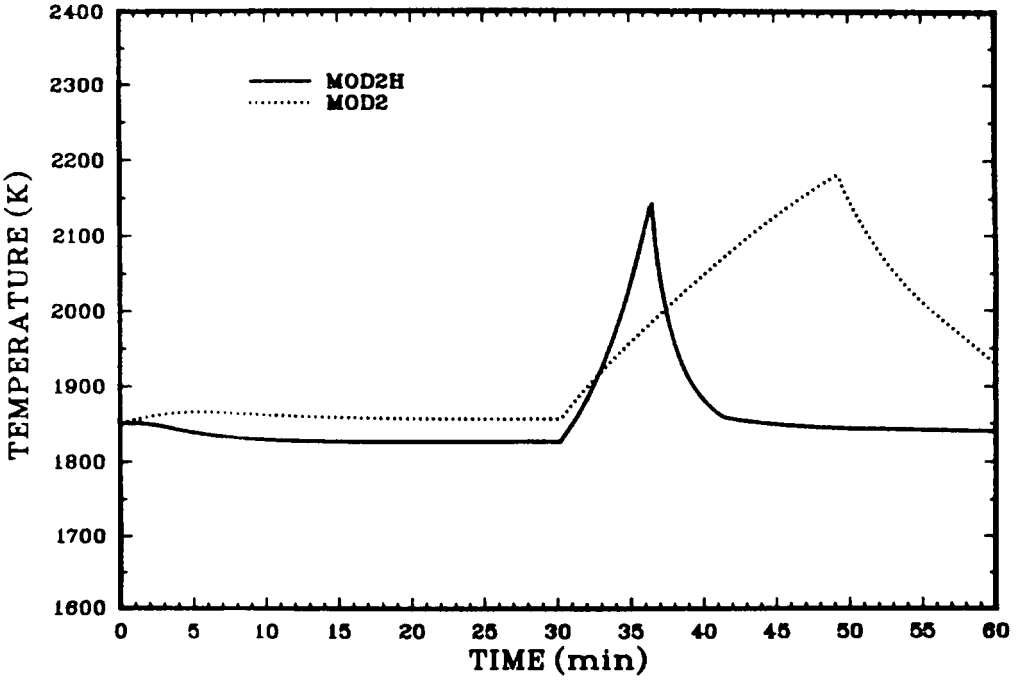

Figure 1.3-11. SURC3 Predicted Melt Temperature

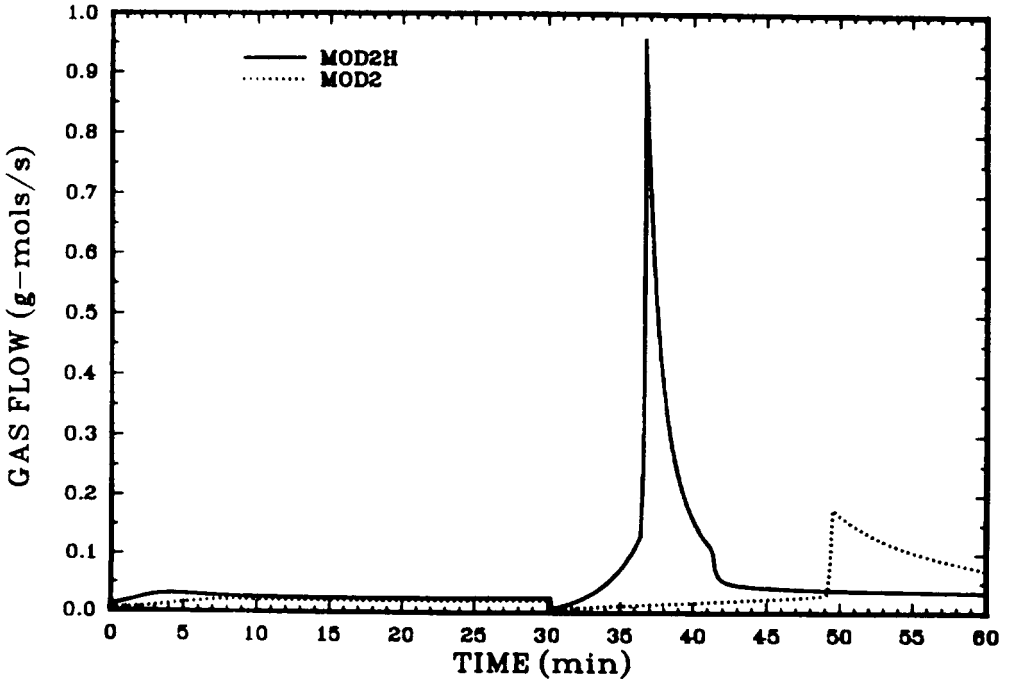

Figure 1.3-12. SURC3 Predicted Gas Flow

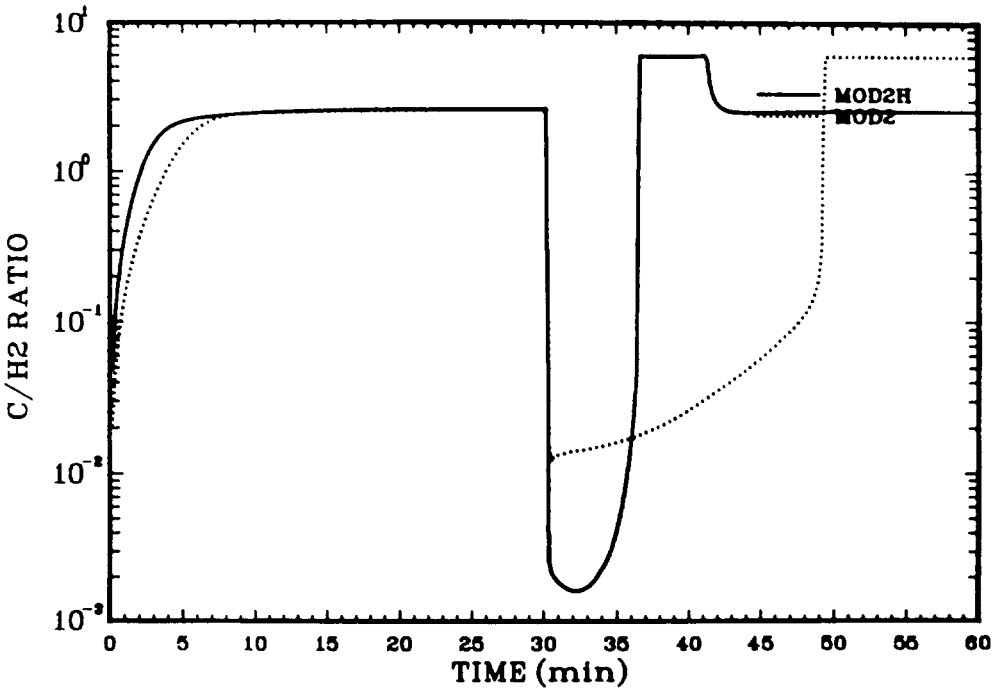

Figure 1.3-13. SURC3 Predicted Molar Ratio of CO + CO_2 to H_2

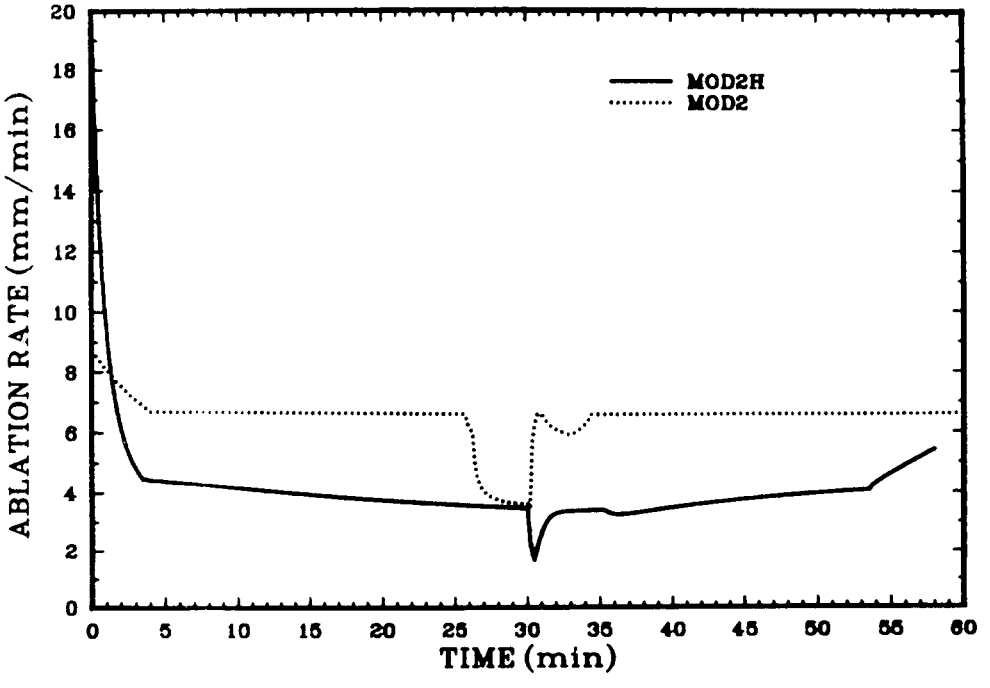

Figure 1.3-14. SURC4 Predicted Ablation Rate

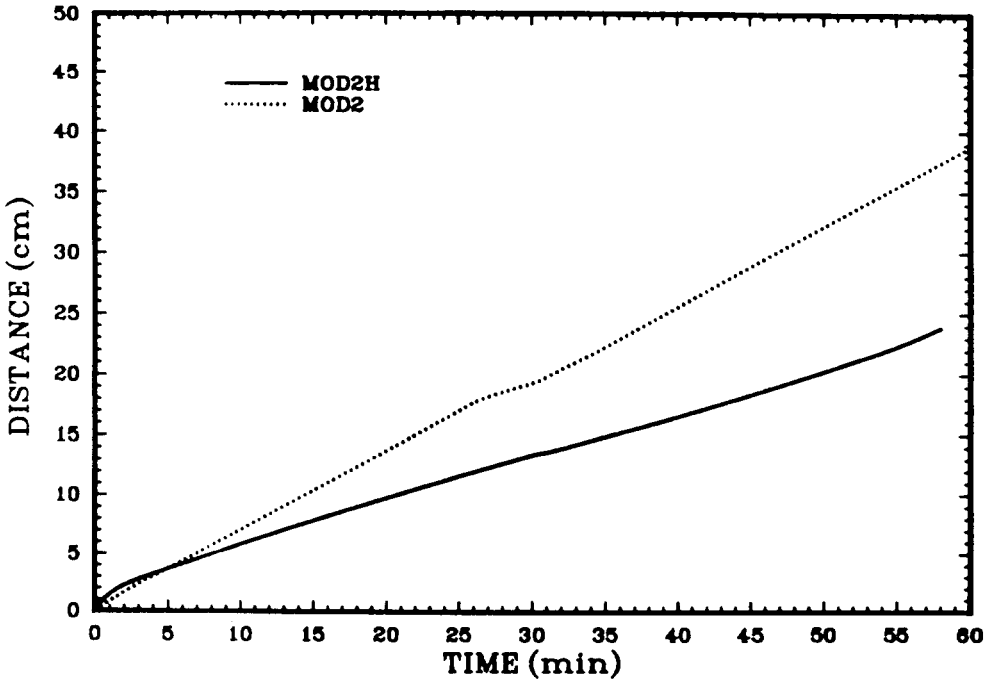

Figure 1.3-15. SURC4 Predicted Ablation Distance

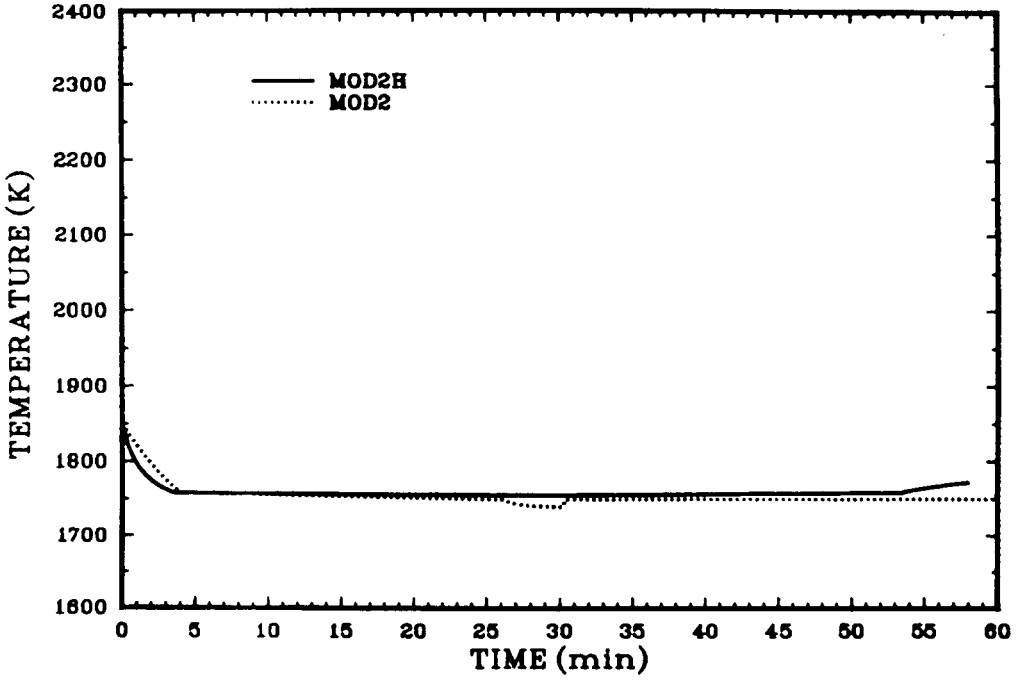

Figure 1.3-16. SURC4 Predicted Melt Temperature

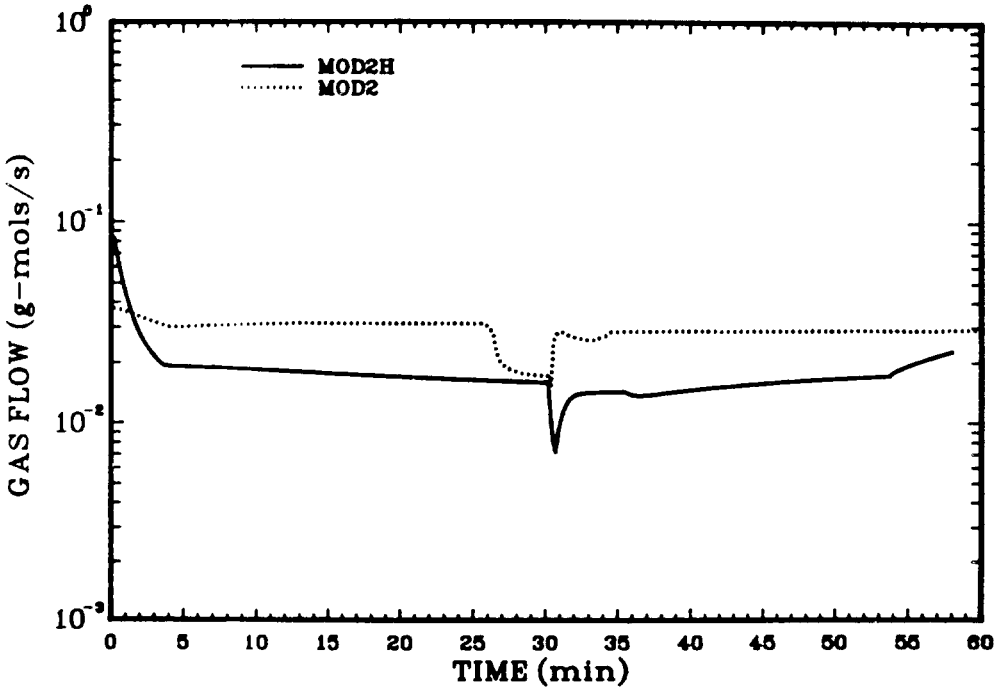

Figure 1.3-17. SURC4 Predicted Gas Flow

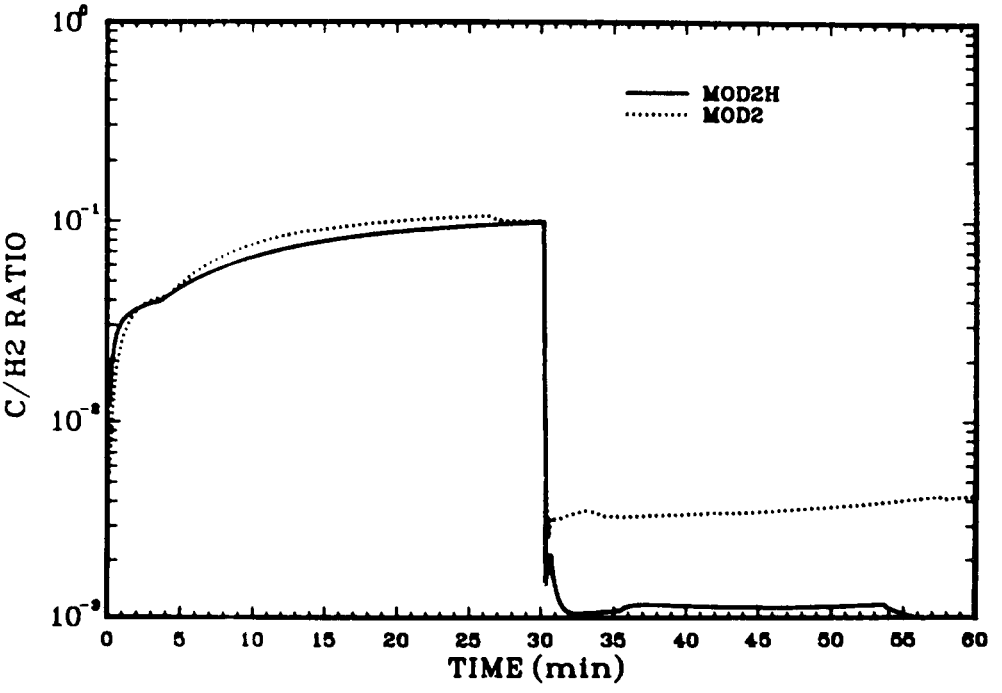

Figure 1.3-18. SURC4 Predicted Molar Ratio of CO + CO_2 to H_2

modified to accept a time-dependent source of mass, aerosol and fission-product release will be calculated for the experiments.

1.4 Molten Fuel-Coolant Interactions
(B. W. Marshall Jr. and M. Berman, 6427)

The objective of this program is to develop an understanding of the nature of fuel-coolant interactions (FCIs) during hypothetical accidents in light water reactors (LWRs). The understanding of FCIs achieved in this program is expected to resolve key reactor safety issues for both terminated and unterminated accidents. Models are being developed to quantitatively determine:

1. The rates and magnitudes of steam and hydrogen generation.

2. The degree of mixing and coarse fragmentation of the fuel.

3. The degree of the fine fragmentation of the individual droplets composing the coarse mixture.

4. The fraction of the available thermal energy that is converted into mechanical energy.

Experiments are being conducted to determine the influence of three classes of important independent variables; thermodynamic conditions (temperature of the fuel and the coolant and the ambient pressure); scale variables (amount of fuel and coolant initially involved); and boundary conditions (pour diameter and rate, shape and degree of confinement of the interactions region, presence of structures, water depth, and fuel-coolant contact mode). Primary measurements and observations made during the experiments included photographic observation of the FCIs, pressures generated in the coolant and the cover gas, steam and hydrogen generation, and the resulting debris characteristics.

1.4.1 Experiments, Data Reduction, and Analysis

1.4.1.1 FITS-D Experiments
(B. W. Marshall, Jr., 6427)

We have begun to prepare the FITS vessel for the completion of the 20-kg experiments in the FITS-D series. The first experiment will be a repeat of the FITS-2D experiment since all of the melt mass did not fall into the small water chamber in the previous experiment. We will construct a funnel on top of the lucite water chamber to ensure that all of the melt enters into the water. The second experiment will be the FITS-3D test and, as far as we know, is the

first experiment conducted with these set of initial conditions. The important initial conditions for each experiment are shown in Table 1.4-1.

Table 1.4-1

Initial Conditions for FITS Experiments

Test	Water Depth (m)	Chamber Width (m)	Drop Height (m)	Water Temp.	Ambient Pressure (MPa)
FITS-2D	0.66	0.38	2.7	Ambient	1.1
FITS-3D	0.15	0.76	1.6	Saturated	1.1

In both of these experiments, we will use on-line mass spectrometers for "real-time" gas analysis. We have been working on the mass spectrometers to be used for these two experiments and have had success detecting peaks for H_2, O_2, N_2, H_2O, Ar, and CO_2. Final calibrations of the systems have begun for each of the species of interest, i.e., H_2, O_2, N_2 and H_2O. Water vapor presents a difficult species to calibrate accurately since it is condensible, and standards are difficult to come by. However, if all other noncondensible species are accurately detected by the mass spectrometer, we can use the chamber pressurization and temperature transients to calculate the water vapor fraction.

1.4.1.2 Jet-Mixing Experiments
(B. W. Marshall, Jr. and M. Berman, 6427;
M. F. Young, 6425)

At the request of the NRC, we have prepared a new program plan, which addresses the important phenomena involving jets of molten fuel mixing and interacting with saturated water.[19] The program will last for the remainder of FY86 and is expected to be concluded by the end of FY87.

In this program, we will begin to develop an understanding of the mixing characteristics and explosibility of molten jets of fuel as they fall through saturated water. The mixing characteristics of boiling jets are not well understood. A review of the literature suggests that there is a limited amount of experimental data pertaining to a combination of nonisothermal jets with high density ratios. Most of the jet-mixing data pertains to very small-scale mixing of isothermal jets with no or relatively small density differences.[20] Thus we feel it necessary to develop an understanding of the mixing characteristics and important scaling variables of these nonisothermal jets.

In the early phases of the proposed program, the mixing behavior and explosibility of jets of molten fuel in saturated water will be addressed in the EXO-FITS facility. In the first series of experiments, we will evaluate the FCI characteristics of single jets of molten fuel interacting with water inside a clear lucite water chamber. The clear lucite will allow high-speed photographic coverage of the phenomena. Subsequent test series in lucite water chambers will evaluate the influence of neighboring jets (three-jet matrix) and of a fully surrounded jet (five-jet matrix). The proposed jet diameter and hole-pitch will represent either full- and half-linear-scale representations of the lower grid distributor plate or half- and quarter-linear-scale representations of the lower core support plate inside the TMI-Unit-2 reactor.

The importance of the lucite experiments cannot be overemphasized. As mentioned, there is very little data about the mixing of boiling jets or jets with relatively high-density ratios, even at very small scale. The behavior of these multiple boiling jets relative to isothermal jets is important to the modeling and analysis of these experiments. If heat transfer and the presence of a vapor blanket influence the mixing processes, as we think they might, then existing correlations will incorrectly predict the mixing behavior, and new correlations should be developed for future modeling efforts.

Following the FCI experiments conducted in a lucite water chamber, we will conduct four experiments in the EXO-FITS facility using rigid-wall water chambers. These experiments will be identical to the proposed tests inside the FITS vessel and will allow us to develop the needed loading criterion for designing a supporting structure for the in-vessel tests. Furthermore, since similar lucite experiments are proposed, the influence of confinement can be determined from these tests.

The three preliminary series of experiments will assist us in the final objective of this program, i.e., to conduct four rigidly confined jet experiments inside the FITS vessel. The final experiments will evaluate the influence of three initial parameters: two different water depths, a three- and five-jet configuration, and the presence of an external trigger. These experiments are expected to provide experimental data about the conversion ratio, the gas- and water-phase-pressures generated during the FCI, the generation of hydrogen and steam, the posttest debris characteristics, the quench rate of the debris during the FCI, the average level swell or void fraction, and the explosibility of the configurations.

1.4.1.3 EXO-FITS Experiments (B. W. Marshall, Jr., 6427)

We began to conduct the newly developed experimental program, described in Section 1.4.1.2, investigating jets of molten fuel falling through relatively deep water chambers. This set of experiments was designed to model the lower grid forging of the Three-Mile Island Unit-2 reactor and to provide information about the mixing behavior of molten jets of fuel falling through water. The experiments conducted have been molten jets of iron alumina falling through both air and water. The preliminary observations, conclusions, and discussion for each type of experiments follow:

1.4.1.3.1 Molten Jets Falling Into Air

We have conducted six experiments in the EXO-FITS facility investigating the behavior of molten jets of iron alumina thermite falling through approximately 1.8 m of air. The experimental series has been named the MDJET series for Melt Development of JETs of molten thermite. The purpose of these experiments is to develop the experimental technology needed to deliver unobstructed molten jets of iron alumina into deep water chambers of various sizes. The general geometry of these experiments is shown in Figure 1.4-1. The crucible and mixer plate construction are shown in Figure 1.4-2. In Tables 1.4-2 and 1.4-3, the initial and boundary conditions of each of the experiments are shown for comparison purposes. Note that there were two MDJET experiments conducted with water as the coolant media. These two experiments were developmental in nature and are described in Section 1.4.1.3.2. To date, there have been two types of molten jet experiments conducted in air incorporating single- and three-jet configurations. Each is described below.

- Single-Jet Tests

  In the single-jet experiments (MDJET-1, -2, -6 and -7), we observed some interesting and somewhat unexpected trends in the jet behavior. Experimentally, the reacted thermite melted through the melt plug in the reaction crucible and fell into the mixer plate. The melt then flowed through a 4-cm hole in the mixer plate and created the desired initial jet diameter. The integral behavior of this jet was unusual in that it could not be described by a single-jet characteristic. Rather, the jet behavior appeared as a combination of characteristics, depending upon the time into the pour. Early into the pour, the jet characteristic resembled that of a jet in the turbulent regime with a transverse disturbance, more commonly referred to as sinuous breakup of the jet. This phase typically lasted for the duration of the melt relocation from the reaction crucible into the

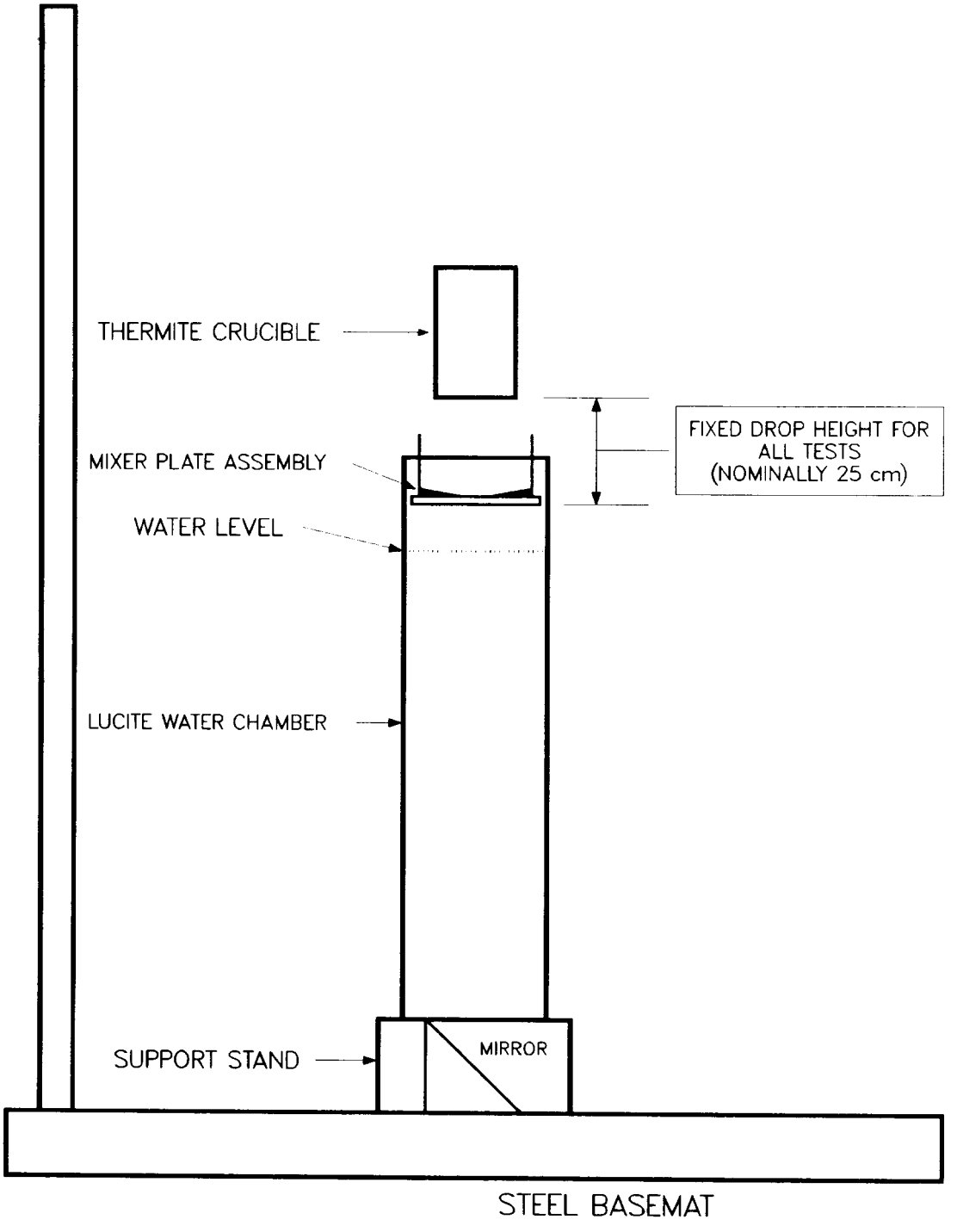

Figure 1.4-1. Geometry of the Molten Jet-Water Experiments Used for the EJET Series

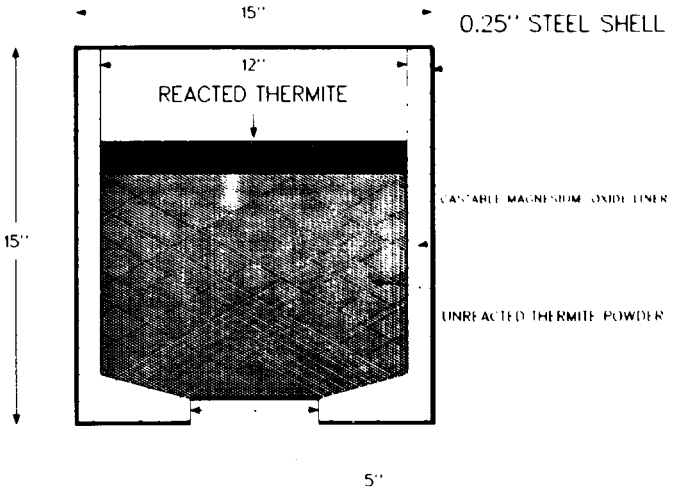

a.

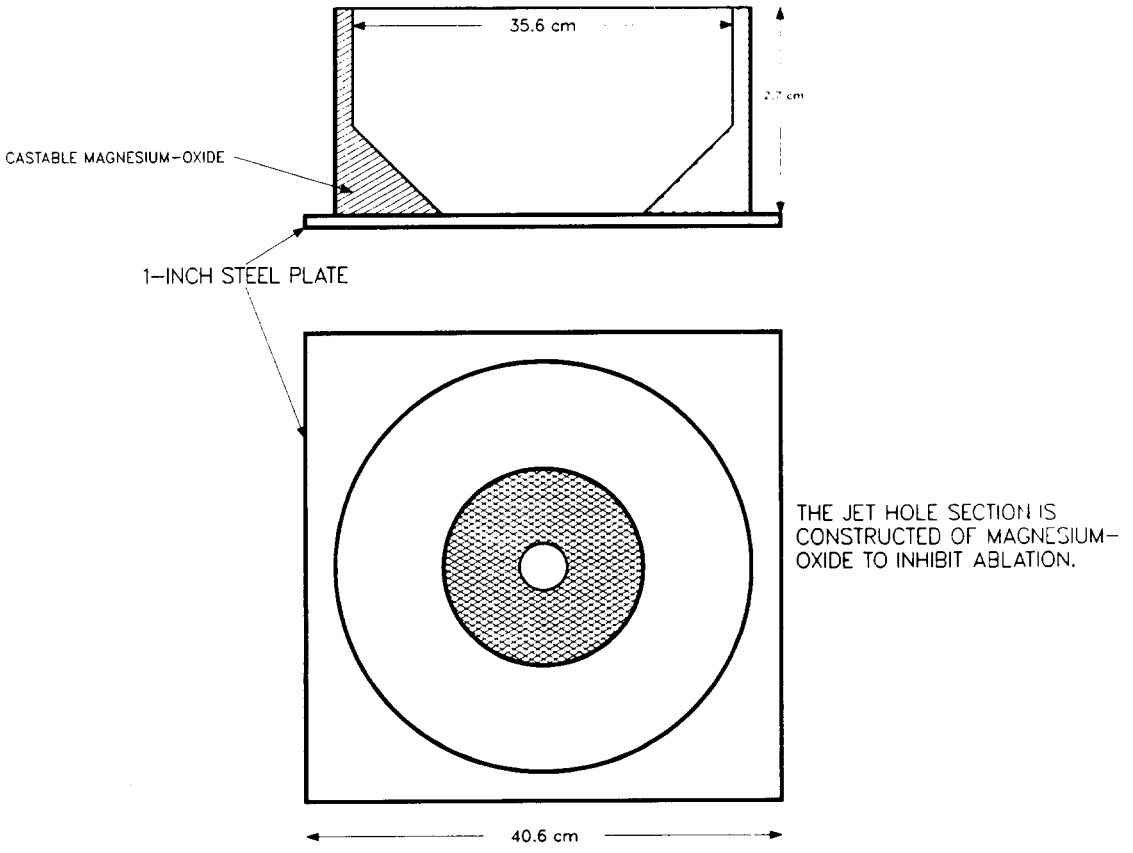

b.

Figure 1.4-2. Thermite Crucible (a) and Mixer Plate (b) Geometry

mixer plate. The jet behavior can be affected by numerous direct and indirect factors inherent in the experiment. Particularly, the turbulence in the reservoir above the nozzle will affect the jet behavior. In addition, the sharpness of the edge of the nozzle, the smoothness of the nozzle walls, and other factors will affect the behavior of the jet as it leaves the nozzle and falls through the coolant media. All of these conditions can lead to turbulent jet conditions for velocities that would not otherwise be turbulent. In these experiments, the turbulence is most likely generated during the melt relocation from the reaction crucible into the mixer plate. Therefore, we currently believe that turbulence in the jet flow field is responsible for the early time sinuous or transverse wave breakup.

Table 1.4-2

Initial and Boundary Conditions of the Molten Jet Air Experiments

Test	M_f[a] (kg)	M_d (cm)	Number of Jets	Jet Fall Distance(m)
MDJET-1	41.5	4	1	~1.8
MDJET-2	40.0	4	1	~1.8
MDJET-4	40.0	4	3[b]	~1.8
MDJET-5	40.0	4	1	~1.8
MDJET-6	40.0	4	1	~1.8
MDJET-7	40.0	4	3[b]	~1.8

[a]Mass of thermite initially loaded into the crucible.
[b]The jet holes were 120° apart and at a pitch of ~5.7 cm.

Table 1.4-3

Initial and Boundary Conditions for the Molten Jet Water Experiments

Test	M_f[a] (kg)	M_d (cm)	M_c (kg)	Coolant Depth (m)	T_c (K)
MDJET-3	37.6	4	269.4	1.20	303
MDJET-8	37.0	4	489.3	1.57	303
EJET-1	47.0	4	472.1	1.57	362
EJET-2	47.0	8	472.1	1.57	361
EJET-3	47.0	16	472.1	1.57	359
EJET-4	47.0	16	489.3	1.57	303

[a]Mass of thermite initially loaded into the crucible.

Subsequent to this early pouring phase, the behavior of the jet changed from sinuous to varicose. Varicose jet breakup is due to surface tension affects, causing the jet to break up to drops having diameters either approximately equal to the size of the jet diameter or smaller depending upon the number of satellites associated with the jet disintegration. This type of behavior would be expected since the jet velocities in these experiments are relatively low and surface tension effects should dominate in the absence of turbulence (e.g., the jets are gravity driven and the Reynolds numbers are relatively low implying that, in the absence of turbulence, varicose behavior would be expected).

Thus, for a single jet of molten thermite falling through an air media, we have observed jet behaviors that range from turbulent dominated phenomena (i.e., sinuous or transverse wave breakup) to jet fragmentation due to surface tension effects (i.e., varicose breakup).

o Three-Jet Tests

Two experiments (MDJET-4 and -5) were conducted using a three-jet geometry. The experimental configuration consisted of three 4-cm diameter jets at a pitch of 5.7 cm. The purpose of these experiments was to analyze the differences and similarities between the single-jet and three-jet configurations.

During these two experiments, we observed the same general type of jet behavior, segmented into two classifications. Early in the pour, the jet behavior was dominated by turbulent sinuous wave breakup while the late times were characterized by surface tension effects (i.e., varicose breakup). Furthermore, during the early pour times, the three jets appeared to spread away from one another and spin slightly about the center line of the three jets. This may be an indication that vortices were being established in the mixer plate above the nozzle, which caused the jet to swirl about the centerline. At late times during the pour, the jets appeared to fall vertically straight down when the influence of turbulence had subsided and surface tension effects again became important. Furthermore, we did not observe the slow swirling behavior as clearly in the late times as we did in the early phases of the pour. There was also a period during the pour in which we observed the influence of both transverse wave breakup and surface tension effects; e.g., the jet first broke up into segments corresponding to the transverse disturbance and then broke up into droplets approximately

equal to the jet diameter, indicating that surface tension and turbulence both play a role in the jet framentation.

1.4.1.3.2 Molten Jets Falling Into Water

o MDJET-8

In this experiment, we used iron-alumina thermite to generate approximately 40 kg of melt. The molten products of the thermite reaction melted through a 0.64-cm-thick plate in the bottom of the reaction crucible and fell onto the mixer plate. The mixer plate had a funnel-type assembly causing the melt to flow through the 4-cm diameter hole. The mixer plate was placed at the upper water level, such that there was no appreciable entrance velocity of the melt into the water. The water chamber was a 55.9-cm square and was filled to a depth of 1.57 m. The water was initially at a temperature of 303 K (30°C).

The melt flowed through the mixer plate and into the water. We could not identify a coherent jet flowing in the water. There appeared to be significant breakup of the melt as it entered the water. The purpose of this experiment was to identify any potential experimental problems in preparation for the two experiments proposed (i.e., a 4- and 8-cm diameter jet falling into saturated water). This experimental data is currently being analyzed and will be reported as the results warrant.

o EJET-1

This experiment was essentially a repeat of the MDJET-8 experiment except the water temperature was 362°K (89°C), and the thermite mass prepared was 50 kg. In this experiment we again observed significant breakup of the melt as it fell through the saturated water. As shown in Figure 1.4-3, the outer diameter of the melt water mixture region entered the water and immediately grew to twice the initial jet diameter. This diameter then continued to fall into the water for approximately 600 ms, corresponding to a penetration of the leading edge of approximately 45 cm. After 600 ms, smaller satellite droplets of melt appeared to continue to fall further into the water chamber at their terminal velocity while the main mass constituting the jet did not penetrate the water any further for the next 700 to 800 ms. At ~1300 ms, the main jet mass began to propagate further into the water chamber at approximately the same speed as the leading edge. This type of segmented behavior suggests that a threshold-type

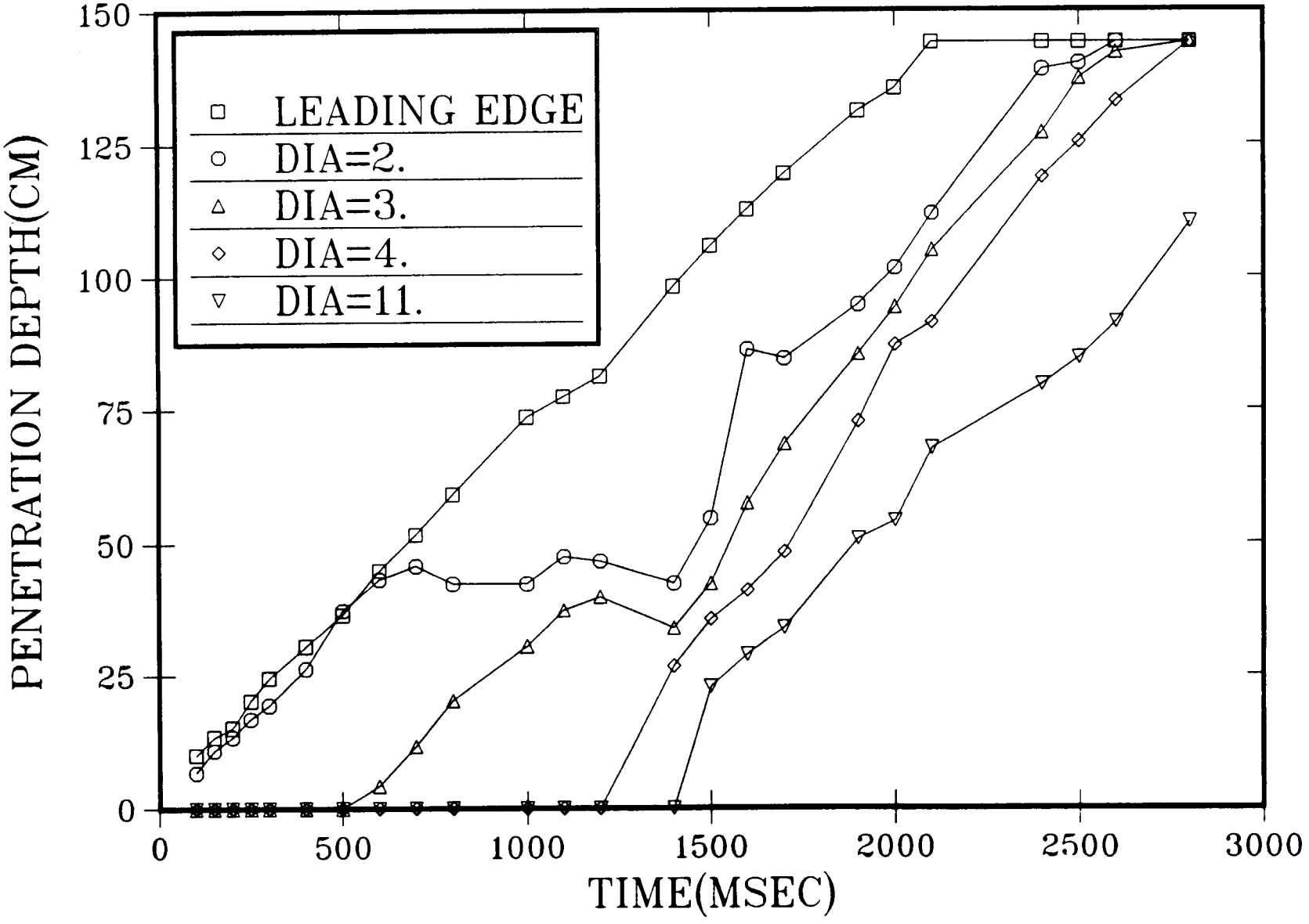

Figure 1.4-3. Penetration of the Initially 4-cm Diameter Jet as a Function of Time for Various Scaled Jet Diameters (Test EJET1)

condition governs the jet-mixing characteristics. The most obvious condition would be the countercurrent flow of steam up towards the incoming jet. Also experimental boundary conditions such as the delivery technique could potentially cause such observations. Therefore, more data is needed before these data and the resulting interpretations can be accepted.

- EJET-2

  In this experiment, 50 kg of iron-alumina thermite were used to generate a molten jet 8 cm in diameter. The water chamber dimensions and water depth were identical to those used in the EJET-1 and MDJET-8 tests. The water temperature was 361°K (88°C), which is approximately six degrees subcooled.

  From the high-speed films, we again observed significant mixing of the melt with the water. As shown in Figure 1.4-4, the same general jet-mixing behavior occurred as in the EJET-1 experiment. The 8-cm jet penetrated approximately 25 to 30 cm before a mixing plateau occurred. As in the EJET-1 experiment, the beginning of the plateau occurred at ~700 ms, but the corresponding penetration depth was roughly half that observed in the EJET-1. After the mixing plateau (i.e., at ~1400 ms), the full jet diameter (8 cm) propagated further into the water at roughly the same velocity as the leading edge. It is apparent that a threshold-type condition plays an important role in the fragmentation and growth process of these jets. However, it is currently unclear what the exact cause of this behavior is.

- EJET-3

  The two experiments described obviously asked more questions than the data base could answer. For example: What causes the threshold-type condition in the mixing behavior observed in both the EJET-1 and -2 experiments? Does this type of behavior scale? Is it important at reactor-scale jet diameters?

  There are numerous questions that must be addressed before we can understand the complex mixing of molten jets of core material with residual coolant water. However, we felt that one of the most important questions that needed to be answered for reactor safety analyses was the question of scaling. We, therefore, conducted an experiment which modeled the full-scale jets inside the TMI-2 reactor; i.e., the 16.3-cm holes in the core forging that could generate the largest jet

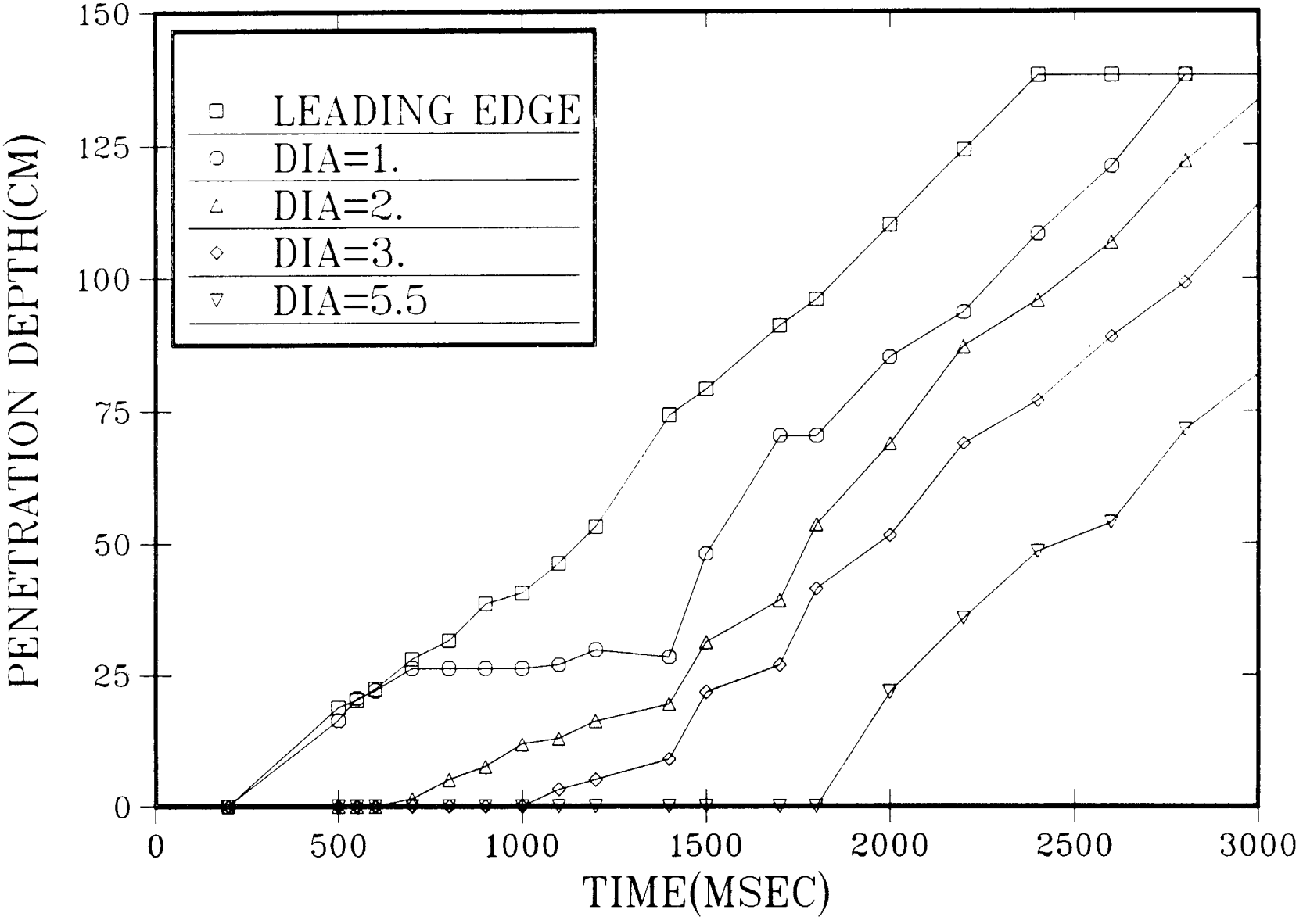

Figure 1.4-4. Penetration of the Initially 8-cm Diameter Jet as a Function of Time for Various Scaled Jet Diameters (Test EJET-2)

diameters. The experiment, EJET-3, was an exact repeat of the EJET-1 and -2 experiments except for the initial jet diameter, making comparisons straightforward and simplified. In this experiment, as shown in Figure 1.4-5, the mixing behavior was noticeably different than the previous two experiments. We did not observe a plateau at anytime during the pour. We note, however, that delivery of a uniform jet having this large of an initial diameter is difficult. We encountered problems with the melt-through plug (the 0.64-cm plate on the bottom of the thermite crucible) uniformly failing, resulting in a leading edge somewhat smaller than the actual desired jet diameter. Furthermore, since only 50 kg of thermite melt were used to generate this jet, the ideal L/d of the jet was less than ~4; not an ideal "jet." However, the behavior shown in Figure 1.4-5 is at least qualitatively different than those observed for the previous two experiments and suggests that more full-scale experiments may be warranted for future work.

We have begun to experimentally evaluate the importance of molten jets falling through saturated water. In all experiments, significant mixing and growth of the initial jet diameter were observed within the time scale of the melt pour. We did not observe a spontaneously triggered steam explosion in any of these experiments, suggesting a potentially benign geometry. However, if an external trigger were available, these configurations might yield a highly explosible configuration. We are currently planning on using an external trigger in future experiments of this type to assess this observation.

1.4.2 Liquid Jet Breakup; Atomization Model (S. Winquist and M. Corradini, University of Wisconsin)

In the event of a nuclear reactor meltdown accident, molten corium may be ejected into the containment as a liquid jet. In order to accurately predict containment pressure loads as a result of steam explosions, direct heating, or both, it is important to assess this liquid jet breakup. Due to the sensitivity of containment code results to the injected corium source term, it is important to make good estimates of:

1. The extent of jet breakup.

2. The size of the resulting fragments.

3. The area over which the fragments will distribute themselves.

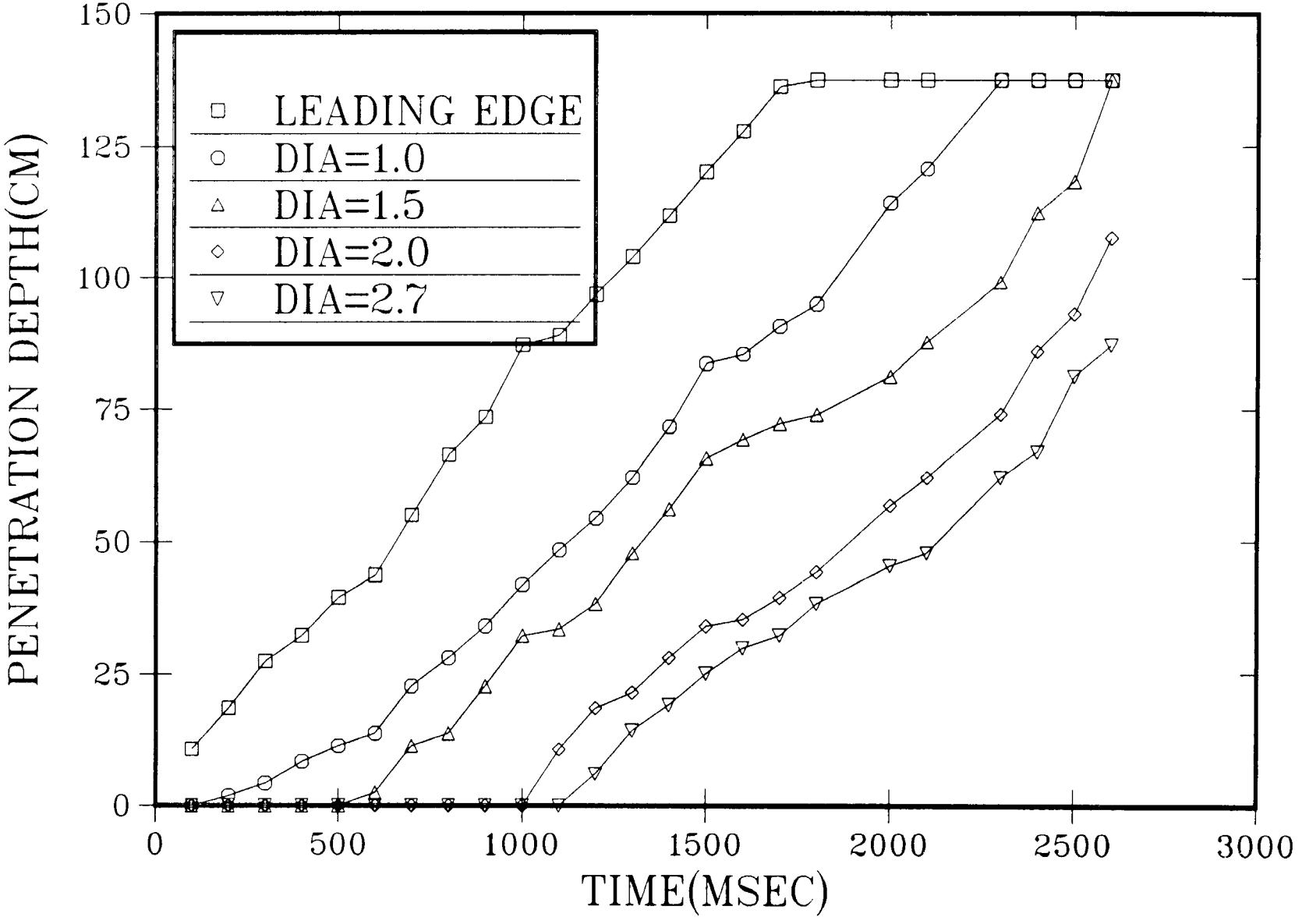

Figure 1.4-5. Penetration of the Initially 16-cm Diameter Jet as a Function of Time for Various Scaled Jet Diameters (Test EJET-3)

We are presently working on a mechanistic, one-dimensional computer model that predicts the atomization of a liquid jet. The following provides a short description of the model, the expected results and limitations, and present progress of the model.

1.4.2.1 Characteristics

This one-dimensional model calculates breakup in the atomization regime based on what many feel is the dominant mechanism for atomization: aerodynamic surface wavegrowth and subsequent droplet separation.[21] It does not account for nozzle geometry effects or breakup effects of the dissolution of gases at this time. It calculates steady-state breakup for gas liquid interface of an isothermal jet. Further breakup or coalescence of the separated droplets is not considered at this time.

This project focuses on aerodynamic atomization because if breakup does occur, atomization is possible, and it is the bounding case for size and amounts of jet fragments created, i.e., the rate of jet breakup will not exceed that given by atomization. Only aerodynamic effects are considered because they will always play a dominant role in high speed jet breakup, and not enough is known about atomization to justify including other effects. Further analysis based on the work of Epstein[22] validate the assumption of a vapor-liquid interface even in the case of corium into water injections.

1.4.2.2 Description

The model represents the liquid jet from the nozzle exit to the end of the continuous core of the liquid jet in a series of control volumes. Using an analytical solution,[23] the model calculates a droplet separation time and a control volume length equal to the jet velocity times the separation time constant. The side of the control volume is taken as a cone whose angle is determined analytically.[23] The number of droplets separated in that control volume and the diameter of the drops are calculated using an analytical solution for the fastest growing wavelength.[23] The deceleration of all previously separated droplets are then calculated across the control volume. A momentum balance between the droplets and the continuous phase accounts for entrainment of the continuous phase. Entrained air or steam is assumed to enter the control volume radially with no axial momentum. The new relative velocity between the jet surface and the continuous phase is used to calculate the growth rate and wavelength of the fastest growing disturbance in the next control volume. This process is repeated until the liquid core has been completely atomized.

1.4.2.3 Limitations

The most glaring limitation of this project is the limited availability of data for code verification. Not only are there only a few published experiments on liquid jets in atomization, but they are for small diameter jets. Also, measurements of droplet sizes and continuous liquid cores are very difficult in dense sprays.

1.4.2.4 Sample Calculation

Figures 1.4-6 through 1.4-11 are the results of a sample calculation of a 2-cm diameter jet being injected into atmospheric air. We are still in the process of making initial modifications to this model, so these results are only illustrative of what kind of output the model does provide. In the figures the distance from the nozzle, Z, is the axial distance from the nozzle exit. The calculation ends when the jet is completely broken up: When the continuous core of the jet ends. For this calculation the breakup length, Zbreakup, is about 7.2 m. The control volume number corresponds to each individual control volume in the calculation, starting with 1 at the nozzle exit and ending with the last number at the end of the continuous core of the liquid jet. This calculation used 58 control volumes. Where droplet characteristics (velocity, diameter, etc.) are plotted as a function of the control volume number, the characteristics are of those droplets separated in that control volume. Likewise, where the velocities of the 1st, 5th, 10th, and 50th droplet groups are plotted as a function of distance from the nozzle, the numbers 1, 5, 10, and 50 refer to the control volume number of the control volume in which the droplets were separated from the jet. Notice that in Figure 1.4-7, that the 10th droplets do not have a velocity until Z = 1.2 m, just after they were formed.

1.4.2.5 Expected Results: Qualitative

With this model we hope to show:

1. The effect of jet diameter on jet breakup (the stabilizing effect of continuous phase entrainment).

2. The effect of initial jet velocity.

3. The effect of nonzero initial ambient velocity (i.e. steam generation).

4. The sensitivity of the breakup to various parameters.

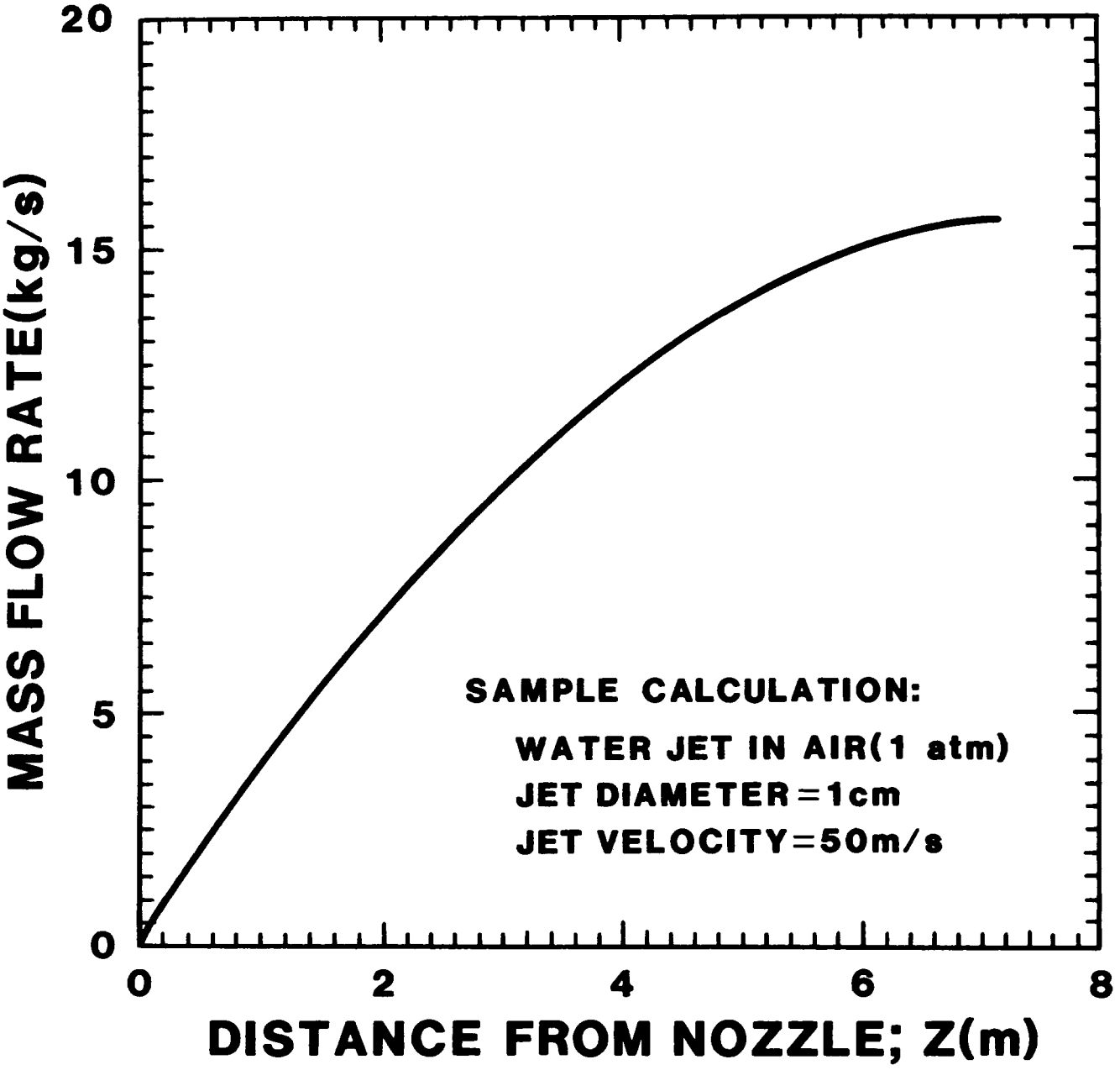

Figure 1.4-6. Separated Mass Flow Rate as a Function of Distance From Nozzle (Droplet Mass Flow Rate)

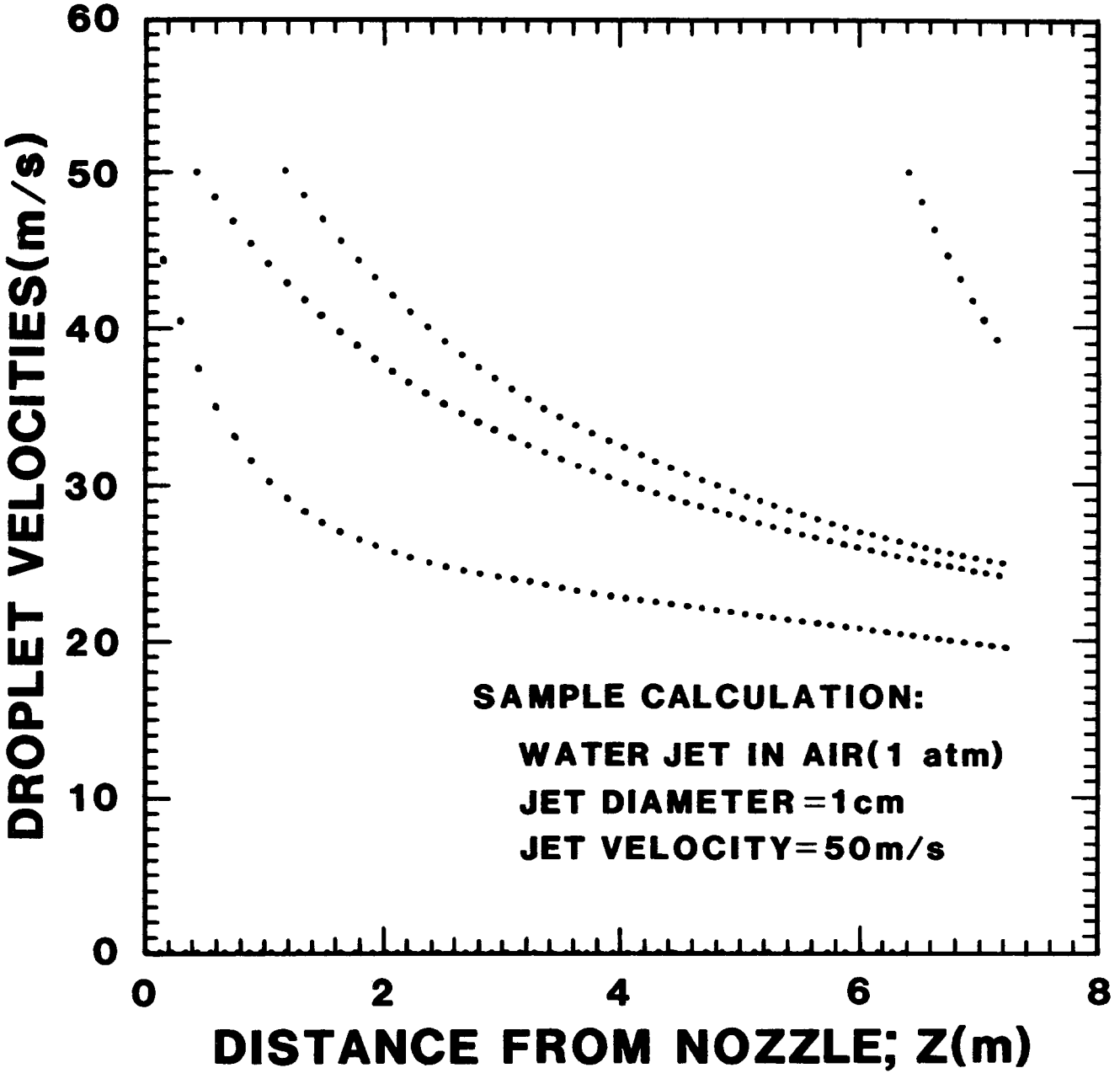

Figure 1.4-7. Droplet Velocities as a Function of Distance From the Nozzle (for the 1st, 5th, 10th, and 50th Droplets)

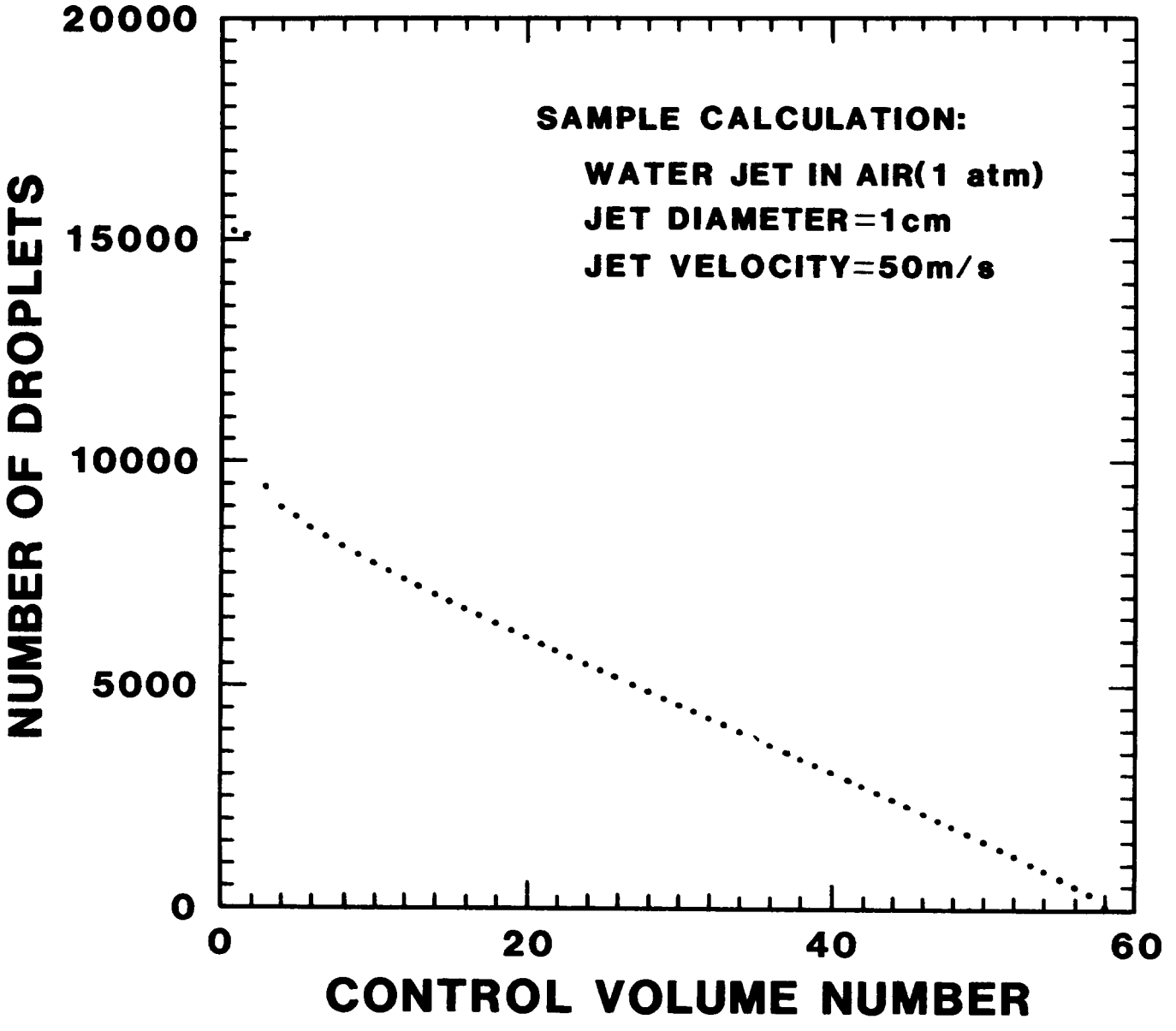

Figure 1.4-8. Number of Droplets Produced in Each Control Volume

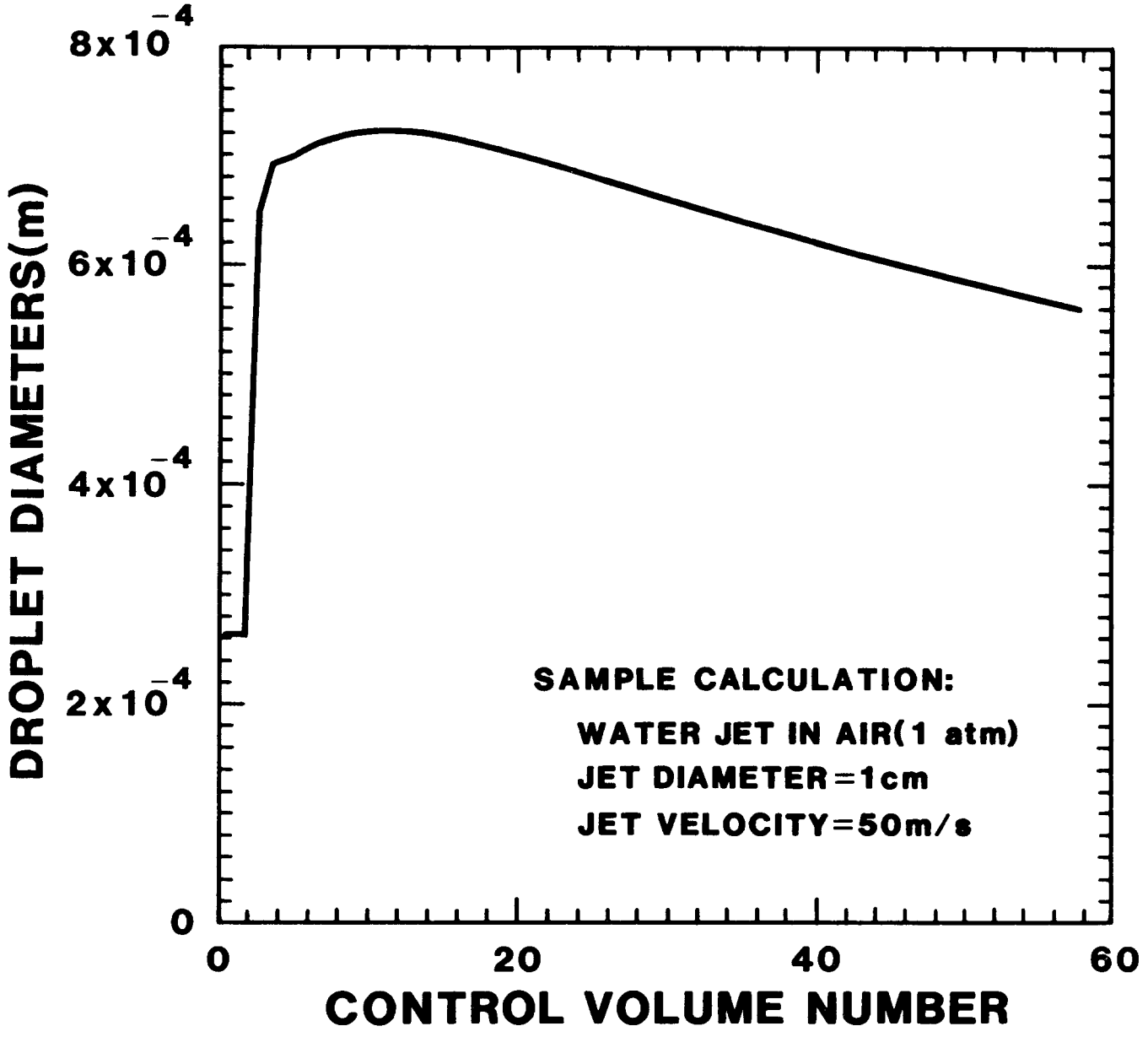

Figure 1.4-9. Droplet Diameter Produced in Each Control Volume

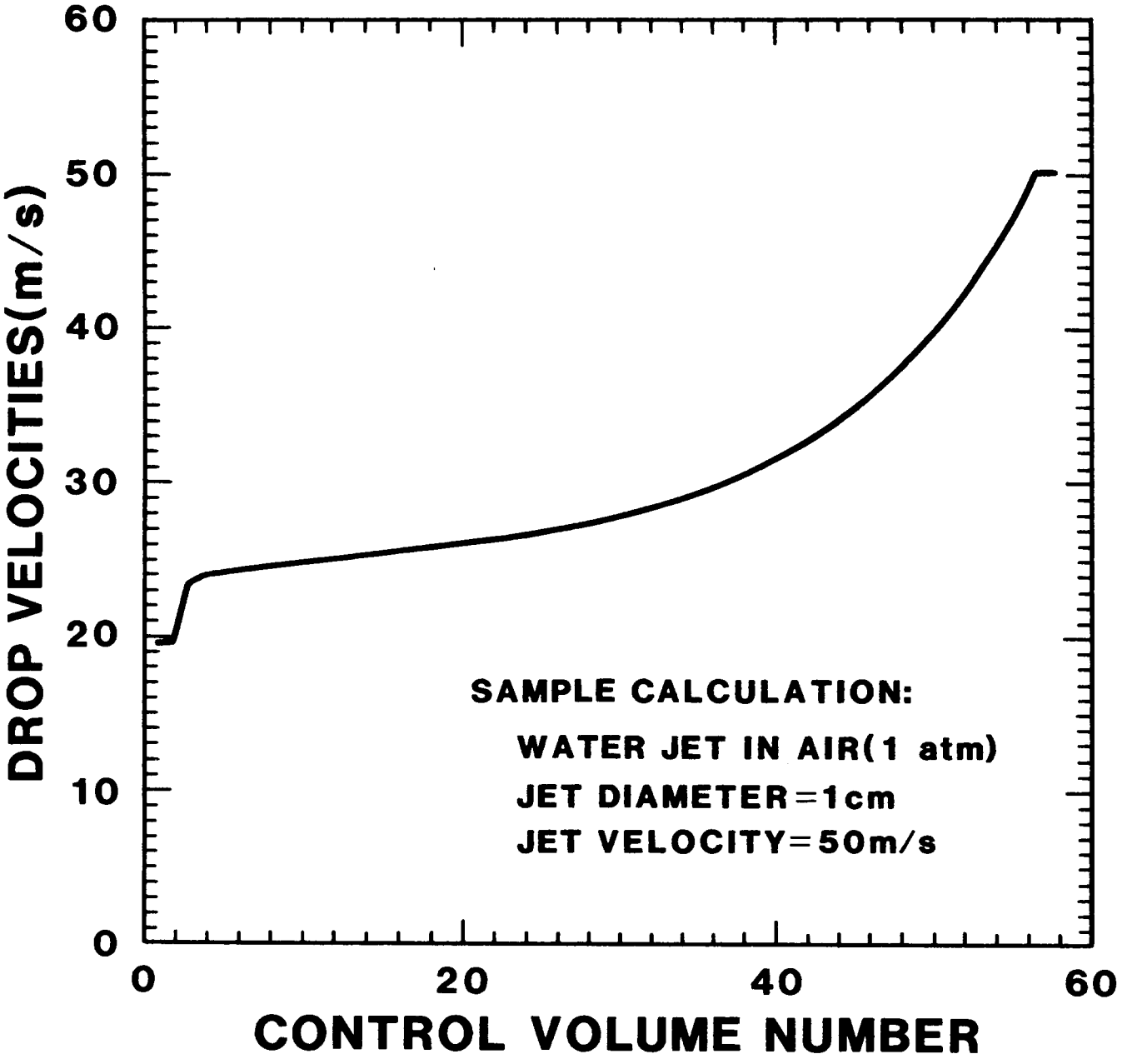

Figure 1.4-10. Velocities of Each Droplet Package at Z = Zbreakup

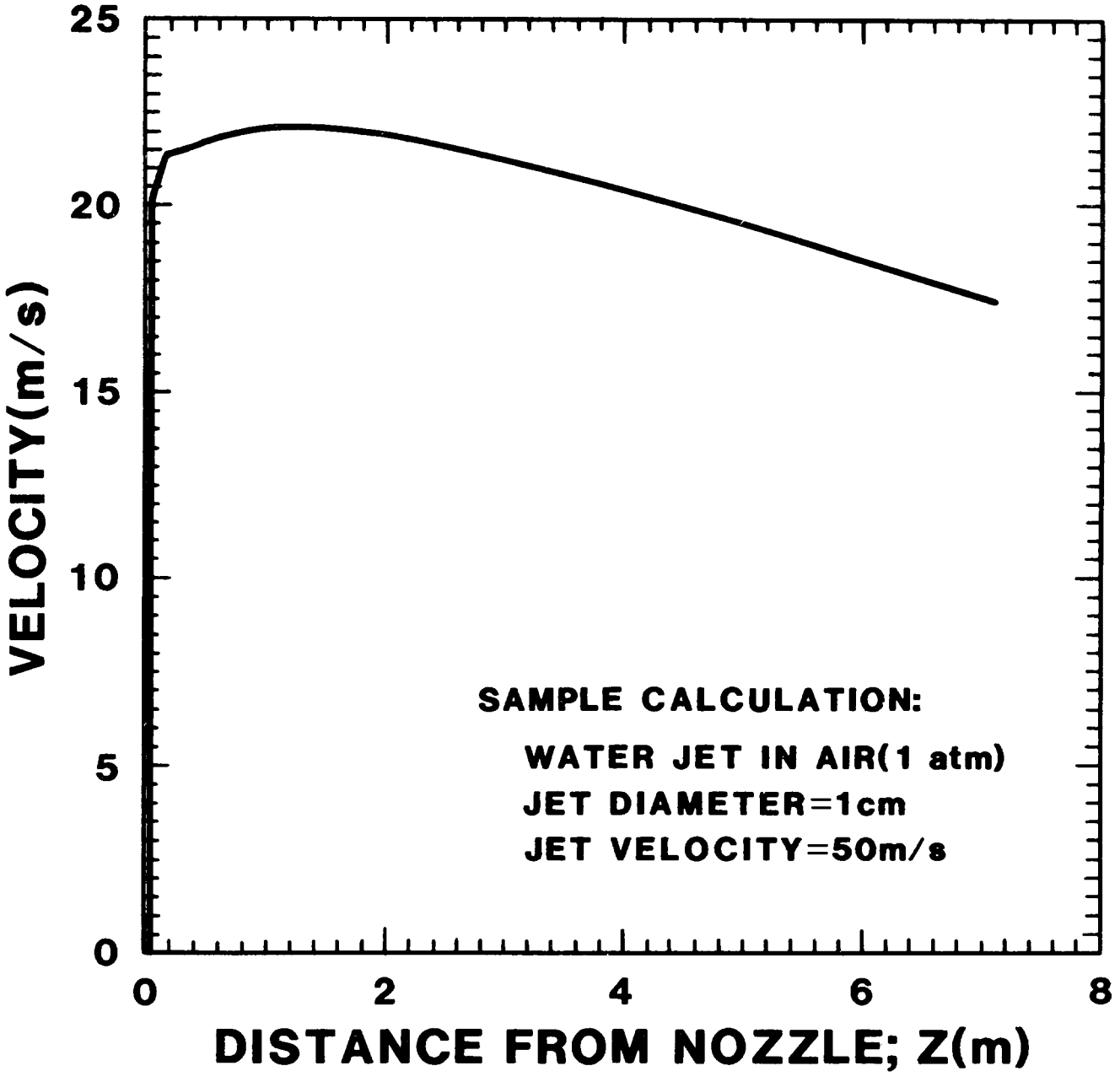

Figure 1.4-11. Continuous Phase Velocity as a Function of Distance From Nozzle (Axial Velocity Is Constant Radially)

1.4.2.6 Expected Results: Quantitative

With this model we hope to be able to provide better estimates than are currently available for:

1. Droplet sizes.

2. Mass flow rates of separated droplets as a function of distance from nozzle (reactor vessel breach).

1.4.3 Presentations, Visits, and Meetings Attended

B. Marshall and M. Berman each presented papers at the ANS/ENS meeting in San Diego on February 2nd - 6th. The titles of these papers were: "Recent Intermediate-Scale Experiments on Fuel-Coolant Interactions in an Open Geometry (EXO-FITS)" and "An Evaluation of the Bases for Estimating Alpha-Mode Failure Probabilities," respectively.

On June 25, 1986, M. Berman, M. Young, and B. W. Marshall attended the peer review of the technical report entitled "An Investigation of Steam Explosion Loadings with SIMMER-II" by B. Bohl of the Los Alamos National Laboratory. M. Berman and M. Young each gave presentations summarizing their comments and review of the report.

1.5 Hydrogen Behavior
(D. W. Stamps and M. Berman, 6427)

The major concerns regarding hydrogen in LWRs are that the static or dynamic pressure loads from combustion may breach containment or that important, safety-related equipment may be damaged due to either pressure loads or high temperatures. In order to assess the possible threats, it is necessary to understand how hydrogen is produced, how it is transported and mixed within containment, and how it combusts.

The objectives of this program are (1) to quantify the threat to nuclear power plants (containment structure, safety equipment, and the primary system) posed by hydrogen combustion, (2) to disseminate information on hydrogen behavior and control, and (3) to provide programmatic and technical assistance to the NRC on hydrogen-related matters.

1.5.1 Standard Problem for HECTR-MAAP Code Comparison
(C. C. Wong, 6427)

Substantial differences exist in the way that IDCOR (Industry Degraded Core Rulemaking) and NRC model hydrogen combustion and transport in a nuclear reactor containment. The major differences lie in the areas of (1) ignition and flame propagation criteria, (2) discrete burning, (3) continuous recombination, and (4) natural circulation. These

differences will give different predictions of pressure and temperature loadings imposed on the containment and equipment by the accumulation and combustion of hydrogen during a severe accident. For example, the NRC model, based on the analyses by the HECTR code, tends to allow the buildup of higher hydrogen concentrations and generally leads to the prediction of higher containment pressures and temperatures. On the other hand, the IDCOR model, based on the analyses by the MAAP code (Modular Accident Analysis Program,[24]) usually does not predict these effects. The objective of this comparison is to determine the impact of these differences and to assist the NRC in determining the acceptability of the models for performing risk assessments.

In order to resolve differences between the NRC and IDCOR on the hydrogen combustion issue, a standard problem has been defined to compare HECTR and MAAP analyses of hydrogen transport and combustion in a nuclear reactor containment. The problem selected is an S2HF accident sequence in a PWR ice-condenser containment. The selection of the S2HF accident sequence is for code comparison only.

1.5.1.1 Description of the HECTR-MAAP Standard Problem

The S2HF accident scenario involves a small break (0.5 to 2 inches in diameter) loss-of-coolant accident with failure of emergency coolant and containment-spray recirculation. All of the water inventory from the sprays, which are only operated in the injection mode, is trapped in the upper compartment due to the failure to remove upper-to-lower-compartment drain plugs. This failure causes the reactor cavity to remain dry throughout the transient. Incomplete hydrogen burns initiated by the deliberate ignition system will occur in the lower and upper compartments. When the reactor vessel fails, the molten fuel slumps onto the floor of the cavity and results in a core-concrete interaction. This interaction generates a substantial amount of combustible gases, which may burn as a standing flame in the cavity. The stability of this standing flame strongly depends on the amount of oxygen present in the cavity and the concentrations of steam, CO_2, and other diluents.

Because our main objective is to assess the importance of modeling differences of hydrogen combustion and transport in the HECTR and MAAP codes, the sources (either steam or any noncondensible gases) and initial conditions predicted by the MAAP code will be put into HECTR to study the containment response. Moreover, for better comparison of both computer codes, we redefined the standard problem into a two-part transient problem.[25] The first part of the transient problem will study hydrogen behavior during the period of in-vessel hydrogen production and the second part

will cover hydrogen behavior during the period of ex-vessel hydrogen production. By setting up the standard problem this way, any discrepancies of the results between HECTR and MAAP in the first part of the problem will not affect the second part of the problem.

In the MAAP analysis of the S2HF accident in an ice-condenser containment,[26] an average clad oxidation of 30 percent was calculated. This corresponds to 248 kg (547 lb) of hydrogen being generated. The hydrogen and steam release rates predicted by the MAAP code for the S2HF accident sequence are plotted in Figure 1.5-1. Since HECTR is using the sources and initial conditions generated by the MAAP code, the following HECTR results do not represent our best estimate of the pressure-temperature response of an ice-condenser containment during an S2HF accident. These HECTR analyses are only designed to better understand differences in the combustion model between two computer codes.

1.5.1.2 Modeling Differences Between HECTR and MAAP

Before presenting HECTR analyses of the first part of the standard problem, a review of the combustion models used in HECTR and in MAAP is provided. Table 1.5-1 lists major differences of the combustion model between these two codes. Since most key parameters in combustion modeling, such as ignition criteria, combustion completeness, burn time, and propagation criteria, are expressed either as an algebraic formula (as in HECTR) or as an analytical formula (as in MAAP), it is not necessary to perform a large amount of HECTR or MAAP calculations in order to compare the combustion models in both codes. By comparing these key combustion parameters, based on the predictions made by both algebraic and analytical formulas, with the measured data obtained from experiments, a better understanding of differences between the combustion models in both codes can be achieved. This approach works well when addressing the modeling of incomplete burning in the lower and upper compartments.

The existing experiments that are used in this comparison are the VGES[27] and NTS[28] experiments. The required input data for both HECTR and MAAP models are listed in Table 1.5-2. A burning velocity multiplier of 1 and drag coefficient of 100 are used in this comparison because these are the values used in containment analyses in Reference 26.

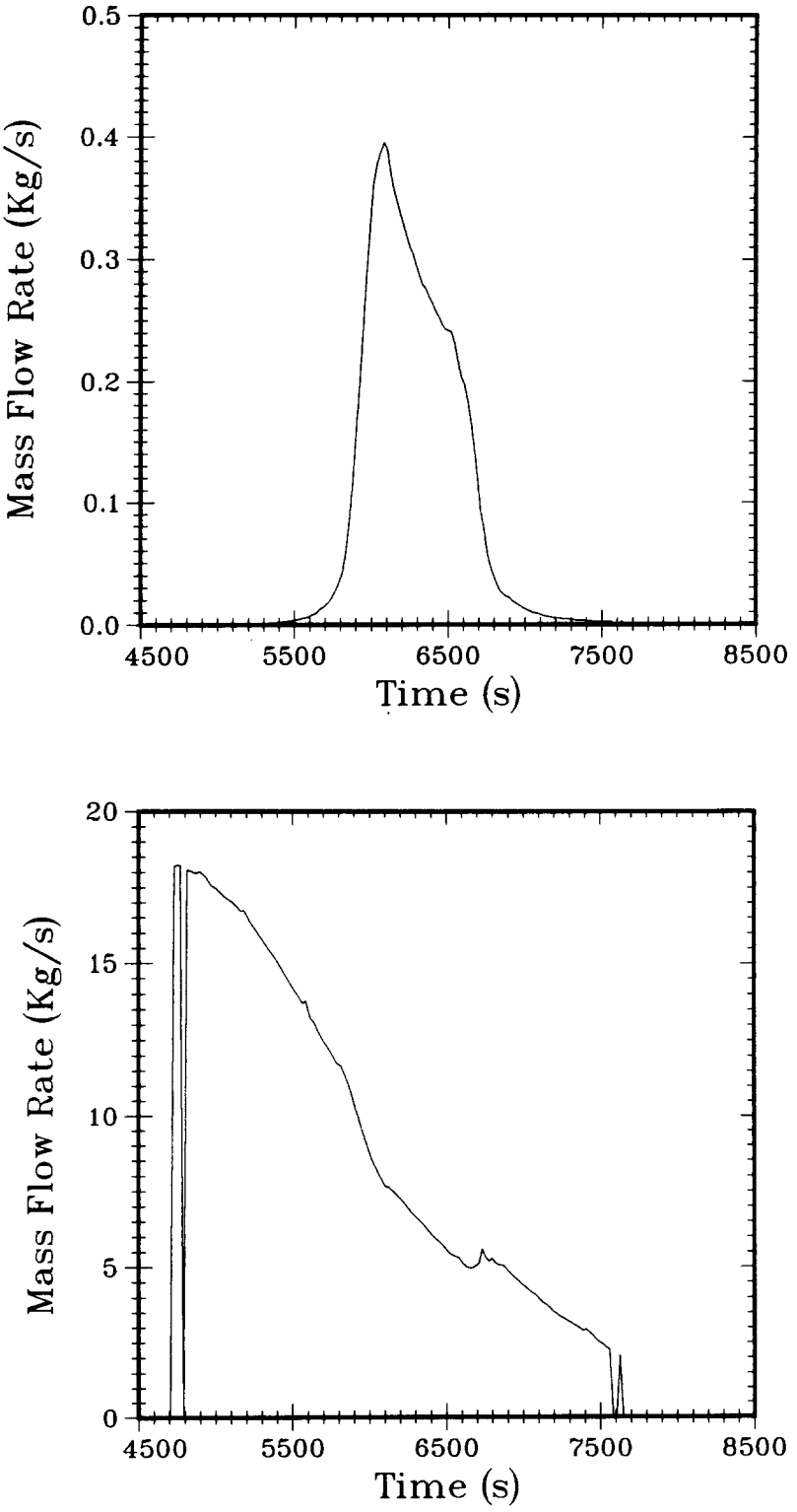

Figure 1.5-1. Hydrogen (Top) and Steam (Bottom) Release Rates Into Reactor Containment Predicted by the MAAP Code

Table 1.5-1

Modeling Differences Between HECTR and MAAP

	HECTR	MAAP
Combustion Model		
Ignition Criterion	Depends on mixture concentration (user input; can be varied parametrically).	For global burn, uses flame speed criterion. For incomplete burn, checks if burning velocity is greater than 1 cm/s.
Combustion Completeness	Calculates based on an empirical formula (a function of H_2 concentration).	Predicts a complete burn if flame temperature criterion is satisfied. For incomplete burn, uses an analytical formula (functions of burning velocity, drag coeff., igniter location).
Burn Time	Characteristic length divided by flame speed.	Regional radius divided by burning velocity for global burn. For incomplete burn, uses an analytical formula (functions of burning velocity, drag coeff., and density)
Flame Propagation	Upward, downward, horizontal propagations depend on H_2 concentration	Upward propagation

- Ignition Criteria

  The ignition criteria in both HECTR and MAAP codes depend heavily on the mixture chemistry. Neither combustion model considers the availabilty of ignition sources or activation energy required to initiate combustion. For example, a substantial cooling by air motion driven by sprays may degrade the performance of igniters and prevent ignition; neither model accounts

for this effect. In HECTR and in MAAP, as long as the built-in ignition criteria are satisfied, combustion will occur. The default ignition criteria in HECTR are: $H_2 \geq 7$ percent, $O_2 \geq 5$ percent, and steam ≤ 55 percent. The user can vary the criteria by changing the value of the mixture concentration and perform parametric studies.

Table 1.5-2

Parameters Used for Case Study of the MAAP Combustion Model

1. VGES Fans-Off and Fans-On Cases	
Burning Velocity Multiplier	= 1
Drag Coefficient	= 100
Characteristic Length	= 3.680 m
Height of the Vessel	= 4.267 m
Radius of the Vessel	= 0.610 m
2. NTS Fans and Sprays Off Cases	
Burning Velocity Multiplier	= 1
Drag Coefficient	= 100
Characteristic Length	= 14.02 m
Use Cylindrical Geometry	
Height of the Vessel	= 15.85 m
Radius of the Vessel	= 6.471 m

In MAAP, the flame temperature criterion is used to determine the potential of a global burn; the critical temperature is set at 983 K. Figure 1.5-2 illustrates how the calculated adiabatic flame temperature varies with hydrogen concentration, based on the initial conditions of the VGES fans-off experiments. Applying this flame temperature criterion, it predicts that a global burn will occur at a hydrogen concentration of 7.3 percent. In MAAP, the specific heat at constant pressure is used to calculate the adiabatic flame temperature, and these gas properties are temperature-independent. Figure 1.5-2 also includes two curves to show how the flame temperature criterion will change if the specific heat at constant volume and constant pressure is calculated taking into account the actual temperature dependence.[29] If a temperature-dependent specific heat at constant pressure is used, it predicts that a global burn will occur at a hydrogen concentration of 8.7 percent; this is quite similar to the findings in Reference 30.

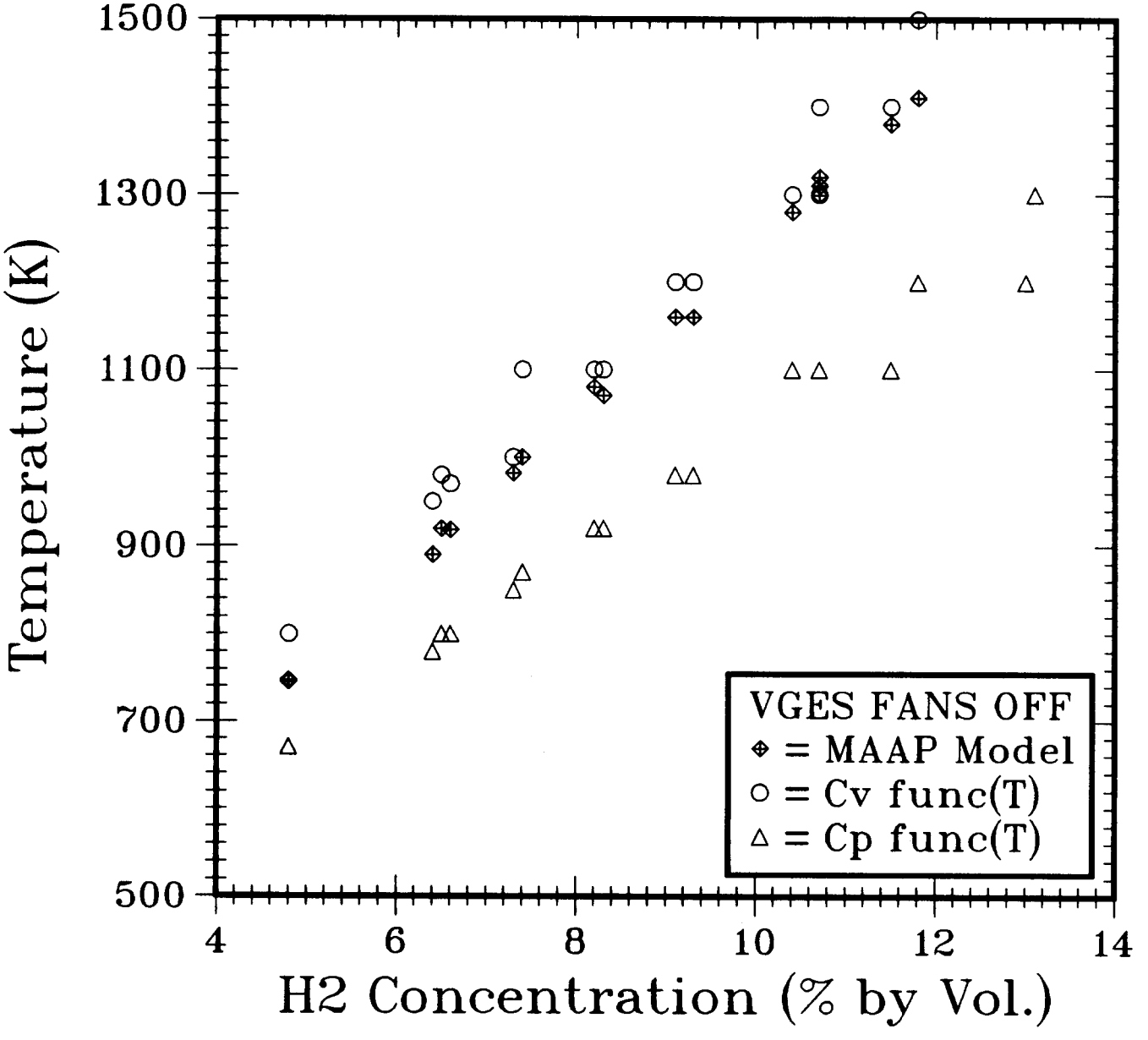

Figure 1.5-2. Adiabatic Flame Temperature as a Function of Hydrogen Concentration

To determine whether an incomplete burn will take place, MAAP will check (1) if the calculated burning velocity is greater than 1 cm/s and (2) if igniters are working. This 1-cm/s burning velocity condition implies that an incomplete burning occurs at a hydrogen concentration of about 4.8 to 5 percent, depending upon the steam mole fraction (Figure 1.5-3). Here, as shown in Figure 1.5-3, the steam inerting effect on initiation of an incomplete burn is rather small. Hydrogen will still combust at a concentration of 5.5 percent even though there is substantial amount of steam in an environment (>55 percent steam). Experiments, which studied flammability of hydrogen-air-steam mixtures,[31,32,33] have shown that combustion will be precluded if the steam mole fraction is greater than 55 percent or much less if the hydrogen concentration is 4 to 6 percent.

In Figure 1.5-4, the ignition criteria used in HECTR and in MAAP for both global and incomplete burns are compiled and plotted against data obtained from FITS combustion experiments[31] to study flammability of hydrogen-air-steam mixtures in a quiescent environment. The ignition criteria in HECTR will prevent any combustion if steam concentration is too high (>55 percent); on the contrary, the MAAP criteria do not consider any steam inerting effect. Neglecting the steam inerting effect may give a very different result when analyzing containment responses during a severe nuclear reactor accident. For example, in Reference 34, during an S_2D accident with 75 percent zirconium-water reaction, HECTR predicted that a substantial amount of steam had already built up in the lower compartment of an ice-condenser containment when the hydrogen was released. Even though igniters were working, combustion in the lower compartment did not occur because of the steam inerting environment. Eventually, combustion took place in the dome and generated a peak pressure of 343 kPa. If combustion were allowed in the lower compartment, neglecting the steam inerting effect, an earlier and more moderate burn leading to a much lower peak pressure would be predicted.

A newly-generated flammability correlation[31] based on the FITS experiments is also plotted in Figure 1.5-4. This correlation is better than the existing criteria used in HECTR and in MAAP to account for the steam inerting effect. Incorporation of this flammability correlation is recommended for both codes when performing containment analysis.

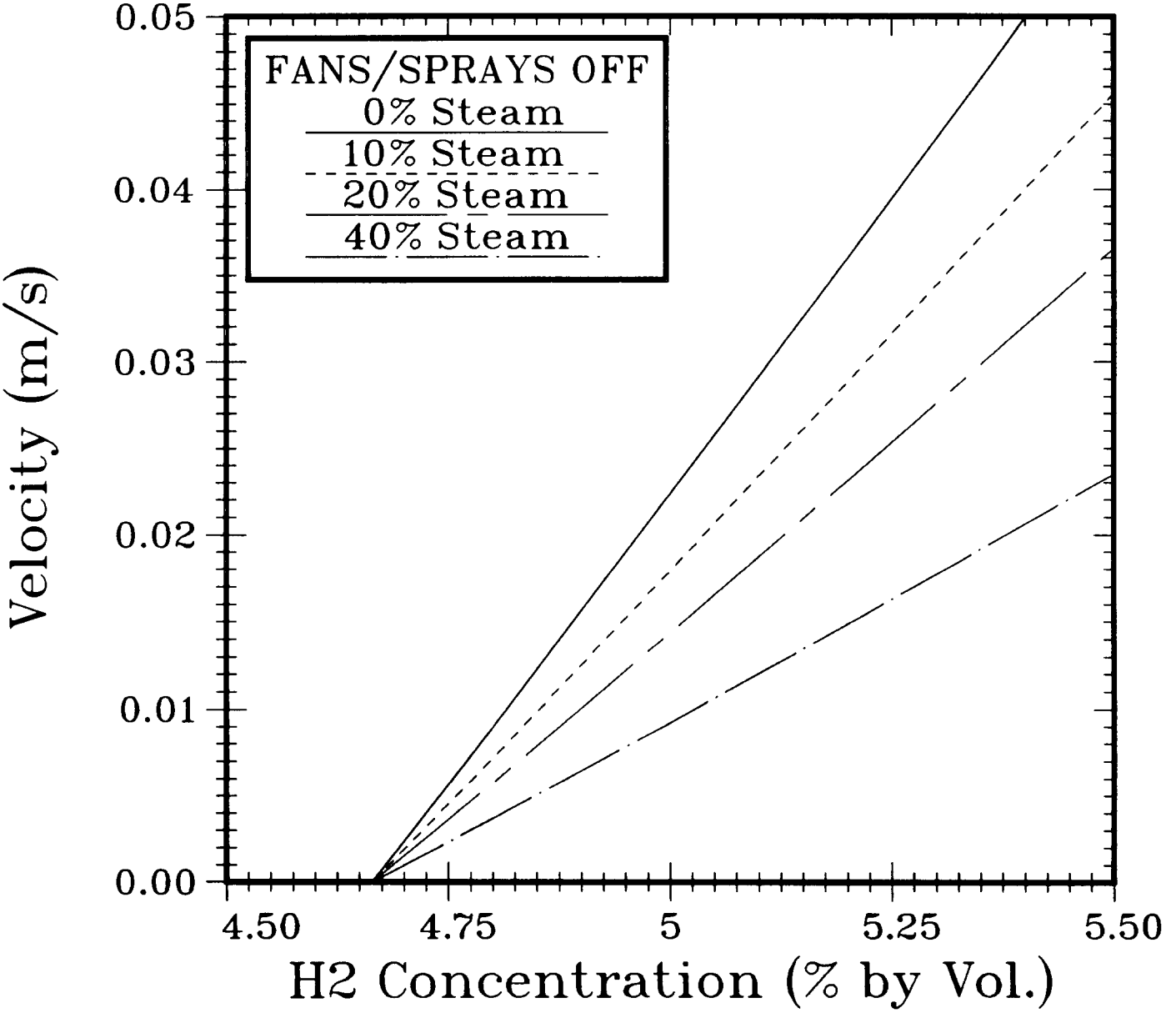

Figure 1.5-3. Burning Velocity as a Function of Hydrogen and Steam Concentrations

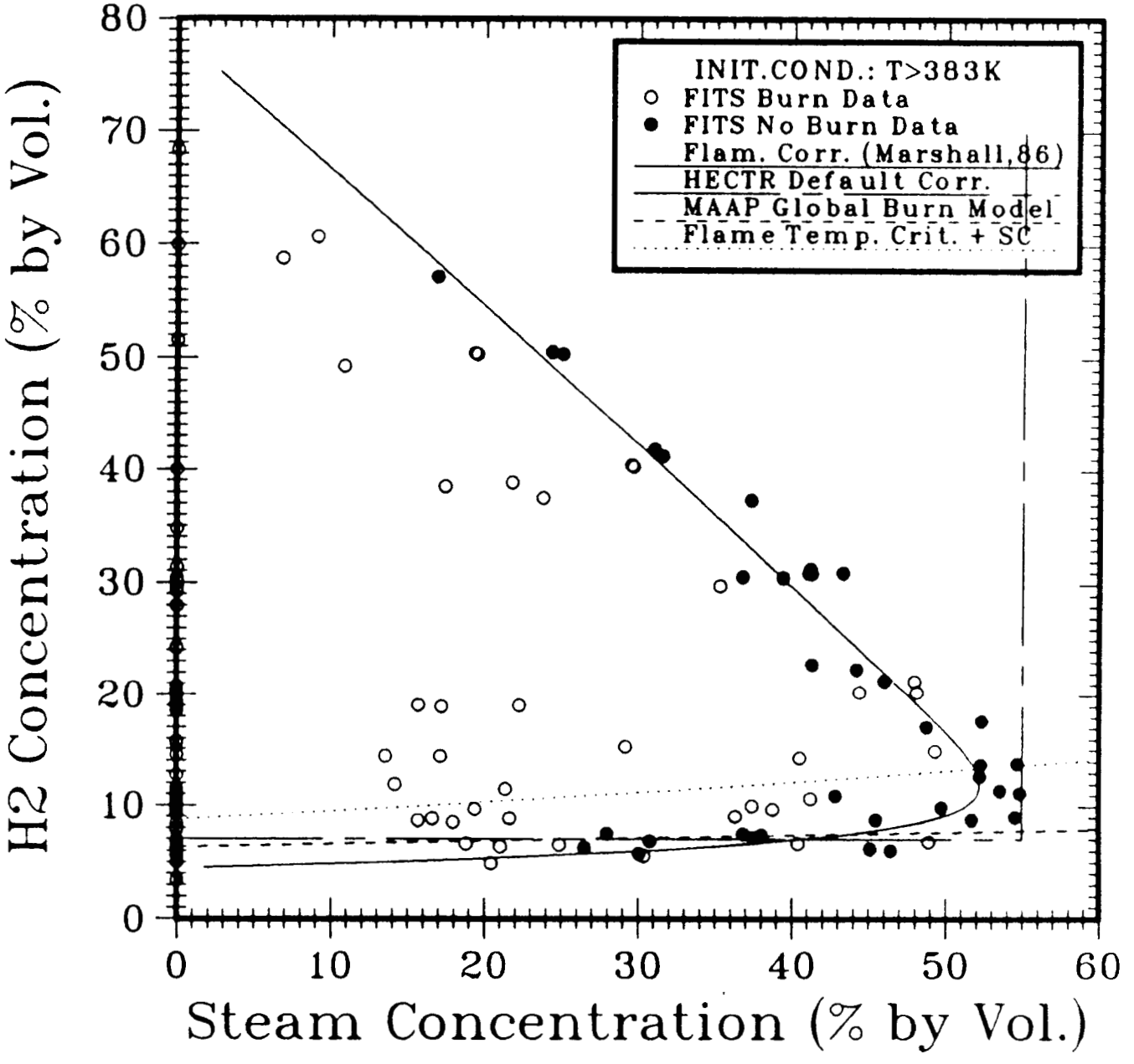

Figure 1.5-4. Flammability of Hydrogen:Air:Steam Mixture in a Quiescent Environment

o Combustion Completeness

At the beginning of a burn, HECTR will determine the amount of hydrogen left when combustion is complete, based upon an empirical formula that depends on the preburn hydrogen concentration. The influence of steam concentration and vessel geometry on combustion completeness is minimal. The results of VGES and NTS experiments (Figures 1.5-5 and 1.5-6) show that the measured combustion completeness data can be correlated in this way. Combustion completeness of 100 percent occurs at a hydrogen concentration of about 8 percent, while minimum burn (less than 1 percent) occurs at a hydrogen concentration of about 3.7 percent. The HECTR predictions of combustion completeness for VGES and NTS experiments using this empirical formula are shown in Figures 1.5-5 and 1.5-6.

Unlike HECTR, MAAP relies on the flame temperature criterion to determine whether a burn in a compartment is complete or incomplete. The default critical flame temperature is 983 K. For an incomplete burn, the burnt volume of the mixture is calculated by an analytical formula, which depends upon burning velocity, drag coefficient, ignition location, and regional radius of the characteristic cylindrical volume.

Based upon this analytical formula,[24] the burned volume was calculated, then divided by the total volume of the vessel to obtain the combustion completeness for the VGES and NTS experiments (Figures 1.5-5 and 1.5-6). Since the combustion chamber in the NTS experiments is spherical rather than cylindrical, we, for these calculations and as suggested in Reference 24, transformed the spherical vessel into an equivalent cylindrical geometry with an equal height and an equal volume before any analyses were performed.

Overall, both the empirical and analytical formulas predict the region of complete burn reasonably well. For an incomplete burn, the analytical formula generally underpredicts the combustion completeness, except in VGES fans-on and fans-off experiments when hydrogen concentration is about 5 percent to 7 percent. Figures 1.5-5 and 1.5-6 show that the incomplete burn model overpredicts the completeness if the propagating flame front hits the wall before reaching the top of the vessel; otherwise, it underpredicts the completeness. In VGES experiments, where the vessel is smaller, the burning radius will intersect the wall before the flame reaches the top. Thus, the model overpredicts the combustion completeness. However, for a very lean

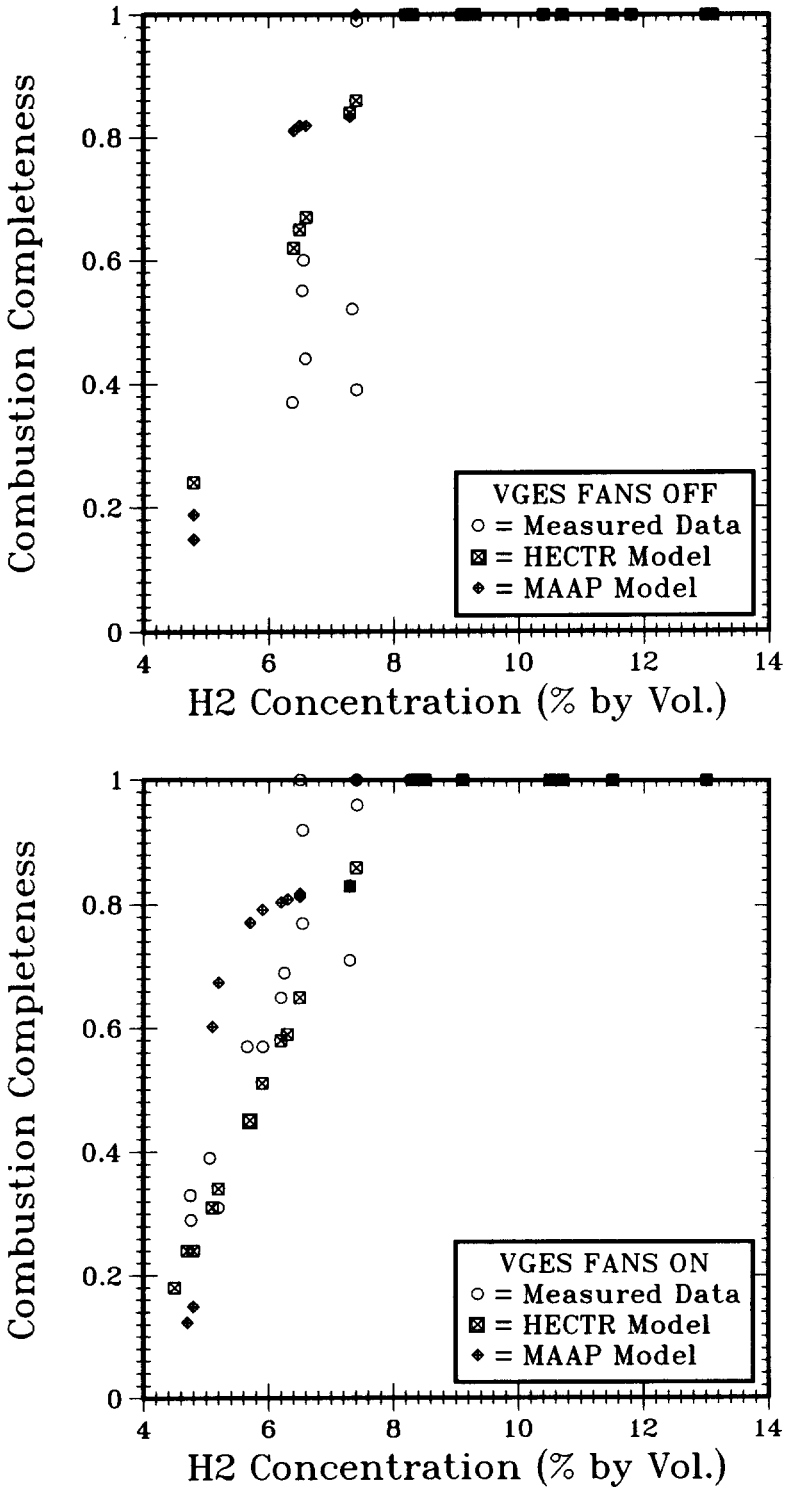

Figure 1.5-5. Comparison of Combustion Completeness Between Measured Data and Prediction by the HECTR and MAAP Models for VGES Fans-Off, Fans-On Experiments

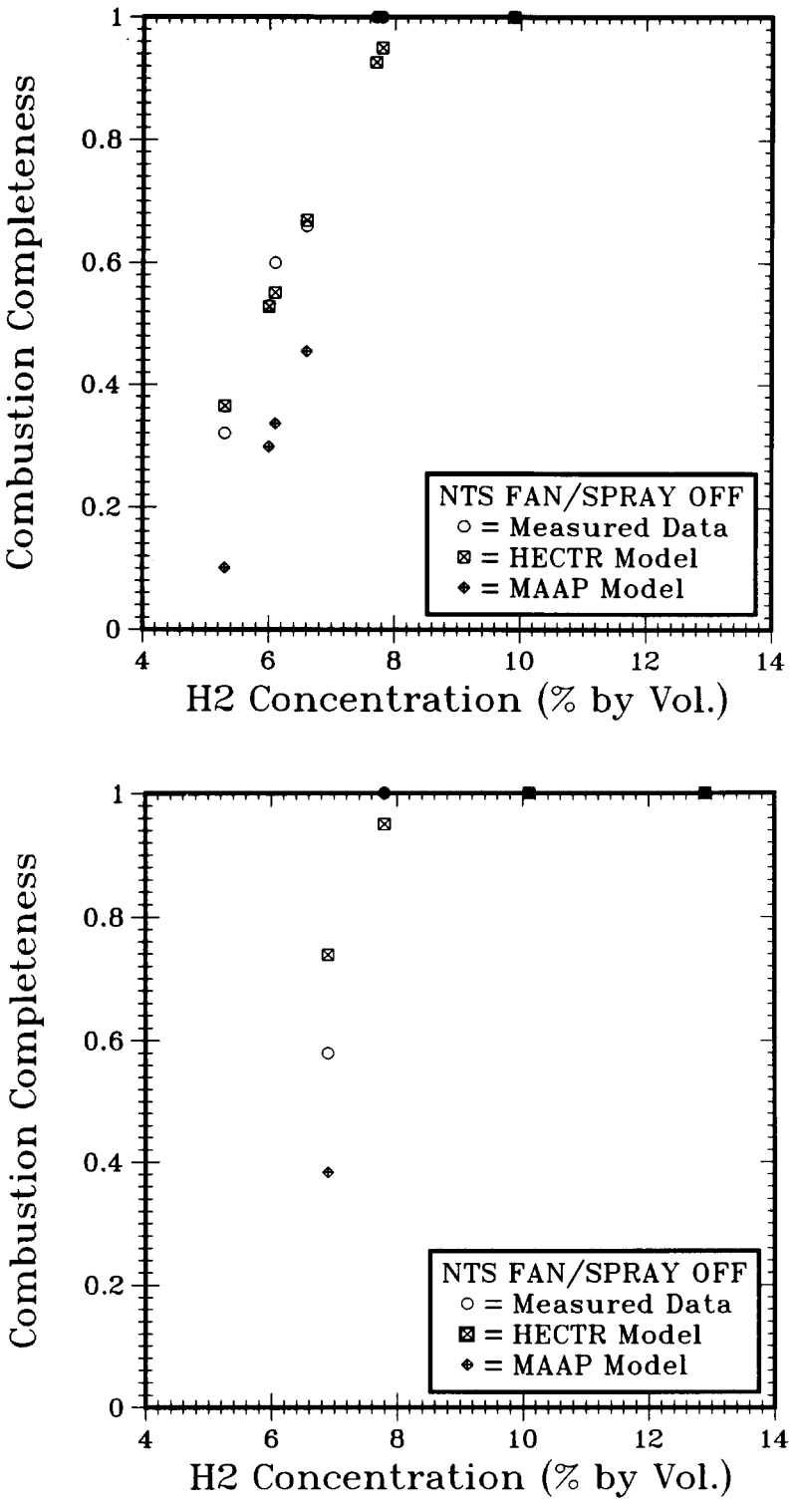

Figure 1.5-6. Comparison of Combustion Completeness Between Measured Data and Prediction by the HECTR and MAAP Models for NTS Low-Steam (5%, Top), High-Steam (30%, Bottom) Experiments

hydrogen combustion case (less than 5 percent), the burning velocity is so small that the flame hits the top of the vessel before it reaches the wall. The analytical formula underpredicts the combustion completeness. Similarly, in NTS experiments, where the vessel is bigger and the region radius of the characteristic cylindrical volume is larger, the flame never hits the side wall as it propagates upward to the top. Hence, the formula underpredicts the completeness. Readjusting the values of drag coefficient and burning velocity multiplier may improve the prediction by the incomplete burn model. However, resetting these values for every containment analysis would be difficult, if not impractical.

- Flame Speed and Burn Time

  In HECTR, an "effective" flame speed is used to calculate the burn time, which in turn determines the burn rate at every time step. Flame speed is defined as the velocity of the propagating flame front in the laboratory frame. The default flame speed correlation is a function of hydrogen and steam concentrations. The burn time is calculated as a user-specified burn characteristic length divided by the flame speed.

  The model in MAAP relies upon the burning velocity to estimate the burn time. Burning velocity is defined as the velocity of the propagating flame front relative to the gas motion downstream from the flame front. For a global burn, burn time is predicted by dividing the regional radius of a characteristic cylindrical volume by the flame velocity. The time for an incomplete burn is expressed as a function of burning velocity, drag coefficient, mixture density, and a characteristic length.

  For the MAAP model, the predicted burn time was used to obtain the "effective" flame speed when comparing the calculated flame speed with the existing experimental data (VGES and NTS) for lean hydrogen combustion cases (less than 15 percent hydrogen concentration). (The "effective" flame speed can be expressed as a characteristic length divided by the burn time.) The results of the flame speed comparison can be found in Figures 1.5-7 and 1.5-8, and the results of the burn time comparison are shown in Figures 1.5-9 and 1.5-10. Since our interest is the burn time, not the pressure-rise time, its values can easily be calculated by either an empirical or analytical formula.

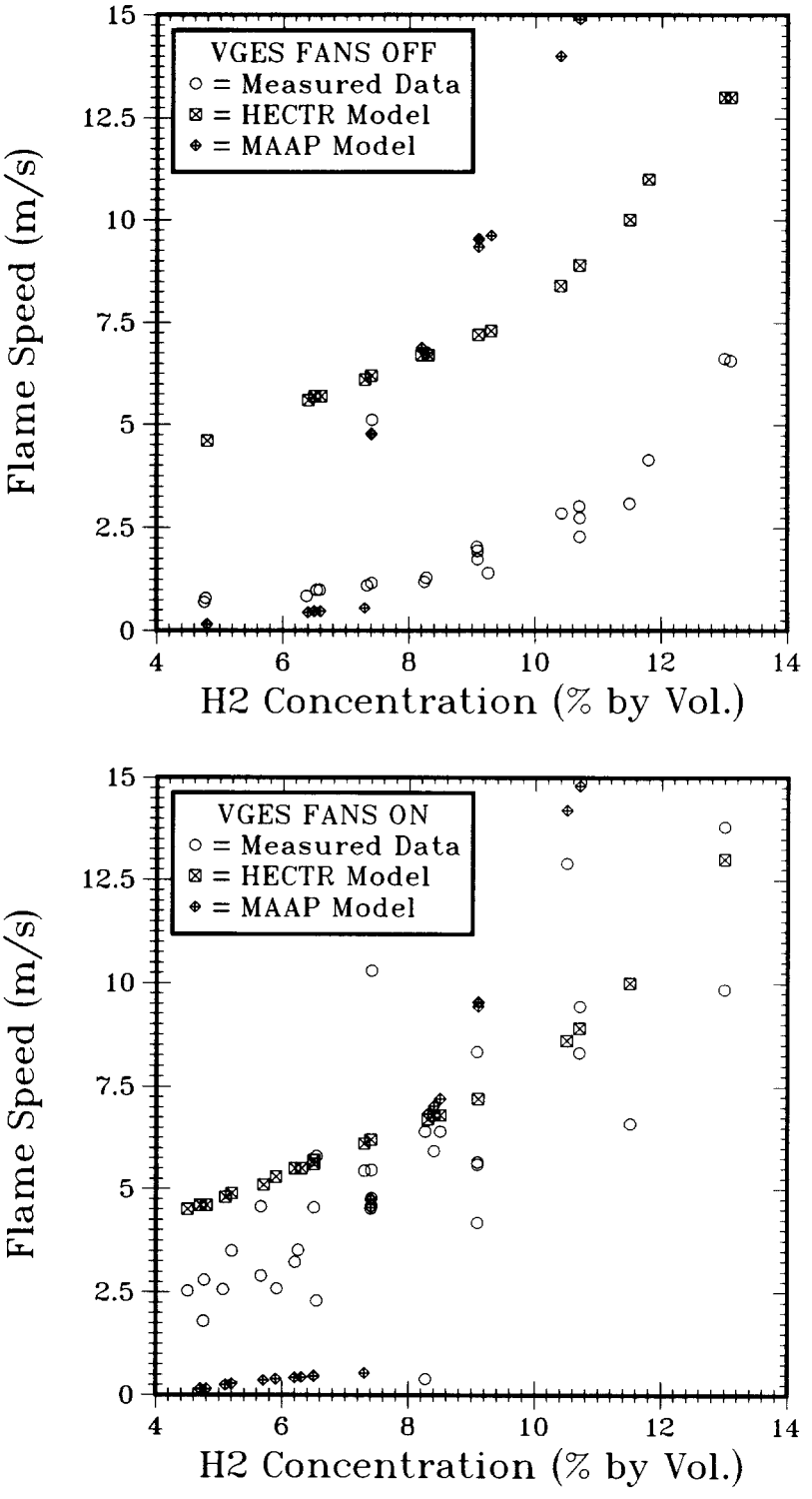

Figure 1.5-7. Comparison of Upward Flame Speed Between Measured Data and Prediction by the HECTR and MAAP Models for VGES Fans-Off, Fans-On Experiments

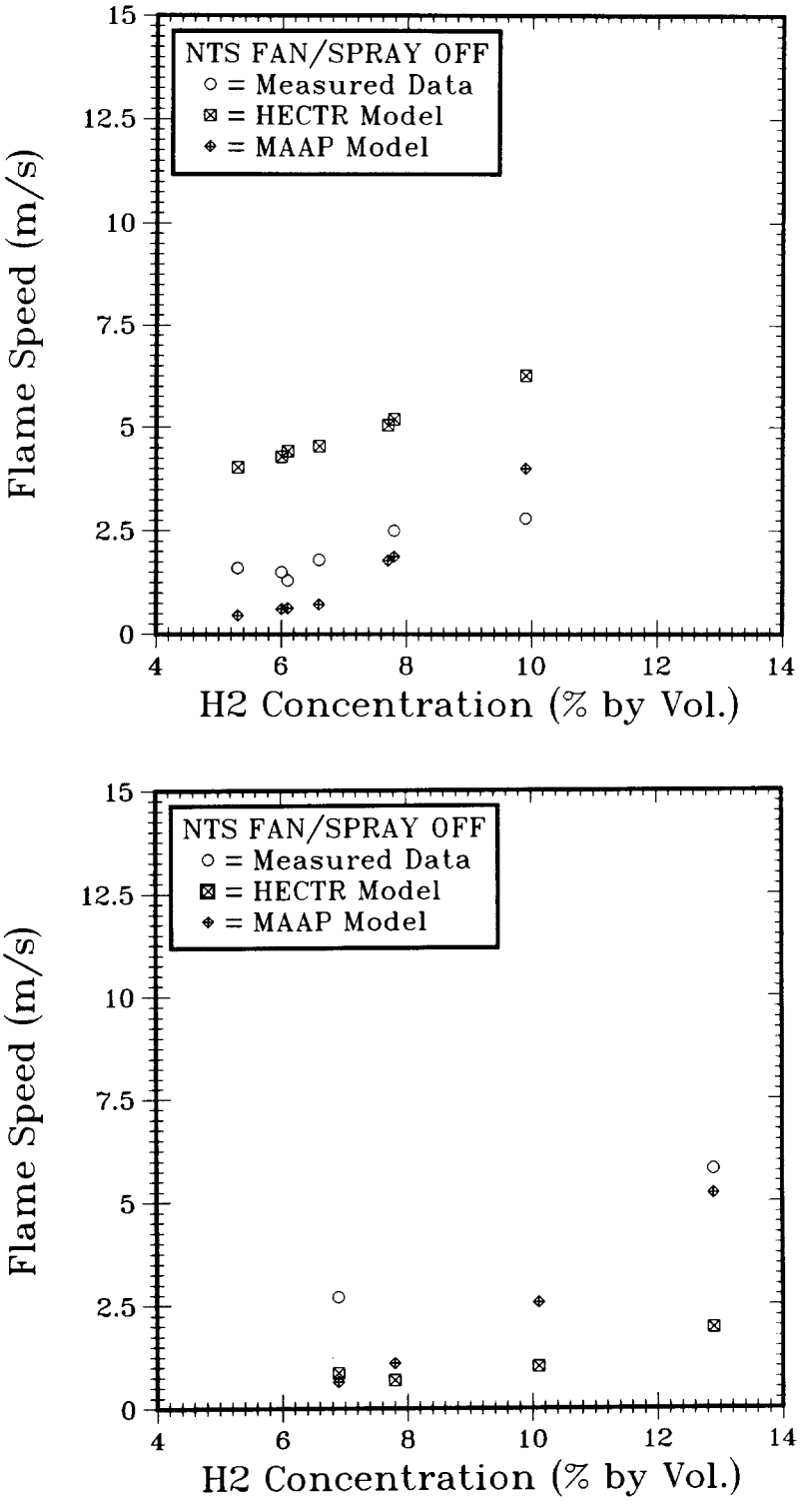

Figure 1.5-8. Comparison of Upward Flame Speed Between Measured Data and Prediction by the HECTR and MAAP Models for NTS Low-Steam (5%, Top), High-Steam (30%, Bottom) Experiments

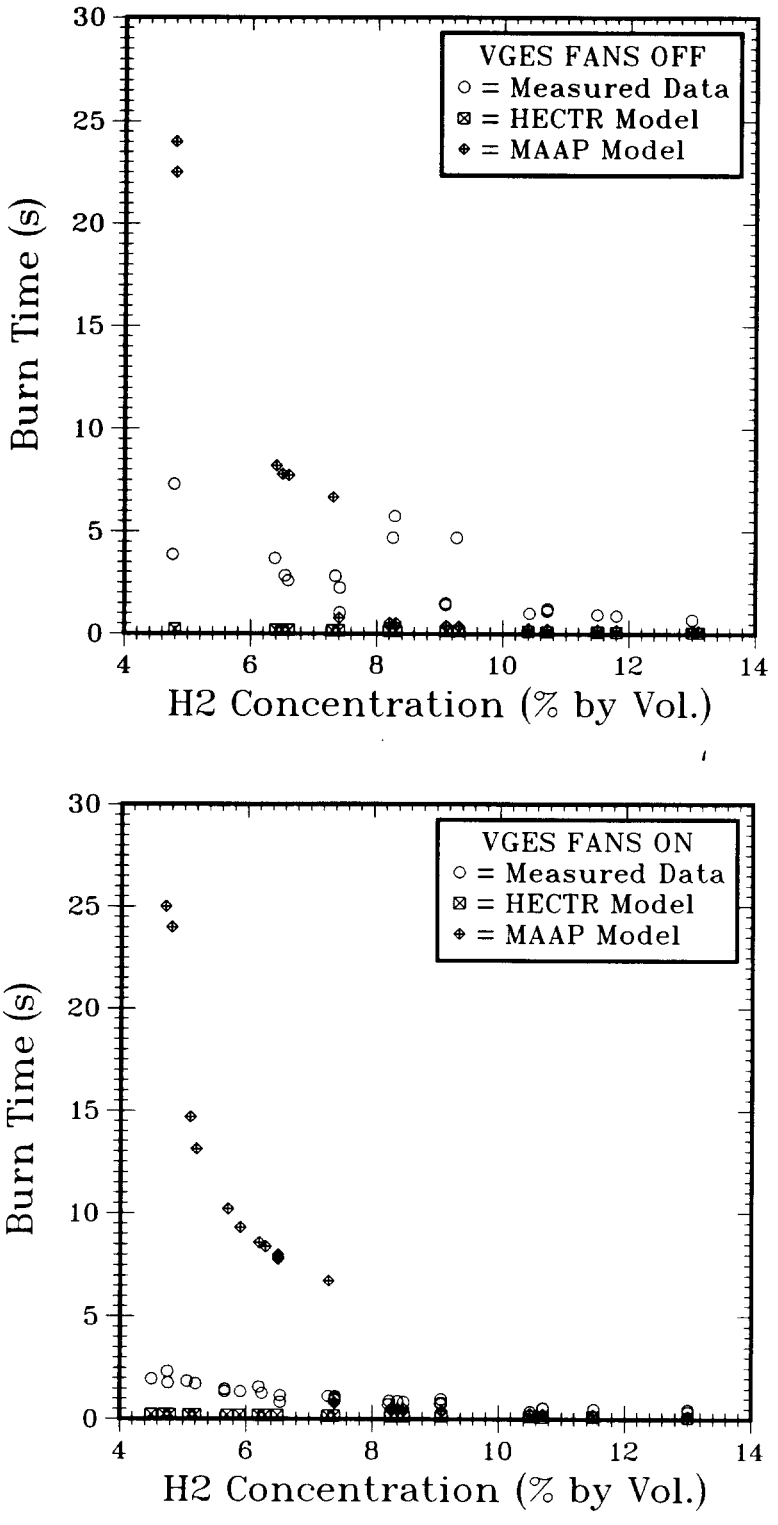

Figure 1.5-9. Comparison of Burn Time Between Measured Data and Prediction by the HECTR and MAAP Models for VGES Fans-Off, Fans-On Experiments

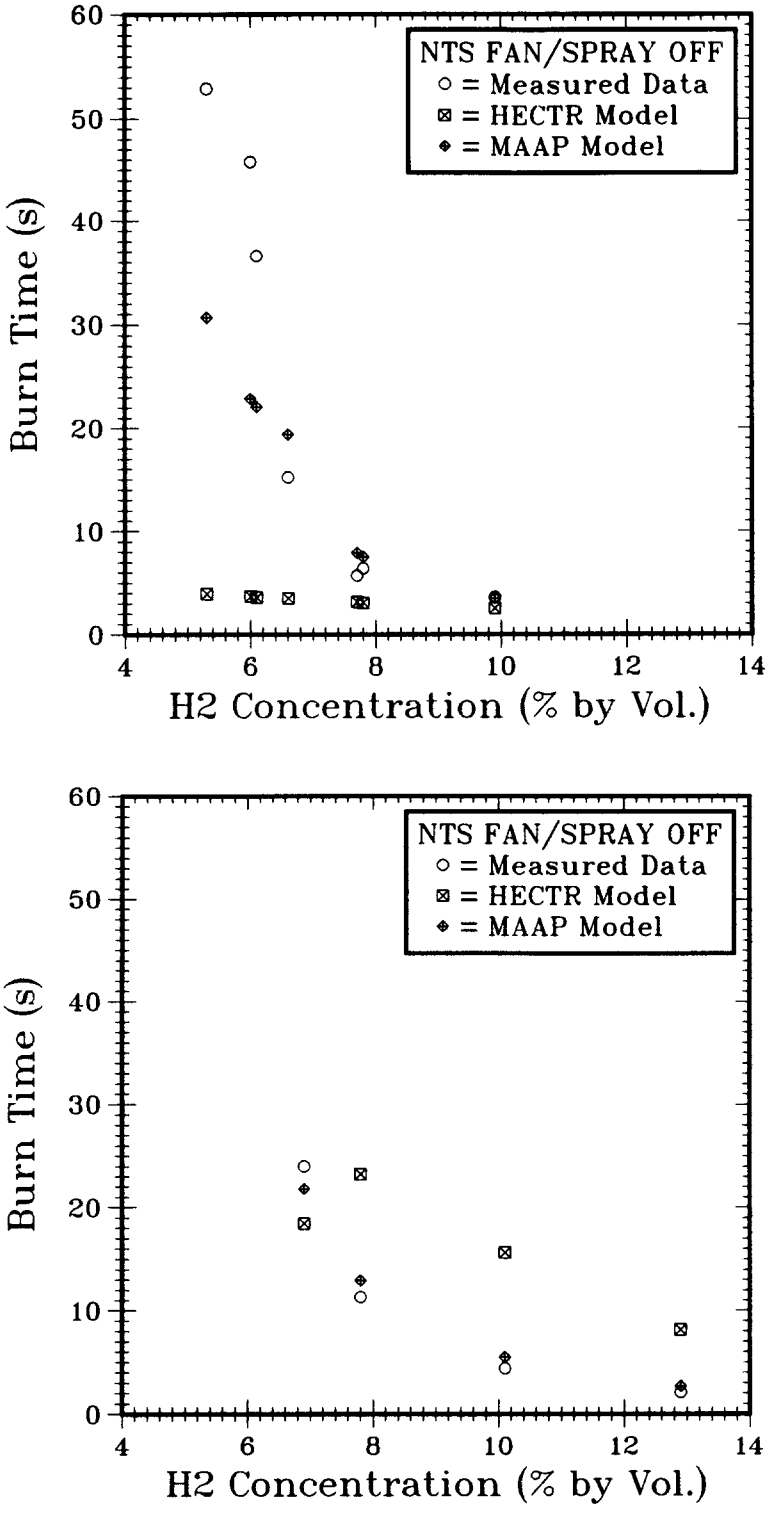

Figure 1.5-10. Comparison of Burn Time Between Measured Data and Prediction by the HECTR and MAAP Models for NTS Low-Steam (5%, Top), High-Steam (30%, Bottom) Experiments

Because the default flame speed correlation in HECTR is based upon the VGES fans-on experiments, HECTR overpredicts the flame speed when compared to the observed values in the VGES fans-off and NTS fans/sprays-off experiments. Obviously, a prediction of a larger flame speed will result in a shorter burn time and a smaller flame speed will lead to a longer burn time (Figures 1.5-7 through 1.5-10). For those cases with high steam concentration, HECTR underpredicts the flame speed (Figure 1.5-8), which leads to a longer burn time. Hence, the influence of steam on flame speed appears to be not well modeled in the present correlation in HECTR. Moreover, from References 35 and 36, when comparing the measured flame speed data from NTS experiments with data from VGES experiments, it has been found that there may be a scaling dependence on the flame speed. Moreover, the existing flame speed correlation in HECTR does not depend upon vessel geometry.

In general, the MAAP burn model underpredicts flame speed and overpredicts burn time when compared with the NTS experimental data; however, for the VGES fans-on and fans-off experiments, the global burn model overpredicts the flame speed when hydrogen concentration is more than 8 percent. The overprediction of flame speed in VGES experiments, but not in NTS experiments, is because in VGES experiments the geometry of the test vessel is different. The ratio of vessel height to regional radius used in VGES calculations is larger than in NTS; therefore, it gives a larger value for the flame speed. (The effective flame speed predicted by the MAAP global burn model depends directly on the ratio of vessel height to regional radius.) This comparison shows that even though the flame speed expression derived from the MAAP model has an implicit scaling dependence, it also appears to be not well correlated.

For those cases with fans or sprays on, the present calculations based on the MAAP model neglect the effect of turbulence on combustion generated by fans and sprays because a burning velocity multiplier of 1 is used. If a larger value of burning velocity multiplier (>10) is used, this would improve the comparison of the analytical results with the experimental data. The MAAP model relies heavily on the laminar burning velocity correlation developed in Reference 37; at present, very few experimental data exist to support this correlation in the lean hydrogen combustion region (less than 15 percent). Uncertainty in this correlation will possibly lead to a larger uncertainty in predicting flame speed and burn time.

o Flame Propagation

Flame is allowed to propagate into any adjacent compartments in HECTR as long as the propagation criteria are satisfied. In MAAP, flame is only allowed to propagate upward into the adjacent compartment, which is located above the burning compartment, as long as the calculated burning velocity is greater than 1 cm/s, which is about 5 percent hydrogen concentration. No horizontal or downward propagation is permitted. This restriction is contradictory to the test results of the VGES and NTS experiments where downward propagation of flame was observed.

When burning occurs within a compartment, neither model explicitly tracks the flame front. Hence, a mixture of both burned and unburned gases will be convected out of the compartment through junctions, even though a junction may be downstream from the flame front. Consider a case with gas flowing from a larger burning compartment to a smaller neighboring compartment with the flow junction downstream from the flame; the present models will allow for both burned and unburned gases instead of only the unburned gases to convect into the smaller compartment. The convected burned gases may inert the smaller compartment and prevent any flame propagation. This may alter the combustion event and result in a lower peak combustion pressure.

In both models, when combustion occurs in a specific compartment, the final mole fraction of hydrogen at the completion of burn is predetermined at the initiation of burn. During the combustion process, if any combustible gases are convected into the burning compartment, the burn rate will be adjusted at every time step so that the final mole fraction of the combustible gases will be consistent with the predicted value. By setting the ignition criterion at a low hydrogen concentration and with a long burn time (usually this is predicted to be the case by the MAAP incomplete burn model), the combustion process will behave like a standing flame rather than a deflagration. This type of burning will not produce a very high peak pressure and temperature.

1.5.1.3 HECTR Analyses of the Standard Problem

In HECTR analyses of the standard problem, three different compartment models are used to represent the reactor containment. They are:

1. 16-compartment model with Sandia geometrical data
2. 6-compartment model with Sandia geometrical data
3. 6-compartment model with MAAP geometrical data

Overall, the completed calculations can be divided into three different sets. The characteristics of each set are:

1. HECTR default calculations
2. Modified HECTR calculations for matching MAAP results
3. Sensitivity studies

The default values in HECTR were used when performing the first set of calculations. The results of these calculations show that there are differences between HECTR and MAAP predictions. In order to match the results predicted by the MAAP code, a modified HECTR calculation was made using the 6-compartment model with the MAAP geometrical data. This calculation involved tuning the HECTR code by changing certain parameters, for example, ignition criterion, combustion completeness, and burn time. Sensitivity studies were also performed to evaluate the importance of sensitive parameters to better understand HECTR predictions. The results of these calculations are summarized in Table 1.5-3.

o Modeling of the Reactor Containment

Three different noding systems were studied; they were:

1. 16-compartment model with Sandia geometrical data
2. 6-compartment model with Sandia geometrical data
3. 6-compartment model with MAAP geometrical data

Both 6-compartment models have the same noding as in the MAAP code for the Sequoyah Ice-Condenser Containment.[24,26] The differences between these two 6-compartment models are the geometrical data used in these calculations (Table 1.5-4). The MAAP geometrical data are those used in the MAAP analysis. The Sandia geometrical data are obtained either from the Final Safety Analysis Report of the Sequoyah Nuclear Power Plant[38] or from Reference 34. The major differences between these two data sets are the total free volume in the lower compartment, the total surface area, and the time delay for the air-return fans to be activated after the set-point is satisfied.

The 16-compartment model is extracted from the 40-compartment model used in Reference 39. Since the recirculation loop in the ice bed region is not a major concern in this problem, a 16-compartment model, which has a one-dimensional ice-condenser model, is sufficient for this standard problem. However, in the second part of this standard problem, for the purpose of studying the natural circulation loop between the lower compartment and the reactor cavity, it is necessary to refine the noding in the lower compartment so that more detailed information can be obtained.

Table 1.5-3

Summary of HECTR Analyses of the Standard Problem

	P_{max} (kPa)	T_{max} (K)	T_w[a] (K)	T_w[b] (K)
MAAP Code	141.3	366.0	-	-
Default Calculations				
HECTR/MAAP-6	162.3	820.6	348.2	375.6
HECTR-6	150.6	788.0	348.5	369.0
HECTR-15	142.9	808.5	351.7	370.5
Modified Calculations				
HECTR/MAAP-6	140.4	536.4	351.5	375.8
Sensitivity Studies				
HECTR-15[c]	133.1	682.4	351.5	370.1
HECTR-15[d]	172.5	962.7	348.8	352.9
HECTR-15[e]	299.7	1049.3	348.8	352.9

[a]Steel equipment in the lower compartment
[b]Concrete in the lower compartment
[c]Ignition Criterion = 6% hydrogen concentration
[d]Ignition Criterion = 8% hydrogen concentration
[e]8% hydrogen combustion in the dome region

In HECTR analyses, the first part of the standard problem begins at the time when core uncovering occurs (1.3 h or 4705 s) and ends at the time when the reactor vessel fails (2.34 h or 8418 s). At 1.3 h, the air-return fans have been on for a period of time and the containment spray system fails because switching over to the recirculation mode is unsuccessful. Hence the discrepancy with respect to the time delay for fan activation does not affect the outcome of this standard problem. However, since the containment spray system was working in the injection mode before it failed to switch over to the recirculation mode, water will have accumulated in various locations including the reactor refilling area. The HECTR input deck has been modified to reflect the water accumulated in the sumps, which, in turn, decreases the gas-free volume of those compartments involved. In the 16-compartment model, the compartment that models the reactor refilling area will be deleted because it is filled with water and becomes useless in our calculations. Therefore, only 15 compartments are used in the present calculations.

Table 1.5-4

Major Differences Between HECTR and MAAP Input Data

		HECTR	MAAP
1.	Reactor Cavity:		
	Wall Area	0	234.86 m^2
2.	Lower Compartment:		
	Total Volume	6334 m^3	8184 m^3
	Sump Area	59.2 m^2	502.6 m^2
	Steel Area	5940 m^2	2780 m^2
	Concrete Area	3569 m^2	1796 m^2
3.	Annular Region:		
	Sump Area	0	446.8 m^2
	Steel Area	1834 m^2	0
	Concrete Area	3257 m^2	1027 m^2
4.	Upper Plenum:		
	Steel Area	1000 m^2	0
5.	Upper Compartment:		
	Concrete Area	4085 m^2	3760 m^2
	Steel Area	2000 m^2	1065 m^2
6.	Ice Condenser:		
	Wall Structure - Wt.	2.0×10^5 kg	-
	- Area	2058 m^2	-
	Baskets - Wt.	1.47×10^5 kg	-
	- Area	9920 m^2	-
7.	Air-Return Fans:		
	Delay Time	600 s	0.167 s
	LC to Annular Region Vol. Flow Rate	1.17 m^3/s	0

In the following discussion, the HECTR 6-compartment model using the MAAP geometrical data will be referred to as the HECTR/MAAP 6-compartment model, while the HECTR 6-compartment and the HECTR 15-compartment model will represent the 6-compartment and 15-compartment models, respectively, using the Sandia geometrical data.

o HECTR Default Calculations

Calculations using the default values in HECTR were performed. In HECTR version 1.5,[40] the default criterion for hydrogen ignition was changed such that combustion will occur if the hydrogen mole fracton

within a compartment is above 7 percent instead of 8 percent. The HECTR 15-compartment model predicted that six sequential burns occurred in the reactor containment, with the burns initiated in the lower compartment where hydrogen and steam sources were located. Each burn propagated into the lower plenum, the ice bed, and eventually into the upper plenum, except one burn that stopped at the top of the ice bed.

On the other hand, the HECTR 6-compartment and HECTR/MAAP 6-compartment models predicted that four and three sequential burns would occur, respectively, with the flame propagation similar to the predicton of the HECTR 15-compartment model. All the burns were initiated in the lower compartment and completed in the upper plenum above the ice-condenser region. The total burn times (the tie between ignition in the lower compartment to extinguishing in the upper plenum) calculated by each model for each sequential burn are quite similar. They are 8.54, 7.79 and 4.15 s for the HECTR 15-compartment, HECTR 6-compartment and HECTR/MAAP 6-compartment models, respectively. In the HECTR 15-compartment model, the steam generator (SG) housing was modeled as a separate compartment. This allowed the flame to propagate into the SG housing compartment and resulted in an additional 17.14 s of burning in the SG housing compartment. Among these three calculations, the HECTR/MAAP 6-compartment model predicted the highest peak pressure and temperature with respect to hydrogen combustion (Table 1.5-3 and Figures 1.5-11 through 1.5-13).

The differences between these HECTR results can be explained by the way the three compartment models were set up. Between the HECTR 6-compartment and HECTR/MAAP 6-compartment models, the lower compartment in the HECTR 6-compartment model had a smaller free volume and more total surface area (Table 1.5-4). Given that the same amount of hydrogen and steam were injected into the lower compartment, the HECTR 6-compartment model, as expected, calculated a higher hydrogen concentration. Since the ignition criterion depended on the hydrogen concentration, the HECTR 6-compartment model predicted an earlier burn and an additional sequential burn. Larger total surface area would improve heat-sink capability and condense more steam, which, in turn, would increase the hydrogen mole fraction. The results of an earlier, less severe burn decreased the peak combustion pressure and temperature.

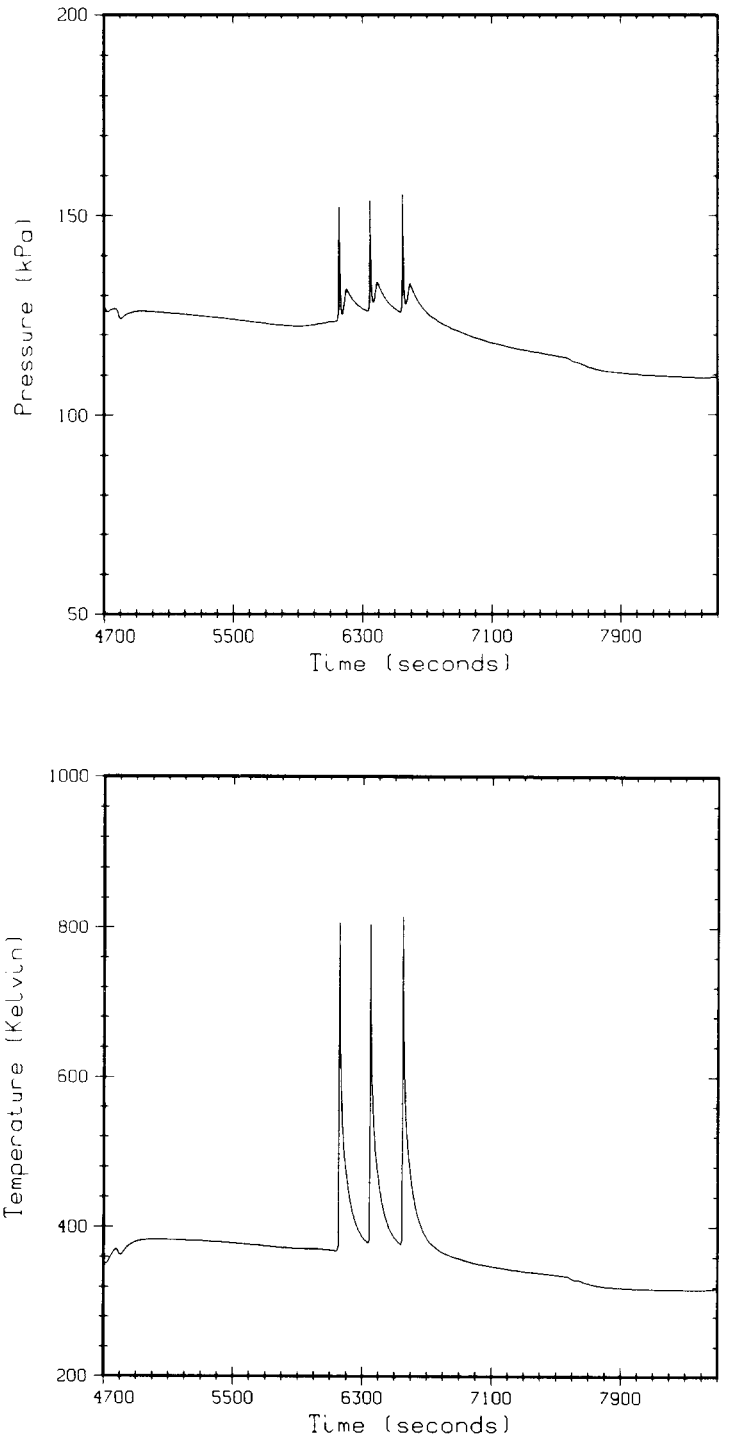

Figure 1.5-11. Pressure and Temperature Responses in the Lower Compartment Predicted by HECTR Using the MAAP 6-Compartment Model (Default Calculation)

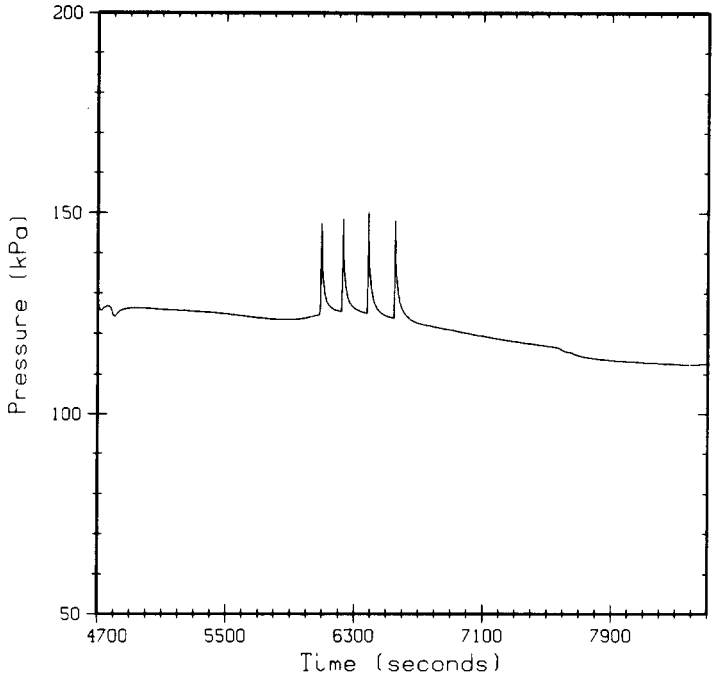

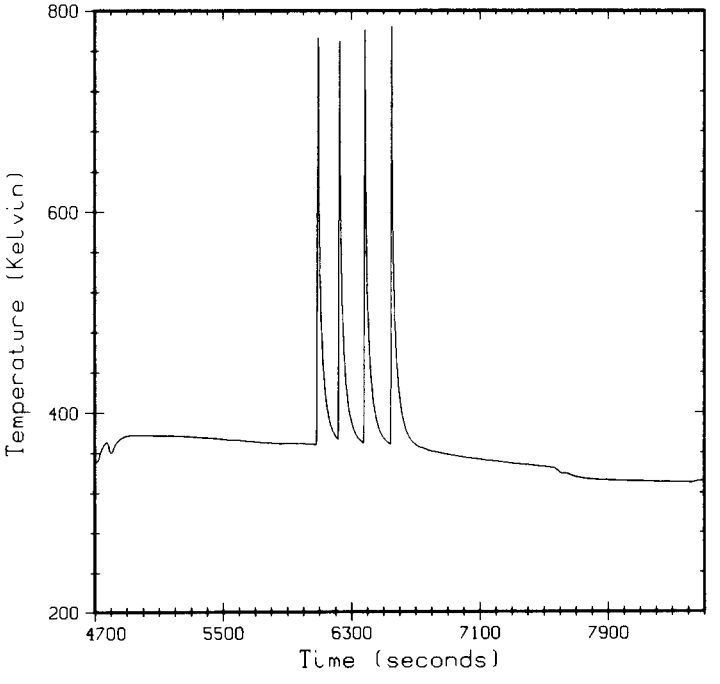

Figure 1.5-12. Pressure and Temperature Responses in the Lower Compartment Predicted by HECTR Using the HECTR 6-Compartment Model (Default Calculation)

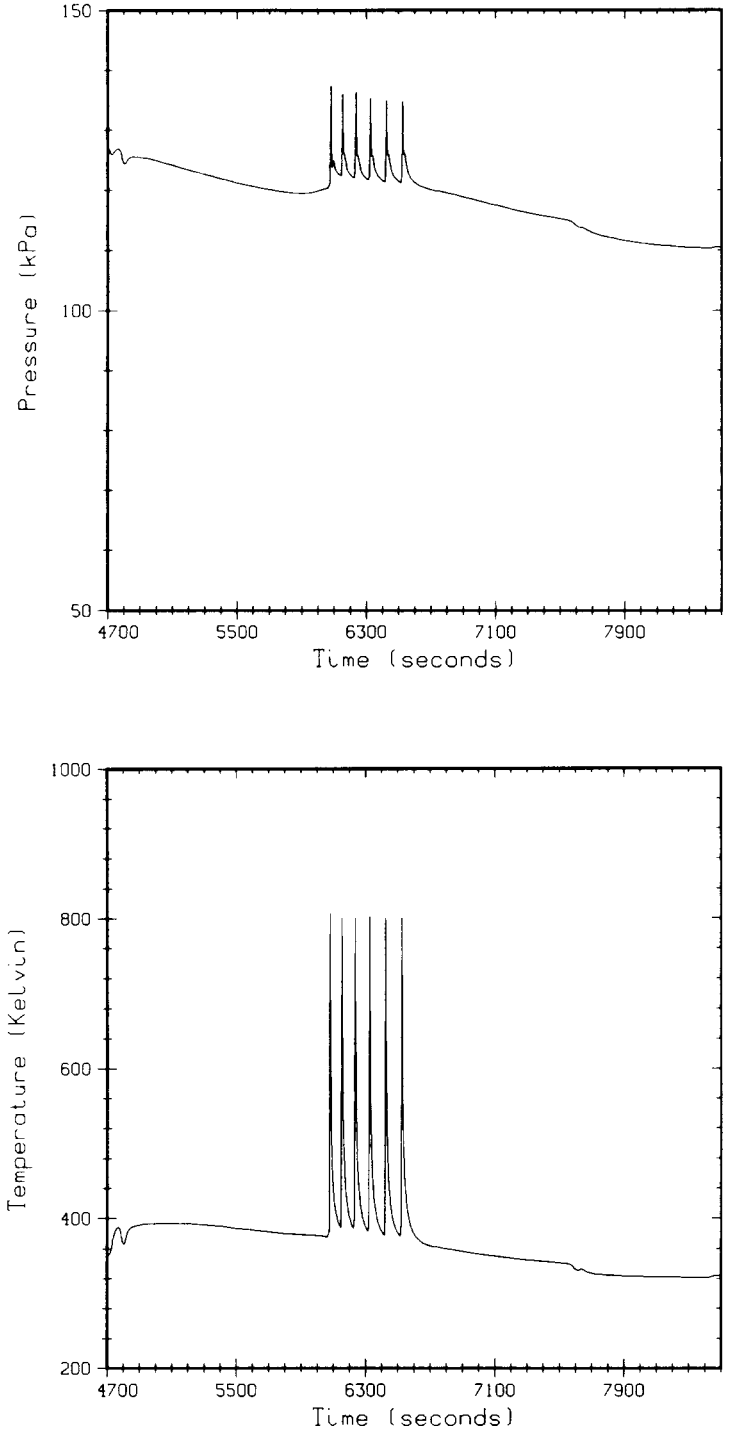

Figure 1.5-13. Pressure and Temperature Responses in the Lower Compartment Predicted by HECTR Using the HECTR 15-Compartment Model (Default Calculation)

The argument discussed in the previous paragraph can also be applied when comparing the results between the HECTR 15-compartment and HECTR 6-compartment model. The HECTR 15-compartment model had a more refined noding in the lower compartment region. Thus it calculated a higher hydrogen concentration in the source compartment, which led to an earlier burn and an additional sequential burn. This resulted in a lower peak combustion pressure. However, the finer noding system in the lower compartment also produced higher gas and wall temperatures because it calculated the temperature distribution within the lower compartment region and identified the local hot spot. The coarse-noding system had only one control volume, which averaged out the temperature distribution by assuming uniform mixing within a compartment.

To summarize the HECTR default calculations, all three compartment models predicted similar magnitudes of pressure and temperature rises with respect to hydrogen combustion. They all predicted a series of moderate burns.

o Modified HECTR Calculations to Match MAAP Results

A set of HECTR calculations using the HECTR/MAAP 6-compartment model were performed with an attempt to match MAAP results given in Reference 26. A few changes were made in HECTR before any calculations were completed. First, several FORTRAN statements were added to the HECTR code so that the ignition would occur at the exact times and locations as they were specified in Reference 26. Burn time for each discrete burn occurring in the corresponding compartment was also adjusted so that it matched the value given in Reference 26. The value of the combustion completeness for each burn was estimated by assuming that only that portion of the hydrogen between igniters and the top of the compartment would combust. As in MAAP, no flame propagation into the neighboring compartment was allowed. The selected combustion parameters which were used for this part of calculations are listed in Table 1.5-5.

The results of this modified HECTR calculation (Figure 1.5-14) compare well with the peak combustion pressure predicted by the MAAP code.[26] Both results show a peak pressure of about 140 kPa. However, the gas temperature in the lower compartment calculated by HECTR disagrees substantially with the MAAP prediction. HECTR shows a peak gas temperature of 536 K while MAAP shows a peak gas temperature of less than 366 K. Several

calculations with different combustion completeness and convective heat transfer coefficients were made in an attempt to decrease the gas temperature in the lower compartment. The gas temperature in the lower compartment did decrease as a result of less complete burns or larger heat transfer coefficient, but the changes were insignificant.

Table 1.5-5

Combustion Parameters Used in Calculations

	Ignition Time (s)	Burn Time (s)	Combustion Completeness
Upper Plenum	5917	6345	19.18%
Lower Compartment	6313	280	42.12%
Upper Compartment	6431	7331	84.40%
Annular Region	6491	7299	53.72%

In reviewing this set of modified HECTR calculations, several items about the combustion model in MAAP will be discussed here. Considering the data given in Table 1.5-5, the MAAP code predicted a burn time on the order of 2 h, except in the lower compartment. If the distance between the location of igniters and the top of compartment given in the MAAP input data[41] is used as the characteristic length, a flame speed of 10^{-4} m/s is calculated. Such a low flame speed is not physically reasonable. In the previous section, it was shown that the MAAP incomplete burn model always underpredicted the flame speed and overpredicted the burn time substantially when compared with experimental results. Hence, a predicted flame speed of 10^{-4} m/s is unacceptable, and that leads to question about the MAAP results of analyzing containment responses with respect to hydrogen combustion.[26]

Next, the results of these modified HECTR calculations will be compared with the results of the 15-compartment model. The pressure rises with respect to hydrogen combustion for both cases compare well. However, the calculated peak temperatures in the lower compartment are far apart: The 15-compartment model predicts a peak value of 808 K while the new HECTR/MAAP 6-compartment model and MAAP code show the peak temperature to be 536 K and 366 K, respectively. The substantial difference in the lower compartment temperature may be important for studying the survivability of equipment.

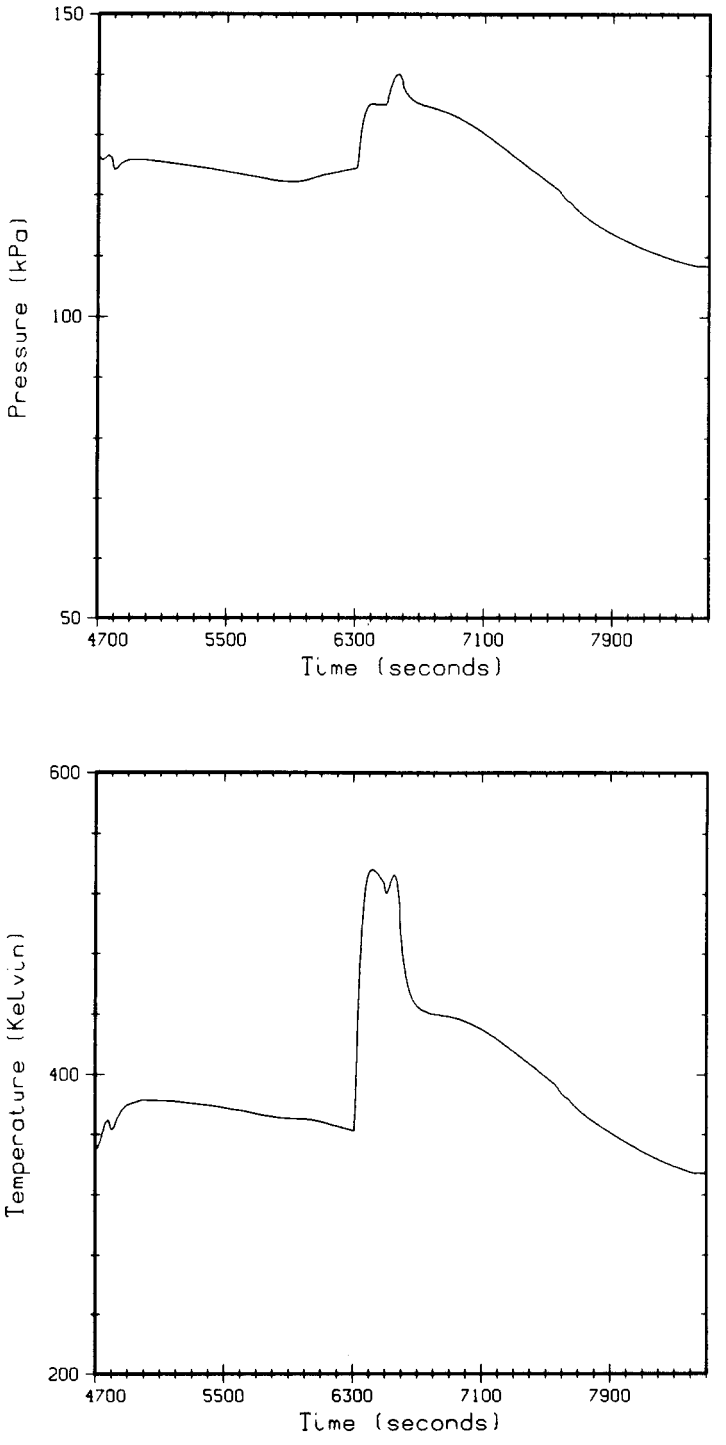

Figure 1.5-14. Pressure and Temperature Responses in the Lower Compartment Predicted by HECTR Using the MAAP 6-Compartment Model (MAAP Ignition Time, Burn Time, and Combustion Completeness)

For equipment survival, energy deposition (the integral of total heat flux over time) is an important parameter to calculate the thermal loading. Figures 1.5-15 through 1.5-18 plot the surface temperature and total heat flux for two kinds of surfaces in the lower compartment (steel and concrete) as predicted by HECTR using two different compartment models. In the 15-compartment model, as a result of a finer noding in the lower compartment, HECTR predicted a higher peak surface temperature and larger heat flux for each discrete burn. However, for the modified HECTR calculation using the HECTR/MAAP 6-compartment model, the total heat flux on the surface behaved like the response to a diffusion flame rather than to a discrete burn. Judging by the graph (without integrating the area under the curve), it seems that the 15-compartment model predicts a much bigger energy deposition rate than the new HECTR/MAAP 6-compartment model.

o Sensitivity Studies

Several sensitivity studies were performed to evaluate the importance of parameters to better understand HECTR predictions. Three such studies are discussed here. Two involved changing the ignition criterion to either 6 percent or 8 percent hydrogen mole fraction. If ignition occurred at 6 percent hydrogen, HECTR predicted an earlier, more moderate burn and more sequential burns in the reactor containment. These burns were all initiated in the lower compartment, then propagated into the ice bed and upper plenum. The results of these burns gave a peak pressure of 133 kPa and peak temperature of 682 K (Figure 1.5-19).

When the ignition criterion was changed to 8 percent hydrogen instead of 7 percent or 6 percent, the flame propagation pattern was quite different. In this case, the flame was initiated in the upper plenum and propagated downward into the ice bed twice and upward into the dome twice. Not a single burn sequence propagated back into the lower compartment in this calculation. In HECTR, the downward flame propagation limit is set at 9 percent hydrogen. Throughout the transient, the hydrogen concentration in the lower compartment never reached 9 percent because of the high steam content. Besides two sequential burns, there were also three local regional burns in the upper plenum predicted by HECTR. Since the burning was at the higher hydrogen mole fraction and at a later time, it was more severe. However, even though the flame did propagate into the dome, only a small fraction of hydrogen present in the dome had been combusted. Therefore, the calculated peak pressure and temperature were slightly higher than other cases:

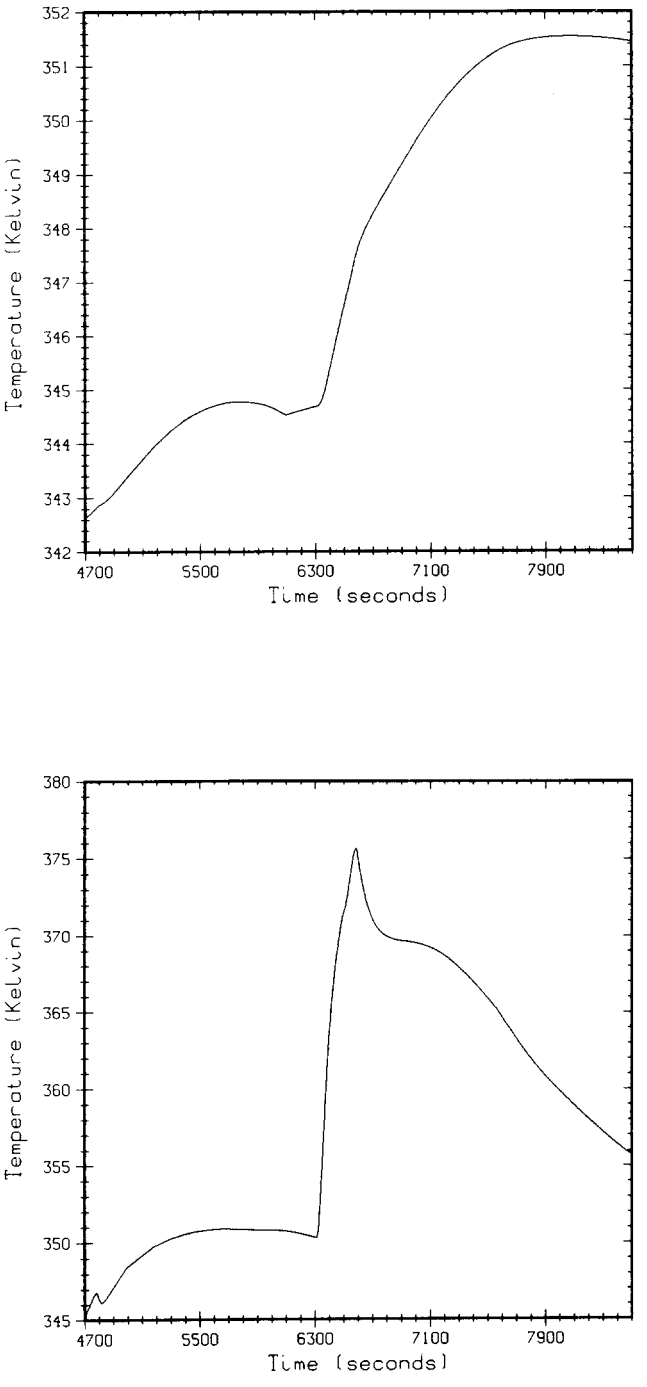

Figure 1.5-15. Surface Temperature Responses of Steel Equipment (Top) and Concrete (Bottom) in the Lower Compartment Predicted by HECTR Using the MAAP 6-Compartment Model (MAAP Ignition Time, Burn Time, and Combustion Completeness)

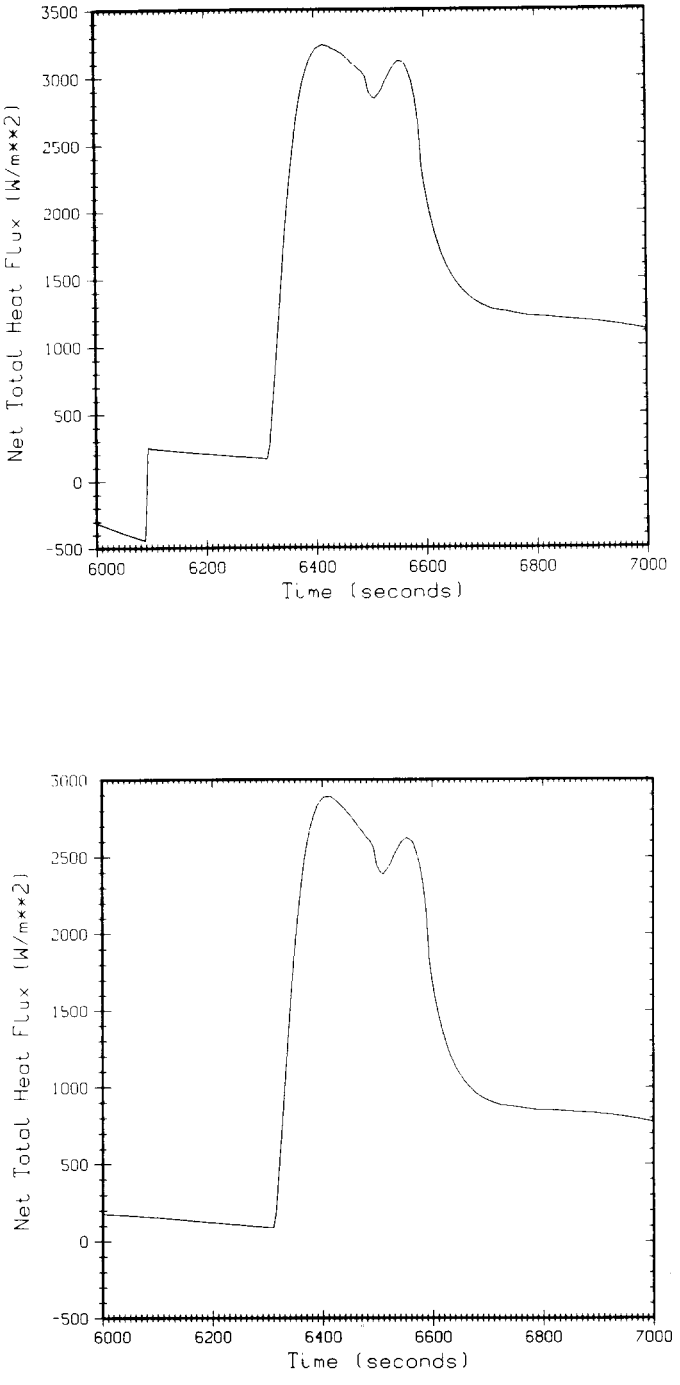

Figure 1.5-16. Total Heat Flux to the Surface of Steel Equipment (Top) and Concrete (Bottom) in the Lower Compartment Predicted by HECTR Using the MAAP 6-Compartment Model (MAAP Ignition Time, Burn Time, and Combustion Completeness)

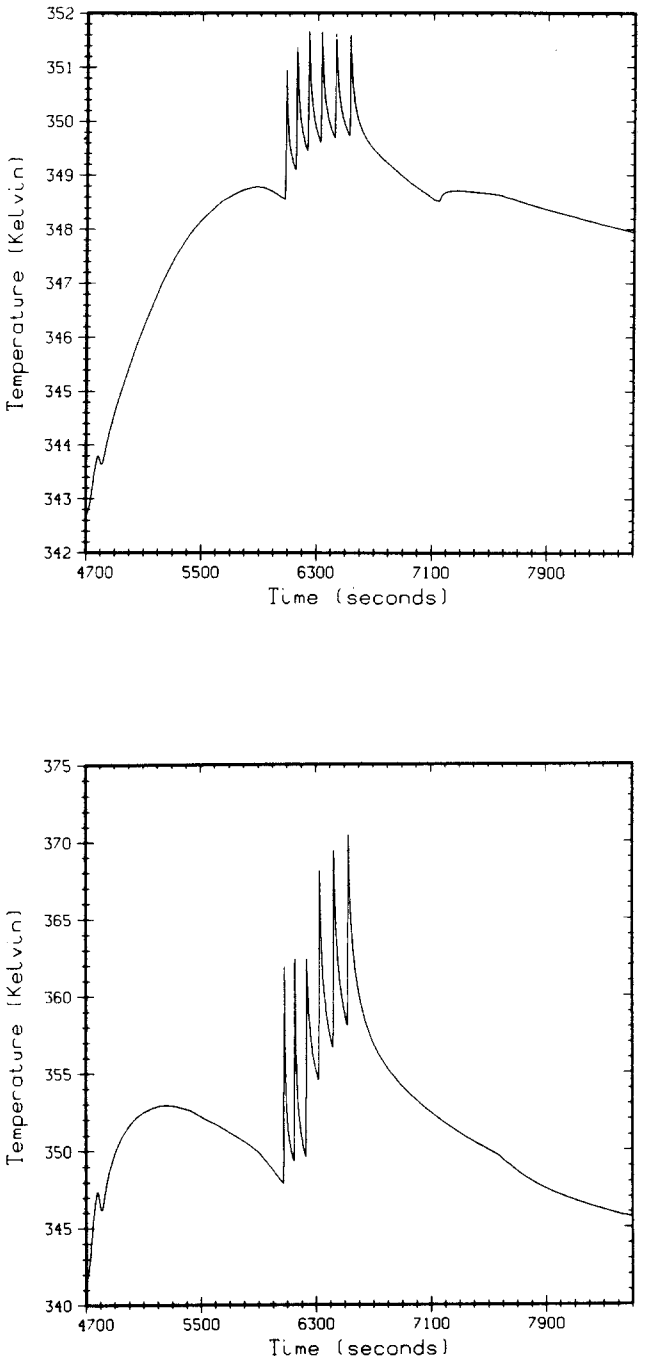

Figure 1.5-17. Surface Temperature Responses of Steel Equipment (Top) and Concrete (Bottom) in the Lower Compartment Predicted by HECTR Using the HECTR 15-Compartment Model (Default Calculation)

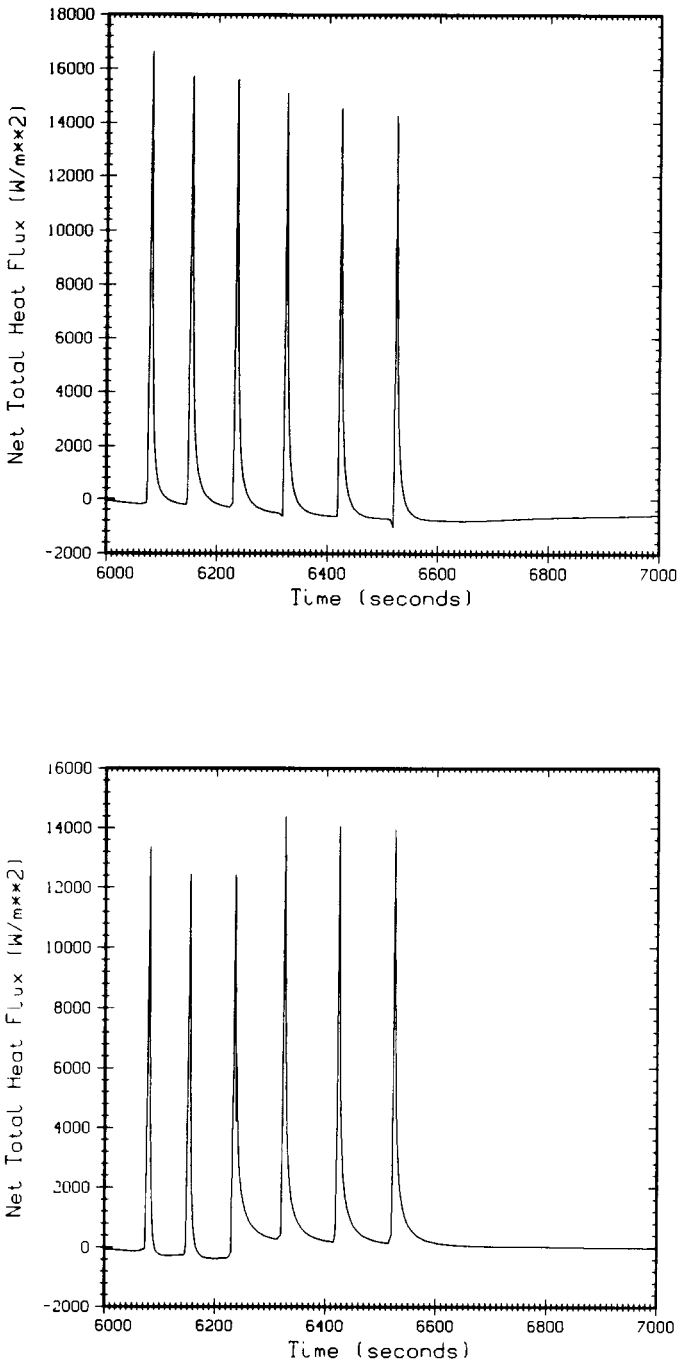

Figure 1.5-18. Total Heat Flux to the Surface of Steel Equipment (Top) and Concrete (Bottom) in the Lower Compartment Predicted by HECTR Using the HECTR 15-Compartment Model (Default Calculation)

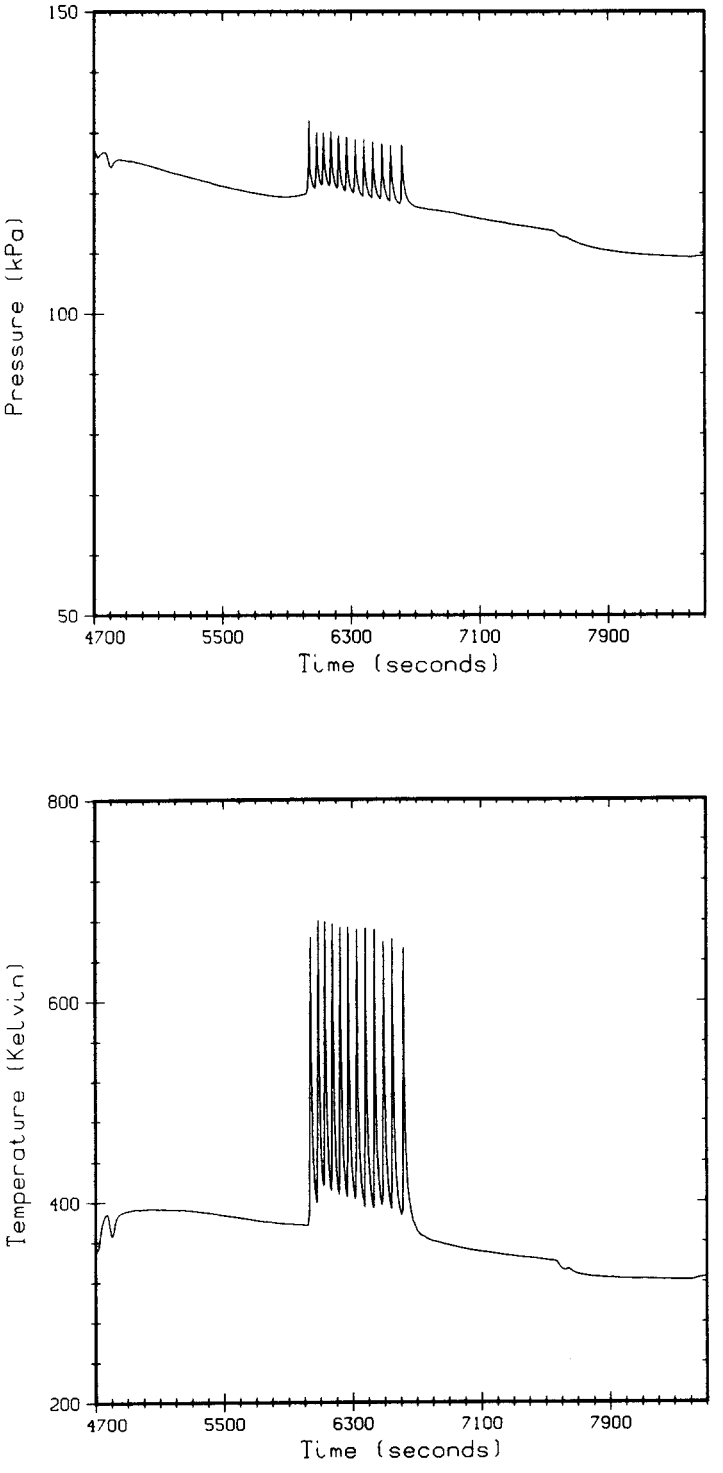

Figure 1.5-19. Pressure and Temperature Responses in the Lower Compartment Predicted by HECTR Using the HECTR 15-Compartment Model (Ignition Criterion: 6% of H_2)

172.5 kPa and 962.7 K (Figure 1.5-20). For equipment survival, there was not much heating of the surface in the upper plenum and in the dome region because the burn time was short and burning was minimal. The surfaces in the lower compartment did not heat up substantially because no combustion took place in that region.

Another sensitivity study was performed to analyze 8 percent hydrogen combustion in the dome. Suppose that igniters in the upper plenum and in the lower compartment were not functioning or igniters did not come on until 6800 s; then 8 percent hydrogen would accumulate in the dome. If ignition occurred in the dome at that time, it would generate pressure and temperature spikes of 299.7 kPa and 1049.3 K, respectively (Figure 1.5-21). However, this global burn happened only in the dome and there was no flame propagation into either the lower region of the upper compartment or into the upper plenum because both compartments never reached 9 percent hydrogen concentration. (Using the generation rates given by MAAP in a well-mixed environment without any combustion, HECTR predicted an 8.4 percent concentration in the ice-condenser containment).

In summary, the preliminary results of HECTR analyses of part 1 of the standard problem show that the calculated peak pressure using various compartment models are close to the MAAP prediction, provided that ignition occurs at hydrogen concentration below 7 percent. With the igniters working during the S2HF accident, it is possible that combustion occurs at hydrogen concentrations below 7 percent. From the FITS tests at Sandia[31], combustion did occur at a hydrogen concentration of 5.5 percent, with 30.4 percent steam concentration and the fans on. One final comment on the completed HECTR analyses is that the probability of the flame at a point flashing back to the source location and burning as a diffusion flame has not been studied thoroughly. It is possible that this can happen, even though the first analysis shows that the flame may be unstable because of the high predicted steam-to-hydrogen mixture ratio at the break (Figure 1.5-22). More work on diffusion flame stability is highly recommended.

1.5.2 HECTR Code Improvement
(C. C. Wong, 6427)

HECTR Analyses of the NTS experiments[43,44] show that the default correlation in HECTR 1.0 overpredicts the flame speed in lean burn cases (less than 8 percent hydrogen concentration) and underpredicts the flame speed in

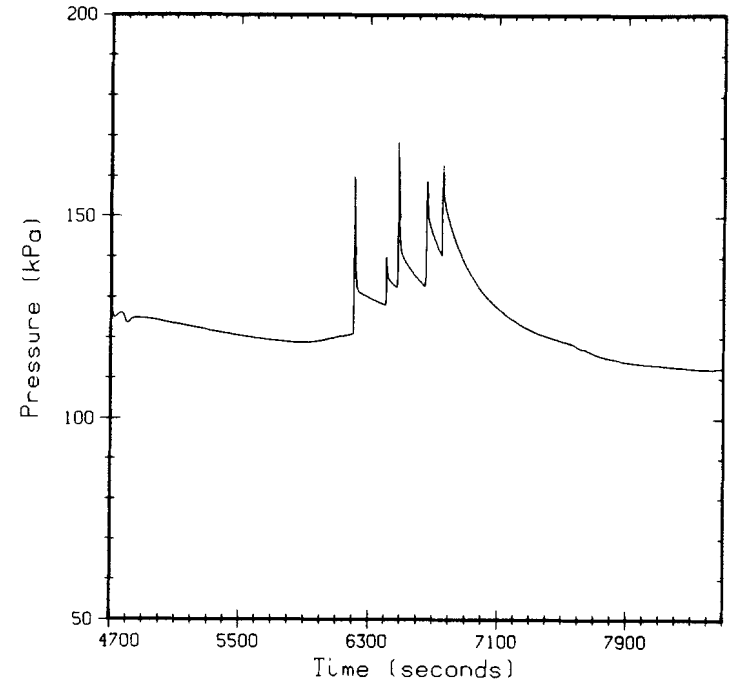

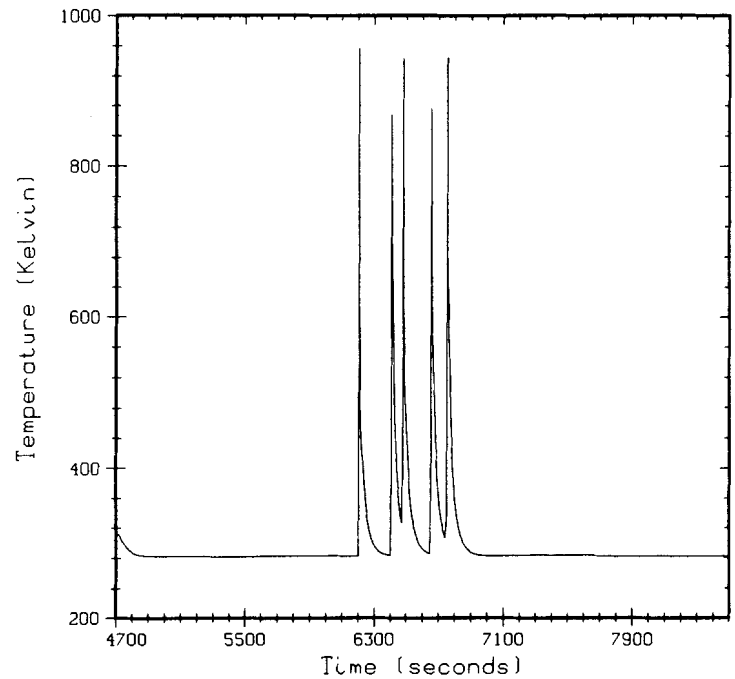

Figure 1.5-20. Pressure and Temperature Responses in the Upper Plenum Predicted by HECTR Using the HECTR 15-Compartment Model (Ignition Criterion: 8% of H_2)

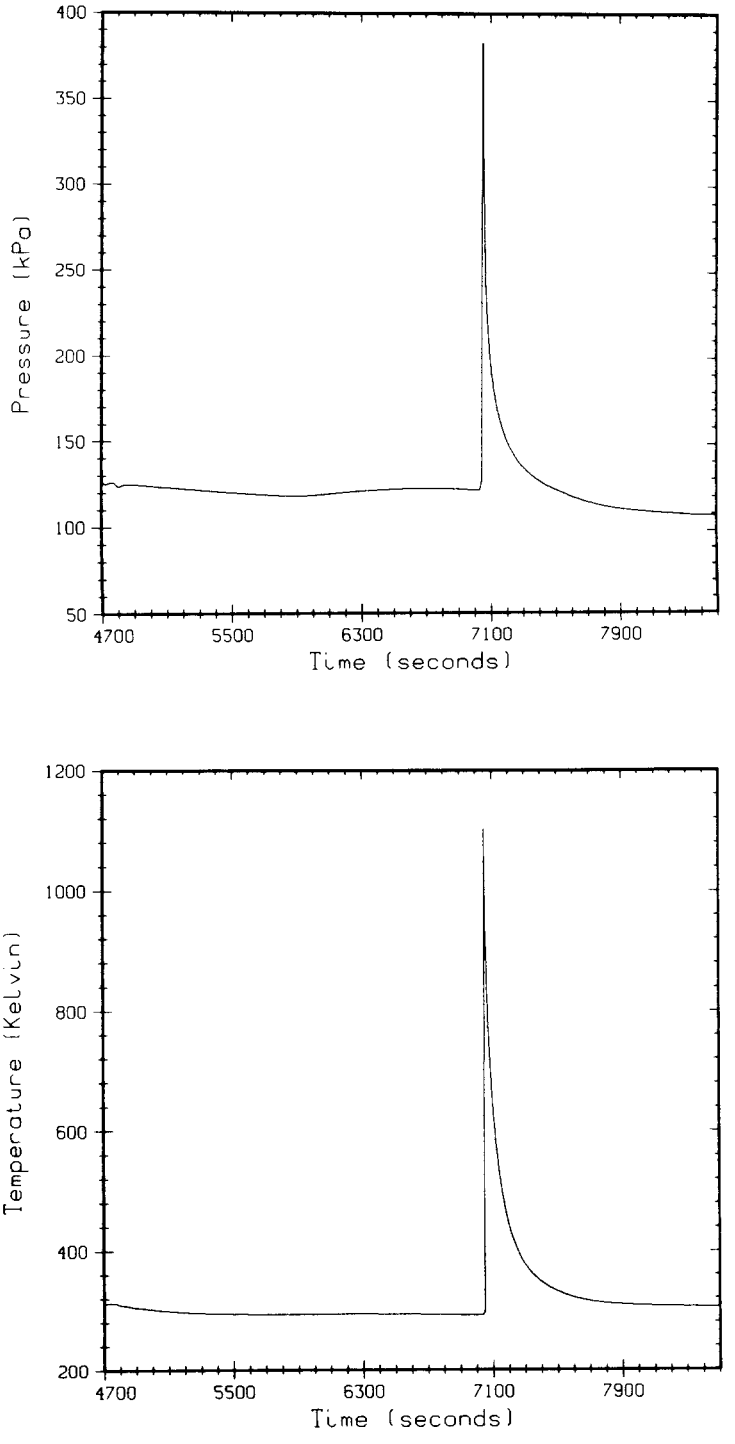

Figure 1.5-21. Pressure and Temperature Responses in the Dome Predicted by HECTR Using the HECTR 15-Compartment Model (Combustion Occurred at 8% H_2 Concentration in the Dome)

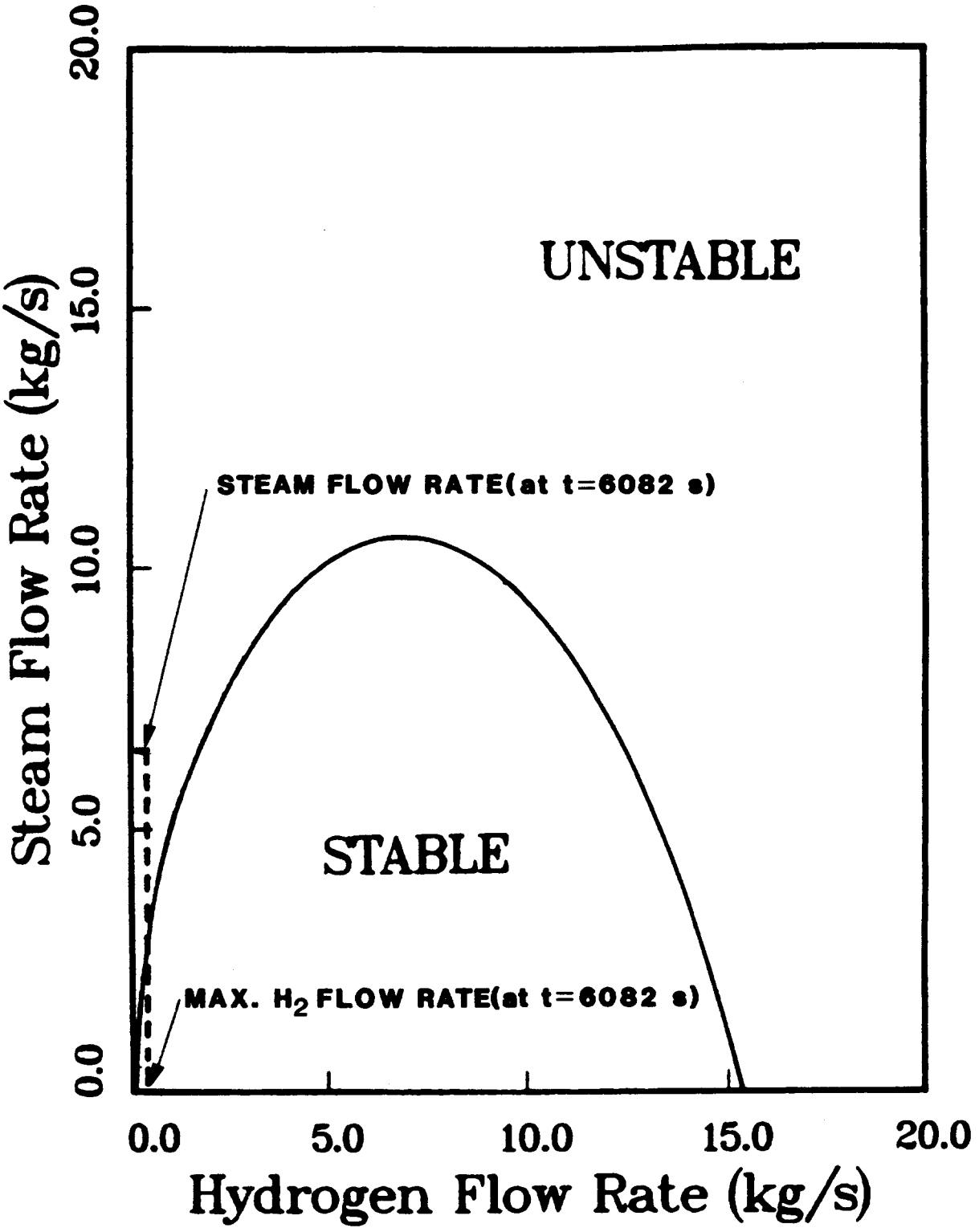

Figure 1.5-22. Calculated Stability Boundaries for a 5-cm Diameter Jet as a Function of Hydrogen and Steam Flow Rates. Jet fluid is at 200°C; the atmosphere is air at room temperature (p. 60 in Reference 42).

high-steam concentration cases. In another NRC program, "Quantitative Uncertainty Evaluation for Containment Loading Analysis," it was determined that the burn time has a substantial effect on the peak combustion pressure and contributes a large uncertainty to containment loading. Since HECTR (and many other computer codes such as MELCOR, CONTAIN, and MARCH) relies on the flame speed correlation to accurately predict the burn time, it was necessary to upgrade the present correlation. Such an effort has been completed. The measured burn time obtained from the FITS experiments and other flame speed data from both VGES and NTS experiments were used to generate this newly developed correlation.

Before any discussion on the development of the improved flame speed correlation is presented, a review of the latest improvement of the combustion completeness correlation will be provided, since more experimental data were available for upgrading the existing correlation.

1.5.2.1 Development of an Improved Combustion Completeness Correlation

The development of an improved combustion completeness correlation for the HECTR code began with the compilation of all existing combustion completeness data from all sources, including NTS. This data base consists of information obtained from Whiteshell,[45] ACUREX,[46] FITS,[31] and VGES[27] experiments and all NTS premixed tests. Combustion completeness versus initial hydrogen concentration in the mixture for both quiescent and turbulent environments is plotted in Figures 1.5-23 and 1.5-24, respectively. A quiescent environment represents the case where neither fans nor sprays are operating; a turbulent environment represents the case where either fans or sprays are operating. As shown in the two figures, the completeness data can be correlated in the following ways: The first is that the combustion completeness is sensitive to initial hydrogen content. No hydrogen will combust until the hydrogen concentration reaches about 4 percent. Then, as hydrogen content increases from 4 percent to 8 percent, the completeness increases linearly to 100 percent. Any burn with hydrogen concentration above 8 percent will always result in 100 percent completeness. The second observation is that the steam has substantial effect on the combustion completeness. Adding more steam in the gas mixture will make the combustion process less complete. Steam will provide an additional heat sink capacity which helps quenching of the flame. The combustion completeness decreases as an exponential function of steam concentration. When the steam content increases to above 50 percent, its effect is enormous and eventually will prevent any burning. (The flammability limit of a hydrogen:air: steam mixture states that 55

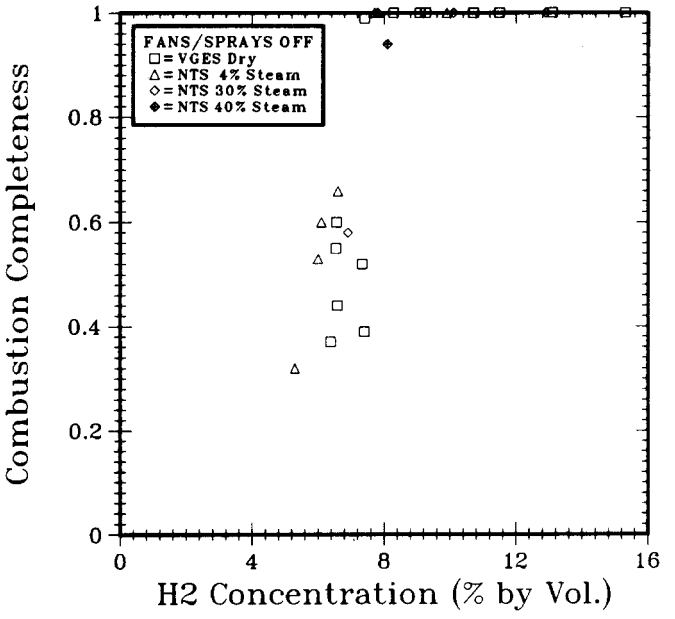

Figure 1.5-23. Combustion Completeness as a Function of Hydrogen Concentration in the Mixture for Combustion in a Quiescent Environment

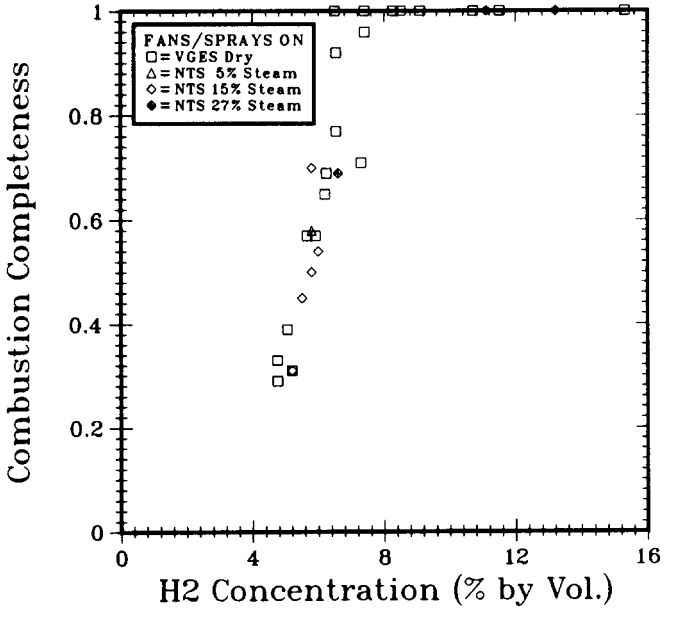

Figure 1.5-24. Combustion Completeness as a Function of Hydrogen Concentration in the Mixture for Combustion in a Turbulent Environment

percent of steam content will preclude any hydrogen burn. Combustion completeness becomes zero at this point.)

The effect of the fans or sprays on combustion completeness is mixed. It depends on the initial hydrogen content. Above 8 percent hydrogen concentration, the effect is minimal. However, it becomes substantial in those tests where very lean hydrogen mixtures exist (less than 6.5 percent as shown in Figures 1.5-23 and 1.5-24). The effect of turbulence on combustion completeness is not as distinct as the effect of turbulence on flame speed data, which is discussed in Section 1.5.2.2. Two combustion completeness correlations have been generated: one for the fans/sprays-on case and the other for the fans/sprays-off case.

The procedure to generate the new and improved combustion completeness correlations is first to compile all completeness data from experiments and group them into different sets according to the amount of steam initially in the combustion chamber. When these sets of data are plotted, they show that the data correlate better against the hydrogen concentration if the concentration is expressed as the gas volume percentage in dry air instead of in the overall mixture (Figures 1.5-23 and -24 versus Figures 1.5-25 and -26). For the plot with hydrogen concentration in dry air as an independent variable, the data points are spread wider apart and become less sensitive to the initial hydrogen concentration; moreover, the effect of steam on combustion completeness is more distinct. Hence the combustion completeness is correlated against hydrogen concentration in dry air. From those experimental results in which the initial conditions of the tests had less than 5 percent of steam concentration, a linear least-squares method is applied to line-fit this particular set of completeness data where the combustion was less than 100 percent completed. Hence a new correlation is generated.

Once the new correlation for the dry case is generated, this newly developed linear expression is applied to predict the combustion completeness for those tests with initially high steam content. The ratio of the measured completeness data to the value predicted by the linear expression is the correction factor to account for the effect of steam. The calculated steam correction factors are plotted against the steam concentration in Figure 1.5-27. An exponential fitting is used to correlate these steam correction factors. Hence, the new combustion completeness correlation can be expressed as a product of a linear function of the hydrogen concentration in dry air and a correction factor to account for the effect of steam. Following these procedures, two combustion completeness correlations are generated, one for the fans/sprays-off case and the other for the fans/sprays-on case.

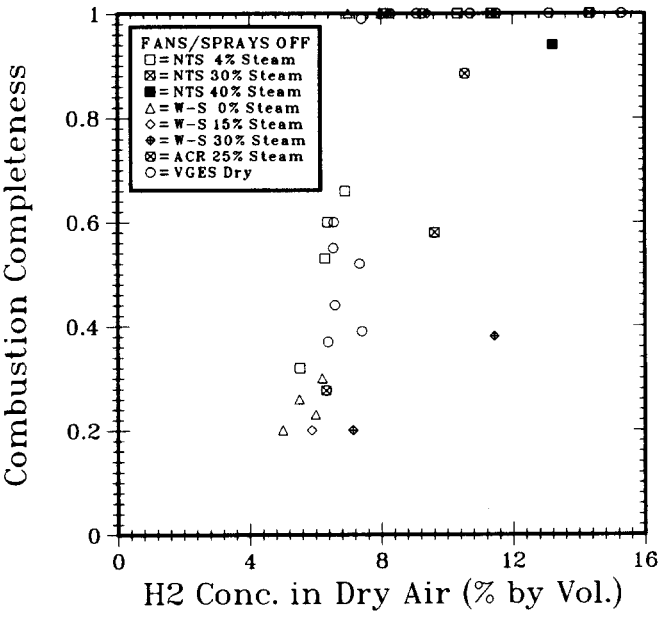

Figure 1.5-25. Combustion Completeness as a Function of Hydrogen Concentration in Dry Air for Combustion in a Quiescent Environment

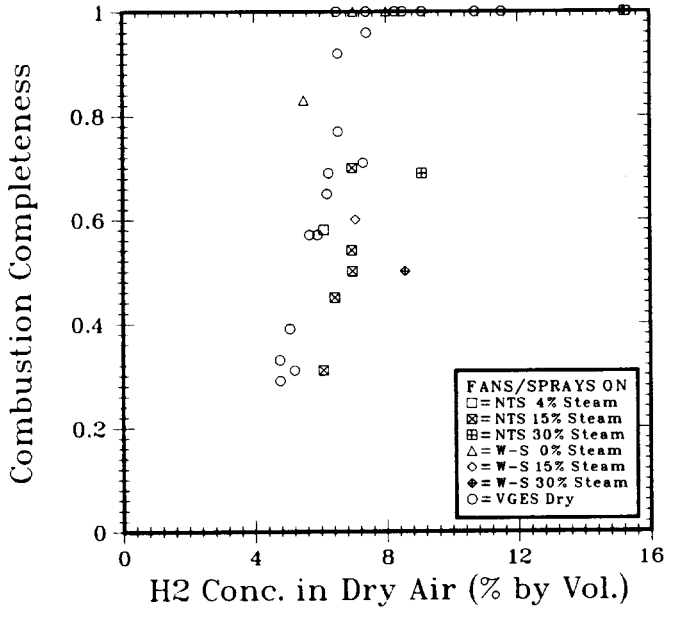

Figure 1.5-26. Combustion Completeness as a Function of Hydrogen Concentration in Dry Air for Combustion in a Turbulent Environment

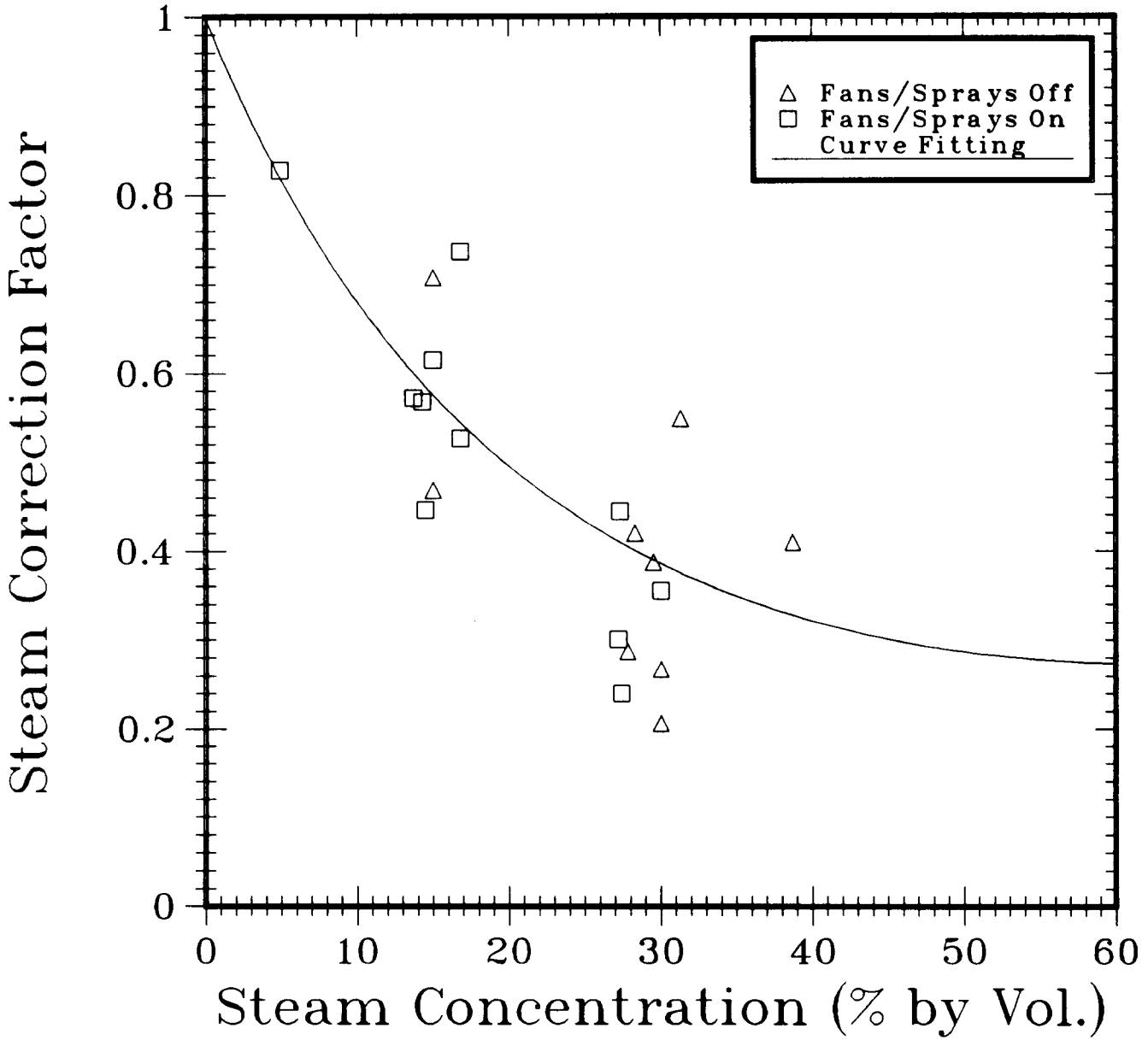

Figure 1.5-27. Steam Correction Factor for Combustion Completeness Correlation

For the fans/sprays-off case, the new correlation is:

$$\text{Completeness} = \text{Min}\,[(30.499\ X_H - 1.2827) * e^a,\ 1.0].$$

For the fans/sprays-on case, the new correlation is:

$$\text{Completeness} = \text{Min}\,[(28.638\ X_H - 1.0463) * e^a,\ 1.0].$$

For both correlations:

$$a = X_S * (-4.1966 + 3.3985 * X_S),$$

X_H = the hydrogen mole fractions in <u>dry</u> air, and

X_S = the steam mole fraction in the mixture.

Up to this point, the development of the new and improved combustion completeness correlations has been presented. Next, the predictability of these newly developed combustion completeness correlations are evaluated by comparing their predicted values with experimental data. Figures 1.5-28 and 1.5-29 show the comparison of the combustion completeness predicted by the new correlations with the experimental data for the quiescent (fans and sprays off) and turbulent (fans and sprays on) cases. Overall, the new correlations show a much better agreement with experimental data than the default correlation in HECTR 1.0. The comparison of the calculated and experimental results show that the accuracy of the fans/sprays-on correlation is good, while the accuracy of the fans/sprays-off correlation is fairly good. The fans/sprays-off correlation works well for the large-scale NTS experiments and tends to overpredict the completeness for the intermediate-scale experiments (VGES and Whiteshell). However, when reviewing the completeness data for fans/sprays-off cases, Figures 1.5-28 and 1.5-29 show that the experimental data are scattered and uncorrelated in the incomplete burn region. One explanation of this inconsistency is that the amount of hydrogen combusted in each quiescent test highly depends on the local hydrodynamic and thermal conditions. The other reason for this inconsistency can be explained by the stochastic nature of the combustion process.

Because of both the stochastic nature of the combustion process and the inconsistency of the data available, future users need to be aware of the uncertainty when using the newly developed correlations to predict the combustion completeness. Performing a parametric study by multiplying the predicted combustion completeness by an uncertainty factor is highly recommended. If a factor of greater than 1 is used, it will predict a larger amount of hydrogen burnt. This, in turn, will produce a higher combustion gas pressure and temperature. Similarly, using a factor of less than 1 will predict a lesser amount of hydrogen burnt.

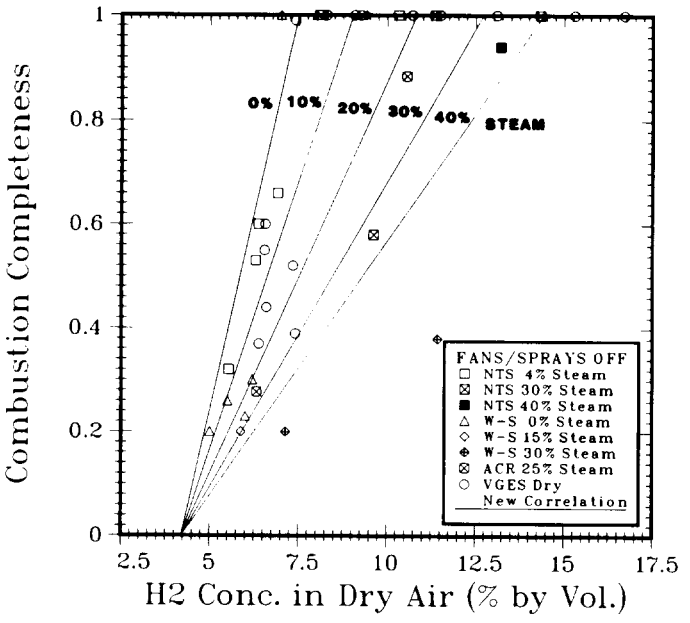

Figure 1.5-28. Comparison of Combustion Completeness Between Predictions and Experimental Data for Combustion in a Quiescent Environment

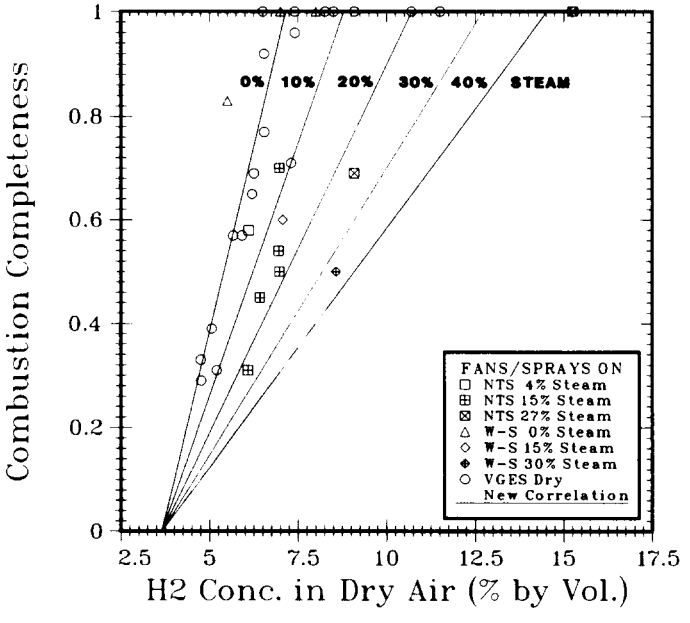

Figure 1.5-29. Comparison of Combustion Completeness Between Predictions and Experimental Data for Combustion in a Turbulent Environment

One reminder on the new correlations is that these new correlations are based on the combustion completeness data where the initial hydrogen concentration is below 20 percent. Since there is not sufficient combustion completeness data to support these correlations in hydrogen concentration near the upper flammability limit (hydrogen concentration of about 75 percent), it may not be valid to use these correlations in that region.

1.5.2.2 Development of an Improved Flame Speed Correlation

The development of a new and improved flame speed correlation is discussed in this section. In order to generate an improved correlation, as many flame speed measurements as are available are needed. Unfortunately, there are not many; besides the VGES fans-on and fans-off experiments, only the NTS experiments had a few additional flame speed data. The compiled data are not sufficient to model the effect of steam, sprays, and scaling well enough to generate a reliable correlation. In responding to this shortcoming, we looked for other means to gather more information about the flame speed. One important variable that can be used to qualify the flame speed, is the reciprocal of the "normalized" burn time.

The "normalized" burn time is defined as the burn time (the time between the initiation of burn to the completion of burn) divided by the characteristic length of a combustion chamber. For a premixed combustion test with bottom ignition, the characteristic length is the distance between the location of the igniter and the top of the combustion chamber. The reciprocal of this "normalized" burn time can be treated as an "effective" flame speed. This is quite similar to the present combustion model in HECTR, which uses the flame speed to calculate the burn time when a combustion occurs in a compartment. There is a substantial amount of burn time data in the FITS experiments. These additional data were used to model the effect of steam on the flame speed.

Care should be taken when applying the burn time data to generate the flame speed correlation. Not all the burn time data are useful. I had to eliminate a portion of the burn time data because it could not be used to calculate the flame speed. When the burn time is plotted against hydrogen concentration (Figure 1.5-30), a small peak is observed in the lean combustion region (hydrogen concentration between 7 and 9 percent). The measured burn time in this region is longer than those cases with hydrogen concentration less than 7 percent. Using the peak value of burn time to

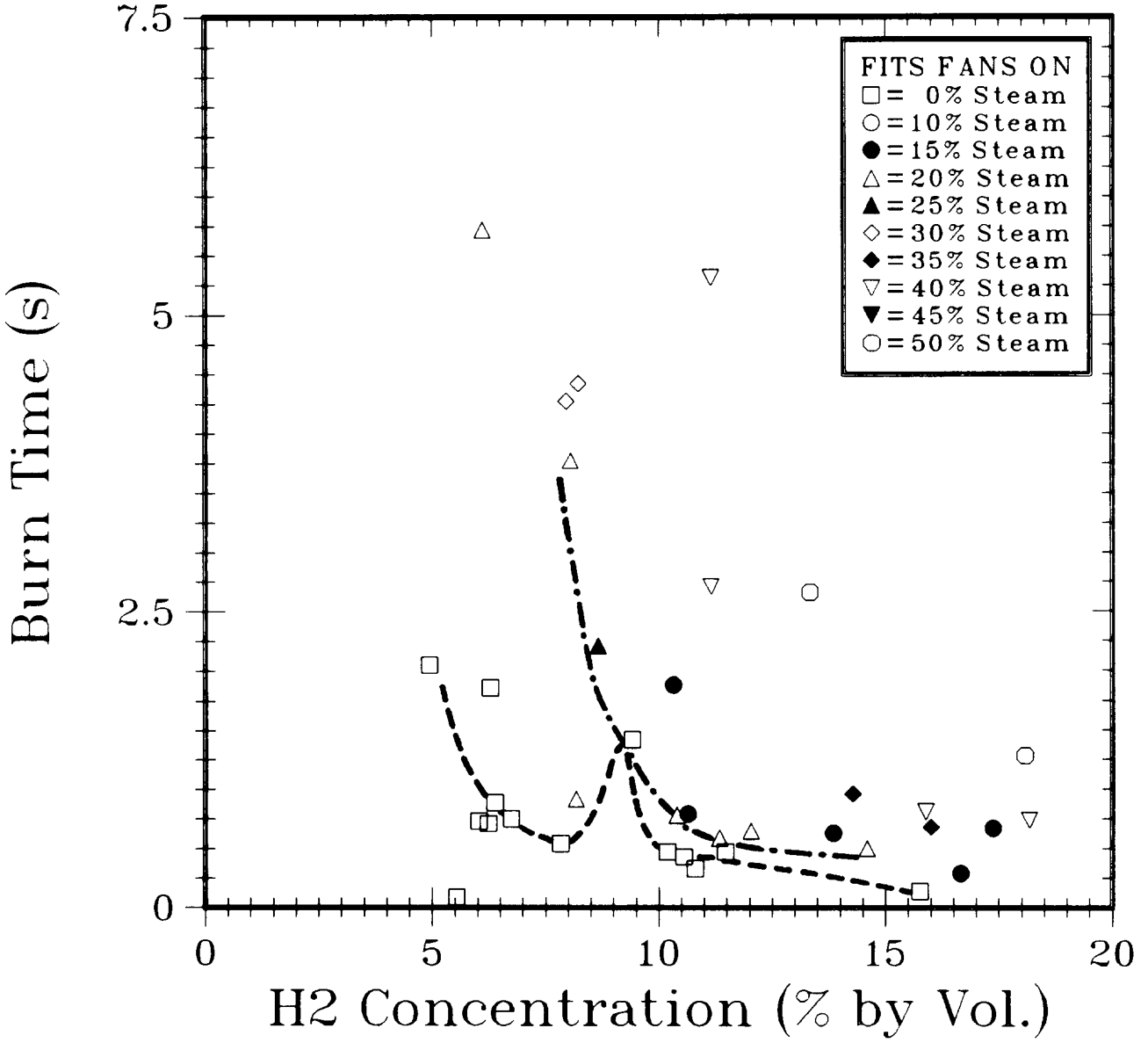

Figure 1.5-30. Burn Time as a Function of Hydrogen Concentration Obtained From the FITS Experiments

estimate the flame speed at this hydrogen concentration will probably give a wrong answer. It underpredicts the flame speed. However, in reality, the flame speed does not peak at a certain value of hydrogen concentration. The flame speed decreases monotonically as hydrogen concentration decreases. The increase of the burn time is due to the complexity of the burn process in this hydrogen concentration. Basically, a simple deflagration can be characterized into three different types of processes. The first one is a simple global, fast, symmetric, and complete burn with flame propagating isotropically. Usually, this happens at a hydrogen concentration above 9 percent. The second is an incomplete burn with flame mainly propagating upward and quenching at the top of the combustion chamber. This occurs at a hydrogen concentration below 6.5 percent. The last one is similar to the second one except when the flame hits the top of the combustion chamber, it does not quench. As the flame kernel travels upward, it accumulates enough energy to readjust itself and then propagate downwards after it hits the top. This phenomenon produces a double peak in pressure (Figure 1.5-31) and results in a longer burn time. Unless the burning characteristic length can be found accurately, using this burn time to generate flame speed may be inaccurate.

Before any data of burn time from the FITS experiments are used to develop an improved flame speed correlation, it would be better to verify whether the reciprocal of the normalized burn time could be treated accurately as an effective flame speed. To verify this, all data of burn time from the VGES experiments were first compiled to generate a set of equivalent effective flame speeds. Then these inferred effective flame speeds were compared with the measured flame speeds from the VGES fans-on and fans-off experiments (Figures 1.5-32 and 1.5-33). As shown in these figures, the agreement is reasonably good. This proves that the reciprocal of the normalized burn time data can be treated as an equivalent effective flame speed.

When comparing the measured flame speed data obtained from the VGES and NTS experiments for a combustion in a quiescent environment, some small differences were found even though the test conditions were quite similar (Figure 1.5-34). One of the suspected factors is the scaling effect. For the lean hydrogen combustion in quiescent environment cases, the duration of the burns is governed by buoyancy-driven gas flow induced by the rising flame. This dynamic gas flow is highly dependent on the geometry and size of the combustion chamber. In order to investigate the scaling effect on the flame speed, an analytical model was set up to relate flame speed with a characteristic length.

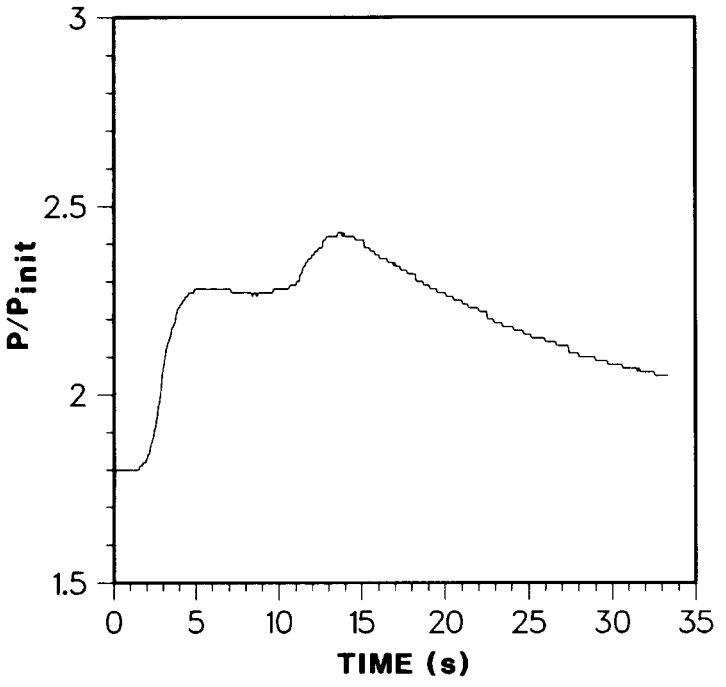

Figure 1.5-31. The Measured Gas Pressure Versus Time for FITS Test No. Burn-24, S50H08

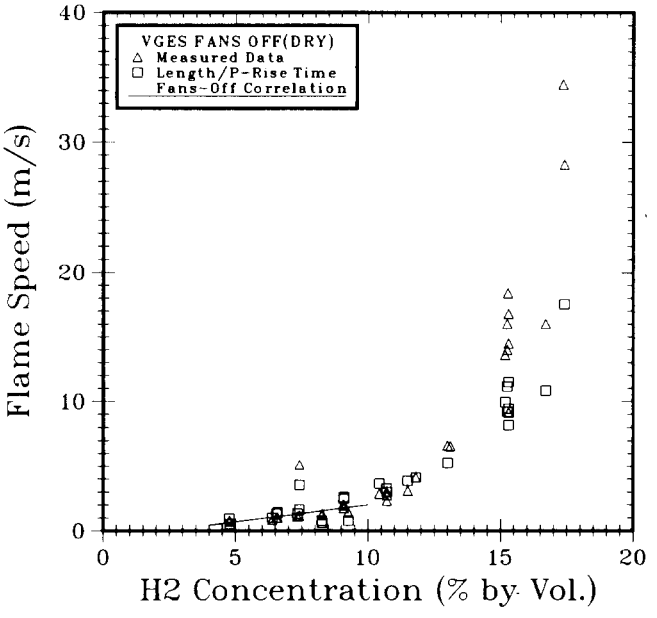

Figure 1.5-32. Comparison of Upward Propagating Flame Speed; Measured Data Versus Inferred Data From the Burn Time (VGES Fans-Off Experiments)

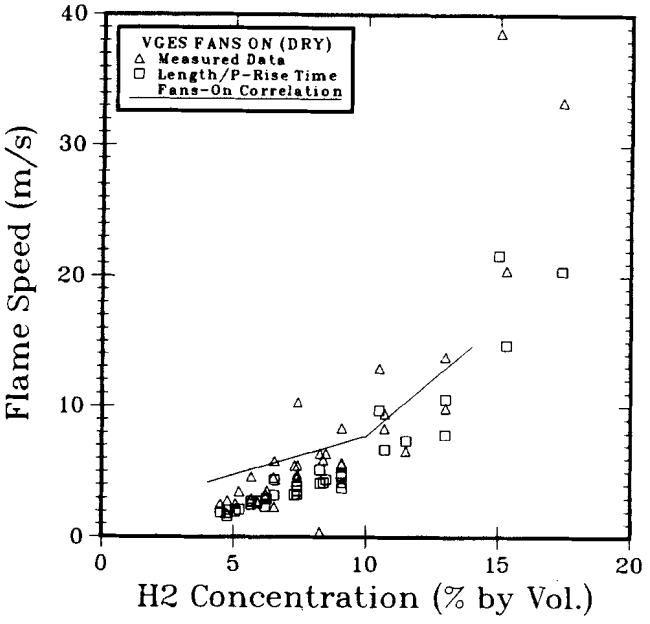

Figure 1.5-33. Comparison of Upward Propagating Flame Speed; Measured Data Versus Inferred Data From the Burn Time (VGES Fans-On Experiments)

Suppose that a deliberate combustion is initiated by an igniter located near the bottom of the chamber. At a lean, quiescent burn condition, the flame will mainly propagate upward and sideways. The burnt zone will be an inverted cone shape with the tip located near the igniter (Figure 1.5-35). Now, define a small control volume with height Δz at the top of the burnt zone. Apply a force balance at this control volume; the buoyancy force generated by the less-dense burnt gases propagating into the unburnt gases is countered by the drag force. The governing equations can be written as

$$\rho_b \pi r_b^2 \Delta z \frac{dU_B}{dt} = \pi r_b^2 \Delta z \, [\rho_u - \rho_b] \, g - C_D \, 2\pi r_b \Delta z \frac{\rho_u U_B^2}{2} \quad , \quad (1.5\text{-}1)$$

where U_B is the local flame propagating velocity,
C_D is the drag coefficient,
ρ_u is the density of the unburnt gases,
ρ_b is the density of the burnt gases, and
r_b is the cross-sectional radius of the burnt zone.

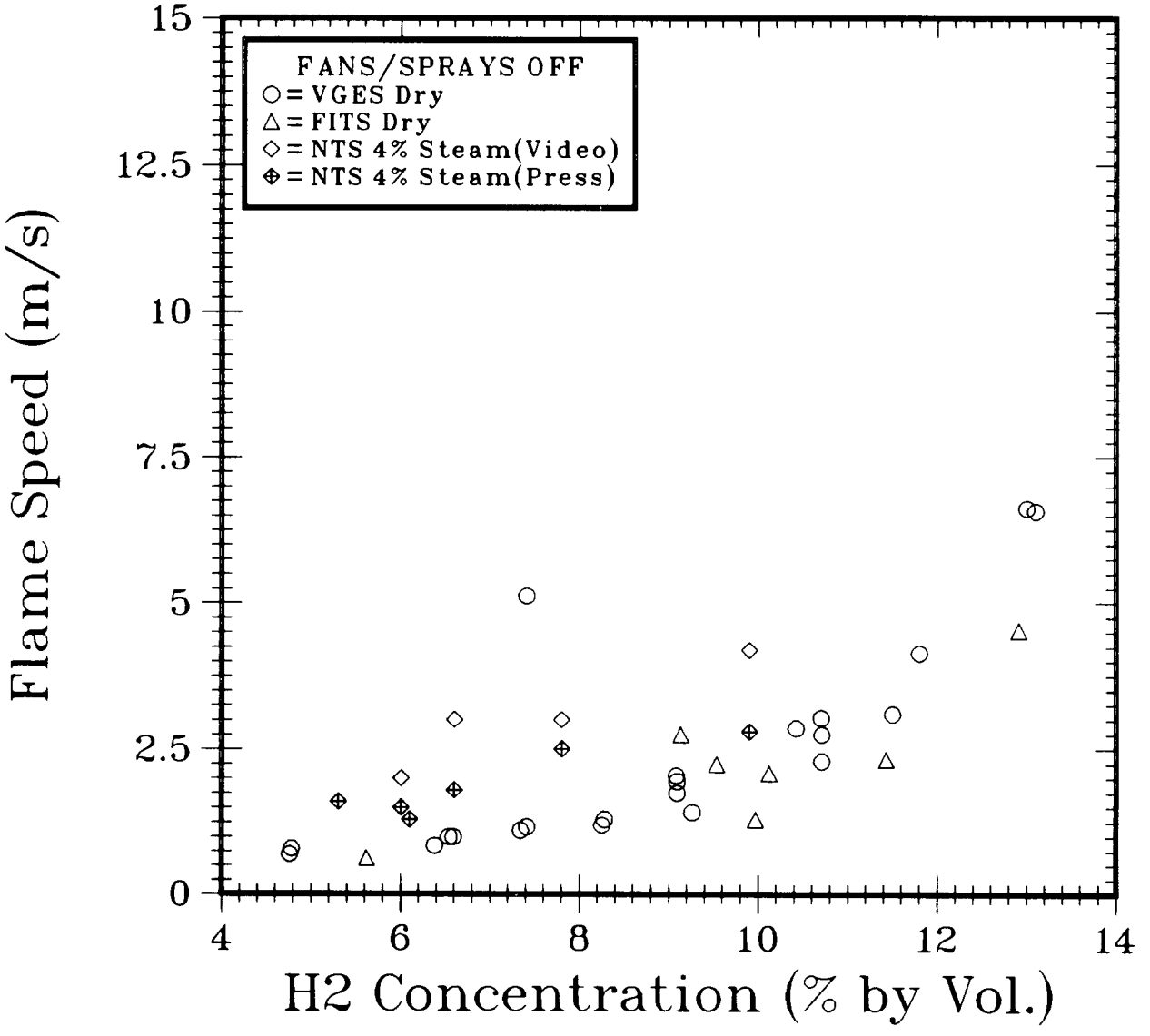

Figure 1.5-34. Comparison of Upward Propagating Flame Speed Between the VGES, FITS (Inferred), and NTS Data for Combustion in a Quiescent Environment

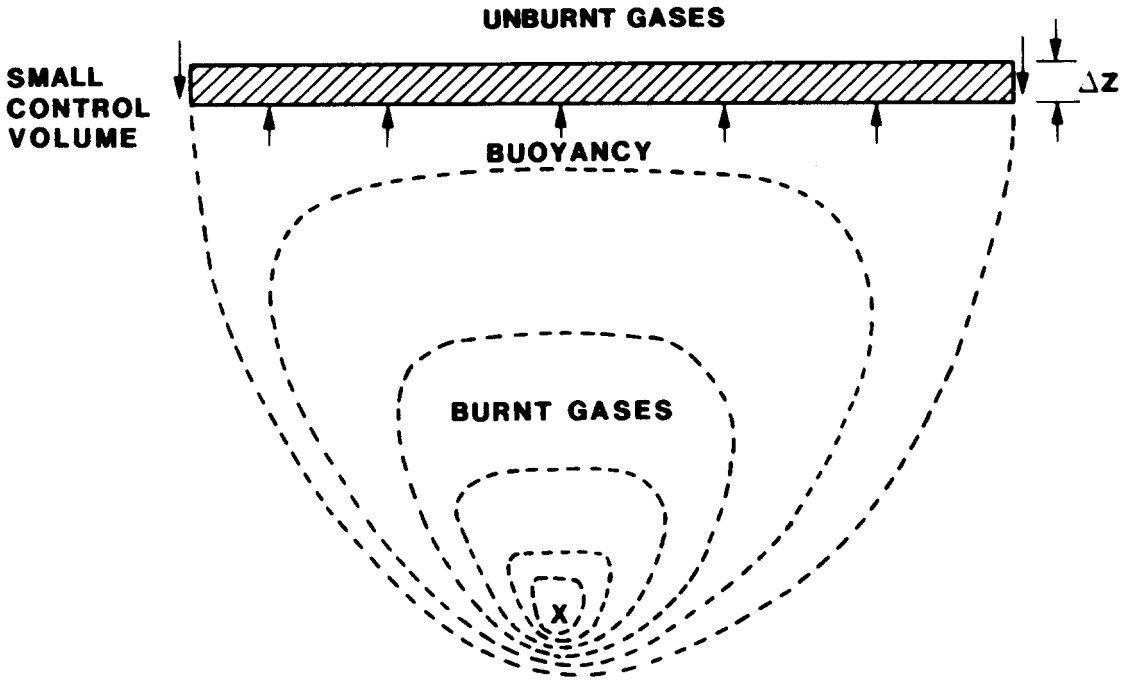

Figure 1.5-35. General Characteristics of Combustion Initiated by an Igniter Located Near the Bottom of the Chamber

Neglecting the inertia effect, the local flame velocity becomes

$$U_B = \sqrt{\left[1 - \frac{\rho_b}{\rho_u}\right] \frac{g}{C_D} r_b} \quad . \tag{1.5-2}$$

Since

$$U_B = \frac{dy}{dt}$$

and from the conservation of mass,

$$r_b = \left[\frac{\rho_u}{\rho_b}\right] * S_u * t \quad ,$$

where S_u is the burning velocity,

$$\frac{dy}{dt} = U_B = \sqrt{\left[1 - \frac{\rho_b}{\rho_u}\right] \frac{g}{C_D} \left[\frac{\rho_u}{\rho_b}\right] * S_u * t} \quad . \tag{1.5-3}$$

$$\therefore y = \frac{2}{3}\sqrt{\left[1 - \frac{\rho_b}{\rho_u}\right]\frac{g}{C_D}\left[\frac{\rho_u}{\rho_b}\right] * S_u} * t^{3/2} \quad . \qquad (1.5\text{-}4)$$

For the flame to rise to the top of the chamber,

let $y = L$ and $t = T$.

$$\therefore L = \frac{2}{3}\sqrt{\left[1 - \frac{\rho_b}{\rho_u}\right]\frac{g}{C_D}\left[\frac{\rho_u}{\rho_b}\right] * S_u} * T^{3/2} \quad . \qquad (1.5\text{-}5)$$

For the upward propagating flame speed,

$$V_f = \frac{L}{T} \qquad (1.5\text{-}6)$$

and

$$V_f = \left[\frac{2}{3}\right]^{2/3}\left[\left[1 - \frac{\rho_b}{\rho_u}\right]\frac{g}{C_D}\left[\frac{\rho_u}{\rho_b} S_u\right]\right]^{1/3} L^{1/3} \quad . \qquad (1.5\text{-}7)$$

From the simple deviation discussed above, the flame speed is shown to depend on the cube root of the characteristic length. For a better comparison, a new parameter defined as the flame speed divided by the cube root of a characteristic length is used to compare the measured data obtained from the VGES, FITS, and NTS experiments (Figure 1.5-36). The data fit well for the VGES, FITS, and NTS experiments. This verifies that to account for the scaling effect, the effective flame speed should depend on the cube root of the characteristic length of the combustion chamber. However, the present analytical model is too simple and crude. Our intention is only to use it to better understand the scaling effect on the upward propagating flame speed, and we will not pursue any further analysis using this analytical model.

Figures 1.5-37 through 1.5-40 compile all the effective flame speed data from either direct measurements (as in the VGES and NTS experiments) or interpretations of burn times (as in FITS) for cases with fans/sprays off and fans/sprays on, respectively. The figures shown plot the effective flame speed against the hydrogen concentration in the dry air as well as hydrogen concentration in the mixture. By comparing these figures, we see that the flame speed is correlated slightly better against the hydrogen concentration in the dry air than in the mixture. Hence the hydrogen concentration in the dry air was selected as one of the independent variables used for the correlation. The other independent variable is steam concentration.

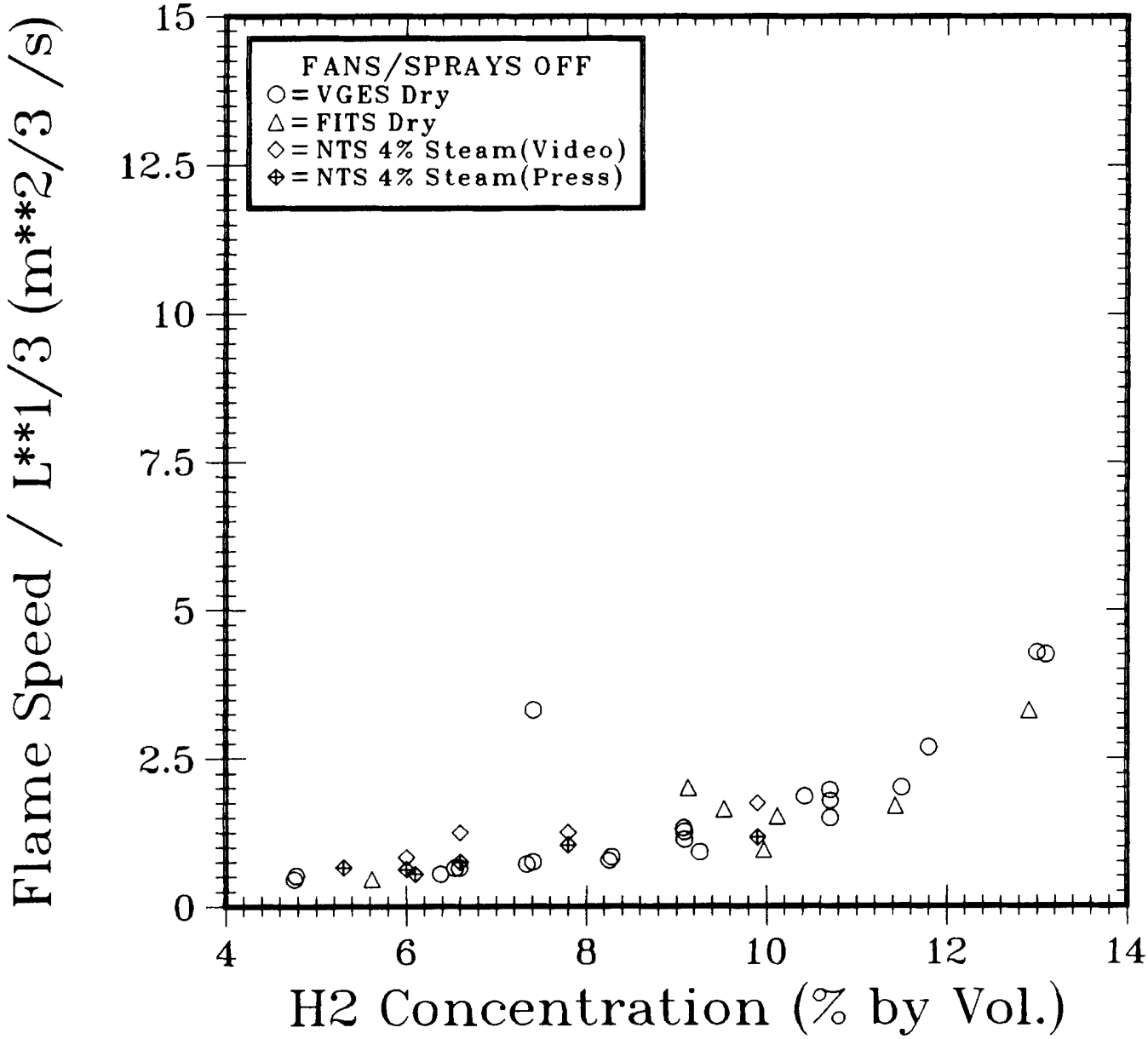

Figure 1.5-36. Comparison of the "Normalized" Flame Speed Between the VGES and NTS Data for Combustion in a Quiescent Environment

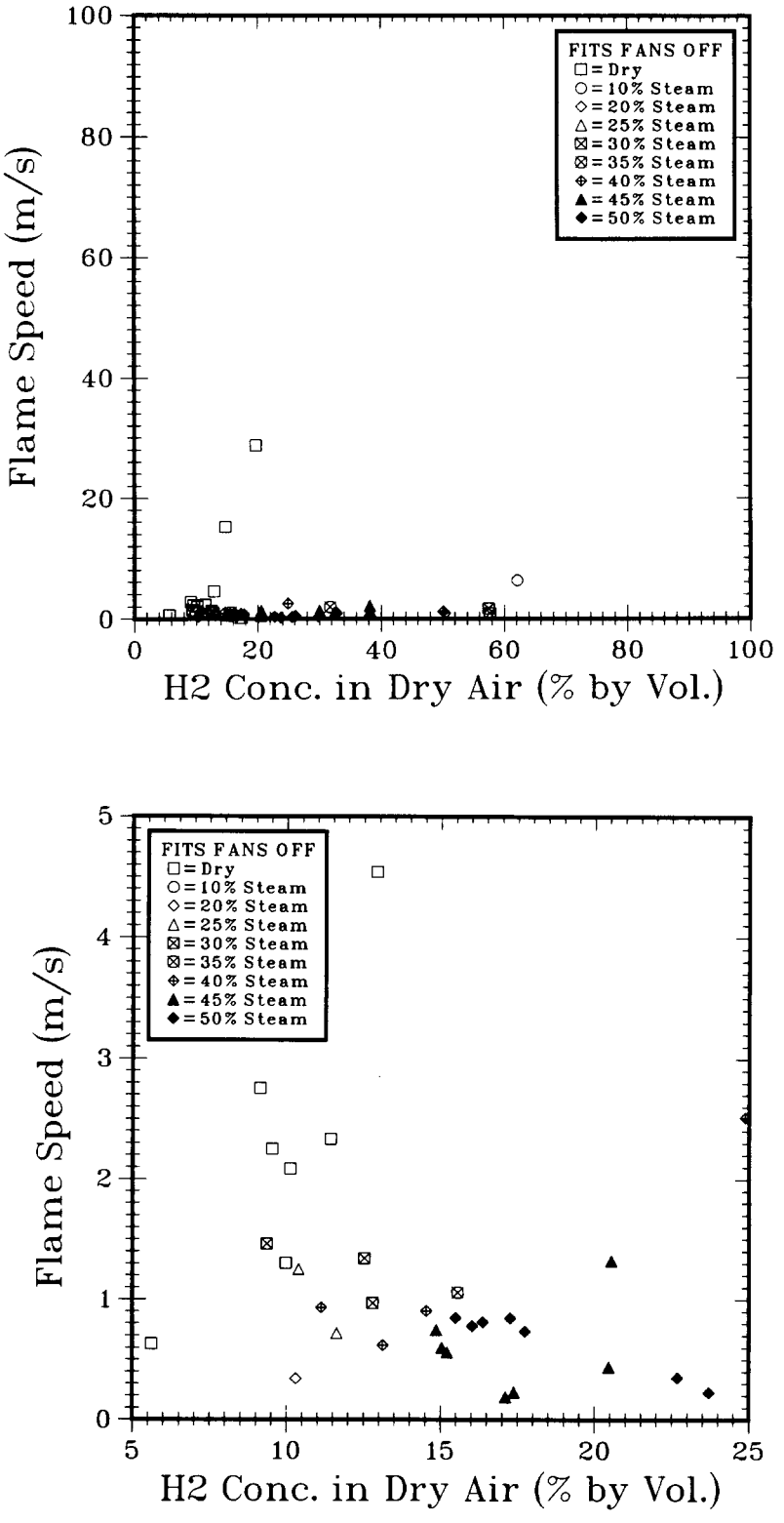

Figure 1.5-37. Normalized Flame Speed as a Function of Hydrogen Concentration in Dry Air for Combustion in a Quiescent Environment

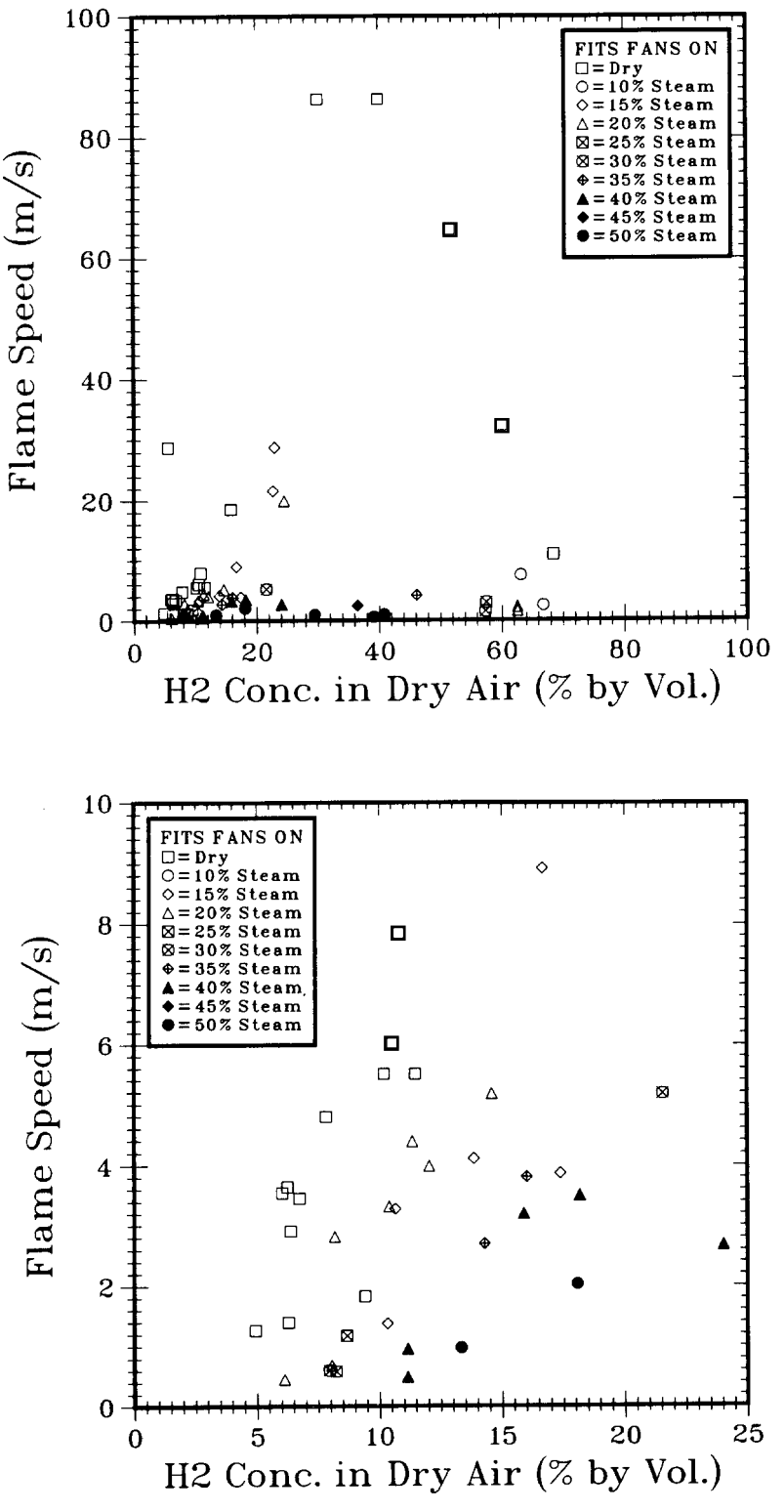

Figure 1.5-38. Normalized Flame Speed as a Function of Hydrogen Concentration in Dry Air for Combustion in a Turbulent Environment

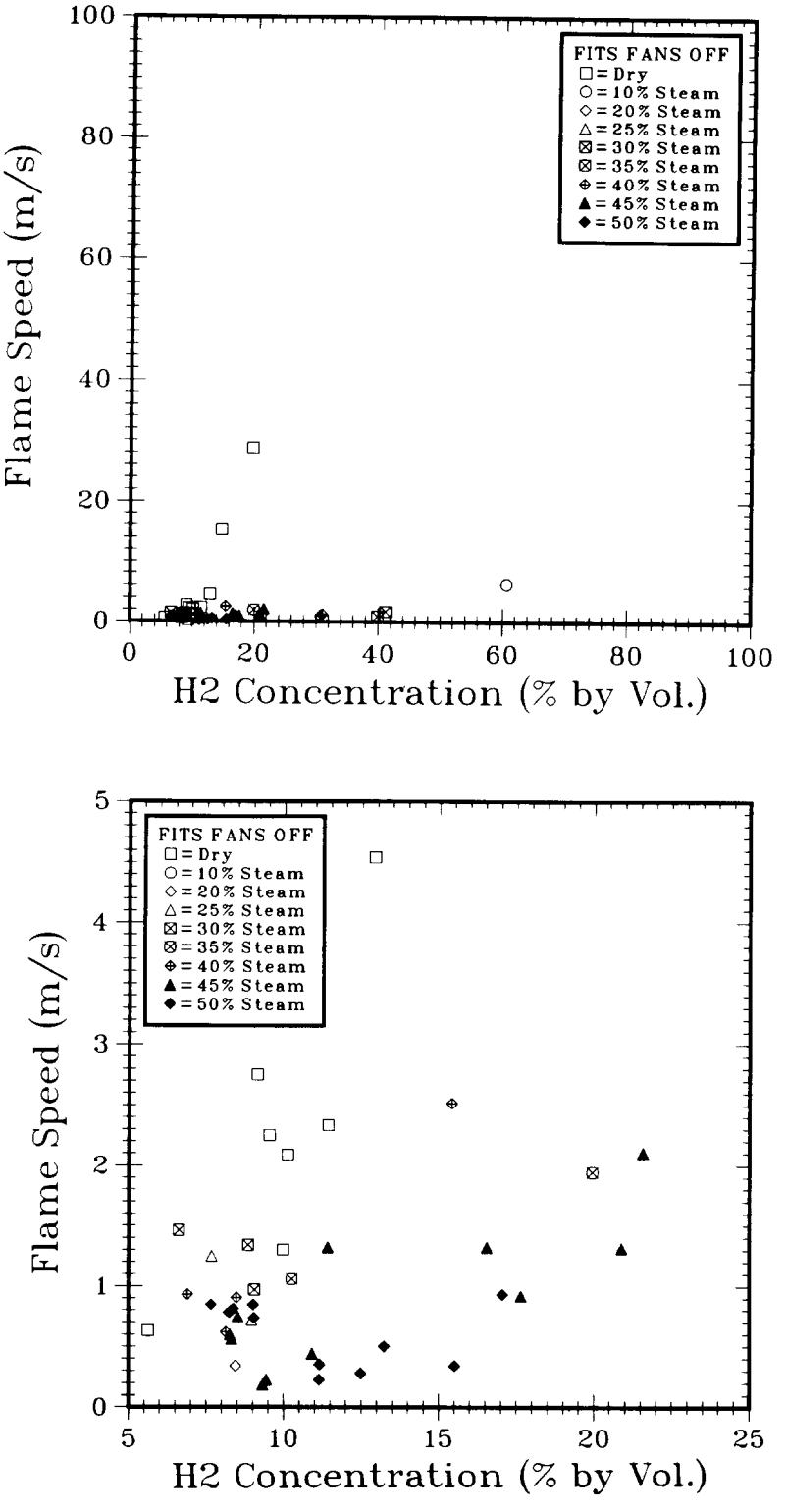

Figure 1.5-39. Normalized Flame Speed as a Function of Hydrogen Concentration in the Mixture for Combustion in a Quiescent Environment

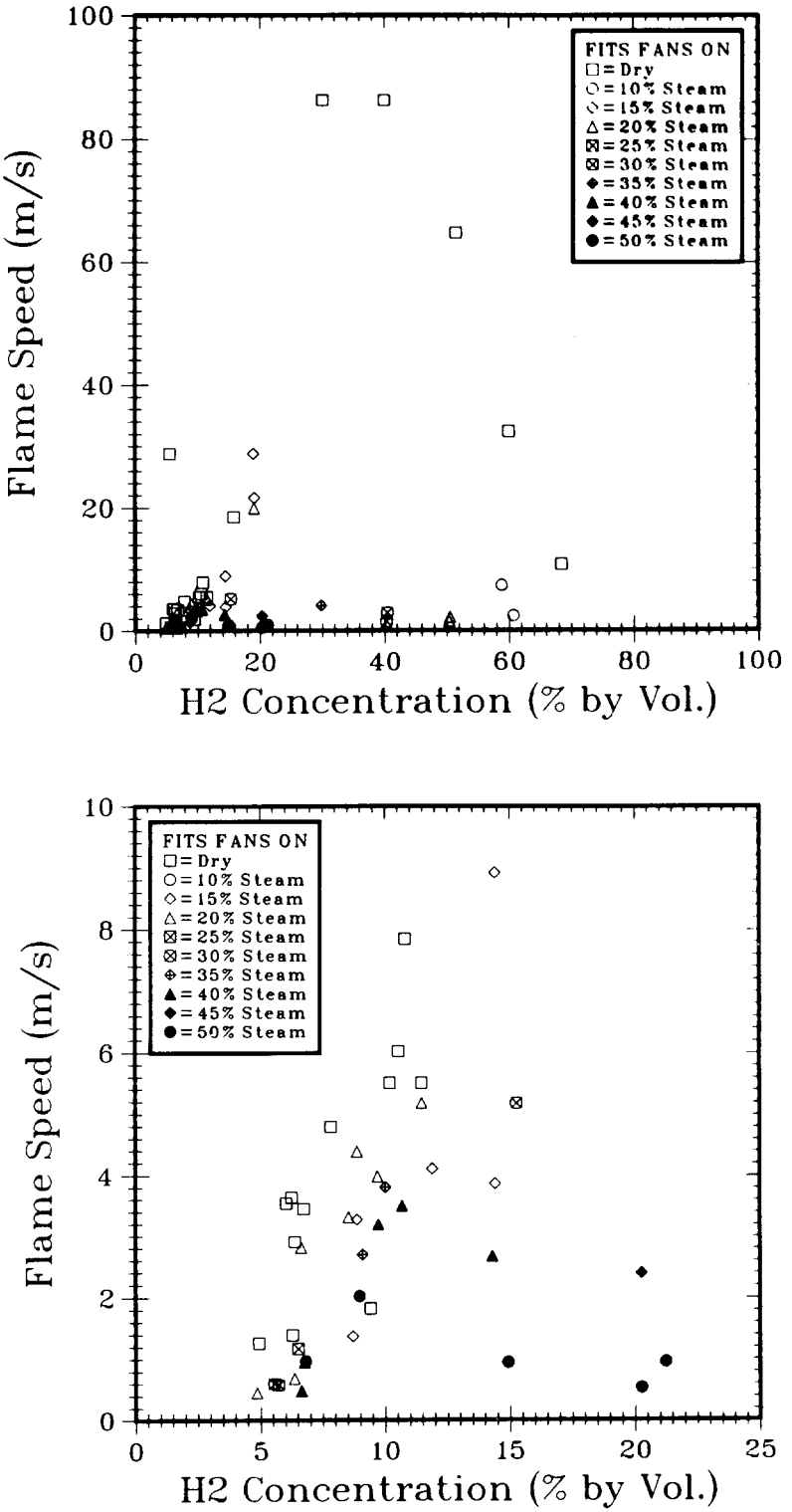

Figure 1.5-40. Normalized Flame Speed as a Function of Hydrogen Concentration in the Mixture for Combustion in a Turbulent Environment

In the mathematical form, the flame speed correlation is expressed as a product of two factors similar to the old default correlation in HECTR 1.0. The first factor is a predictor to calculate the flame speed as a linear or quadratic function of hydrogen concentration in the dry air neglecting the steam effect. The second factor, which is a corrector, does include the steam effect. Thus the flame speed is assumed to depend mainly on the hydrogen concentration in dry air and the addition of steam will monotonically decrease the flame speed. The effects of initial gas pressure and temperature are minimum and neglected.

To generate the flame speed correlation, first those flame speed data obtained from the tests with no steam content are selected, and then the whole spectrum of hydrogen concentration is divided into 6 regions of interest: (1) 0 to 10 percent, (2) 10 to 18 percent (3) 18 to 20 percent, (4) 20 to 35 percent, (5) 35 to 45 percent, and (6) 45 to 80 percent. For the first, fourth, and sixth regions, a linear least-square fitting curve is used to correlate all the experimental data. However, for the second region, a quadratic function fits the data better than a linear function and is used. In order to maintain a smooth and continuous transition between regions, interpolations are applied in both the third and fifth region.

After the flame speed correlations for combustion in a dry environment (no steam content) are generated, they are used to predict the flame speed for other tests that had substantial amount of steam initially. By comparing the predicted flame speed and the measured flame speed, the value of the steam correction factor is obtained and plotted against the steam concentration (Figures 1.5-41, 1.5-42, and 1.5-43). These plots show that the steam factor behaved as an exponential function of steam concentration. The expression to best-fit these steam correction factor data is exp $[X_S(a+b*X_S)]$, where X_S is the concentration of steam.

The effect of turbulence generated by either fans or sprays was substantial at a hydrogen concentration below 18 percent. Separate flame speed correlations were generated for combustion occurring in a quiescent environment and in a turbulent environment. However, at a hydrogen concentration above 18 percent, the flame began to accelerate so fast that the turbulence generated by fans or sprays became unimportant. There is no distinction of the flame speed data between the quiescent environment and the turbulent environment. A single correlation is recommended.

The new and improved flame speed correlations are listed as follows:

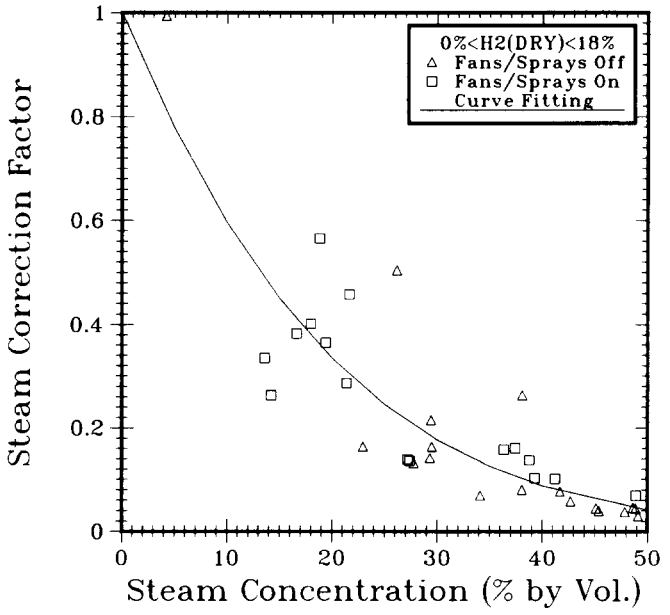

Figure 1.5-41. Steam Correction Factor for Flame Speed Correlation (Combustion With Initial Hydrogen Concentration = 0 to 18 percent)

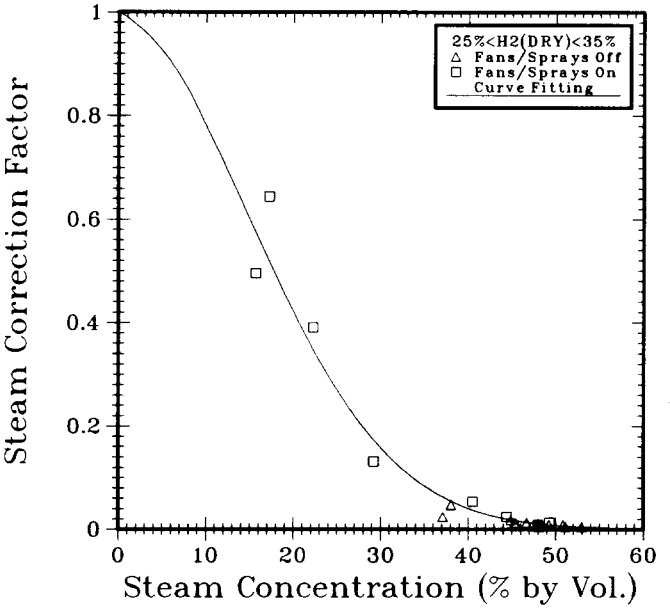

Figure 1.5-42. Steam Correction Factor for Flame Speed Correlation (Combustion With Initial Hydrogen Concentration = 20 to 35 percent)

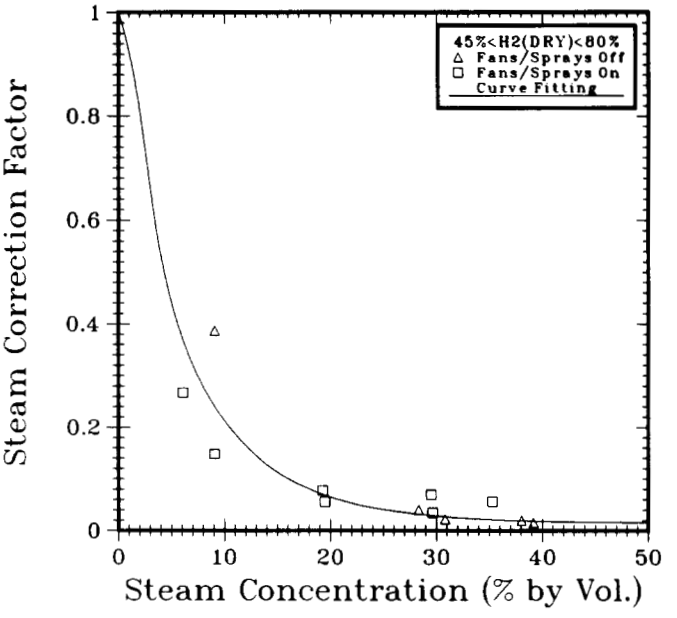

Figure 1.5-43. Steam Correction Factor for Flame Speed Correlation (Combustion With Initial Hydrogen Concentration = 40 to 80 percent)

(1) For $0\% < H_2 \leq 10\%$:

With either fans or sprays on,

$$V_f = L^{1/3} * (59.65\ X_H - 1.248) * \exp\left[X_S\ (a + b\ X_S)\right] \quad . \qquad (1.5\text{-}8)$$

With both fans and sprays off,

$$V_f = L^{1/3} * (23.70\ X_H - 0.862) * \exp\left[X_S\ (a + b\ X_S)\right] \quad , \qquad (1.5\text{-}9)$$

where $a = -4.877$ and $b = -3.008$.

(2) For $10\% < H_2 \leq 18\%$:

With either fans or sprays on,

$$V_f = L^{1/3} * (2074\ X_H^2 - 347.23\ X_H + 18.700) * \exp\left[X_S\ (a + b\ X_S)\right] \qquad (1.5\text{-}10)$$

With both fans and sprays off,

$$V_f = L^{1/3} * (1724\ X_H^2 - 267.28\ X_H + 10.996) * \exp\left[X_S\ (a + b\ X_S)\right] \quad , \qquad (1.5\text{-}11)$$

where a = -4.877 and b = -3.008.

(3) For 18% < H_2 < 25%: Use interpolation.

(4) For 25% ≤ H_2 < 35%: For all cases,

$$V_f = L^{1/3} * (289.73\ X_H - 33.769) * \exp\left[X_S\ (a + b\ X_S)\right] \quad , \qquad (1.5\text{-}12)$$

where a = -0.641 and b = -18.38.

(5) For 35% < H_2 < 45%: For all cases, use interpolation.

(6) For 45% ≤ H_2 ≤ 80%: For all cases,

$$V_f = L^{1/3} * (145.07 - 199.62\ X_H) * \exp\left[X_S\ (a + b\ X_S)\right] \quad , \qquad (1.5\text{-}13)$$

where a = -17.279 and b = 18.07.

For all the flame speed correlation equations, X_H is the hydrogen concentration in dry air and X_S is the steam concentration in the mixture.

The development of the new and improved upward propagating flame speed correlations have been presented throughout this section. Next, these newly developed flame speed correlations are evaluated by comparing their predictions with experimental data. Figures 1.5-44 through 1.5-47 show the comparison of the flame speed predicted by the new correlations with the experimental data for the quiescent (fans and sprays off) and turbulent (fans and sprays on) cases. Overall, the predictability of the new flame speed correlations is reasonably good. The most difficult part of developing the new flame speed correlation is that there are many variables to be considered: hydrogen concentration, steam concentration, turbulence, initial temperature, igniter location, compartment size and geometry, and possibly others. Hydrogen and steam concentrations, turbulence, and scaling are the most important variables with respect to the reactor safety analysis, and they have been modeled in the present correlations. Other effects, by assumption, are minimum.

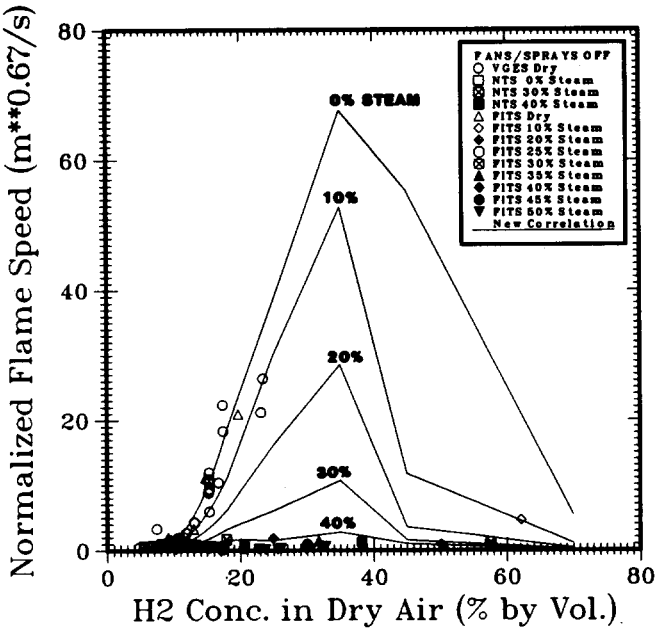

Figure 1.5-44. Comparison of Flame Speed Between Predictions and Experimental Results for Combustion in a Quiescent Environment (Initial Hydrogen Concentration = 0 to 80 percent)

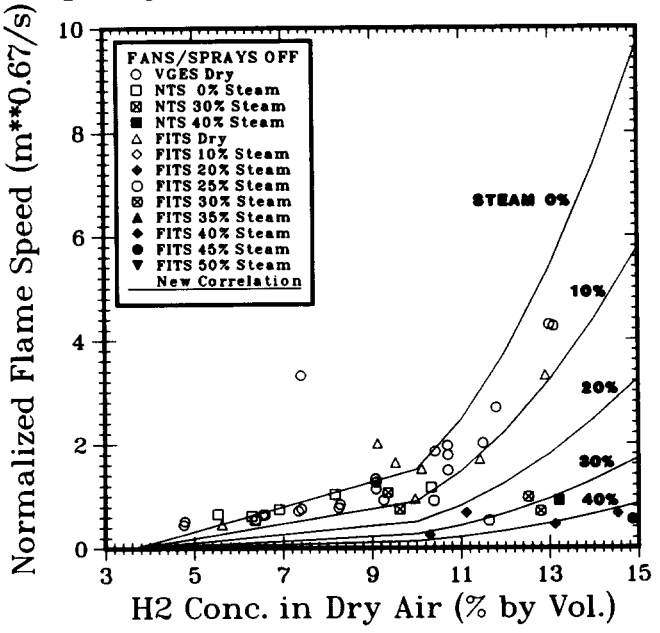

Figure 1.5-45. Comparison of Flame Speed Between Predictions and Experimental Results for Combustion in a Quiescent Environment (Initial Hydrogen Concentration = 0 to 20 percent)

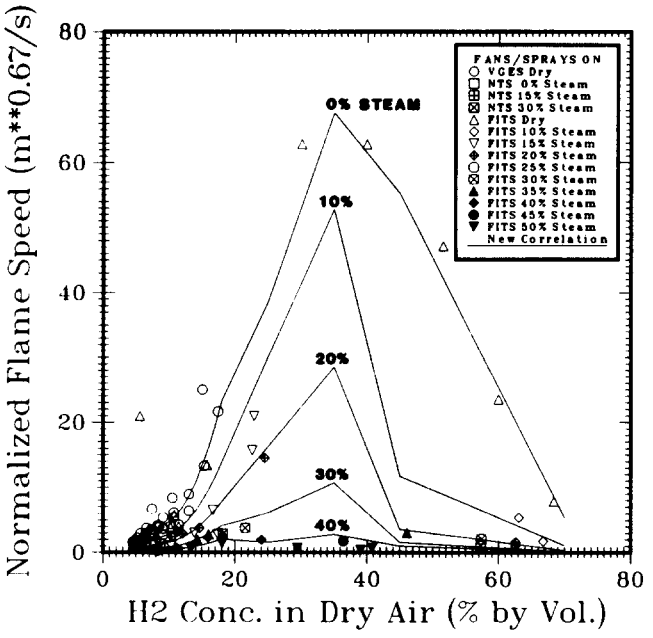

Figure 1.5-46. Comparison of Flame Speed Between Predictions and Experimental Results for Combustion in a Turbulent Environment (Initial Hydrogen Concentration = 0 to 80 percent)

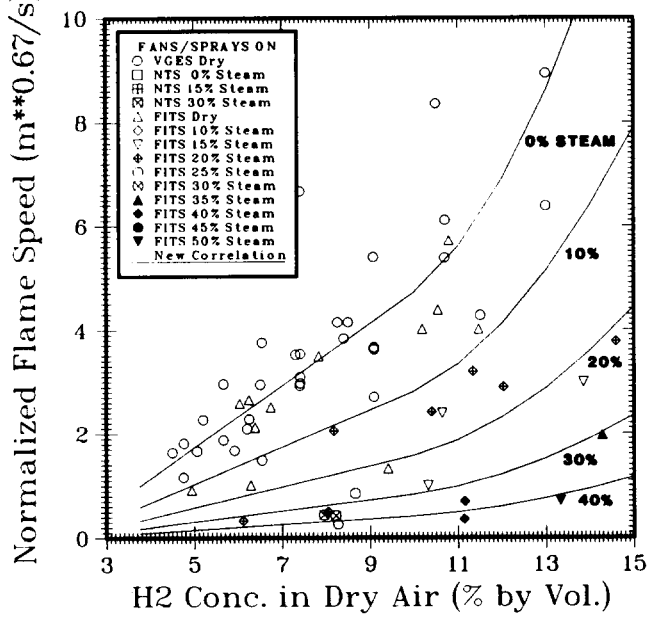

Figure 1.5-47. Comparison of Flame Speed Between Predictions and Experimental Results for Combustion in a Turbulent Environment (Initial Hydrogen Concentration = 0 to 20 percent)

Because of the difficulty to obtain accurate flame speed measurements and possibly because of the stochastic nature of the combustion process as shown in the scattering of data, there is some uncertainty when using these new correlations to predict the flame speed and the burn time. Hence, performing a parametric study by multiplying the predicted flame speed with an uncertainty factor is highly recommended. Using a factor of greater than 1 will give a larger flame speed than the value predicted by these correlations. This in turn will result in a shorter burn time. A faster burning process will produce a higher combustion gas pressure and temperature because there will be less amount of heat lost to surfaces. On the contrary, if a factor of less than 1 is used in the calculation, the slower flame speed and longer burn time will result in a lower peak combustion pressure and temperature because more heat is lost to surfaces.

1.5.3 The FLAME Facility

(M. P. Sherman and S. R. Tieszen, 6427;
W. B. Benedict, 1131)

1.5.3.1 Introduction

FLAME is a large horizontal channel used to study hydrogen combustion problems relevant to nuclear reactor safety including flame acceleration and transition to detonation. A single bridgewire ignition is used at the closed end of the channel, and the combustion propagates toward the open end. The degree of transverse venting along the top of the channel can be varied. Obstacles can be attached to the side walls and floor. FLAME was built to be a half-scale model of an ice condenser upper plenum region. It is 30.5 m long, 2.44 m high, and 1.83 m wide (100 x 8 x 6 ft).

Since an understanding of the effects of scale are vital in relating the results from smaller models to nuclear reactor containments, a test series with 8 percent scale models of the FLAME channel, MINIFLAME, were carried out. The MINIFLAMES were made of transparent plastic and plywood. Instrumentation was minimal: Three pressure transducers mounted in the floor and high speed kinematography through the transparent side walls. Since there was no budget for scale-model testing, the models were built on vacation time, and the tests completed within three working days.

The first 20 FLAME facility tests, F-1 through F-20, investigated the effects of various hydrogen concentrations and degrees of tranverse venting on flame acceleration and deflagration to detonation transition (DDT) in a large channel free of obstructions (other than instrumentation and mixing fans). The later tests, F-21 to F-30, involved the effects of obstructions in the channel on flame acceleration

and DDT. The results of tests F-1 to F-20 and F-21 to F-23 have been reported in previous semiannual reports and in several publications. The results of the later tests, F-24 to F-30, are reported in this semiannual report. The present series ended with F-30, pending additional funding by the NRC.

1.5.3.2 The FLAME Tests With Obstacles

Ten tests were conducted in FLAME with obstacles in the channel. Eight tests used simple baffle obstacles consisting of 1.2-cm (0.5-in) thick plywood sheets mounted in pairs opposite one another on the side walls (Figure 1.5-48). The obstacles extended the full length from the floor to the ceiling of the channel, and inward from the wall 30.8 cm (1 ft), blocking 33 percent of the channel cross section. The obstacle pairs were placed 1.8 m (6 ft) along the channel axis. Two tests involved half-scale models of the air handlers in the upper plenum of ice condenser containments, as shown in Figure 1.5-49. These were boxes blocking 11 percent of the channel cross section. A summary of the test conditions and some of the results are shown in Table 1.5-6.

The results of the entire set of FLAME tests are summarized graphically in Figures 1.5-50 through 1.5-52. From these figures comparison of results between tests with an empty channel and tests with obstacles can be made. Figure 1.5-50 shows the conditions for DDT as a function of H_2 mole fraction and degree of transverse venting. Figure 1.5-51 presents the equivalent planar flame speed, and Figure 1.5-52 the overpressure, as a function of H_2 mole fraction for various degrees of transverse venting, with and without the presence of obstacles. The "equivalent planar flame speed" is the volumetric rate of burning divided by the channel cross-sectional area. The presence of obstacles greatly reduces the lean limits for deflagration-to-detonation transition. In fact, the DDT in test F-22 at 15 percent hydrogen occurred with a mixture leaner than the lean detonation limit cited in the older combustion literature.

In tests without obstacles, there was a clear division between the results of tests with and without DDT. Without DDT the peak overpressures were low, below 1 atmosphere. With DDT, the peak overpressures were much higher, a highly luminous detonation wave was photographed leaving the channel, and a clear retonation wave (returning detonation-shock wave) was observed.

With obstacles, the flames are accelerated to sonic speeds of the burned gas, 600 to 800 m/s. The peak overpressures are large even without DDT. A retonation wave was not

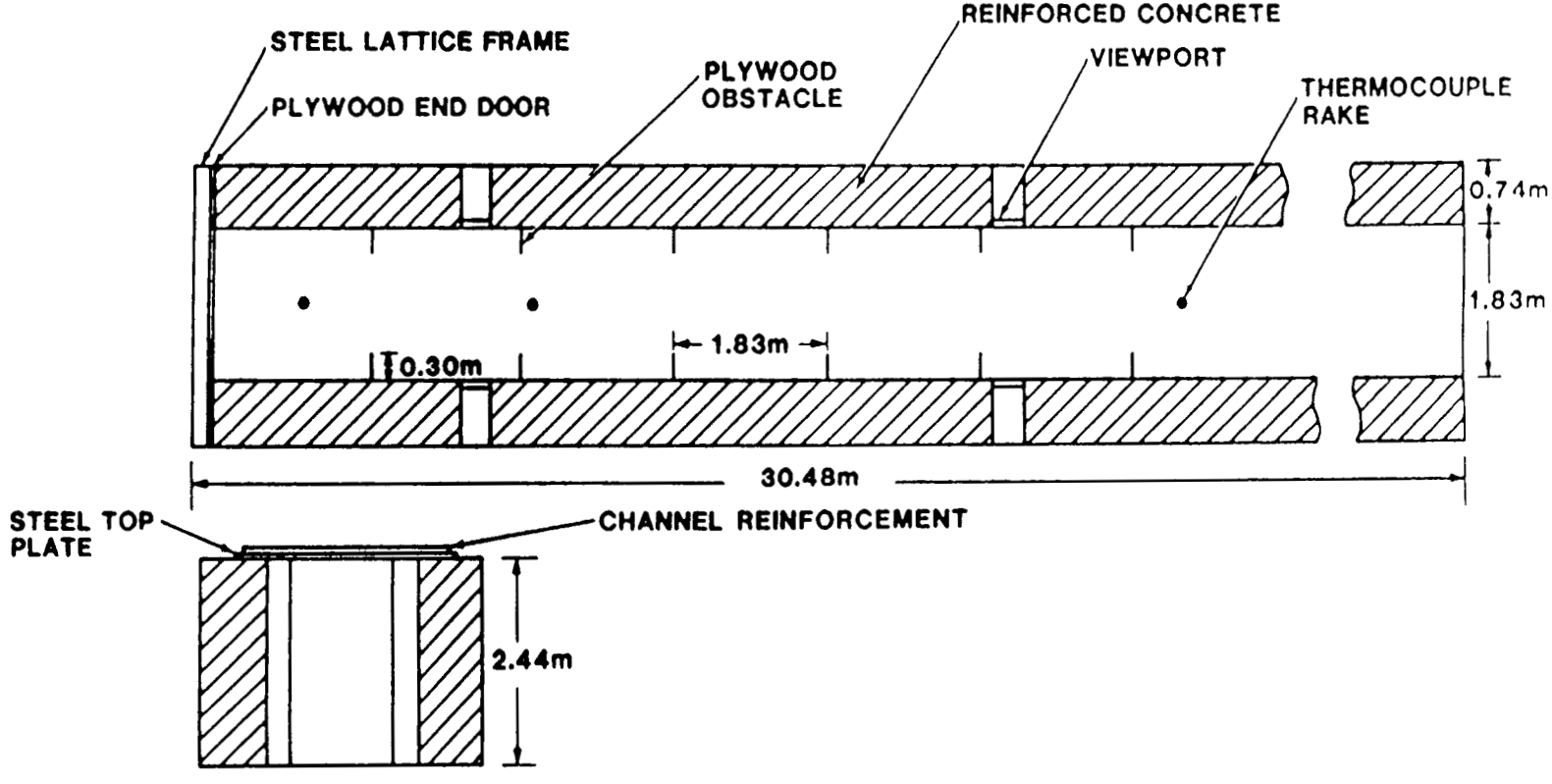

Figure 1.5-48. Schematic of FLAME Facility With Simple Obstacles Installed, 33% Blockage Ratio

Figure 1.5-49. FLAME Half-Scale Models of the Air Handlers in the Upper Plenum of Ice Condensor Containments

Table 1.5-6

FLAME Obstacle Tests

Test Number F-	Top Venting Area (%)	Hydrogen Mole Fraction (%)	Peak Overpressure (kPa)	Peak Equivalent Planar Flame Speed (m/s)	Comments
21	0	10-15	650	580	Inop. fans
22	0	15	3100	700	DDT
23	0	14.5	1200	540	
24	50	15.5	a	46	
25	50	19.7	1650	890	DDT
26	50	28.5	1970	1860	BOXES, DDT
27	50	13.1	9?	15?	
28	50	14.9	9?	33.4	
29	50	18.5	22?	130	
30	50	20			BOXES

a = signal in noise level.

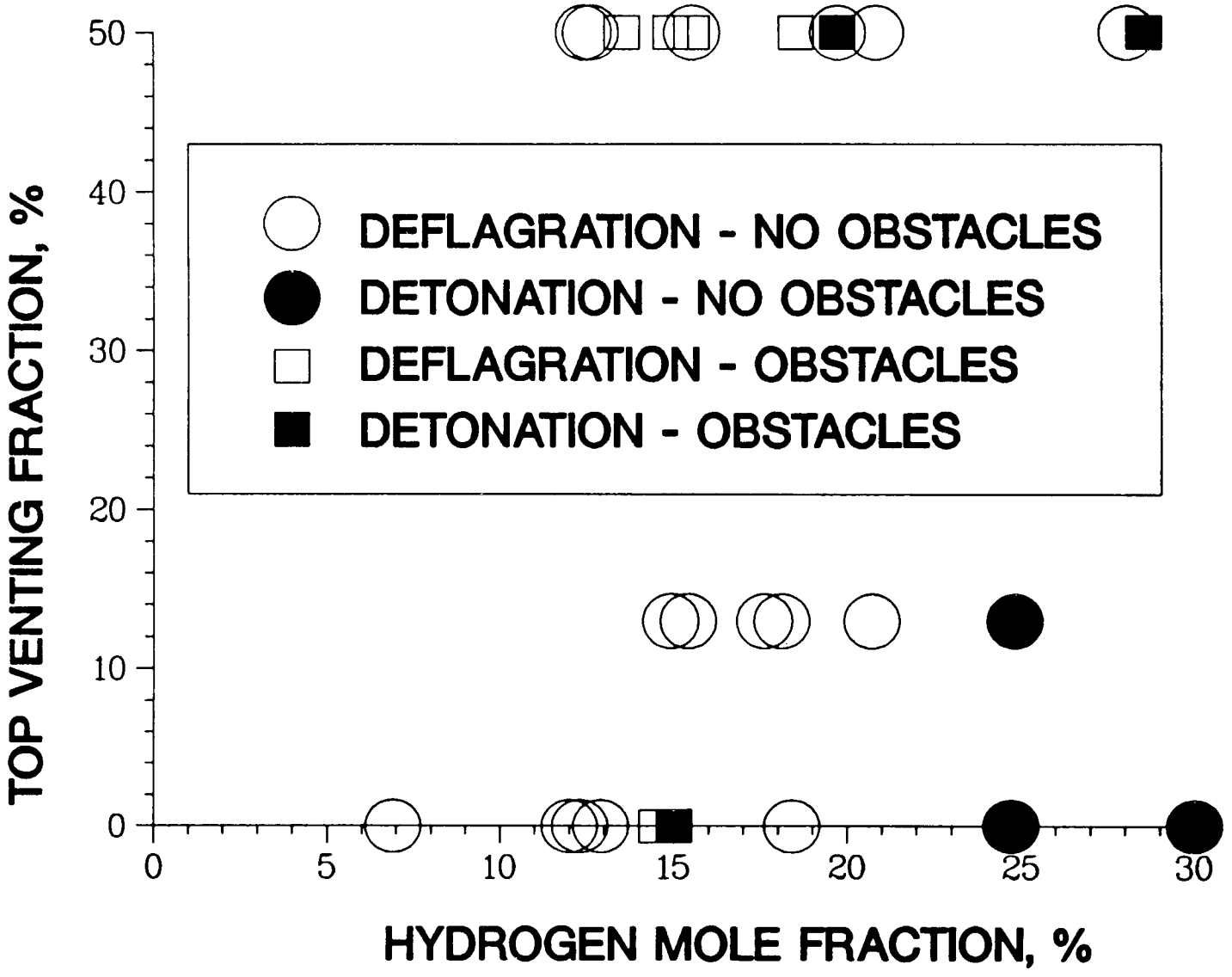

Figure 1.5-50. FLAME DDT Results

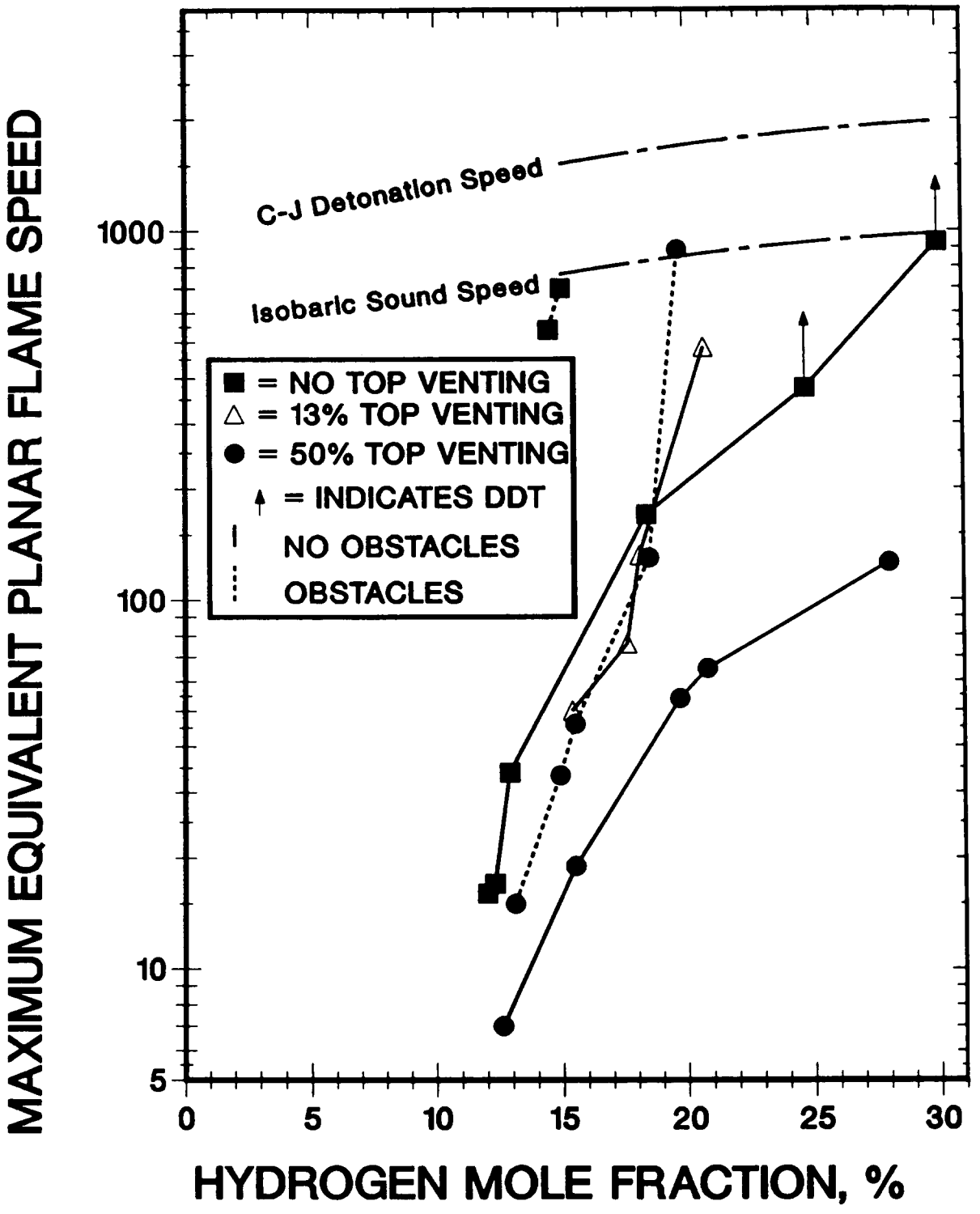

Figure 1.5-51. FLAME Velocity Results

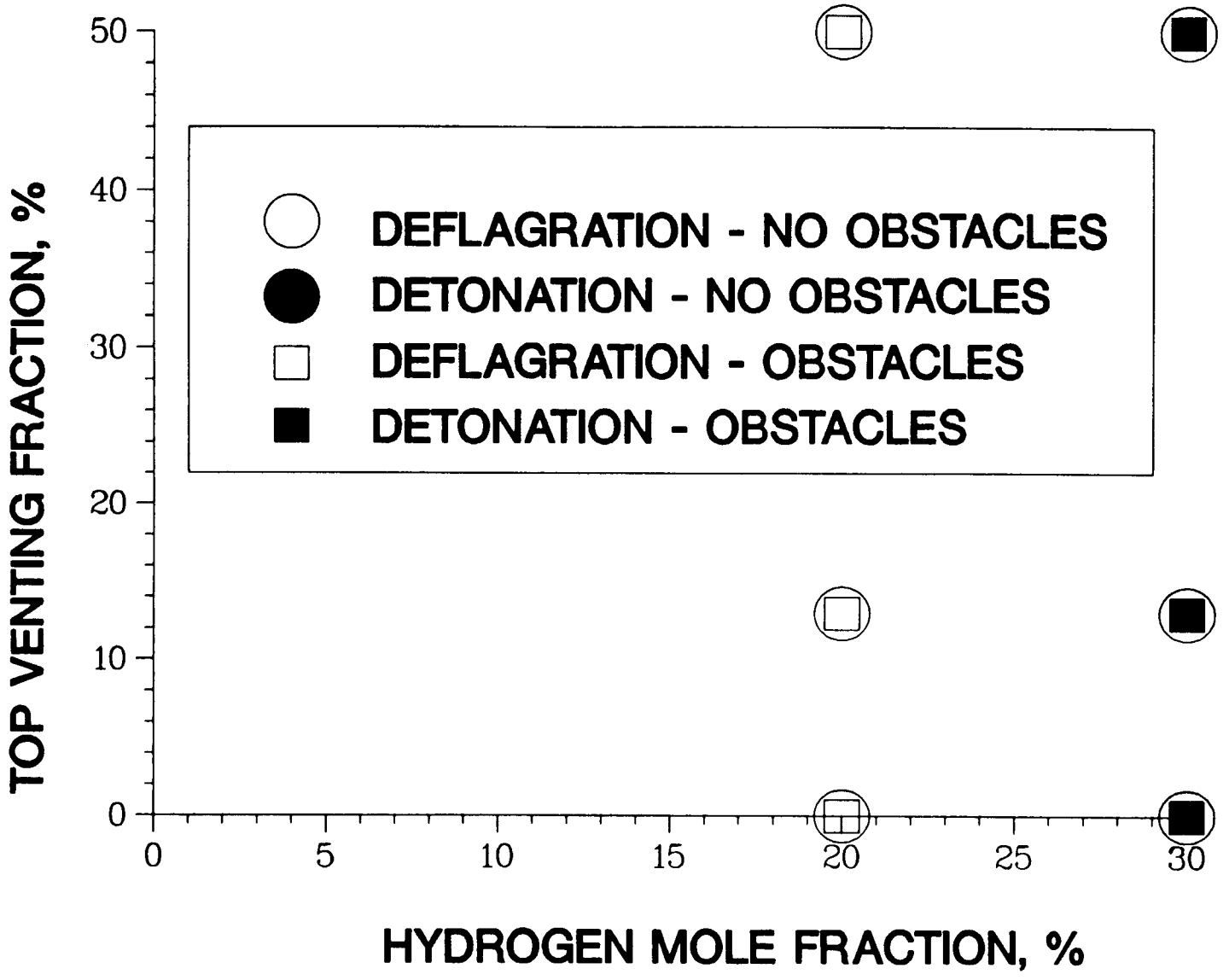

Figure 1.5-52. MINIFLAME DDT Results

observed except in test F-25. The luminousity of the wave leaving the channel for the leaner mixtures tested (≈15 percent H_2) is low. It becomes difficult to distinguish between a shock wave leaving the channel and a detonation wave. We state there was DDT in test F-22 and not in test F-23 because the weakly luminous wave leaving the channel was moving at detonation speeds (1700 m/s) in the first case, but the almost nonluminous wave was moving at slower speeds (1200 m/s) in the second case. The distinction between deflagration and detonation becomes somewhat blurred when there are strong flame acceleration mechanisms present. From the safety point of view, the distinction between a deflagration and a detonation may not be very important when the deflagration is highly accelerated. In both cases there are strong pressure waves, giving dynamic loads on containment in addition to quasi-static loads.

1.5.3.3 MINIFLAME Tests

A complete test matrix of 12 tests was carried out using the MINIFLAME models. The variables were:

1. Hydrogen mole fraction - 20 and 30 percent
2. Degree of transverse venting - 0, 13 and 50 percent
3. Obstacles - none or simple baffles

There were plans to test at 15 percent hydrogen; however, no useful data would have been obtained since the overpressures would have been too small to record accurately, and the flame front would not have been luminous enough to record. Even with 20 percent hydrogen, the visibility of the flame fronts in the high speed kinematography was poor.

The MINIFLAME results are summarized in Figures 1.5-53 through 1.5-55. Comparison with similar FLAME results in Figures 1.5-50 through 1.5-52 shows dramatic differences. The region of DDT on the lean side is much smaller. No detonations are observed at 20 percent hydrogen, and no detonations are observed without obstacles in the channel even at 30 percent hydrogen. The overpressures and flame speeds are much lower than in tests in FLAME with the same hydrogen mole fraction.

The significance of the MINIFLAME results are that scale-model testing of flame acceleration and DDT phenomena with identical combustible mixtures does not accurately model the full scale results. There is a limited set of experimental results that indicate that if the scale-model combustible mixture is made more reactive than the full-scale mixture, such that the ratio of geometric size to detonation cell size is identical, then scale-model testing will be valid.[47] This result should be checked, since the use of scale models can result in a great saving in cost and time.

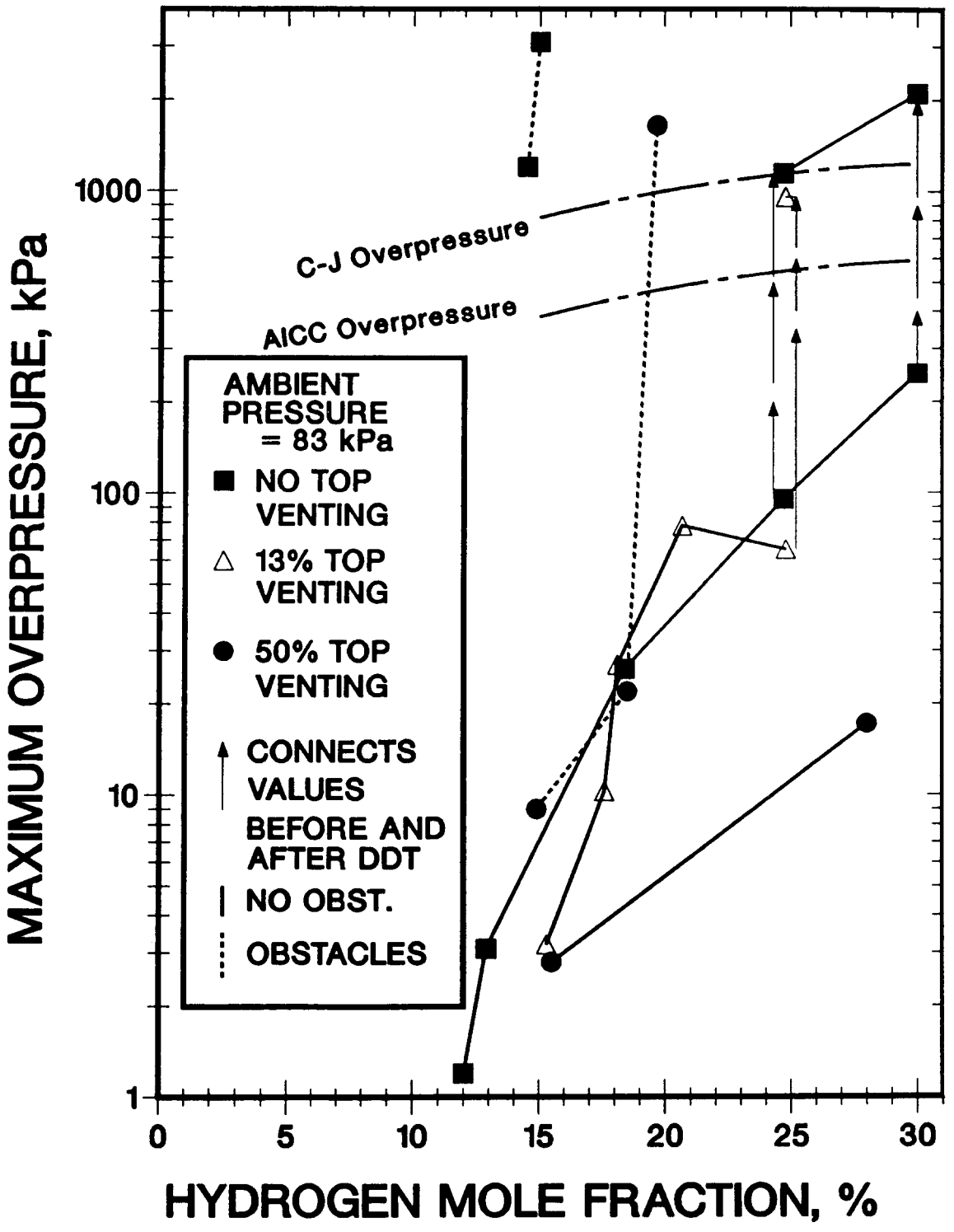

Figure 1.5-53. FLAME Overpressure Results

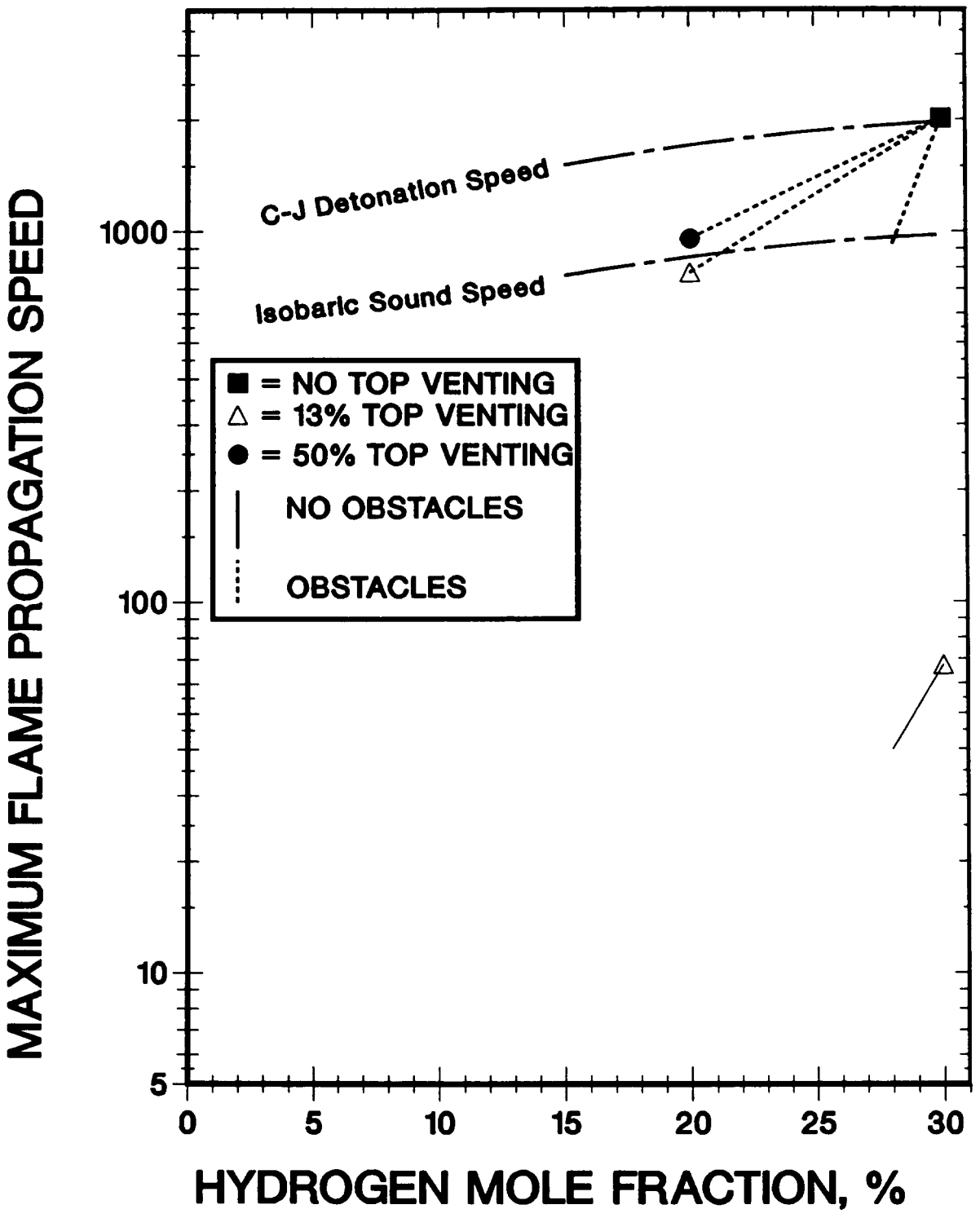

Figure 1.5-54. MINIFLAME Velocity Results

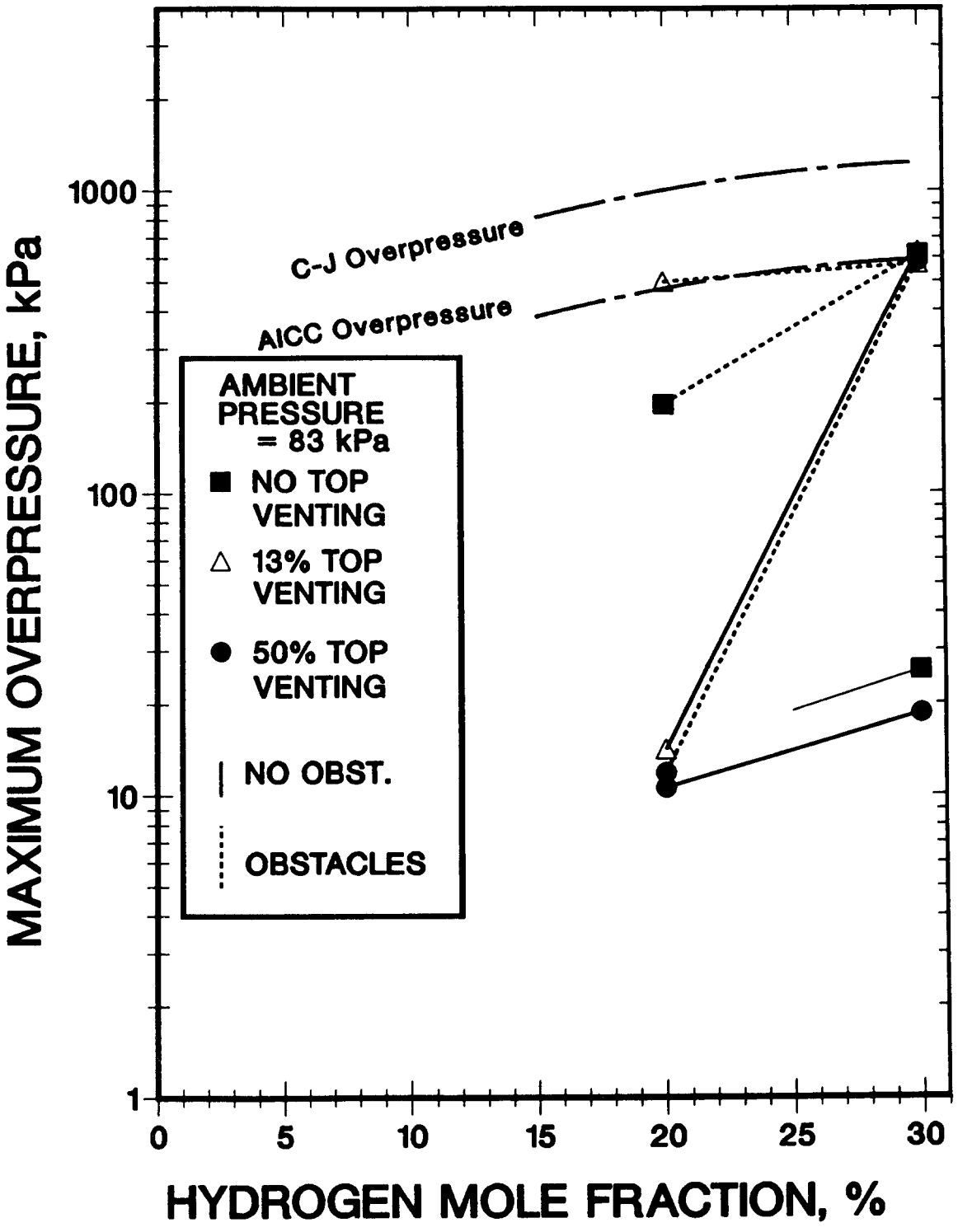

Figure 1.5-55. MINIFLAME Overpressure Results

1.5.4 CONCHAS-SPRAY Modeling of Flame Acceleration (K. D. Marx, 8363)

We have completed a simulation of FLAME Experiment F-23. This was a burn of 14.5 percent hydrogen with no top venting. The side walls were fitted with 16 pairs of symmetrically placed obstacles. The blockage ratio was 0.33. The entire length of the 30-m facility was included in the simulation. Figure 1.5-56 shows contour plots of some of the flow variables that evolve during the calculation. Figure 1.5-57 gives a comparison of the computational flame trajectory with that measured experimentally.[48]

The computational flame trajectory is seen to be in good qualitative agreement with the experimental data. In many respects the quantitative agreement is quite good as well. The flame velocity at the time the flame reached the end of the facility was 570 m/s, compared to 540 m/s measured in the experiment. The structure of the computed flame trajectory does differ from the experiment in that it does not exhibit as sharp an acceleration in the middle of the burn.

One of the greatest attributes of this computation is that it involved a minimum of adjustable parameters. We have adopted a new flame model for the (large scale) FLAME simulations. We adjusted the initial thermal conductivity, diffusion coefficient, and combustion rate artificially to achieve (1) agreement between the initial numerical and experimental turbulent burn velocities and (2) a spreading of the flame over some specified number of numerical mesh points (approximately 5). It was necessary to do this because (1) we cannot provide enough mesh points to resolve the flame structure and obtain an accurate computation of the initial burn velocity, and (2) the flame must be spread over a few grid points for adequate numerical performance. Adjustment of the thermal conductivity and diffusion coefficient determines (artificial) threshold turbulence parameters (turbulent kinetic energy, κ, and dissipation rate, ε). We then maintain the influence of these threshold values of κ and ε in the determination of thermal conductivity, diffusion coefficient, and combustion rate throughout the calculation. That is, the turbulence generated (behind obstacles, for example) in the flow only influences the flame if the true values of κ or length scale, L, exceed the threshold values. This is plausible because, as noted above, there must be turbulence at the flame front to maintain at least the initial flame velocity, and this cannot be calculated on our coarse computational grid. Futhermore, it results in a turbulent flame velocity that has a linear dependence on turbulence intensity, and this qualitatively agrees with flame velocity data from some other experiments.

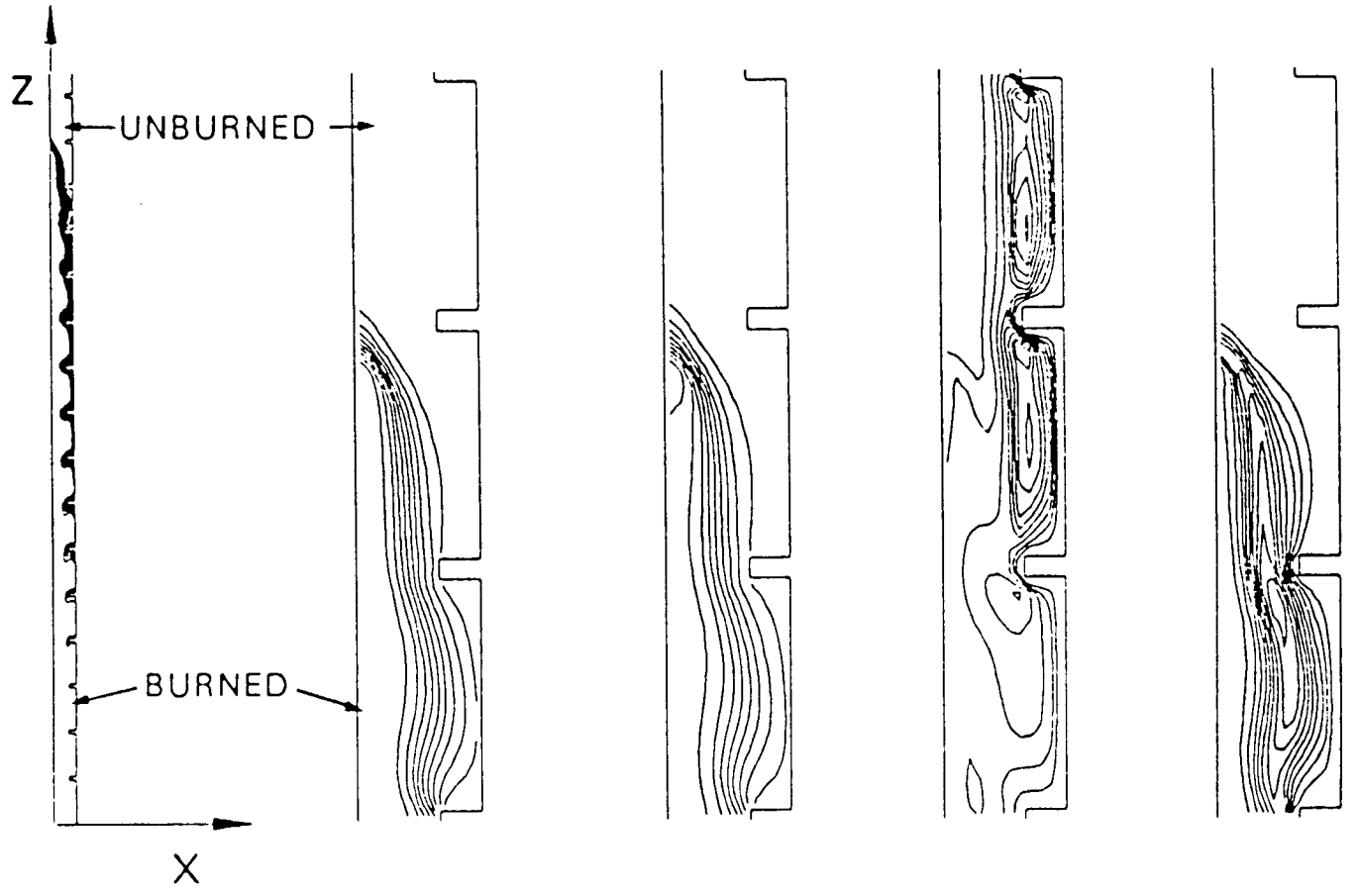

Figure 1.5-56. Contour Plots of Flow Variables in the Simulation of FLAME Experiment F-23. The leftmost figure shows the hydrogen mass fraction over the entire 16 chambers included in the computation. The calculation is two-dimensional: The configuration is assumed symmetric about the vertical midplane. Hence what is shown is a top view of half of the facility, with the vertically aligned obstacles appearing on the right boundary. The flame front is just reaching the 16th chamber. The remaining four figures are expanded views of various quantities in the last three chambers. From left to right they are contours of hydrogen mass fraction, isotherms, and contours of turbulent kinetic energy and hydrogen burn rate.

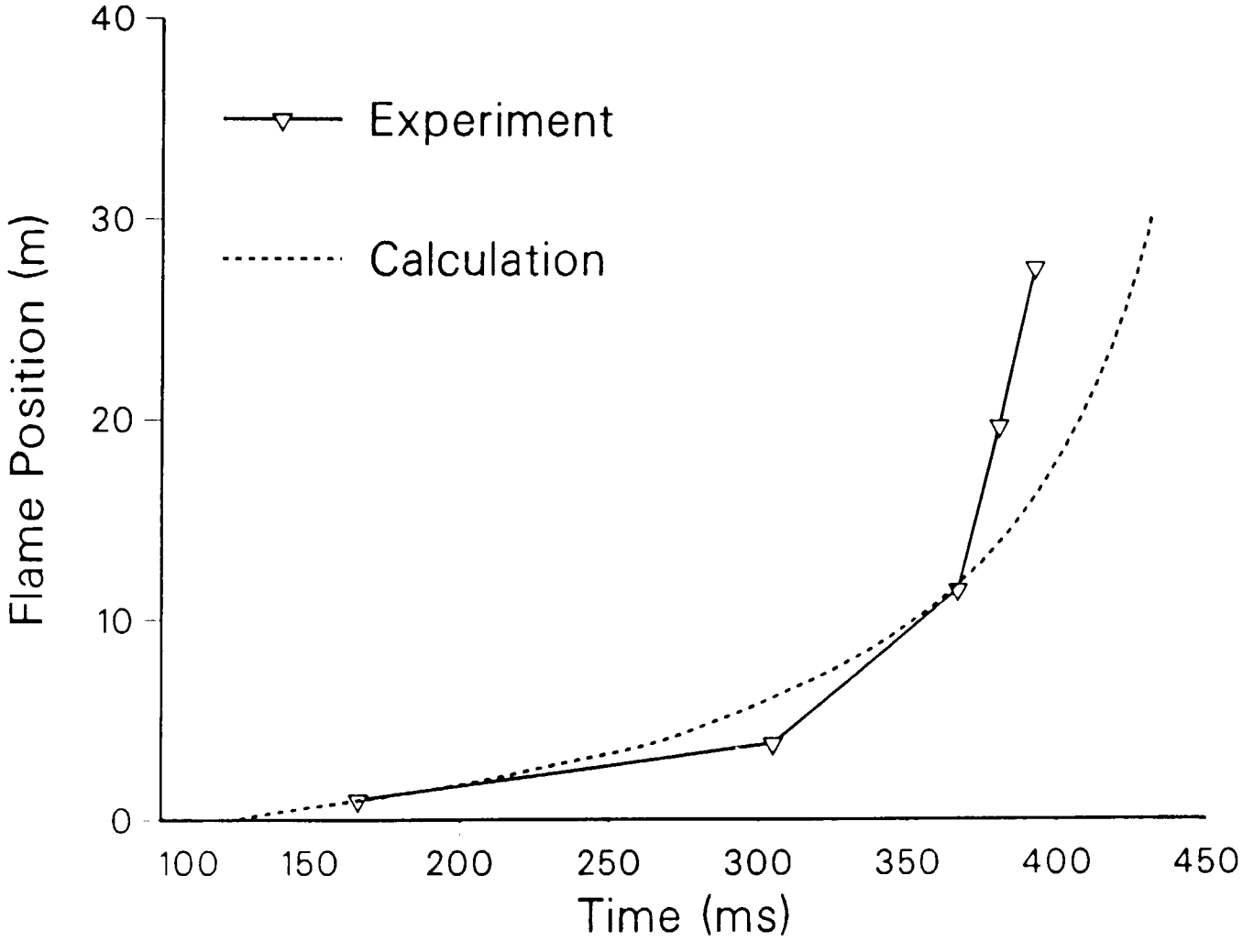

Figure 1.5-57. Comparison of Computed Flame Trajectory (Flame Position on the Central Axis Versus Time) With That Measured in Experiment F-23. The experimental data is that obtained from thermocouples on the central axis of the FLAME facility. Experimental flame arrival times vary with elevation; since the vertical direction is assumed to be an ignorable coordinate in the calculation, this variation is unobtainable from the simulation.

With this model in place, the above results were obtained by running the code with the standard κ-ε turbulence model[49,50] and with a somewhat modified version of the Magnussen-Hjertager[51] combustion model without any further optimization. (The modification to the M-H model was not made with a view to obtaining agreement with any particular experiment.)

The computation was carried out on a grid of 13 by 396 mesh points. It required 2.4 h of Cray time. This grid is extremely coarse, and we intend to halve the gird size for better accuracy in some calculations. Such grid refinement will result in run times of between 10 and 20 h if a complete simulation is performed. Hence, we will first make comparisons on smaller domains.

Other plans for the immediate future involve comparison with other experiments. In particular, it is of interest to investigate variations with hydrogen concentration predicted by the computational model.

1.5.5 Heated Detonation Tube

(D. W. Stamps and S. R. Tieszen, 6427; W. B. Benedick, 1131)

The Heated Detonation Tube (HDT), which is a cylindrical tube 13.1 m long and 0.43 m in internal diameter, is capable of being operated at temperatures up to 100°C. The purpose of the HDT program is to develop an experimental data base on H_2-air-steam detonability. This data can be used to develop models to assess the possibility of detonation inside containment.

Work has been done for the Severe Accident Risk Rebaselining Program (SARRP) on the possibility of local detonations during a hypothetical degraded core accident at the Bellefonte nuclear power plant. The sequence of questions that must be answered to identify the pressure loads from hydrogen combustion is summarized in Figure 1.5-58. The first question of what the mixture composition is in each compartment is addressed by A. Peterson and D. King[52] and J. Travis using the accident analysis codes HECTR and HMS, respectively. With the results from Reference 52, the question of a detonation propagating in a mixture in a given compartment is answered by S. R. Tieszen and D. W. Stamps[53,54] using a chemical kinetics code to calculate the detonation cell size. The third question of the possibility of deflagration to detonation transition (DDT) in mixtures that can propagate a detonation is discussed by M. P. Sherman and M. Berman.[55]

The possibility that a mixture in a given compartment will propagate a detonation is investigated using a chemical

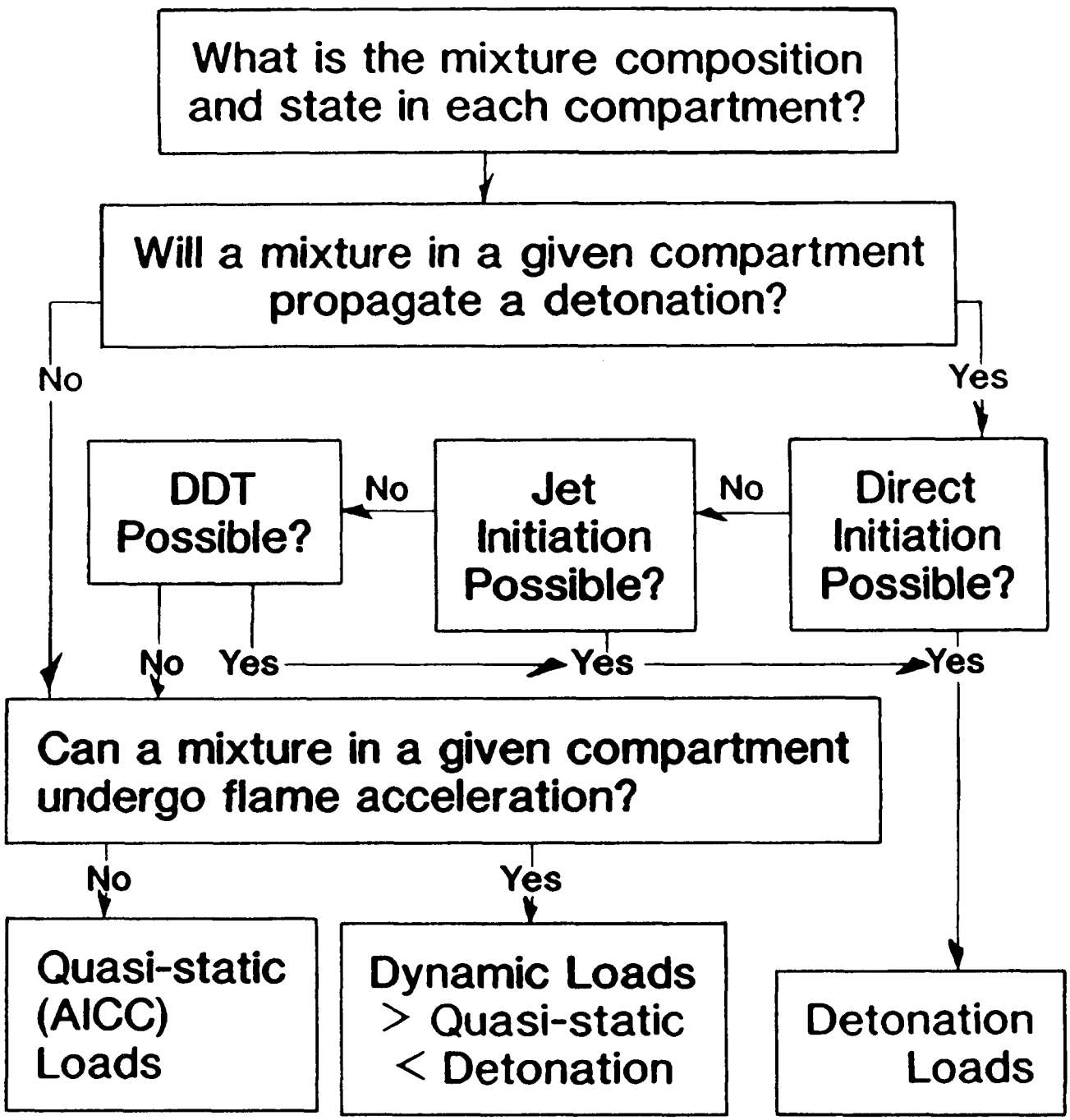

Figure 1.5-58. Detonation and Accelerated Flame Loads

kinetics code with a ZND model,[56] which calculates a reaction length. The relation between the reaction length and detonation cell width is empirical. The experimental H_2-air data from the HDT was used to determine the proportionality constant. The chemical kinetics code has predicted all existing H_2-air-steam data to within a factor of 4 (x/ 4) and represents the best available predictive tool for estimating detonation cell width. Two notes of caution are required. First, the model does not always err on the conservative side; that is, it may predict larger detonation cell widths than the actual value. Second, most of the mixtures from the calculations of A. Peterson and D. King[52] have 100° to 300°C higher temperatures than the existing data base against which the model has been assessed. The calculations from the code indicate that the propagation of a detonation is possible in one compartment of Bellefonte for two different types of accidents. The specific details of the compartment and type of accident are listed in Reference 55.

Additionally, calculations were performed using a chemical kinetics code to predict the effectiveness of CO_2 dilution to suppress detonations. As a consequence of an inquiry by A. K. Oppenheim (member of the NRC-sponsored NAS H_2 Program Review Panel), detonation cell widths for stoichiometric H_2-air mixtures with up to 50 percent CO_2 dilution have been calculated and the results from Reference 57 are presented in Table 1.5-7. The calculations were performed using the chemical kinetics code described previously.[56] The relation between the reaction length (listed as Z.75 in Table 1.5-7) and the detonation cell width is empirical. However, the ZND model that the chemical kinetics code is based on has predicted all existing H_2-air data to within a factor of 4 (x/ 4) and all existing H_2-air-CO_2 data to within a factor of 3 (x/ 3). To our knowledge, this model represents the best available predictive tool for estimating the detonation cell width for these mixtures. The model has been compared to H_2-air-CO_2 data up to 15 percent CO_2 dilution. A new test series will extend the existing data to 20 percent CO_2 dilution. The results of the new test series will help to quantify the use of CO_2 as a steam simulant.

1.6 Hydrogen Mitigative and Preventive Schemes

(L. S. Nelson and M. Berman, 6427)

The objective of the Hydrogen Mitigative and Preventive Schemes Program is to provide the NRC with information to evaluate proposed equipment concepts and operational schemes to prevent or mitigate the effects of hydrogen combustion during hypothetical LWR accidents. To provide this information, we are investigating the operability and consequences

of operation of deliberate ignition systems and their components during hypothetical hydrogen-producing accidents in nuclear power plants.

Table 1.5-7

Detonation Cell Width Calculations for H_2-Air-CO_2 Systems

Mole Fraction Air	Mole Fraction H_2	Mole Fraction CO_2	Pressure	Temp.	Z.75 (cm)	Cell Width (m)
0.7047	0.2953	0	1	298	0.06905	0.015
0.6695	0.2805	0.05	1	298	0.105	0.023
0.6343	0.2657	0.1	1	298	0.257	0.0565
0.5990	0.2510	0.15	1	298	0.867	0.191
0.5638	0.2362	0.2	1	298	2.77	0.609
0.4933	0.2067	0.3	1	298	29.2	6.42
0.4228	0.1772	0.4	1	298	439	96.6
0.3524	0.1476	0.5	1	298	11,080	2438

1.6.1 Behavior of Resistively Heated Igniters During the Operation of Water Sprays in Containment
(L. S. Nelson and K. P. Guay, 6427)

During the completion of experiments and analyses of data relating to the behavior of resistively heated hydrogen igniters during the operation of water sprays in containment, we discovered several new aspects of the behavior of the igniters:

1. Both the cylindrical and the helical igniters will withstand greater water fluxes when initially hot compared to initially cold when first exposed to the spray. We have designated these types of operations as Type B and Type A, respectively.

2. The tip of the cylindrical igniter will remain hot in airflows considerably greater than will the sides of the igniter.

3. The cylindrical igniter is much less affected by water sprays than the helical igniter in the presence of combined water sprays and airflows. Thus the airflows mostly govern the operating temperature of the cylindrical igniter, while a combination of airflows and water drop flux governs the surface temperature of the helical igniter.

A discussion of these phenomena follows:

1.6.1.1 Behavior of Igniters in Spray Fluxes Alone

As previously described,[58] both the helical Tayco igniter and the cylindrical General Motors AC 7G diesel glow plug igniter were studied in a variety of spray fluxes. These fluxes were obtained by positioning the igniters at various coordinates in a well-characterized spray field. The experiments were performed with the igniters in a quiescent atmosphere in a wind-protective enclosure. The surface temperatures of the igniters were measured by four thermocouples spot welded to the bottom of the igniters. Thermocouple outputs were measured with the DAASY Data Acquisition and Analysis System.

In our early experiments, the cold igniter and the solenoid spray that turned on the water spray were energized simultaneously (Type A operation). In later experiments, however, the valve was actuated at least 100 s after the igniter was energized, that is, after the igniter had reached its plateau temperature (Type B operation). Significant differences in behavior were observed between the two modes of operation.

The plateau surface temperatures of the helical igniter for Type A and Type B operation are plotted as a function of water-spray flux in Figure 1.6-1. At the right edge of Figure 1.6-1, we have indicated the minimum surface temperature (NRC) recommended for thermal igniters in nuclear plant containments by the Nuclear Regulatory Commission and also the average igniter surface temperature (IGN-H), at which a 6.5 volume percent hydrogen-air mixture was ignited by the helical igniter in VGES experiments described in previous semiannual reports (see, for example, Reference 59).

It can be seen in Figure 1.6-1 that the helical igniter is able to maintain elevated temperatures at roughly twice the spray flux if hot when initially exposed to the spray than when cold. (Also shown in Figure 1.6-1 are data points supplied by another laboratory for Type B operation.[60,61])

Analogous differences between Type A and Type B exposure of the cylindrical igniter to water spray fluxes were also observed; however, these differences were not as dramatic. The plateau temperatures for the cylindrical igniter operated at 14 Vac (RMS) and 12 Vac (RMS) are presented in Figures 1.6-2 and 1.6-3, respectively. It can be seen from these figures that there are some differences but they are only about half as great as those indicated in Figure 1.6-1 for the helical igniter.

Since both Type A and B operations could occur in various accident scenarios in containment, these phenomena should be recognized in any accident evaluation. It is obvious, of

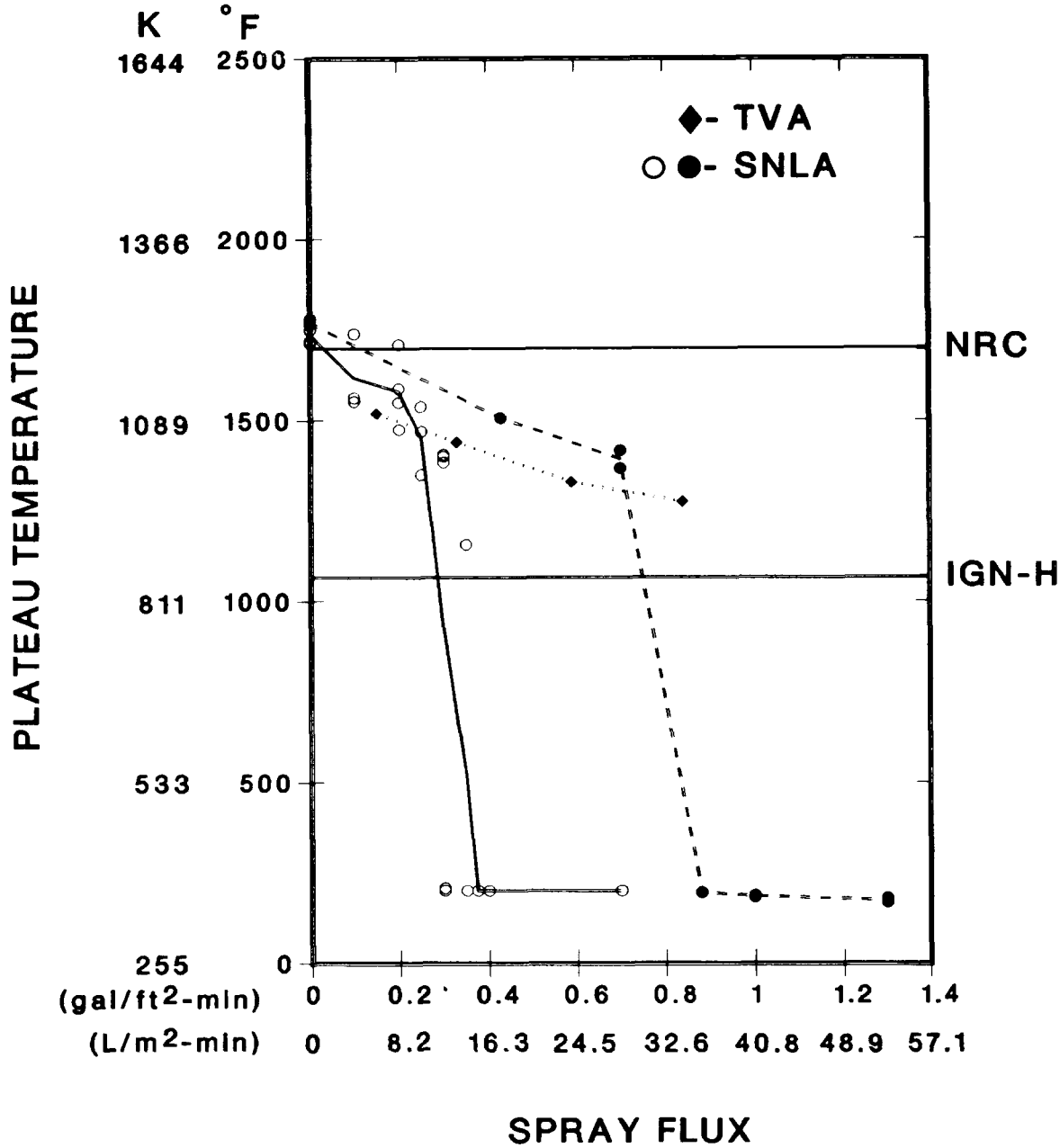

Figure 1.6-1. Plateau Temperatures for a Tayco Model 193-3442-4 Helical Igniter Operated in Various Spray Fluxes; the Igniter Was Energized at 120 Vac (RMS). The curve at left and right are for Type A and Type B operation, respectively. Data points indicated by diamonds are taken from Reference 60.

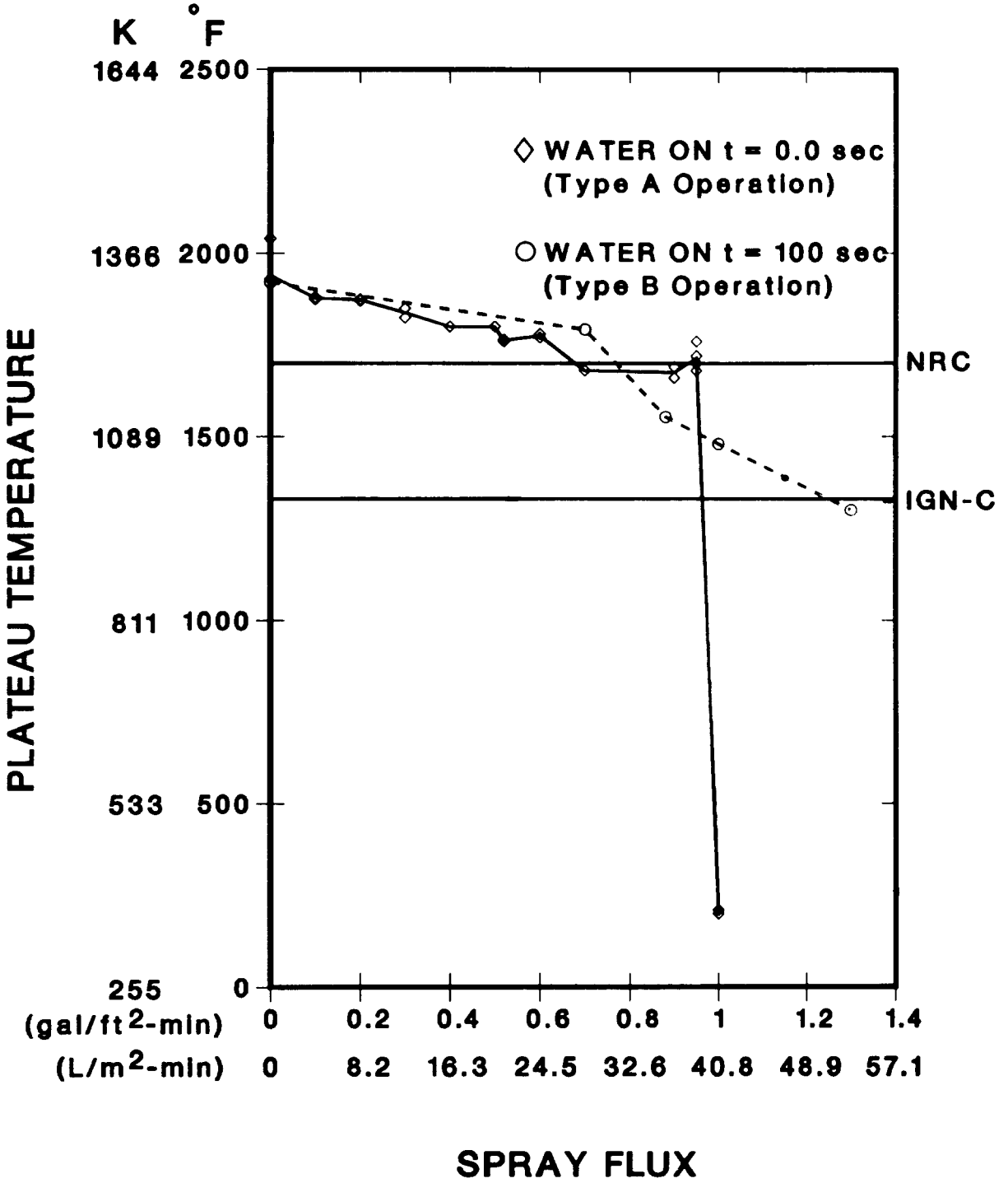

Figure 1.6-2. Comparison of Plateau Temperatures Achieved During Type A and Type B Operation of a General Motors AC 7G Cylindrical Glow Plug Igniter When Exposed to Various Water Spray Fluxes Under Quiescent Conditions.

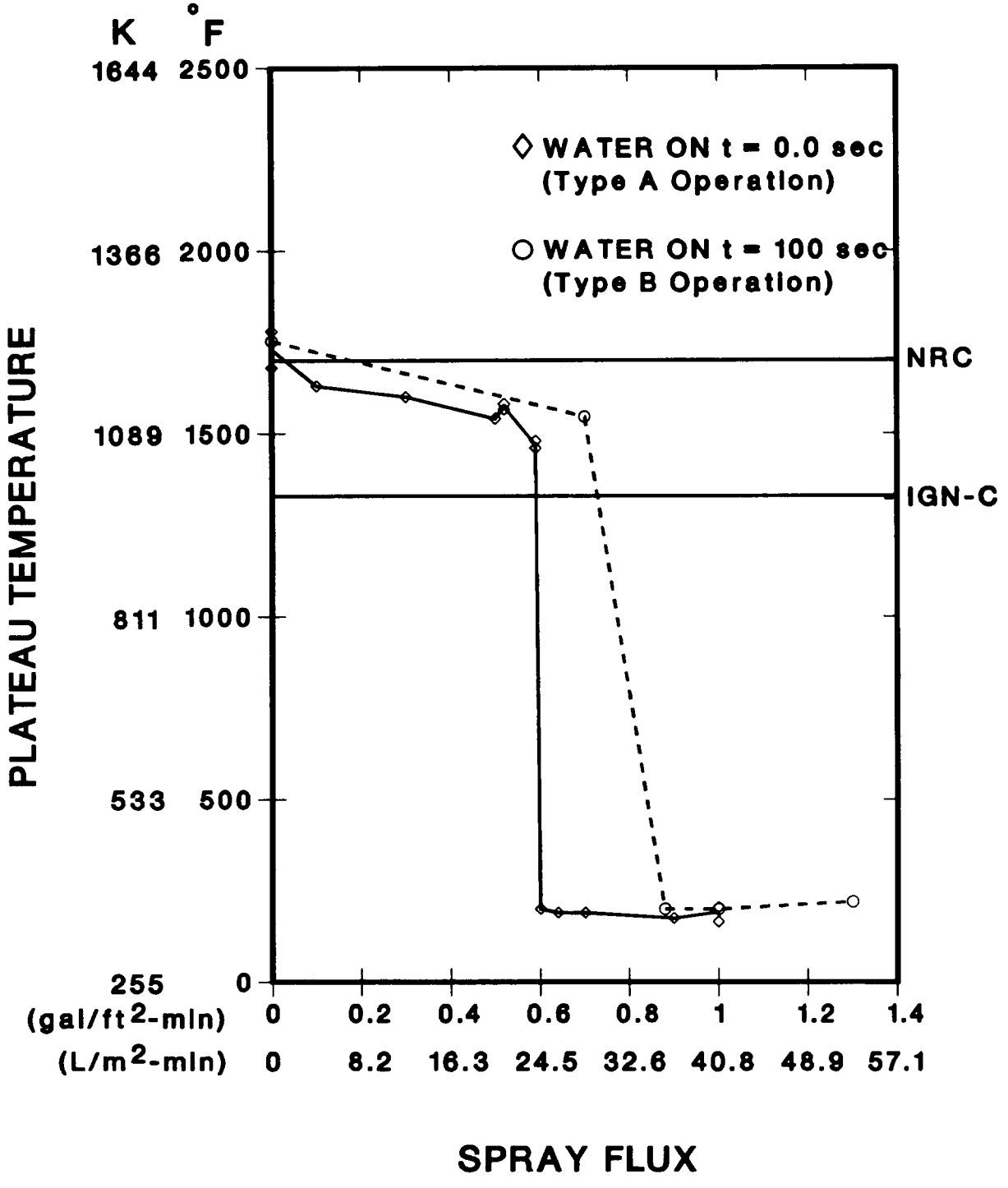

Figure 1.6-3. Comparison of Plateau Temperatures Achieved During Type A and Type B Operation of a General Motors AC 7G Cylindrical Glow Plug Igniter When Exposed to Various Water Spray Fluxes Under Quiescent Conditions.

course, that the assumption of Type A operation would be the more conservative for such analyses.

1.6.1.2 Behavior of the Cylindrical Igniter in Airflows Alone

As we performed cleanup experiments and analyzed our data for the behavior of the cylindrical igniter in airflows alone, we discovered that as airflows increased, the tip of the igniter was behaving somewhat differently than the sides. In these experiments the airflows were produced with the exhaust from an industrial vacuum cleaner. The airflows were measured with a baratron gauge operated as a pitot tube.

In our earlier descriptions of the effects of airflows on the cylindrical igniter, we showed operation of the igniter at both 14 and 12 Vac (RMS) (see Figure 1.6.2 of Reference 44). In that report we indicated that the igniter failed to maintain the temperature for ignition of 6.5 percent hydrogen-in-air mixtures (IGN-C) at airflows of approximately 13 and 5 m/s for the two voltages. These data were taken with a thermocouple placed at the midpoint of the igniter, as shown in Figure 1.6-1 of Reference 44. However, when we analyze the thermocouple responses for all four positions on the igniters, shown in Figure 1.6-1,[44] we discover a somewhat different behavior, as indicated in Figures 1.6-4 through 1.6-7. The sides of the igniter (locations 1/4, 1/2, and 3/4) will remain above IGN-C at airflows of about 13 and 5 m/s for 14- and 12-Vac (RMS) operation, respectively. However, as shown in Figure 1.6-7, the tip of the igniter dips below IGN-C at airflows of about 20 and 9 m/s, respectively. If the tip of the igniter can be regarded as an efficient ignition source, this relaxes the airflow considerations that arise from the combination of this work and the recently reported work of Marx.[62]

1.6.1.3 Behavior of Igniters in Combined Spray Fluxes and Airflows.

In order to investigate whether some unusual behavior of igniters might occur when water sprays and airflows impinge simultaneously on the igniters, we performed experiments in a wind-free enclosure with a variety of spray fluxes and airflows. All spray fluxes and airflows were measured at the location of the igniter by means of a rain gauge and pitot tube, respectively.

The plateau temperatures of the helical igniter exposed simultaneously to various combinations of water spray and horizontal airflow are shown in Figure 1.6-8 (showing the three parameters in three dimensions) and in Figure 1.6-9 (showing the effects spray flux for the different airflows in two dimensions). Most of the data points were recorded

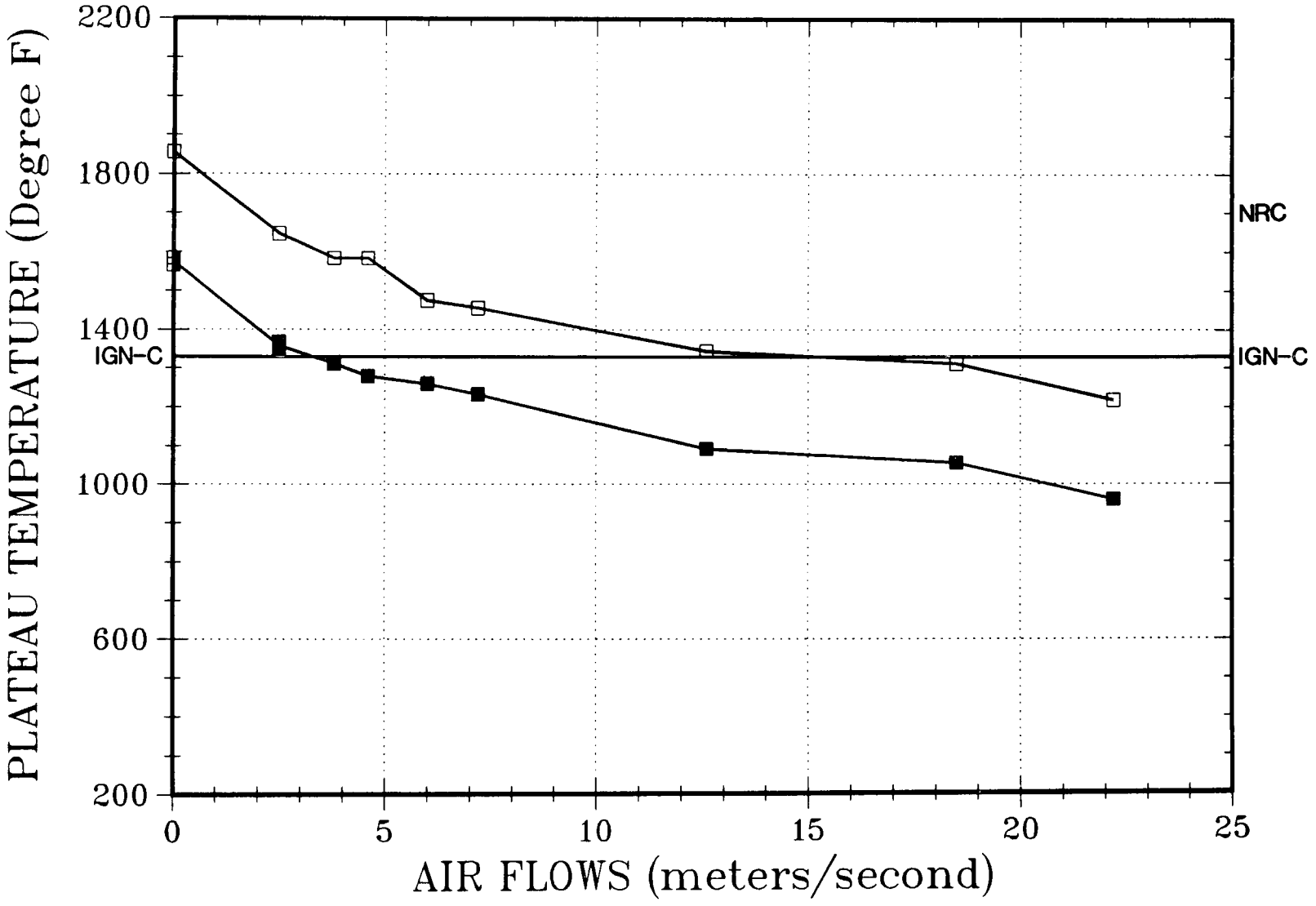

Figure 1.6-4. The Effect of Airflows Alone on Cylindrical Igniters Operated at 14 and 12 Vac (RMS). The source of the airflows was a vacuum cleaner (new data). The location of the thermocouples was at 1/4 (□ for 14 V and ■ for 12 V).

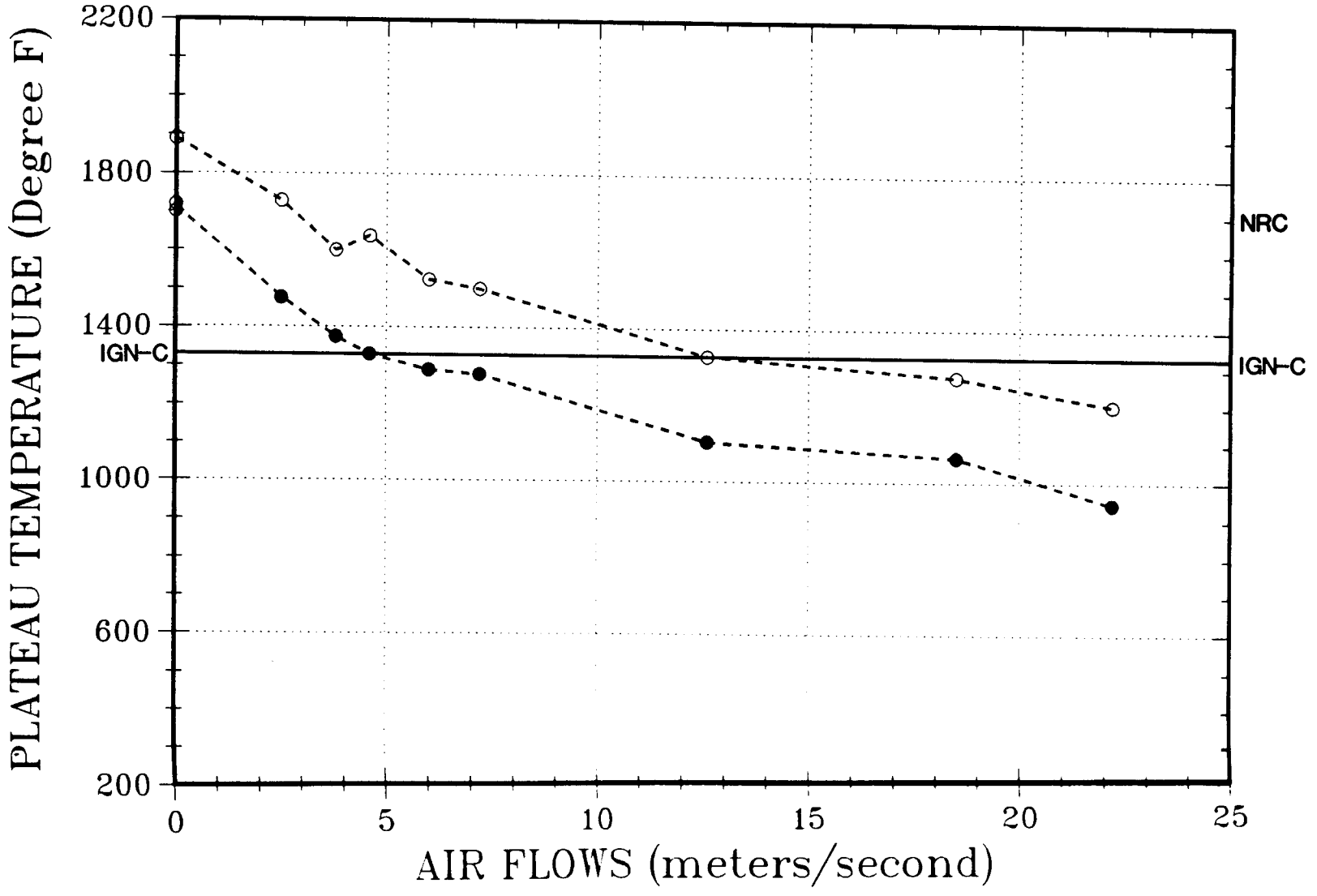

Figure 1.6-5. The Effect of Airflows Alone on Cylindrical Igniters Operated at 14 and 12 Vac (RMS). The source of the airflows was a vacuum cleaner (new data). The location of the thermocouples was at 1/2 (O for 14 V and ● for 12 V).

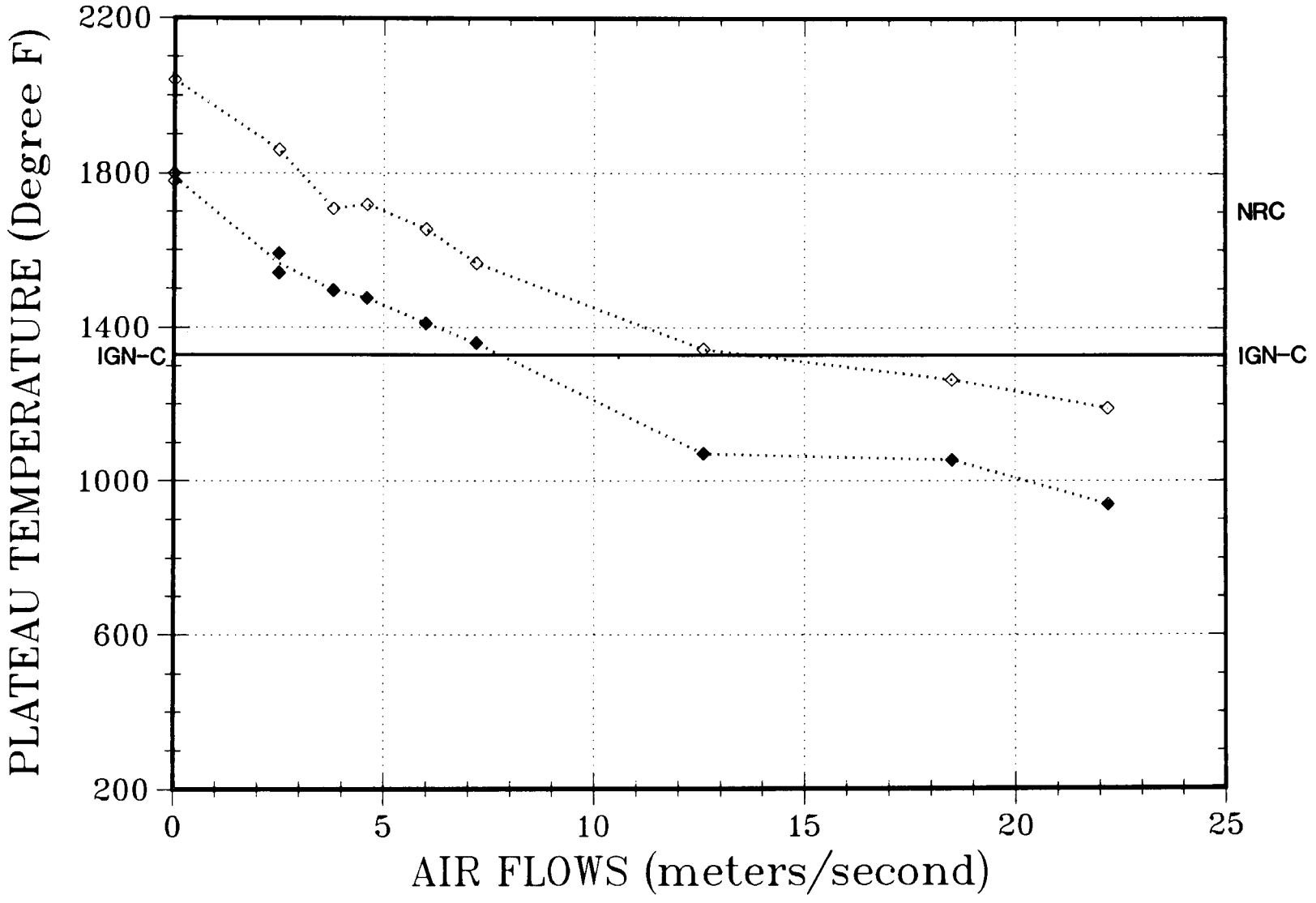

Figure 1.6-6. The Effect of Airflows Alone on Cylindrical Igniters Operated at 14 and 12 Vac (RMS). The source of the airflows was a vacuum cleaner (new data). The location of the thermocouples was at 3/4 (◊ for 14 V and ♦ for 12 V).

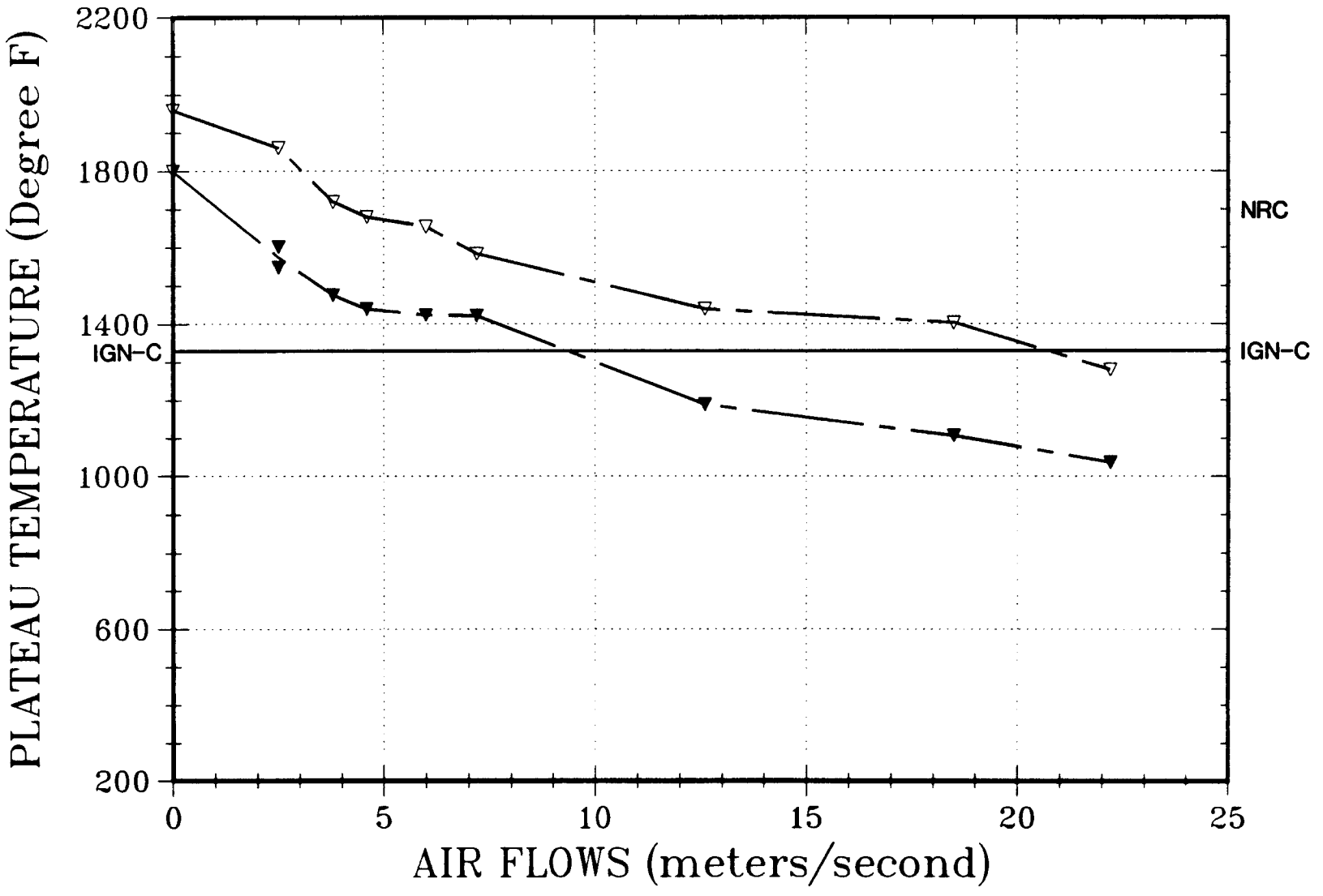

Figure 1.6-7. The Effect of Airflows Alone on Cylindrical Igniters Operated at 14 and 12 Vac (RMS). The source of the airflows was a vacuum cleaner (new data). The location of the thermocouples was tip (▽ for 14 V and ▼ for 12 V).

in the Type B operation where the igniter was allowed to heat in the airflow for 100 s before the spray unit was activated. For completeness, the data points from Figure 1.6-1 are included for the Type A operation of exposure for zero airflow. Also indicated in both figures is the temperature, IGN-H, below which the igniter failed to ignite a 6.5 percent hydrogen-in-air mixture in the VGES chamber.

In the zero water flux plane at the rear of Figure 1.6-8, we note again the cooling of the igniter caused by the airflow alone. When the igniter spray is progressively added to the airflow, however, there is a further steep decline in plateau temperatures in all but the highest airflows where the decline becomes considerably less steep. We suggest that this effect at the highest airflows is caused by blowing away the water that collects on and cools the igniter as a film or as drops in film boiling.

The plateau temperatures of the cylindrical igniter exposed simultaneously to various combinations of water sprays and horizontal airflows are shown in Figures 1.6-10 and 1.6-11 and Figures 1.6-12 and 1.6-13 for 14- and 12-Vac (RMS) operation, respectively. (Again, as in Figures 1.6-8 and 1.6-9, the three- and two-dimensional representations are used.)

In the planes at zero water flux at the rear of Figures 1.6-10 and 1.6-12, we again note the cooling of the igniter caused by the airflow alone. However, when water spray is progressively added to the airflow, unlike the helical igniter, there is only a small cooling effect on the cylindrical igniter in the quiescent cases. At the lower airflows, this cooling effect becomes still smaller and may even reverse at the higher airflows. As noted with the helical igniter, the cylindrical igniter, even though its plateau temperature is reduced by the airflow, also remains hot at much higher water spray fluxes than in the absence of airflow. Again, we attribute this behavior to the higher airflows blowing away the water film that probably collects on and cools the igniter.

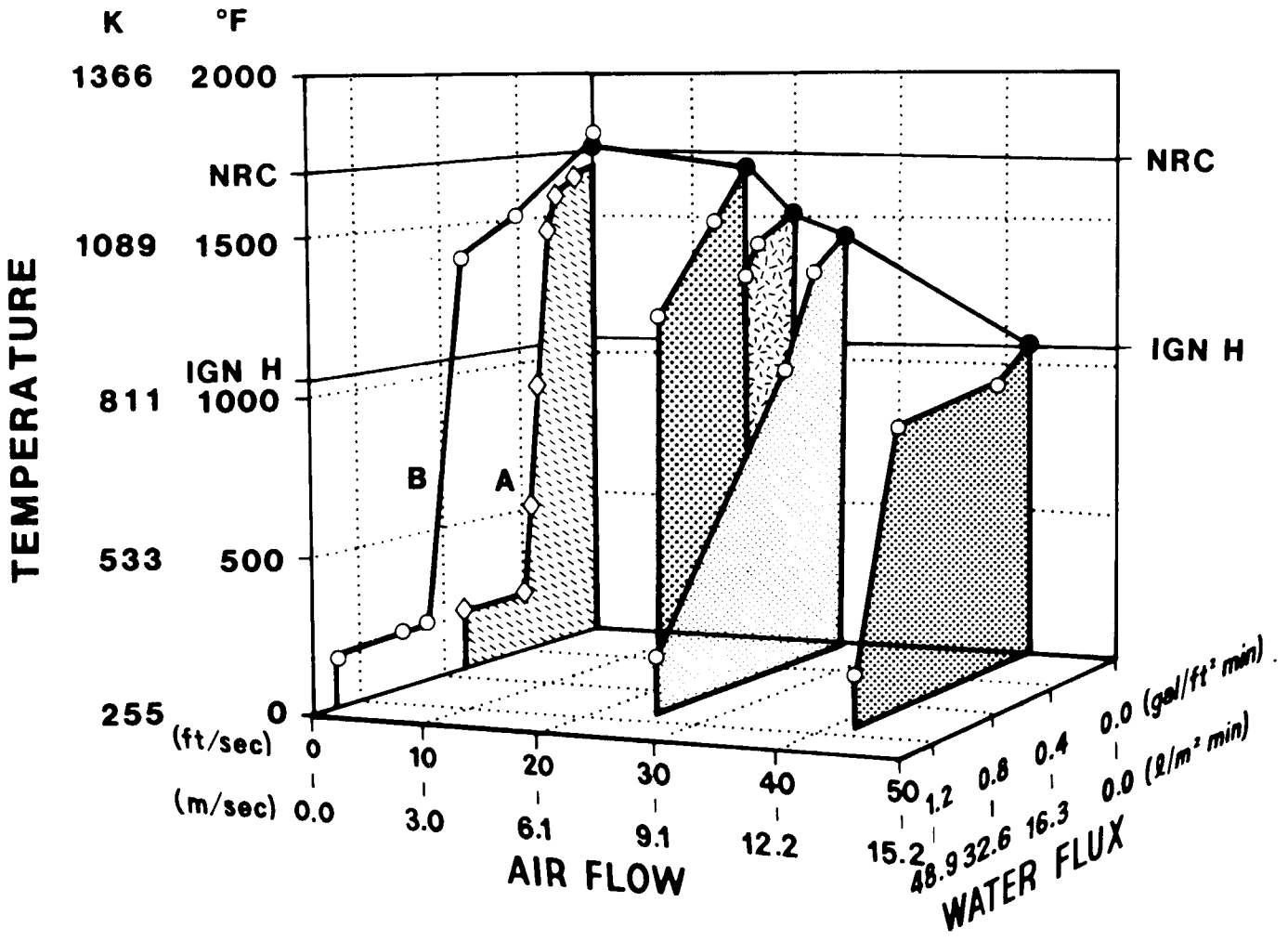

Figure 1.6-8. Plateau Temperatures Versus Water Spray Fluxes for the Helical Igniter Exposed Simultaneously to Several Airflows; Igniter Was Operated at 120 Vac (RMS). All data are recorded for Type B operation except for one plot at zero airflow, which was Type A operation and is so marked.

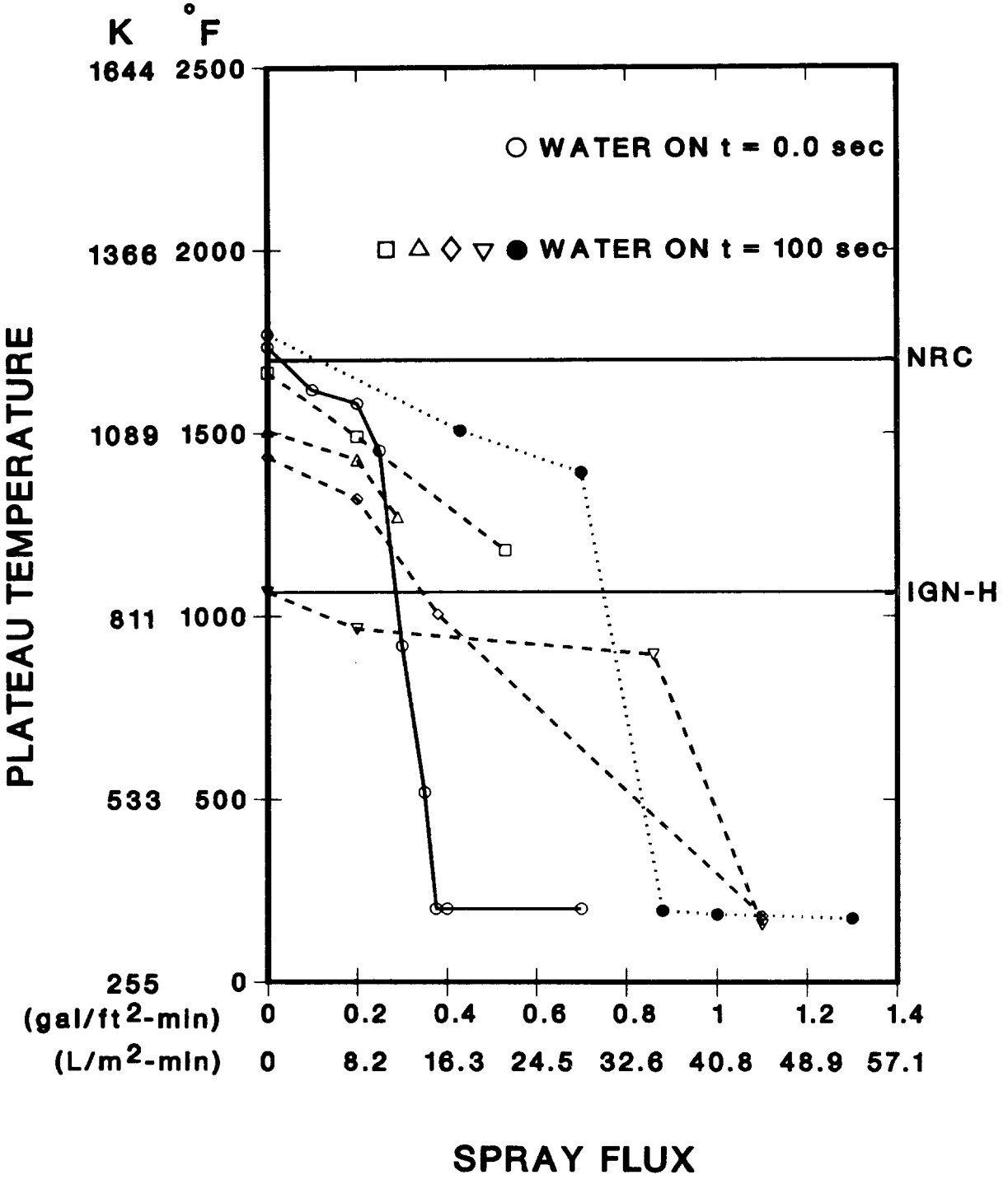

Figure 1.6-9. Plateau Temperatures Versus Water Spray Fluxes for the Helical Igniter Exposed Simultaneously to Several Airflows; Igniter Was Operated at 120 Vac (RMS). Type A operation at zero airflow (○), Type B operation at airflows of 0 (●), 4.7 (□), 6 (△), 7.6 (◊), and 12.8 (▽) m/s.

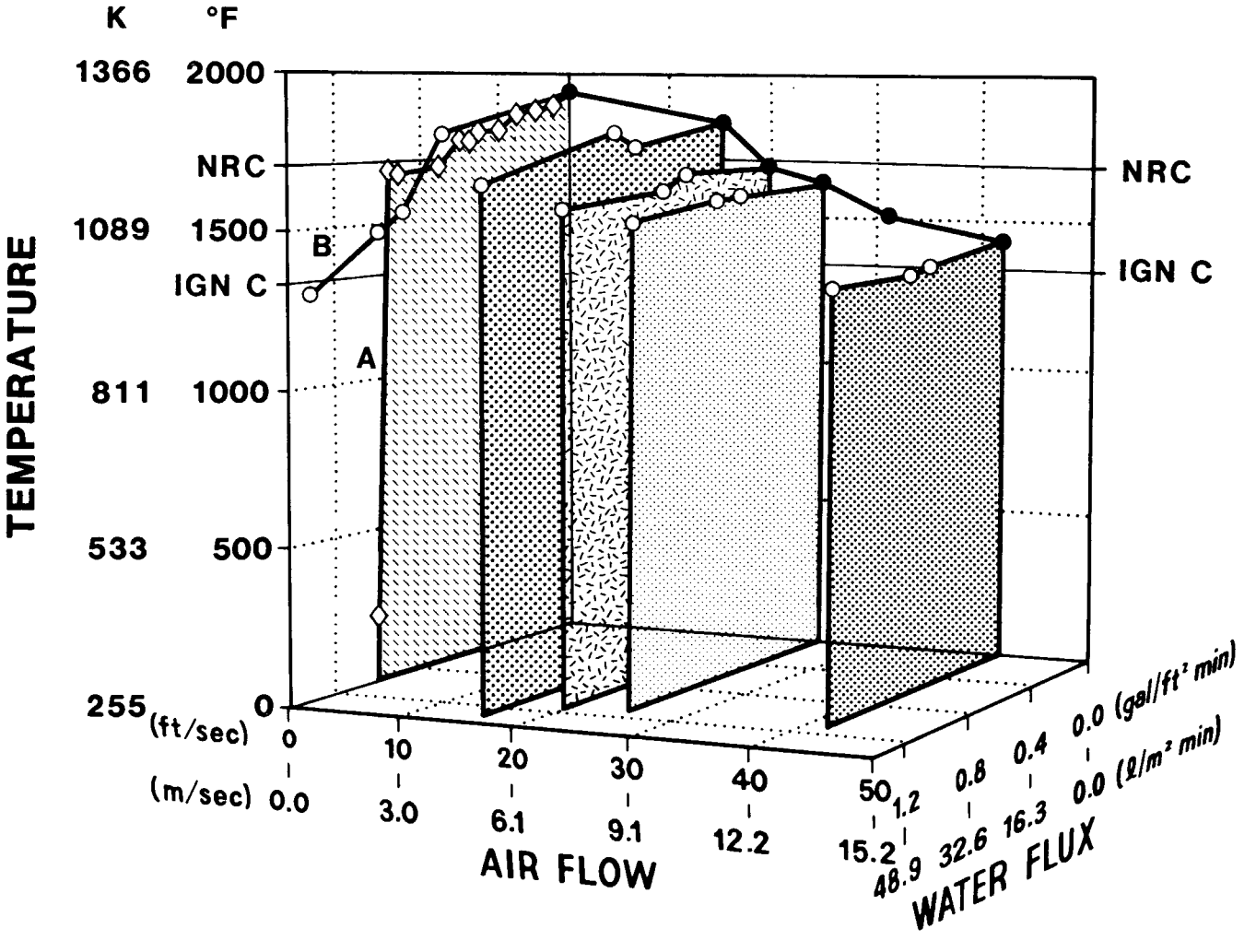

Figure 1.6-10. Plateau Temperatures Versus Water Spray Fluxes for the Cylindrical Igniter Exposed Simultaneously to Several Airflows; Igniter Was Operated at 14 Vac (RMS). All data are recorded for Type B operation except for one plot at zero airflow, which was Type A operation and is so marked.

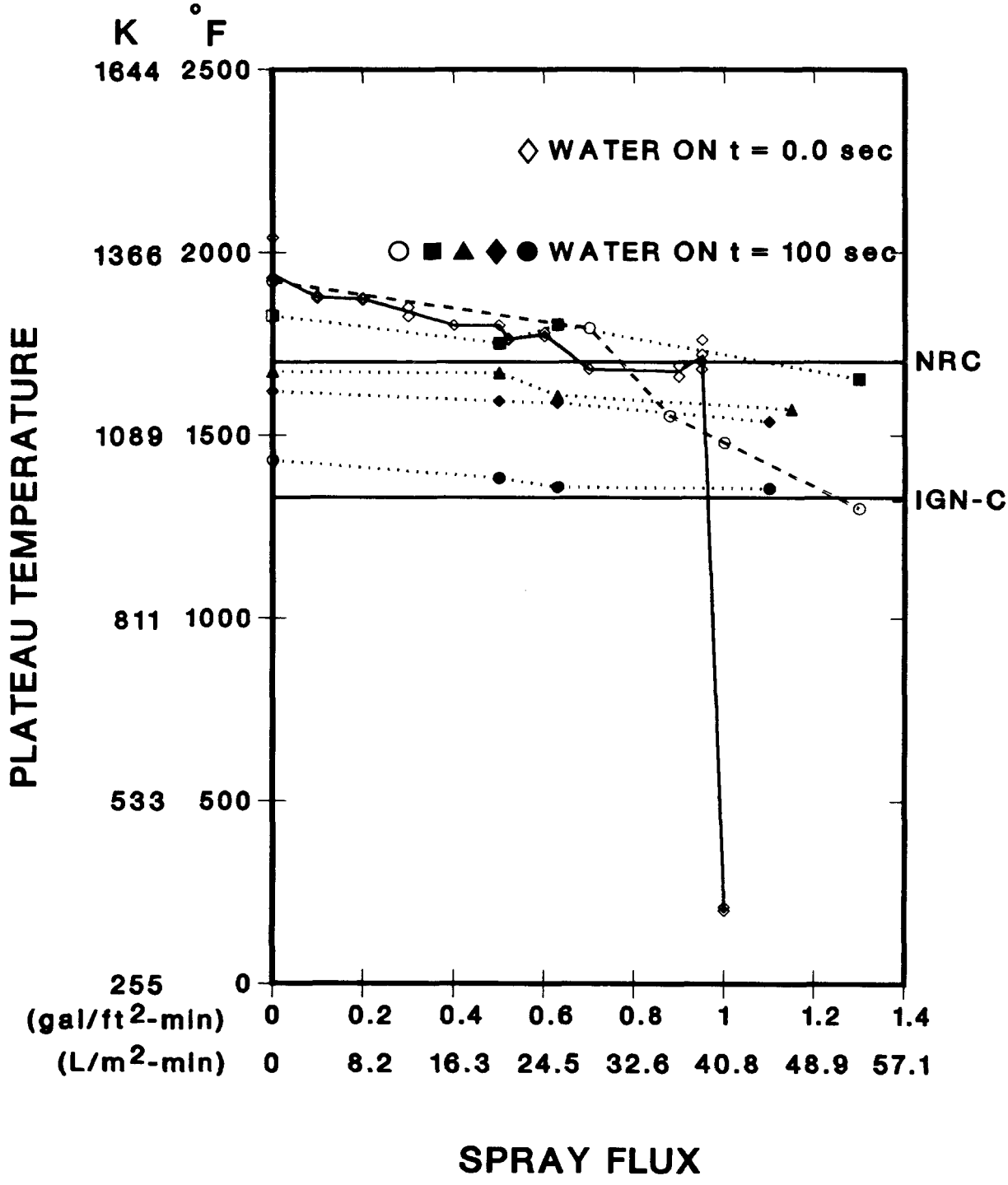

Figure 1.6-11. Plateau Temperatures Versus Water Spray Fluxes for the Cylindrical Igniter Exposed Simultaneously to Several Airflows; Igniter Was Operated at 14 Vac (RMS). Type A operation at zero airflow (◊); Type B operation at airflows of 0 (○), 4.7 (■), 6 (▲), 7.6 (◆), and 12.8 (●) m/s.

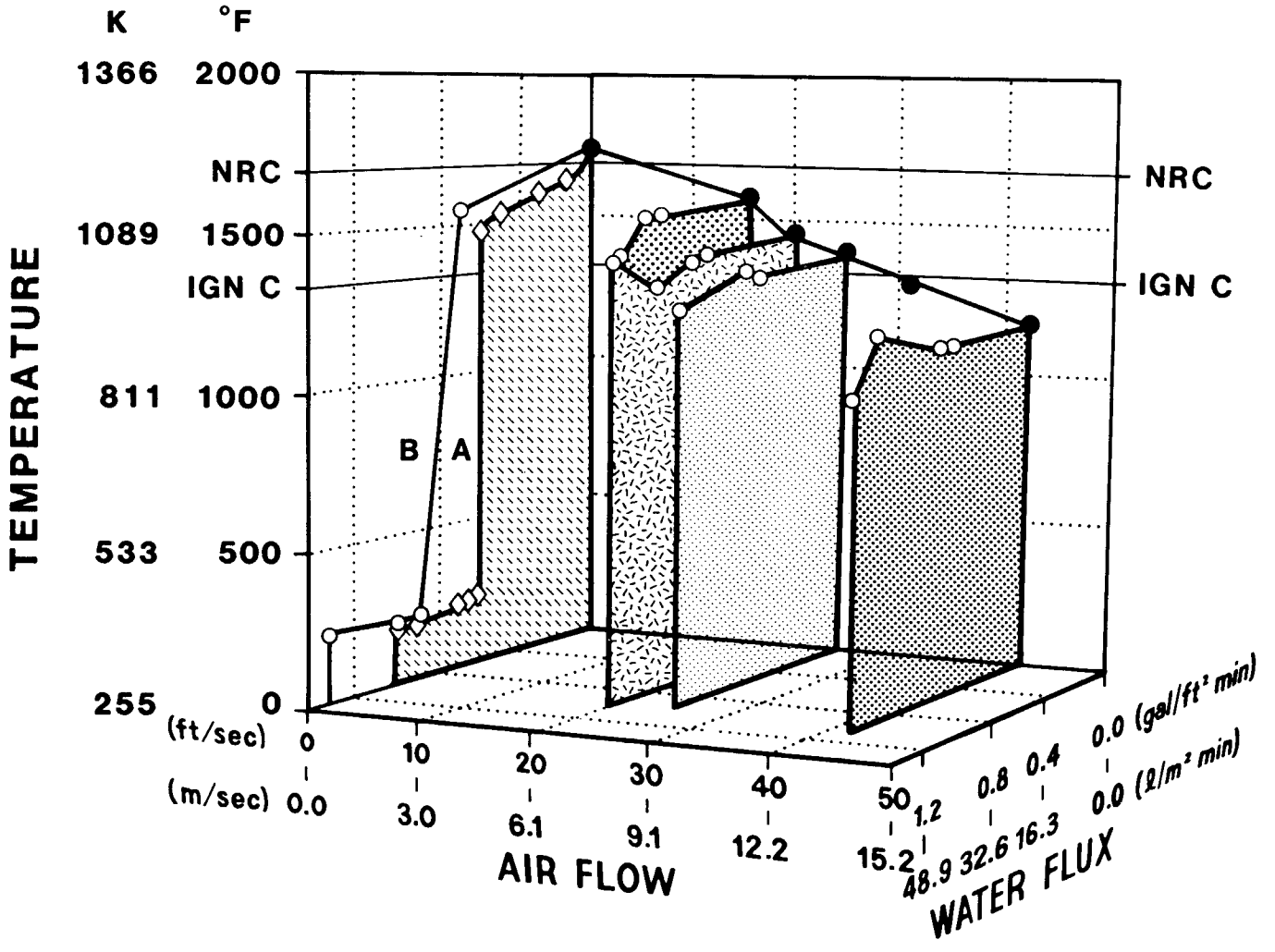

Figure 1.6-12. Plateau Temperatures Versus Water Spray Fluxes for the Cylindrical Igniter Exposed Simultaneously to Several Airflows; Igniter Was Operated at 12 Vac (RMS). All data are recorded for Type B operation except for one plot at zero airflow, which was Type A operation and is so marked.

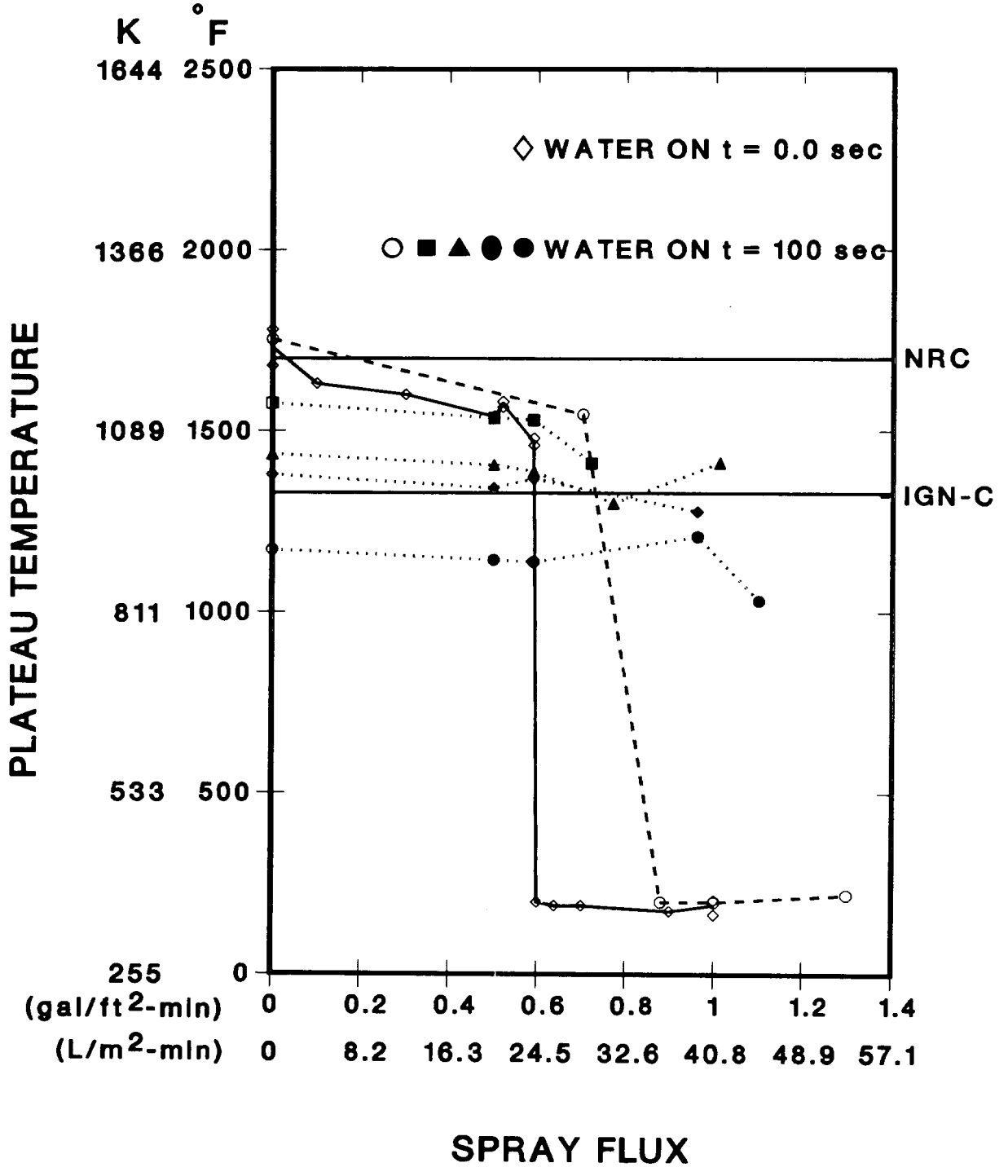

Figure 1.6-13. Plateau Temperatures Versus Water Spray Fluxes for the Cylindrical Igniter Exposed Simultaneously to Several Airflows; Igniter Was Operated at 12 Vac (RMS). Type A operation at zero airflow (◇); Type B operation at airflows of 0 (○), 4.7 (■), 6 (▲), 7.6 (◆), and 12.8 (●) m/s.

2. FISSION-PRODUCT SOURCE TERM

2.1 High-Temperature Fission-Product Chemistry and Transport (R. M. Elrick and D. A. Powers, 6422; R. A. Sallach, 1846)

The purpose of the High-Temperature Fission-Product Chemistry and Transport Program is to obtain data on the chemistry and processes that affect the transport of fission products under accident conditions. The program now consists of three tasks related to one another. Baseline thermodynamic and reactivity data are being collected for compounds of fission-product elements of particular interest. An experiment facility has been built to allow the chemistry of fission products in prototypic steam-hydrogen environments to be studied. The interaction of fission products with reactor materials such as stainless steel can be examined in this facility. Results of these experimental studies are compared to predictions of thermochemical models to determine if reaction kinetics play an important role in fission-product transport.

Little of the chemistry of fission products in high-temperature, steam-plus-hydrogen environments is well characterized. The physical and chemical processes taking place can be categorized into those between vapors (gas-phase reactions) and those between a vapor and a condensed-phase surface (heterogeneous reactions). In the latter category are condensation on, adsorption by, and chemical reaction with surfaces. Conversely, should conditions change, the fission-product species may evaporate, desorb, or leave a surface as the result of decomposition of a compound.

If these reaction surfaces are surfaces of structural materials, control rods, cladding, or bulk fuel, then the fission products can be retained in the primary system. However, the same reactions on the same materials in an aerosol form can result in transport out of the primary system.

Thermodynamic calculations[63] have shown that under some accident conditions cesium, in a steam environment, will form CsOH. In the presence of iodine, the more stable compound CsI may form. At elevated temperatures, however, CsI in steam can dissociate to form CsOH and atomic iodine. With a significant concentration of hydrogen, the atomic iodine can form HI. Because of these types of possible reactions, the stability of the compounds CsOH and CsI were studied in their relation to accident environments in the primary system. The studies were (1) a model to describe the reaction of CsOH with stainless steel in the primary system and (2) the stability of CsI in an accident environment.

2.1.1 Experiment Arrangement and Procedures

The system used for all of the experiments, the Fission Product Reaction Facility, is shown schematically in Figure 2.1-1. It consists of (in the direction of steam flow) (1) a water reservoir and preheater, (2) a boiler for producing saturated steam, (3) a critical orifice for regulating the flow, (4) a steam superheater, (5) a generator for vaporizing the fission product species and mixing them with the superheated steam, (6) a flow section in which reactions take place, and (7) a steam condenser.

The test procedure was similar for all runs. All steam carrying tubes downstream of the superheater were lined with a 0.0125-cm thick sheet of either 304 stainless steel or Inconel 600. A number of coupons of the same material as the liner were arranged along the reaction tube. The coupons used were (1) as-received, (2) cold worked by glass bead peening, or (3) preoxidized at several conditions. The system was brought to temperature over a period of several hours with argon flowing continuously from the gas manifold upstream of the orifice through the condenser. System temperatures and pressures and argon, helium, and steam flow rates were controlled and recorded, condensate steam samples taken, and noncondensed gas levels monitored by a mass spectrometer.

After each test coupons were weighed to determine weight gain and the surface or cross section of coupons were analyzed by electron microprobe, x-ray fluorescence or both. Average condensation rates were determined from the masses of the steam condensate samples and their respective collection times.

The condensates were analyzed for chemical species by pH measurements, by ion chromatography, and by atomic absorption spectroscopy and by titration for iodide ion and total acidity. The rate of hydrogen production was calculated from the ratio of H_2 to argon signals, the known argon flow rate, and a prior calibration of the mass spectrometer system.

2.1.2 Model for Reaction of CsOH With Structural Material

In the steam and hydrogen vapor phase expected during an accident, the primary cesium-containing vapor species is thought to be CsOH. (Since there is about 10 times as much cesium as iodine in the fuel and release rates for the two are similar, the principle iodine species for our experiment conditions was CsI and the principle cesium species was CsOH.) This CsOH vapor will encounter the surfaces of the primary system. Two alloys have been considered--Inconel 600 and 304SS--with oxide layers forming on these alloys as

a result of their reaction with steam. A comparison was made of these oxides for similar thermal histories. The oxide produced on Inconel 600 was relatively thin and consisted largely of Cr_2O_3 while that produced on 304SS was much thicker and consisted of an outer layer of Fe_3O_4 (spinel-type) and an inner layer of Cr+Fe+Mn spinels. After 3 h at 1270 K, the oxide on 304SS grew to about 150 μm in thickness compared to the several-micrometer-thick oxide on the Inconel.

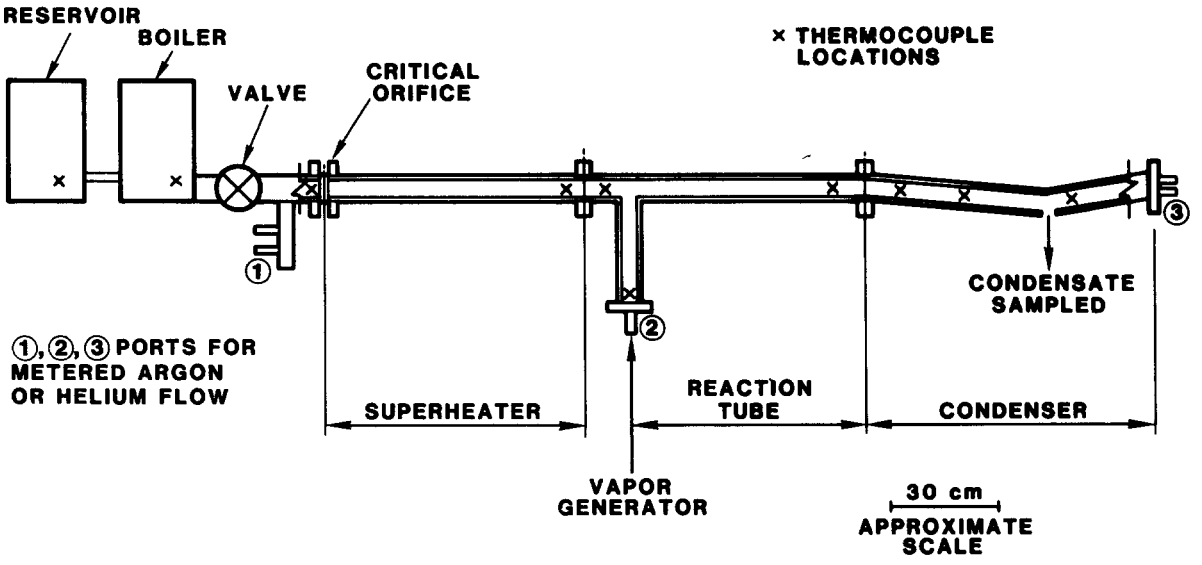

Figure 2.1-1. Schematic of the Fission-Product Reaction Facility

Silicon is a minor component of both alloys but plays a major role in our model. As the alloys were oxidized, our microprobe data indicated that silicon was not incorporated uniformly into the oxide layers but was segregated at the grain boundaries of the Cr_2O_3 layer in the case of Inconel-600 and only in the inner oxide for 304SS. (This was most apparent in tests conducted at the higher temperatures.) The oxide form was presumed to be SiO_2.

Retention of fission-product cesium will occur by its reaction with a component of the oxide layer. Our

microprobe data for both 304SS and Inconel 600 showed positive correlations between the cesium and silicon locations. The correlation was particularly good for 304SS (Figure 2.1-2) and the quantitative agreement indicated that (1) the reaction product was $Cs_2Si_4O_9$ (Figure 2.1-3), (2) all SiO_2 had been consumed, and (3) no other cesium silicates were formed. The reaction can be represented by the equations

$$2CsOH + 4SiO_2 \rightarrow Cs_2Si_4O_9 + H_2O \text{ and} \qquad (2.1\text{-}1)$$

$$2CsOH + Cs_2Si_4O_9 \rightarrow 2Cs_2Si_2O_5 + H_2O. \qquad (2.1\text{-}2)$$

This conclusion is supported by laboratory tests in which various prepared cesium silicates were exposed to steam at 1170 to 1270 K. Only $Cs_2Si_4O_9$ was stable in that environment. $Cs_2Si_2O_5$ and Cs_2SiO_3 both exhibited a loss of cesium. The corresponding numbers obtained on Inconel-600 showed a much larger variability (mostly due to the much smaller amounts of Cs and Si present) but suggest an incomplete reaction in that Si/Cs > 2.

We interpret these data as showing the diffusion of Cs through the oxide layer as being very rapid through the spinel-type layers formed on 304SS but being impeded by the Cr_2O_3 layer on Inconel-600.

The amount of cesium that diffused and reacted in the inner oxide on 304SS was used to calculate effective surface reaction rate constants shown in Table 2.1-1 at three test temperatures--1020, 1120, and 1270 K. An Arrhenius plot (Figure 2.1-4) of these rate constants gives an activation energy for the reaction of 15 kcal/mol.

Little is known about the effect of oxygen potential, temperature, and time on the compositional changes in the formation of the stainless steel oxide and how these changes might influence the cesium reaction. Some of our studies, however, have shown changes in surface oxide characteristics with changes in the H_2/H_2O ratio. Within the range studied (H_2/H_2O from 0.1 to 2), the compound $Cs_2Si_4O_9$ formed from CsOH vapor and the stainless steel oxide was unchanged. As shown in Figure 2.1-5, the surface composition of the oxide formed on 304SS appears to be influenced by the hydrogen to steam ratio as determined from several Sandia tests. The dashed lines connect composition points for tests at the same temperature (1270 K) but different H_2/H_2O ratios. Points at H_2/H_2O ratios ≥ 1 were from a test in which argon was the main carrier gas. This argon dilution may affect composition in a yet unknown way. The other 1270 K test had H_2/H_2O ratios that (time) averaged between 0.13 to 0.30 depending on the location of the coupon in the reaction tube. Compositions for a test at 1020 K and one at 1120 K

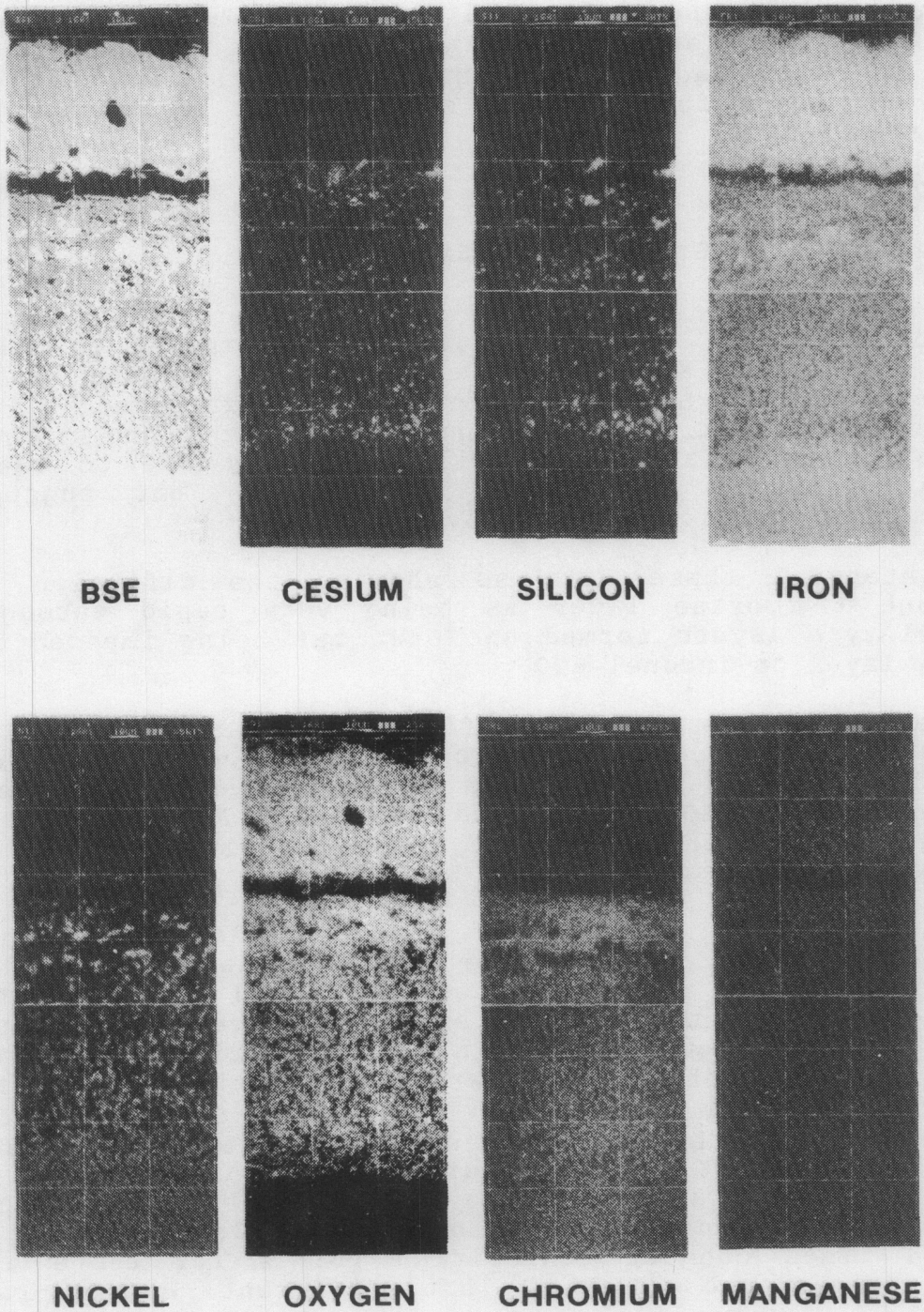

Figure 2.1-2. Cross Section of Oxide Formed on 304 Stainless Steel Exposed to CsOH Vapor and Steam at 1273 K and Examined by Electron Microprobe (Test 11)

with H_2/H_2O ratios in this lower range are placed on the graph, but none of the points are differentiated by test. We conclude from Figure 2.1-5 that at 1270 K, the surface content of Fe decreases while that of Cr and Mn increase with increasing H_2/H_2O ratios. We have no evidence to predict the influence of H_2/H_2O on the subsurface composition, which will probably be more strongly influenced by time and temperature than is the surface composition. The temperature change, at least from 1020 to 1270 K, has little effect on the surface composition for similar H_2/H_2O ratios (0.13 to 0.30). It is interesting to note that analysis of surfaces of lead screws taken from the TMI-2 core gave surface compositions[64] ranging from 10 to 40 w/o for Fe and 1 to 20 w/o for Cr. Figure 2.1-5 data indicate similar surface compositions would result from H_2/H_2O ratios of about 0.5 to 5. There are data from TMI-2 analysis[64] showing a correlation between cesium and silicon in the inner oxide on stainless steel lead screws that indicate there was probably a cesium-silica reaction product formed there.

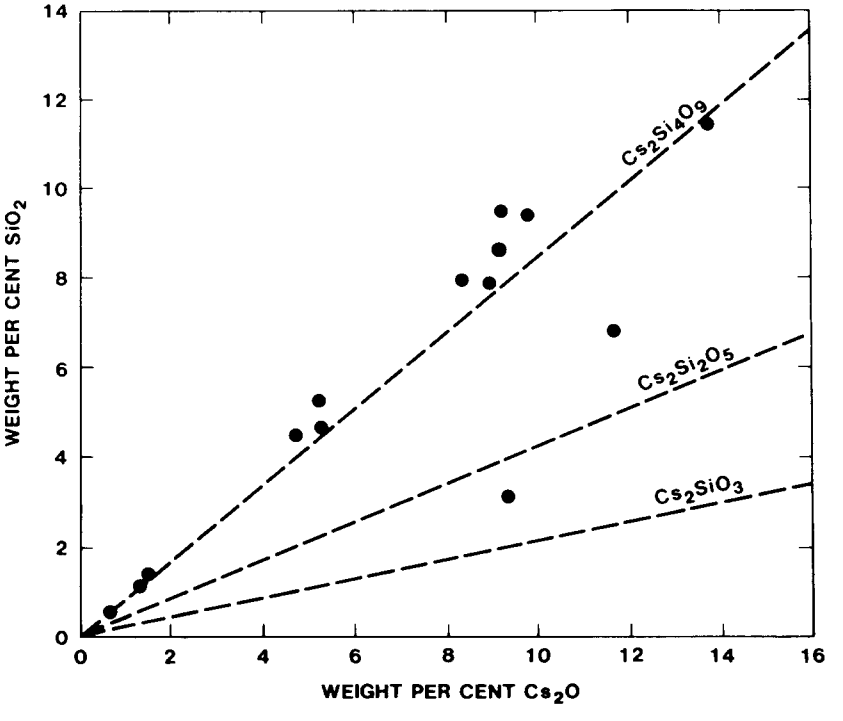

Figure 2.1-3. Correlation Between SiO_2 and Cs_2O in the Inner Oxide on 304SS for Test 11

Table 2.1-1

Summary of Surface Reaction Rate Constants

Conditions	Temperature (K)	$\frac{H_2\ (mol)}{H_2O(mol)}$	$\frac{Species\ (mol)}{H_2O\ (mol)}$	Rate Constant (m/s)
CsOH/304SS	973	0.2 -0.3	$2.3x10^{-4}$	$4.4x10^{-5}$
	1123	0.03-0.2	$7.0x10^{-5}$	$1.6x10^{-4}$
	1273	0.07-0.3	$5.0x10^{-5}$	$2.5x10^{-4}$
CsOH/INCONEL 600	1273	0.05-0.08	$1.1x10^{-4}$	$2.1x10^{-5}$
CsI/304SS	1273	0.1 -0.2	$4x10^{-5}$	Cs $<3x10^{-7}$ I $<3x10^{-7}$
CsI/INCONEL 600	1273	0.03-0.08	$4x10^{-5}$	Cs $2.5x10^{-6}$ I $<3.10^{-7}$
CsI/RADIATION CYCLED	1173	~0.1	$1.2x10^{-4}$	Cs $\sim 8x10^{-5}$ I $\sim 8x10^{-7}$

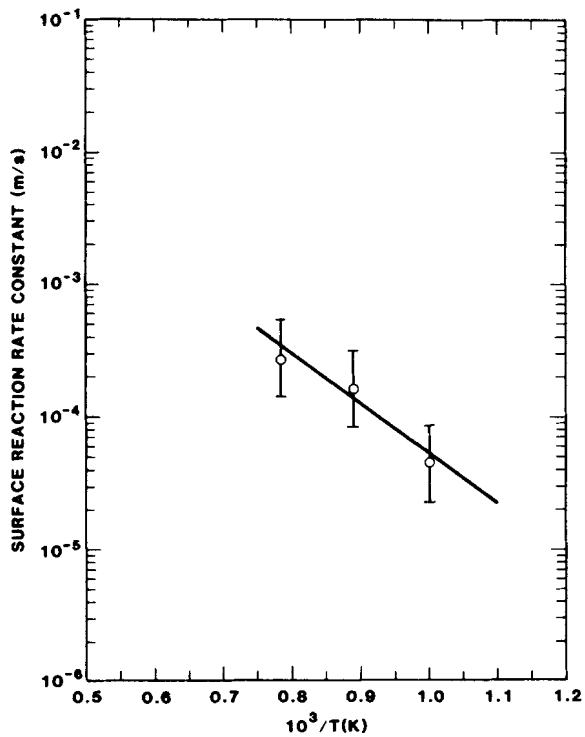

Figure 2.1-4. An Arrhenius Plot of Surface Reaction Rate Constants for the Reaction of CsOH Vapor With 304SS

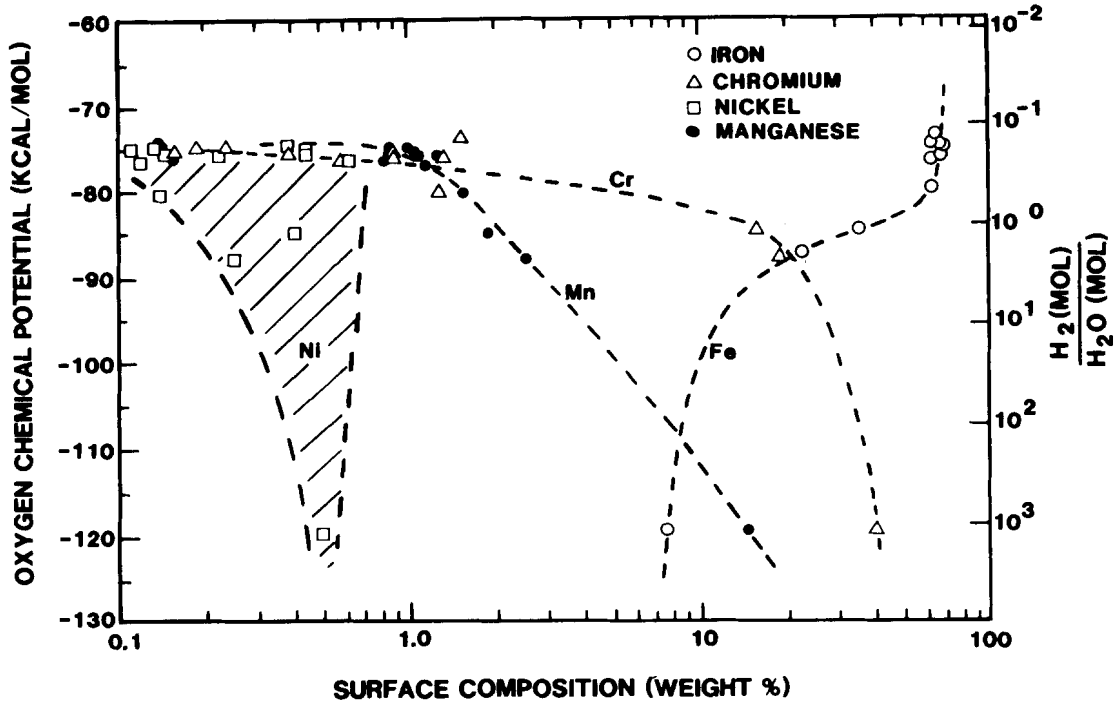

Figure 2.1-5. Surface Composition of Oxide Formed on 304SS in Steam and Hydrogen Mixtures at 1270 K

Our reaction model assumes that retention of fission-product cesium is accomplished by the formation of $Cs_2Si_4O_9$ and thus is limited by the SiO_2 content of the oxides formed on metal alloys. The model further assumes that Si does not preferentially diffuse to the metal-oxide interface so that the amount of available SiO_2--i.e., the retentive capacity of the oxide layer--is only related to the extent of oxidation. A surface that has been more severely oxidized has a larger capacity for Cs retention. It does not matter if the oxidation occurs concurrently with or prior to fission-product cesium release.

Thus, given a thermal history of an alloy and data for the oxidation rate of that alloy, the retention capacity of the oxide layer for cesium (or alternately stated the maximum amount of cesium that could be retained in the oxide) can be calculated. Whether this capacity is achieved depends on several parameters. One is the arrival rate of cesium at the oxide surface. A second parameter is the diffusion rate of cesium through the oxide layer. This parameter is dependent on oxide structure--spinel-type phases appear to facilitate diffusion while the Cr_2O_3 layer (on Inconel-600) may impede or restrict diffusion. A third parameter

is the reaction rate of cesium with silica. Any of these parameters may be controlling the overall reaction at any one time.

The various limiting reaction steps are illustrated in Figure 2.1-6. For simplicity, the case depicted is assumed to be isothermal. The parabolic curve is the calculated cesium retention capacity of the oxide. It is proportional to the accumulated amount of oxide present or to the accumulated amount of SiO_2 present in the oxide.

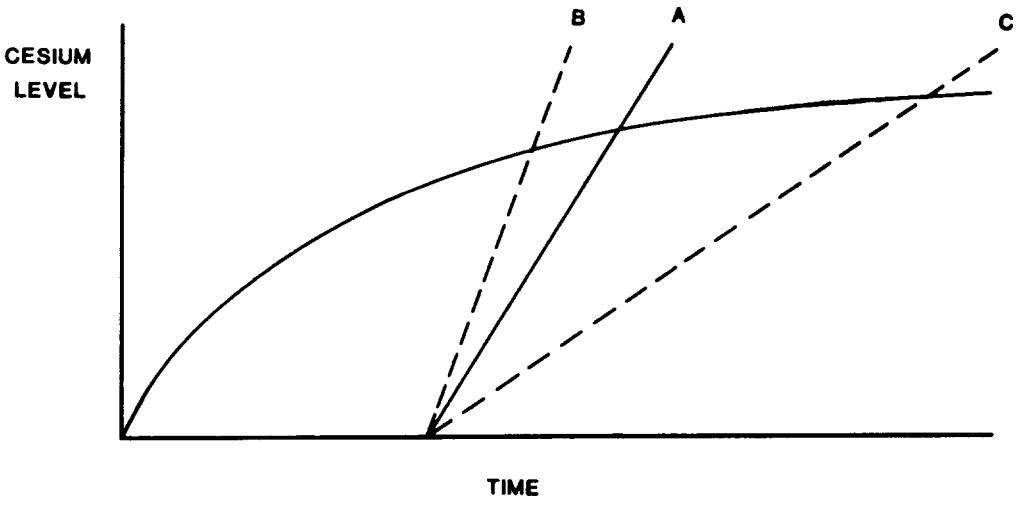

Figure 2.1-6. Schematic of a Cesium Hydroxide - Stainless Steel Reaction Model

Curve A depicts the maximum production of $Cs_4Si_2O_9$ that could occur from the reaction of a diffusing cesium species with silica. It assumes that the resupply rate of either reactants is not a limiting step in the reaction mechanism. When Curve A intersects the parabola, the formation of SiO_2 becomes the limiting step in the reaction process.

Curves B and C depict the integrated flux of CsOH arriving at the oxide-gas interface. These curves are proportioned to the partial pressure of CsOH at the interfaces. As B lies above A, the arrival flux of cesium vapor species at the surface is greater than the intrinsic reaction rate of a

diffusing cesium species with silica, therefore, Curve A is the limiting reaction step.

However, when the partial pressure of CsOH is smaller as in Curve C, then the intrinsic reaction rate of cesium with silica is greater than the arrival rate. Hence the limiting step is the arrival rate of CsOH at the oxide-gas interface. Other possible limiting steps could also be depicted. Ultimately the amount of cesium in the oxide is the lower envelope of these potential reaction steps.

In our experiments, some limiting steps can be identified. For the 1270 K test, the limiting step by the end of the run was the oxidation rate, since the reaction had by then gone to completion allowing us to identify the species. At the other two test temperatures--1020 and 1120 K--the limiting rate was probably not the oxidation rate (since reaction species could not be identified), but the rate at which the CsOH could react with the oxide (Curve A), given no other limitations. An adequate supply of CsOH vapor for all the tests did not limit the reaction. The rate constant for CsOH vapor in intimate contact with SiO_2 was recently measured as 5×10^{-3} m/s. This rate is considerably larger than the rate of 2.5×10^{-4} m/s measured in the 1270 K test so the reaction with the larger rate would not be limiting. An estimate of the reaction rate between CsOH vapor and the oxide at 1270 K, with no other limitations and corresponding to Curve A, could be made by extrapolating the similar data from 1020 and 1120 K in Figure 2.1-4 to 1270 K. This gives a value of 5×10^{-4} m/s instead of 2.5×10^{-4} m/s. This new value then is probably a better estimate for the rate at which the cesium species travels through the outer oxide to the reaction site at 1270 K and reacts with the silica.

The gaseous environment could also affect the oxide structure or its composition as discussed earlier. For instance, the "steam-starved" environment in which hydrogen is the predominant gas can have a low oxygen potential. Under such conditions, the iron in 304SS could not be oxidized and a surface enhanced in chromium oxides would result. This might, as appears to happen with Inconel oxidation, inhibit the rate at which the CsOH reacts.

2.1.3 Stability of CsI in an Accident Environment

The stability of CsI in a steam and hydrogen environment was demonstrated in both a 304SS- and Inconel 600-lined system at 1270 K. Levels of reacted cesium and iodine on the surface of 304SS coupons were less than the detection limit for the electron microprobe (~0.1 $\mu g/cm^2$) giving a reaction rate constant of less than 3×10^{-7} m/s for cesium iodide. (See Table 2.1-1 for a summary of all reaction rate constants.)

A cross section of a coupon from the reaction tube showed an oxide structure that resembled that found on 304SS from the CsOH tests. No cesium or iodine was detected within these oxides by microprobe so there was no significant diffusion of CsI (or cesium or iodine alone) into the oxide. Analysis of the steam condensate samples confirmed the conclusion that there was essentially no preferential holdup of cesium or iodine in the system since the cesium-to-iodine mass ratio was 1.06 ± 0.04.

In the case where CsI vapor was exposed to oxidizing Inconel, the cesium preferentially reacted with the oxide as determined from microprobe scans of the oxide surface (Figure 2.1-7). There was no indication that iodine was similarly retained. Corresponding rate constants were 2.5×10^{-6} m/s for cesium and $<2 \times 10^{-7}$ m/s for iodine.

This same chemical system, that of cesium iodide vapor with 304SS in steam and hydrogen, was examined to see if its behavior could be influenced by the presence of a radiation field. The steam facility used for the irradiation experiment was similar to that shown earlier but configured to fit the Gamma Irradiation Facility (Figure 2.1-8). The radiation source consists of an array of ^{60}Co pins stored in a water pool below the experiment room and raised on an elevator to irradiate the experiments. The radiation field was measured in the vicinity of the reaction volume by placing thermoluminescent dosimeters on the reaction tube and exposing the steam system to the ^{60}Co source for 10 min. The dose rate varied along the reaction tube from about 1000 to 1600 rad/min. This level is about one-thousandth of that in the reactor core during an accident.

The test was run by cycling the ionizing field on and off to compare the field and no-field effects. This was accomplished by running the test in the GIF, first with the source down (no field) for a period of 3 h and then with the source up for 3 h. This complete cycling of the source was performed twice over a 12-h period. The steam condensates were sampled periodically during the test and analyzed for concentration of cesium and iodide. To check the analytic results, cesium was measured by both atomic absorption and ion chromatography (IC) and the iodide by ion-selective electrode and IC; comparable measurements agreed within 7 percent in 11 out of 12 cases. Ion chromatography measurements of Cs and I, on a blind standard, agreed to within 4 percent of actual values. The ratio of cesium to iodide in the condensates is shown in Figure 2.1-9 as a function of time. Two things are noted in the figure. First, the cesium iodide is initially unstable as shown for a Cs/I molar ratio of less than 1, indicating that some of the cesium relative to iodine was retained in the system.

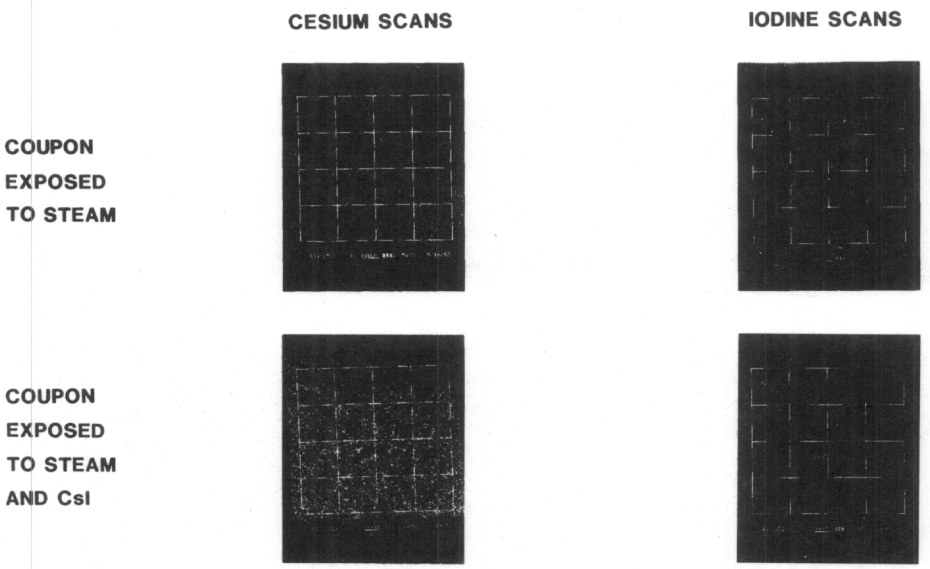

Figure 2.1-7. Microprobe Photographs of the Surface of Inconel 600 Exposed to Steam at 1270 K

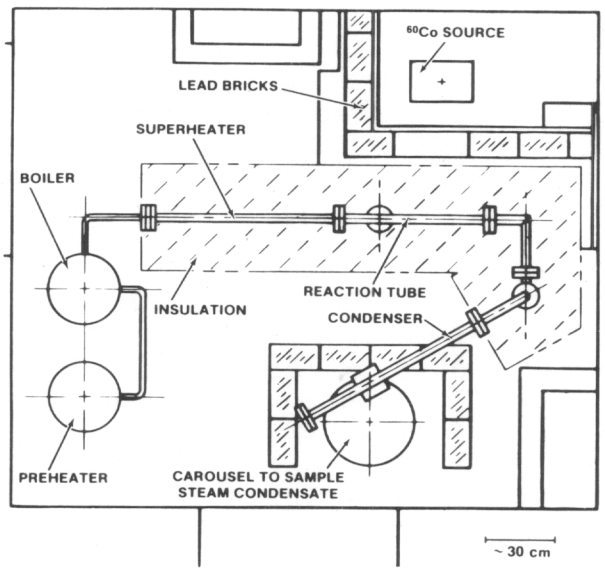

Figure 2.1-8. Schematic of the Steam Apparatus Used in the Gamma Irradiation Facility

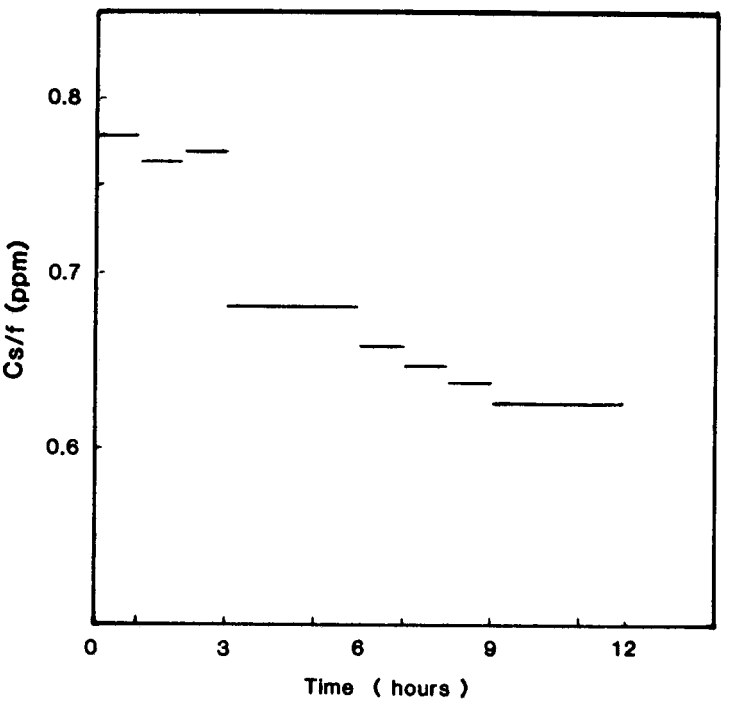

Figure 2.1-9. Cesium to Iodine Ratio (in ppm) in the Steam Condensates Versus Time for Test 52

Second, the instability increased monotonically during the 12 h period beginning with a Cs/I ratio of 0.78 and decreasing to a Cs/I ratio of 0.63.

Instability of cesium iodide determined from condensate analysis was first observed in a similar CsI experiment exposed to ionizing radiation. This instability was solely attributed to radiation although the field was too weak for the effect to be caused by a gas-phase reaction.

In stronger ionizing fields, more CsOH would exist in equilibrium with CsI and could react with stainless steel to produce the degree of instability observed. There is evidence from earlier ionizing field experiments that some of the cesium but none of the iodine from CsI reacted in the inner oxide and that the cesium is coincident with the silicon as seen in Figure 2.1-10. This observation indicates a cesium reaction similar to that observed between CsOH and stainless steel.

In two subsequent tests, CsI instability was again observed but this time in the absence of a radiation field. A program was initiated to analyze the steam system and its contents during a CsI test to determine the level of any contaminants. With the exception of 100 ppm of Cl^-

(higher for the cycled test just discussed), levels of other impurities were on the order of several ppm. Chlorine was attributed to HCl used in the cleaning processes. The HCl has since been removed. In a test performed with the new cleaning procedure, the level of Cl^- was considerably reduced and the CsI instability was also less. However, the case for chlorine playing a role in the stability of CsI is not strong. The greatest instability did not occur in the tests with the highest level of Cl^-, and in the cycling test, the instability increased as the Cl^- level decreased during the 12 h. With the exception of the presence of chlorine from an earlier cleaning process, the system probably contained only those elements proposed for the study: The reaction of CsI vapor with stainless steel or Inconel in a steam environment.

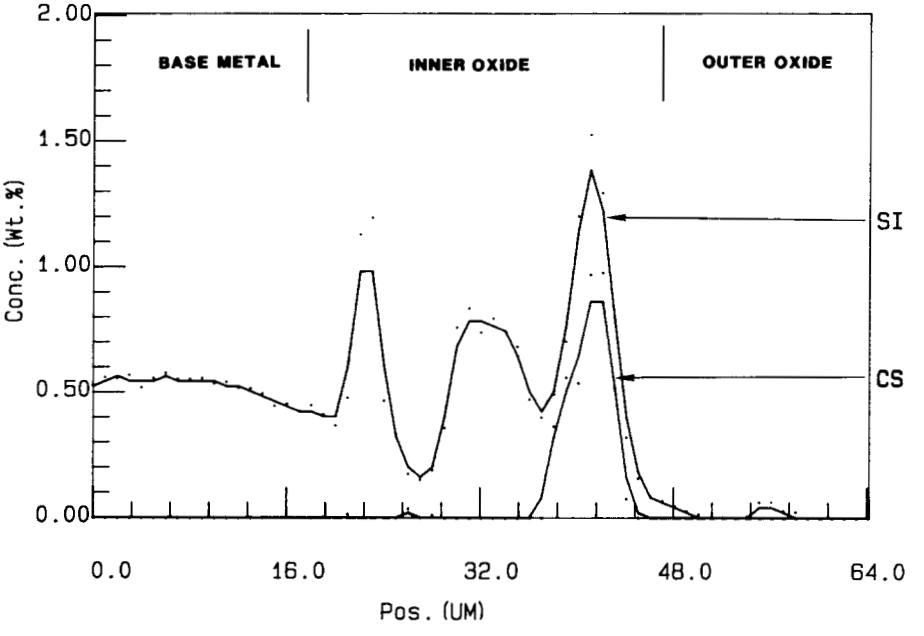

Figure 2.1-10. A Microprobe Scan Showing the Correlation Between Silicon and Cesium in the Inner Oxide Formed on 304SS in Steam (Test 40)

It seems certain that under the conditions of these experiments, CsI was unstable to varying degrees both in the presence and absence of ionizing radiation. First the causes of the instability outside a field and their relevance to reactor accidents must be determined before irradiated effects are studied. The present interpretation for the CsI stability is that (1) CsI or a cesium-bearing species in equilibrium with CsI, perhaps CsOH, reacts with

304SS as well as with Inconel, (2) this species reacts with the SiO_2 in the oxide formed, and (3) the rate and extent of the reaction depend on the thermodynamic conditions of the experiment and the accessibility of the reacting material, which is a function of the initial oxide thickness and the physical defects in the oxide.

2.1.4 Conclusions

The reaction of CsOH vapor with 304SS in steam and hydrogen has been studied over a range of conditions, which include those that are thought to have existed during the TMI-2 accident. In all cases the cesium reaction product existed in the inner oxide formed on the steel. Where a correlation could be established, it was between cesium and silicon (as silica). In a few of these cases, where the reaction had gone to completion, the product was identified as $Cs_2Si_4O_9$. A model was developed for the kinetics of this reaction as controlled by the temperature, oxide growth, and availability of CsOH. A similar reaction between cesium and silicon was observed to have occurred in the TMI-2 accident.

Results of early work showed CsI to be quite stable in a steam environment in the presence of structural materials. CsI instability was first observed in a radiation field and was attributed to the ionizing radiation. Subsequent work has shown that this instability can be produced by only thermal effects. The magnitude of the instability varies from test-to-test. Some pattern to the instability may be obtained by examining the kinetics of the reaction of the cesium bearing compound resulting from decomposition.

2.2 ACRR Source Term Tests

(K. O. Reil and M. D. Allen 6422; A. J. Grimley, 6425; H. W. Stockman, 1543)

Understanding the release of radionuclides during fuel degradation in a core uncovery accident is the first stage in determining the amount and chemical nature of the radioactive species released from a damaged nuclear plant. Current estimates of the release of the principal fission products over the range of relevant accident conditions are subject to significant uncertainty (e.g., see the QUEST Study). A key element in reducing the uncertainty in predicted releases is an improved understanding of fission-product release from the fuel under severe fuel damage conditions. Major progress is being made in the development of mechanistic release models (e.g., MELPROG's VICTORIA model) to substantially reduce these uncertainties. The ACRR Source Term (ST) program is being conducted to provide a data base for fission-product release over a range of fuel temperatures, system pressures, and fuel damage states. Significantly, these experiments will be performed in the

presence of ionizing radiation and at elevated pressure, where little or no data currently exist, to allow the validation of these improved fission-product release models.

2.2.1 Introduction

The major activities in this program currently involve evaluation of filter sampler designs and components, the continued development of the VICTORIA code and application of VICTORIA to the ST experiments, completion of design and fabrication of the ST experiment package, and modification of the Sandia Area V Hot Cell Facility.

2.2.2 Source Term Sampler System

The goals for the source term (ST) sampler system are to (1) measure the quantity of each primary fission product (Cs, I, Te, Ba, Sr, Sb, Ru, Ce, Eu, Kr, and Xe) and structural material (Sn) released from the fuel bundle; (2) determine the release rates; and (3) qualitatively establish some of the chemical forms that exist close to the fuel bundle under high-temperature accident conditions.

A functional diagram of the fission-product gas and aerosol sampling system for the ST experiments is shown in Figure 2.2-1. Seven identical filter thimbles are arranged vertically in a concentric arc over a ceramic mixing plenum. The upstream end of the filter thimbles are located approximately 10 cm above the irradiated fuel bundle. The filter thimbles are plumbed in parallel between the ceramic plenum and a manifold. The entire exhaust stream carrying fission-product vapors and aerosols will flow through each filter sampler individually. The samplers will be changed sequentially using solenoid valves located on the outlet end of the filter thimble. The sampling schedule will be predetermined using the computer code VICTORIA. There are also five grab sample cylinders connected to the manifold that will sample inert gases and control the pressure in the recirculating closed loop.

The filter thimbles must be designed and tested to meet the following requirements: (1) 61 cm long with an outside diameter of 1.6 cm to fit inside the pressure boundary, (2) have a high overall collection efficiency (> 99 percent) for fission-product vapors and particles, (3) sample at high pressures (the nominal pressure in the ST-2 experiment will be 30 atm) and in large temperature gradients (calculations indicate that the temperature of the filter thimble near the ceramic plenum will be approximately 1130 K and the downstream end will be less than 400 K), and (4) provide information on fission-product mass and chemical species during posttest analyses.

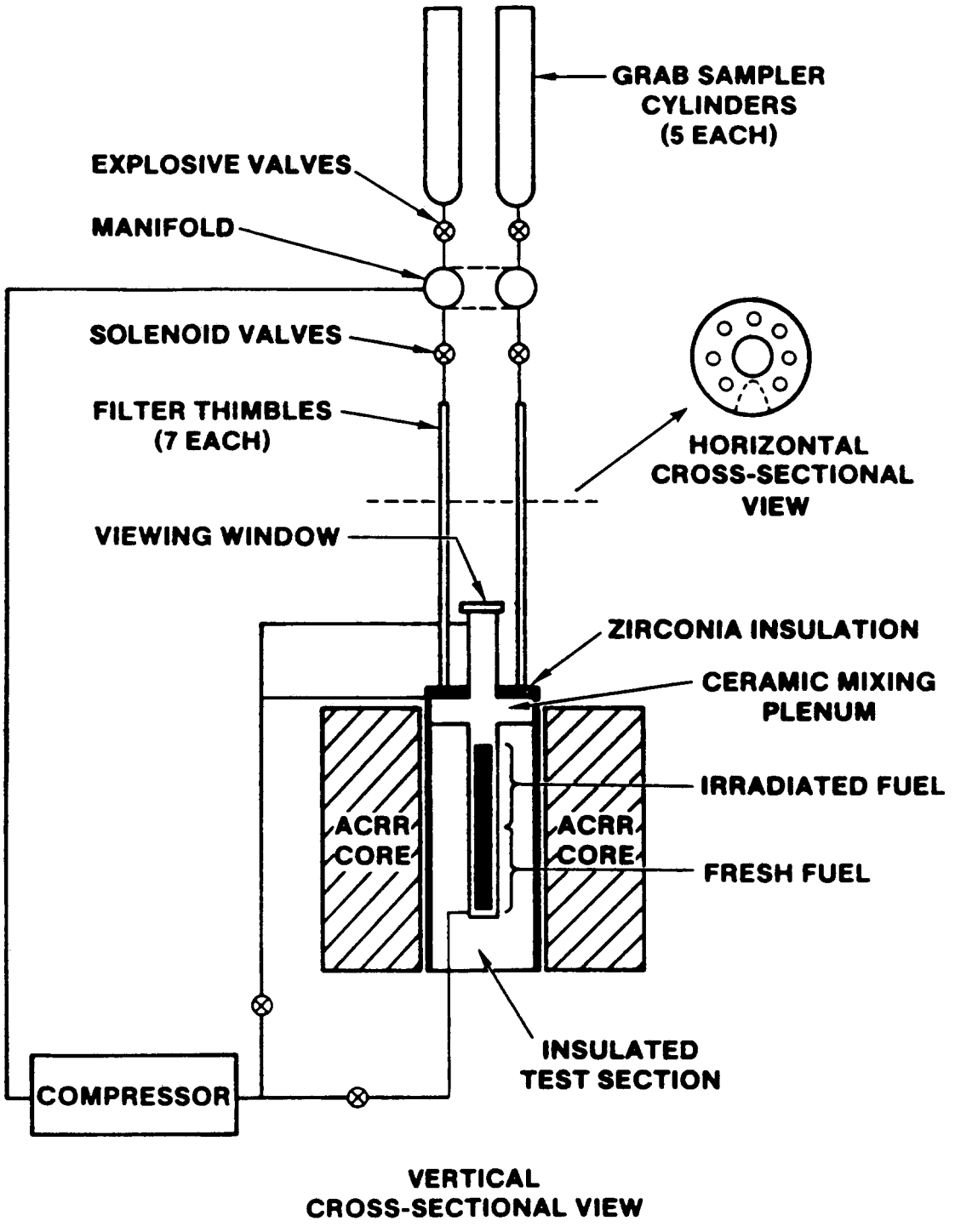

Figure 2.2-1. Functional Diagram of the Gas and Aerosol Sampling System for the Source Term Experiment

The preliminary design for the filters is shown in Figure 2.2-2. Each filter will contain a 15-cm section of substrates, which are known to be chemically reactive with major fission-product gases. For example, nickel metal is known to have a diffusion-limited chemical reaction with Te_2, H_2Te, and SnTe gas. The second section of the filter will be a 17-cm platinum thermal gradient tube. Platinum metal is inert to most fission products, except Te at high temperatures and it will dissolve in Cs°. The flow will pass through a 25-cm long fiber filter composed of Pt-10%Rh wire with a diameter of 0.076 mm. The flow will then pass through a 2-cm granular charcoal filter which will collect noncondensed vapors such as HI, I_2, and H_2Te. This filter design is preliminary and may change based on the results of our filter systems tests.

VICTORIA predicts that metallic Cs° will dominate Cs species interacting with filters in the first ST test. Hence, the initial tests of the filter assembly have been run with Cs° as the dominant species and are characterized by extremely reducing conditions. However, it is possible that CsOH will be more prevalent in the first ST test due to two factors that are difficult to consider in VICTORIA: (1) poorly known oxidation state of the fuel and (2) contamination of the system with O_2 from materials in the experimental package. To illustrate the second possibility, consider that a 1000 A coating of Fe_3O_4 on 0.4-m^2 steel, when reacted with H_2, would provide enough H_2O to convert 0.5 g Cs° to CsOH, yet this coating would appear as little more than a tarnish. It will therefore be necessary to run some tests with CsOH as the dominant Cs species.

The first filter systems test for the ST experiment was performed in February using the setup diagrammed in Figure 2.2-3. A fission-product mixture was simulated by separately heating CsI, Cs, I, Ba, and Te and then sweeping the vapors with He into an Inconel-lined tube furnace. Tin vapor, which is released as zircaloy cladding melts, was also introduced into the tube furnace. The primary gas flow inside the tube furnace was a 2:1 by volume Ar to H_2 mixture at a flow rate of about 700 cm^3/min. The fission-product simulants were generated for 3 h. The filter sampler consisted of parallel SiO_2 slats that were intended to collect CsOH (if present), Ni slats that were intended to collect Te and SnTe, and Ag slats that were intended to collect I_2 and HI. Downstream of these parallel slats was a fiber filter which was about 12 cm in length and consisted of fibers of Ni metal, which were between about 0.076 and 0.25 mm in diameter. The upstream end of the filter assembly was maintained at approximately 850°C, and the fiber filter was cooled to less than 100°C. Vapors and particles that passed through the filter assembly were collected downstream in a condensate trap and a deionized water impinger.

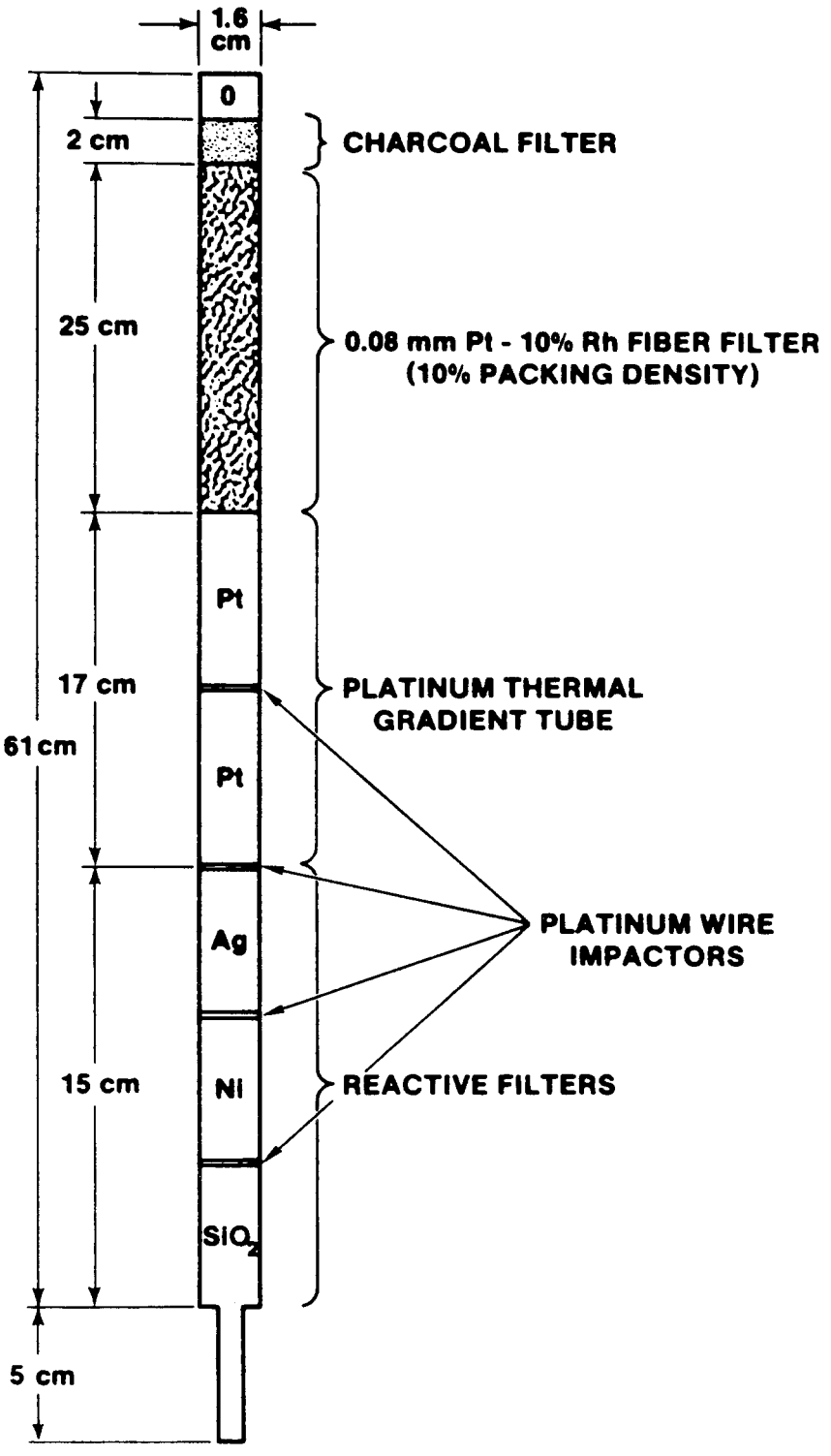

Figure 2.2-2. Preliminary Filter Design

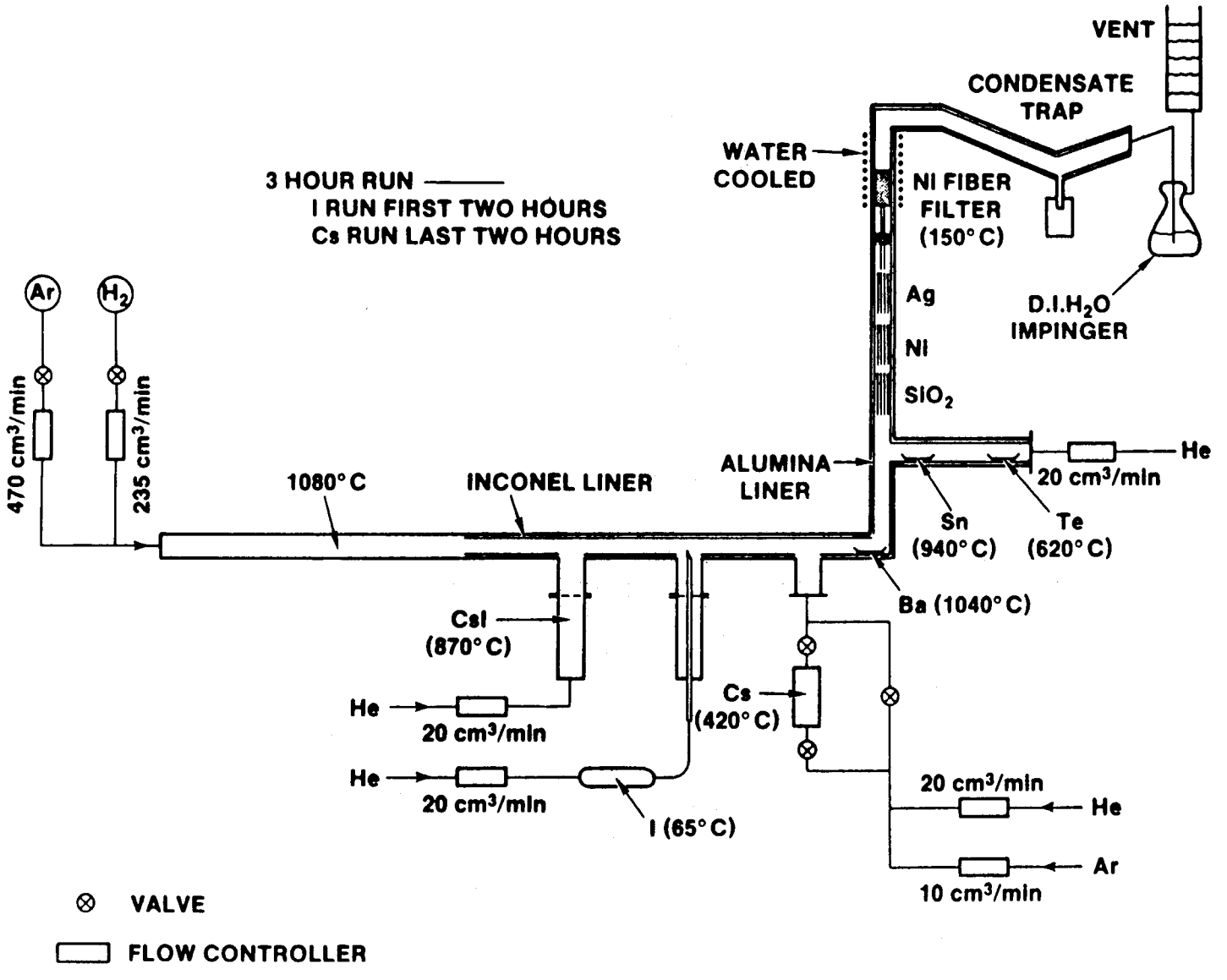

Figure 2.2-3. Systems Test 1 for ST Filters

The results of filter systems test 1 are plotted in bar graphs in Figures 2.2-4 through 2.2-6. Five segments of the filter assembly were analyzed separately: SiO_2 slats, Ni slats, Ag slats, Ni fiber filter, and condenser liner and also the deionized water in the impinger. Each segment of the filter was first washed with deionized water and then with 6M nitric acid. Each water sample was analyzed for iodine using a specific ion electrode. The water and nitric acid leachates were analyzed for Cs, Ba, and Sn using a DC plasma emission spectrometer and for Te by voltammetry. Also, qualitative electron microprobe analyses were performed on the slats.

The results from systems test 1 indicate the following conclusions: The filter was very efficient, with less than 2 percent of the collected mass depositing past the fiber filter. All of the detectable Cs was soluble in water. CsI collected on the Ni and Ag slats as agglomerated aerosol particles; there was no reaction between the Ag and I, which indicates that no HI or I_2 passed over the Ag slats. The SiO_2 slats were surprisingly inert. Almost all Te and Sn species, which were probably SnTe, H_2Te, and Te_2, were collected on the Ni slats. No Te or Sn was soluble in water. Barium appeared to deposit as an aerosol along the thermal gradient in the filter. There was evidence of contamination in the test, especially H_2O, Na, and Cl. This test demonstrated the need for several more carefully controlled filter systems tests with a simpler setup.

Filter assembly tests 2 and 3 were run during early March using the experimental setup shown in Figure 2.2-7. The setup consisted of a vertical tube furnace capable of temperatures up to 1300°C. A silica tube with an OD of 3.8 cm and a length of 120 cm passed through the tube furnace with about 15 cm protruding out of the bottom of the furnace and 60 cm out of the top. Above the tube furnace, a calrod was wrapped around the silica tube and was packed with insulation to create the temperature gradient expected in the ST experiments. The stainless steel filter thimble was sealed by Viton O-rings in a second silica tube with a 3.1-cm OD that was positioned inside the outer silica tube. A brass plug was sealed by Viton O-rings in the inner silica tube at the bottom of the tube furnace. Stainless steel plungers, which passed through the brass plug, contained individual silica crucibles containing Ba, Te, SnTe, and CsI. The plungers were adjusted to a position in the tube furnace where the temperature was adequate to reach the partial pressures necessary to vaporize the desired amount of fission-product simulants. Cesium vapor was generated by sweeping a 2:1 by volume Ar-to-H_2 gas mixture at a flow rate of 600 cm^3/min over molten Cs metal. Each experiment was run for 40 min.

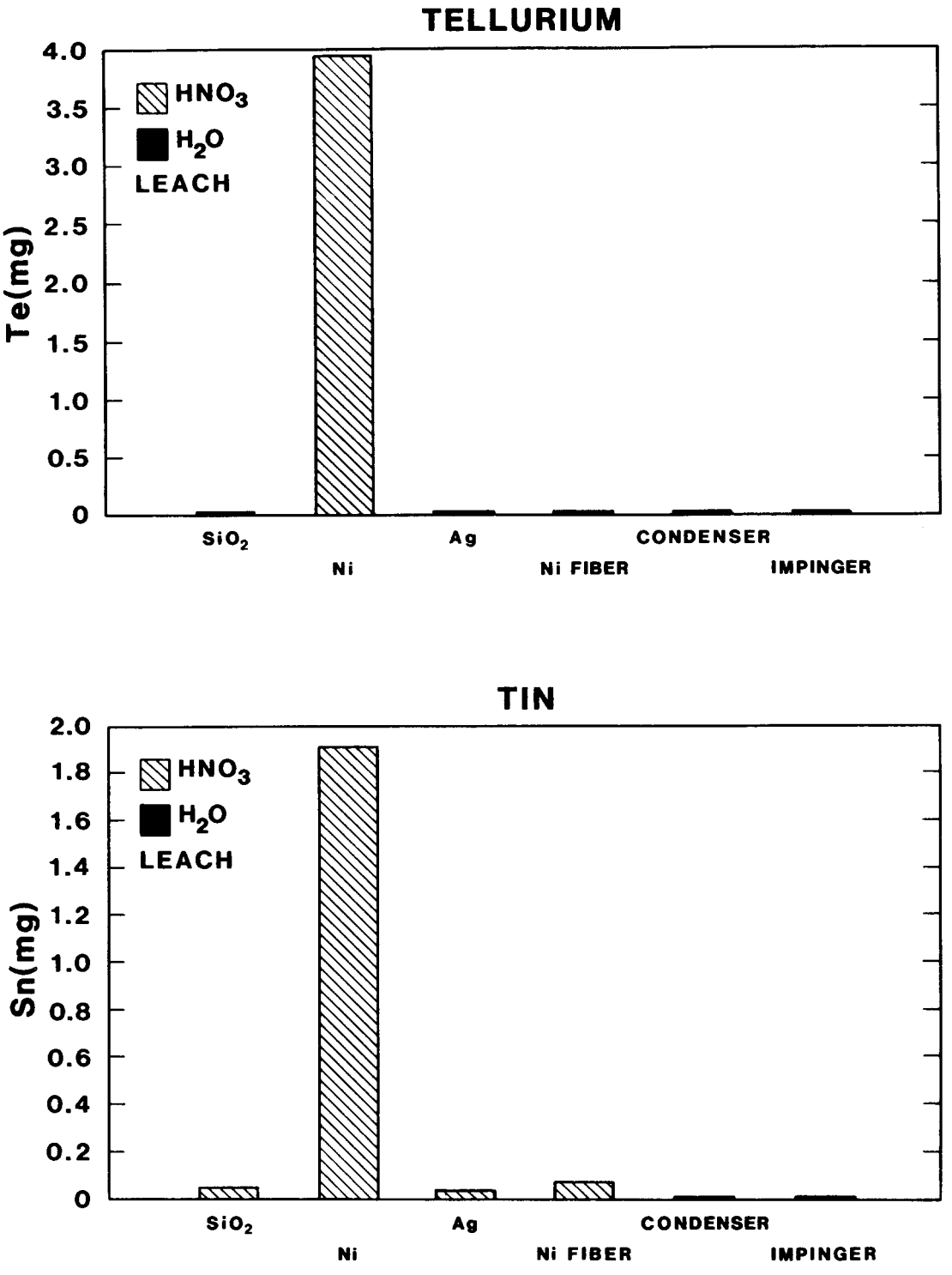

Figure 2.2-4. Filter Systems Test 1 Results for Tellurium and Tin

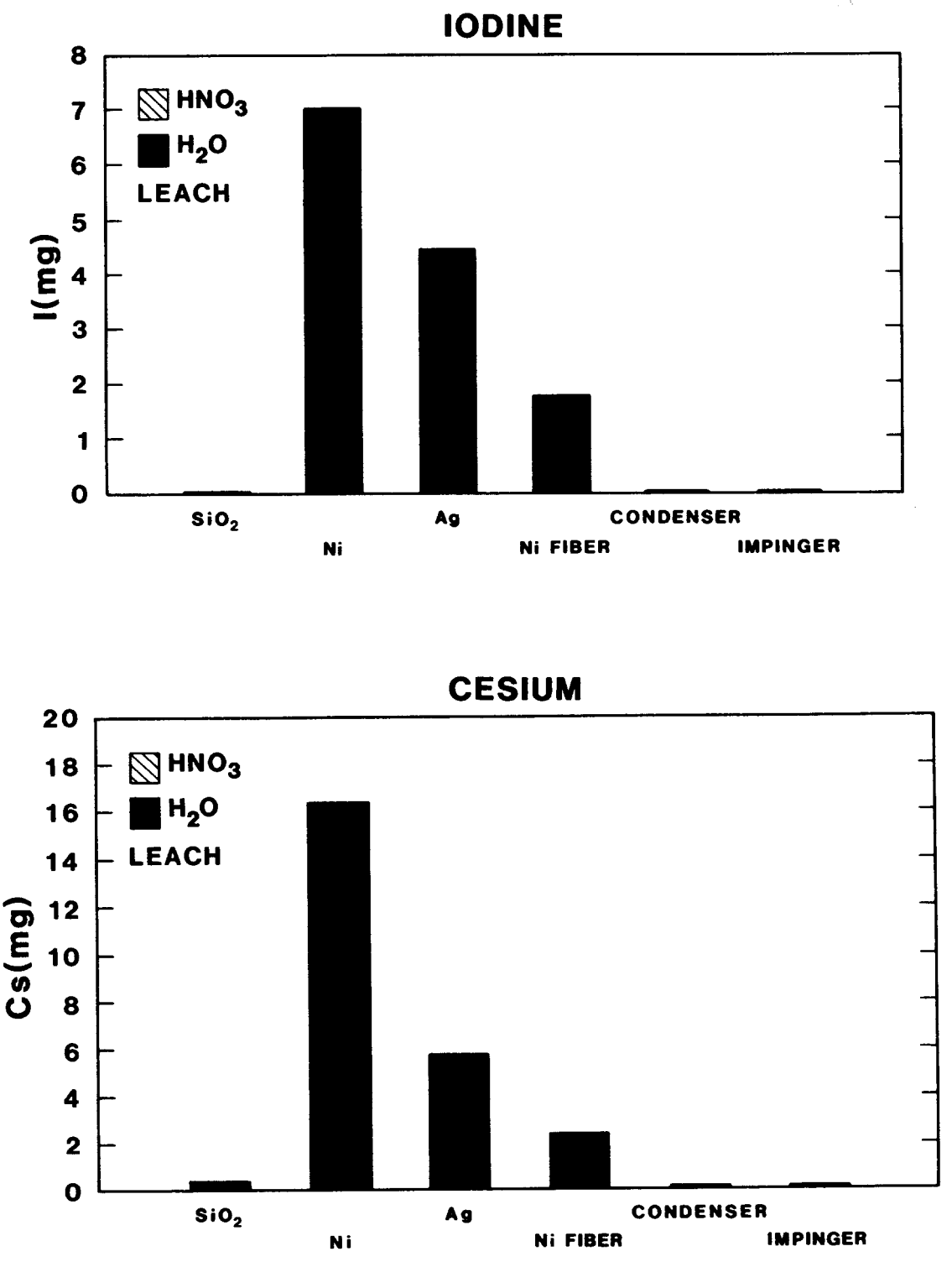

Figure 2.2-5. Filter Systems Test 1 Results for Iodine and Cesium

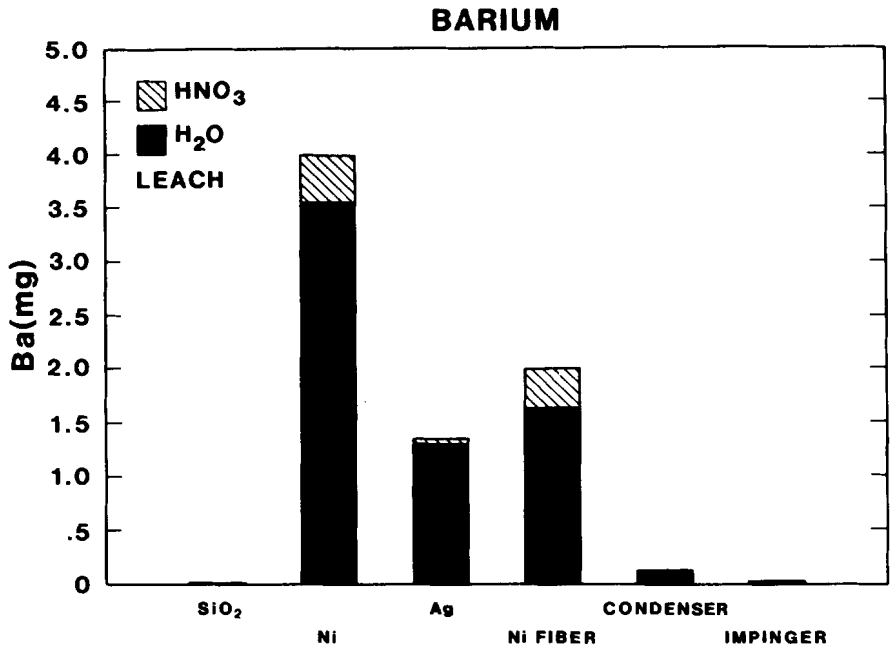

Figure 2.2-6. Filter Systems Test 1 Results for Barium

The filter assembly consisted of a stack of tubes composed of materials known to be chemically reactive with certain fission products. These tubes slid inside the stainless steel filter thimble. The length and material of the filter tubes from the hot region to the cooler top end of the filter were 5-cm Ni, 5-cm SiO_2, 5-cm Ni, 8.4-cm Pt-lined Ni, 5-cm Ag, 8.4-cm Pt-lined Ni, 8.4-cm Ni, 8.4-cm Ni, 3-cm fiber filter (0.0076-cm diameter Pt-10%Rh wire with 10 percent packing density), and a 2-cm granular charcoal filter. The filter thimble was positioned with the bottom end protruding into the tube furnace where the temperature was approximately 850°C. The top end of the filter assembly was air cooled to approximately 75°C. Fission-product vapors and aerosols that passed through the filter assembly were collected downstream using a dry trap and a deionized water impinger.

It appeared that the Cs metal had been exposed to O_2 and H_2O vapor in test 2, so chemical analyses were not performed on the filter components. The Cs metal container was redesigned for test 3. The results of filter test 3 are given in the bar graphs in Figures 2.2-8 through 2.2-12. Twelve segments of the filter assembly were analyzed individually: the nozzle end of the filter thimble, the Ni,

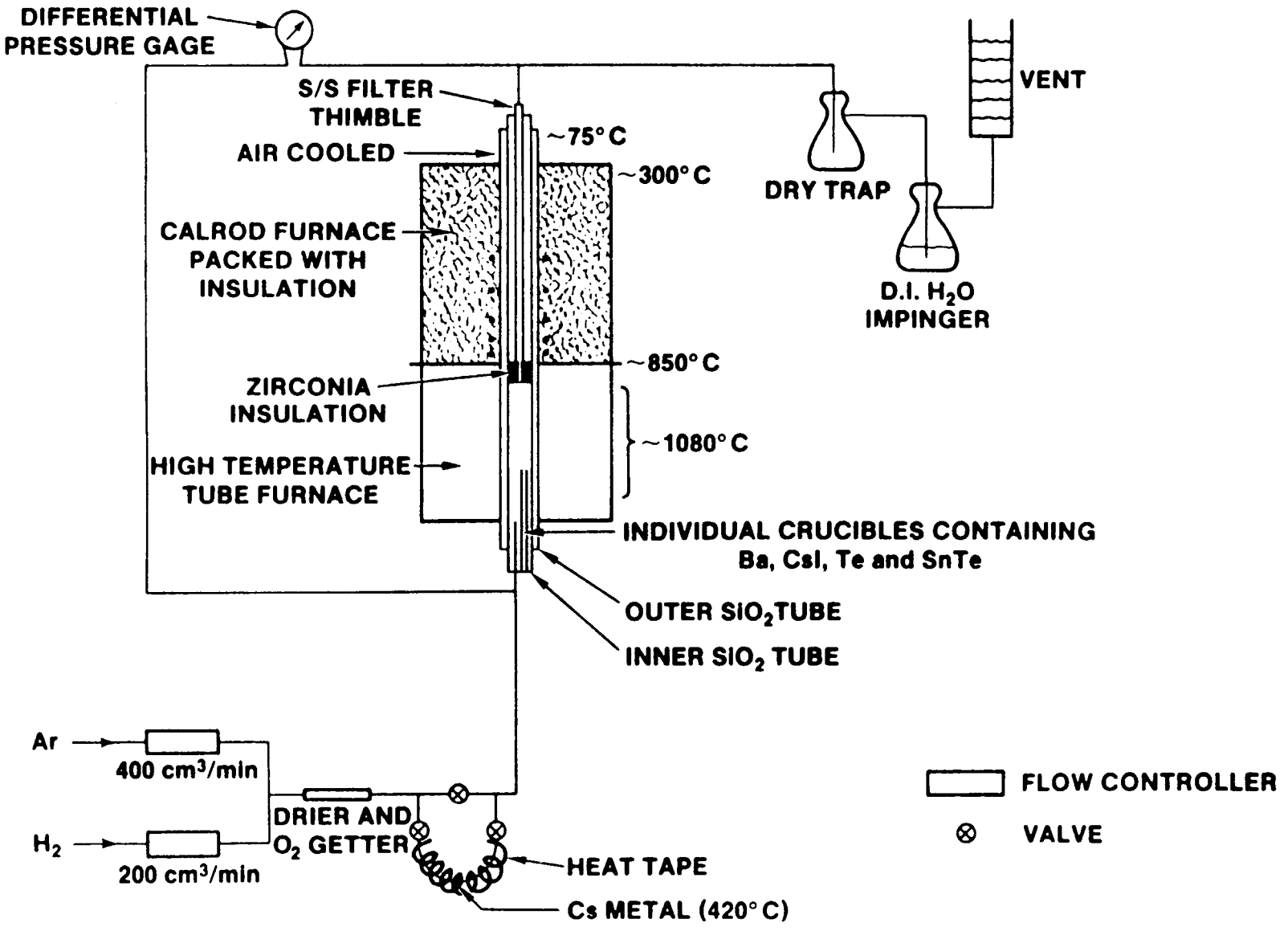

Figure 2.2-7. Experimental Setup for ST Filter Tests

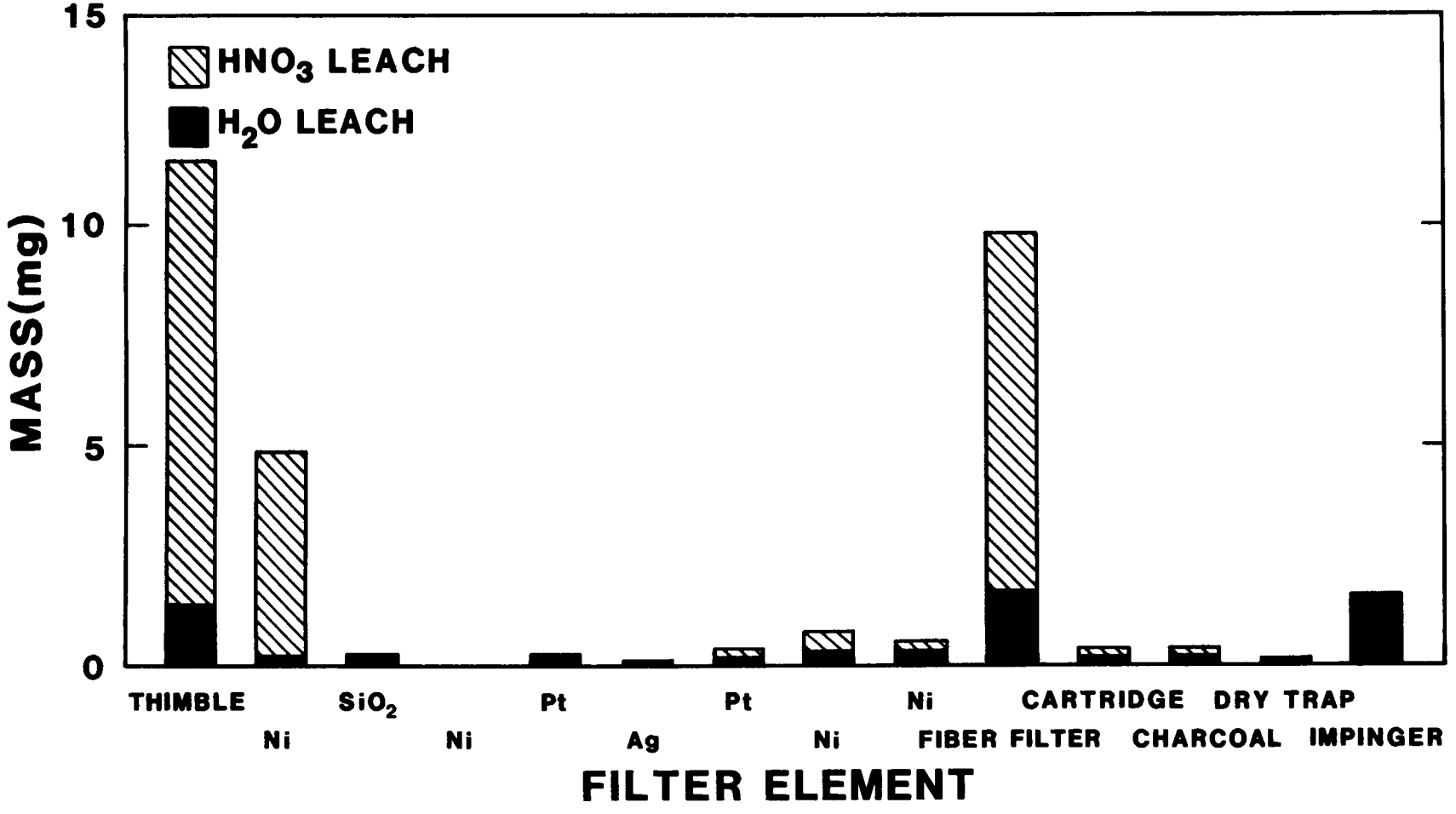

Figure 2.2-8. Filter Systems Test 3 Results for Tellurium

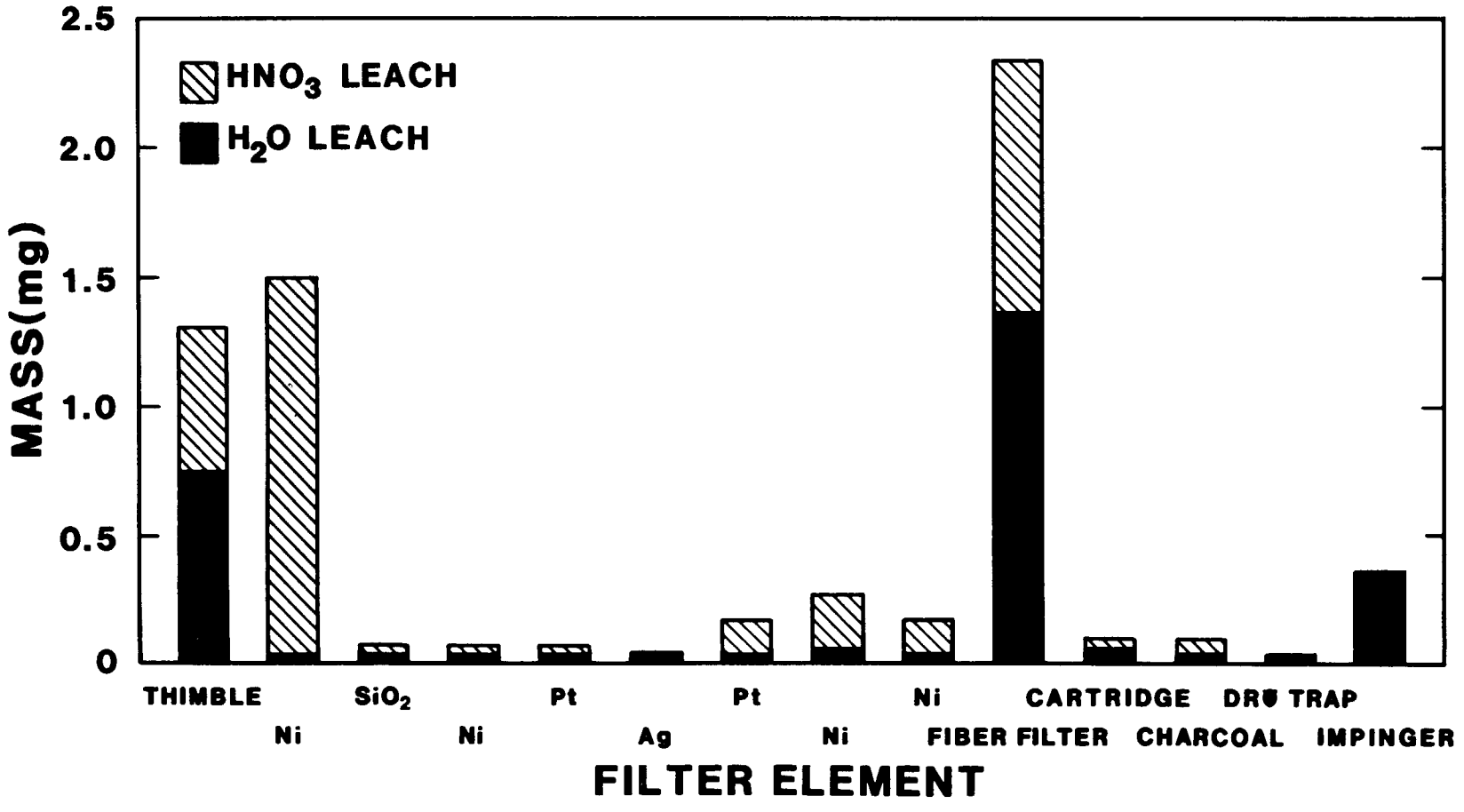

Figure 2.2-9. Filter Systems Test 3 Results for Tin

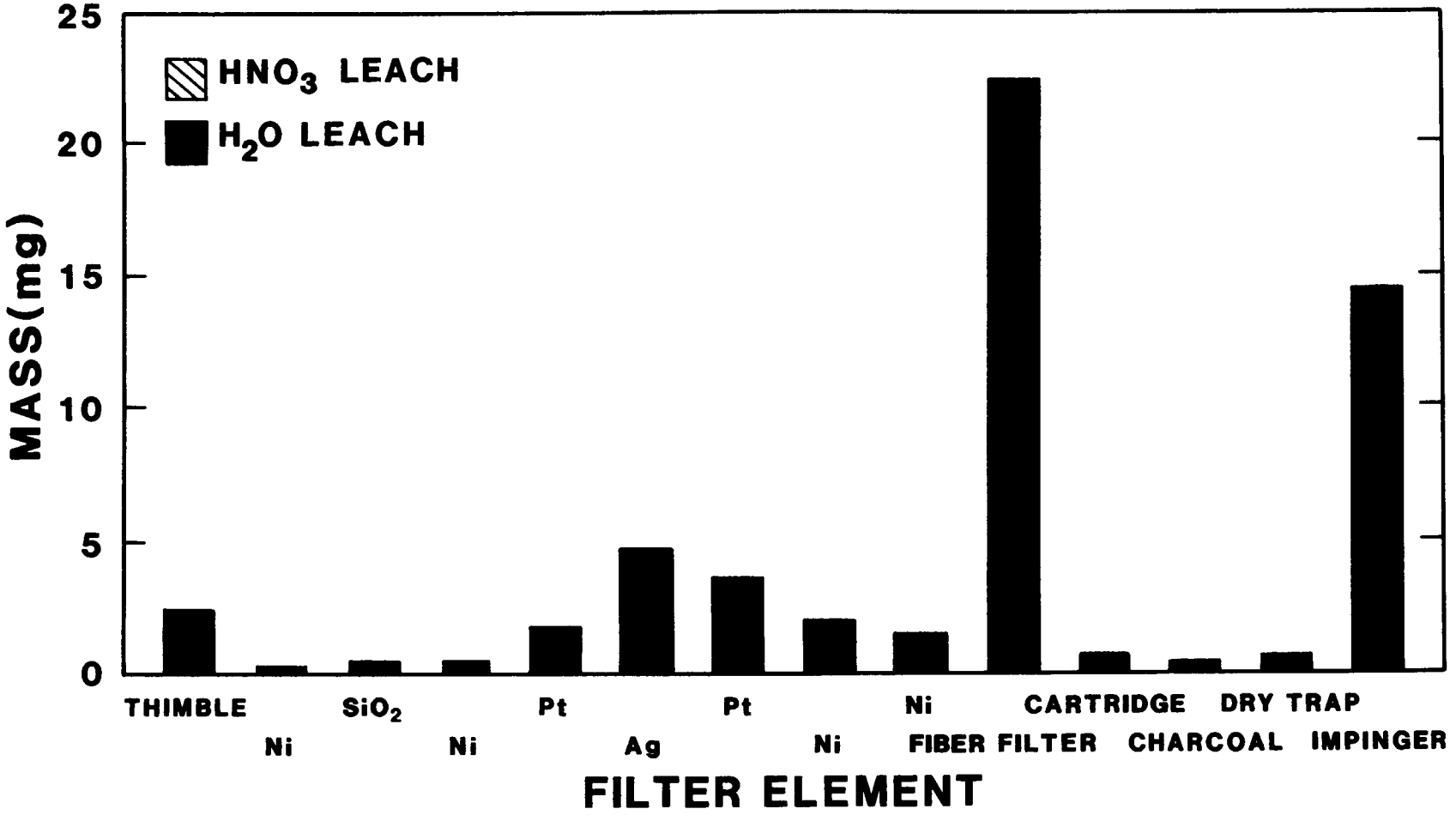

Figure 2.2-10. Filter Systems Test 3 Results for Iodine

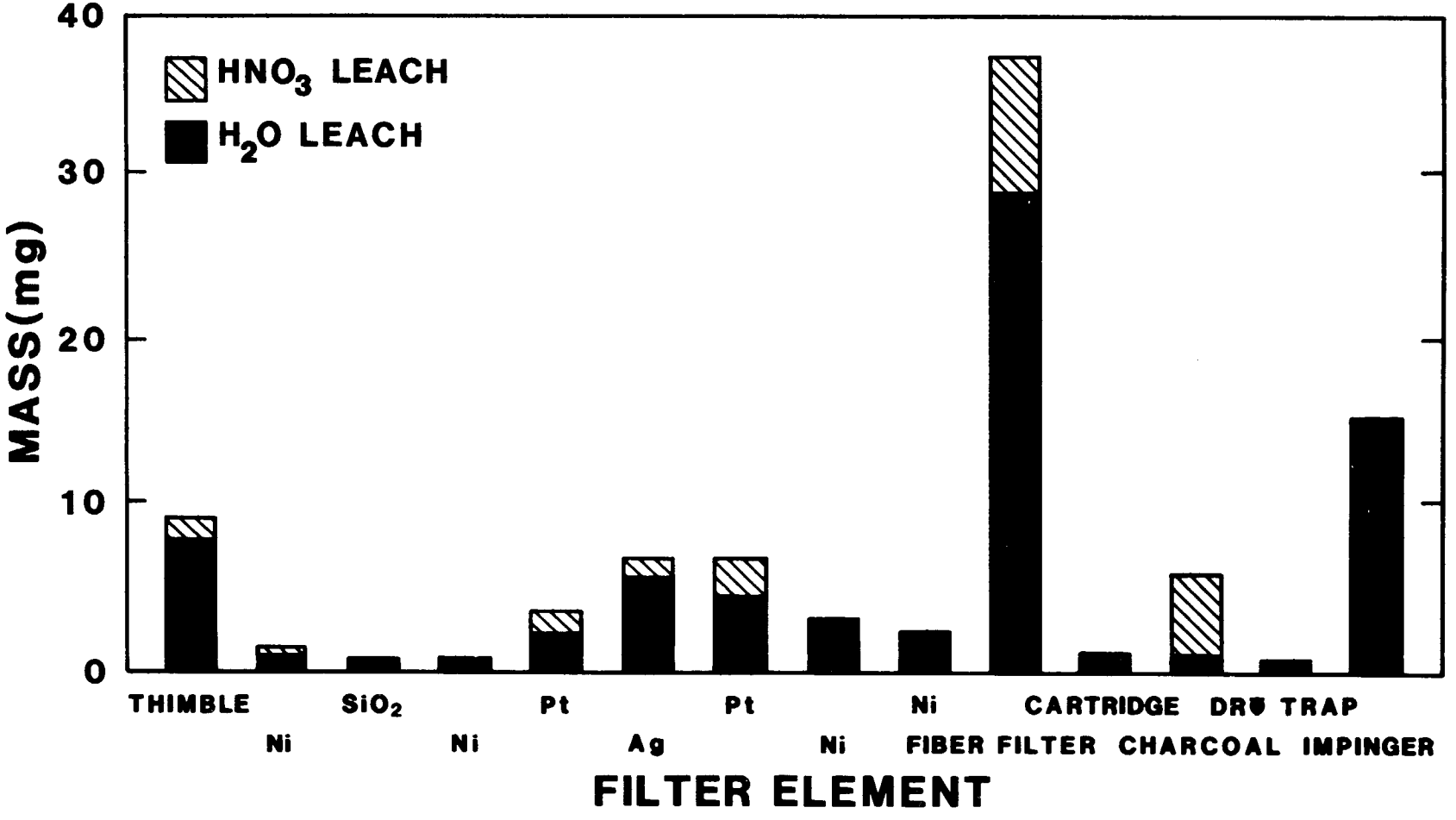

Figure 2.2-11. Filter Systems Test 3 Results for Cesium

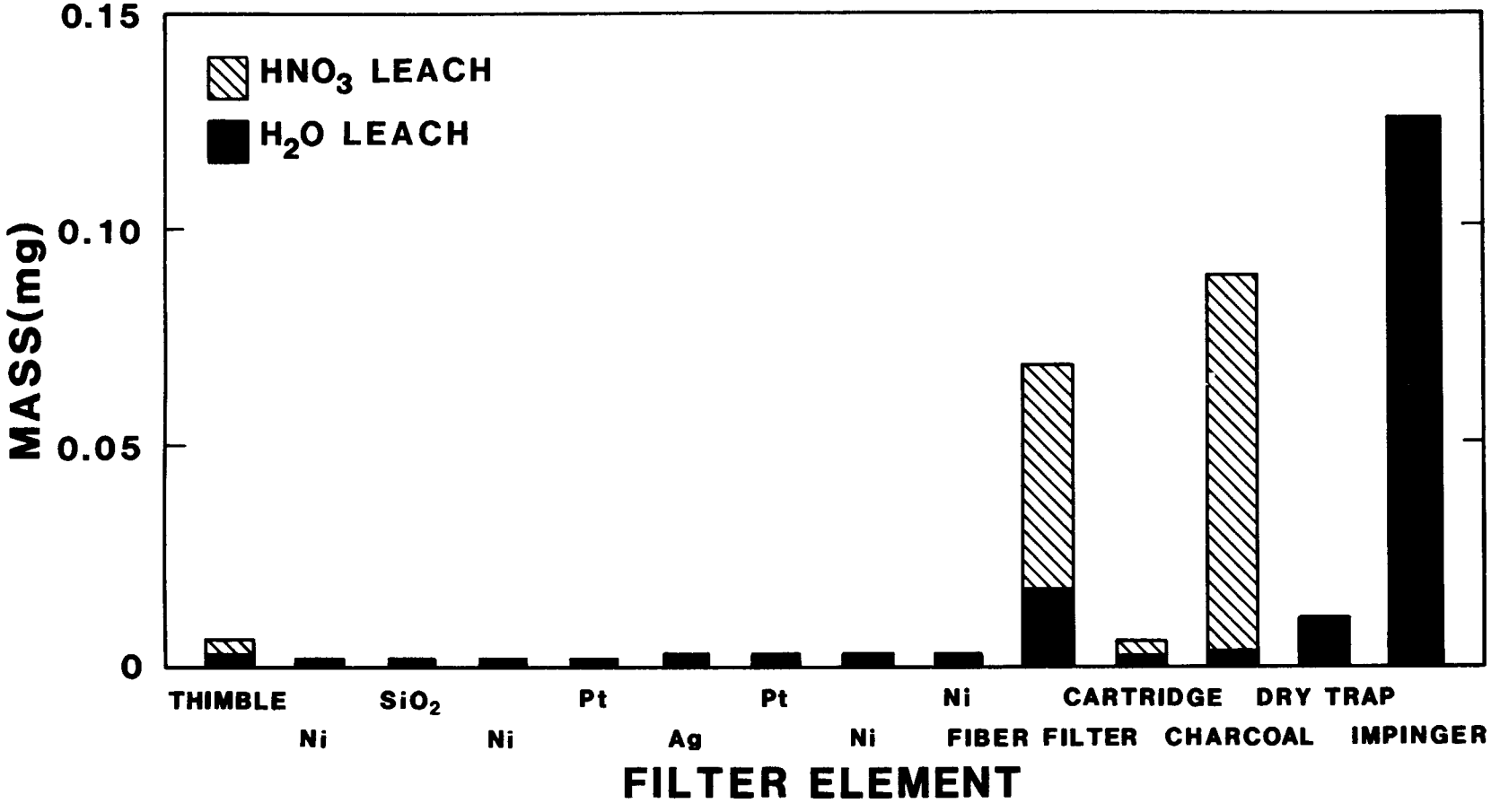

Figure 2.2-12. Filter Systems Test 3 Results for Barium

SiO_2, Ni, Pt, Ag, Pt, Ni, and Ni tubes, the Pt-10%Rh fiber filter, the cartridge that held the charcoal, and the charcoal granules and also the dry trap and the deionized water in the impinger. Each segment was first leached with water and was then leached with 6M nitric acid. The water leachates were analyzed for iodide using a specific ion electrode. The water and nitric acid leachates were analyzed for Cs, Te, Sn, and Ba using a DC plasma emission spectrometer.

The results from systems test 3 indicate the following conclusions: The fiber filter was not very efficient, primarily because as the filter became overloaded with particles and plugged, the aerosol tended to flow around the outside of the tube containing the fibers. This indicated that the tube holding the Pt-10%Rh fibers must be redesigned with outside O-rings to seal it in the filter thimble. The Cs tended to deposit as an aerosol along the thermal gradient in the filter thimble; it showed no obvious chemical reactivity with any of the substrates. Not all of the Cs was water soluble; the fraction of the Cs that was soluble in nitric acid might have been Cs_2Te. The iodine bar graph was similar to the one for cesium, indicating that most of the iodine was in the form of CsI particles. The Te and Sn tended to collect on the stainless steel nozzle of the filter thimble, on the first nickel tube, and in the fiber filter. The Sn was probably in the form of SnTe, but since there was approximately 5 times more Te than Sn, there were other forms of Te present, possibly Te, Te_2 and H_2Te; these forms would also be reactive with the Ni in the stainless steel nozzle and with the first Ni tube in the filter thimble. Cs_2Te probably also formed, but was less reactive with the filter materials (discussed later). Barium collected primarily on the fiber filter, in the charcoal, and in the impinger water. The barium bar graph (Figure 2.2-12) may indicate that the majority of the Ba vaporized late in the experiment after the filter was plugged and, therefore, may have flowed around the fiber filter. Filter test 3 showed the need for several more filter system experiments. In particular, this test showed that the fiber filter must be more efficient and sealed in the filter thimble with O-rings, and it showed that the majority of the reactive substrates, with the exception of Ni, acted as no more than a thermal gradient tube. This experiment indicated the need for a simpler reactive substrate section in the filter since most of the samples gave little or no information on chemical speciation.

Filter systems test 4 was run in early May using the same experimental setup used in tests 2 and 3 (Figure 2.2-7). The filter was redesigned based on the results of earlier tests. The stainless steel filter thimble contained three

sections: (1) a 34-cm-long nickel thermal gradient tube that had 0.5-mm-diameter wires of Ni, Pt, and Ag running parallel to its walls; (2) a 24-cm-long fiber filter composed of a 0.076-mm diameter Pt-10%Rh wire with a graded packing density of 3-5-6.3 percent; and (3) a 3-cm-long granular charcoal filter. The wires that stretched along the length of the thermal gradient tube were inserted to provide better information on chemical speciation. The wires were analyzed using the new SEM located in the Hot Cell Facility by wavelength and energy dispersive analyses. The Ni wire was included because it is the same material as the thermal gradient tube and will give an indication of chemical species deposited in the thermal gradient tube; the Pt wire was included because it is chemically inert to most fission products, except possibly Te at high temperatures; and the Ag wire was included to react with the gaseous iodine species HI and I_2. The Pt-10%Rh fibers were held in a stainless steel tube by stainless steel screens that were tack welded on each end. The tube had outside O-rings on each end to seal it inside the filter thimble and to prevent the flow of aerosol around the fiber filter, which was observed in test 3. A graded packing density was used to obtain the necessary filter efficiency and preclude a high pressure drop and filter plugging. The pressure drop across this filter was about 0.6 psi at a flow rate of 12 L/min. The granular charcoal filter was included to collect HI and I_2 gases.

Results of filter systems test 4 are plotted in the bar graphs in Figures 2.2-13 through 2.2-16. Five segments of the filter assembly were analyzed individually: the nozzle end of the filter thimble, two equal sections of the Ni thermal gradient tube, the fiber filter, and the granular charcoal and also the dry trap and the deionized water in the impinger. Each filter segment was first leached with water and then with 6M nitric acid. The water leachates were analyzed for iodine using a specific ion electrode, and the water and nitric acid leachates were analyzed for Cs, Te, Sn, and Ba using a DC plasma emission spectrometer.

The data from filter systems test 4 result in the following conclusions: The filter assembly appeared to be greater than 99 percent efficient. About 1.3 g of Cs was collected; most of the Cs deposited on the fiber filter as Cs metal aerosol. Wavelength dispersive analyses also identified individual particles composed of Cs alone (probably Cs_2CO_3 formed by oxidation of Cs metal and reaction with CO_2 after exposure to the atmosphere), CsI, and $Cs_{2-x}Te$ on the wires. The iodine generated appeared to exist primarily as CsI aerosol particles. The Sn appeared to be deposited as SnTe. However, since the Te-to-Sn ratio was about 8.6, Te probably also existed as Te, Te_2, H_2Te, and $Cs_{2-x}Te$. Metallic Te vapor and H_2Te are known to

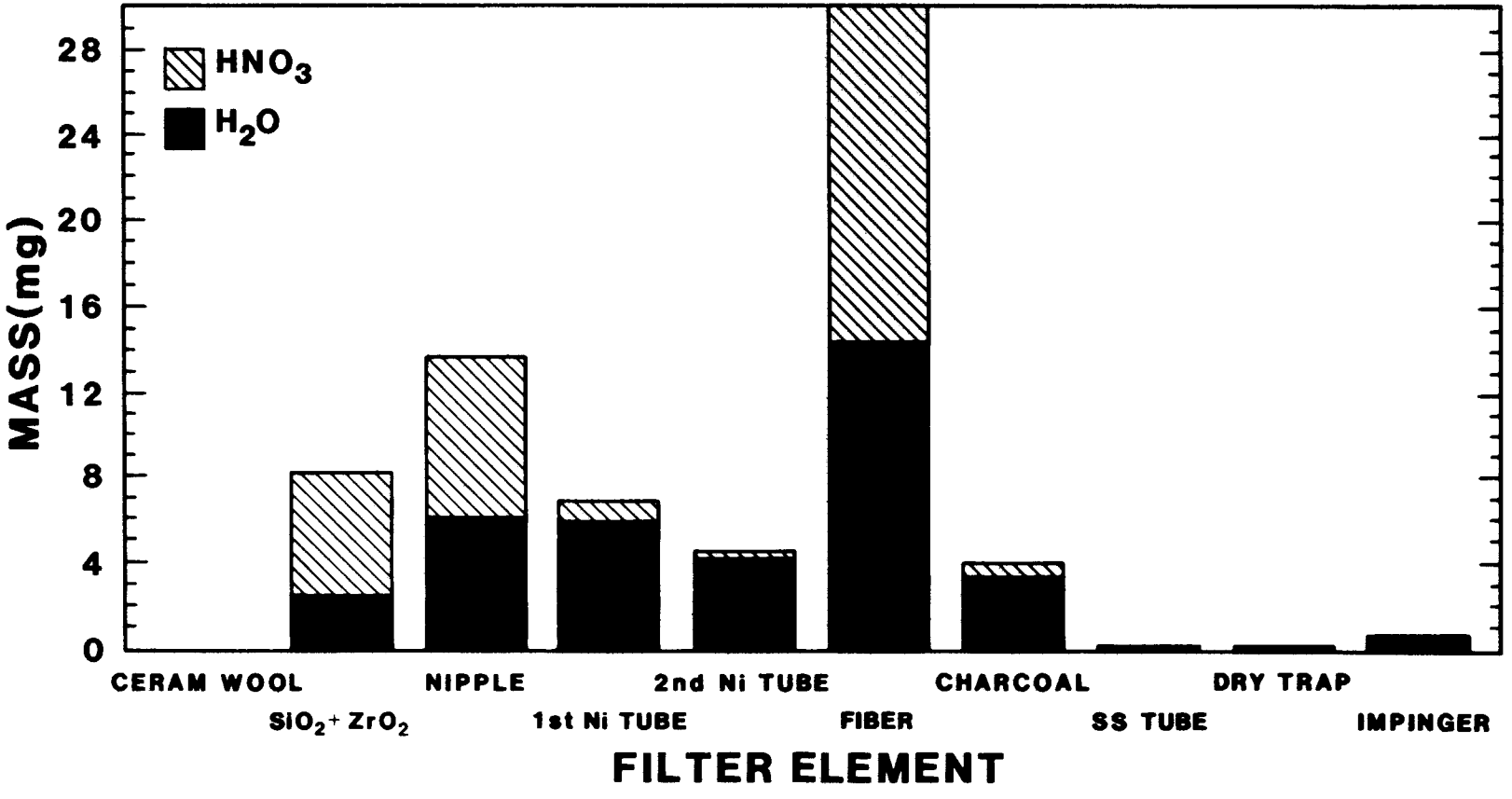

Figure 2.2-13. Filter Systems Test 4 Results for Tellurium

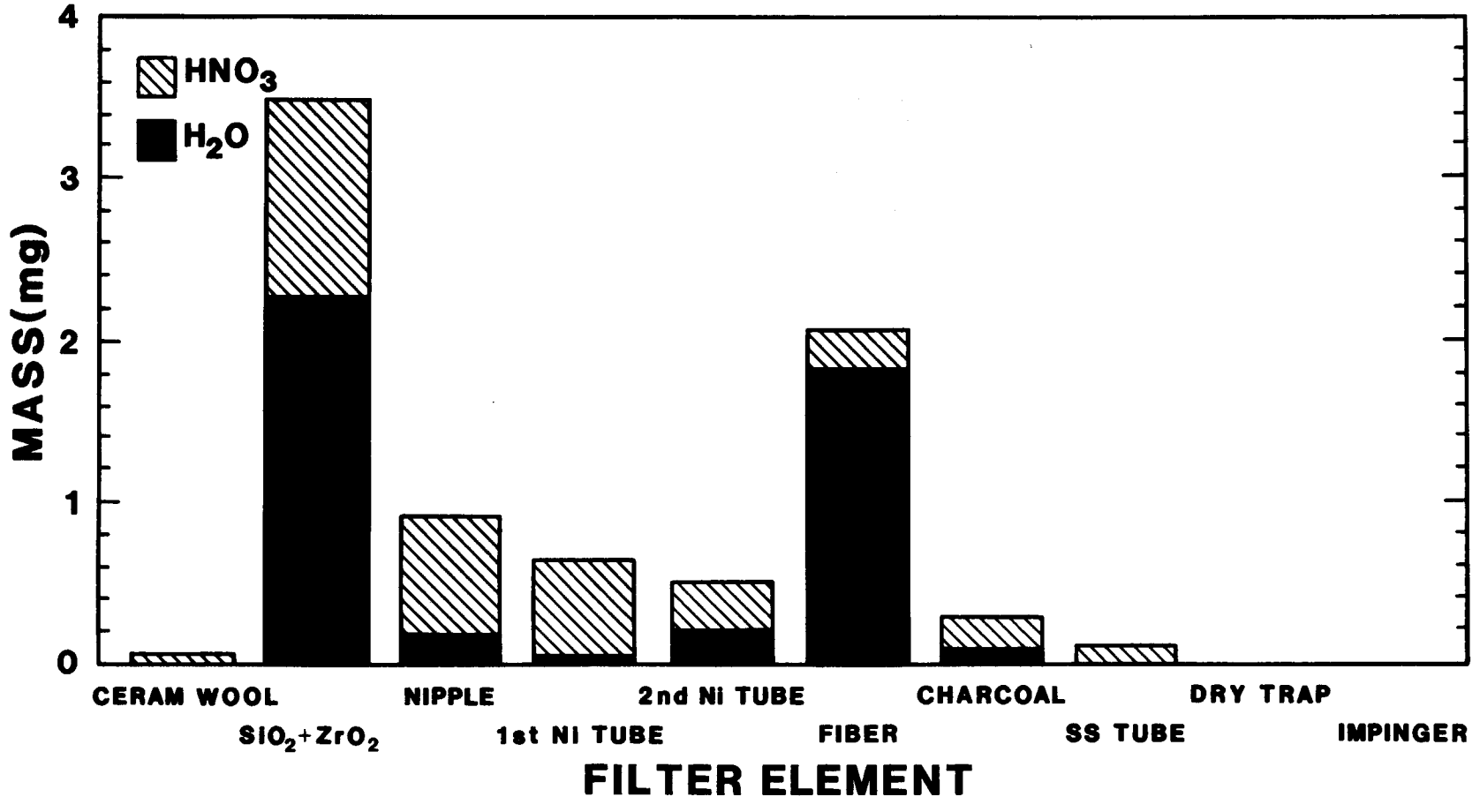

Figure 2.2-14. Filter Systems Test 4 Results for Tin

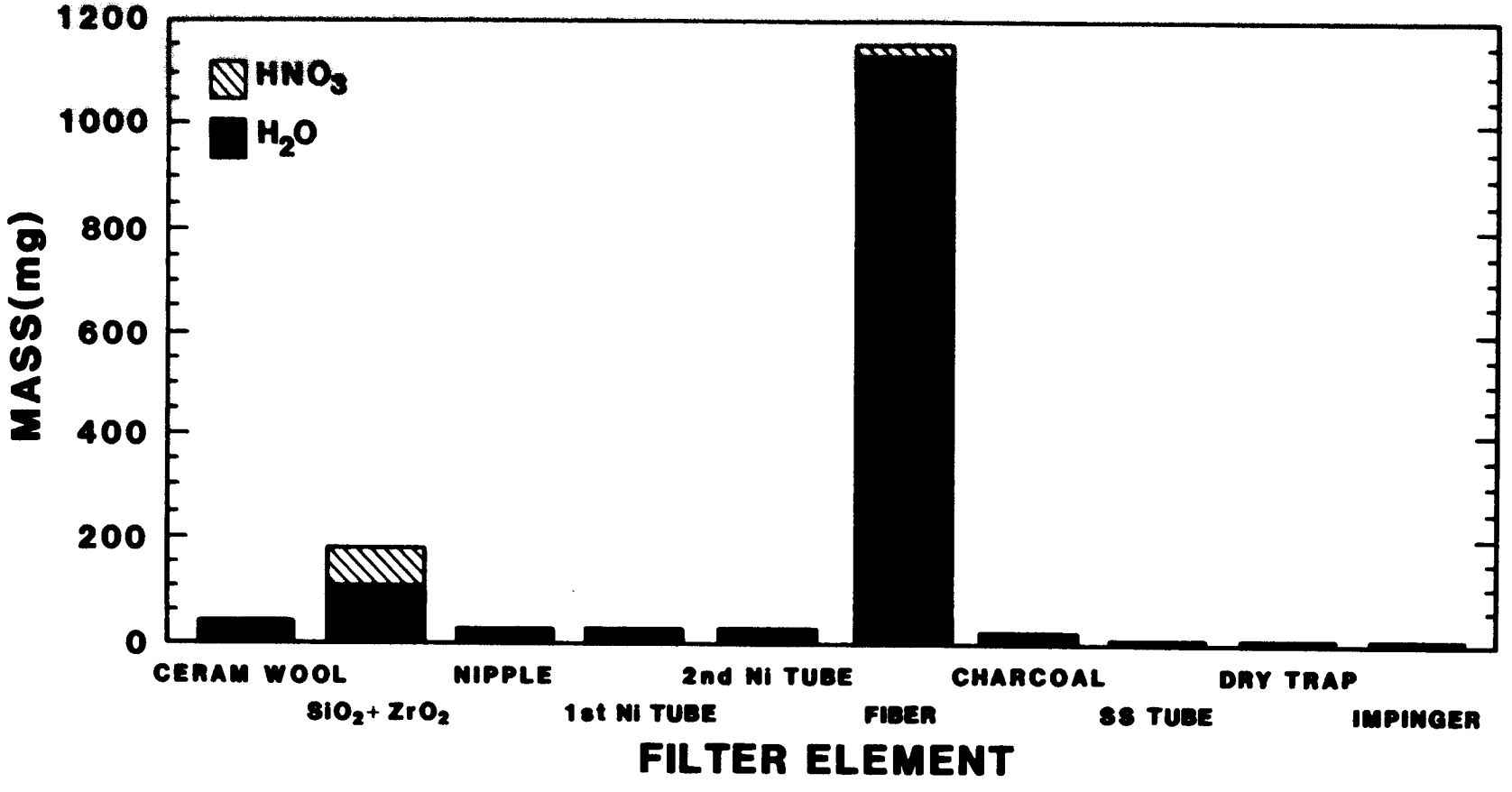

Figure 2.2-15. Filter Systems Test 4 Results for Cesium

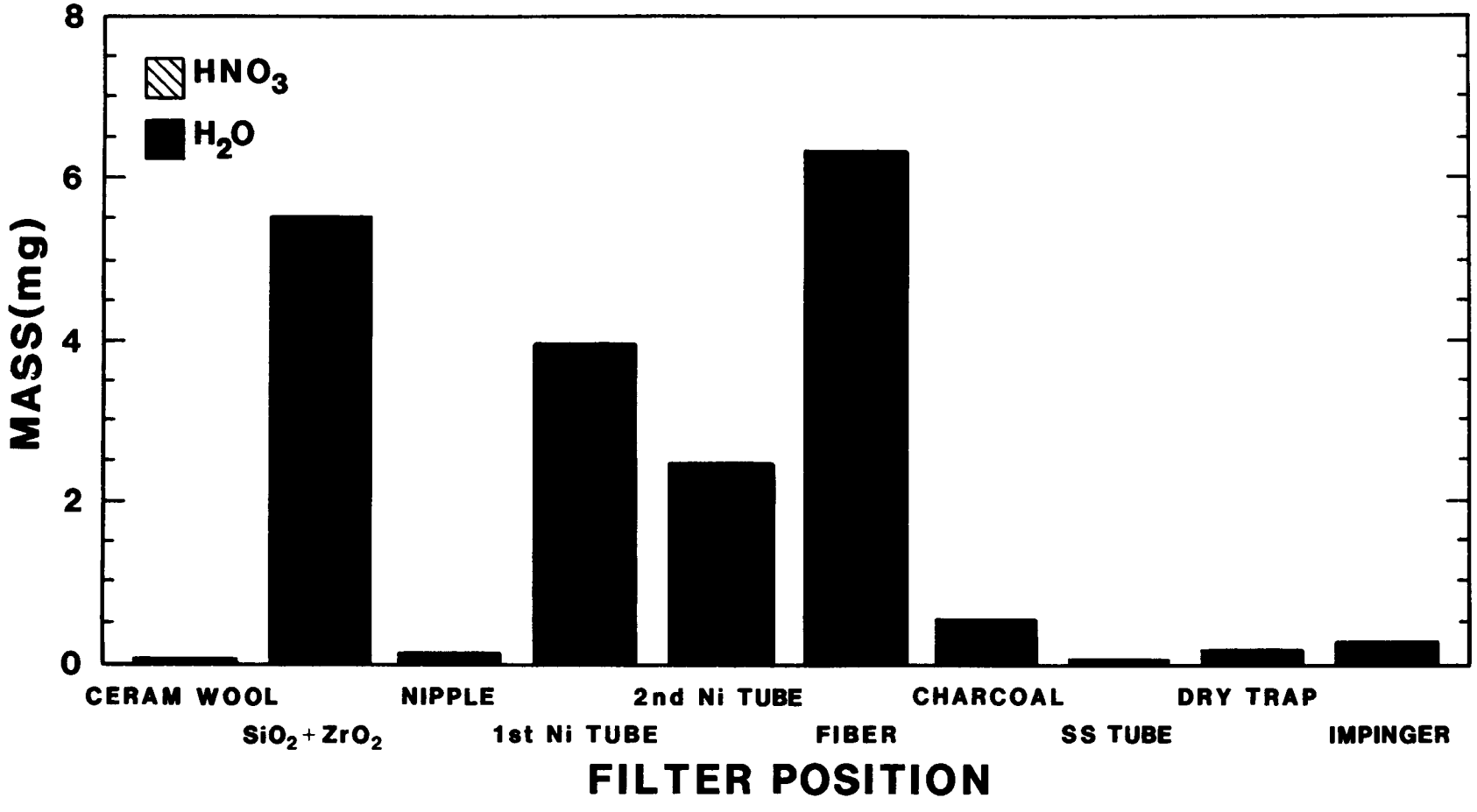

Figure 2.2-16. Filter Systems Test 4 Results for Iodine

react strongly with Ni and steel; however, under the test conditions, reaction of Cs_2Te with Ni and steel may be weak or even thermodynamically unfavorable. Estimated thermochemical data[65] suggest the reaction

$$3Ni_{(s)} + 2(Cs_2Te)_{(l)} \quad Ni_3Te_{2(s,l)} + 4Cs_{(g)}$$

is favorable at 700°C when Cs° pressure is less than about 0.2 atm and at 850°C (the maximum temperature of the filter assembly) when Cs° pressure is less than about 1 atm. Dissolution of Cs_2Te in Cs° liquid would lower the maximum Cs° pressure. Cesium pressures in the filter tests may have approached 0.2 to 1 atm at times, and given the uncertainty in the thermochemical data, the reaction of Cs_2Te with Ni may not have been favorable. The quantities of Ba that were generated were so close to the detection limit that the measured values were meaningless. This filter systems test was successful in that the filter was very efficient and our analyses gave some insight into chemical speciation. The final filter design will not be much different from the one used in test 4.

2.2.3 VICTORIA Modeling

The VICTORIA code is being developed both as a fission-product release/transport/chemistry module for MELPROG and as a stand-alone experiment analysis code. Both versions have been upgraded by the incorporation of a new chemical equilibrium solver, which is more than an order-of-magnitude faster than the previous version. This solver reduces the number of equations to be solved at the expense of introducing significant additional nonlinearity into the problem. The new package offers the advantages of greater speed of the solution and the ability to deal with zero quantities of some elements. The main drawback is that changing the species considered requires an extensive amount of algebra and code modification.

In addition to adding the new solver, a new chemistry data base has been adopted. This new set includes approximately 40 new chemical species. The most important changes have been the addition of uranates, zirconates, and molybdates, which makes the fuel chemistry portion of the code much more extensive and accurate than before.

The stand-alone version of the code has been used to perform scoping calculations for the first two tests of the ST series. The difference in the parameter space of the two experiments is an order of magnitude change in pressure with its concomitant changes in gas density and gas flow velocity. The scoping calculations performed, using the proposed test parameters, show that the release of fission products is hindered in the high-pressure test. The calculated

reduction in release is about 50 percent for all species except the noble gases (where only the timing of release is affected). This reduction demonstrates the competition between the intra- and intergranular mechanisms in the release phenomenon. The calculations show that an order-of-magnitude increase in the pressure is sufficient to show an effect while not being so large as to swamp out all other effects. The information obtained in these calculations concerning the chemical form of the released fission products has been useful in understanding the systems tests performed on the filter assemblies. In the very strongly reducing atmosphere planned for these tests, marked differences (versus an oxidizing atmosphere) are observed. In particular, the chemistry of iodine, barium, cesium, and tellurium are found to be quite different. The barium and cesium are found to be in the elemental form rather than as a compound; tellurium is carried largely as H_2Te, and iodine is found to be either elemental or as HI. These findings demonstrate the need for a vapor trap, i.e., charcoal filter, at the outlet of the filter assembly along with reactive filters.

The stand-alone version of VICTORIA is currently being modified for use in analyzing the results of the HI test series at ORNL. Changes in the code input to accommodate the different geometry of these tests have been made, and a zirconium oxidation model has been developed. Once this latter model (based on the Urbanic and Heidrick data) has been verified, detailed modeling of these experiments and a comparison of the experimental results with calculations will be made.

2.2.4 Experiment Preparations

The design of the ST experiment package has been completed, and all components for the first two ST experiments have been ordered or are being fabricated. It is anticipated that most components will be available in late August. The major modifications to the Sandia Hot Cell facilities are nearing completion. The development of the posttest analysis methods and development of hot cell tooling and fixturing are continuing.

3. LWR DAMAGED FUEL PHENOMENOLOGY

Sandia's LWR Damaged Fuel Phenomenology Program includes analyses and experiments that are part of the integrated NRC Severe Fuel Damage (SFD) Research Program. Sandia is investigating, both analytically and in separate-effects experiments, the important "in-vessel" phenomenology associated with severe LWR accidents. This investigative effort provides for two related research programs: the Debris Formation and Relocation (DFR) Program and the Degraded Core Coolability (DCC) Program. The focus of these activities is to provide a data base and improved phenomenological models that can be used to predict the progression and consequences of LWR severe core damage accidents. The DFR experiment program provides unique data on in-vessel fuel damage processes that are of central importance in determining the release and transport of fission products in the primary system. The DCC experiment program, completed early in this semiannual period, provided data on the ultimate coolability of damaged fuel configurations. Models coming from both programs are used directly in the MELPROG code.

3.1 ACRR Debris Formation and Location (DFR)
(R. O. Gauntt and K. O. Riel, 6423)

3.1.1 Introduction

Evaluation of the potential consequences of severe core damage accidents requires the development and verification of computer models that account for the complex fission-product release and fuel damage phenomena occurring in core uncovery accidents. The NRC-sponsored DRF experiments are being performed at Sandia to provide data on the effects of key variables and conditions on the progression and severity of core damage processes. Examined in the DFR experiments are a range of conditions of initial clad oxidation, steam flow rates, system and rod internal pressures, and the effect of control rod materials on damage. The purpose of these experiments is to provide a data base of core damage phenomenology over a broad parameter space for use in model development and verification.

The DFR test series consists of four experiments using fresh fuel. The first two tests, DF-1 and DF-2, were designed to investigate fuel degradation under conditions of low and intermediate early clad oxidation and were intended to provide a comparison to later data on irradiated fuel. Initial oxidation conditions were achieved by holding the fuel at elevated temperature for a controlled period prior to the power increase and subsequent rapid oxidation transient. A higher initial clad oxidation condition led to more robust

oxidized clad shells, which seemed to "channel" the molten cladding along one side of the fuel rod. This resulted in more nonuniform fuel erosion along the side of the pellet that experienced the channeled clad relocation. A lower initial clad oxidation condition led to a more coherent and rapid slumping of the molten cladding and more uniform fuel pellet erosion.

The DF-3 and DF-4 tests were designed to investigate the effect of control materials on fuel degradation and to obtain phenomenological data on behavior of control materials in a severe accident. In DF-3, the central rod of a nine-rod bundle was replaced by a stainless steel tube containing the silver-indium-cadmium control alloy with the steel tube, in turn, enclosed inside a zircaloy guide tube. The DF-4 experiment includes a structure representative of the boron carbide filled control blade used in boiling water reactors. The control blade is surrounded by a zircaloy channel box, which represents the fuel element canister in the BWR. In this test 14 fuel rods are used instead of the usual nine. Current progress has been focused upon analysis of DF-3 and the design and pretest analysis of DF-4. These efforts are discussed further in the following sections.

3.1.2 The DF-3 Ag-In-Cd Control Rod Experiment

The DF-3 experiment addressed the influence of a PWR control rod, containing AG-In-Cd alloy, upon the fuel and clad damage phenomenon. Specific goals of the PWR control rod experiment were to characterize the timing and magnitude of the control material aerosols and to assess the effect of the control materials on structure interaction and relocation with specific emphasis on Ag-Zr alloying, clad relocation and oxidation, and blockage formation. The center rod in the nine-rod experiment geometry was replaced with a zircaloy sheathed control rod containing Ag, In, and Cd (proportions 80/15/5) sealed in a stainless steel tube. Steam flow to the test bundle was 0.07 g/s/rod and the bundle heatup rate from fission heating in the fuel rods was ~1 K/s. The on-line data characterizing the test progression is presented in the following section. A subsequent section details the metallurgical characterization with respect to key questions addressed by this experiment.

3.1.2.1 Test Progression

The average power generation in the DF-3 test bundle is shown in Figure 3.1-1. In the early portion of the fuel heating history, the bundle power was adjusted to maintain the fuel heatup rate on a nominal 1 K/s ramp, with numerous small boosts in power applied to maintain heatup rate as the fuel temperature rose and the radial heat loss increased.

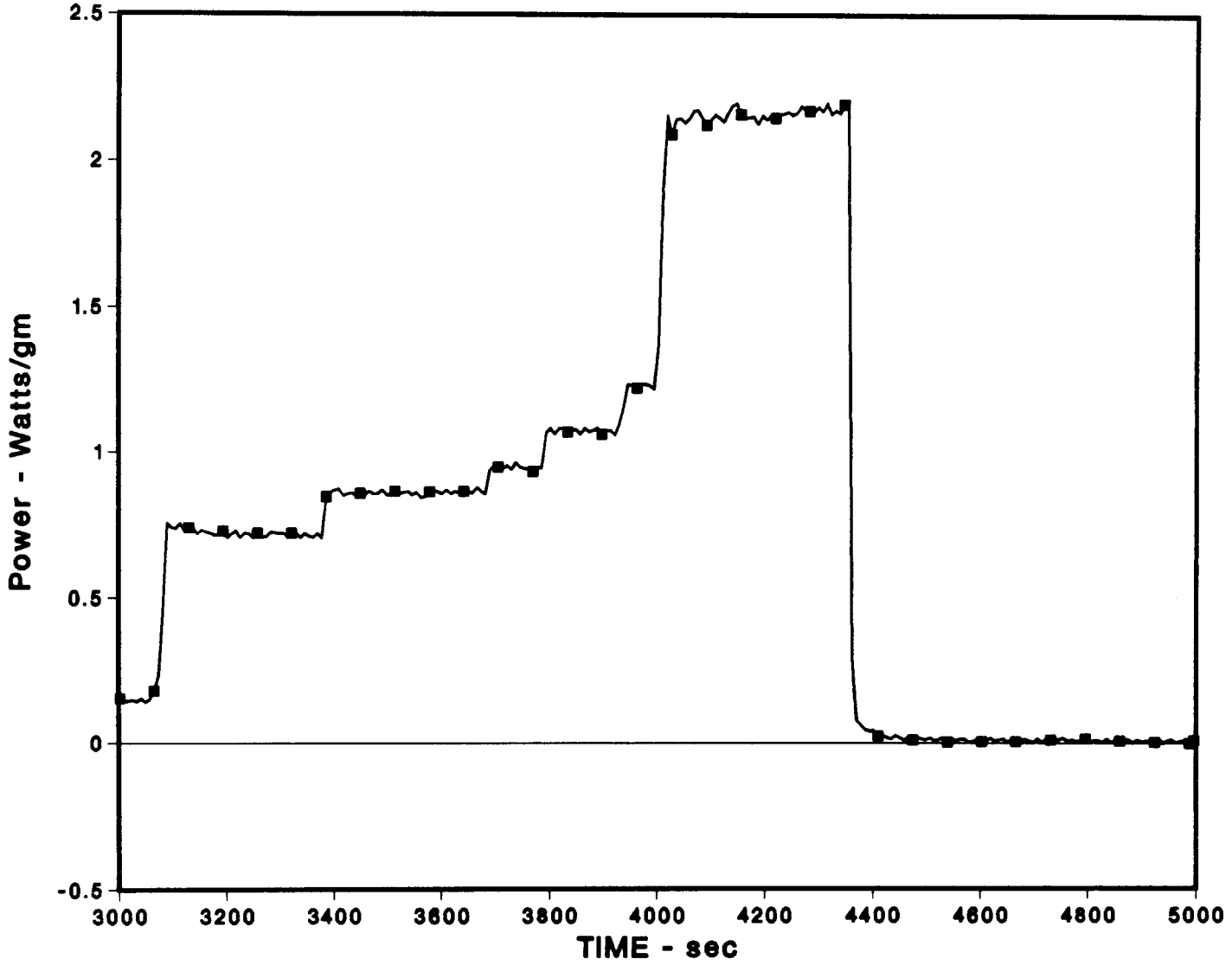

Figure 3.1-1. Fission Power Generated in the DF-3 Test Bundle

This moderate heating rate was maintained over the largest part of the bundle until about 3900 s, at which point, peak fuel temperatures exceeded 1500 K. At that time, an intense localized oxidation front developed in the upper portion of the bundle and heatup rates increased significantly due to rapidly increasing oxidation power generation. The bundle power was then boosted significantly at 4000 s to support the rapidly increasing radial heat loss during the high temperature phase of the test. The development of the localized oxidation front is evident in the W/Re thermocouple data, plotted on an axial basis in Figure 3.1-2. (W/Re thermocouples affect the temperature measurement by virtue of the thermal inertia and heat conducting properties of the thermocouple assembly, and because of this, measure a temperature that is on the order of 200 K lower than the actual fuel surface temperature.) Relative to the bottom of the fissile fuel zone, the zircaloy oxidation power peaked at ~36 cm. The oxidation reaction subsequently proceeded downward toward the bottom of the bundle and the source of the steam. The control rod guide tube surface temperature at the 44-cm location is shown in Figure 3.1-3. This zone heated at a rate of 1.12 K/s up until the measuring thermocouple failed at 4000 s (1775 K). After this, the W/Re instrumentation (Figure 3.1-4) indicated much more rapidly escalating temperatures. Relocation of control rod materials was first detected (viz., lower fuel support plate temperature, Figure 3.1-5) at 3910 s at which time the control rod guide tube temperature (slightly above the peak oxidation zone) was 1670 K. This suggests that control rod failure did not occur before the inner steel tube reached its melting point at ~1700 K, a few centimeters below the 44-cm thermocouple location.

Although control rod failure and relocation was detected at 3910 s, significant aerosol release was not observed in the film record until 4035 s. This observation suggests that the aerosol observed was not from the control materials because the onset of control material aerosol should have occurred 75 s earlier. The peak fuel temperature at the time of dense aerosol production is estimated to be ~2000 K, very near the melting point of zircaloy (~2030 K), and therefore, the optical occlusion may have been primarily due to the formation of tin aerosol released from the zircaloy. This is a somewhat unexpected result. Cadmium vapor released at ~1700 K should have formed an aerosol in the upper steam mixing chamber since its dew point is ~1100 K, and the mixing chamber temperature should have been below this value.

At 4200 s, steam flow was interrupted by a buildup of noncondensible gas pressure (evidently hydrogen) in the test section (Figure 3.1-6). Steam flow was recovered

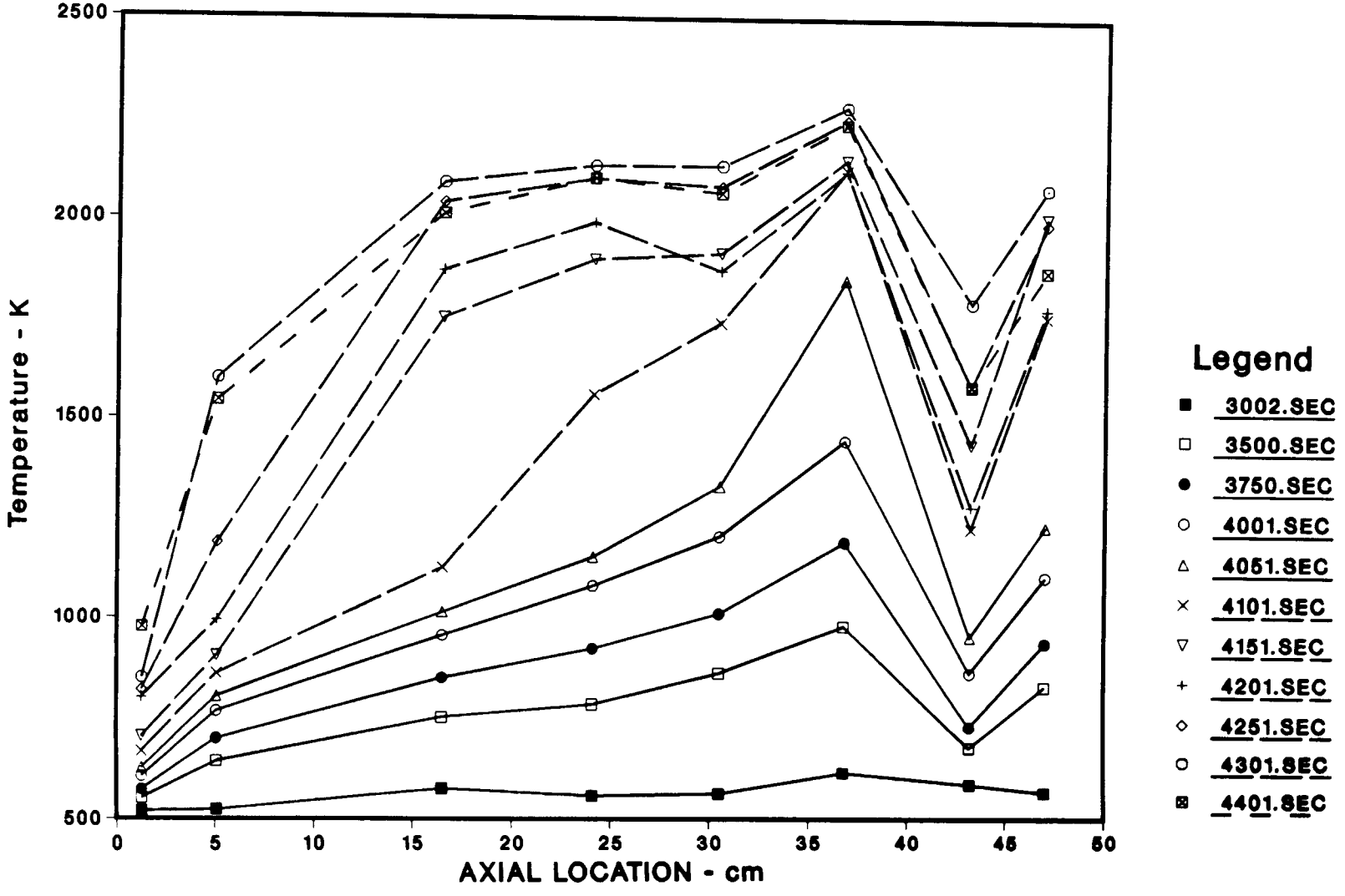

Figure 3.1-2. Axial Temperature Profile of DF-3 Test Bundle Based on W/Re Thermocouple Data

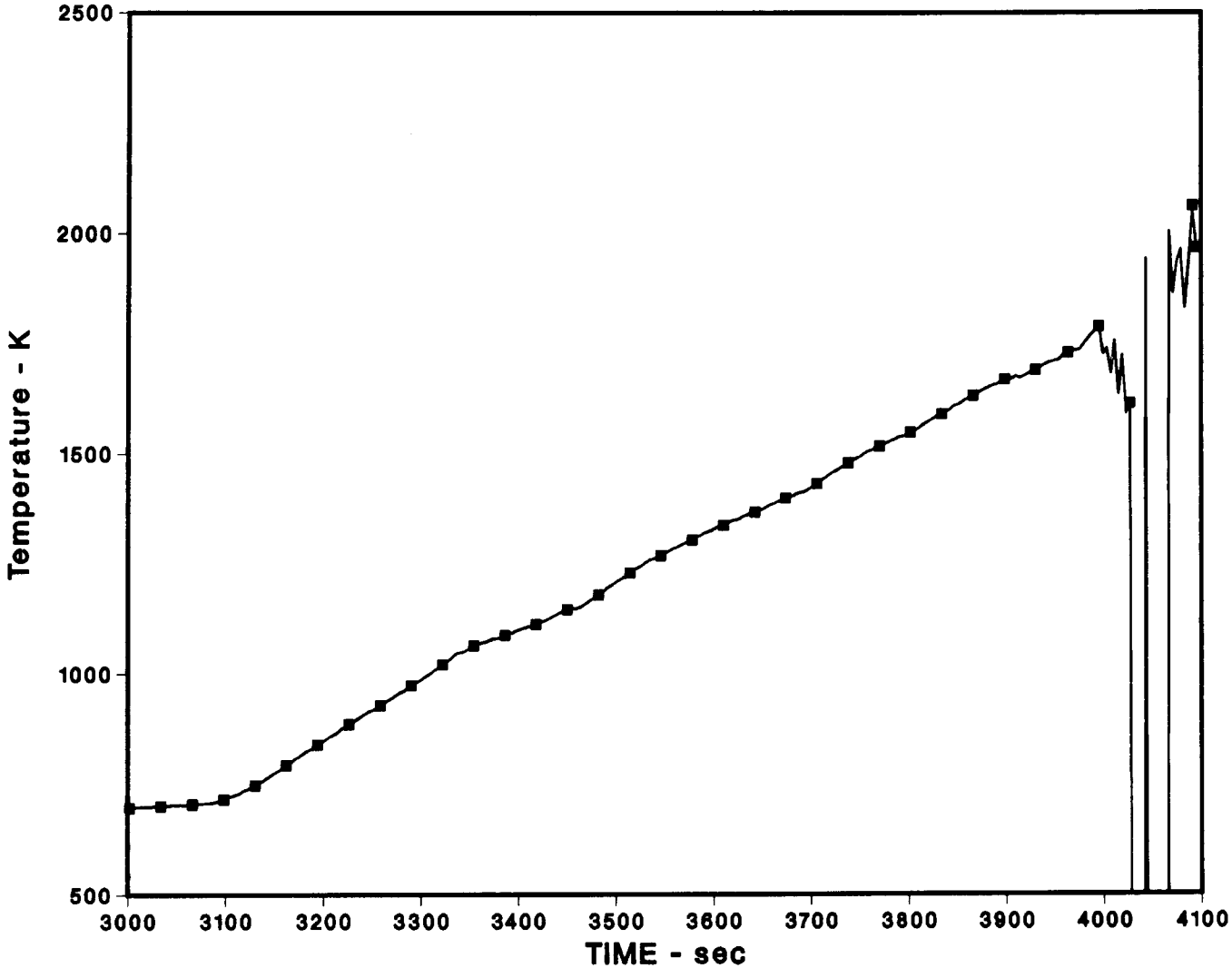

Figure 3.1-3. Temperature of the DF-3 Control Rod Guide Tube at the 44-cm Location. Heatup rate at this location proceeds at 1.12 K/s until thermocouple failure at 4000 s (Pt/Rh thermocouple data).

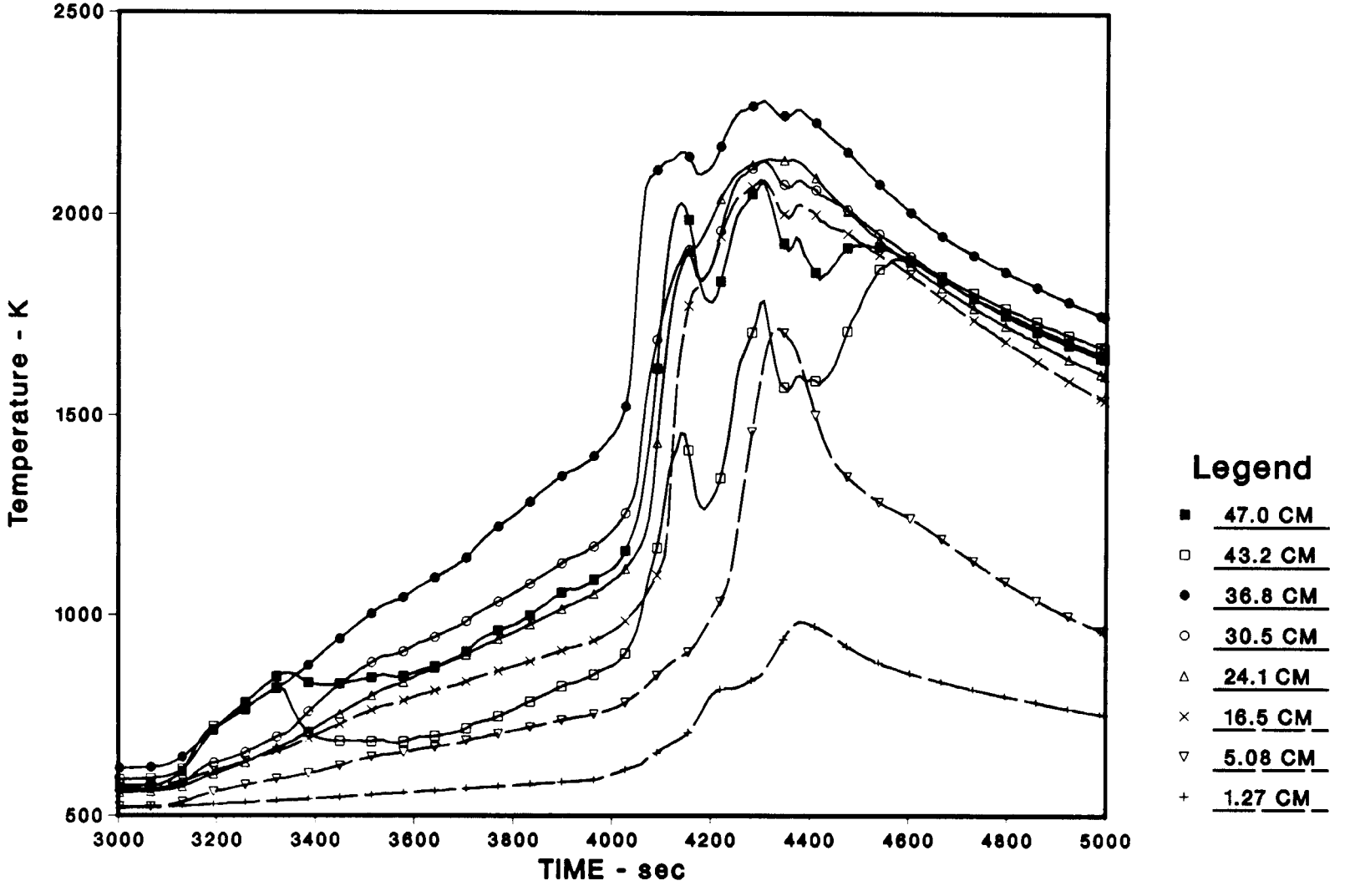

Figure 3.1-4. W/Re Thermocouple Instrumentation in DF-3 Test Bundle Shown on a Time Basis

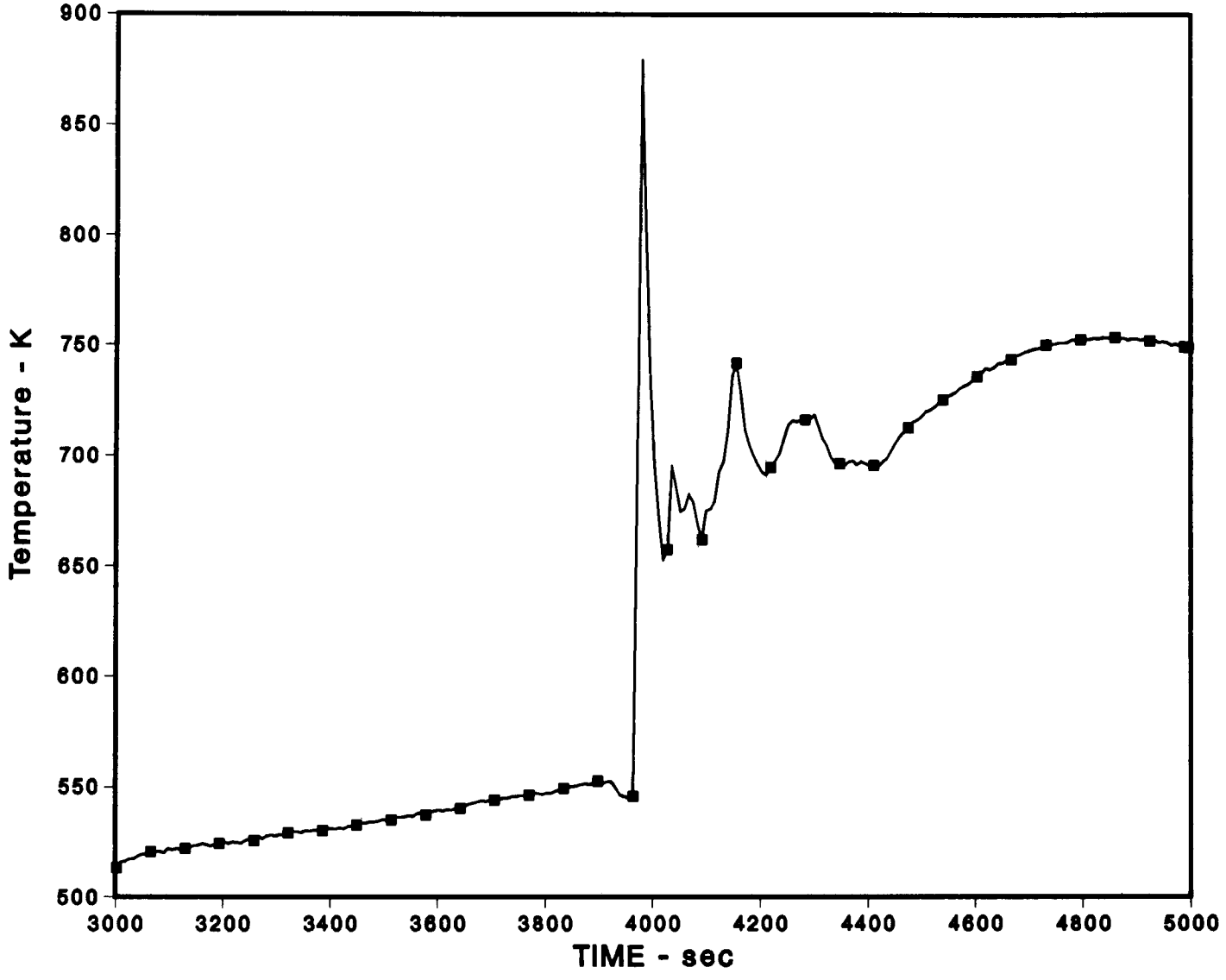

Figure 3.1-5. Response of Lower Fuel Support Plate Thermocouple (DF-3). The sudden discontinuity in response at 3910 s indicates arrival of molten control material at the bottom of the rod bundle.

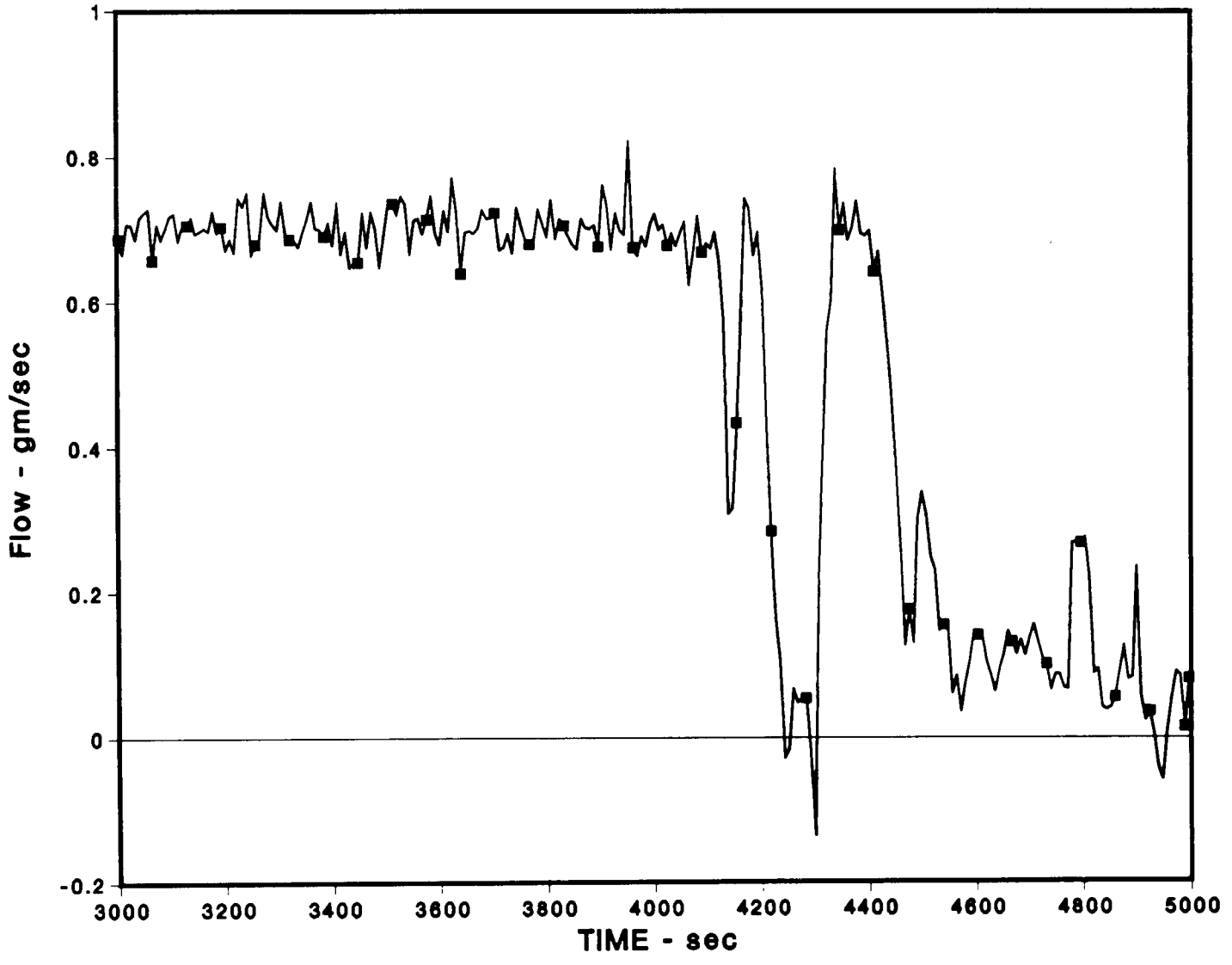

Figure 3.1-6. Steam Flow Introduced to the DF-3 Test Bundle. Loss of steam flow occurs after 4000 s due to hydrogen accumulation in the test section.

temporarily but was lost again at 4420 s, again by test section pressurization. After this, the test was terminated.

Determination of the hydrogen production in DF-3 is complicated by the fact that the CuO reaction beds failed to operate, allowing the test section to pressurize with unreacted hydrogen. Hydrogen production will be estimated based upon this measured pressurization after some analysis has been performed.

3.1.2.2 Posttest Examination of DF-3

Posttest examination of DF-3 involved both x-radiography (tomography) and destructive examination. The tomographic characterization was performed using 32-view x-radiographic reconstruction, whereby cross-sectional views of the test section were generated at numerous axial locations. Figure 3.1-7 shows the tomographic cross-section reconstruction of several axial planes. The features revealed in the reconstructed views serve to "interpolate" between the limited number of actual cuts prepared. After being stabilized with epoxy resin, the DF-3 test section was cut at five axial locations and polished for metallograhic examination. The axial locations of the cross-sectional cuts were 30, 45, 135, 295, and 460 mm relative to the bottom of the fuel fissile zone. Low magnification photographs of the fuel bundle cross sections were prepared. Based upon the cross-sectional samples and x-radiographs (tomographs) of the posttest bundle configuration, it is evident that fuel damage and erosion in DF-3 was less extensive than in previous tests. High magnification photographs of the cross sections gave information on the degree of interaction between the control rod components and the fuel and cladding. Low magnification photographs of the test bundle are shown in Figures 3.1-8 through 3.1-12. Salient features of each of the cross sections are described in the following paragraphs.

Cross Section at 460 mm: The eight fuel rods in this cross section--located just below the top of the fissile zone--moved very little from their original positions. (Rod 3 was broken from the sample during cutting.) The fuel pellets were intact although some circumferential cracking was seen; loss due to dissolution averaged 5 percent. The cladding was completely oxidized to ZrO_2. The cladding shells were each split in at least one place and did not maintain their original radius of curvature. Loss of material from the clad ranged from 40 to 85 percent of the theoretical, fully oxidized area. A collapsed ZrO_2 shell was found in the region of the control rod. Ceramic melts were seen between the rods and the cladding shells and in the control rod shell in two principal morphologies. One, a single-phase

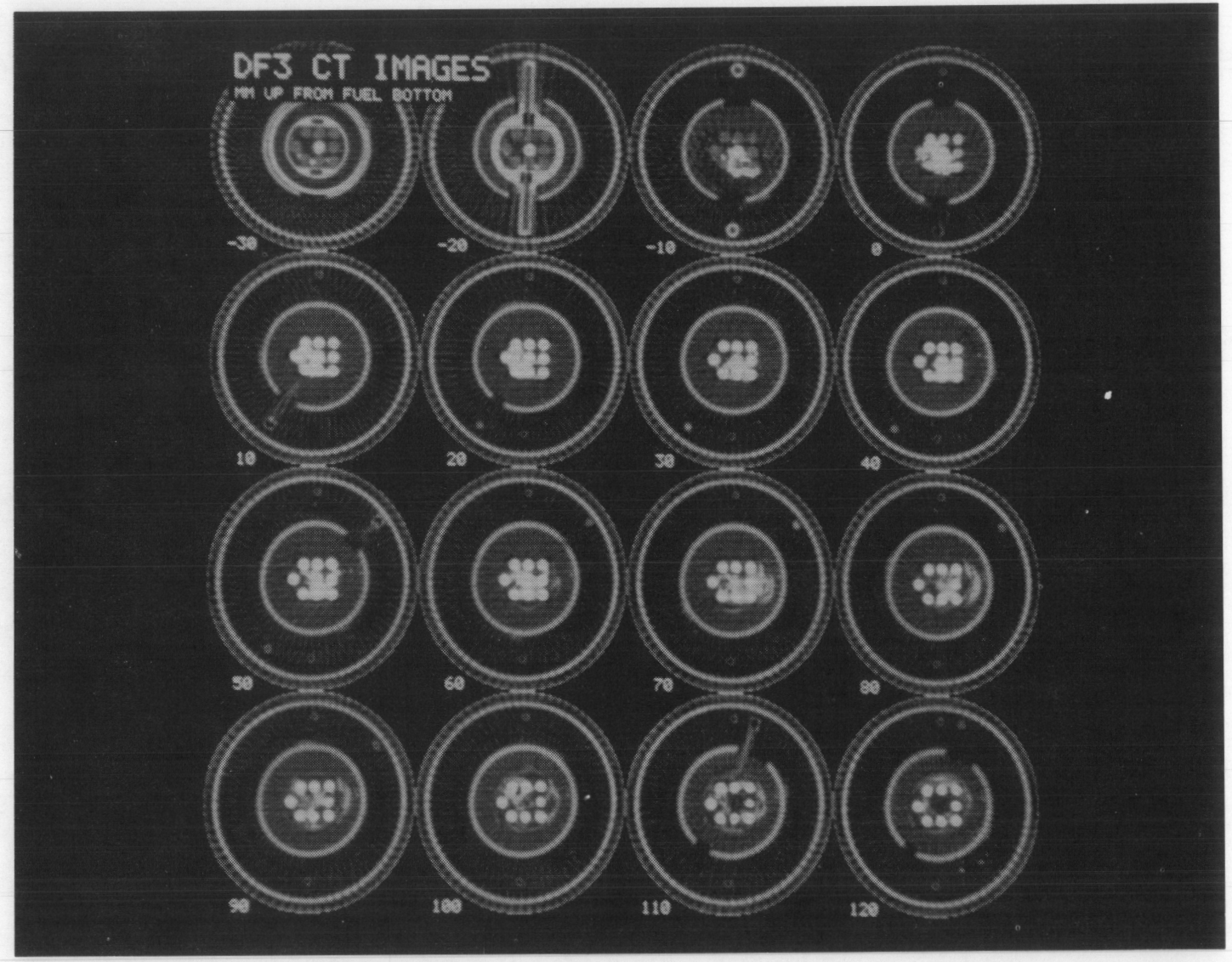

Figure 3.1-7. Tomographic Cross-Sectional Views of the DF-3 Test Bundle Showing the Extent of Control Rod Failure and Relocation

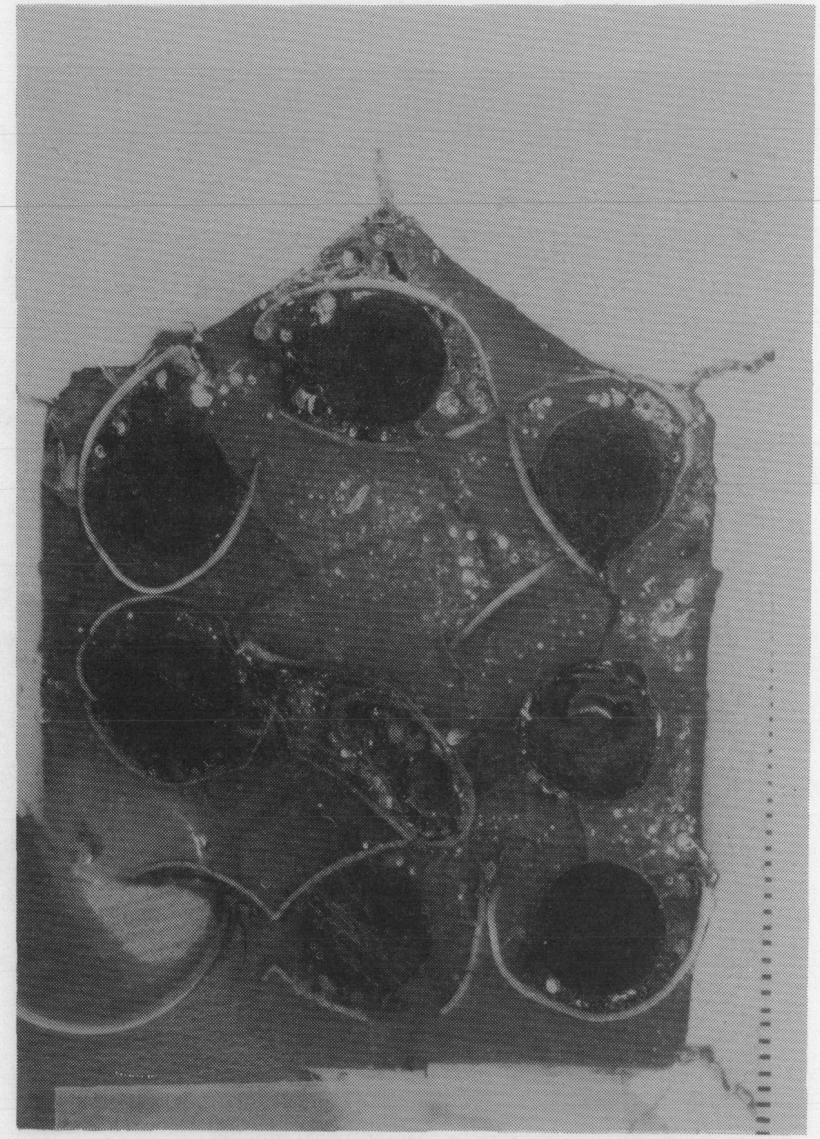

Figure 3.1-8. DF-3 PIE: Cross Section at the 460-mm Location Near the Top of the Bundle

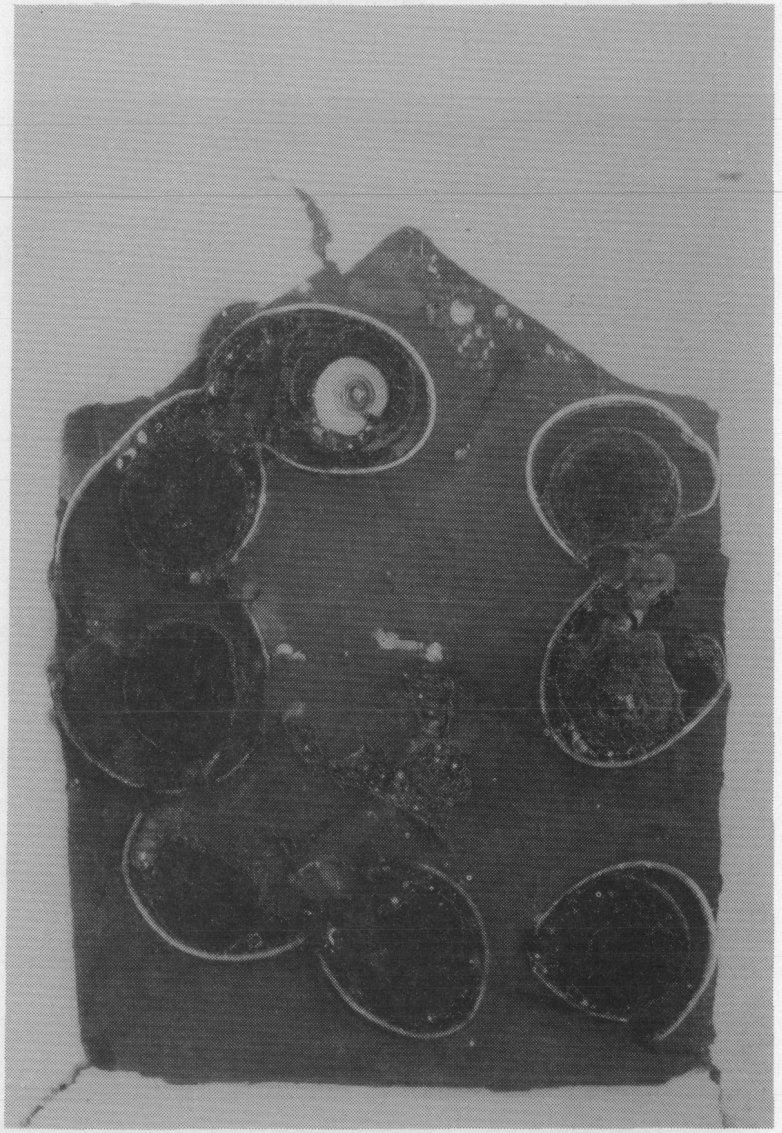

Figure 3.1-9. DF-3 PIE: Cross Section at the 295-mm Location Near the Middle of the Bundle

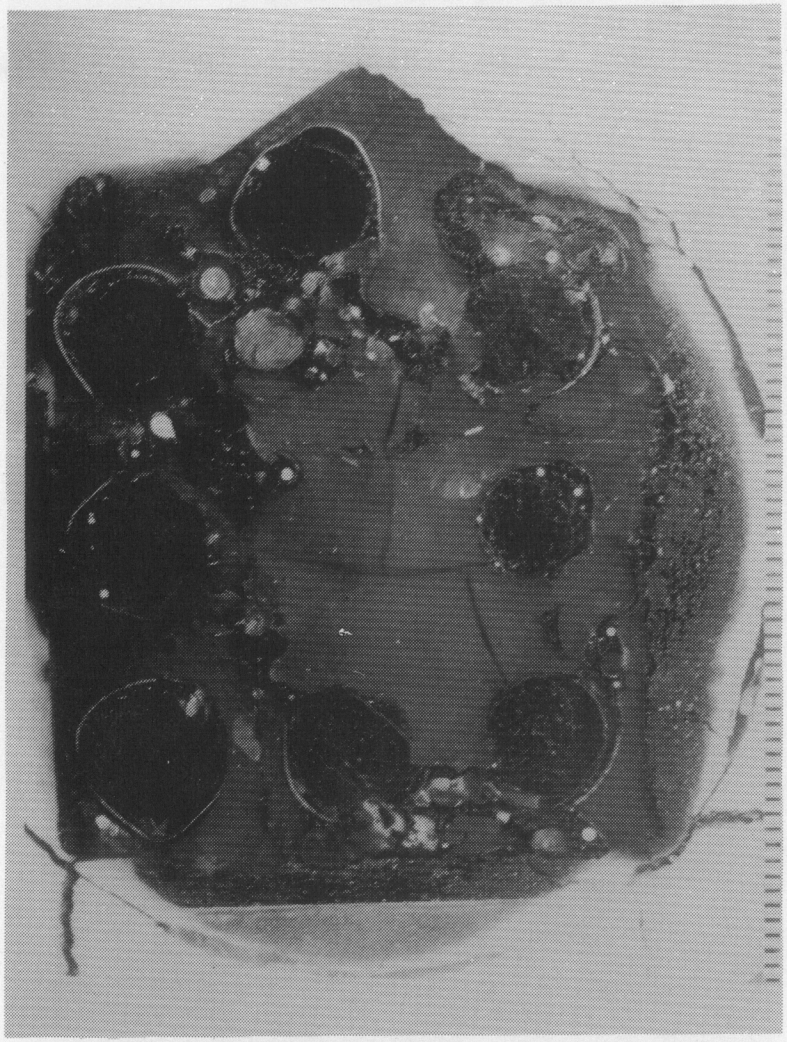

Figure 3.1-10. DF-3 PIE: Cross Section at the 135-mm Location at the Grid Spacer Region

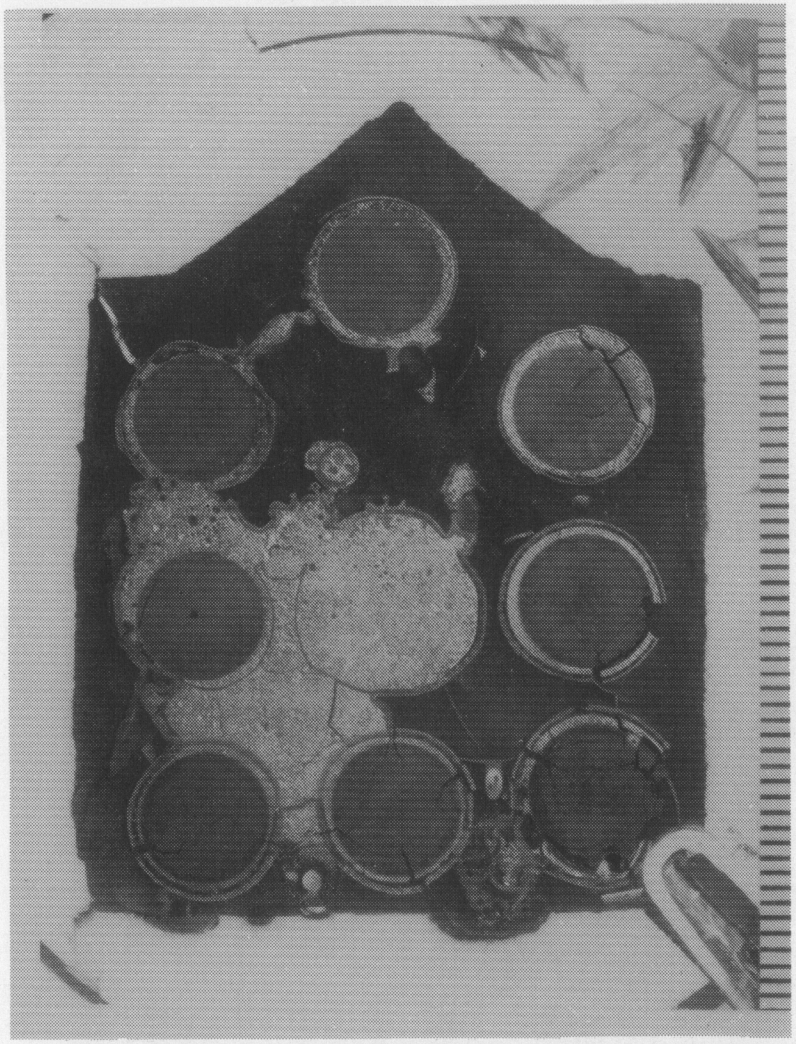

Figure 3.1-11. DF-3 PIE: Cross Section at the 45-mm Location Below the Grid Spacer Region Where Relocated Material Accumulated

ceramic with a marked columnar grain structure, was found near oxidized cladding shells and free surfaces. The other, a porous, equiaxed ceramic comprised of two ceramic and one metallic phases, was seen near regions of fuel attack. Some large metallic particles were also found in the melt.

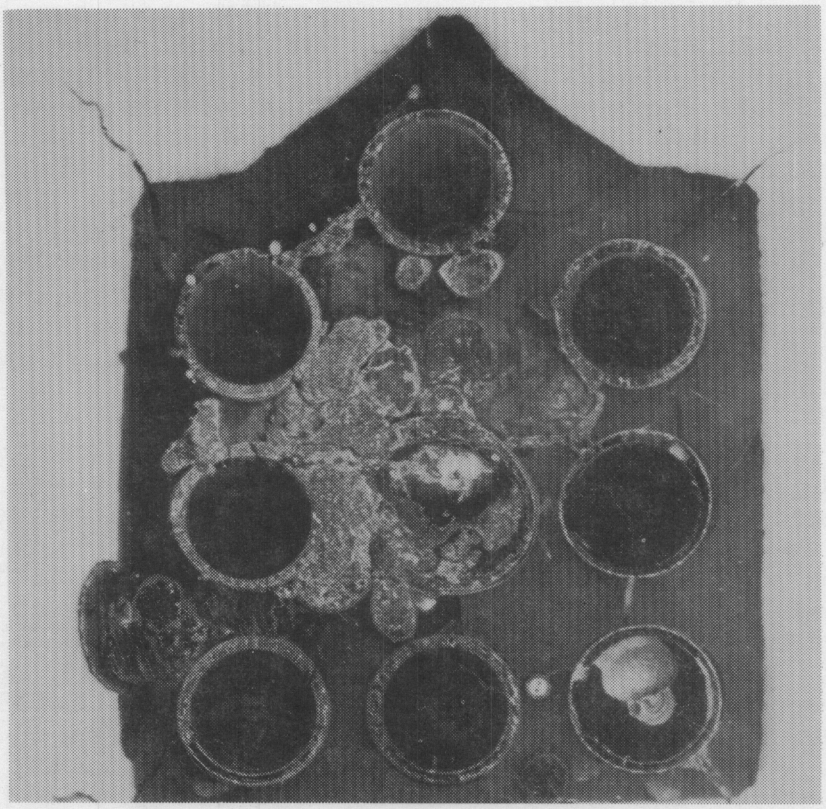

Figure 3.1-12. DF-3 PIE: Cross Section at the 30-mm Location

Cross Section at 295 mm: The fuel rods were slightly displaced from their original positions in this cross section, which was near the middle of the bundle. Some circumferential cracking of the pellets was seen, and fuel loss from Rod 3 due to fallout could not be ruled out. Fuel loss caused by flowing material was apparent on all of the pellets. (Al_2O_3 was not associated with this dissolution.) Losses ranged from 5 to 35 percent, averaging 15 percent. The clad, completely oxidized, had a layered, columnar structure and was split and opened as in Sample 460. Clad losses averaged 70 percent. The two melts are also seen in this cross section. The multiphase melt was particularly associated with attacked areas of pellets. The melts were located primarily between pellets and clad, although there was some flow on the outer clad surface. Remnants adhered to almost all of the inner clad surfaces, indicating that large quantities of molten material flowed through this

elevation during the experiment. Otherwise, very little material was found in the central channel. There was minimal shroud attack.

Cross Section at 135 mm: In this cross section, cut through the area of minimal control rod density and located in the original grid spacer position, the fuel rods maintained their original positions. Some minor circumferential cracking of the fuel was seen, but fuel loss, which averaged 15 percent, could clearly be ascribed to dissolution by flowing material. The clad, completely oxidized, had a multilayered columnar structure. Considerable thinning of the cladding occurred; losses ranged from 80 to 100 percent, averaging 90 percent. The same two melt morphologies were seen at this elevation. The melts were located between the pellet and clad and throughout the flow channel, except for the region occupied by the control rod, which was void. Shroud ablation and attack were evident.

Cross Section at 45 mm: In this cross section, which was made through the region of material gain below the original grid spacer location, the fuel rods maintained their original spacing. Cooldown cracks traversed most of the rods at this elevation. Although shallow interaction zones were visible on the pellet surfaces, there was no discernible removal of fuel. The completely oxidized clad maintained its integrity until late in the test when some segments were dissolved by flowing molten material. There appeared to have been in situ attack of oxidized clad by the same melt. The melt, which varied little in makeup over the cross section, was comprised of a two-phase matrix containing spheres of Ag and was enclosed in a shell of impure ZrO_2. Although of metallic reflectivity, the melt exhibited ceramic mechanical behavior. The same melt occupied the control rod position and was found in the pellet-clad gaps. Limited shroud attack was seen where molten droplets contacted it. In contact with Rod 9 was a sheathed W/Re thermocouple.

Cross Section at 30 mm: This cross section was cut just below Sample 45 where the deposition of relocated molten material had shifted towards Rods 1 and 4. Complex fuel-melt interaction zones had formed but there was no fuel removal. A very thin oxide shell was found around the outside of the clad; although in some areas a structure resembling prior ß-Zr was seen, this did not represent original clad. In spite of the proximity of this section to the one above, the nature of the melts here was very different. The material in the control rod position consisted of an outer shell of ZrO_2, a layer rich in Fe, and a central deposit of silver. Four complex structures were seen in the clad-pellet gaps. There was slight shroud attack where molten droplets had contacted it.

3.1.2.3 Interactions Involving Control Materials

Ag Interactions: In DF-3, the silver control alloy quickly relocated to the lower nonfissile region of the test upon melting of the stainless steel tube, beginning at 3910 s, with all regions above the grid spacer failed and relocated by 4150 s. The silver was found to be basically immiscible with other components and very little Zr was found to be alloyed with the relocated Ag. Alloying between Ag and Zr might have been discouraged by the ZrO_2 crust on the cladding.

Stainless Steel Interactions: Components of stainless steel, namely Fe and Cr, were found to form a complex eutectic involving Zr, U, and O. The only major effect that Fe and Cr might have on fuel attack would be in lowering the freezing point of the liquid carrying the Zr, thereby prolonging the time of UO_2 attack. Neither Fe nor Cr should reduce UO_2 based upon the free energy for these reactions. Although stainless steel and zircaloy form a low melting point eutectic, and could lead to an early control rod failure mechanism, no evidence of this mode of failure was seen in DF-3.

In summary, the effects of PWR control materials upon the fuel damage processes appear to be minimal. The Ag-In-Cd alloy melted and relocated early in the damage sequence and relatively little interaction between control alloy components and other structures occurred. The control rod failure was closely correlated with reaching the melting point of the stainless steel tube wall encasing the control alloy. Silver was found to be generally immiscible with other components. Steel components, Fe and Cr, were found to form a eutectic with U-Zr-O, possible lowering the freezing point of the liquid carrying Zr thus extending slightly the time of $Zr-UO_2$ attack. Cadmium aerosol in DF-3 could not be verified and, as yet, is an unresolved question in this experiment. It is suspected that Cd ultimately may be found in the low pressure-low temperature condenser region of the experiment; however, this has not been pursued at this time.

3.1.3 The DF-4 BWR B_4C Control Blade Experiment

Previous experimental investigations into severe fuel damage phenomenon have been focused primarily on PWR related damage processes. In that BWR designs are very different from PWR designs and because of the lack of any experimental studies of BWR geometry effects on severe core damage, the DF-4 experiment has been designed to specifically address BWR geometry effects. The key BWR geometry to be investigated in DF-4 is the zircaloy fuel assembly channel box and the

stainless steel B_4C filled control element. These components are shown in Figure 3.1-13. Major uncertainties concerning BWR accident progression to be addressed in DF-4 include:

1. The relative heatup rate and oxidation behavior of the BWR fuel clad, canister wall, and control blade structures.

2. The potential interaction between the B_4C powder in the control element and steam, which may constitute an additional vigorous heat source as well as a source of volatile boric acid species that can affect Cs and I fission-product transport.

3. The interaction effects between the steel control structures and the zircaloy channel box wall.

4. The integrity of the channel box with respect to side wall damage, and the potential for tight blockage formation within the channel box.

(The latter issue relates to IDCOR assertions that BWR hydrogen production in BWR severe core damage accidents is significantly diminished by the formation of tight blockage formation in the lower canister region, which prevents steam from reaching the upper fuel cladding and channel box zircaloy.)

Figures 3.1-14 shows the relation between the actual BWR geometry under investigation and the DF-4 experimental representation. Because of the increased thermal mass of the can wall and control structure over previous DFR test designs, the number of fuel rods in DF-4 was increased to 14. As seen in Figure 3.1-14, two distinct flow channels exist in this design, one flow path associated with the fuel rod zone and the other, with the intercanister flow path where the control blade is located. This allows different steam flow rates to be administered to the fueled zone and the interstitial control blade zone, since in the BWR, these zones are discrete and have largely differing steaming rates during a core uncovery accident. In DF-4, the control blade tip region is being modeled since this region is supplied the richest steaming rate in the actual BWR and, therefore, is likely to be the region where the severest oxidation initiates.

Pretest analysis of the DF-4 test is facilitated by use of a computer code which was developed at Oak Ridge National Laboratories by the BWR Severe Accident Technology (BWR-SAT) Division. The computer code, MARCON-DF4, is based upon new models incorporated in MARCON 2.1B for BWR analysis and models the unique BWR features in DF-4 including the effects of fission heating, conduction-convection-radiation heat

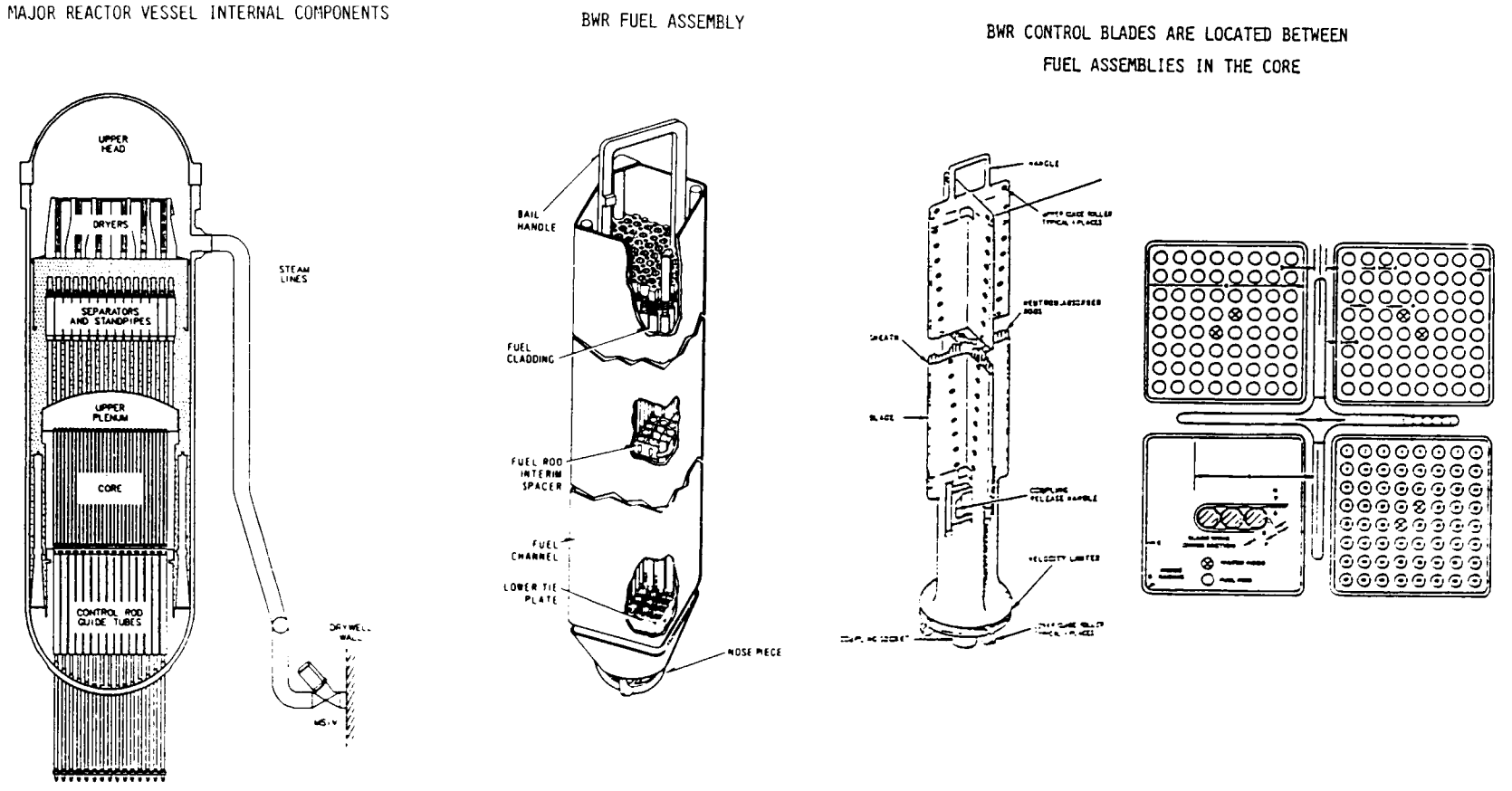

Figure 3.1-13. Major Components of the BWR Design Showing Fuel Canister Design and Control Blade Configuration

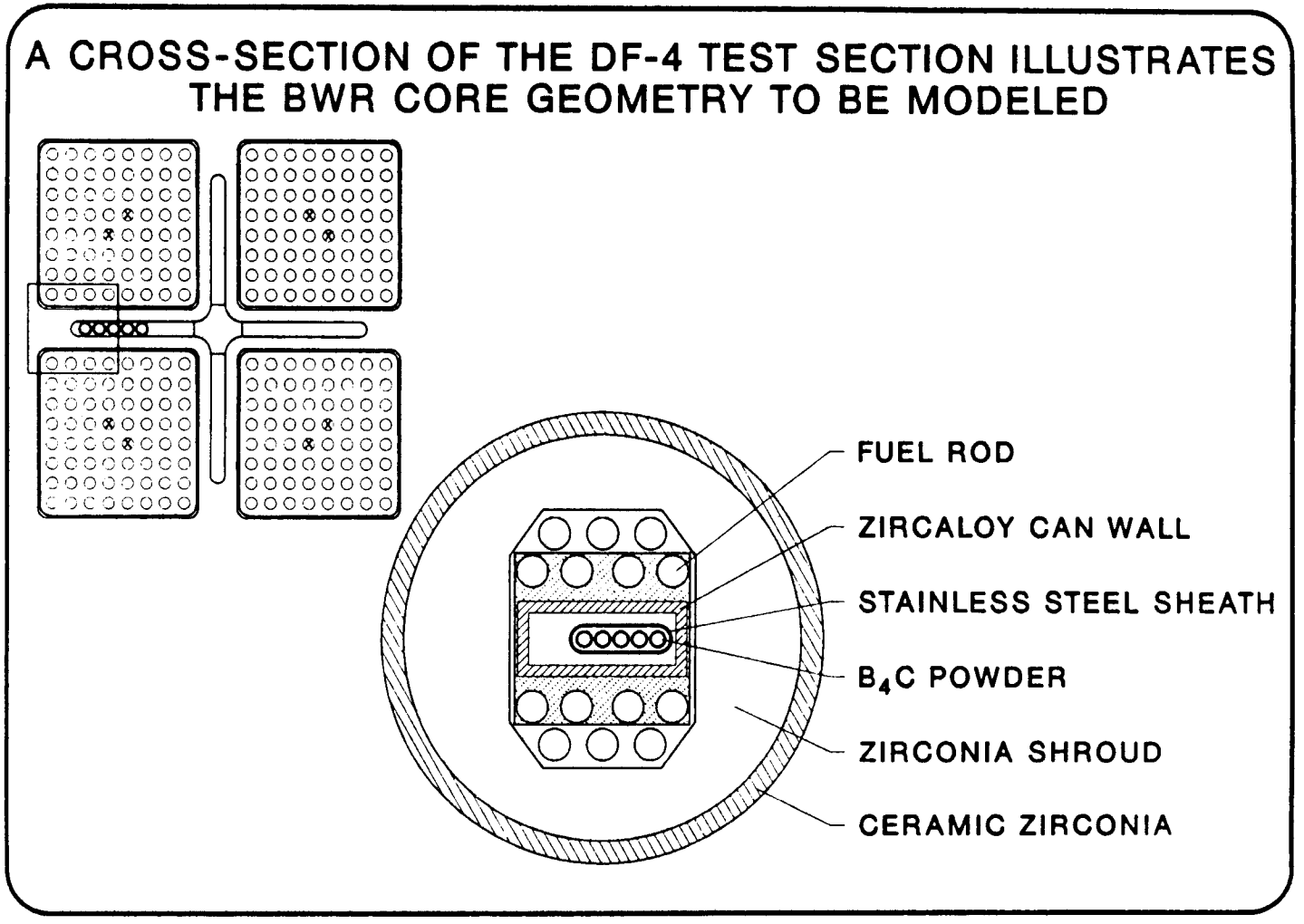

Figure 3.1-14. Representation of Key BWR Features in the DF-4 Test Section Design (Cross-Sectional View of Test Bundle)

transfer, and metal-steam oxidation. The BWR-SAT Division is also providing assistance in determining appropriate parameters for DF-4 based upon information gained in their involvement with the NRC BWR-Severe Accident Sequence Analysis (SASA) program. The MARCON-DF4 code will be the principal posttest evaluation tool for interpreting the DF-4 results. The posttest evaluation will both aid in evaluating MARCON 2.1B BWR models as well as characterize the raw experiment data sufficiently well that MELPROG or SCDAP evaluations may be attempted.

Preliminary calculations with MARCON-DF4 have been carried out; the results are embodied in Figures 3.1-15 through 3.1-18. Shown in Figure 3.1-15 is the anticipated ACRR power transient proposed to drive the fission heating of DF-4. This power history provides for:

1. A coupling factor calibration phase with several small step increases in power.

2. A larger power increase to quickly bring fuel temperatures up to ~900°C after which the channel box and control blade will be allowed to equilibrate with the fuel.

3. A final power increase during which the fuel cladding will be heated at roughly 1.5 K/s as rapid Zr-steam oxidation takes over as the dominant fuel/structure heating source.

The fuel clad, channel box, and control blade response to this power history is seen in Figures 3.1-16 through 3.1-18. The fuel clad temperature (Figure 3.1-16) shows a sharply developing zircaloy-steam reaction front at the top of the fissile zone (50 cm) after the second power increase is applied. The reaction front then progresses downward toward the steam source. Predicted peak fuel clad temperatures are 2500 K. The channel box heatup (Figure 3.1-17) proceeds much the same as the fuel, except at a faster rate with more extensive structural melting. Shown in Figure 3.1-18 is the predicted response of the stainless steel control blade. Because of the much lower melting point of stainless steel (~1700 K), the predicted extent of blade damage is large. Phenomena not addressed by the calculation, but expected to occur in the experiment, is material interaction, e.g., alloying and eutectic formation, between the different melting and relocating materials. These events are expected to influence the character of the damage progression and will be investigated by posttest metallurgical examination of the test section. Small scale out-of-pile experiments are currently under way at KfK, Karlsrhue,

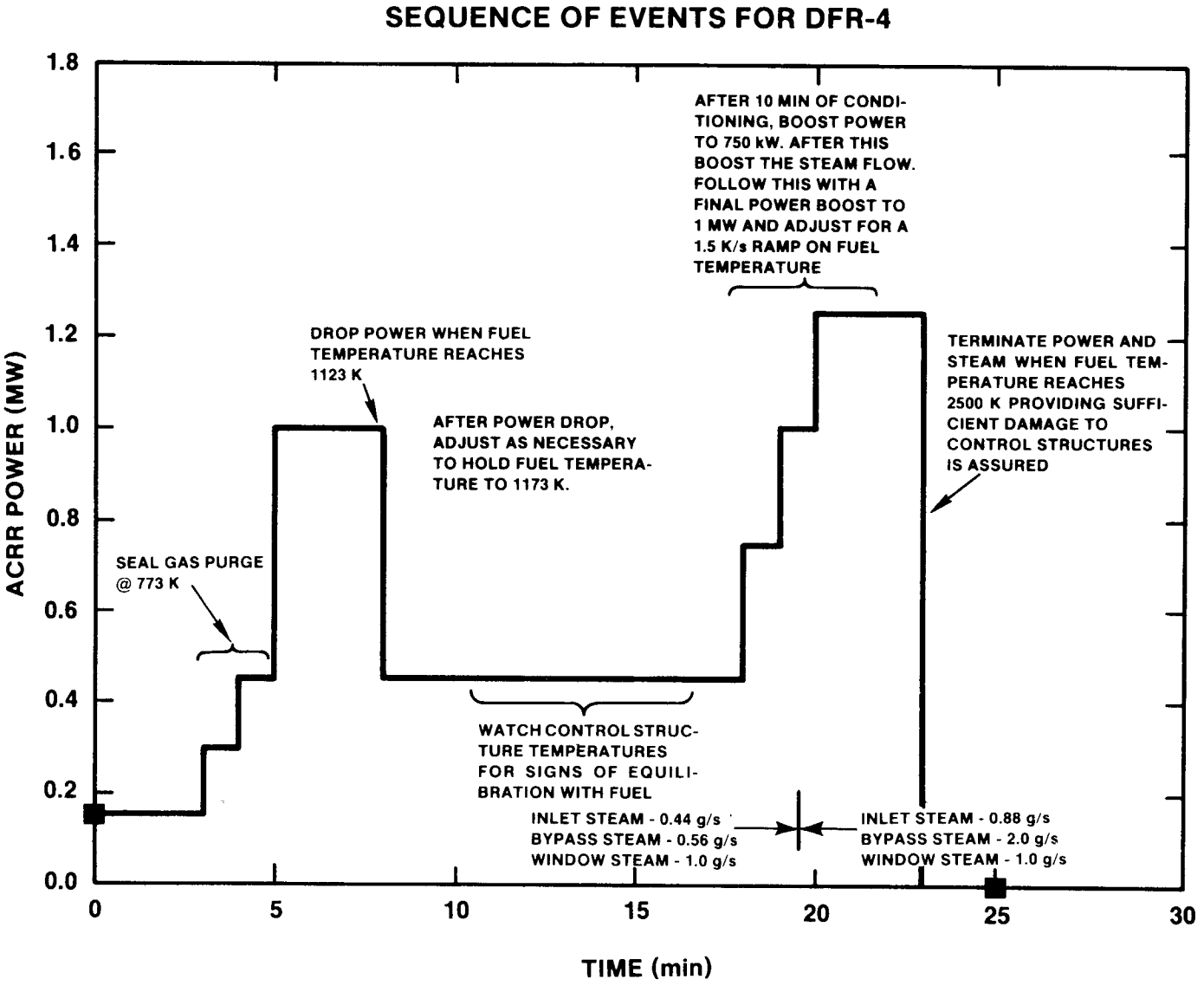

Figure 3.1-15. Proposed ACRR Power Transient for the DF-4 Test, Showing Anticipated Test Progression

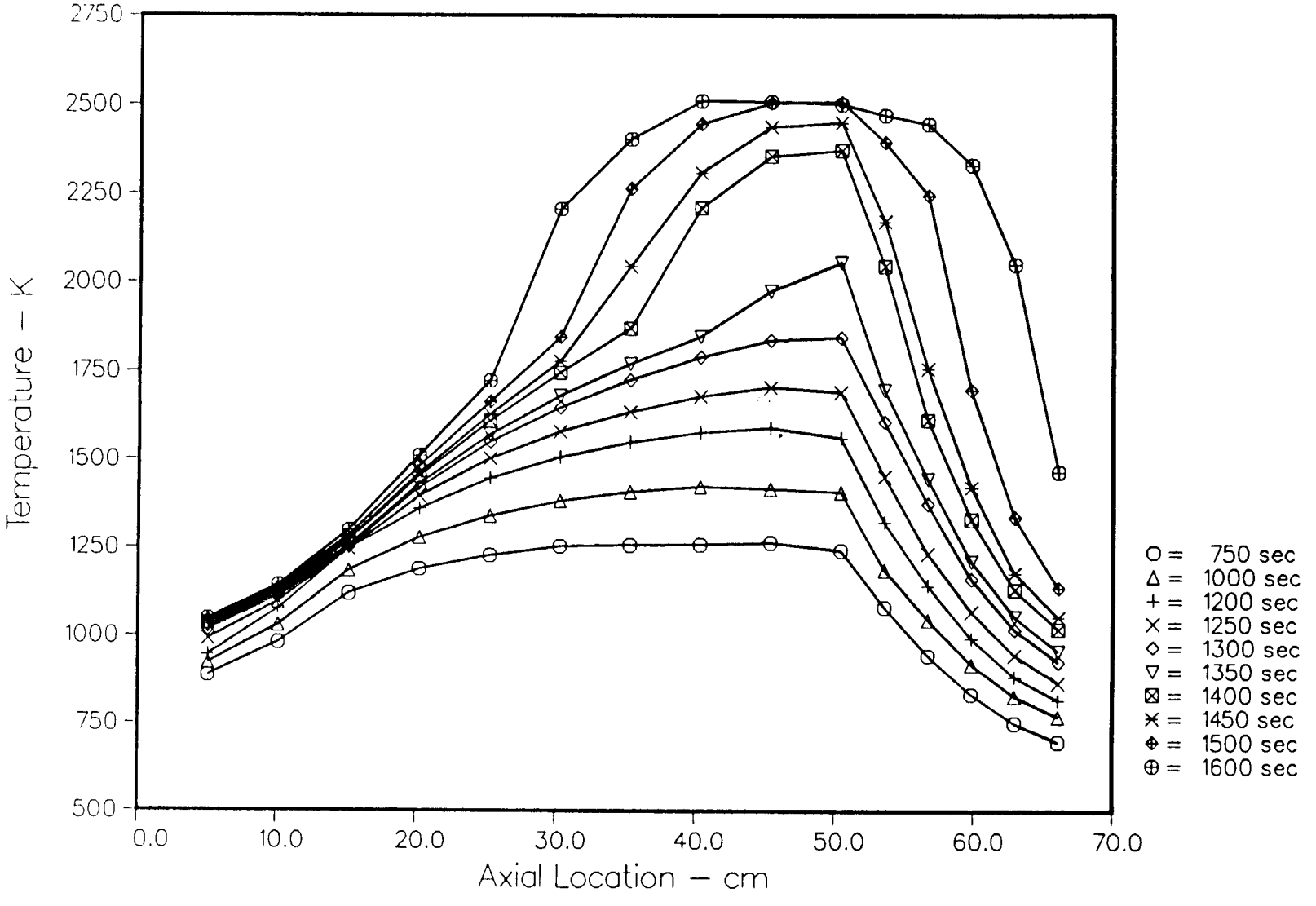

Figure 3.1-16. Axial Temperature Profiles Predicted by MARCON-DF-4 for the Fuel Rods

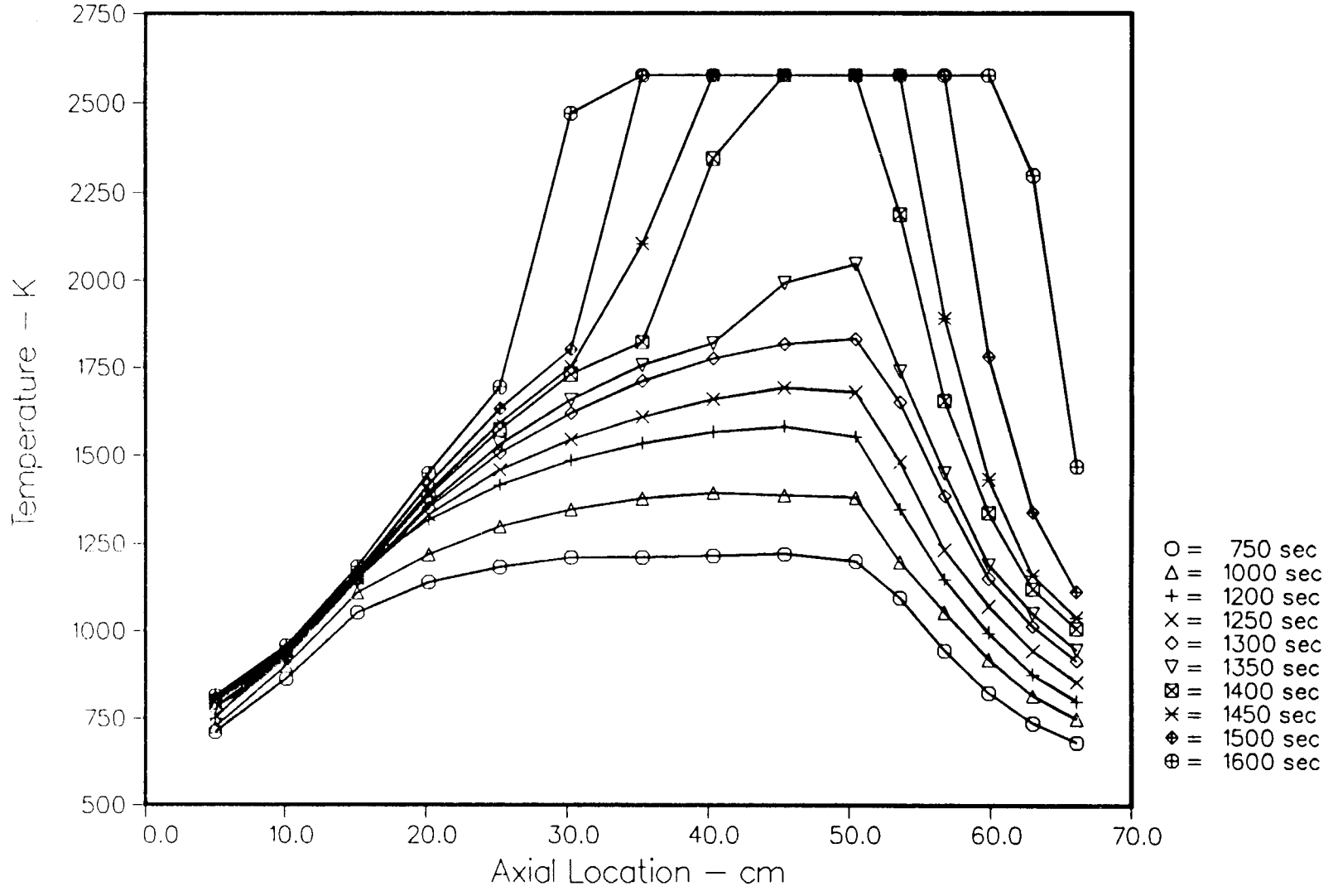

Figure 3.1-17. Axial Temperature Profiles Predicted by MARCON-DF-4 for the Zircaloy Channel Box

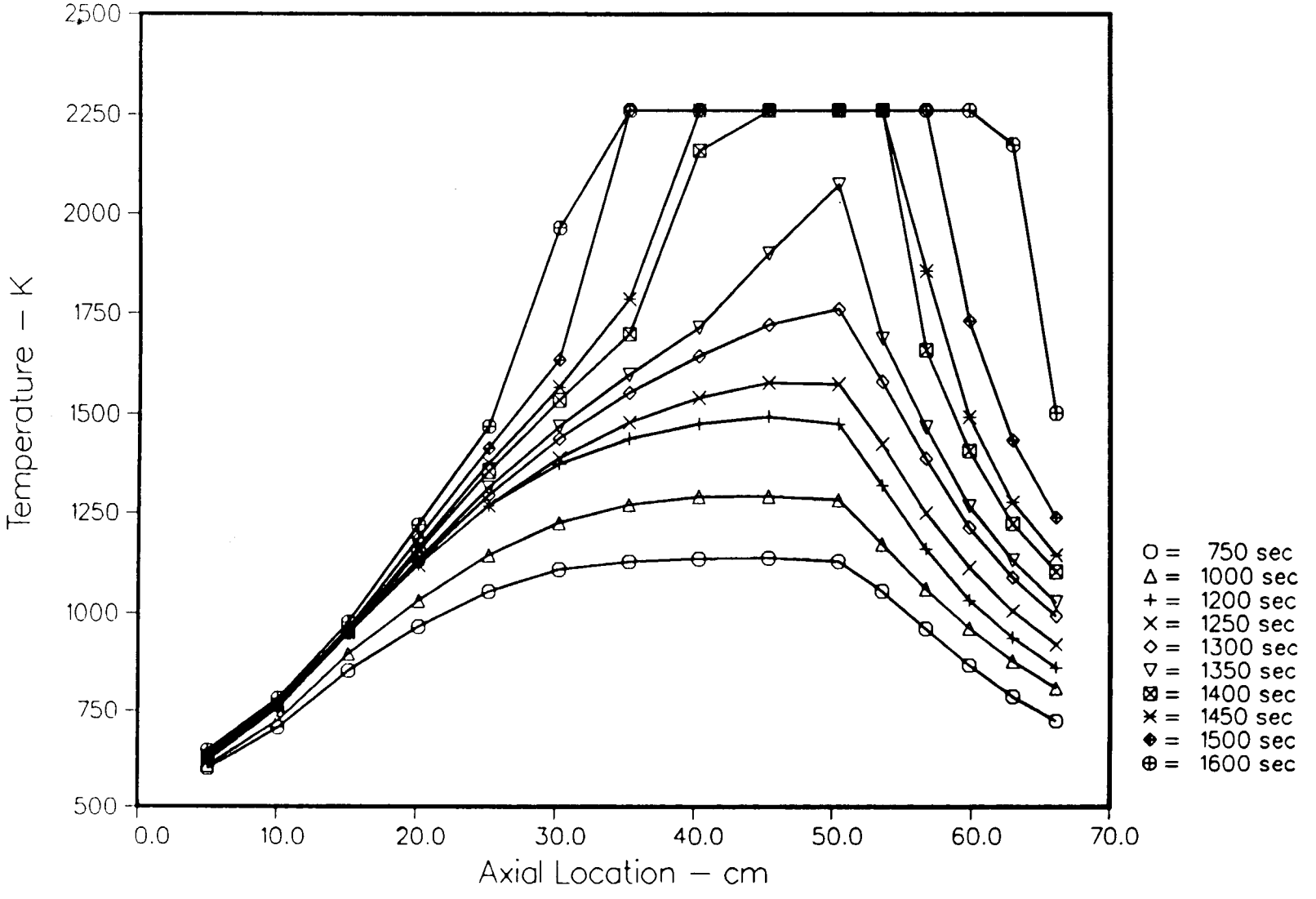

Figure 3.1-18. Axial Temperature Profiles Predicted by MARCON-DF-4 for the Stainless Steel/B_4C Control Blade

Germany. These experiments, by Siegfrid Hagen, are investigating the heatup behavior and interactions between zircaloy -4 clad UO_2 fuel rods and B_4C filled stainless steel tubes. These tests will aid in the design evaluation of DF-4.

With the design phase of the experiment completed, assembly of DF-4 is currently underway and the experiment is expected to be carried out in September 1986.

3.2 ACRR LWR Degraded Core Coolability

(K. R. Boldt, 6222; A. W. Reed, 6425; T. R. Schmidt, 6423)

The LWR Degraded Core Coolability (DCC) Program investigated the coolability of damaged core debris in water. The debris was fission heated in the Annular Core Research Reactor (ACRR) to simulate the decay heat expected in an LWR severe core-damage accident. The governing phenomenological uncertainties investigated were pressure effects, deep bed behavior, particle size distributions, stratified beds, bottom coolant feed, and coolability in three thermal regimes: (1) convection/boiling, (2) dryout, and (3) extended dryout. The staff used experimental results to confirm and/or modify the present analytical models used to predict degraded-core coolability.

Three experiments constituted the DCC Program. The DCC-1 experiment was designed to look at boiling in deep beds with a broad distribution of small particulate. The DCC-2 experiment was also a deep bed composed of a narrow distribution of medium-sized particles with a small amount of "fines" added. The DCC-3 experiment was a stratified bed in which a thin layer of small particulates (effective diameter: 0.919 mm; 100-mm deep) was placed on top of a thick layer of large particles (effective diameter: 3.64 mm; 400-mm deep). In addition, DCC-3 provided for inlet flow of coolant at the bottom of the debris. The first two experiments were conducted over the full PWR pressure range (17 MPa) while DCC-3 was conducted only up to the peak of the pressure curve (7 MPa). No other high-pressure data for debris coolability has been generated. The three experiments have been successfully concluded and the analyses completed. The following is a summary of the results and analysis of the DCC-3 experiment. The experiment hardware and procedures were discussed in the July-December 1985 Semiannual Report.[44]

3.2.1 Dryouts Without Inlet Flow

The DCC-3 dryout data without inlet flow is shown in Figure 3.2-1. The dryout points are based on an average calibration value of 0.722 $W/kg_{fuel}\text{-}kW_{reactor}$ corresponding to a bed average saturation of 0.5, a total bed loading of

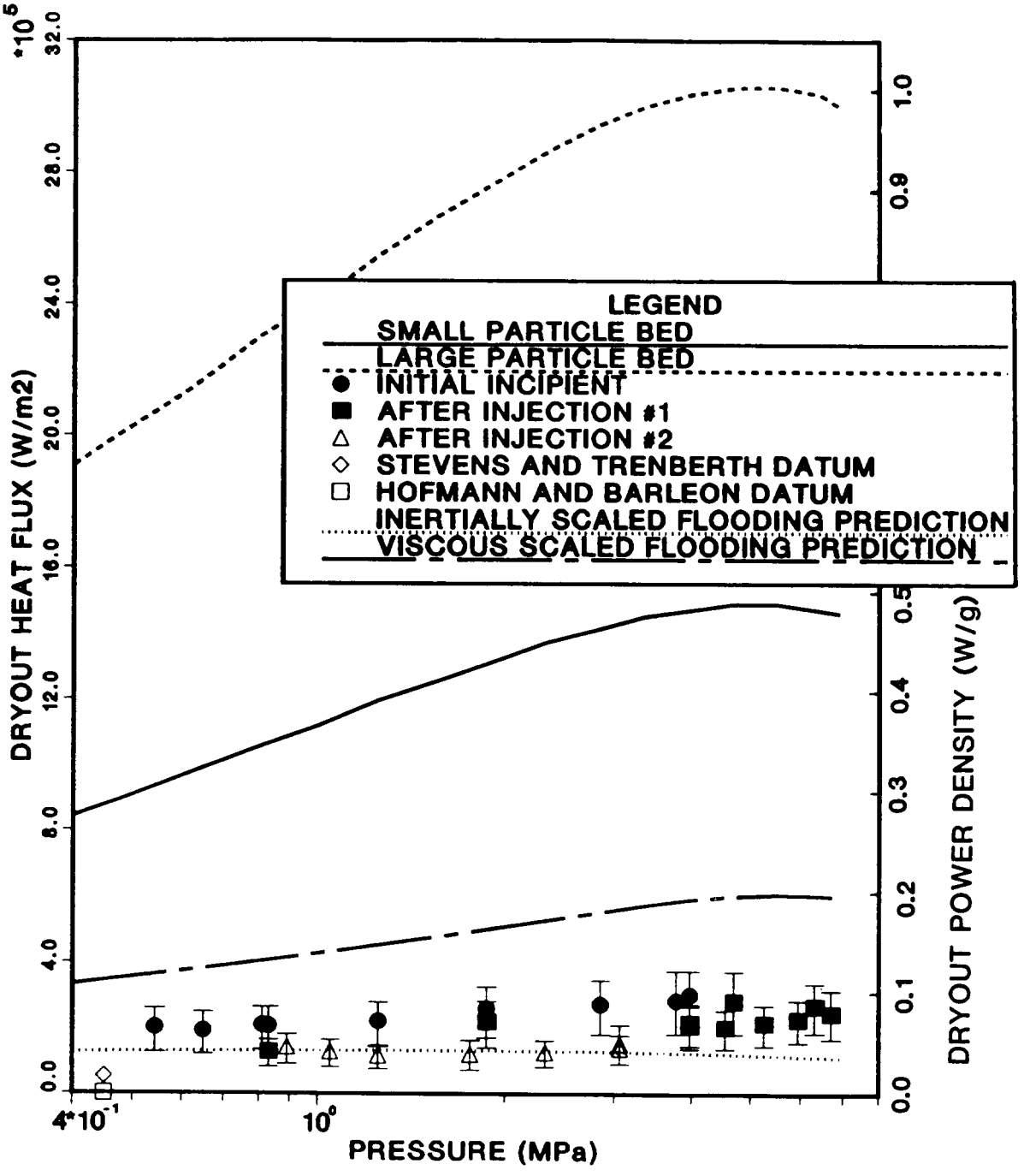

Figure 3.2-1. DCC-3 Dryout Data (No Inlet Flow)

24.133 kg of fuel, and a bed area of 0.00811 m^2. The bars on the data reflect the span in possible saturation (from 0 to 1).

The upper line in the plot is the predicted (Lipinski model) dryout heat flux for a bed composed entirely of the larger particulate having the same height (0.5 m) and porosity (0.42) as the DCC-3 bed. The next line is the predicted dryout heat flux for a bed composed entirely of the smaller particles. Both of these homogeneous beds are predicted to be coolable, having dryout powers in excess of 0.2 W/g. By contrast, the dryout levels of the DCC-1 bed were less than 0.1 W/g and would be uncoolable under accident conditions. In other words, one cannot conservatively estimate the dryout level of a stratified bed based upon the dryout level of the smallest particles. The bottom two lines refer to predictions based on flooding measurements.

The predicted saturation profile for a stratified bed is useful in explaining this phenomenon. Figure 3.2-2 shows the predicted saturation profile for a bed like the DCC-3 bed in which the power generation is uniform. Above the particle interface, the saturation is nearly unity. Immediately below the interface, the saturation jumps to a very small value, exhibits a steep gradient to a value near unity, and then increases slowly as the bottom of the bed is approached. The point of minimum saturation is the "throat" where the critical flooding condition takes place. This saturation is much lower in a stratified bed than would exist in a homogeneous bed. As a consequence, the liquid pressure gradient in this region is much larger, and the corresponding vapor pressure gradient required for dryout is much smaller. Hence dryout heat fluxes are lower in stratified beds than in homogeneous beds. The saturation profile in the DCC-3 experiment can deviate from that of a bed with uniform energy generation. However, the location of the saturation "throat" is expected to remain the same.

The reason for the sudden jump in saturation is found in the capillary pressure/saturation curve. Figure 3.2-3 shows the capillary pressure curves for the two DCC-3 particle sizes at 100°C based upon a fit to the Leverett correlation. If both phases are continuous across the interface, then the pressure of each phase must be continuous. This means that the pressure difference between the two phases, the capillary pressure, must be continuous across the interface.

The top curve in Figure 3.2-3 is the capillary pressure for the smaller particles. The saturation of the smaller particles just above the interface is found by integrating the differential equation for saturation from the top of the bed to the interface. This determines the capillary pressure at the interface.[66] The figure indicates that, for continuity of capillary pressure to exist, a high value of

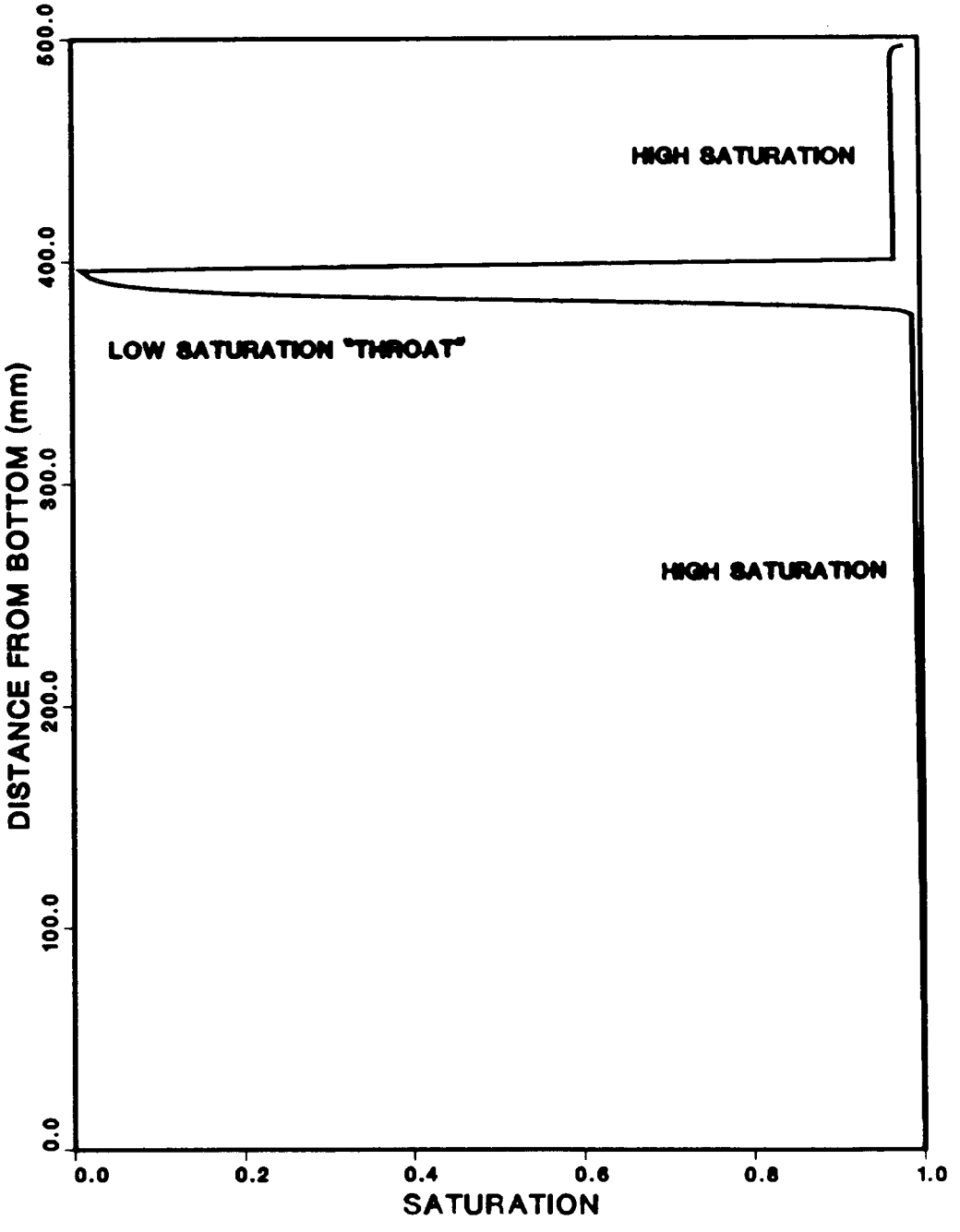

Figure 3.2-2. Predicted Saturation Profile (No Inlet Flow, Uniform Heating)

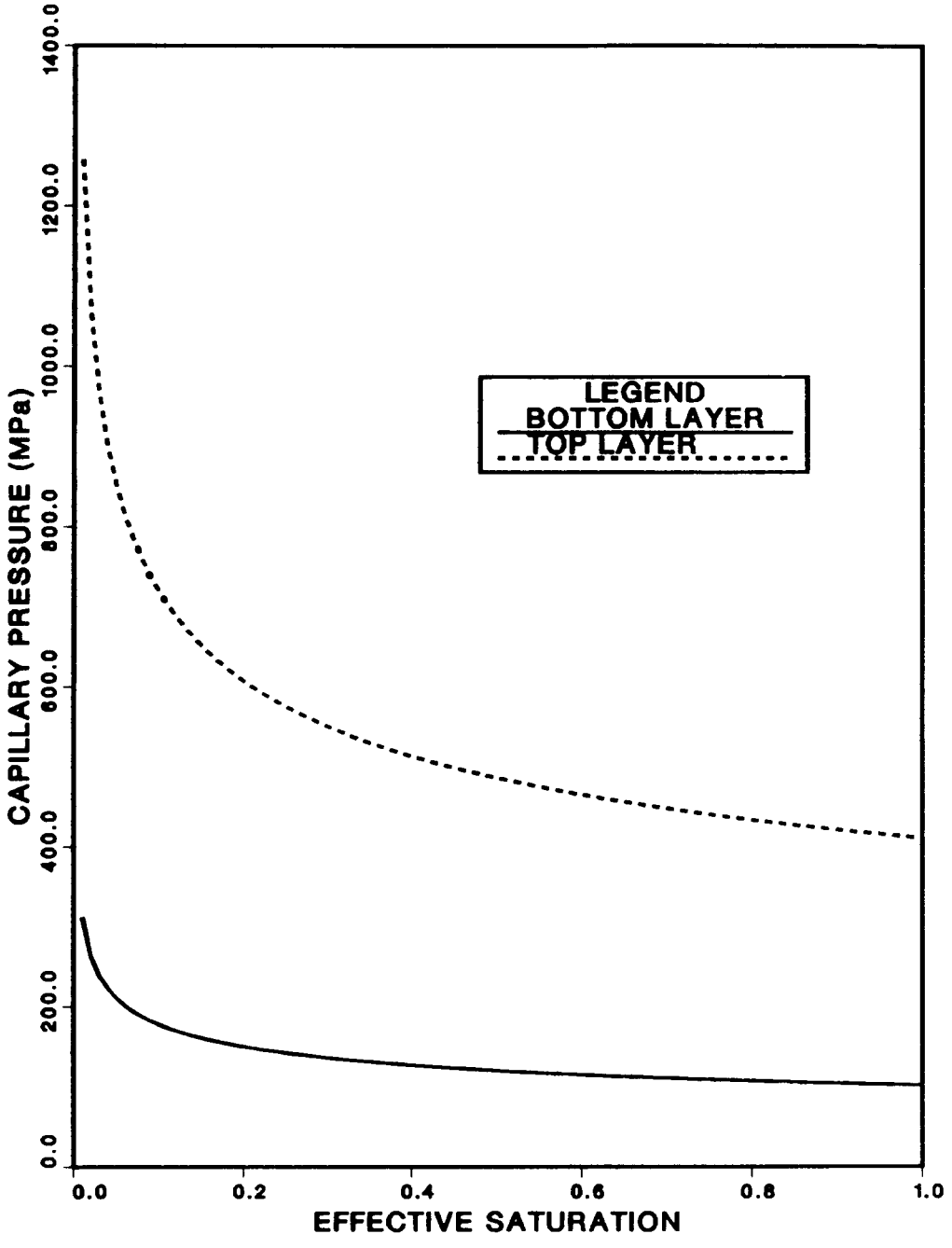

Figure 3.2-3. DCC-3 Capillary Pressures

saturation in the smaller particles produces a very small saturation in the larger particles.

The data from Stevens and Trenberth[67] and Hofmann and Barleon[68] are shown with the DCC-3 data (Figure 3.2-1). Since both out-of-pile experiments were conducted at a pressure of 0.1 MPa, the data appear shifted to the left on the plot. The Stevens and Trenberth datum is for a stratified bed in which 40 mm of 1.2-mm diameter metal spheres overlay 60 mm of 4-mm diameter metal spheres. This produced a dryout heat flux of 53 kW/m^2. The Hofmann and Barleon datum is for 50 mm of 1-mm cylinders overlying 570 mm of 3-mm spheres. To the limits of experimental accuracy, the dryout heat flux for this later configuration was zero; incipient boiling led to incipient dryout.

This latter point was explained by hypothesizing an upper limit on the dimensionless capillary pressure of 1.2. The argument is that if the breakthrough pressure of the small particles is greater than the maximum capillary pressure in the large particles, the continuity of capillary pressure across the interface is impossible. For one-dimensional flow, this means that the liquid phase cannot be continuous across the interface, and the liquid below the interface will simply boil away without resupply from above.

At first glance, the DCC-3 data appear closer to the Stevens-Trenberth data than the Hofmann-Barleon data. However, out-of-pile flooding measurements indicated that the DCC-3 data were influenced by the thermocouples. Some water bypassed the stratification interface between the thermocouples and the wall. The conclusion made from the flooding measurement is that if thermocouples had not penetrated the interface, incipient boiling would have led to incipient dryout in DCC-3. This is the same conclusion found by Hofmann-Barleon.

In light of the capillary pressure measurements and the extreme thoroughness of the Hofmann-Barleon experiments, it seems reasonable to adopt the lower values of dryout heat flux. The apparent lack of agreement in the experimental data does not obscure the major feature of the experiments; stratification can have a large detrimental impact on the coolability of core debris.

3.2.2 Dryouts With Inlet Flow

The bed power calibration for dryouts with inlet flow differed from that for uninjected dryouts. For all runs in which inlet flow was used, the dryout was located at the stratification interface. This fact allows for a more precise specification of the bed power without further specifying the bed saturation.

The injected dryout data is plotted in Figures 3.2-4 and 3.2-5. The upper line is the prediction for a uniform bed of small particles with uniform heating. The lower line is the prediction for a DCC-3 bed with uniform heating. The predicted dryout heat flux for the stratified bed is linear because the dryout is predicted to always occur at the interface. This means that the dryout power is directly proportional to the inlet flow.

At the point where the predictions for a uniform and stratified bed merge, the stratified prediction deviates from the linear relationship with inlet flow and becomes the same as that of the uniform bed. This can be explained with the aid of a saturation diagram. Figure 3.2-6 shows the saturation profile for the DCC-3 bed with uniform heat generation at 166°C. The inlet flow is 0.63 mm/s and the bed power is 1.6 MW/m^2. This is very close to the dryout flux of 1.65 MW/m^2. The saturation profile reveals two possible throats that can cause dryout. The first is just below the interface where the stratification has forced a low saturation. The second occurs in the smaller particles of the upper layer. The location of this latter throat is the same as it would be in a homogeneous bed composed of the smaller particles.

At sufficiently low inlet flows, the critical flooding conditions are never met in the upper throat, and the stratification dominates the dryout characteristics. If the inlet flow is sufficiently high, the critical flooding condition in the upper throat is realized even though the lower bed is being adequately cooled. When this occurs, the dry zone will occur above the stratification. The power where this occurs is the dryout power of a homogeneous bed of smaller particles. In other words, if the inlet flow is sufficiently high, the stratification will play no role in the dryout and the bed will behave like a deep bed of the smaller particles. The inlet flow where this occurs increases as the saturation pressure increases. Hence the predicted effect is shown at 166°C (Figure 3.2-4) and not at 210°C (Figure 3.2-5).

The measurements of injected dryout flux come very close to the predictions. Most of the discrepancy is attributable to the flat power profile assumed in the prediction. In DCC-3, the power generation in the upper layer was lower than in the rest of the bed. Hence the total bed power at the time of dryout in the DCC-3 experiment was lower than for a uniformly heated bed.

The main discrepancy between measurement and prediction occurs when the inlet flow is zero. As stated before, the reason for this is the impact of the thermocouples on the interface. This does not obscure the obvious benefits of

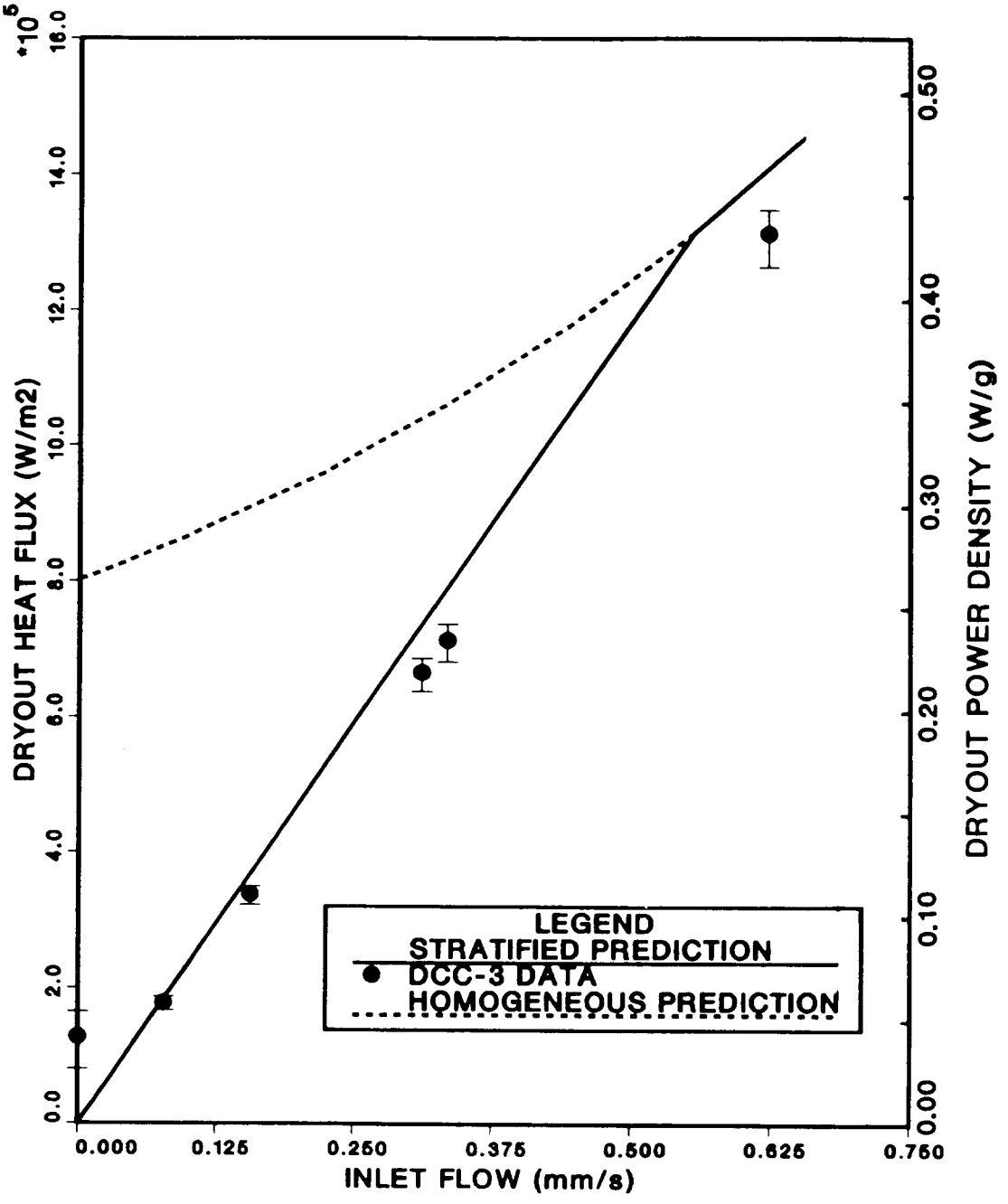

Figure 3.2-4. DCC-3 Dryout Data (Inlet Flow, 166°C, 0.718 MPa)

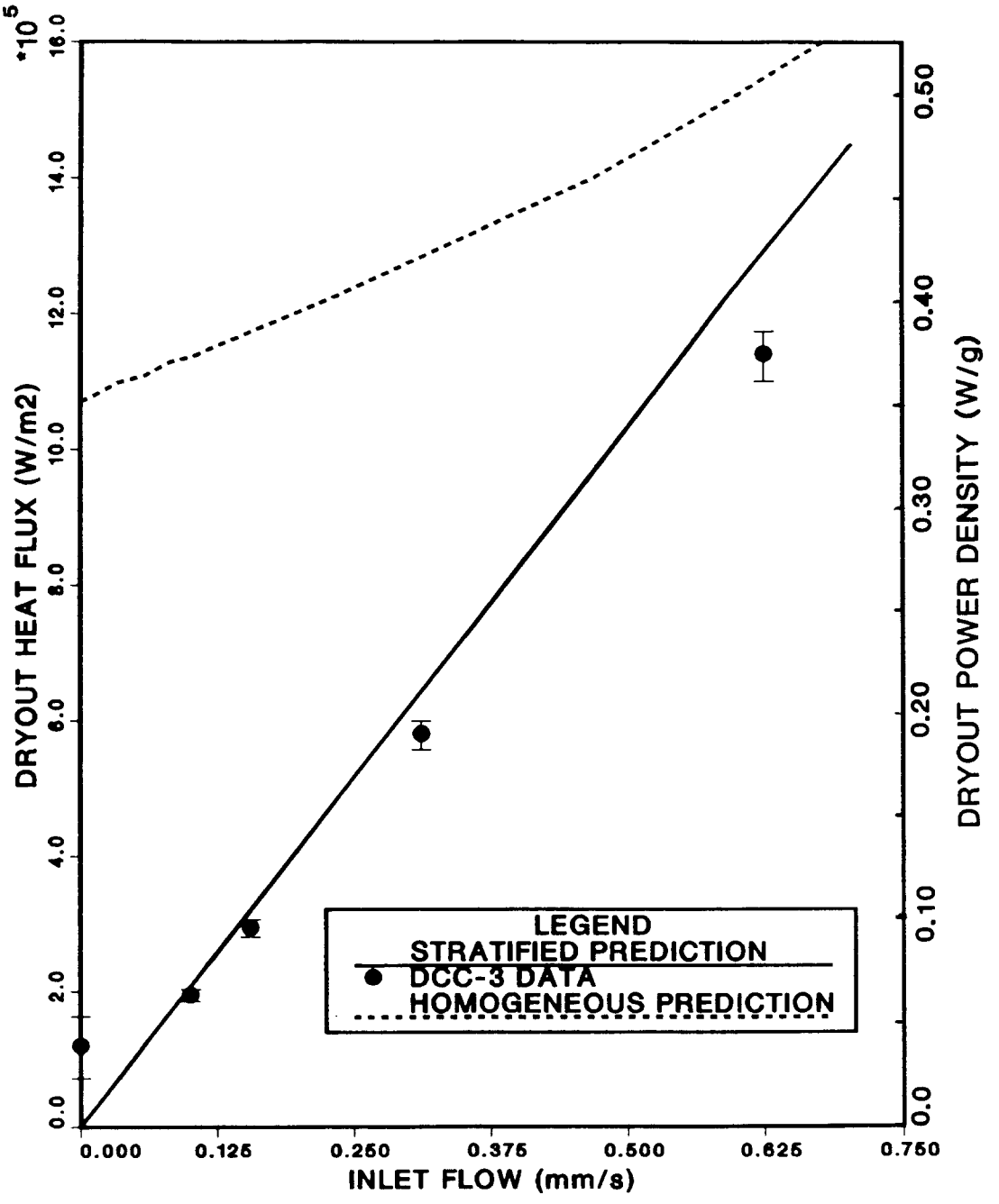

Figure 3.2-5. DCC-3 Dryout Data (Inlet Flow, 210°C, 1.906 MPa)

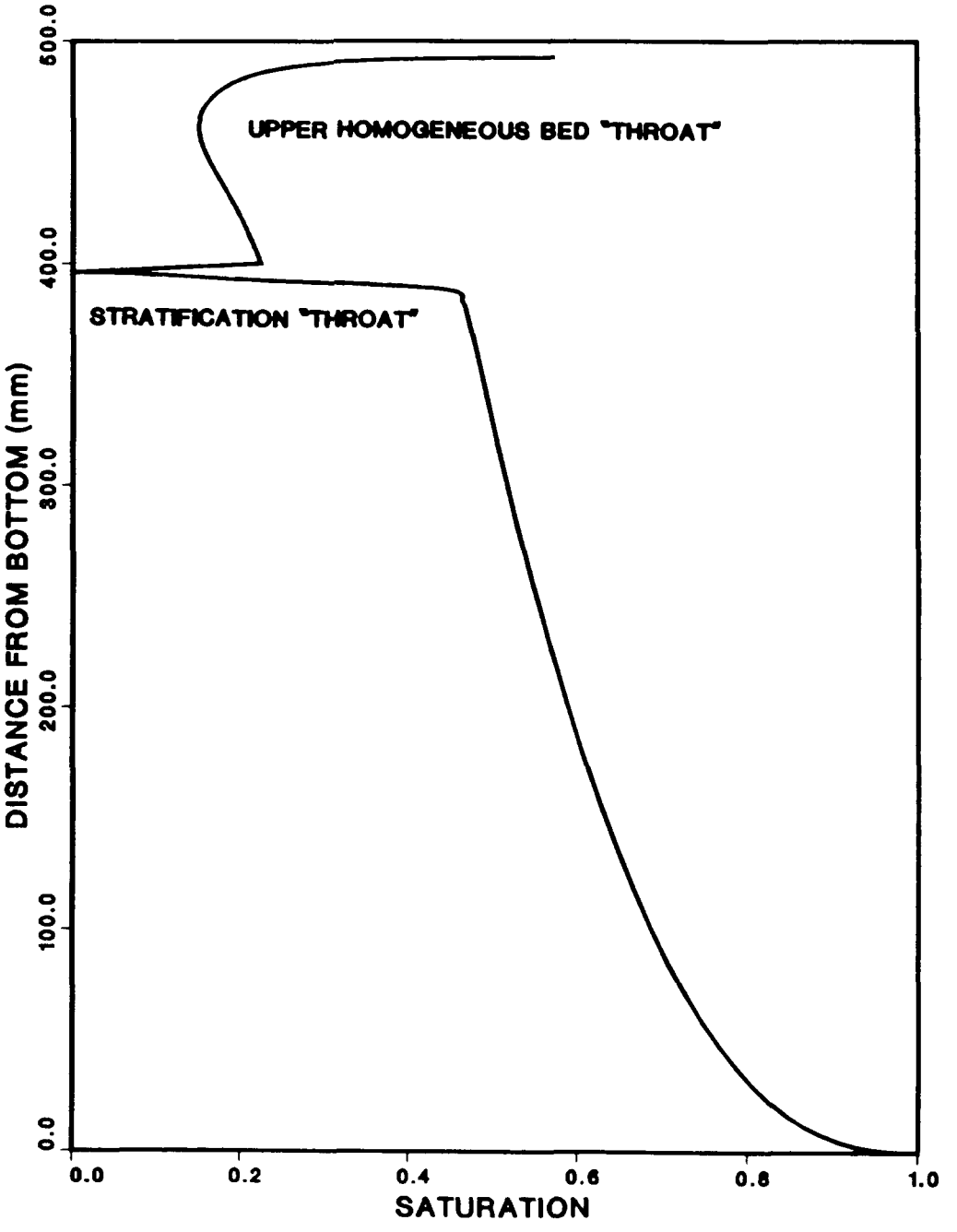

Figure 3.2-6. Predicted Saturation Profile (Inlet Flow, Uniform Heating)

water injection. Without injection, the bed is uncoolable, having a dryout level of less than 0.05 W/g. With water injection, the bed is made coolable with dryout levels in excess of 0.2 W/g.

3.2.3 Quench Behavior

Quench behavior was also studied in the DCC experiments because it relates to the question of accident management: If a dry debris bed forms and heats up, can it be returned to a coolable state by flooding it with water from the top? Several out-of-pile experiments, as well as the DCC-1 and DCC-2 experiments, have investigated the quench behavior of heated particulate. In large particulate, the quench front was two-dimensional. A core of water penetrated the center of the debris bed while vapor escaped along the bed sides. Once the water reached the bottom of the bed, the remaining dry part of the bed was quenched from the bottom.

This process contrasts with the quenches observed for beds of smaller particulate. In such beds, the quench front tended to be horizontal while progressing uniformly downward. More importantly, the bed power at which quenching took place was less than half of the dryout power.

DCC-1 quenches (effective particle diameter of 0.31 mm) had uniform quench fronts resembling the small particle out-of-pile tests. DCC-2 quenches (effective particle diameter of 1.41 mm) were two-dimensional like the large particle out-of-pile experiments. In both experiments, the heat flux during the quenching process was significantly lower than the measured dryout heat flux.

The quench behavior of the three extended dryouts of the DCC-3 experiment was also analyzed. In particular, the total heat flux during the quench was estimated from the temperature data. An average temperature was calculated for the initial zone at various times during the quench as shown in Figure 3.2-7. The heat flux was then computed using energy conservation.

The quench behavior of all three DCC experiments has shown the quench heat flux to be significantly below the dryout heat flux. In particular, the DCC-2 experiment demonstrated a marginally coolable debris bed with a quench heat flux less than 20 percent of the dryout heat flux. Such a bed is probably not quenchable even though it is coolable. Because of its implications in accident management, the ability to predict quench behavior is important. As mentioned earlier, there have been two distinct types of behavior observed in quench. While the quench types have been attributed to the differences between "large" and "small" particles, the physics of the debris quenching have not been fully

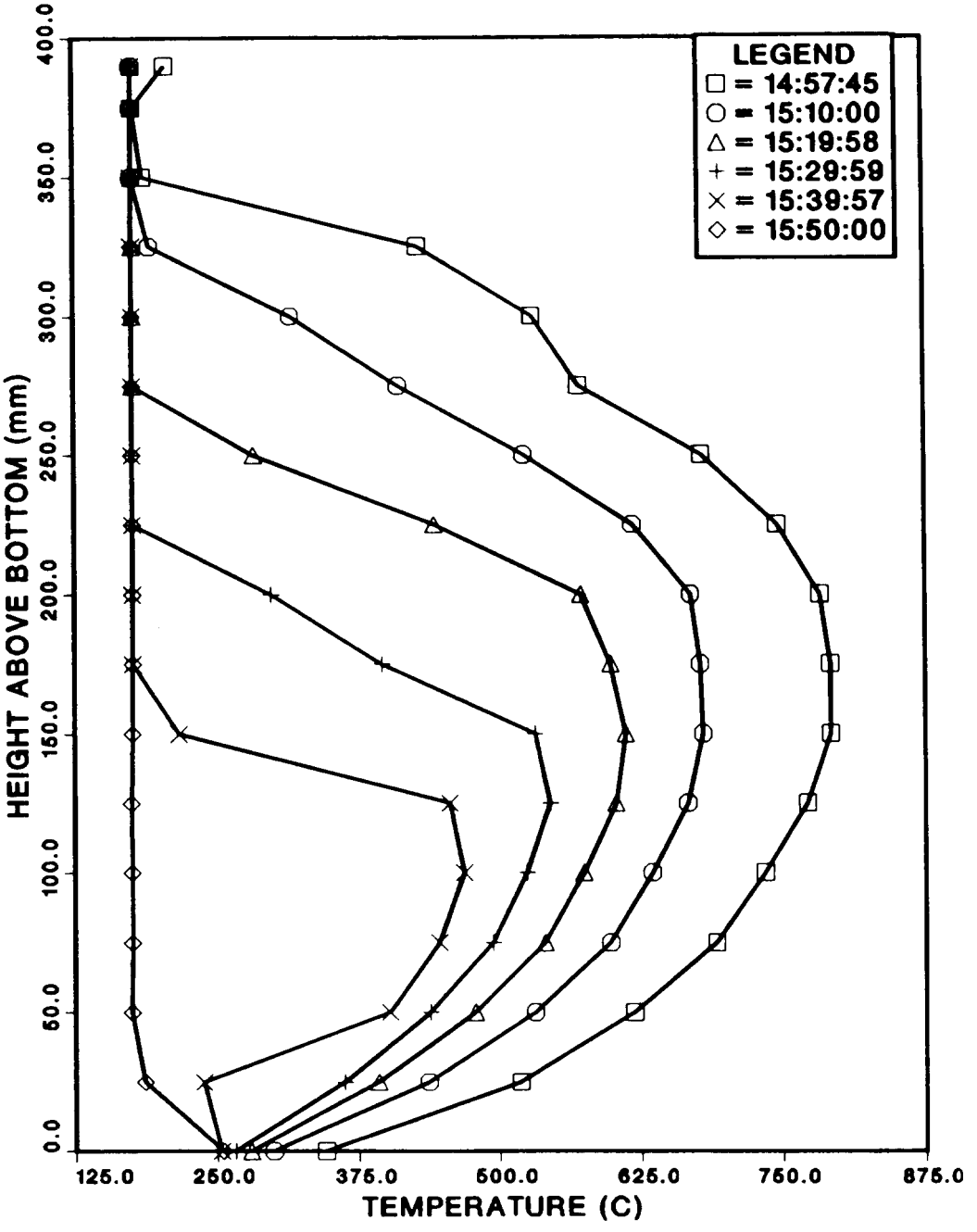

Figure 3.2-7. Quench at 10/2 15:00

explained. Further work on debris quenching is necessary before a satisfactory model is obtained.

3.2.4 Conclusions

The DCC-3 experiment was the third and final experiment of the DCC series. This experiment addressed the problems of stratification and inlet flow in a deep bed of large UO_2 particulate. The data demonstrated two important features of debris coolability: Stratification can sharply reduce the coolability of a debris bed, and inlet flow can effectively increase the coolability of a bed.

Without inlet flow, the DCC-3 debris bed would be uncoolable in a prototypic reactor accident. This is counterintuitive since a bed composed solely of the smaller particles would be coolable. The cause of the seemingly premature dryout is the surface tension force at the stratification interface. The top layer of smaller particles acts like a sponge and holds water, preventing it from flowing into the lower bed. This same surface tension force is at work during the quench of a hot dry bed. In fact, the quench heat fluxes are even lower than the dryout heat fluxes.

The great importance of surface tension in the DCC-1 experiments is at odds with the heuristic argument that surface tension is unimportant in beds composed of "large" particles. "Large" particles are usually thought to be greater than or equal to 1 mm. The justification for this argument is that the capillary rise in such particles is much smaller than the depth of the debris bed. The argument is valid for homogeneous beds where the length scale governing dryout is the height of the bed. In stratified beds, capillary forces can make strong changes in the saturation profile over a length equal to the capillary rise. The length scale governing dryout for such changes is much smaller than the bed height and, in DCC-3, is the same order of magnitude as the capillary rise.

The heuristic argument about particle size is not without appeal. One would not expect the same sort of behavior seen in DCC-3 if the particles had been a factor of 10 larger. The difference in expected behavior probably lies in the question of stability. The configuration observed in the flooding experiment, in which liquid occupied the upper layer of particles and gas occupied the lower level of particles, should be unstable. The heavier fluid was on top and the lighter fluid, below. The stabilizing force was the surface tension.

If the absolute value of the capillary forces is sufficiently small, the pressure fluctuations will exceed the stabilizing force and the configuration can become

unstable. The most probable result of the instability would be a two-dimensional flow of water and gas in which the water flows into the lower bed on one side and gas is released into the upper bed on the other side. The instability probably has a critical wavelength. Test sections having a diameter smaller than this wavelength will exhibit the stable behavior while those having a larger diameter will exhibit two-dimensional flow. It is possible that the DCC-3 dryout heat fluxes would have been larger if the debris bed diameter had been larger.

The realm of this problem is not confined to stratified beds. The two-dimensional quench behavior observed in large particles could be the result of a simple gravity instability. Presumably, the surface tension forces in the small particle quenches are sufficiently large to keep the flow one-dimensional. Another potential impact is in incipient dryout behavior. The test section diameters of all experimental apparatus were small compared to the diameter of a reactor vessel. The heating technique usually places a severe restriction on the section diameter. In principle, it is possible that the flow in a larger test section would be two-dimensional and the resulting dryout heat flux would be higher than existing data indicated. To date, no one has examined the stability of flows in boiling debris beds.

The configuration of the DCC-3 bed was designed to test models for nonuniform beds and is not expected to represent a particular accident scenario. However, it is anticipated that nonuniformities will be present in degraded core debris, thus requiring their understanding.

The injection of water at the bottom of the DCC-3 debris bed increased the dryout powers above that which would be observed in a reactor accident. The inlet flows required for this were within the capacity of the High Pressure Injection System (HIPS). This demonstrates that the HIPS might be useful in cooling debris beds in the pressure vessel. This is subject to the condition that the lower boundary of the debris bed is not impermeable.

The DCC experimental series has provided a data base for debris coolability in which prototypic materials were used and prototypic pressures were realized. DCC-1 exhibited an unexpected pressure dependence, and DCC-2 displayed the effects of inhomogenities. Both of these effects are believed to be due to the particle size distributions. In spite of these new effects, the data from DCC-1 and DCC-2 fit in well with the world data. The dryout behavior of beds composed of prototypic materials appears to be similar to that observed in out-of-pile experiments using simulant materials.

The behavior of debris beds at this point is reasonably well understood. Several analytical models, among them the Lipinski model, do a reasonable job of predicting dryout heat fluxes. The obvious problem is in determining the proper debris bed configuration for LWR reactor accidents. In particular, more information is needed on the particle size distribution, void fraction, bed depth, and degree of stratification (if it occurs). Given this information, reasonably accurate predictions can be made about the coolability of an actual debris bed. Further efforts in the area of debris coolability should concentrate on the questions of debris formation and settling. This concludes the reporting of the DCC program in the Semiannual reports.

4. MELT PROGRESSION CODE DEVELOPMENT (MELPROG)
(W. J. Camp and J. E. Kelly, 6425)

The objective of this program is the development of a mechanistic computer model for the analysis of the in-vessel phases of severe accidents in LWRs. This model, MELPROG, is implicitly linked with the TRAC-PF1 thermal hydraulics code to provide a complete, integrated treatment of the reactor primary system from accident inception through release of core materials and fission products from the reactor vessel. The model also provides materials and thermohydrodynamic input to the CONTAIN reactor containment analysis model.

The work involves both developing the MELPROG computer code and applying the code to accident scenarios and to experiments. In the code development phase, models needed to treat the phenomena associated with severe accidents have been extracted from the open literature as well as being formulated specifically for this effort. The application effort involves both testing the code and assessing the modeling.

4.1 MELPROG Code Development
(J. E. Kelly, P. J. Maudlin, J. L. Tomkins, P. K. Mast, K. L. Schoenefeld, M. F. Young, and R. C. Smith, 6425)

MELPROG consists of several explicitly linked modules, which, in turn, are comprised of models that treat the physical processes that occur during a severe accident sequence. The approach used in MELPROG has been to develop these modules as stand-alone codes. Then these modules have been explicitly linked together in the MELPROG code in order to treat the entire accident sequence in an integrated manner. The advantage of this approach is that it allows for both accurate modeling of specific phenomena and accurate predictions of the coupling between phenomena. This approach allows key quantities, such as fission-product release and transport, to be calculated in a realistic and consistent manner. Additionally, the modular structure of the code has the advantage that it is relatively easy to improve or substitute new models into the code as warranted.

The first version of MELPROG, MELPROG-PWR/MOD0, was completed and is being tested prior to release. This version uses a one-dimensional fluid dynamics model (FLUIDS module) and contains PWR core structure models (STRUCTURES module). This version also includes the DEBRIS module for debris bed analysis, the RADIATION module for radiation heat transfer analysis, and the PINS module for fuel and control rod analysis. Major development on this version has ceased in order to devote more effort to developing the improved versions of the code.

The second version, MELPROG-PWR/MOD1, is currently under development. This version will include all features of the original code plus many significant enhancements. In particular, this version includes a two-dimensional fluid dynamics model (FLUIDS-2D module), a fission-product model (VICTORIA module), an improved core structures model (CORE module), a melt-water interaction model (IFCI module), and a melt ejection model (EJECT module). This version represents a major improvement over the original version. In addition, substantial development on the FLUIDS-2D, VICTORIA, and CORE modules also occurred.

The new FLUIDS-2D module replaces the one-dimensional fluid dynamics treatment in MOD0 with a full two-dimensional (R-Z) capability. In addition, four momentum fields are treated instead of three (the corium field is split into solid and liquid fields). This version was completed at Los Alamos National Laboratory as part of the MELPROG effort. The major advantage gained through the new FLUIDS module is the ability to treat the important effects of natural circulation in the core and vessel. This new module is completely operational in MELPROG.

While the MOD1 version of MELPROG is still under development, the initial results from the testing of the 2-D hydrodynamics are quite promising. The new module works well, and no major obstacles have been found. Additionally, the preliminary results illustrate the importance of natural circulation within the vessel. Relative to a one-dimensional treatment, a strong radial variation in the meltdown progression has been found. This difference will influence in-vessel fission-product release as well as the mode of core slump.

The VICTORIA module in MELPROG treats release and transport of fission products in the core and vessel. The philosophy behind the development of VICTORIA was to adapt from other fission-product codes and research programs the models, methods, and in some cases, even software needed to build a fission-product behavior module suitable for MELPROG. This module treats the appropriate physical processes at a level of modeling detail consistent with MELPROG and has a software structure compatible for coupling to MELPROG. In addition, the structure of VICTORIA is designed such that (1) further changes of the code as dictated by appropriate experiments will be straightforward to implement, and (2) it can be used in either a stand-alone mode or in a coupled mode with MELPROG.

VICTORIA, in stand-alone form, has been completed and is being assessed. The stand-alone code is also being used to perform scoping studies for the ACRR source term (ST) experiments. Incorporation of this module into MELPROG has been initiated.

The new CORE module has been designed to treat PWR and BWR core structures in one consistent and flexible framework. The module was also designed to be consistent with the existing treatment of in-vessel and ex-core structures (the STRUCTURES module). The actual level of modeling detail, both geometrical and physical, are user controlled. For example, one can use very detailed geometry for experiment analyses and considerably less detail for reactor accident calculations. Such flexibility allows the user to determine the impact on accident calculations of the level of physics and geometry detail.

The CORE module is designed to treat fuel rods, PWR control rods, BWR control blades, poison rods, dummy rods, and BWR can walls. MELPROG is a 2-D code (R-Z geometry). Within each radial ring, a model can be provided for each different type of core structure. Each model then represents the actual number of such structures in that ring. Each core structure modeled may have its own power factor and its own axial structure. Thus, for example, multiple fuel rods within a ring may be modeled with the axial detail of the rods (fission gas plenum, insulator pellets, active fuel, etc.) explicitly treated.

Each core structure is treated as consisting of one or more material regions. For example, a fuel rod would initially be modeled as a two-region structure, i.e., fuel and cladding. During the course of the calculation the number of material regions can change. For example, oxidation of the zircaloy cladding leads to formation of a layer of ZrO_2, which is explicitly treated as a separate material region. Similarly, formation of a U-Zr-O solution that forms and flows down the exterior or interior or both the exterior and interior of the fuel rod also creates new material regions. Therefore, the model allows for the formation and loss of material regions for all core structures in order to calculate the important physical processes.

A 1-D finite-difference solution for heat conduction through the various material regions forms the basis for the CORE module. Oxidation kinetics for solid and liquid zircaloy and steel as well as for U-Zr-O solutions on structure outer surfaces are treated. Cladding plastic deformation and failure are modeled. Candling on inner and outer surfaces is treated. Fuel rod and other core structure failure by melting or fracture are modeled.

The major development effort has been centered in developing subroutine CANDLE, which determines how molten core material flows over core structures in response to gravitational and other forces. The subroutine consists of basically two parts. In the first part, the routine loops through the

axial layers of the structure to determine the geometry of flow paths and the location and initial conditions of liquefied core material, which will subsequently be referred to as eutectic. In the second part, mass, energy, and momentum conservation equations are solved iteratively for each flow path to determine the extent of motion during the time step. The routine then compares the initial conditions to the final conditions to calculate incremental changes in eutectic mass and energy for later use by the CRMESH subroutine in the overall remesh calculation. Each part will be explained in more detail in the following paragraphs.

In part one of the CANDLE subroutine, initial conditions and flow geometry are determined by looping through axial layer data provided by other CORE subroutines. At each axial layer, the routine loops over the radial regions to identify eutectic regions, regions occupied by eutectic or empty regions into which eutectic may flow, and cracked or porous solid regions that permit flow between eutectic regions within the same axial layer. Two types of eutectic regions are considered: The eutectic is assumed to be a homogeneous fluid in annular regions between confining solids (region type 5) or a film on an underlying solid substrate (region type 6). Figure 4.1-1 is a schematic of a typical situation that is addressed by the model. Initial conditions and geometric characteristics from the region data are stored in CANDLE working arrays one layer at a time. In part one, the subroutine also determines which eutectic regions in adjacent axial layers are connected and where multiple connections (junctions) occur. This information is used to construct path arrays which identify the eutectic regions at each axial layer that define a particular path. Paths that can communicate through either shared junctions or crack/hole flow are grouped together to be solved simultaneously in part two of the CANDLE subroutine. If too many paths or junctions are identified (based upon allocated array space), the routine prints a diagnostic message and aborts.

In part two of the CANDLE subroutine mass, energy and momentum equations are solved iteratively along each path in a group to determine how the eutectic moves during the time step. Figure 4.1-2 is a flow chart of the CANDLE solution algorithm. The conservation equations are solved simultaneously along each path in a group. Initial conditions are obtained from the arrays constructed in part one at the beginning of the MELPROG time step. The sub-time-step used by CANDLE is initially set equal to the MELPROG-time-step. The equations are pseudo-two-dimensional with variations in the axial direction treated by a typical discretization scheme and flow between connected paths (crack or junction flow) treated with "old" iterate values. The difference equations are solved with a direct tridiagonal matrix

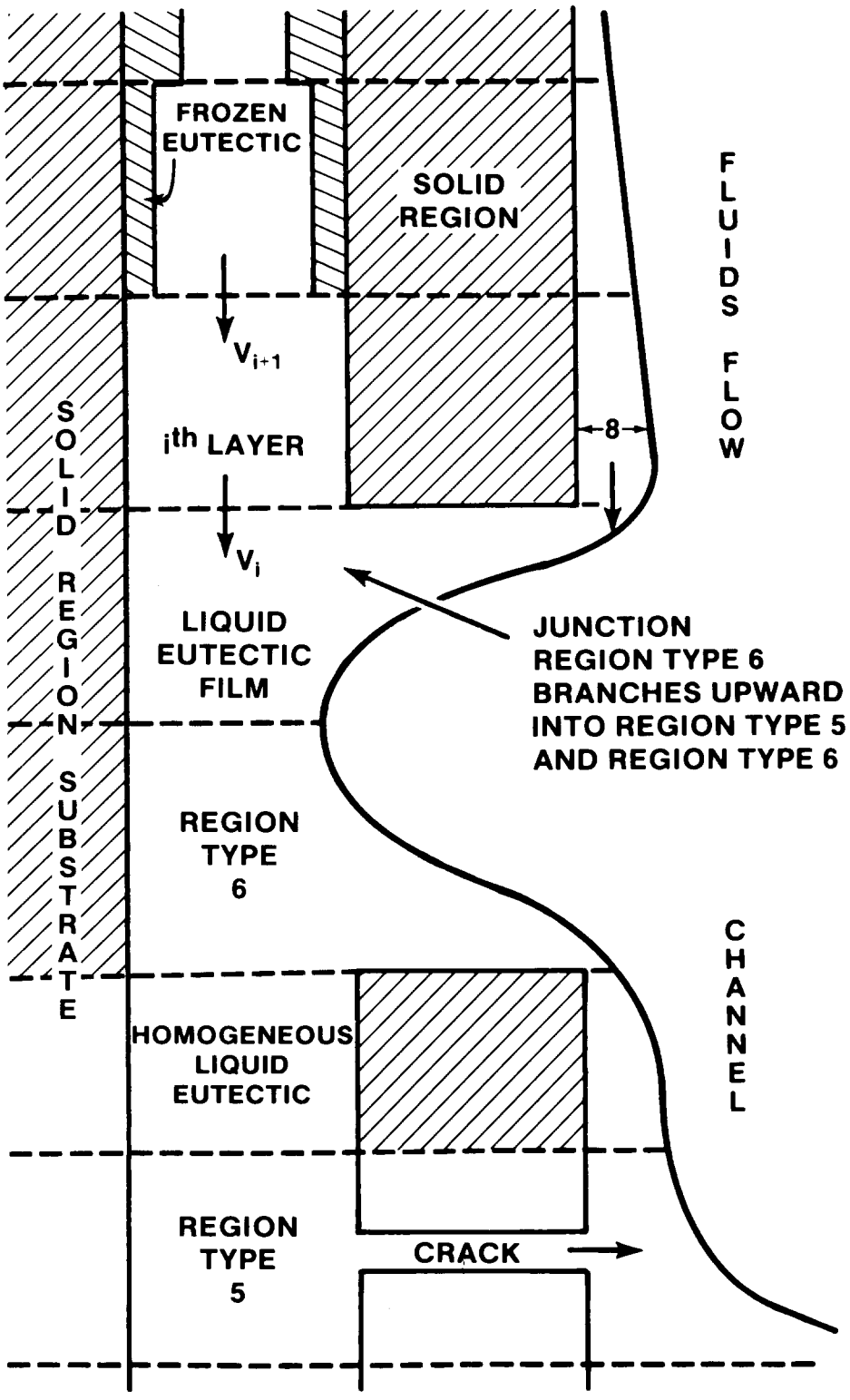

Figure 4.1-1. Typical CANDLE Geometry

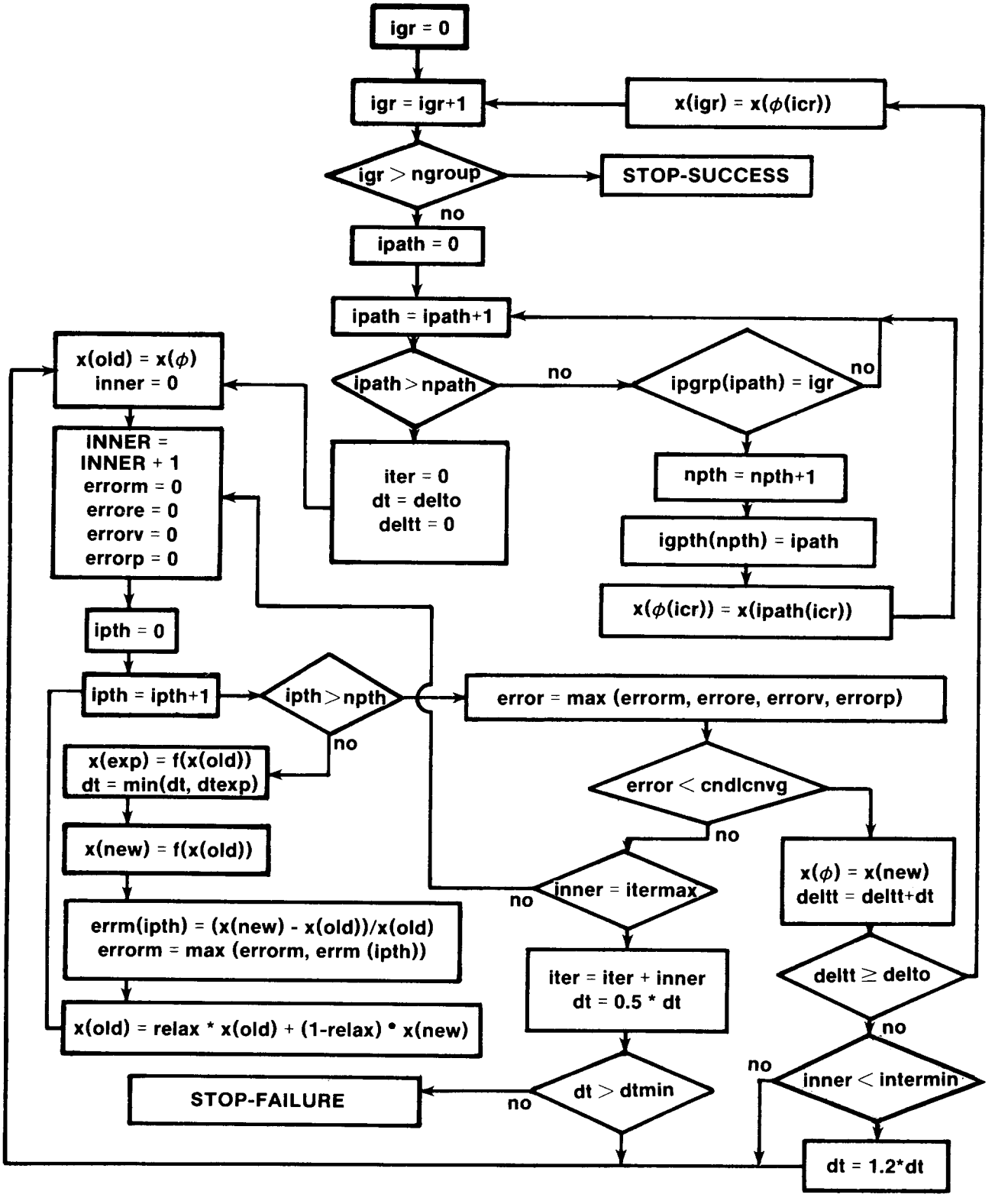

Figure 4.1-2. CANDLE Solution Algorithm

algorithm over the axial layers to obtain "new" iterate values of the dependent variations from the "old" ones. "Old" iterate values are updated with relaxed values of the "new" iterates, and mass, energy, velocity, and pressure relative errors are evaluated at each iteration. Convergence is obtained when the maximum error for every dependent variable in the group is less than the input convergence criteria. If the number of iterations exceeds an input limit, the sub-time-step is halved and the process is repeated until convergence occurs or the sub-time-step becomes smaller than a specified value (currently 10^{-5} s). At this time the process has failed; a diagnostic message is then printed, and the calculation shifts to the next group. If it is necessary to subdivide the MELPROG time-step to obtain convergence, then the converged values are used as initial conditions for the next sub-step until the sum of the sub-time-steps equals the MELPROG-time-step.

When the calculation successfully reaches the end of the MELPROG-time-step for a group of paths, the solution is examined to identify cells with "small" eutectic masses that may cause numerical problems in subsequent calculations. To prevent that possibility, a simple algorithm combines the small masses with the mass in a neighboring cell. Then incremental changes in the eutectic mass and energy in each region of each layer (a cell) are calculated by subtracting the initial values of mass and energy from the final values.

The CORE module has been coupled to MELPROG-PWR/MOD0 (1-D fluids) and is presently being debugged. Coupling of the CORE module to MELPROG-PWR/MOD1 has begun. The development of the BWR core structure models is the major step in making the BWR version of MELPROG--MELPROG-BWR/MOD0. This effort will begin in FY87.

4.2 MELPROG Applications and Testing

(K. A. Williams, T. J. Heames, and J. E. Kelly, 6425)

The first complete, coupled, and mechanistic analysis of a reactor core meltdown sequence has been made with MELPROG-PWR/MOD1. The sequence analyzed was a station blackout accident sequence (TMLB') for the Surry plant. The MELPROG calculation was initiated at the point where the primary coolant saturated (estimated from a TRAC-PF1 calculation) and was run through the point that the reactor vessel failed. Betwen the beginning and the end, all important aspects of the meltdown sequence were calculated with MELPROG. While this calculation is the first one performed with the new version of MELPROG and must be viewed as preliminary at this point, the current analysis does demonstrate the advanced capabilities that this version of MELPROG possesses for core meltdown accident analyses.

In the TMLB' scenario, the primary system heat rejection path through the steam generators is unavailable due to a complete loss of feedwater; also the emergency core cooling systems and the containment safety features are unavailable due to the loss of all electric power. Decay heating following reactor shutdown results in complete boiloff of the water in the secondary side of the steam generators. After steam generator dryout, the primary system pressure rises to the relief valve setpoint and the primary coolant temperature rises to the saturation temperature for that pressure. At this point, over 6000 s after neutronic shutdown, the vessel and core are near the coolant saturation temperature and have very low thermal gradients. It is at this point that the MELPROG analysis began.

The model used for this analysis is shown in Figure 4.2-1. Five radial rings and 13 axial cells are used in a cylindrical grid to represent the reactor vessel. (A total of 65 nodes are used.) The calculation is bounded on the bottom by the lower head, on the top by the upper head, and on the outer radial side by the vessel wall. The first three radial rings are used to model the core region, the fourth ring represents the core bypass region, and the fifth ring represents the downcomer. The three radial rings in the core region subdivide the fuel assemblies equally by volume. This equal volume separation is assumed to be adequate to describe the radial heat transfer and failure incoherence. However, the number of rings and axial cells is user input; more can be used at the cost of computer time and memory. The 13 axial cells include six in the fuel rod region to enable computation of the axial gradients necessary to follow melt progression. These six cells include the fuel rods, the control rods, and poison rods. All of the major vessel structures are modeled, as shown in Figure 4.2-1. The major plates are located at cell boundaries to allow accurate, structural thermal calculations to be performed. In the axial cells below the core, additional structures associated with instrumentation and core support have been added as heat sinks with the appropriate volume and surface area. In developing the lower plenum noding, the volume of the liquid contained in the plenum was made consistent with the actual volume.

All the geometric data for the core, barrel, and vessel are readily available from either the Surry FSAR[69] or the BMI-2104[70] documents. The geometric data for the core plate, support plate, and diffuser plate as well as the structural support columns can be inferred from other Westinghouse plants.

Steady-state values of pressure drops and flows were used to calibrate the model. Specifically, 1 percent of the total vessel flow cools the upper head from the spray cooling

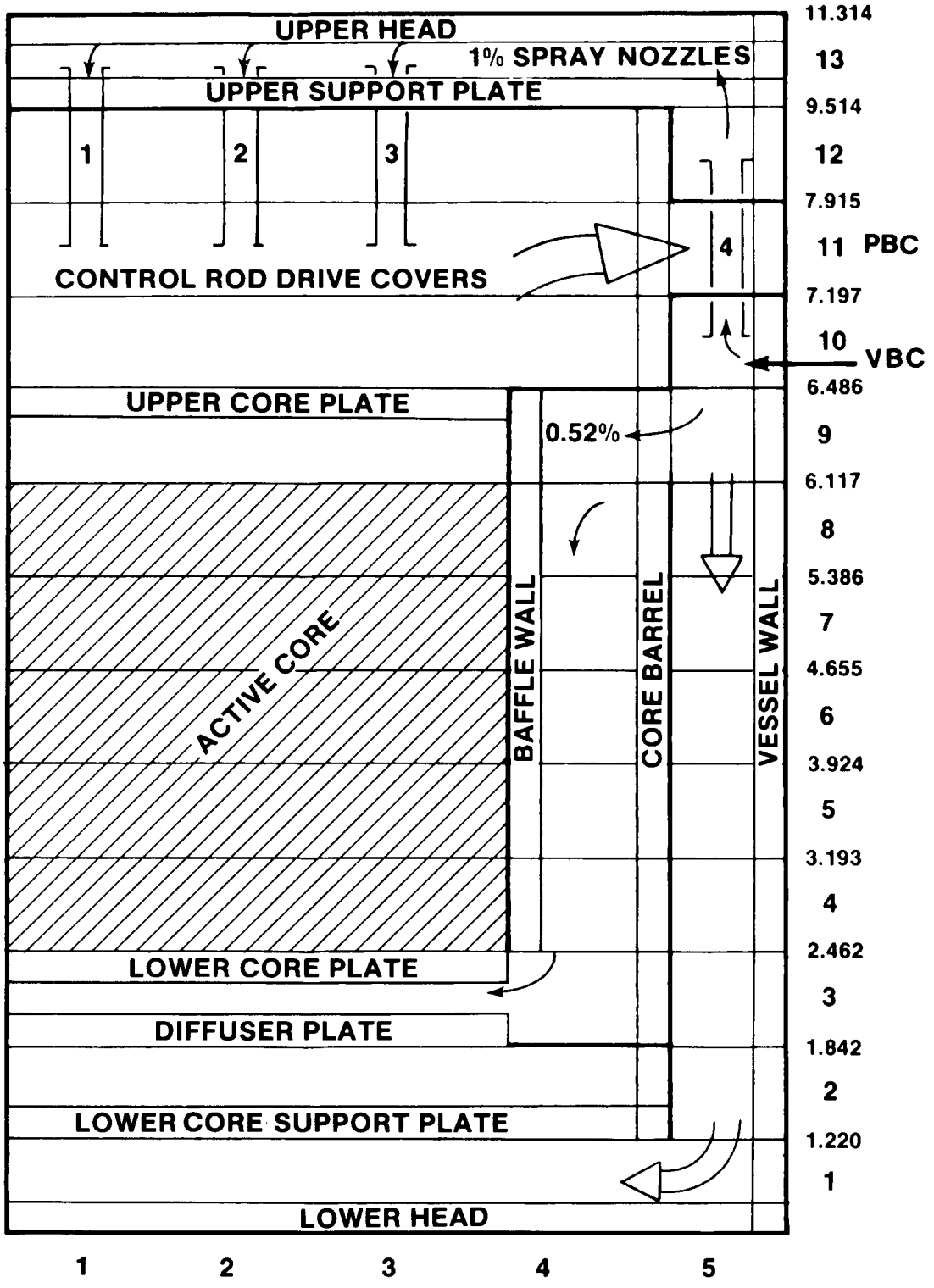

Figure 4.2-1. MELPROG Analysis Model

nozzles. The amount of flow penetrating the core barrel and flowing down the core bypass was adjusted to 0.52 percent. Flow resistances were adjusted to achieve the required pressure drops between the inlet nozzles and diffuser plate and between the diffuser plate and outlet nozzles. Axial lengths of cells representing the upper and lower heads were adjusted to achieve the appropriate fluid volume of these hemispherical regions. Finally, FSAR values of total vessel flow and power produced the required temperature rise and core average velocity.

A TRAC-PF1[71] calculation[72] for Zion-1 PWR was used to provide initial conditions for MELPROG at a point 6500 s into the transient, when boiling began in the core. The cold-leg flow calculated by TRAC was equal to 3.5 percent of nominal full power flow at this point. This flow is due to a natural circulation loop within the primary system and was calculated by TRAC to decrease to zero beginning about 300 s after boiling began in the core. For simplicity, the flow through the cold leg was set to zero at the beginning of the MELPROG calculation. This condition was chosen to allow comparison with the results of a previous calculation with similar assumptions.[73] The pressure boundary condition representing the hot legs was set to the PORV setpoint of 16.3 MPa.

In performing this analysis, a base-case calculation has been defined. This calculation is simply the complete calculation that has been made. It is not necessarily the most accurate calculation possible. Nevertheless, it is this base-case calculation which will serve as a reference point in future comparative analyses currently under way.

The sequence of important events for this base-case calculation is given in Table 4.2-1. This list does not give great detail concerning the various events, but serves to place the events in the proper sequence. As the calculation is described, further detail will be given.

In describing this calculation, the accident sequence has been divided into five sections. These sections chronologically cover the entire sequence (with some overlap) and lump together related phenomena and similar events. The first section is the boiloff and core heating to the start of oxidation phase. This section includes the period from the beginning of the calculation until the maximum cladding temperature exceeds 1273 K. Relative to Table 4.2-1, this is from 6500 to 9300 s.

The second section is the cladding oxidation and fuel rod failure phase. This section includes the period during which the Zr cladding is oxidizing and generating heat. The core rapidly heats during this period leading to fuel and

Table 4.2-1

TMLB' Event Sequence

Time(s)	Event
0	Loss of offsite power, loss of feedwater
4170	Steam generators dry
6500	Incipient boiling, begin MELPROG calculation
7070	Core "uncovered"
8350	Core empty
9280	Hydrogen generation begins at top of core
9970-10145	Control rods fail in rings 1 and 2, nodes 7, 8, and 9; steam temperature > 1700 K
10156	Cladding begins to melt in ring 1, node 8; cladding temperature > 2180 K
10181	Fuel rods fail in ring 1, node 8; cladding molten and temperature > 2200 K
10216-10221	Control rods fail in ring 3, at top of core
10241-10303	Cladding melts and fuel rods fail in rings 1 and 2, nodes 6 through 9
10319-10377	Cladding melts and fuel rods fail in ring 3, nodes 6 through 9
10377-10403	Fuel rods fail in rings 1 and 2, node 5
10387	Upper core plate melts in ring 1
10808	Fuel rods fail in ring 3, node 5
11345-10260	"Thin" metal in upper plenum melts
11522	Control rods fail in ring 1, node 4
11680	Core baffle fails mechanically
11824	Core baffle begins to melt
14877	Debris region crust fails, core slumps
14878	All remaining fuel rods fail
15371-15874	Lower support structures melt
15928	Lower head fails, end MELPROG calculation

control rod failures. Relative to Table 4.2-1, this phase includes the period from 9300 to 10400 s.

The third section is the debris region formation and behavior phase. This section includes the initial formation of debris regions, their heating and eventual relocation. Relative to Table 4.2-1, this phase includes the period from 10180 to 14877 s.

The fourth section is the core slump phase. This section includes the slumping of the core debris into the lower plenum. The core slump is a very fast event, but is very significant. As noted in Table 4.2-1, this event occurs at 14877 s.

The fifth and final section is the vessel heating and failure section. This section includes the core debris heating in the lower plenum and the eventual failure of the vessel head. Particular attention is given to the state of the core debris at the time of vessel failure. Relative to Table 4.2-1, this section covers the period from 14877 to 15928 s.

Until cladding oxidation begins, the transient is simply a slow back-off process. When the cladding temperatues exceed 1273 K, the cladding oxidation calculation begins. This process becomes highly exothermic as the temperature increases and accelerates the fuel-rod heating. Throughout this time, the cladding temperatures are increasing as core decay energy and energy from cladding oxidation are deposited in the rods, fluids, and structures. The rapidly increasing fluid and structural temperatures in the core region will cause failure and the formation of debris regions. The first component to fail will be those portions of the control rods whose stainless steel cladding have reached the 1700 K melting point. The liquefied control materials drain from the failed rods into the intact core and proceed downward until they have given up enough heat to cooler structures to cause them to freeze.

When the cladding temperatures reach 1850 K, the oxidation kinetics change and the cladding oxidation rate increases markedly. Fuel-rod cladding begins to melt when cladding temperatures exceed 2180 K. The rods are assumed to fail in those portions where the cladding is completely molten and above 2200 K. The current model assumes that failed fuel rods are fragmented, and the debris, which is formed, is of a particulate nature. Recent evidence indicates that the fuel rods may not simply fragment at such a low temperature and that more refined models such as the MELPROG CORE module are needed. The debris formed by fuel-rod failure will move downward and freeze or lodge in the lower sections of the core.

In the TMLB' calculation, the exothermic metal-water reaction (oxidation) becomes a significant heat source when it begins in the ring 1 rods at approximately 9300 s in nodes 6 through 9. The heating rate in these nodes changes from 0.3 to 0.8 K/s as is indicated in Figure 4.2-2. Figures 4.2-2 through 4.2-4 give the cladding surface temperatures for the upper five nodes for each of the three radial rings in the core region. Ring 2 cladding begins to oxidize approximately 100 s later in nodes 6 through 8. Ring 3 cladding oxidation begins approximately 300 s after ring 1 at 9600 s.

A closer examination of the figures reveals that for this part of the accident the temperature increases upwards through the core in ring 1 (the axial temperature gradient is positive), whereas in ring 3 it increases downward through the core (the axial temperature gradient is negative). Ring 2 increases upwards except for the uppermost node (node 9). The temperature distribution can be explained by the flow patterns present in the vessel. Flow is found to be upward in ring 1 and most of ring 2 (except for node 9) and downward in ring 3. A pattern similar to this persists until 9970 s when the gas in the hottest node of the core reaches the stainless steel melting point (1700 K). At 1700 K, it is assumed that the stainless steel control rod cladding fails, releasing the molten silver-indium-cadmium absorber alloy that it contains. In the next 175 s, all of the control rods in the top four nodes of rings 1 and 2 fail. The absorber material, whose freezing point is 1070 K, flows downward through the core. The minimum rod temperature in the core when absorber material begins to move is approximately 1200 K in node 4 at the bottom of the core. Therefore, the absorber material does not freeze until it contacts water in the lower plenum. Heat transfer from the absorber material to the water causes steaming in the lower plenum, which, in turn, cools node 4 rods in all three rings and node 5 rods in rings 2 and 3. Continued heating results in the hottest rods reaching 1850 K at 10115 s at which point a change in the ZrO_2 lattice structure causes an increase in the oxidation rate. The increased oxidation is manifested in a change in the rod heating rate from 0.8 to 2 to 5 K/s, which can be seen in the rod temperature plots (Figures 4.2-2 through 4.2-4). With increased heating the rods rapidly reach the cladding melting point (2180 K) and then the failure temperature (2200 K). In ring 1 at node 5 (the hottest location in the core), these events occur at 10156 s and 10181 s, respectively. Rod failure is indicated by the point at which the line ends in the rod temperature plots.

The total hydrogen mass produced by oxidation of cladding is given by Figure 4.2-5. Most of the hydrogen is produced when the rods are intact and above 1850 K (between 10115 s

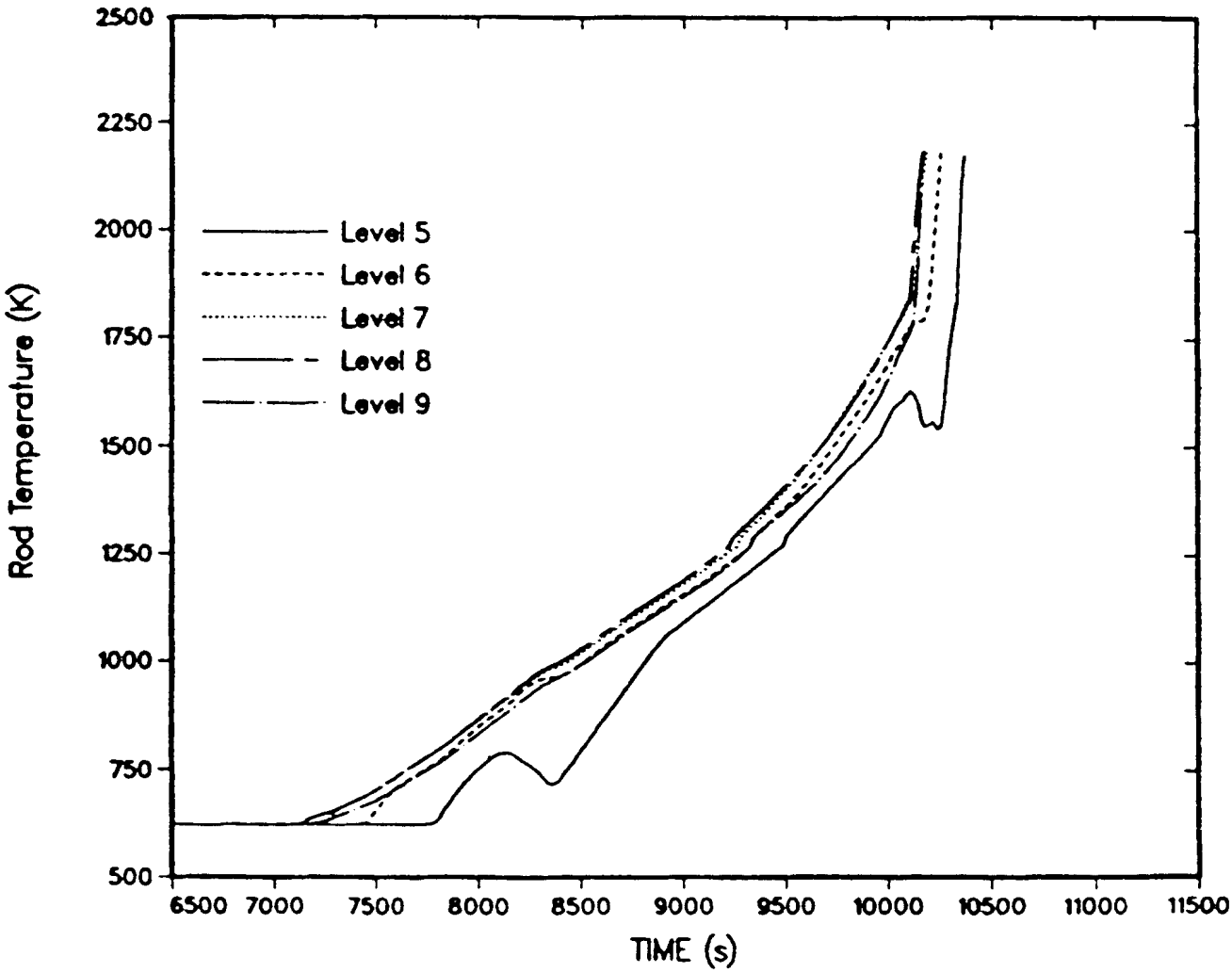

Figure 4.2-2. Cladding Wall Temperature in Ring 1

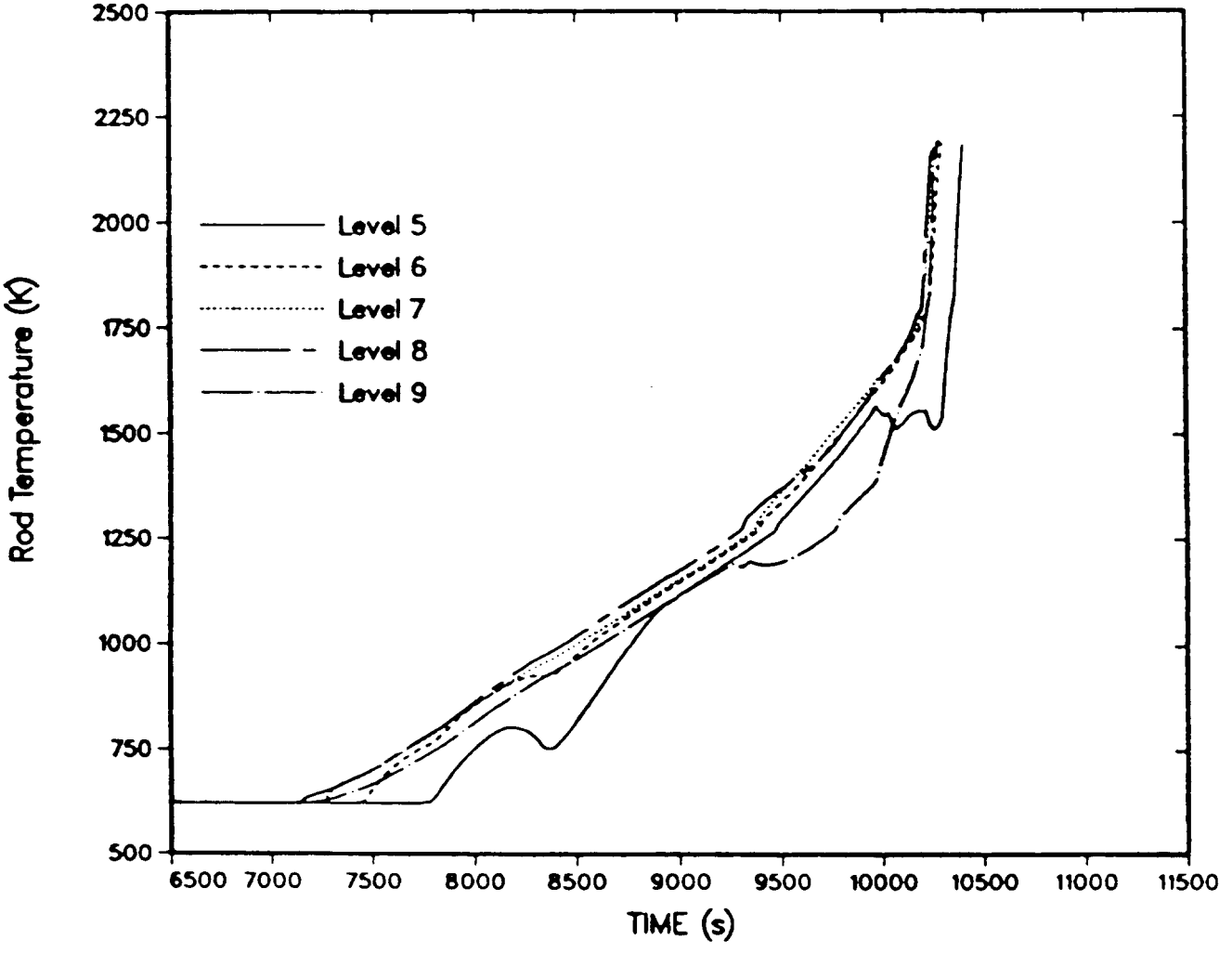

Figure 4.2-3. Cladding Wall Temperature in Ring 2

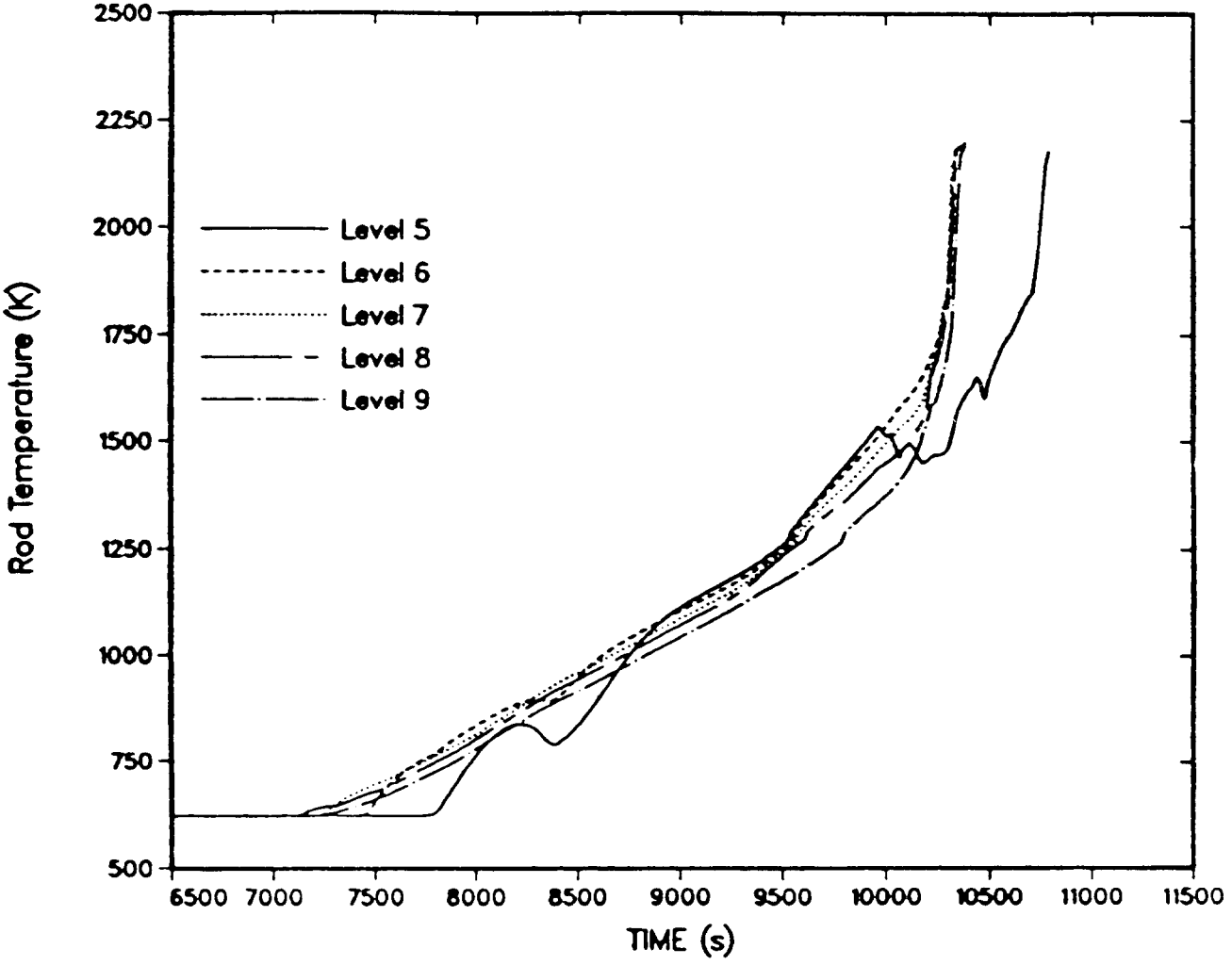

Figure 4.2-4. Cladding Wall Temperature in Ring 3

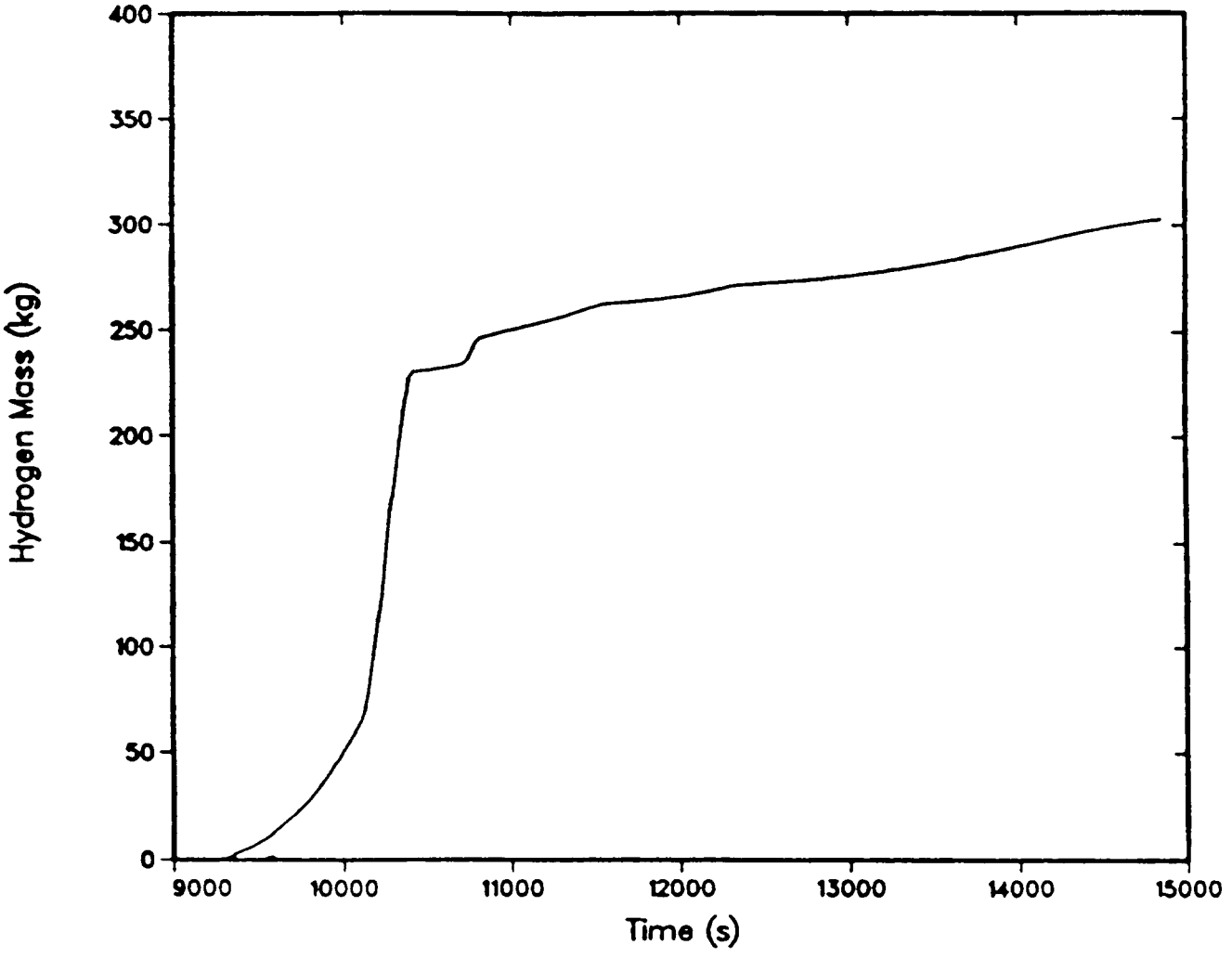

Figure 4.2-5. Total Hydrogen Mass Produced

and 10403 s). It is during this time period that all of the rods except those at node 4 and those in ring 3, node 5 are oxidizing rapidly and fail. The small addition of hydrogen at approximately 10800 s is due to the oxidation of the node 5 rods in ring 3. Figure 4.2-6, which gives the total pressure and hydrogen partial pressure at the top of the core, shows that steam starved conditions were not reached in the base-case calculation. The abrupt changes in hydrogen partial pressure are caused by the quenching of control rod material and induced steaming in the lower plenum. The resulting steam sweeps the gas, including the hydrogen, from the vessel. The steam flow from the lower plenum also lowers the temperature in the bottom of the core region. The low rod failure temperature (2200 K) used in the base case limited the amount of cladding oxidation; the average oxidation fraction at failure was only 0.4.

In the current case, the debris material is calculated to be molten and begins to flow downward. As it moves, it loses energy, cools, and eventually freezes. Depending on the degree of superheat, some material may flow into the plenum. However, the usual case is that the material freezes on intact rods in the lower section of the core. As material accumulates on intact rods, a debris region will eventually form. In the current model, a debris region forms when a cell is at least half full of corium at the minimum packing fraction (37 percent). This means that the corium occupies a minimum of 18.5 percent of the free volume of a cell before a debris region forms.

Once it is determined that a debris region exists, the DEBRIS module begins to perform a detailed calculation of the heating and melting of the region. As time progresses the intact rods upon which the debris region formed fail, and their mass is added to that in the debris region. As other rod sections fail above the region, their mass is relocated downward until reaching the top of the region. At this point, the mass is added to the region. This process continues and leads to increases in the size of the region.

When the support for a region fails, it is assumed that the debris can relocate. At this point, FLUIDS resumes control of the debris behavior calculation. This means that a detailed debris calculation is not performed until a debris region reforms. Hence, if the debris region is supported on the lower plate and the plate fails, then the debris will relocate into the lower plenum. The debris will usually encounter water in the plenum, and the resulting quench will generate copious quantities of steam and hydrogen. Eventually, a debris region will form on the vessel bottom and begin to reheat.

In this calculation, the first fuel rod section fails at 10181 s in ring 1, node 8. A debris region forms shortly

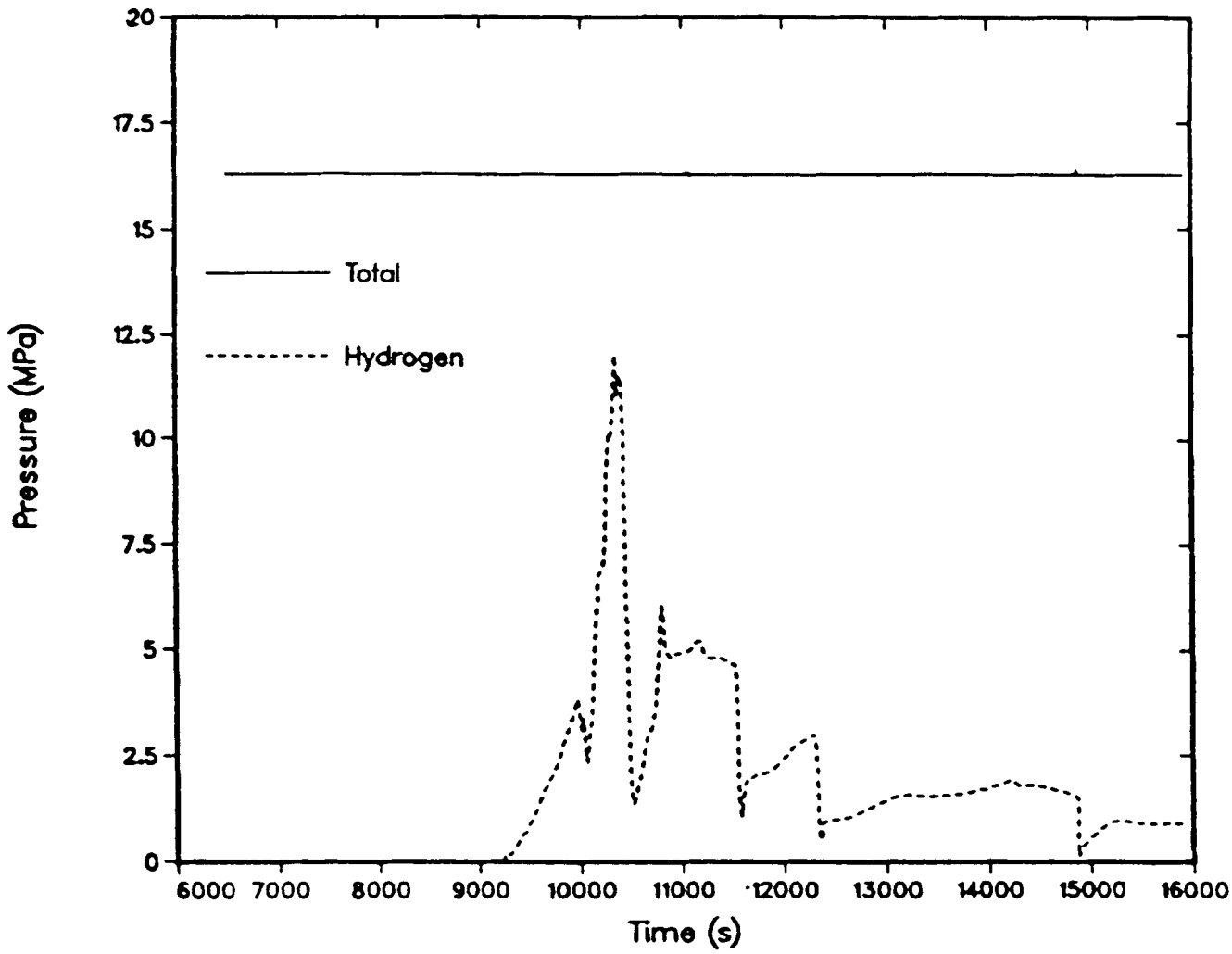

Figure 4.2-6. Total Pressure and Hydrogen Partial Pressure at Top of Core

thereafter in ring 1, node 7. The rod section in ring 1, node 9, fails at 10197 s followed by the rod section in ring 1, node 7, at 10199 s. By 10206 s, the debris region in ring 1 is 1.25 m high and has an average temperature of 2140 K. The region is fairly porous and has steam flowing through it. Consequently, the unoxidized Zr in the region continues to oxidize.

At 10273 s, the rod section in ring 1, node 6, fails. This failure causes the debris region to lose its support, and consequently the debris relocates downward. However, the debris does not have much superheat, and a new debris region forms in ring 1, cell 5. By 10303 s, sufficient remelting and relocation of material (mainly Zr) in the debris region has occurred so that a crust (5-cm thick) has formed at the bottom of the region. At this point, the steam flow through the region ceases, and this terminates the Zr oxidation in this debris region.

This region continues to melt and relocate internally, but remains stable because the bottom of the region is cooled by steam from below. In the current model, the crust at the bottom of the region is assumed to be stable until it attains the Zr melting temperature (2200 K) or loses its support. Due to the poor heat transfer in the region and the cool steam below the region, the time scale to reach a failure limit is long. In fact, not until 14877 s does the crust fail by melting. The long time to failure seems too large and is currently believed to be due to a heat transfer coupling error between the debris and the gas. A development effort is currently under way to correct this problem.

The pattern of rod section failure and debris region formation is similar in the other rings and occurs during the same time that the sections in ring 1 are failing. In ring 2, the debris region ultimately forms in node 5, while in ring 3 it ultimately forms in node 4. While the actual locations of the debris regions are not exactly the same, the general meltdown behavior is the same in each ring.

As the sequence proceeded, the debris regions in all rings continued to heat, melt, and relocate internally. The region in ring 1 began in node 5 and was 2.2 m high. In ring 2, the region also began in node 5 and was 2.4 m high. The region in ring 3 began in node 4 and was 3.1 m high. At 14877 s, the crusts in ring 1 and 2 failed, which marked the beginning of the core slump phase. At this time, it was arbitrarily assumed that the region in ring 3 would also release.

At this time, the average temperature of the core debris was 2840 K. This high temperature is directly related to the

long time required to fail the crust. An earlier crust failure time would have resulted in a lower temperature. Of the debris, approximately 72 percent was molten. Due to the large degree of superheat and large molten fraction, a significant amount of the core debris entered the lower plenum after the debris regions in the core released. At the time just prior to core slump, there was approximately 3000 kg of saturated water in the lower plenum.

The code calculates that within 5 s after the initiation of core slump approximately 75000 kg of debris relocated into the plenum. This implies an average corium fraction of 76 percent. This high packing fraction is due to the large molten fraction in the debris prior to slump. While the current version of the code does not contain a fuel-coolant interaction model, it does model the heat transfer between the corium and the water and steam. When the corium and water mix, the corium partially quenches while the water rapidly boils by means of film boiling. Within 5 s, 95 percent of the plenum has been voided. The voiding occurs due to vaporization and to sweep-out of the water (by entrainment and displacement). Most of the remaining water is in the downcomer region. This water enters the plenum and vaporizes as it enters. Within 15 s, the plenum is devoid of water and the average corium temperature is 2350 K.

The steam produced during the rapid vaporization raises the pressure in the interaction zone (the bottom of the lower plenum) to 17.9 MPa. During the interaction, a 0.6 MPa pressure drop develops across the downward falling corium above the interaction zone. This pressure drop is not large enough to levitate the corium. This pressure drop is enough, however, to move steam upward through the falling corium with a velocity in excess of 2 m/s. The steam flows through the core, the upper plenum, and out of the vessel. The vessel exit area corresponds to the flow area of one hot leg. Even with this relatively large flow area (0.426 m^2), exit velocities in excess of 200 m/s were seen during the core-slump interaction.

The corium that enters the lower plenum after core slump is only partially quenched by the water in the plenum. This is due to the low inventory of water and the high debris temperature. The debris quickly accumulates into debris regions in the first 3 rings throughout the lower plenum. In fact, the debris regions extend from the bottom of the vessel up to node 4 in the core (>2 m high). After boiling the water away, the debris has an average temperature of 2350 K.

As time progresses, the debris regions heat, remelt, and compact. The heating is due primarily to decay heat since there is no steam flow through the regions, which could

oxidize the unoxidized Zr. The heat generated in the regions is transferred upward by radiation and downward to the vessel by conduction.

As indicated above, the core slump occurs at 14877 s. At this point the average vessel temperature is 610 K. Even though the heat transfer between the debris and the vessel is poor, the high debris temperature results in a rapid heating of the vessel. The average temperature of the vessel bottom in the central ring increases at a rate of 1.5 K/s. This high heating rate results in the rapid failure of the vessel bottom.

In the current calculation, the vessel was predicted to fail in ring 1 at 15928 s (over 2.5 h after the start of voiding). The mode of failure was a creep-rupture type and not a complete melt through. At the time of failure, the average temperature of the vessel bottom was 1428 K, and ablation of the vessel had begun. It should be noted that no instrumentation tube weld had been modeled in this calculation, and hence no failure of this type could be predicted. After the vessel bottom failed, the calculation was terminated.

At this time, the debris in the vessel was 30 percent molten on average. The debris in the lower plenum consisted of both the core material and structural steel. Table 4.2-2 gives a brief summary of the state of debris regions at the time of vessel failure. This information provides the compositional basis to indicate the distribution of the debris. Included here is the amount of steel in the debris, most of which is added to the debris after core slump. Also included here is the amount of unoxidized Zr. This amount (9575 kg) represents 58 percent of the original inventory. The average temperature of the debris was 2460 K.

This "base case" calculation has provided the timing of the major events occurring in the accident, the amount and timing of hydrogen produced by oxidation of zircaloy cladding, and the condition and composition of the disrupted material at the time of vessel failure. Because this calculation is preliminary, a limited number of sensitivity studies are currently being performed. These studies are useful for identifying the key phenomena in a meltdown sequence. While these studies are not yet complete, two important observations have already been made.

In particular, this work has confirmed that natural circulation reduces the rate of core heating, but increases the rate of heating of upper plenum structures. This implies that a significant amount of core energy is deposited in the plenum and primary piping. This increased heating can inhibit fission-product deposition and increase the

amount of molten structural steel in the melt at vessel failure. It is also shown that the coupling between vessel flow and primary system flow may lead to rapid heating and early failure of the primary system. Natural convection cooling of the top of a debris region, such as in the lower head, also lengthens the time to vessel failure. Hence natural circulation within the vessel with coupling to the primary system can completely change the course and timing of a meltdown sequence. This underlines the importance of a multidimensional vessel flow capability coupled to a complete treatment of the primary system such as will be provided by TRAC-MELPROG/MOD1.

Table 4.2-2

State of Debris at Vessel Failure

	Mass (kg)	% Molten/ Liquefied
UO_2	96000	14
Zr	9600	100
ZrO_2	9250	0
Steel	19300	78
Control Rod	2850	100
TOTAL	137000	30

T_{ave} = 2460 K

In addition, the calculation sensitivity to the modeling of the initial fuel rod melting and relocation has been found to be important. Variations in the assumptions are found to strongly affect hydrogen production and the subsequent course and timing of the accident (total hydrogen production was doubled and vessel failure occurred earlier for a higher failure and relocation temperature). Thus, it is shown that more accurate models, such as provided by the MELPROG CORE module, are needed.

5. ADVANCED REACTOR ACCIDENT ENERGETICS

The Advanced Reactor Accident Energetics Program was initiated in 1975 to address the important phenomenological uncertainties involved in LMFBR core disruptive accidents. The Accident Energetics Program consisted of 10 major in-pile experimental programs addressing all phases of in-core phenomenology. These programs drew significant international attention and were jointly funded and staffed by the German KfK, Japanese PNC, and the UKAEA. With the completion of the STAR-7 test in the Initiation Phase, the GAP-2 experiment in the Transition Phase, and the irradiated Equation-of-State experiments in the Disassembly Phase, the major elements of the program have now been completed.

5.1 Initiation Phase
(S. A. Wright and P. S. Pickard, 6421)

The Sandia Initiation Phase Fuel Dynamics Program provided experimental data and analysis for the initiation phase of an LMFBR core-distruptive accident. The motion of clad and fuel in the initiation phase of an LOF accident is an important consideration in the subsequent progression of the accident. Early fuel dispersal can lead to neutronic termination while limited dispersal and blockage formation continue the accident into the transition phase and the possibility of further neutronic activity.

To obtain data on the important phenomena involved in this phase of an LMFBR accident, the Sandia Transient Axial Relocation (STAR) experiments were performed in the Annular Core Research Reactor (ACRR). The purpose of the seventh and last experiment in the STAR program, STAR-7, was to investigate the upper bound loss-of-flow (LOF) accident scenario for the MONJU fast breeder reactor. The experiment was performed successfully and analyses are currently in progress at PNC.

The experiment reproduced the heating conditions for the proposed MONJU LOF accident scenario. Preliminary analysis of the data and film shows limited prebreakup fuel motion due to fuel crumbling during the clad melting phase of the accident scenario. Late pin break up due to fuel melting is observed at high power levels, and this is accompanied by significant axial fuel motion. Much later an energetic event is observed which destroyed the quartz tube and dispersed fuel over the inside of the containment. This "explosion" is believed to have been caused by steel vaporization, which began its heating to possibly superheated levels when breakup was observed (about 200 ms earlier). Simple extrapolation of the clad heating rates indicates that the local entrained clad temperatures may have been as high as 3700 K. Theoretical models indicate

that this "vapor explosion" was probably due to rapid heat transfer from superheated liquid fuel to a liquid steel droplet.

5.2 Transition Phase
(R. O. Gauntt, 6423; P. S. Pickard, 6421)

If sufficient fuel dispersal does not occur in the initiation phase of a core disruptive accident, the accident may progress to a "transition" or "meltout" phase. The key questions in the transition phase, highlighted in the CRBR safety review, are whether fuel or clad blockages form, leading to a confined or "bottled" core configuration, and the behavior and reactivity implications of this pool of fuel-steel in the core region if the fuel blockages do lead to this state.

The TRAN program addressed the question of fuel-inventory reduction by penetration into the upper core structure through subassembly gaps to the lower core structure. If deep penetrations occur, nonenergetic shutdown is probable while shallow penetrations will lead to a transition phase and the possibility of further energetics. First-of-a-kind in-pile experiments have been conducted to provide data to evaluate the various models describing fuel penetration.

The last experiment in the TRAN program, GAP-2, addressed the large fuel removal paths presented by the subassembly gap regions of the LMFBR core. This experiment involved the melting of a 1.7-kg UO_2 fuel load and the downward injection by applied gas pressure of this melt into a channel representative of the subassembly can wall gaps. The fuel load was successfully melted, and a temperature of about 4000 K was attained. Analysis of the channel thermocouples indicated the arrival of a substantial amount of melt at all axial locations along the length of the channel (~70 cm). In addition, thermocouples situated at the bottom of the dump tank showed ~200 K heating of this massive component, an indication that a substantial amount of molten material penetrated the full length of the freezing channel. Preliminary interpretation of GAP-2 at KfK suggests that conduction freezing dominates fuel removal processes and that potentially large fuel removal capability exists through these fuel paths.

5.3 Disassembly Phase--Effective Equation-of-State (EEOS) Experiments
(W. Breitung and P. S. Pickard, 6421)

5.3.1 Introduction

In the safety evaluation of LMFBRs, the severity of Core Disruptive Accidents (CDAs) is a primary concern. One of

the significant sources of uncertainty in the mechanistic modeling of such CDAs is the lack of thermo-physical data for irradiated fuel. The Effective Equation-of-State (EEOS) experiments investigate the pressure source from irradiated mixed oxide fuels (U, Pu) under severe accident conditions. The tests are sponsored by the Fast Breeder Project/KfK through the NRC and are being conducted in the ACRR.

5.3.2 Research Goal

The working fluid during a CDA core expansion phase is generally liquid irradiated fuel. To calculate the mechanical excursion of the core disruption, the pressure--enthalpy and pressure--temperature relation of the fuel is needed up to about 6000 K.

The EEOS experiments have been designed to investigate the pressure buildup from irradiated fuel under three different conditions:

1. In-channel conditions
2. In-pin conditions
3. Vacuum environment

The individual test objectives of these three experiments (EEOS-10, -11, and -12) are summarized in Table 5.3-1. The test parameters were carefully selected from the experimentally accessible parameter space to simulate the above given conditions as closely as possible.

5.3.3 EEOS Technique

The experimental concept was developed in the very first in-pile vapor pressure measurements on UO_2.[74] In a succeeding test series on fresh reactor fuels, sponsored jointly by the NRC and the Fast Breeder Project/KfK, this technique was further improved. The pressure cell (Figure 5.3-1) was redesigned and an in-pile calorimeter was added to reduce the uncertainties in the fuel enthalpy evaluation (Figure 5.3-2). The results of the fresh fuel EEOS tests were recently described in a final paper.[75]

The irradiated fuel test used the same experimental technique as previous ACRR EEOS tests. The test fuel was prepared from HEDL pin P15-2A, which had a peak burnup of 5.1 percent. The composition of the irradiated fuel and the fresh fuel, which was used in the calorimeter, is shown in Table 5.3-2.

Table 5.3-1

Irradiated Fuel EEOS Experiment Objectives

Experiment	Test Objectives
EEOS-10	Determine irradiated fuel vapor pressure for typical LMFBR coolant channel conditions (low fuel smear density and low ambient pressure).
EEOS-11	Determine irradiated fuel vapor pressure for typical in-pin conditions (high fuel smear density and high ambient pressure).
EEOS-12	Measure fission-product release kinetics without fill gas contribution. Compare to fresh fuel results.

5.3.4 EEOS Tests

The three tests, EEOS-10, -11, and -12, were performed during this reporting period. At this point no detailed analysis of the raw data has yet been done. Only a preliminary discussion of the measured data will be given here.

5.3.4.1 EEOS-10

EEOS-10 simulated the conditions that liquid fuel would typically encounter in a CDA scenario after it is ejected from a failed pin into the surrounding coolant channel. The EEOS test volume was filled with 0.95 g of 5.1 percent burnup $(U_{0.77}, P_{0.23})$ O_2 fuel, then evacuated and back filled with argon to a pressure of 0.03 MPa at 300 K. This fill-gas pressure resulted in about 0.5 MPa ambient pressure at 3600 K, with the thermal fuel expansion taken into account.

The ACRR transient was a double pulse with about 3000 J/g prompt energy deposited into the test fuel (Figure 5.3-3). The coupling factor of the irradiated fuel was determined by combining a calorimetric measurement for fresh fuel with TWODANT calculations for fresh and irradiated fuel. The measured and calculated coupling factor for fresh fuel agreed within 8 percent. The error limits on the irradiated fuel coupling factor are estimated to be less than ± 5 percent.

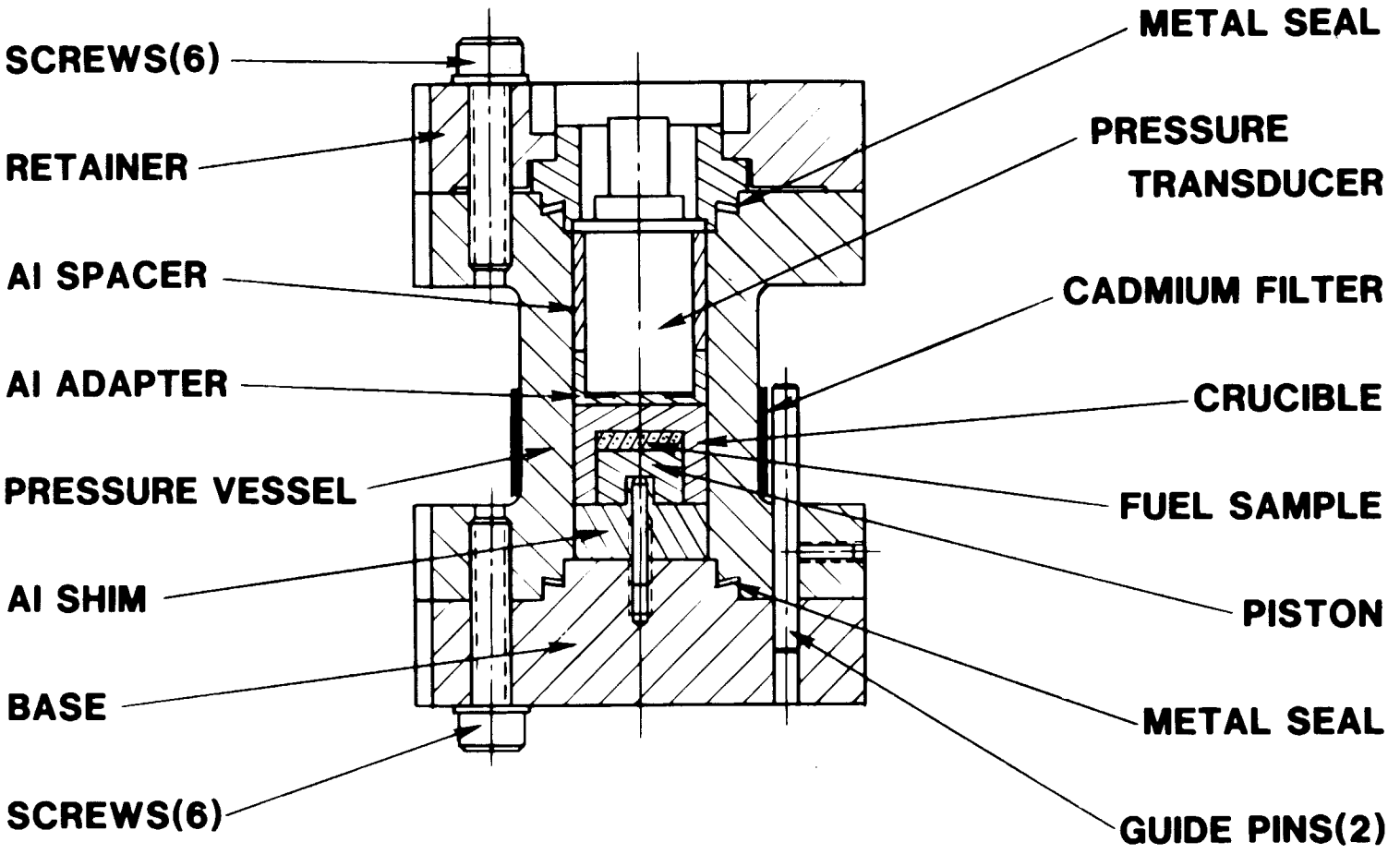

Figure 5.3-1. In-Pile Pressure Cell for Transient Measurement of the Test Fuel Vapor Pressure

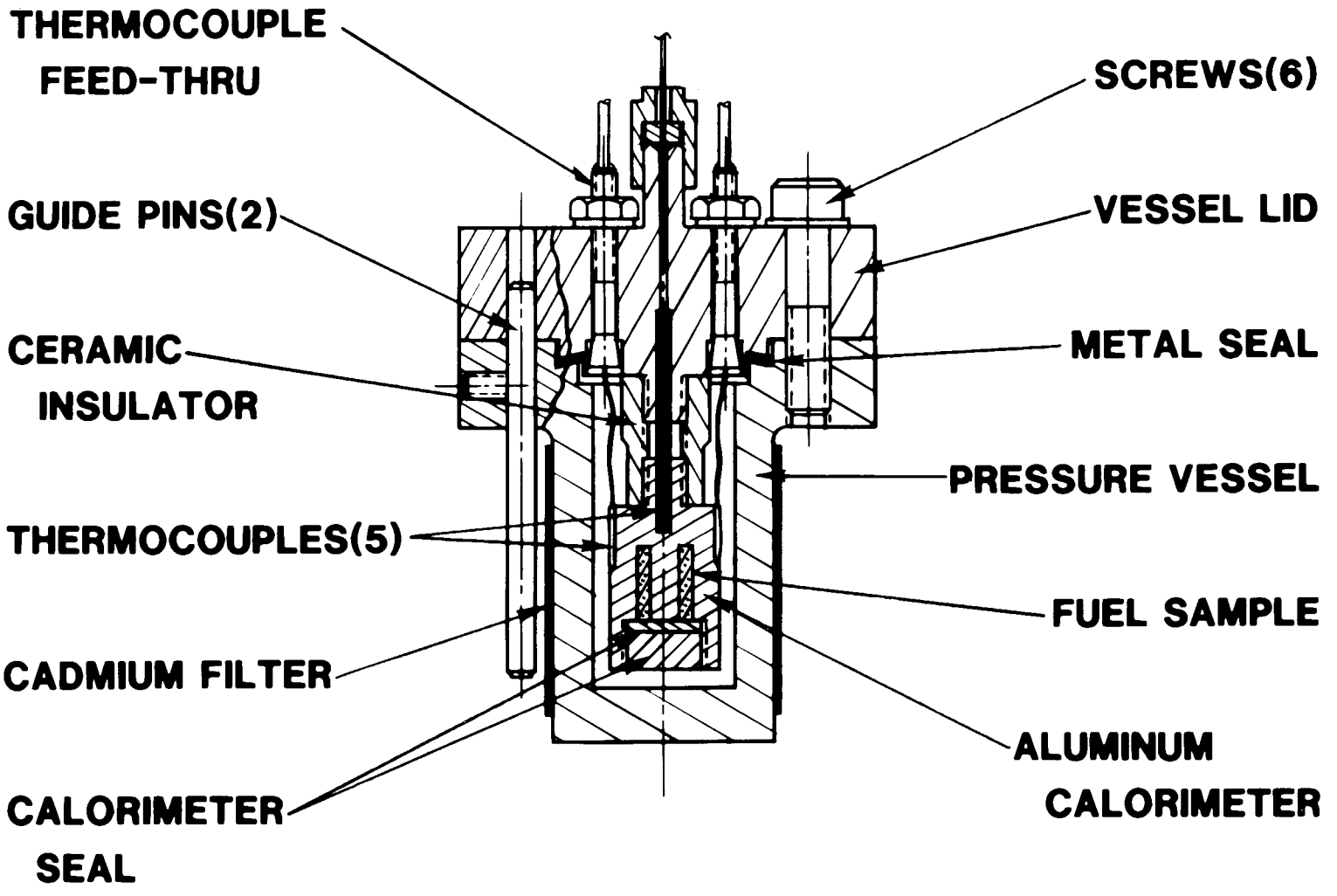

Figure 5.3-2. In-Pile Calorimeter for Measurement of the Total Energy Deposition Into the Test Fuel

Table 5.3-2

EEOS Test Fuel Composition
(Percent of Total Metal)

Isotope	Fresh Mixed Oxide (LASL)	Irradiated Mixed Oxide (Pin P15-2A)
U-235	0.15	0.45
U-238	76.83	73.57
Pu-239	20.01	22.52
Pu-240	2.66	3.46
Pu-241	0.27	0.39
Total Fissile	20.43	23.36

Figure 5.3-4 summarizes the measured pressure data. The noise signal in the pressure transducer (bottom curve) was measured in a separate background shot without fuel. When this background is subtracted from the pressure signal obtained with fuel (middle curve), the true net signal is obtained (top curve). The following observations can be made from this net pressure curve:

- The timing of the pressure sequence is consistent with the heating sequence: The first pressure plateau is reached at the end of the first pulse and the second plateau at the end of the second pulse.

- The pressure arrest from about 0.342 to 0.347 s agrees very closely with the fuel melting interval as calculated from the coupling factor, the energy deposition history (Figure 5.3-3), and the enthalpy data of fresh mixed oxide. This good agreement can be considered an independent confirmation of the fuel coupling factor evaluation.

- The succeeding pressure rise to about 1.7 MPa is due to further heating of the now liquid fuel. The slight decay to the pressure plateau at 1.6 MPa can probably be attributed to the ongoing convective mixing of cooler and hotter regions in the liquid fuel, with the heating power being very small at these times.

- During the times of the first pressure plateau, the test fuel temperature should be around 3700 K, if nearly adiabatic conditions exist. The total

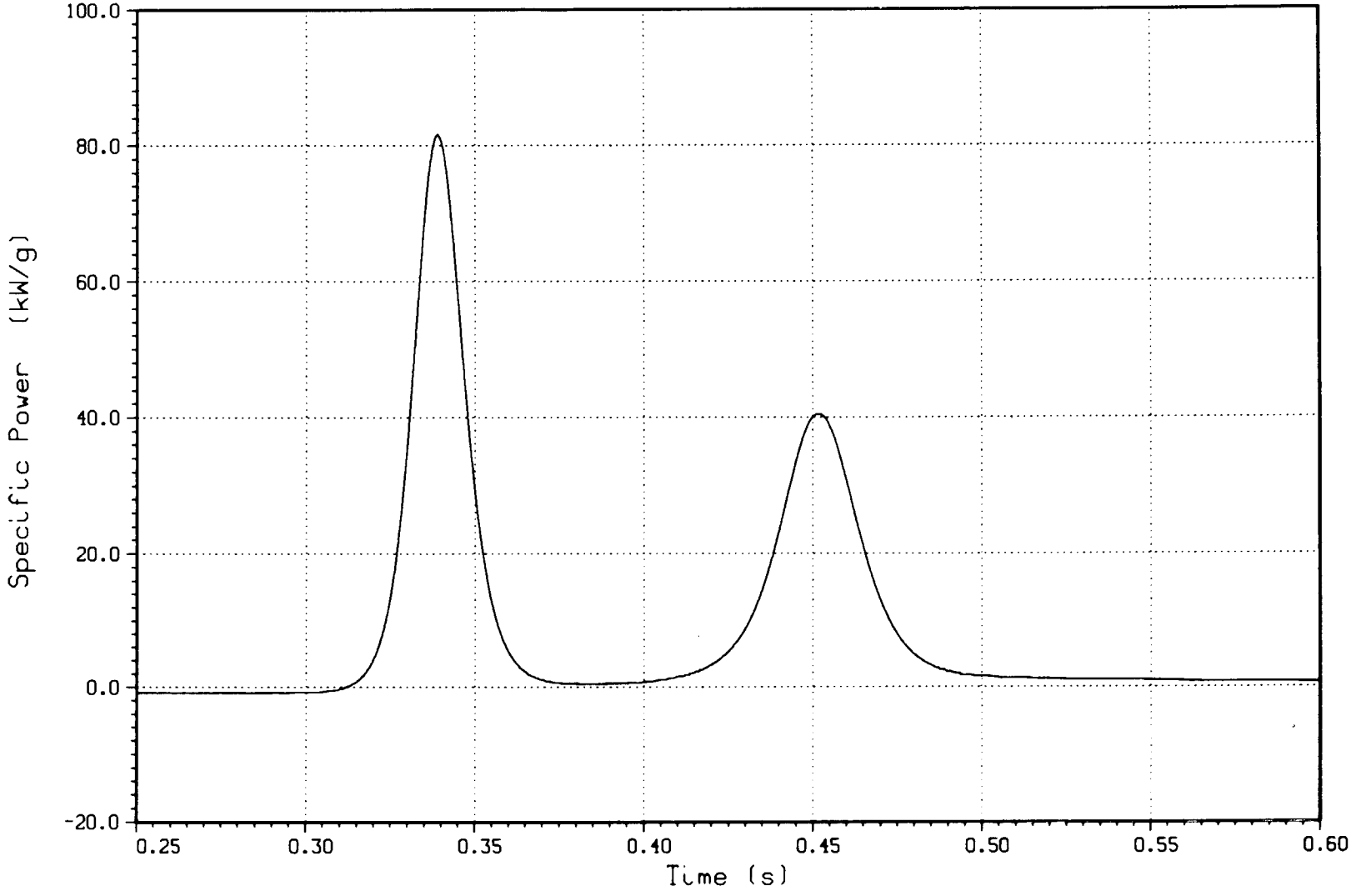

Figure 5.3-3. Specific Power of the Test Fuel in Experiment EEOS-10. The total prompt energy deposition was about 3000 J/g.

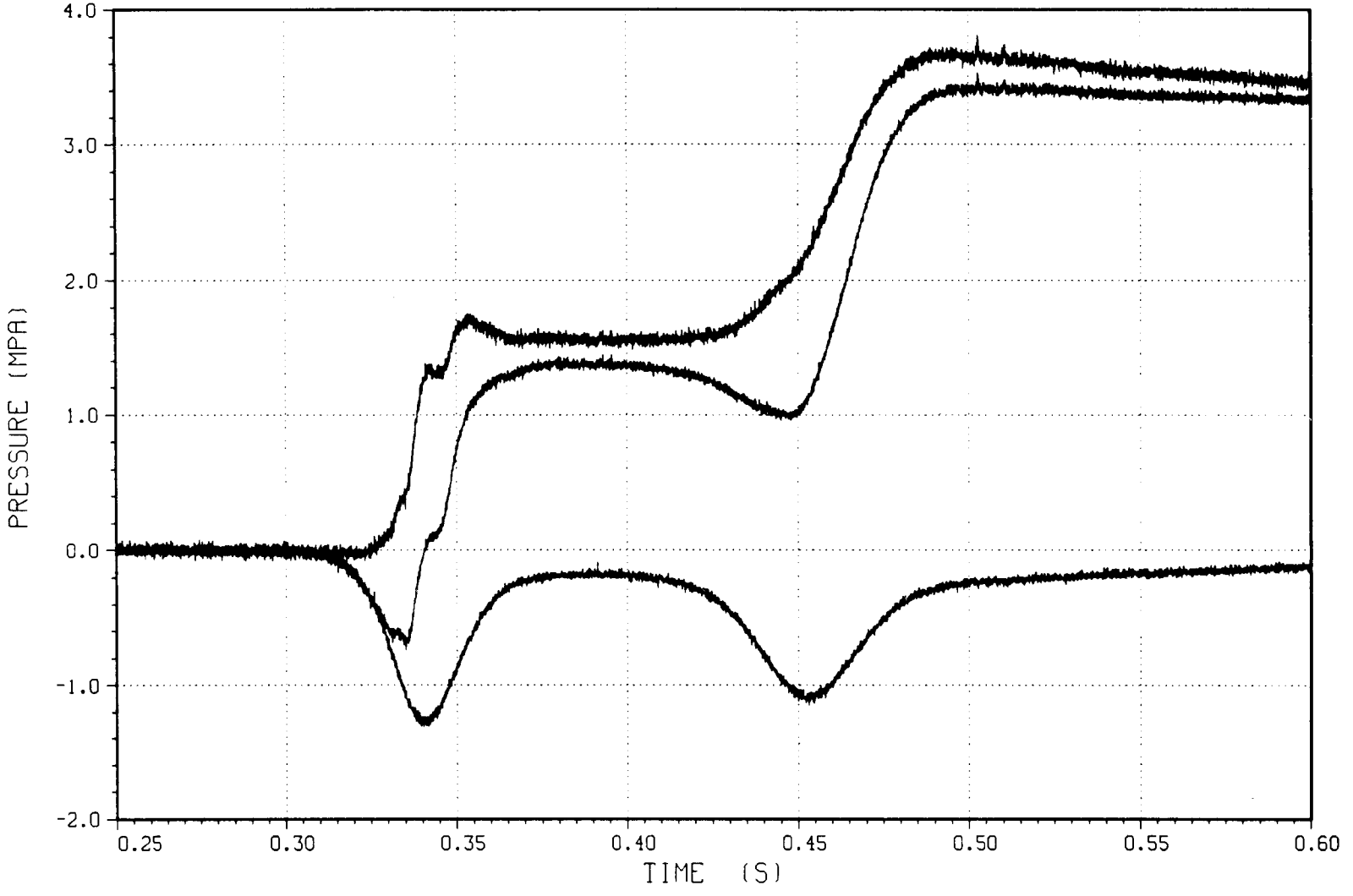

Figure 5.3-4. Measured Pressure Signal Without Fuel (Bottom Curve), With Fuel (Middle Curve), and True Net Pressure (Top Curve) for Experiment EEOS-10

pressure increase of about 1.6 MPa could be due to the argon fill gas (0.5 MPa) and released fission products (1.1 MPa). Most of the fission products appear to have been already released from the solid fuel. Fuel vapor is negligible at these temperatures.

- The second pressure plateau should correspond to a fuel energy of about 3000 J/g or 6800 K, if heat losses are neglected. At this temperature, fresh fuel exhibited a vapor pressure of 15 MPa. However, the additional pressure increase seen here is only about 2.1 MPa, part of which is due to further heating of argon and released fission products. This suggests a very low pressure contribution from the fuel itself. Heat loss calculations will be performed to estimate the actual enthalpy of the fuel sample after the first pulse. The final value may be significantly below the adiabatic value of 3000 J/g because the pressure decrease at 0.353 s has already occurred at a rather high power (about 20 KW/g, Figure 5.3-3).

5.3.4.2 EEOS-11

This test simulated the vaporization of a liquid irradiated mixed oxide into the free volume of a fuel pin, prior to pin failure. These conditions are characterized by a high ambient pressure, resulting from the previous steady-state fission gas release, and little free volume for accommodation of vapor species. The test volume (0.191 cm^3) contained 1.3 g of test fuel, corresponding to a fuel smear density of 60 percent theoretical density, and argon fill gas at a pressure of 0.25 MPa (at 300 K). This amount of fill gas exerted a pressure of about 4.3 MPa after fuel melting (at 3030 K). This fuel-gas system was subjected to a simple ACRR pulse (Figure 5.3-5), which deposited about 2700 J/g into the test fuel. The measured pressure history including the noise contribution is shown in Figure 5.3-6. The noise contribution was not measured for the single pulse shown in Figure 5.3-5, but rather for a double pulse. In view of the possible significant heat losses in EEOS-10, the planned double pulse of EEOS-11 was replaced by a single pulse. The noise signal for this single pulse will be derived theoretically--using a transfer function approach--from the measured double pulse noise signal. A maximum noise signal of about -2.5 MPa at peak power (0.314 s) is expected.

The following observations can be made from Figure 5.3-6:

- Fuel melting is again visible as a distinct change in the pressure rise rate. The pressure plateau starts and ends at the expected times, times at which about

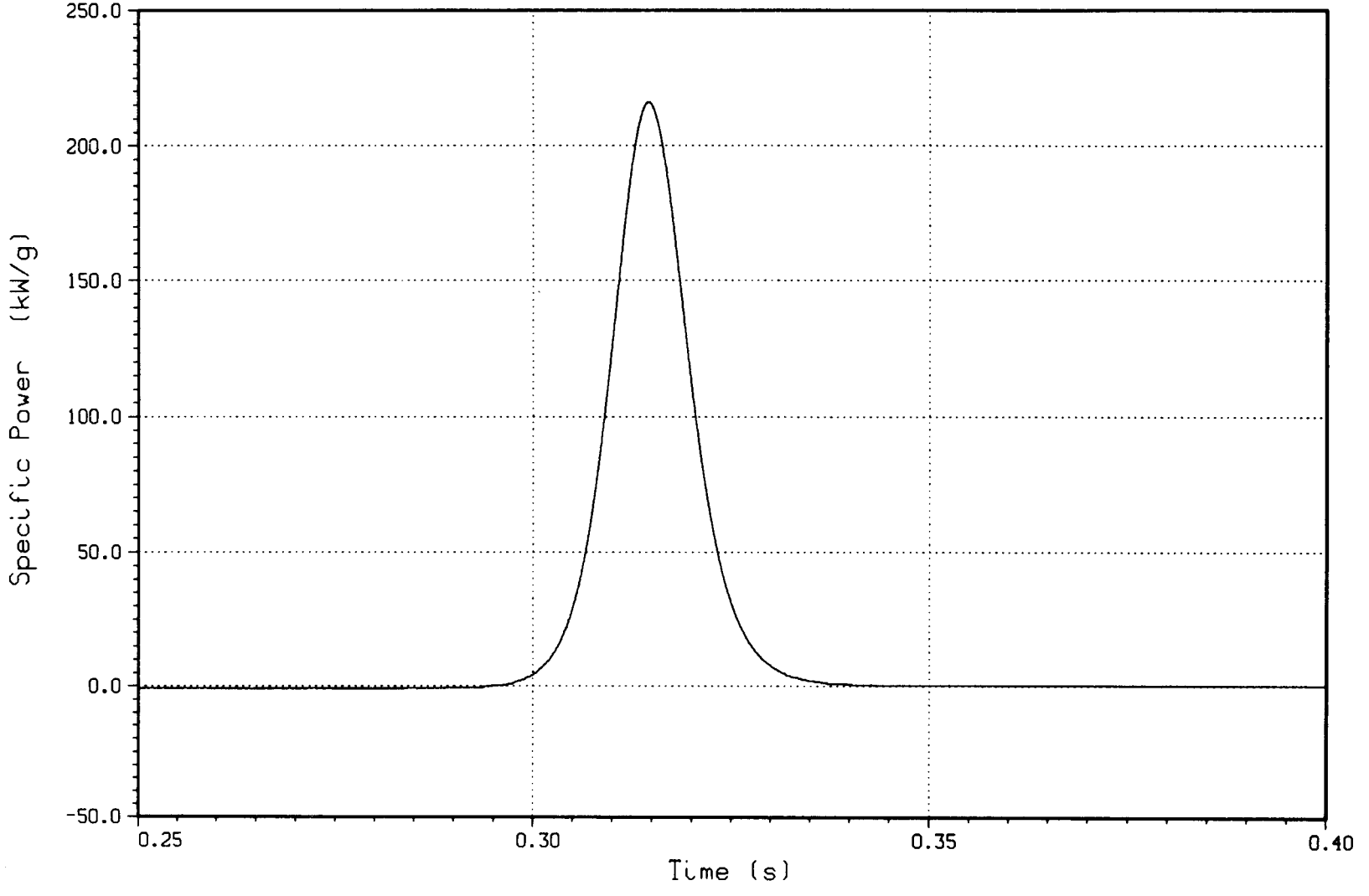

Figure 5.3-5. Specific Power of the Test Fuel in Experiment EEOS-11. The total prompt energy deposition was about 2700 J/g.

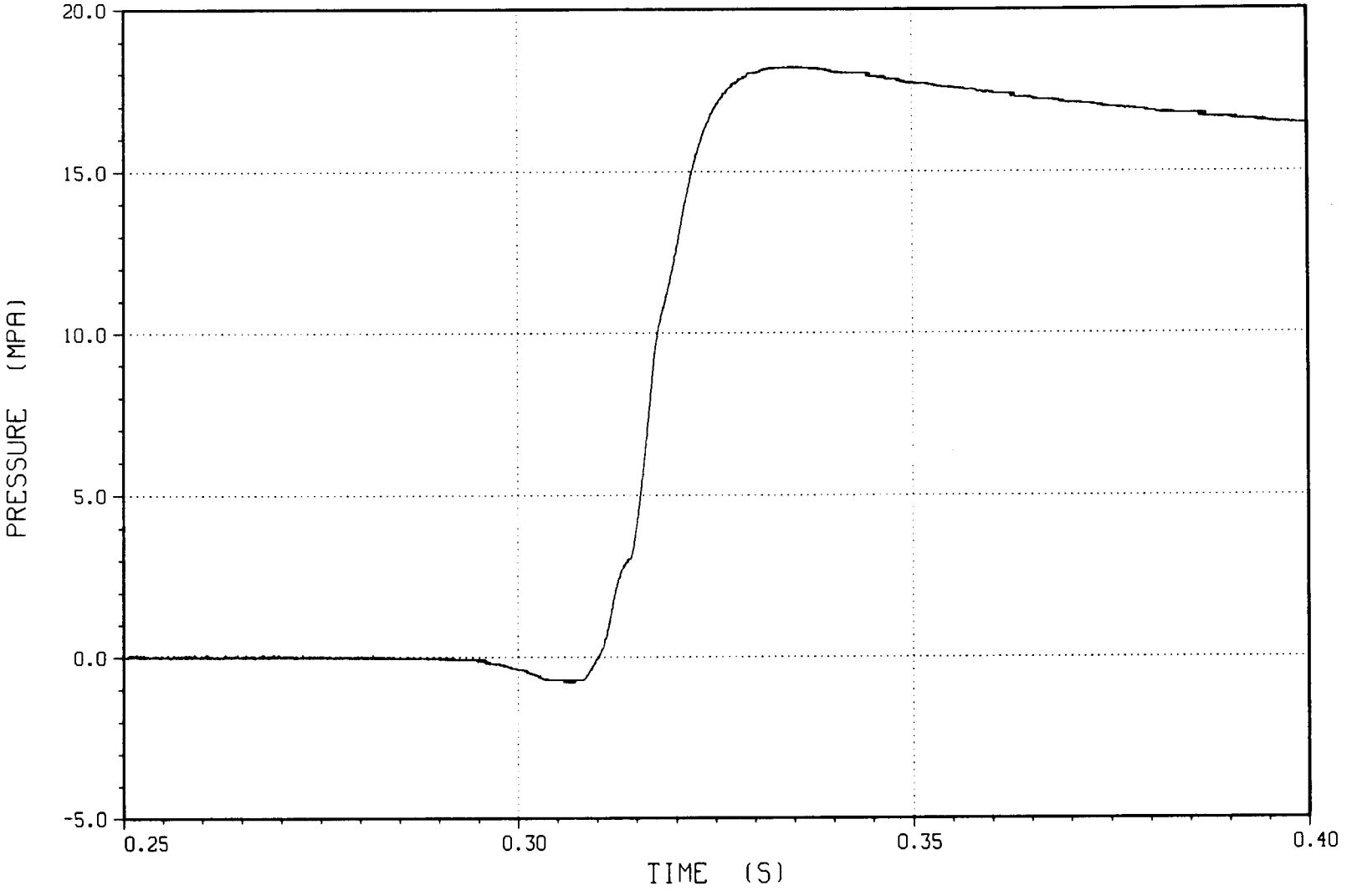

Figure 5.3-6. Measured Pressure Signal (Not Corrected for Background Contribution) of Experiment EEOS-11

1040 J/g (= solidus) and 1310 J/g (= liquidus) are deposited into the test sample.

- The approximate total pressure rise at this time is about 5.5 MPa, assuming a noise contribution of -2.5 MPa. Such a total rise is consistent with the expected fill gas heating of 4.3 MPa plus the fission-product release estimated for EEOS-10 (1.1 MPa).

- At the end of the prompt pulse the fuel reaches about 2700 J/g or 6000 K. At this temperature the argon fill gas and the release fission products could contribute around 12 MPa to the total pressure rise of about 18 MPa. This would leave about 6 MPa for the fuel vapor pressure contribution, which is somewhat less than the fresh fuel vapor at this fuel state (7.5 MPa).

- The pressure rise again follows the heating sequence. The fact that the pressure reaches the maximum value at the end of the prompt pulse (0.334 s) may be taken as an indication of very small heat losses in the pressure determining inner hot sample region. At 0.334 s the neutronic heating amounted to 5 kW/g, which means the heat loss should be on the order of only 5 J/g/ms.

- The slight change in slope at about 10 MPa appears to be a real event because the disassembly of the EEOS-11 pressure cell after the test confirmed that no fuel was lost from the test volume. It may be related to a switch over on the dominant release process from mainly fission product to mainly fuel vaporization.

5.3.4.3 EEOS-12

The test objective of EEOS-12 was to investigate the pressure source from irradiated fuel without the influence of a fill gas. The results provided a direct comparison between irradiated fuel and fresh fuel EEOS measurements. About 0.95 g of irradiated fuel powder were heated in a single ACRR pulse (Figure 5.3-7) to 3200 J/g, which corresponds to about 7300 K, assuming fresh fuel heat capacity values.

The measured pressure data are summarized in Figure 5.3-8. The bottom curve represents the noise signal as measured for an identical ACRR pulse without fuel. The middle curve shows the measured signal with fuel including the noise contribution. The top curve shows the difference, the net pressure signal without noise contribution.

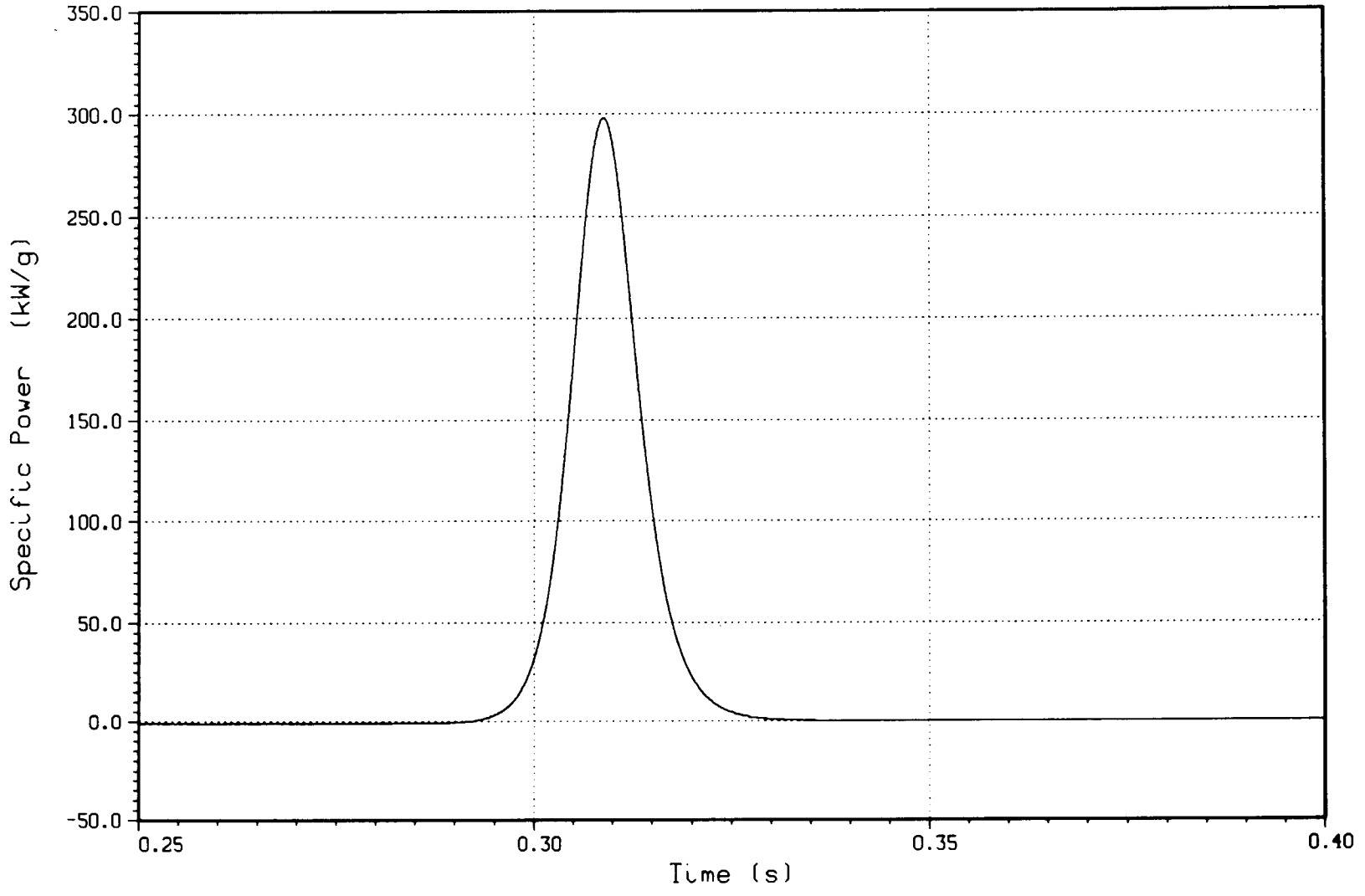

Figure 5.3-7. Specific Power of the Test Fuel in Experiment EEOS-12. The total prompt energy deposition was about 3200 J/g.

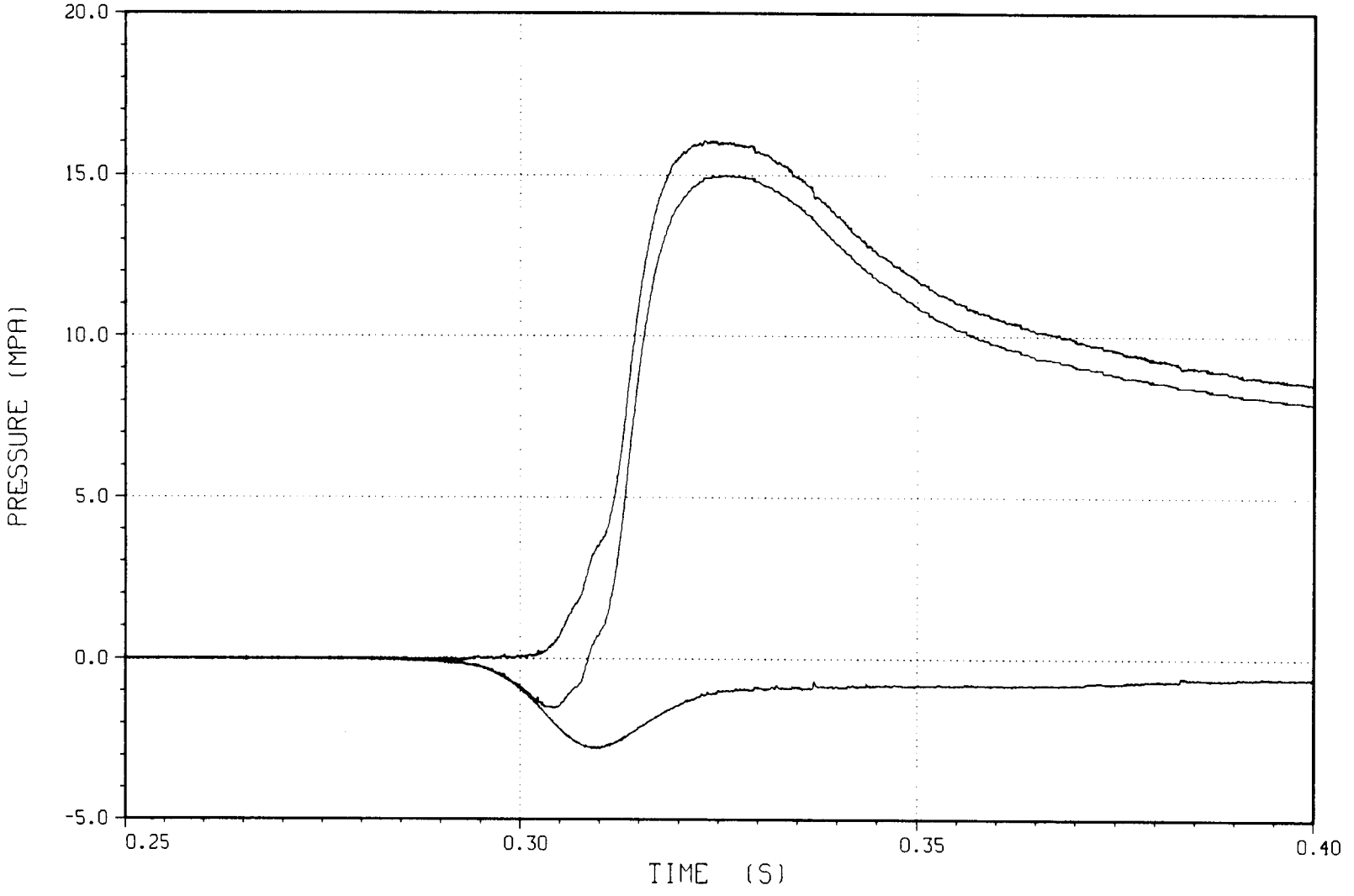

Figure 5.3-8. Measured Pressures in Experiment EEOS-12. The net pressure (top curve) is the difference between the pressure signal with fuel (middle curve) and pressure signal without fuel (bottom).

The following points are apparent from Figure 5.3-8:

- There is again a slight, but still noticeable change in the pressure slope at the expected time of fuel melting (about 0.307 to 0.308 s). Up to this time the pressure rise due to fission-product release from the solid fuel amounts to about 1.6 MPa.

- After melting the pressure continues to rise rapidly to about 4 MPa. At this time (0.31 s), the fuel temperature is around 4200 K.

- Thereafter a transition phenomenon appears to occur as in EEOS-11, which may have to do with fuel vapors becoming the dominant vapor species. Possibly the increasing fuel vapor pressure in the hottest fuel parts ceases fission-product release processes in other fuel regions by forcing them from a two-phase (boiling) configuration into a compressed liquid state.

- The maximum pressure of about 16 MPa occurs again at the end of the prompt ACRR pulse (0.323 s). The fuel should be close to 3200 J/g or 7300 K at this time if the heat losses here are indeed as small as with fresh fuel. The fission-product contribution, which was about 3 MPa at 4200 K, can be expected to be around 6 MPa at this time, leaving roughly 10 MPa for the fuel vapor contribution. This is about one-half of the fresh fuel vapor pressure measured previously with the same technique (22 MPa at 3200 J/g).

- The fast pressure drop seen after the end of the energy deposition indicates that about 8 MPa of the pressure was indeed due to condensible vapor species, e.g., fuel or less volatile fission products. The other two tests with fill gas showed little pressure decay at late times (Figures 5.3-4 and -6). The pressure remaining at the end of the condensation process is probably indicative of the amount of the released incondensible fission gases xenon and krypton.

5.3.5 Summary

These experiments have provided the first Equation-of-State data on irradiated mixed-oxide fuels. The data discussed above appear to support the following preliminary findings:

- Significant amounts of fission products are released from the <u>solid</u> fuel, generating pressures around 1 to 2 MPa.

- Fission-product release continues as the liquid fuel is heated to higher temperatures, which results in the pressure being raised by several MPa.

- Somewhere between 4000 and 5000 K, fuel vapor seems to become dominant over the fission-product species.

- In all cases, however, this fuel vapor contribution appears to be below that of fresh fuel at the same temperature.

- Fill gas may hamper the vaporization of condensible fission products and fuel species.

The total pressure from liquid irradiated fuel should be some combination of the pressures from its individual constituents, e.g., different classes of fission products and fuel species. The measured raw data suggests that the interaction of these constituent pressures may not follow simple models, e.g., ideal solubility pressure addition, ideal insolubility behavior, or boiling point suppression.

A main goal of the final analysis will be to derive a model for the total pressure of irradiated fuel in terms of constituent pressures and ambient gas pressures. Such a model would allow some further extension of the experimental results to other fuels or vaporization conditions.

5.3.6 Planned Experimental Work

An additional fourth test, EEOS-13, is planned to further extend the experimental data base with respect to the fuel vapor pressure contribution. The test will use about 0.9 g of irradiated fuel, no fill gas, and a very high energy deposition to generate a clear fuel vapor signal that is much larger than fission-product pressures. Such an additional measurement of the fuel contribution will allow a better separation of the incondensible gases in EEOS-10, -11, and -12. It will also be a reproducibility check of the apparently low fuel vapor contributions seen before.

6. REFERENCES

1. R. K. Cole et al., CORCON-MOD2: A Computer Program for Analysis of Molten-Core Concrete Interactions, Sandia National Laboratories, Albuquerque, NM, NUREG/CR-3920, SAND84-1246, August 1984.

2. D. A. Powers et al., VANESA: A Mechanistic Model of Radionuclide Release and Aerosol Generation During Core Debris Interactions With Concrete, Sandia National Laboratories, Albuquerque, NM, NUREG/CR-4308, SAND85-1370, 1986.

3. M. Pilch and W. W. Tarbell, Preliminary Calculations on Direct Heating of a Containment Atmosphere by Airborne Core Debris, Sandia National Laboratories, Albuquerque, NM, NUREG/CR-4456, SAND85-2439, July 1986.

4. W. Tarbell et al., Pressurized Melt Ejection Into Scaled Reactor Cavities, Sandia National Laboratories, Albuquerque, NM, NUREG/CR-4512, SAND86-0153, Oct 1986.

5. J. Brockmann, "Range of Possible Dynamic and Collision Shape Factors," Appendix F in Uncertainty in Radionuclide Release Under Specific LWR Accident Conditions, Vol. 2, Sandia National Laboratories, Albuquerque, NM, SAND84-0410, Feb 1985.

6. USNRC, Reactor Safety Study: An Assessment of Accident Risks in US Commercial Nuclear Power Plants, WASH 1400, NUREG 75/04, October 1975.

7. J. F. Muir, R. K. Cole, M. L. Corrandini, and M. A. Ellis, CORCON-MOD1 - An Improved Model for Molten Core-Concrete Interactions, Sandia National Laboratories, Albuquerque, NM, NUREG/CR-2415, SAND80-2415, 1981.

8. J. E. Gronager, A. J. Suo-Anttila, D. R. Bradley, and J. E. Brockmann, TURC1: Large Scale Metallic Melt-Concrete Interaction Experiments and Analysis, Sandia National Laboratories, Albuquerque, NM, NUREG/CR-4420, SAND85-0707, 1985.

9. J. E. Gronager, A. J. Suo-Anttila, and J. E. Brockman, TURC2 and TURC3: Large Scale $UO_2/ZrO_2/Zr$ Melt-Concrete Interaction Experiments and Analysis, Sandia National Laboratories, Albuquerque, NM, NUREG/CR-4521, SAND86-0318, 1986.

10. R. E. Blose, J. E. Gronager, A. J. Suo-Anttila, and J. E. Brockmann, SWISS: Sustained Metallic Melt-Concrete Interactions With an Overlying Water Pool - Experiments and Analysis, Sandia National Laboratories, Albuquerque, NM, SAND85-1546 (to be published).

11. H. Alsmeyer and M. Reimann, "Large Scale Experiments on Core-Concrete Interactions: BETA Experiments and WECHSL Code Verification," Proceedings of the International ANS/ENS Topical Meeting on Thermal Reactor Safety, San Diego, CA, February 1986.

12. M. Reimann, "Verification of Core-Concrete Interaction Codes, KAVERN and WECHSL," Fifth Annual Information Exchange Meeting on Core Meltdown Research, Shelter Island, NY, October 1985.

13. H. Alsmeyer and M. Reimann, "Preliminary BETA V3.3 Results," presented at the BETA Workshop, Kernforschungszentrum Karlsruhe, FRG, June 1986.

14. R. K. Cole, "Analysis of the KfK BETA Experiments with the CORCON Code," Fifth Annual Information Exchange Meeting on Core Meltdown Research, Shelter Island, NY, October 1985.

15. S. S. Kutateladze and I. G. Malenkov, "Fluid and Gasdynamical Aspects of Heat Transfer in the Injection Bubbling and Boiling of Liquids," High Temperature, 14, 703 (1976).

16. S. S. Kutateladze and I. G. Malenkov, "Boiling and Bubbling Heat Transfer Under the Conditions of Free and Forced Convection," Proceedings, Sixth Int. Heat Transfer Conf., Paper FB-2, Toronto, Canada, 1978.

17. O. E. Dwyer, Boiling Liquid Metal Heat Transfer, A.N.S. Publication, 1976.

18. "Heat Conduction Problem," in Nuclear Engineering and Design 53, (North-Holland Publishing Company, 1979).

19. B. W. Marshall, Jr. and M. Berman, "FY86 Draft Program Plan for the Fuel-Coolant Interactions Program," memorandum to J. Telford, USNRC, 1986.

20. M. J. McCarthy and N. A. Molloy, "Review of Stability of Liquid Jets and the Influence of Nozzle Design," The Chemical Engineering Journal, Vol. 7, pp 1-20, 1974.

21. F. V. Bracco, "Modeling of Engine Sprays," Society of Automotive Engineers, 1985 Congress, paper 850394, February-March 1985.

22. M. Epstein and H. K. Fauske, "Steam Film Instability and the Mixing of Core Melt Jets and Water," Fauske & Associates, Inc., January 1985.

23. G. K. Batchelor (editor), Collected Works of G. I. Taylor, (Cambridge Univ. Press, Cambridge, Mass., 1958).

24. MAAP, Modular Accident Analysis Program, User's Manual - Volume II, IDCOR Technical Report 16.2-3, August 1983.

25. Letter, Marty Plys, Fauske & Associates, Inc., to C. Channy Wong, Sandia National Laboratories, dated October 8, 1985.

26. Sequoyah Nuclear Plant - Integrated Containment Analysis, IDCOR Task 23.1 Final Report, December 1984.

27. W. B. Benedick, J. C. Cummings, and P. G. Prassinos, Combustion of Hydrogen:Air Mixtures in the VGES Cylindrical Tank, Sandia National Laboratories, Albuquerque, NM, NUREG/CR-3273, SAND83-1022, May 1984.

28. A. C. Ratzel, Data Analyses for Nevada Test Site (NTS) Premixed Combustion Tests, Sandia National Laboratories, Albuquerque, NM, NUREG/CR-4138, SAND85-0135, May, 1985.

29. J. P. Holman, Thermodynamics, (McGraw-Hill Book Company, New York, NY, 1980) Tables 2-3 and 2-3M, P. 64-65.

30. S. S. Tsai, N. J. Liparulo, J. E. Olhoeft, and D. F. Paddleford, "Flame Temperature Criteria Tests," Proceedings of the Second International Conference on the Impact of Hydrogen Water Reactor Safety, NUREG/CP-0038, EPRI RP1932-35, SAND82-2456, pp. 609-632, October 1982.

31. B. W. Marshall, Hydrogen:Air:Steam Flammability Limits and Combustion Characteristics in the FITS Vessel, Sandia National Laboratories, Albuquerque, NM, SAND84-0383, (to be published).

32. M. G. Zabetakis, Research on the Combustion and Explosion Hazards of Hydrogen-Water Vapor-Air Mixtures, Bureau of Mines, Division of Explosives Technology, Pittsburgh, PA., NTIS, USAEC Report AECU-3327, September 1957.

33. H. Tamm, R. K. Kumar, and W. C. Harrison, "A Review of Recent Experiments at WNRE on Hydrogen Combustion," Proceedings of the Second International Conference on the Impact of Hydrogen Water Reactor Safety, NUREG/CP-0038, EPRI RP1932-35, SAND82-2456, pp. 633-650, October 1982.

34. A. Camp, V. Hehr, and F. Haskin, MARCH-HECTR Analysis of Selected Accidents in an Ice-Condenser Containment, Sandia National Laboratories, Albuquerque, NM, NUREG/CR-3912, SAND83-0501, December 1984.

35. L. B. Thompson et al., Large-Scale Hydrogen Combustion Experiments, Electrical Power Research Institute, Palo Alto, CA, EPRI NP-3878, Research Project 1932-11, (to be published).

36. C. C. Wong, "HECTR Analyses of Large-Scale Premixed Hydrogen Combustion Experiments," Proceedings of the International ANS/ENS Topical Meeing on Thermal Reactor Safety, San Diego, CA, Volume 2, Section XI.4, February 1986.

37. W. B. Benedick, J. C. Cummings, and P. G. Prassinos, "Experimental Results from Combustion of Hydrogen:Air Mixtures in an Intermediate-Scale Tank, Proceedings of the Second International Conference on the Impact of Hydrogen Water Reactor Safety, NUREG/CP-0038, EPRI RP1932-35, SAND82-2456, P. 665-680, October 1982.

38. Sequoyah Nuclear Plant, Units 1 and 2. License Application, Final Safety Analysis Report, Volume 5, Tennessee Valley Authority, DOCKET-50327-77, April, 1981.

39. S. Dingman and A. Camp, Pressure-Temperature Response in an Ice-Condenser Containment for Selected Accidents, Sandia National Laboratories, Albuquerque, NM, SAND85-1824C, October 1985.

40. S. Dingman, A. Camp, C. C. Wong, D. King, and R. Gasser, HECTR Version 1.5 User's Manual, Sandia National Laboratories, Albuquerque, NM, NUREG/CR-4507, SAND86-0101, April 1986.

41. Letter, Marty Plys, Fauske & Associates, Inc., to C. Channy Wong, Sandia National Laboratories, dated July 8, 1985.

42. J. E. Shepherd, Hydrogen-Steam Jet-Flame Facility and Experiments, Sandia National Laboratories, Albuquerque, NM, NUREG/CR-3638, SAND84-0060, February 1985.

43. Reactor Safety Research Semiannual Report, January-June 1985, Volume 33, Sandia National Laboratories, Albuquerque, NM, NUREG/CR-4340 (1 of 2), SAND85-1606 (1 of 2), October 1985.

44. Reactor Safety Research Semiannual Report, July-December 1985, Volume 34, Sandia National Laboratories, Albuquerque, NM, NUREG/CR-4340 (2 of 2), SAND85-1606 (2 of 2), July 1986.

45. R. K. Kumar, H. Tamm, and W. C. Harrison, Intermediate-Scale Combustion Studies of Hydrogen-Air-Steam Mixtures, Electric Power Research Institute, Palo Alto, CA, EPRI NP-2955, June 1984.

46. R. Torok et al., Hydrogen Combustion and Control Studies in Intermediate Scale, Electric Power Research Institute, Palo Alto, CA, EPRI NP-2953, June 1983.

47. M. Berman, "A Critical Review of Recent Large-Scale Experiments on Hydrogen-Air Detonation," Nuclear Science and Engineering: 93, pp. 321-347 (1986).

48. M. P. Sherman, Sandia National Laboratories, personal communication, 1985.

49. W. P Jones, "Models for Turbulent Flows with Variable Density and Combustion," in Prediction Methods for Turbulent Flows, (W. Kollmann, ed., McGraw-Hill, New York 1980).

50. W. Rodi, Turbulence Models and Their Application in Hydraulics, (International Association for Hydraulic Research, Rotterdamseweg 185-P.O. Box 177, 2600 MH Delft, The Netherlands, 1980).

51. B. Magnussen and B. Hjertager, "On Mathematical Modelling of Turbulent Combustion with Special Emphasis on Soot Formation and Combustion," Proceedings, Sixteenth Symposium, pp. 719-729, The Combustion Institute, Pittsburgh 1976.

52. D. B. King and A. C. Peterson, Hydrogen Transport in a Large, Dry Containment for Selected Arrested Sequences, Sandia National Laboratories, Albuquerque, NM, SAND85-1787C, 1985.

53. S. R. Tieszen and D. W. Stamps, "Detonation Cell Width Calculations for Bellefonte," Memorandum to A. C. Peterson, January 29, 1986.

54. D. W. Stamps, "Detonation Cell Width Calculations for Bellefonte," Memorandum to A. C. Peterson, February 12, 1986.

55. M. P. Sherman and M. Berman, The Possibility of Local Detonations During Severe Accidents in the Bellefonte Nuclear Power Plant, Sandia National Laboratories, Albuquerque, NM, SAND86-1180, 1986.

56. J. E. Shepherd, "Chemical Kinetics of Hydrogen-Air-Diluent Detonations," Proceedings of the 10th International Colloquium on Dynamics of Explosions and Reactive Systems, Berkeley, CA, August 4-7, 1985 (to be published).

57. D. W. Stamps and M. Berman, "Detonation Cell Width Calculations for H_2-Air-CO_2 Systems," Private Communications to A. K. Oppenheim, May 12, 1986.

58. L. S. Nelson and K. P. Guay, Reactor Safety Research Quarterly Report, April-June 1984, Vol. 30, Sandia National Laboratories, Albuquerque, NM, NUREG/CR-3816 (2 of 4), SAND84-1072 (2 of 4), December 1984.

59. L. S. Nelson, W. B. Benedick, and P. G. Prassinos, Light Water Reactor Safety Research Program Semiannual Report, April-September 1983, Sandia National Laboratories, Albuquerque, NM, NUREG/CR-3784, SAND84-0689, 1984.

60. Letter, L. M. Mills, TVA, to E. Adensam, USNRC, with enclosure, entitled "Proposed Test Program to Demonstrate Igniter Operability in a Spray Environment," dated January 31, 1983.

61. Letter, L. M. Mills, TVA, to E. Adensam, USNRC with two enclosures, Enclosure 1, entitled "Additional Testing Performed on Tayco Igniters, Sequoyah Nuclear Plant," dated January 31, 1983.

62. K. D. Marx, "Air Currents Driven by Sprays in Reactor Containment Buildings" Sandia National Laboratories, Livermore, CA, NUREG/CR-4102, SAND84-8258, May 1986.

63. Technical Bases for Estimating Fission Product Behavior During LWR Accidents, U.S. Nuclear Regulatory Commission, NUREG-0772, June 1981.

64. V. F. Baston and K. J. Hofstetter, Adherent Activity on TMI-2 Internal Surfaces, ACS Symposium Series 293, The Three Mile Island Accident Diagnosis and Prognosis, 189th ACS National Meeting, Miami Beach, FL, April 28 - May 3, 1985.

65. M. G. Adamson, E. A. Aitken, and T. B. Lindemer, "Chemical Thermodynamics of Cs and Te Fission Product Interactions in Irradiated LMFBR Mixed-Oxide Fuel Pins," J. Nuclear Materials, Vol. 130, pp. 375-392, (1968).

66. R. J. Lipinski, "A Coolability Model for Postaccident Nuclear Reactor Debris," Nuclear Technology, 65, pp. 53-66, (April 1984).

67. G. F. Stevens and R. Trenberth, "Experimental Studies of Boiling Heat Transfer and Dryout in Heat Generating Particulate Beds in Water at 1 Bar," Proceedings of the Fifth Post Accident Heat Removal Information Exchange Meeting, Karlsruhe, Germany, pp. 108-113, July 28-30, 1982.

68. G. Hofmann and L. Barleon, "Reduced Coolability of Particle Beds Caused by Capillary Effects at Horizontal Phase Boundaries," Presented at the International ANS/ENS Topical Meeting on Thermal Reactor Safety, San Diego, California, USA, February 2-6, 1986.

69. Surry Power Station Final Safety Analysis Report (FSAR), Vol. 1, 2, and 3, Virginia Electric and Power Company, December 1969.

70. J. A. Gieseke, P. Cybulskis, R. S. Denning, M. R. Kuhlman, and K. W. Lee, Radionuclide Release Under Specific LWR Accident Conditions--Volumes I-VII (drafts), Battelle Columbus Laboratories, Columbus, OH, BMI-2104, 1983.

71. TRAC-PF1: An Advanced Best-Estimate Computer Program for Pressurized Water Reactor Analysis, Los Alamos National Laboratory, NM, NUREG/CR-3567, LA-9944-MS, 1984.

72. B. E. Boyack, Loss-of-Offsite Power Transient for the Zion-1 PWR, Los Alamos National Laboratory, NM, LA-UR-83-1714, 1983.

73. K. A. Williams, T. J. Heames, and J. E. Kelly, "Mechanistic Calculation of a Station Blackout Accident (TMLB') in a Large PWR Using MELPROG-PWR/MOD0," Internal Memo, Sandia National Laboratories, Albuquerque, NM, November 1985.

74. K. O. Reil, "Effective Equation of State Measurements on Uranium Dioxide," Dissertation, Nucl. Eng. Dept., University of New Mexico, Albuquerque, NM, 1977.

75. W. Breitung and K. O. Reil, "In-Pile Vapor Pressure Measurements on UO_2 and $(U,Pu)O_2$ from 4700 to 8500 K." Conf. on Science and Technology of Fast Reactor Safety, Guerusey, UK, 12-16 May 1986.

DISTRIBUTION:

U.S. Government Printing Office
Receiving Branch
(Attn: NRC Stock)
8610 Cherry Lane
Laurel, MD 20707
(550 Copies for R3, R5, and R7)

U.S. Nuclear Regulatory Commission (17)
Division of Accident Evaluation
Office of Nuclear Regulatory Research
Washington, D.C. 20555
Attn: B. W. Morris
D. Ross
C. N. Kelber
G. Marino
W. S. Farmer
P. Worthington
M. Fleishman
B. Burson
M. Silberberg
J. T. Han
L. Chan
T. Lee
J. Mitchell
R. Meyer
J. Telford
R. W. Wright
C. W. Nilsen

U.S. Nuclear Regulatory Commission (13)
Office of Nuclear Reactor Regulation
Washington, D.C. 20555
Attn: V. Benaroya
W. R. Butler
G. W. Knighton
R. Barrett
R. Palla
K. I. Parczewski
G. Quittschreiber
Z. Rosztoczy
T. M. Su
C. G. Tinkler
D. D. Yue
B. Hardin
F. Eltawila

U.S. Department of Energy
Office of Nuclear Safety Coordination
Washington, D.C. 20545
Attn: R. W. Barber

U.S. Department of Energy (2)
Albuquerque Operations Office
P.O. Box 5400
Albuquerque, NM 87185
Attn: J. R. Roeder, Director
Transportation Safeguards Division
J. A. Morley, Director Energy
Research Technology Division
For: C. B. Quinn
R. N. Holton

Applied Sciences Association, Inc.
P.O. Box 2687
Palos Verdes Pen., CA 90274
Attn: D. Swanson

Argonne National Laboratory (6)
9700 South Cass Avenue
Argonne, IL 60439
Attn: J. Rest
L. Baker
L. Neimark
Dae Cho
R. Anderson
B. Spencer

Astron
2028 Old Middlefield Way
Mountain View, CA 94043

Battelle Columbus Laboratory (3)
505 King Avenue
Columbus, OH 43201
Attn: R. Denning
P. Cybulskis
J. Gieseke

Battelle Pacific Northwest Laboratory (2)
P.O. Box 999
Richland, WA 99352
Attn: M. Freshley
G. R. Bloom

Brookhaven National Laboratory (4)
Upton, NY 11973
Attn: R. A. Bari
T. Pratt
T. Ginsberg
G. Greene

University of California
Chemical and Nuclear Engineering Dept.
Santa Barbara, CA 93106
Attn: T. G. Theofanous

Duke Power Co. (2)
P.O. Box 33189
Charlotte, NC 28242
Attn: F. G. Hudson
A. L. Sudduth

EG&G Idaho (3)
Willow Creek Building, W-3
P.O. Box 1625
Idaho Falls, ID 83415
Attn: Server Sadik
D. Croucher
R. Hobbins

Electric Power Research Institute (6)
3412 Hillview Avenue
Palo Alto, CA 94303
Attn: W. Loewenstein
M. Leverett
G. Thomas
B. R. Sehgal
R. Vogel
J. Haugh

Fauske and Associates
16W070 West 83rd St.
Willow Brook, IL 60521
Attn: R. Henry

Factory Mutual Research Corporation
P.O. Box 688
Norwood, MA 02062
Attn: R. Zalosh

General Electric Corporation
Advanced Reactor Systems Department
P.O. Box 3508
Sunnyvale, CA 94088
Attn: M. I. Temme, Mgr.,
Probabilistic Risk Assessment

General Electric Corporation
175 Curtner Avenue
Mail Code N 1C157
San Jose, CA 95125
Attn: K. W. Holtzclaw

Institute of Nuclear Power Operation
Suite 1500
1100 Circle 75 Parkway
Atlanta, GA 30339
Attn: Henry Piper

International Technology Corporation
Attn: M. H. Fontana Director, Nuclear Programs
575 Oak Ridge Turnpike
Oak Ridge, TN 37830

Los Alamos National Laboratory (4)
P.O. Box 1663
Los Alamos, NM 87545
Attn: M. Stevenson
R. Henninger
J. Carson Mark
J. Travis

Massachusetts Institute of Technology
Nuclear Engineering Dept.
Cambridge, MA 02139
Attn: N. C, Rasmussen

McGill University
315 Querbes
Outremont, Quebec
CANADA H2V 3W1
Attn: J. H. S. Lee

University of Michigan
Department of Aerospace Engineering
Ann Arbor, MI 47109
Attn: Prof. M. Sichel

University of Michigan
Nuclear Engineering Department
Ann Arbor, MI 48104

Mississippi Power Light
P.O. Box 1640
Jackson, MS 39205
Attn: S. H. Hobbs

Northwestern University
Chemical Engineering Department
Evanston, IL 60201
Attn: S. G. Bankoff

Oak Ridge National Laboratory (2)
NRC Programs
P.O. Box X. Bldg. 4500S
Oak Ridge, TN 37831
Attn: A. P. Malinauskas
T. Kress

Power Authority State of NY
10 Columbus Circle
New York, NY 10019

Stratton & Assoc., Inc.
2 Acoma Lane
Los Alamos, NM 87544
Attn: W. Stratton

Dr. Roger Strehlow
505 South Pine Street
Champaign, IL 61820

Texas A&M University
Nuclear Engineering Dept.
College Station, TX 77843

UCLA
Nuclear Energy Laboratory (2)
405 Hilgaard Avenue
Los Angeles, CA 90024
Attn: I. Catton
D. Okrent

Westinghouse Corporation (3)
P.O. Box 355
Pittsburgh, PA 15230
Attn: N. Liparulo
J. Olhoeft
V. Srinivas

Westinghouse Electric Corporation
Bettis Atomic Power Lab
P.O. Box 79
West Mifflin, PA 15122-0079
Attn: Frances Emert

University of Wisconsin
Nuclear Engineering Department
1500 Johnson Drive
Madison, WI 53706
Attn: M. L. Corradini

Atomic Energy Canada Ltd.
Chalk River, Ontario
CANADA K0J 1J0
Attn: P. Fehrenbach

AEC Ltd. (2)
Whiteshell Nuclear Research Establishment
Pinawa, Manitoba
CANADA
Attn: D. Liu
D. Wren

Institute of Nuclear Energy Research
P.O. Box 3
Lungtan
Taiwan 325
REPUBLIC OF CHINA
Attn: Sen-I-Chang

Belgonucleaire S.A.
Rue de Champ de Mars 25
B-1050 Brussels
BELGIUM
Attn: H. Bairiot

Director Research, Science Education
CEC
Rue De La Loi 200
1049 Brussels
BELGIUM
Attn: B. Tolley

Battelle Institute E. V. (3)
Am Roemrhof 35
6000 Frankfurt am Main 90
FEDERAL REPUBLIC OF GERMANY
Attn: Dr. Werner Geiger
Dr. Guenter Langer
Dr. Manfred Schildknecht

Projekt Schneller Brueter (6)
Kernforschungszentrum Karlsruhe GMBH
Postfach 3640
7500 Karlsruhe
FEDERAL REPUBLIC OF GERMANY
Attn: Dr. Kessler
Dr. Heusener
Dr. S. Hagen
Dr. J. P. Hosemann
Dr. W. Schock
A. Fiege

Gesellschaft für Reaktorsicherheit (2)
8046 Garching
Forschungsgelande
FEDERAL REPUBLIC OF GERMANY
Attn: Dr. E. F. Hicken
Dr. H. L. Jahn

Gesellschaft für Reaktorsicherheit (GRS)
Postfach 101650
Glockengasse 2
5000 Koeln 1
FEDERAL REPUBLIC OF GERMANY

Institute für Kernenergetik und
Energiesysteme (2)
University of Stuttgart
Stuttgart
FEDERAL REPUBLIC OF GERMANY
Attn: M. Buerger
A. Unger

Kraftwerk Union
Hammerbacher Strasse 12 14
Postfach 3220
D-8520 Erlangen 2
FEDERAL REPUBLIC OF GERMANY
Attn: Dr. M. Peehs

Departmento Di Costruzioni
Meccaniche E Nucleari
Facolta Di Ingegneria
Via Diotisalvi 2, 56100
ITALY
Attn: M. Carcassi

ENEA Nuclear Energ Alt Disp (2)
Via V. Brancati
00144 Roma
ITALY
Attn: P. L. Ficara
G. Petrangeli

Japan Atomic Energy Research
Institute (3)
Tokai-mura, Naku-gun, Ibaraki-ken, 319-11
JAPAN
Attn: Dr. K. Soda
Dr. T. Fujishiro
Mr. K. Sato

Power Reactor Nuclear Fuel Development
Corporation (PNC)
Fast Breeder Reactor Development Project
(FBR)
9-13, 1-Chome, Akasaka
Minato-Ku, Tokyo
JAPAN
Attn: Dr. Watanabe

Korea Advanced Energy Research Institute
P.O. Box 7
Daeduk Danji
CHUNGNAM, KOREA
Attn: H. R. Jun

Netherlands Energy Research Foundation
P.O. Box 1
1755ZG Petten NH
NETHERLANDS
Attn: K. J. Brinkmann

Juan Bagues
Cowesjo de Seguridad Nuclear
SOR Angela de LaCruz Nº 3
MADRID, SPAIN 28046

Statens Karnkraftinspektion
P.O. Box 27106
S-10252 Stockholm
SWEDEN
Attn: L. Hammar

Studsvik Energiteknik AB
S-611 82 Nykoping
SWEDEN
Attn: K. Johansson

Swedish State Power Board
S-162 Fach 87 Vallingby
SWEDEN
Attn: Wiktor Frid

AERE Harwell (2)
Didcot
Oxfordshire OX11 ORA
UNITED KINGDOM
Attn: J. R. Matthews
Theoretical Physics Division

National Nuclear Corp. Ltd.
Cambridge Road
Whetestone, Leicester, LE83LH
UNITED KINGDOM
Attn: R. May

Simon Engineering Laboratory
University of Manchester
M139PL,
UNITED KINGDOM
Attn: Prof. W. B. Hall

UKAEA, AEA Winfrith (7)
Dorset DT2 8DH
UNITED KINGDOM
Attn: A. Nichols
B. Bowsher
T. Butland
M. Bird
R. Potter
A. Wickett
S. Board

UKAEA, Culham Laboratory (2)
Abingdon
Oxfordshire OX14 3DB
UNITED KINGDOM
Attn: F. Briscoe
D. Fletcher

UKAEA Safety and Reliability Directorate (7)
Wigshaw Lane
Culcheth
Warrington WA3 4NE
Cheshire
UNITED KINGDOM
Attn: J. H. Gittus (2)
M. R. Hayns (2)
A. Taig
B. Cowking
D. Hicks

SANDIA DISTRIBUTION:

1131 W. B. Benedick
1510 J. W. Nunziato
Attn: 1512 J. C. Cummings
1530 L. W. Davison
Attn: 1534 J. R. Asay
1541 H. C. Hardee
3141 S. A. Landenberger (5)
3151 W. L. Garner
6400 D. J. McCloskey
6410 N. O. Ortiz
6411 A. Benjamin
6412 A. L. Camp
6415 F. E. Haskin
6420 J. V. Walker
6421 P. S. Pickard
6422 D. A. Powers
6422 M. D. Allen
6422 J. E. Brockmann
6422 E. R. Copus
6422 R. M. Elrick
6422 W. W. Tarbell
6423 K. O. Reil
6423 R. O. Gauntt
6425 W. J. Camp
6425 D. R. Bradley
6425 J. E. Kelly
6425 M. Pilch
6425 A. W. Reed
6425 M. F. Young
6427 M. Berman
6427 D. Beck
6427 B. W. Marshall, Jr.
6427 L. S. Nelson
6427 M. P. Sherman
6427 S. Slezak
6427 D. Stamps
6427 S. R. Tieszen
6427 C. C. Wong
6440 D. A. Dahlgren
6447 D. L. Berry
6449 K. D. Bergeron
6450 T. R. Schmidt (1)
Attn: 6451 T. F. Luera
6454 G. L. Cano
7530 T. B. Lane (1)
Attn: 7537 N. R. Keltner
7537 R. U. Acton
7537 T. Y. Chu
7550 T. S. Edrington (1)
Attn: 7551 O. J. Burchett
7552 J. H. Gieske
8024 P. W. Dean
8363 B. R. Sanders
Attn: 8363 K. D. Marx

NRC FORM 335 (2-84) NRCM 1102, 3201, 3202

U.S. NUCLEAR REGULATORY COMMISSION

BIBLIOGRAPHIC DATA SHEET

SEE INSTRUCTIONS ON THE REVERSE

1 REPORT NUMBER (Assigned by TIDC and Vol. No. if any)

NUREG/CR-4805 (1 of 2)
SAND86-2752 (1 of 2)

2 TITLE AND SUBTITLE

REACTOR SAFETY RESEARCH SEMIANNUAL REPORT
January-June 1986

3 LEAVE BLANK

4 DATE REPORT COMPLETED

MONTH	YEAR
December	1986

5 AUTHOR(S)

Reactor Safety Research Department
Sandia National Laboratories

6 DATE REPORT ISSUED

MONTH	YEAR
May	1987

7 PERFORMING ORGANIZATION NAME AND MAILING ADDRESS (Include Zip Code)

Sandia National Laboratories
Albuquerque, NM 87185

8 PROJECT TASK WORK UNIT NUMBER

9 FIN OR GRANT NUMBER

A1016 etc.

10 SPONSORING ORGANIZATION NAME AND MAILING ADDRESS (Include Zip Code)

Office of Nuclear Regulatory Research
U.S. Nuclear Regulatory Commission
Washington, DC 20555

11a TYPE OF REPORT

progress-technical

b PERIOD COVERED (Inclusive dates)

January-June 1986

12 SUPPLEMENTARY NOTES

13 ABSTRACT (200 words or less)

Sandia National Laboratories is conducting, under USNRC sponsorship, phenomenological research related to the safety of commercial nuclear power reactors. The research includes experiments to simulate the phenomenology of the accident conditions and the development of analytical models, verified by experiment, which can be use to predict reactor and safety systems performance and behavior under abnormal conditions. The objective of this work is to provide NRC requisite data bases and analytical methods to (1) identify and define safety issues, (2) understand the progression of risk-significant accident sequences, and (3) conduct safety assessments. The collective NRC-sponsored effort at Sandia National Laboratories is directed at enhancing the technology base supporting licensing decisions.

14 DOCUMENT ANALYSIS - a KEYWORDS/DESCRIPTORS

b IDENTIFIERS/OPEN ENDED TERMS

15 AVAILABILITY STATEMENT

GPO Sales
NTIS

16 SECURITY CLASSIFICATION

(This page)
Unclassified

(This report)
Unclassified

17 NUMBER OF PAGES

18 PRICE

☆ U.S. GOVERNMENT PRINTING OFFICE: 1987—773-049/41048